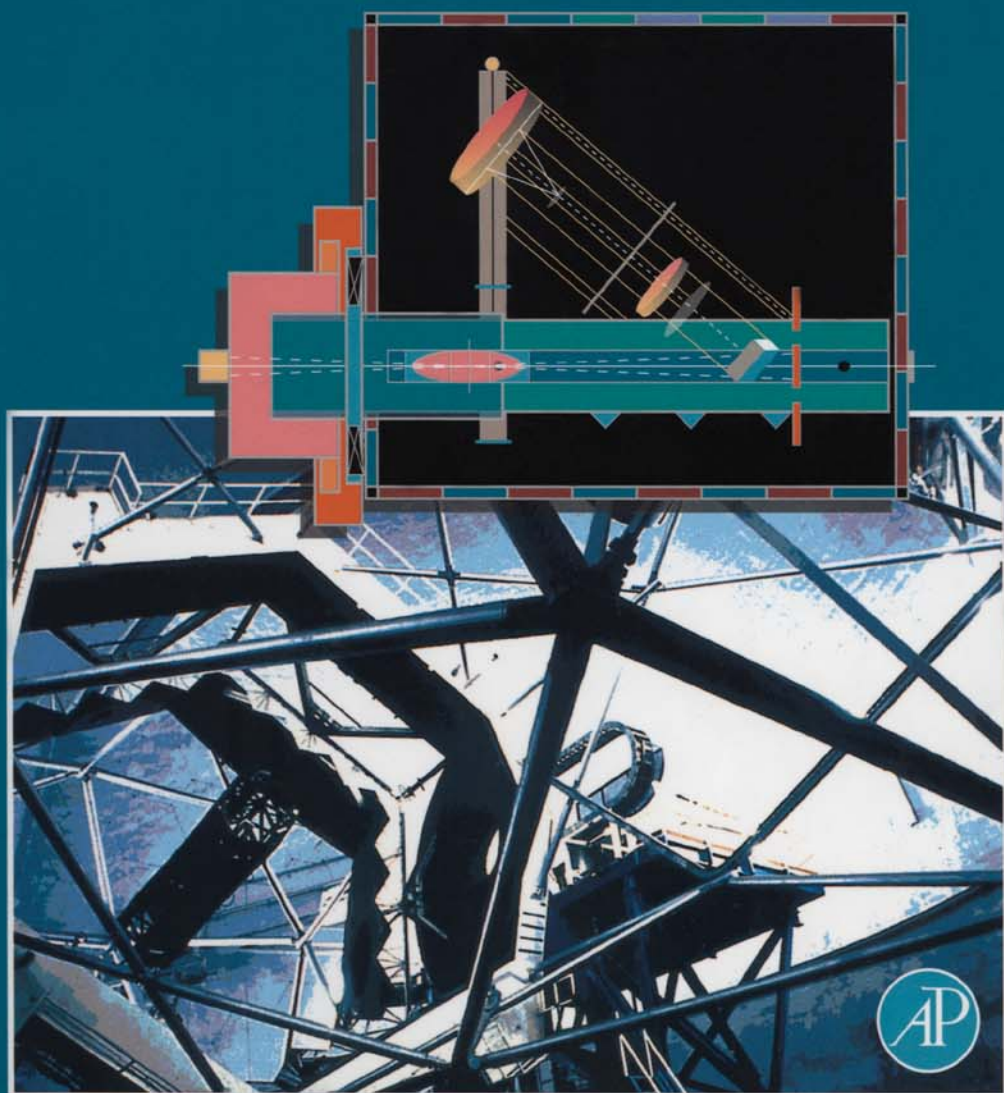


SECOND EDITION

# ASTRONOMICAL OPTICS

DANIEL J. SCHROEDER



**Astronomical Optics**  
**Second Edition**

This Page Intentionally Left Blank

# Astronomical Optics

Second Edition

DANIEL J. SCHROEDER

Professor of Physics and Astronomy, Emeritus  
Department of Physics and Astronomy  
Beloit College,  
Beloit, Wisconsin



**ACADEMIC PRESS**

A Harcourt Science and Technology Company

San Diego San Francisco New York Boston  
London Sydney Tokyo

This book is printed on acid-free paper. 

Copyright © 2000 by Academic Press

All rights reserved.

No part of this publication may be reproduced or transmitted in any form or by any means, electronic or mechanical, including photocopy, recording, or any information storage and retrieval system, without permission in writing from the publisher.

Requests for permission to make copies of any part of the work should be mailed to: Permissions Department, Harcourt Brace & Company, 6277 Sea Harbor Drive, Orlando, Florida, 32887-6777.

Cover picture (photo): A view of the 10-m Keck I telescope on Mauna Kea, Hawaii. A portion of the primary mirror with its 36 hexagonal segments is seen at the lower left, and the secondary mirror housing is partly visible at the top. One of the Nasmyth platforms is seen in the right background. (The photograph was taken by Eric Hill and is a courtesy of the W. M. Keck Observatory with permission from Fred Chaffee, Director.)

Cover picture (schematic): Schematic diagrams from the top and side of the High Resolution Echelle Spectrometer (HIRES) in operation on a Nasmyth platform of the Keck I telescope. A portion of the telescope primary is mirror is seen at the left. (Diagrams are courtesy of Steve Vogt and Jack Osborne, University of California Observatories/Lick Observatory.)

## ACADEMIC PRESS

*A Harcourt Science and Technology Company*

525 B Street Suite 1900, San Diego, California 92101-4495, USA

<http://www.academicpress.com>

## ACADEMIC PRESS

24-28 Oval Road, London NW1 7DX, UK

<http://www.hbuk.co.uk/ap/>

Library of Congress Cataloging Number: 99-65098

ISBN: 0-12-629810-6

PRINTED IN THE UNITED STATES OF AMERICA

99 00 01 02 03 MB 9 8 7 6 5 4 3 2 1

To my wife, LaVern

This Page Intentionally Left Blank

# Contents

<i>Preface</i>	xiii
<b>Chapter 1</b> Introduction	
1.1. A Bit of History	1
1.2. Approach to Subject	4
1.3. Outline of Book	4
<b>Chapter 2</b> Preliminaries: Definitions and Paraxial Optics	7
2.1. Sign Conventions	8
2.2. Paraxial Equation for Refraction	9
2.3. Paraxial Equation for Reflection	12
2.4. Two-Surface Refracting Elements	14
2.5. Two-Mirror Telescopes	17
2.6. Stops and Pupils	22
2.7. Concluding Remarks	25
Bibliography	26
<b>Chapter 3</b> Fermat's Principle: An Introduction	27
3.1. Fermat's Principle in General	28
3.2. Fermat's Principle and Refracting Surfaces	31
3.3. Wave Interpretation of Fermat's Principle	36
3.4. Fermat's Principle and Reflecting Surfaces	37
3.5. Conic Sections	41
3.6. Fermat's Principle and the Atmosphere	42

3.7. Concluding Remarks	45
References	47
Bibliography	47
<b>Chapter 4 Introduction to Aberrations</b>	<b>48</b>
4.1. Reflecting Conics and Focal Length	49
4.2. Spherical Aberration	50
4.3. Reflecting Conics and Finite Object Distance	57
4.4. Off-Axis Aberrations	59
4.5. Aberration Compensation	61
References	69
Bibliography	69
<b>Chapter 5 Fermat's Principle and Aberrations</b>	<b>70</b>
5.1. Application to Surface of Revolution	70
5.2. Evaluation of Aberration Coefficients	75
5.3. Ray and Wavefront Aberrations	78
5.4. Summary of Aberration Results, Stop at Surface	84
5.5. Aberrations for Displaced Stop	88
5.6. Aberrations for Multisurface Systems	93
5.7. Curvature of Field	97
5.8. Aberrations for Decentered Pupil	103
5.9. Concluding Remarks	109
Appendix A: Comparison with Seidel Theory	110
References	111
Bibliography	111
<b>Chapter 6 Reflecting Telescopes</b>	<b>112</b>
6.1. Paraboloid	113
6.2. Two-Mirror Telescopes	115
6.3. Alignment Errors in Two-Mirror Telescopes	132
6.4. Three-Mirror Telescopes	144
6.5. Four-Mirror Telescopes	154
6.6. Concluding Remarks	161
References	162
Bibliography	162
<b>Chapter 7 Schmidt Telescopes and Cameras</b>	<b>164</b>
7.1. General Schmidt Configuration	165
7.2. Characteristics of Aspheric Plate	167
7.3. Schmidt Telescope Example	174
7.4. Achromatic Schmidt Telescope	177

7.5. Solid- and Semisolid-Schmidt Cameras	181
References	184
Bibliography	184
<b>Chapter 8</b> Catadioptric Telescopes and Cameras	185
8.1. Schmidt-Cassegrain Telescopes	185
8.2. Cameras with Meniscus Correctors	197
8.3. All-Reflecting Wide-Field Systems	204
References	205
<b>Chapter 9</b> Auxiliary Optics for Telescopes	206
9.1. Field Lenses, Flatteners	207
9.2. Prime Focus Correctors	210
9.3. Cassegrain Focus Correctors	216
9.4. Cassegrain Focal Reducers	220
9.5. Atmospheric Dispersion Correctors	225
9.6. Fiber Optics	237
References	239
Bibliography	239
<b>Chapter 10</b> Diffraction Theory and Aberrations	240
10.1. Huygens-Fresnel Principle	241
10.2. Perfect Image: Circular Aperture	246
10.3. The Near Perfect Image	257
10.4. Comparison: Geometric Aberrations and the Diffraction Limit	270
10.5. Diffraction Integrals and Fourier Theory	271
References	275
Bibliography	275
<b>Chapter 11</b> Transfer Functions; Hubble Space Telescope	277
11.1. Transfer Functions and Image Characteristics	277
11.2. Hubble Space Telescope, Prelaunch Expectations	291
11.3. Hubble Space Telescope, Postlaunch Reality	298
11.4. Concluding Remarks	302
References	303
Bibliography	303
<b>Chapter 12</b> Spectrometry: Definitions and Basic Principles	304
12.1. Introduction and Definitions	305
12.2. Slit Spectrometers	308

12.3. Fiber-Fed Spectrometers	317
12.4. Slitless Spectrometers	318
12.5. Spectrometers in Diffraction Limit	318
References	320
Bibliography	320
<b>Chapter 13</b> Dispersing Elements and Systems	321
13.1. Dispersing Prism	321
13.2. Diffraction Grating; Basic Relations	323
13.3. Echelles	327
13.4. Grating Efficiency	331
13.5. Fabry-Perot Interferometer	342
13.6. Fourier Transform Spectrometer	347
13.7. Concluding Remarks	350
References	350
Bibliography	350
<b>Chapter 14</b> Grating Aberrations; Concave Grating Spectrometers	352
14.1. Application of Fermat's Principle to Grating Surface	353
14.2. Grating Aberrations	357
14.3. Concave Grating Mountings	362
References	367
Bibliography	367
<b>Chapter 15</b> Plane Grating Spectrometers	368
15.1. All-Reflecting Spectrometers	369
15.2. Pixel Matching	377
15.3. Fast Spectrometers	378
15.4. Fiber-Fed Spectrometers	383
15.5. Echelle Spectrometers	384
15.6. Nonobjective Slitless Spectrometers	396
15.7. Concluding Remarks	407
References	407
Bibliography	407
<b>Chapter 16</b> Adaptive Optics: An Introduction	409
16.1. Effects of Atmospheric Turbulence	410
16.2. Correction of Wavefront Distortion	415
16.3. Adaptive Optics: Systems and Components	421
16.4. Concluding Remarks	423
References	424
Bibliography	424

<b>Chapter 17</b>	<b>Detectors, Signal-to-Noise, and Detection Limits</b>	<b>425</b>
17.1.	Detector Characteristics	426
17.2.	Signal-to-Noise Ratio	433
17.3.	Detection Limits and Signal-to-Noise Ratio	435
17.4.	Detection Limits: Stellar Photometry	438
17.5.	Detection Limits: Spectroscopy	440
	References	443
	Bibliography	443
<b>Chapter 18</b>	<b>Large Mirrors and Telescope Arrays</b>	<b>444</b>
18.1.	Large Mirrors	444
18.2.	Telescope Arrays; Interferometers	451
	References	457
	Bibliography	457
	Table of Symbols	459
<b>Index</b>		<b>467</b>

This Page Intentionally Left Blank

## Preface

When I began thinking about and working on this second edition, it became clear early on that substantive additions to the first edition were in order. Although the optical principles upon which the earlier text was based have not changed, the ingenuity and resourcefulness of astronomers in the intervening years have led to many exciting new instrumental developments. These developments, in turn, have meant a greatly increased efficiency in gathering data from celestial sources. As one example to illustrate this change, note the use of optical fibers to feed light from a hundred or more galaxies at a time into a spectrometer, rather than the traditional one galaxy at a time approach.

Other dramatic developments within the past decade include implementing or planning for techniques of adaptive optics to compensate for the atmosphere, and the almost total adoption of solid-state detectors arrays. But the biggest change of all is only starting to become reality, that of a significant number of ground-based telescopes of near diffraction-limited quality and apertures greater than six meters in diameter. This greatly increased light gathering power will undoubtedly revolutionize observational astronomy.

In view of these developments, and in response to the many comments I received on the first edition, my thrust in this rework has been two-fold. First, many portions of the text were rewritten or amended to make the explanations more clear and to correct errors. In some cases this meant adding additional material, such as spot diagrams or wavefront maps; in other cases words and figures were removed. Second, new sections were added to many chapters and one new chapter, on adaptive optics, was added. The overall format of the first

edition has not been changed, and I hope the reader will find the changes in this edition to be positive ones.

As in the first edition, my intent is to emphasize basic principles of optics and how these principles are used in the designs of specific types of instruments. The treatment is limited to telescopes and cameras that use near-normal incidence optics and spectrometers with dispersive elements or interferometers. Numerous examples of system characteristics are given to illustrate the optical performance that can be expected. An outline of the topics covered is given in Chapter 1.

The level of presentation and approach are appropriate for a graduate student in astronomy approaching the subject of astronomical optics for the first time. Although the basic principles of optics are discussed, it is assumed that the reader has the equivalent of an intermediate-level optics course at the undergraduate level. This book should also serve as a useful reference for active researchers.

Because the presentation is not simply a compilation of types of telescopes and spectrometers, the reader should consult the original sources for details on specific instruments or telescopes. I have given an expanded bibliography and list of references, including conference proceedings, to facilitate further exploration. I have also added a table of symbols and their meanings as an aid to the reader.

A number of persons contributed directly or indirectly to the writing of the first edition and this revision. First and foremost I thank Arthur Code, who gave me the opportunity of participating in the development of the Wisconsin Experiment Package of the first Orbiting Astronomical Observatory. Since that time I have been privileged to draw upon his wealth of knowledge and to teach jointly with him on one occasion a course on astronomical optics. For his contributions I am especially grateful. My thanks also to Arthur Hoag, Robert Bless, and Donald Osterbrock for their help and support over the years, and to Robert O'Dell for his encouragement to take part in NASA's Hubble Space Telescope Project.

Although many persons contributed to this rework, I mention only a few by name. Robert Lucke gave several pedagogical suggestions, especially on my discussion of distortion, that have been incorporated into the text. Derek Salmon asked some questions about misaligned telescopes and that section has been greatly expanded in this edition. The excellent book *Reflecting Telescope Optics I* by Raymond Wilson has been an important resource during the revision process. For their input, and the numerous other comments I have received, I am grateful.

Finally, and most importantly, I acknowledge the support, encouragement, and patience of my wife LaVern while I worked on both editions of this book.

Daniel J. Schroeder

Errata: *ASTRONOMICAL OPTICS*, 2nd Edition,

by Daniel J. Schroeder, ISBN 0-12-629810-6, © 2000 by Academic Press

Page	Location	Correction
43	Eq. (3.6.1)	Replace $K$ with $\mathcal{K}$
77	Fig. 5.3 caption	... $s = s' = R = -1000$ mm ...
122	Table 6.9	Replace $(3m^2 - 2)$ in ADI with $\beta(3m^2 - 2)$
129	Line 18 of text	Delete entire line
132	Table 6.13	Replace $(1 - k)$ in $B_{1s}$ with $(1 - k)^2$
154	Line 8 of text	Replace parabolic with hyperbolic
174	Table 7.2	Spherical mirror, $B_5 = \frac{3n_0}{8R^5}$
195	First line of text	Replace ( with $\rho$
179	Table 7.6	Replace $n - 1$ with $\langle n \rangle - 1$
250	Table 10.1	Replace $\nu$ with $\mathcal{V}$ in last line
282	Two lines below Eq. (11.1.13)	Replace $\nu$ with $\mathcal{V}$
435	Four lines above Eq. (17.3.1)	Reference is Code (1973)
437	Eq. (17.3.6)	Replace $\mathcal{K}$ with $\mathcal{K}^2$
446	Lines 3, 9	Replace paraboloid with hyperboloid

This Page Intentionally Left Blank

The increasing rate of growth in astronomical knowledge during the past few decades is a direct consequence of the increase in the number and size of telescopes and the efficiency with which they are used. Most celestial sources are intrinsically faint and observations with small refracting telescopes and insensitive photographic plates that required hours of observing time are now done in minutes with large reflecting telescopes and efficient solid-state detectors. The increased efficiency with which photons are collected and recorded by modern instruments has indeed revolutionized the field of observational astronomy.

### **1.1. A BIT OF HISTORY**

Early in the 1900s the desire for larger light gathering power led to the design and construction of the 100-in Hooker telescope located on Mount Wilson in California. This reflecting telescope and its smaller predecessors were built following the recognition that refracting telescopes, such as the 36-in one at Lick Observatory in California and the 40-in one at Yerkes Observatory, in Wisconsin, had reached a practical limit in size. With the 100-in telescope, it was possible to start systematic observations of nearby galaxies and start to attack the problem of the structure of the universe.

Although the 100-in telescope was a giant step forward for observational astronomy, it was recognized by Hale that still larger telescopes were necessary for observations of remote galaxies. Due largely to his efforts, work began on the

design and construction of a 200-in (5-m) telescope in the late 1920s. The Hale telescope was put into operation in the late 1940s and remained the world's largest until a 6-m telescope was built in Russia in the mid-1970s.

The need for more large telescopes became acute in the 1960s as the boundaries of observational astronomy were pushed outward. Plans made during this decade and the following one resulted in the construction of a number of optical telescopes in the 4-m class during the 1970s and 1980s in both hemispheres. These telescopes, equipped with efficient detectors, fueled an explosive growth in observational astronomy.

Large reflectors are well-suited for observations of small parts of the sky, typically a fraction of a degree in diameter, but they are not suitable for surveys of the entire sky. A type of telescope suited for survey work was first devised by Schmidt in the early 1930s. The first large Schmidt telescope was a 1.2-m instrument covering a field about  $6^\circ$  across, and put into operation on Palomar Mountain in the early 1950s. Several telescopes of this type and size have since been built in both hemispheres. The principle of the Schmidt telescope has also been adapted to cameras used in many spectrometers.

While construction of telescopes was underway during the 1970s and 1980s, astronomers were already planning for the next generation of large reflectors. In the quest for still greater light-gathering power, attention turned to the design of arrays of telescopes and segmented mirrors, and to new techniques for casting and figuring single mirrors with diameters in the 8-m range. The fruits of these labors became apparent in the late 1990s with the coming online of a significant number of telescopes in the 8- to 10-m class.

The array concept was first implemented with the completion of the Multiple-Mirror Telescope (MMT) on Mount Hopkins, Arizona, a telescope with six 1.8-m telescopes mounted in a common frame and an aperture equivalent to that of a single 4.5-m telescope. Beams of the separate telescopes were directed to a common focal plane and either combined in a single image or placed side-by-side on the slit of a spectrometer. Although the MMT concept proved workable, advances in mirror technology prompted the replacement of the separate mirrors with a single 6.5-m mirror in the same telescope structure and building.

The segmented mirror approach was the choice for the Keck Ten-Meter Telescope (TMT), with 36 hexagonal segments the equivalent of a single filled aperture. This approach requires active control of the positions of the segments to maintain mirror shape and image quality. Even before the first TMT had been pointed to its first star, its twin was under construction on Mauna Kea, Hawaii, and together these two telescopes are obtaining dramatic observational results. Another segmented mirror telescope is the Hobby-Eberly Telescope designed primarily for spectroscopy.

Although it seemed in the 1980s that multiple and segmented mirrors were the wave of the future, new techniques for making large, “fast” primary mirrors and controlling their optical figure in a telescope led to the design and construction of several 8-m telescopes. Among these are the Very Large Telescopes (VLT) of the European Southern Observatory, the Gemini telescopes, Subaru, and Large Binocular Telescope (LBT). Used singly or as components of an interferometric array (for the VLT and LBT), observations are possible that could only be dreamed of in the 1970s.

Instrumentation used on large telescopes has also shown dramatic changes since the time of the earliest reflectors. Noting first the development in spectrometers, small prism instruments were replaced by larger grating instruments at both Cassegrain and coude focus positions to meet the demands for higher spectral resolution. In recent years many of these high resolution coude instruments have, in turn, been replaced by echelle spectrometers at the Cassegrain focus. On the largest telescopes, such as the TMT and VLT, most large instrumentation is at the Nasmyth focus position on a platform that rotates with the telescope. Nearly all spectrographic instruments and imaging cameras now use solid-state electronic detectors of high quantum efficiency that, coupled with these telescopes, make possible observations of still fainter celestial objects.

Although developments of ground-based optical telescopes and instruments during the last three decades of the 20th century have been dramatic, the same can also be said of Earth-orbiting telescopes in space. Since the first Orbiting Astronomical Observatory in the late 1960s, with its telescopes of 0.4-m and smaller, the size and complexity of orbiting telescopes have increased markedly. The 2.4-m Hubble Space Telescope (HST), once its problem of spherical aberration was fixed, has made observations not possible with ground-based telescopes. Although its light gathering power is significantly smaller than that of many ground-based telescopes, its unique capability of observing sources in spectral regions absorbed by our atmosphere and of imaging to the diffraction limit are leading the revolution in astronomy.

Because of the high cost of a telescope in space, there has been significant effort to improve the quality of images of ground-based telescopes. These efforts include controlling the thermal conditions within telescope enclosures and incorporating active and adaptive optics systems into telescopes. With these techniques it becomes possible to obtain images of near-diffraction-limited quality, at least over small fields and for brighter objects.

This brief excursion into the development of telescopes and instruments up to the present and into the near future is by no means complete. It is intended only to illustrate the range of tools now available to the observational astronomer.

## 1.2. APPROACH TO SUBJECT

Most of the optical principles that serve as the starting point in the design and use of any optical instrument have been known for a long time. In intermediate-level optics texts these principles are usually divided into two categories: geometrical optics and physical optics. Elements from both of these fields are required for full descriptions of the characteristics of optical systems.

The theory of geometrical optics is concerned with the paths taken by light rays as they pass through a system of lenses and/or mirrors. Although the ray paths can be calculated by simple application of the laws of refraction and reflection, a much more powerful approach is one that starts with Fermat's Principle. With the aid of this approach it is possible to determine both the first-order characteristics of an optical system and deviations from these characteristics. The latter leads to the theory of aberrations or image defects, a subject to be discussed in detail.

The theory of physical optics includes the effects of the finite wavelength of light and such topics as interference, diffraction, and polarization. Analyses of the characteristics of diffraction gratings, interferometers, and telescopes such as the Hubble Space Telescope require an understanding of these topics. The basics of this theory are introduced prior to our discussions of these types of optical systems.

The approach, therefore, is to emphasize the basic principles of a variety of systems and to illustrate these principles with specific designs. Although the specifics of telescopes and instruments have changed, and will continue to change, the basic optical principles are the same.

## 1.3. OUTLINE OF BOOK

The 17 chapters that follow the Introduction can be grouped into six distinct categories. Chapters 2 through 5 cover the elements of geometrical optics needed for the discussion of optical systems. The first three chapters of this group are an introduction to this part of optics seen from the point of view of Fermat's Principle, with Chapter 5 a detailed treatment of aberrations based on this principle.

Chapters 6 through 11 cover the characteristics of a variety of telescopes and cameras, including auxiliary optics used with them. The characteristics of diffraction-limited telescopes are covered in the last two chapters of this group, with application to the Hubble Space Telescope.

Chapters 12 through 15 are a discussion of the principles of spectrometry and their application to a variety of dispersing systems, with the emphasis on diffraction gratings. In this group Chapter 14 is the counterpart of Chapter 5, a treatment of grating aberrations from the point of view of Fermat's Principle.

The remaining three chapters (16, 17, and 18) are distinct in themselves with each chapter drawing upon results given in preceding chapters and applying these results to selected types of observations for both ground-based and space-based systems.

A closer look at the contents of each chapter is now in order. Chapter 2 is an introduction to the basic ideas of geometrical optics, and the reader who is well versed in these ideas can cover it quickly. One topic covered in this chapter, not part of the usual course in optics, is the definition of normalized parameters for two-mirror telescopes.

Chapter 3 is an introduction to Fermat's Principle with a number of examples illustrating its utility, including a brief discussion of atmospheric refraction and atmospheric turbulence. Chapter 4 is an introduction to aberrations, with emphasis on spherical aberration. The concept of aberration compensation is introduced and applied to two optical systems.

The discussions of the preceding three chapters set the stage for an in-depth discussion of the theory of third-order aberrations in Chapter 5. The results of the analysis are summarized in tables for easy reference.

In Chapter 6 we draw on the results from Chapter 5 to derive the characteristics of a number of types of reflecting telescopes. Comparisons of image quality are given for several of these types, including examples of image quality for misaligned two-mirror telescopes. Chapter 7 covers the characteristics of Schmidt systems, including a discussion of the achromatic Schmidt and solid and semi-solid cameras.

Chapter 8 covers various types of catadioptric systems, including Schmidt-Cassegrain telescopes and cameras with meniscus correctors substituted for aspheric plates. The following chapter (9) is a discussion of various types of auxiliary optics used with telescopes, including field lenses, field flatteners, prime and Cassegrain focus correctors, focal reducers, atmospheric dispersion correctors, and fiber optics.

In Chapter 10 we discuss the basics of diffraction theory and aberrations and the characteristics of perfect and near-perfect images. Perfect and near-perfect images are discussed in terms of classical and orthogonal aberrations in Chapter 10, followed by a discussion in terms of transfer functions in Chapter 11. The results are illustrated with a discussion of the optical characteristics of the Hubble Space Telescope, both expected before launch and as measured after launch.

Chapter 12 covers the basic principles of spectrometry, followed by application of these principles to a variety of dispersing elements and systems in Chapter 13.

The following two chapters are devoted entirely to the diffraction grating, with Chapter 14 an analysis of grating aberrations and concave grating mountings and Chapter 15 the application of these results to a variety of plane grating instruments.

Chapter 16 is an introduction to adaptive optics and the approach to correction of wavefront distortion due to atmospheric turbulence to restore image quality. In Chapter 17 we discuss detectors in terms of transfer functions and Nyquist sampling, signal-to-noise ratio (SNR), and the detection limits that are reached at a given SNR level for several types of observations. The final chapter is two separate topics: residual errors of real mirrors and effects of these errors on image quality, and diffraction-limited images given by telescope arrays.

The reader approaching the topic of astronomical optics for the first time is encouraged to work through the basic theory. This exercise will facilitate the understanding of its application to a specific optical system and the bounds within which this system is usable. Other readers, on the other hand, will be interested only in specific systems and their characteristics. We hope that their needs are met with the tables and equations that are given. Whatever the motivation, a selected bibliography is given at the end of each chapter for additional reading.

A more complete understanding of any optical system is achievable if an analysis using the basic theory is supplemented with data from one of the many optical design packages now available. Such packages generally provide a large number of analysis tools and can give the user a detailed picture of how an optical system will perform. Tasks ranging from simple tracing of rays to complete diffraction analysis are essential in the design of complex optical systems.

In preparing the figures in this book, we have made extensive use of the optical design program **ZEMAX** from Focus Software, Inc. of Tucson. As a help to the reader, many of the optical systems used as examples in our discussions are available from the public free download part of the web site **www.focus-software.com**. An interested reader is encouraged to use the supplied design files as a starting point for further self-study of the examples in the text.

The analysis of any optical system generally proceeds along a well-defined route. First one arrives at a basic layout of optical elements: lenses, mirrors, prisms, gratings, and such, by using first-order or Gaussian optics. Such an analysis establishes such basic parameters as focal length, magnification, and locations of pupils, among others. The next step often involves using a ray-trace program on a digital computer to trace rays through the system and calculate aberrations of the image. Such an analysis might dictate changes in the basic layout in order to achieve image quality within certain specified limits. Ray trace and optical analysis programs are now quite sophisticated and are particularly useful in systems with many optical elements. Tracing of rays is especially useful in optimizing system performance.

In order to efficiently use the results generated by a ray-trace program it is necessary to understand the theory of third-order aberrations. In subsequent chapters we go into considerable detail on the nature of these aberrations and how they can be eliminated or minimized in different kinds of optical systems. In many cases an analysis of aberrations is a useful intermediate step following the setup of the basic system and the analysis using a ray-trace program. Details of how such programs work are not discussed.

Each of the steps along this route requires a systematic approach to measurements of angles and distances. In this chapter we define the sign conventions used and determine the equations of first-order optics. We apply these equations to several systems including two-mirror telescope systems.

### 2.1. SIGN CONVENTIONS

The coordinate system within which surface locations and ray directions are defined is the standard right-hand Cartesian frame shown in Fig. 2.1. For a single refracting or reflecting surface the  $z$ -axis coincides with the optical axis, with the origin of the coordinate system at the vertex  $O$  of the surface. For an optical system in which the elements are centered, the optical axis is the line of symmetry along which the elements are located. In a system in which one or more of the elements is not centered, the optical axis for such an element will not coincide with that for a different element, a complication that is dealt with later. In the following discussion only centered systems are considered.

Figure 2.1 illustrates refraction at a spherical surface with an incident ray directed from left to right. Rays from an initial object are always assumed to travel in this direction. The indices of refraction are  $n$  and  $n'$  to the left and right of the surface, respectively, with points  $B$ ,  $B'$ , and  $C$  on the optical axis of the surface. The line  $PC$  is the normal to the interface between the two media at point  $P$ , and a ray directed toward  $B$  is refracted at  $P$  and directed toward  $B'$ .

The unprimed symbols in Fig. 2.1 refer to the ray before refraction, while the primed symbols refer to the ray after refraction. The slope angles are  $u$  and  $u'$ , measured from the optical axis, and the angles of incidence and refraction, respectively, are  $i$  and  $i'$ , measured from the normal to the surface. The symbols  $s$  and  $s'$  denote the object and image distances, respectively, and  $R$  represents the radius of curvature of the surface, measured at the vertex.

The sign convention for distances is the same as for Cartesian geometry. Hence distances  $s$ ,  $s'$ , and  $R$  are positive when the points  $B$ ,  $B'$ , and  $C$  are to the right of the vertex, and distances from the optical axis are positive if measured

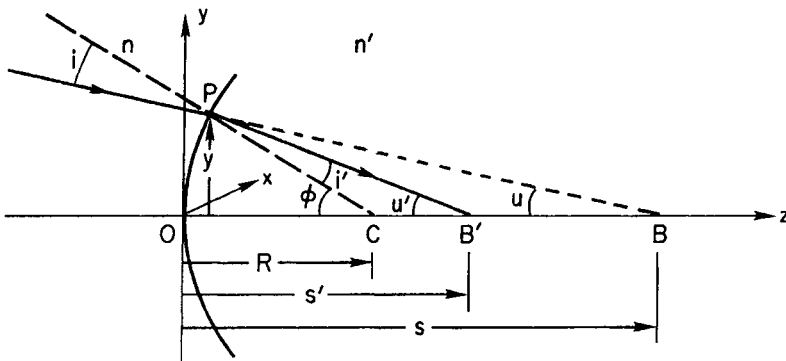


Fig. 2.1. Refraction at spherical interface. All angles and distances are positive in diagram; see text for discussion.

upward. The sign convention for angles is chosen so that all of the angles shown in Fig. 2.1 are positive. Slope angles  $u$  and  $u'$  are positive when a counter-clockwise rotation of the corresponding ray about  $B$  or  $B'$  brings the ray into coincidence with the  $z$ -axis. The angles of incidence and refraction,  $i$  and  $i'$ , are positive when a clockwise rotation of the corresponding ray about point  $P$  brings the ray into coincidence with the line  $PC$ . All rotations are made through acute angles.

The advantage of these conventions for distances and angles is that both refracting and reflecting surfaces can be treated with the same relations. As we show, formulas for reflecting surfaces are obtained directly by letting  $n' = -n$  in the formulas derived for refracting surfaces. The meaning of a negative index of refraction is discussed in Section 2.3.

The sign conventions for distances and angles are similar to those used by Born and Wolf (1980) and by Longhurst (1967). Although the conventions for angles may at times seem awkward, they have the advantage of universal applicability and are especially appropriate in third-order analysis of complex systems.

## 2.2. PARAXIAL EQUATION FOR REFRACTION

In this section we develop some of the basics needed for a first-order analysis of an optical system. It is worth noting that our discussion is not intended as a comprehensive one, and should more details be needed the reader should refer to any of a number of excellent texts in optics. Examples of such texts are those by Longhurst (1967), Hecht (1987), or Jenkins and White (1976). You should be aware, however, that the sign conventions used in the latter two of these books differ from that used here.

With the help of Fig. 2.1 we can easily determine the relation between  $s$  and  $s'$  when the distance  $y$  and all angles are small. By small we mean that point  $P$  is close enough to the optical axis so that sines and tangents of angles can be replaced with the angles themselves. In this approximation any ray is close to the axis and nearly parallel to it, hence the term *paraxial approximation*.

The exact form of Snell's law of refraction is

$$n \sin i = n' \sin i', \quad (2.2.1)$$

which in the paraxial approximation becomes  $ni = n'i'$ . From Fig. 2.1 we find

$$i + u = \phi, \quad i' + u' = \phi. \quad (2.2.2)$$

Solving these relations for  $i$  and  $i'$ , and substituting into the paraxial form of Snell's law gives

$$n'u' - nu = (n' - n)\phi. \quad (2.2.3)$$

Applying the paraxial approximation to the distances, we get  $\phi = y/R$ ,  $u = y/s$ , and  $u' = y/s'$ . Substituting, and canceling the common factor  $y$ , we get

$$\frac{n'}{s'} - \frac{n}{s} = \frac{n' - n}{R}. \quad (2.2.4)$$

The points at distances  $s$  and  $s'$  from the vertex are called *conjugate* points, that is, the image is conjugate to the object and vice versa. If either  $s$  or  $s' = \infty$ , then the conjugate distance is the *focal length*, that is,  $s = f$  when  $s' = \infty$  and  $s' = f'$  when  $s = \infty$ .

### 2.2.a. POWER

In Eq. (2.2.4) we see that the right side of the equation contains factors relating to the surface and surrounding media, and not to the object and image. It is useful to denote this combination by  $P$ , where  $P$  is the *power* of the surface. The power is unchanged when the direction of light travel in Fig. 2.1 is reversed, provided  $n$  and  $n'$  are interchanged and each is made negative. This invariance of  $P$  to the direction of light travel makes it a useful parameter. Note also that  $s$  and  $s'$  change places when the light is reversed in Fig. 2.1, and Eq. (2.2.4) is unchanged.

Combining Eq. (2.2.4) with the defined focal lengths and power we get

$$\frac{n'}{s'} - \frac{n}{s} = \frac{n' - n}{R} = P = \frac{n'}{f'} = -\frac{n}{f}. \quad (2.2.5)$$

This is the first-order or Gaussian equation for a single refracting surface and is the starting point for analyzing systems that have several surfaces. For multi-surface systems the image formed by a given surface, say the  $i$ th one, serves as the object for the next surface, the  $(i + 1)$ st in this case. A surface-by-surface application of Eq. (2.2.5), starting with the first surface, will be illustrated in examples to follow.

Equation (2.2.5) does not contain height  $y$  and hence applies to any ray passing through  $B$  before refraction, provided of course the paraxial approximation is valid. This equation also applies to object and image points that are not on the optical axis, provided these points are close to  $B$  and  $B'$  and lie on a line passing through point  $C$ . This is illustrated in Fig. 2.2, where  $Q$  and  $Q'$  denote an object and image point, respectively, for a case where  $B$  and  $B'$  lie on opposite sides of the surface vertex. In Fig. 2.2 the line  $QCQ'$  can be thought of as a new axis of the spherical surface, where  $Q$  and  $Q'$  are conjugate points along the new axis just

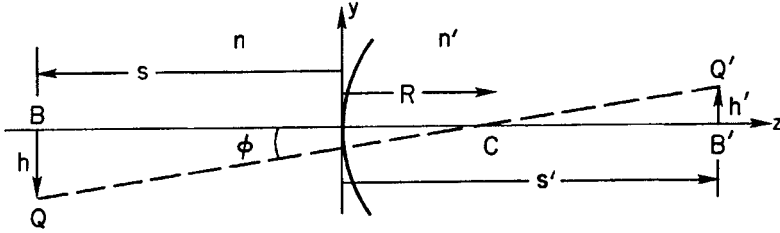


Fig. 2.2. Conjugate points in the paraxial region. Here  $B$  and  $B'$ ,  $Q$  and  $Q'$  are pairs of conjugate points. See Eq. (2.2.7) for definition of transverse magnification.

as  $B$  and  $B'$  are conjugate points on the original axis. If the angle  $\phi$  in Fig. 2.2 is small, then the line segments  $BQ$  and  $B'Q'$  can be taken perpendicular to the original axis. In general, of course,  $BQ$  and  $B'Q'$  are short arcs of circles whose centers are at  $C$ .

### 2.2.b. MAGNIFICATION

The geometry in Fig. 2.2 can be used to determine the *transverse* or *lateral magnification*  $m$ , defined as the ratio of image height to object height. In symbols we have  $m = h'/h$ , where

$$h' = -(s' - R) \tan \phi, \quad h = -(s - R) \tan \phi, \quad (2.2.6)$$

and the sign convention has been applied to each quantity. Note that the paraxial approximation has not been applied in Eq. (2.2.6) in order to emphasize the fact that for this definition the object and image lie in planes perpendicular to the axis.

In Fig. 2.2 we have  $s'$  and  $R > 0$  and  $s$  and  $\phi < 0$ , hence  $h$  and  $h'$  have opposite signs. Therefore

$$m = \frac{h'}{h} = \frac{s' - R}{s - R} = \frac{ns'}{n's}, \quad (2.2.7)$$

where the final step follows by substitution of Eq. (2.2.4). Because  $h$  and  $h'$  have opposite signs in Fig. 2.2, the transverse magnification is negative for the case shown. If  $m < 0$ , as in Fig. 2.2, the image is *inverted* relative to the object; in the case where  $m > 0$  the image is said to be *erect*.

In Fig. 2.3 a ray joining conjugate points  $B$  and  $B'$  has slope angles  $u$  and  $u'$ . The *angular magnification*  $M$  is defined as  $\tan u' / \tan u$ , where from the geometry of Fig. 2.3 we see that  $y = s \tan u = s' \tan u'$ . Therefore

$$M = \frac{\tan u'}{\tan u} = \frac{s}{s'} = \frac{n}{n'm} = \frac{nh}{n'h'}. \quad (2.2.8)$$

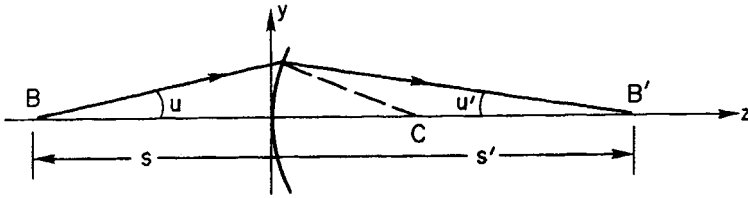


Fig. 2.3. Angular magnification. See Eq. (2.2.8) for definition.

Equation (2.2.8) relates the transverse and angular magnification for a pair of conjugate planes. Rewriting this relation we get

$$nh \tan u = n' h' \tan u', \quad (2.2.9)$$

which in the paraxial approximation becomes

$$nhu = n' h' u'. \quad (2.2.10)$$

If, as is customary, we let  $H = nh \tan u$ , then Eq. (2.2.9) states that  $H$  before refraction is the same as  $H$  after refraction. Thus in any optical system containing any number of refracting (or reflecting) surfaces,  $H$  is an invariant. This follows because the combination  $n'h'u'$  for the first surface is  $nhu$  for the second surface, and so on. Called the Lagrange invariant,  $H$  is important in at least one other respect; the total flux collected by an optical system from a uniformly radiating source of light is proportional to  $H^2$ . Its invariance through an optical system is thus a consequence of conservation of energy.

### 2.3. PARAXIAL EQUATION FOR REFLECTION

With the aid of Fig. 2.4 we now find the Gaussian equation for a reflecting surface in the paraxial approximation. Applying the sign conventions to the symbols shown gives distances  $s$ ,  $s'$ , and  $R$ , and angles  $i$ ,  $\phi$ ,  $u$ , and  $u'$  as negative. The law of reflection is  $i = -i'$ , hence the angle of reflection  $i'$  is positive in Fig. 2.4. From the geometry shown we get

$$i = \phi - u, \quad i' = \phi - u', \quad \phi = \frac{y}{R}, \quad u = \frac{y}{s}, \quad u' = \frac{y}{s'}.$$

Substituting into the law of reflection,  $i = -i'$ , gives

$$\frac{1}{s'} + \frac{1}{s} = \frac{2}{R}. \quad (2.3.1)$$

As in the case of Eq. (2.2.4), this relation applies generally to any object position provided we use the appropriate signs for the distances. At this point it is

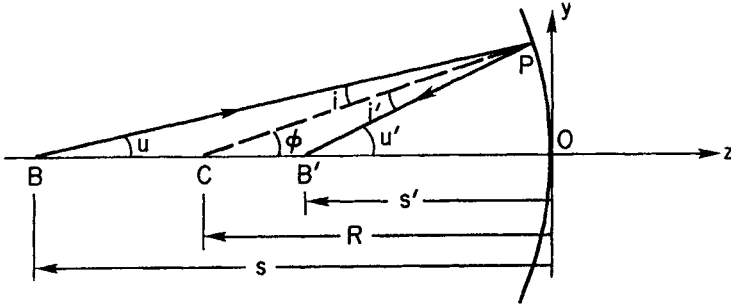


Fig. 2.4. Reflection at spherical surface. Here  $B$  and  $B'$  are conjugate axial points.

important to point out that the law of reflection follows directly from Snell's law of refraction if we make the substitution  $n' = -n$ . Specifically, note that this substitution into Eq. (2.2.4) gives Eq. (2.3.1) directly. The fact that the relations for reflecting surfaces are thus directly obtained is very useful because we need only consider relations for refracting surfaces and simply put  $n' = -n$  as needed. As an example we apply this substitution to Eqs. (2.2.5) and (2.2.7) and get

$$\frac{1}{s'} + \frac{1}{s} = \frac{2}{R} = -\frac{P}{n} = \frac{1}{f'} = \frac{1}{f}, \quad (2.3.2)$$

$$m = -\frac{s'}{s}. \quad (2.3.3)$$

Using Eq. (2.3.2) it is easy to verify that  $P > 0$  for a concave mirror and  $P < 0$  for a convex mirror, where a mirror is concave or convex as seen from the direction of the incident light. Note, however, that the focal length of a concave mirror changes sign when the direction of the incident light is reversed. This is expected because the reversal of Fig. 2.4, left for right, changes the signs of  $s$  and  $s'$ . But because  $n$  also changes sign in this reversal,  $P$  is invariant.

The meaning of a negative index of refraction simply means that the light is traveling in the direction of the  $-z$ -axis, or from right to left. Consistent use of this convention, together with the other sign conventions in Eq. (2.2.2), allows one to work with any set of refracting and/or reflecting surfaces in combination.

In many situations it is convenient to take  $f > 0$  for a concave mirror and  $f < 0$  for a convex mirror, independent of the direction of the incident light. We will adopt this convention for convenience, keeping in mind that it violates the strict sign convention. The sign convention for  $s$ ,  $s'$ , and  $R$  will *always* be observed.

## 2.4. TWO-SURFACE REFRACTING ELEMENTS

We now apply the results of Section 2.2 to several systems with two refracting surfaces, a thick lens, a thin lens, and a thick plane-parallel plate. We first consider a thick lens, a lens in which the second refracting surface is distance  $d$  to the right of the first surface.

## 2.4.a. THICK LENS

A schematic cross-section of a thick lens is shown in Fig. 2.5. If we assume the lens has index  $n$  and is located in air, then  $n_1 = n'_2 = 1$ , and  $n'_1 = n_2 = n$ . Applying Eq. (2.2.5) to each surface gives

$$\frac{n}{s'_1} - \frac{1}{s_1} = \frac{n-1}{R_1} = P_1, \quad \frac{1}{s'_2} - \frac{n}{s_2} = \frac{1-n}{R_2} = P_2, \quad (2.4.1)$$

where  $s_2 = s'_1 - d$ .

With this system we find only the net power  $P$  or, equivalently, the effective focal length  $f'$ , where  $P = 1/f'$ . Figure 2.5 shows a ray with  $s_1 = \infty$  intersecting the first surface at height  $y_1$  and the second surface at height  $y_2$ . From similar triangles in Fig. 2.5 we get

$$\frac{y_2}{y_1} = \frac{s'_1 - d}{s'_1} = \frac{s'_2}{f'}. \quad (2.4.2)$$

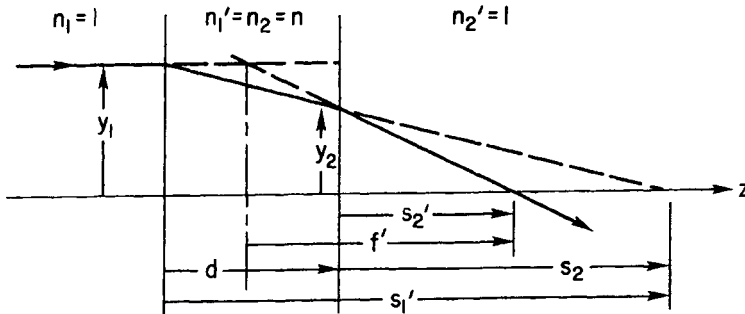


Fig. 2.5. Cross section of thick lens. See Eq. (2.4.3) for lens power. In the thin lens limit,  $f' = s_2 = s'_1$ .

We can now find the effective focal length by setting  $s_1 = \infty$  and  $s_2 = s'_1 - d$  in Eq. (2.4.1) and combining the result with Eq. (2.4.2). After a bit of algebra we get

$$P_1 = \frac{n}{s'_1}, \quad P_2 = \frac{1}{s'_2} - \frac{n}{s'_1 - d},$$

$$P = \frac{1}{f'} = \frac{1}{s'_2} \left( \frac{s'_1 - d}{s'_1} \right) = \left( P_2 + \frac{n}{s'_1 - d} \right) \left( \frac{s'_1 - d}{s'_1} \right).$$

Multiplying out the preceding equation we finally get the result sought in the form

$$P = \frac{1}{f'} = P_1 + P_2 - \left( \frac{d}{n} \right) P_1 P_2. \quad (2.4.3)$$

In the steps leading to Eq. (2.4.3), both  $n$  and  $d$  are positive. If the directions of the arrows in Fig. 2.5 are reversed, the foregoing derivation reproduces Eq. (2.4.3), with  $P_1$  and  $P_2$  exchanging roles. In this case both  $d$  and  $n$  change sign and the ratio  $(d/n)$  is unchanged in sign. Thus  $P$  in Eq. (2.4.3) is the same for either direction of light. Note that the effective focal length  $f'$  in Fig. 2.5 is measured from the intersection of two extended rays, the incident ray to the right and the refracted ray to the left.

#### 2.4.b. THIN LENS

A thin lens is defined as one in which the separation of the two surfaces is negligible compared to other axial distances, that is,  $s_2 = s'_1$  effectively. For a thin lens in air, Eqs. (2.4.1) apply directly. Letting  $s_1 = s$  and  $s'_2 = s'$ , the addition of these equations gives

$$\frac{1}{s'} - \frac{1}{s} = (n - 1) \left( \frac{1}{R_1} - \frac{1}{R_2} \right) = P_1 + P_2 = P = \frac{1}{f'} = -\frac{1}{f}. \quad (2.4.4)$$

The net power of a thin lens is simply the reciprocal of its focal length and is the same as that of a thick lens with  $d = 0$ , as expected. Although a thin lens has two surfaces, it is of interest to note that the Gaussian relations that describe the lens are actually somewhat simpler than those for a single refracting surface.

The transverse magnification of each surface is given by Eq. (2.2.7) with the results  $m_1 = s'_1/ns_1$  and  $m_2 = ns'_2/s_2$ . The net transverse magnification of a thin lens is then  $m = m_1 m_2 = s'/s$ .

As a final item for thin lenses, we note that Eq. (2.4.3) also applies to two thin lenses separated by distance  $d$ , where  $n = 1$  in the space between the lenses. The simple analysis showing this is left to the reader.

2.4.c. THICK PLANE-PARALLEL PLATE

A thick plane-parallel plate, as shown in Fig. 2.6, has a zero power but also has an image that is displaced laterally along the optical axis relative to the object. Applying Eq. (2.2.5) at each surface gives  $n'_1/s'_1 = n_1/s_1$  and  $n'_2/s'_2 = n_2/s_2$ . Assuming the plate of index  $n$  is in air,  $n_1 = n'_2 = 1$ ,  $n'_1 = n_2 = n$ , and noting that  $s_2 = s'_1 - d$ , we get  $s'_1 = ns_1$ ,  $s'_2 = s_1 - (d/n)$ . The distance from object to image is  $\Delta = s'_2 - s_2 + d$ , or

$$\Delta = d[1 - (1/n)]. \tag{2.4.5}$$

Note that the displacement  $\Delta$  is independent of the object distance and, as is true in all cases in the paraxial approximation, independent of height  $y$ . For a typical glass with  $n \cong 1.5$ , we see that  $\Delta \cong d/3$ .

In the paraxial approximation an optical system is free of any aberrations, that is, an object point is imaged precisely into an image point. When the exact form of Snell's law is used however, most systems will have some form of aberration. A thick plate is a good example of a simple system with aberration, that is, it fails to take all rays from a single object point into a single image point. This is easily shown by applying Snell's law in its exact form at each surface. With the intermediate steps left to the reader, the geometry of Fig. 2.6 leads to

$$\Delta = d \left( 1 - \frac{\cos i_1}{n \cos i'_1} \right). \tag{2.4.6}$$

A comparison of Eqs. (2.4.5) and (2.4.6) gives

$$\Delta_{\text{exact}} - \Delta_{\text{par}} = \frac{d}{n} \left( 1 - \frac{\cos i_1}{\cos i'_1} \right) \cong \frac{y_1^2 d (n^2 - 1)}{2s_1^2 n^3}, \tag{2.4.7}$$

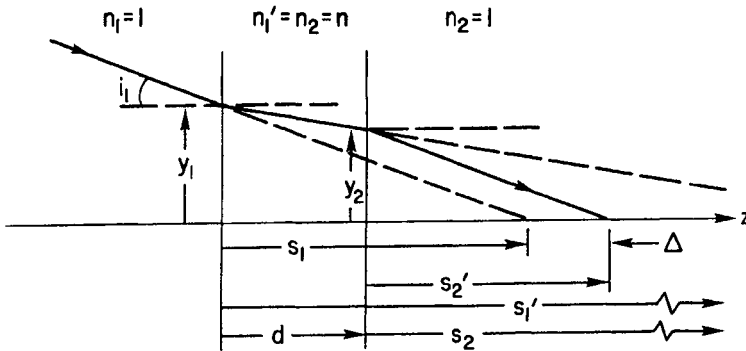
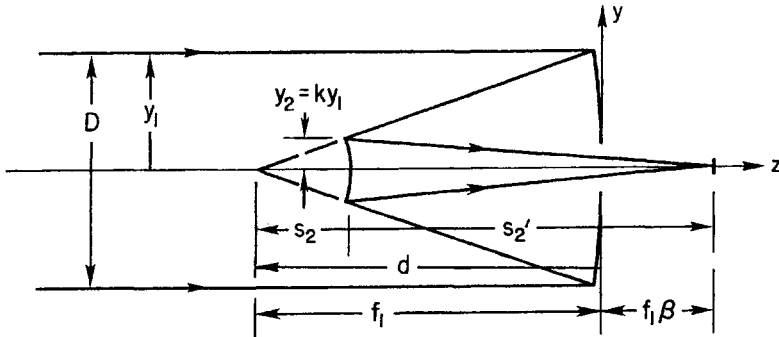


Fig. 2.6. Image shift  $\Delta$  for plane-parallel plate of thickness  $d$  and index  $n$  in air. See Eqs. (2.4.5)–(2.4.7) for discussion.

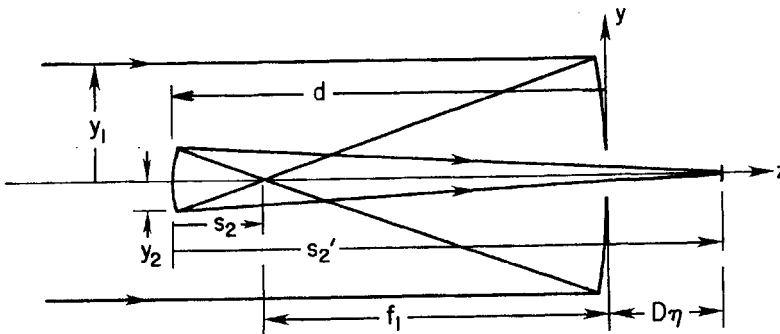
hence the image position depends on the ray height at the first surface. We consider the aberrations of a thick plate in more detail later.

### 2.5. TWO-MIRROR TELESCOPES

We now apply the results of the preceding sections to the general class of two-mirror systems. In this section we are concerned only with the paraxial properties



(a)



(b)

**Fig. 2.7.** Schematic diagrams of two-mirror reflecting telescopes: (a) Cassegrain; (b) Gregorian. Designated parameters are  $y_1$  and  $y_2$ , height of ray at margin of primary and secondary, respectively;  $D$ , telescope diameter =  $2|y_1|$ ;  $2|y_2|$ , diameter of secondary mirror;  $R_1$  and  $R_2$ , vertex radius of curvature of primary and secondary mirror, respectively;  $s_2$  and  $s_2'$ , object and image distance of intermediate object (located at focal point of primary) measured from the secondary mirror vertex;  $f_1$ , focal length of primary mirror; and  $d$ , distance from primary to secondary,  $d < 0$ . See Table 2.1 for definitions of normalized parameters.

of such systems, and will limit our discussion to the case where  $s_1 = \infty$ . Two examples of particular two-mirror systems are shown in Fig. 2.7, the so-called Cassegrain and Gregorian types, of which the Cassegrain is the more common type for an optical telescope.

Symbols in Fig. 2.7 are defined in the legend. Note that subscript 1 refers to the first mirror (primary) and 2 refers to the second mirror (secondary) in the optical train. For convenience, the sign of  $f_1$  is taken positive when the primary is concave. Following the sign convention,  $y_1$  and  $y_2$  have the same signs for a Cassegrain and opposite signs for a Gregorian.

### 2.5.a. NORMALIZED PARAMETERS

It is very helpful to describe any two-mirror system in terms of a set of dimensionless or *normalized* parameters, defined as given in Table 2.1. Among the things to note for the entries in Table 2.1 are: (1) the focal ratios are defined as positive quantities; and (2) the dimensionless parameters do not change sign when the diagrams in Fig. 2.7 are reversed left for right.

In Fig. 2.7 we have  $\beta > 0$  when the focal point lies outside the space between the primary and secondary. Depending on whether the system is Cassegrain or Gregorian, the signs of some of these dimensionless parameters differ. In particular,  $k$  and  $m$  are each positive for a Cassegrain and negative for a Gregorian, hence the product  $mk$  is positive for each of the telescopes shown in Fig. 2.7.

The relationships between these parameters are obtained with the aid of Eqs. (2.3.1) and (2.3.3) applied to the secondary, and the relation  $s_2 = kR_1/2$ . The steps are as follows:

$$\frac{1}{s'_2} = \frac{2}{R_2} - \frac{2}{kR_1} = \frac{2}{R_1} \left( \frac{1}{\rho} - \frac{1}{k} \right) = \frac{1}{s_2} \left( \frac{k - \rho}{\rho} \right) = -\frac{1}{ms_2}.$$

**Table 2.1**

Normalized Parameters for Two-Mirror Telescopes

---

$k = y_2/y_1 =$ ratio of ray heights at mirror margins,
$\rho = R_2/R_1 =$ ratio of mirror radii of curvature,
$m = -s'_2/s_2 =$ transverse magnification of secondary,
$f_1\beta = D\eta =$ back focal distance, or distance from vertex of primary mirror to final focal point,
$\beta$ and $\eta$ , back focal distance in units of $f_1$ and $D$ , respectively,
$F_1 =  f_1 /D =$ primary mirror focal ratio,
$W = (1 - k)f_1 =$ distance from secondary to primary mirror,
= location of telescope entrance pupil relative to the secondary when the primary mirror is the aperture stop,
$F =  f /D =$ system focal ratio, where $f$ is the telescope focal length.

---

Solving for  $m$ , and for  $\rho$  and  $k$  in turn, we get

$$m = \frac{\rho}{\rho - k}, \quad \rho = \frac{mk}{m - 1}, \quad k = \frac{\rho(m - 1)}{m}. \quad (2.5.1a)$$

We also find

$$1 + \beta = k(m + 1), \quad \eta = F_1\beta. \quad (2.5.1b)$$

It should be kept in mind that the relations in Eq. (2.5.1a,b) apply specifically to the case where the original object is at infinity. Given this caveat we will see that it is convenient to describe telescope characteristics in term of these parameters, especially system aberrations.

The net power of a two-mirror telescope is found by using Eq. (2.4.3), which can be rewritten as

$$P = P_1 \left( 1 + \frac{P_2}{P_1} - \left( \frac{d}{n} \right) P_2 \right).$$

From Eq. (2.3.2) we find  $P_1 = -2/R_1$ ,  $P_2 = 2/R_2$ , hence  $P_2/P_1 = -1/\rho$ . In using Eq. (2.3.2) note that  $n = 1$  for the primary and  $n = -1$  for the secondary, according to the sign convention. For the arrangements shown in Fig. 2.7, both  $d$  and  $n$  are negative; the light is traveling from right to left and the secondary mirror is to the left of the primary. Hence  $d/n$  is positive. In terms of the dimensionless parameters from Eq. (2.5.1), we find that  $d/n = (1 - k)P_1$ , and

$$P = P[1 - (k/\rho)] = P_1/m, \quad (2.5.2)$$

hence the telescope power is positive for a Cassegrain telescope and negative for a Gregorian. In accord with our convention for single mirrors, we take telescope focal length positive for a Cassegrain and negative for a Gregorian. In terms of the focal lengths and focal ratios, therefore,

$$m = f/f_1, \quad F = |m|F_1. \quad (2.5.3)$$

The difference in sign between the focal lengths of a Cassegrain and Gregorian, and their magnifications, requires some discussion.

Consider the rays reflected from the secondary in Fig. 2.7(a). If these rays are extended to the left until they intersect their corresponding incident rays, the distance between the intersection plane and the focal point, measured along the axis, is the focal length. The focal point lies to the right of the intersecting rays, hence the focal length is positive. This is similar to the situation shown in Fig. 2.5 for a thick lens. Following the same procedure for the Gregorian in Fig. 2.7(b), the incident rays and the rays reflected from the secondary must be extended to the right to locate the intersection plane, hence the focal length is negative.

As for the magnification, its sign according to our convention is positive if the image made by the secondary has the same orientation as the object for the

secondary. This is the case for the secondary mirror in a Cassegrain telescope as shown in Fig 2.7(a). But this telescope has a final image that is inverted with respect to the original object on the sky. This is because the image given by the primary is inverted, hence the final image is also inverted. For the Gregorian telescope the final image is erect relative to the object on the sky because each mirror inverts its object. Thus these two types of telescopes might simply be characterized as follows:

Cassegrain:  $f > 0$ ,  $m > 0$ , final image inverted;  
 Gregorian :  $f < 0$ ,  $m < 0$ , final image erect.

### 2.5.b. OTHER TELESCOPE CHARACTERISTICS

Given our introduction of normalized parameters for two-mirror telescopes, it is appropriate to discuss other characteristics in terms of them. Among these are telescope scale, effect of secondary mirror displacement on focal surface location, secondary mirror to focal point separation, diameter of secondary mirror as a function of field size, and overall telescope length.

We are limiting our discussion here to optical systems for which the original object is effectively at an infinite distance, hence it is not possible to give a useful formula for the magnification of the system. Rather it is the *telescope scale* that provides a useful parameter of the telescope. For a telescope of focal length  $f$ , the scale is

$$S(\text{arc-sec/mm}) = \frac{206265}{f(\text{mm})}, \quad (2.5.4)$$

where the units of arc-sec/mm are those most often used. For conversion to radian measure the identities  $0.206 \text{ arc-sec} = 1 \mu\text{rad}$  and  $3.44 \text{ arc-min} = 1 \text{ mrad}$  can be used. Equation (2.5.4) applies to a telescope with any number of mirrors.

For a given pair of primary and secondary mirrors the location of the telescope focal surface depends on the location of the secondary, as given by Eq. (2.5.1). If the secondary is moved along the optical axis, then both  $m$  and  $k$  are changed, and so also is the position of the focal surface.

Let  $ds'_2$  be the displacement of the focal surface, or *focal surface shift*, when the secondary is displaced by  $ds_2$ . Differentiating Eq. (2.3.1) while holding  $R_2$  constant, we find that

$$ds'_2 = -m^2 ds_2, \quad (2.5.5)$$

where  $ds_2 < 0$  when the secondary is moved closer to the primary.

The displacement given by Eq. (2.5.5) is measured relative to the secondary, which is now in a new position. Relative to the object at the focal point of the

primary, or relative to the primary, the focal surface has moved by  $ds'_2 - ds_2 = -(m^2 + 1)ds_2$ . This relation can easily be checked by working with the dimensionless parameters. From Eq. (2.5.1) we have

$$\beta = k(m + 1) - 1 = k\left(\frac{2\rho - k}{\rho - k}\right) - 1, \quad (2.5.6)$$

$$\frac{d\beta}{dk} = \frac{\rho^2}{(\rho - k)^2} + 1 = m^2 + 1,$$

where  $dk = -ds_2/f_1$ , and  $d\beta$  = shift of focal surface relative to the primary mirror vertex in units of  $f_1$ .

Although Eq. (2.5.6) does not set any apparent limit on how far the secondary can be moved, there is a limit set by the onset of aberrations. Two-mirror telescopes generally have a mirror separation set to make the on-axis aberration zero. For a different secondary position the on-axis aberration is no longer zero, and its size sets a practical limit to the amount of secondary displacement. These limits will be considered during our discussion of telescope aberrations.

Both Cassegrain and Gregorian telescopes, especially the former, can have a long overall focal length in a mechanical structure that is many times shorter. From Fig. 2.7 we see that a typical Cassegrain telescope has a secondary mirror to focal surface separation comparable to  $f_1$ , or about  $m$  times smaller than  $f$ . More precisely, the *secondary mirror-focal surface distance* is  $f_1(1 + \beta - k)$ , or  $1 + \beta - k$  in units of  $f_1$ . Using Eq. (2.5.1) we get

$$\text{secondary-focal surface distance} = mkf_1, \quad (2.5.7)$$

a relation that applies to both Cassegrain and Gregorian types. We show in Chapter 6 that a Gregorian telescope is significantly longer than a Cassegrain if both telescopes have the same values of  $|m|$  and  $f_1$ , hence the same focal length. The advantages of a relatively short structure from an engineering point of view are obvious because there will be less flexure in a short telescope than in a long one.

Another difference between these two types of telescopes is the size of the secondary required to accept all of the light reflected from the primary. Each diagram in Fig. 2.7 shows a secondary mirror whose diameter is  $|k|D$ , the minimum required for a single point source. To cover a field on the sky of angular diameter  $2\theta$  without vignetting any light from the primary, the secondary must be larger by  $2\theta(1 - k)f_1 = 2\theta F_1(1 - k)D$ . Thus the full diameter of the secondary is

$$D_2 = D[|k| + 2\theta F_1(1 - k)]. \quad (2.5.8)$$

Because  $k < 0$  for a Gregorian, the diameter  $D$  of the Gregorian secondary is larger for the same  $\theta$  and  $F_1$ , hence it blocks a larger fraction of the light headed for the primary.

These two-mirror designs have the added feature that the system focal length is easily changed simply by putting in a different secondary mirror, without changing the physical length by a large factor. As an example, consider a Cassegrain telescope with parameters  $F_1 = 3$ ,  $\beta = 0.25$ , and  $m = 3$ . Using Eqs. (2.5.1) we find  $k = 0.3125$  and the normalized secondary mirror-focal surface separation is 0.9375. If we choose to increase the telescope focal length by a factor of three, hence making  $m = 9$ , while keeping  $\beta = 0.25$ , then  $k = 0.125$  and  $mk = 1.125$ . The modified telescope is only 1.2 times longer than the original one.

A final, and very significant, advantage of two-mirror systems is the additional freedom provided for controlling image quality. With proper choices of surface parameters it is possible to have the aberrations of the primary canceled, entirely or in part, by those of the secondary, thus giving a system with better image quality. We discuss these considerations in detail in subsequent chapters.

## 2.6. STOPS AND PUPILS

We now turn our attention to the important topic of stops and pupils. Our discussion, although brief, will cover the essential points. For a more complete discussion the reader should consult any of the intermediate-level texts listed in the bibliography at the end of the chapter.

### 2.6.a. DEFINITIONS AND BASICS

The *aperture stop* is an element of an optical system that determines the amount of light reaching the image. This stop is often the boundary of a lens or mirror, although it may be a separate diaphragm. In addition to controlling the amount of light entering the system, it also is one of the determining factors in the sizes of system aberrations. For most telescopes the primary mirror serves as the aperture stop, although in many infrared telescopes the secondary mirror is the aperture stop.

The *field stop* is an element that determines the angular size of the object field that is imaged by the system. In most systems the boundary of the field stop is the edge of the detector, although it may also be a separate diaphragm in an image plane ahead of the detector.

In a general optical system the image of the aperture stop formed by that part of the system preceding it in the optical train is called the *entrance pupil*. For two-mirror telescopes in which the primary mirror is the aperture stop, as well as for prime focus (single mirror) and refracting telescopes, no imaging elements precede the aperture stop. In this case the entrance pupil coincides with the

aperture stop. For infrared telescopes the aperture stop (secondary mirror) is preceded by the primary mirror. In this case the entrance pupil is the same diameter as the primary mirror, an exercise left for the reader.

The image of the aperture stop formed by that part of the system following it is called the *exit pupil*. The significance of the exit pupil is that rays from the boundary of the aperture stop approach the final image point as if coming from the boundary of the exit pupil, for all incidence angles at the aperture stop boundary. If the secondary mirror is the aperture stop, then there are no telescope optics following the aperture stop and the telescope exit pupil coincides with the stop.

### 2.6.b. PUPILS FOR TWO-MIRROR TELESCOPES

We now apply these definitions to telescopes of the type shown in Fig. 2.7. Taking the aperture stop at the primary, at distance  $W = (1 - k)f_1$  from the secondary, the exit pupil is the image of the primary formed by the secondary. Figure 2.8 shows the exit pupil location for a Cassegrain telescope; for a Gregorian the exit pupil is located between the primary and secondary mirrors.

Applying Eq. (2.3.1) to the geometry in Fig. 2.8, with  $f_1\delta$  defined as the distance from the exit pupil to the telescope focal point, and converting to normalized parameters, gives

$$\delta = \frac{m^2 k}{m + k - 1} = \frac{m^2(1 + \beta)}{m^2 + \beta}, \quad (2.6.1)$$

where  $\delta > 0$  when the focal surface of the system lies to the right of the exit pupil, as shown in Fig. 2.8. Although Eq. (2.6.1) was derived from the diagram

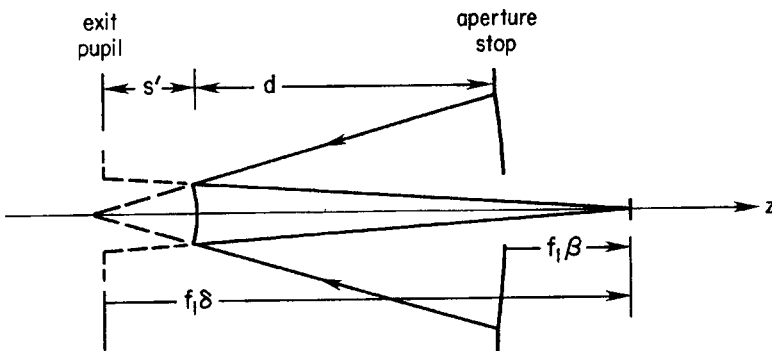


**Fig. 2.8.** Location of exit pupil for Cassegrain telescope. The exit pupil is closer to the secondary than is the primary focal point. See Eq. (2.6.1).

for a Cassegrain, it also applies to a Gregorian telescope. The distance from the secondary mirror to the exit pupil, in normalized parameters, is  $mk - \delta$ . From Eqs. (2.5.7) and (2.6.1) we find

$$\text{secondary-exit pupil distance} = \frac{mk(k-1)}{m+k-1}f_1. \quad (2.6.2)$$

Using Eqs. (2.3.3) and (2.2.3) we find that the exit pupil diameter is

$$D_{ex} = D|\delta/m| = f_1|\delta/F|. \quad (2.6.3)$$

Because the centers of the aperture stop and exit pupil are on the axis of the telescope, the so-called chief ray appears to come from the center of the exit pupil after reflection from the secondary. The *chief ray* is defined as the ray that passes through the center of the aperture stop. If the angle of incidence of the chief ray at the primary is  $\theta$ , its angle with respect to the telescope axis is  $\psi$  after reflection from the secondary. The relation between these angles is easily derived from the geometry shown in Fig. 2.9, where the focal length of a thin-lens refracting telescope equivalent to a Cassegrain type is  $f$ . From Fig. 2.9

$$\psi f_1 \delta = f\theta = m f_1 \theta, \quad (2.6.4)$$

hence  $\psi/\theta = m/\delta$ . Because  $\delta$  is generally of order unity, the chief ray angle at the focal surface is of order  $m$  larger than the incident chief ray angle.

If the secondary mirror is the aperture stop, then the exit pupil coincides with the stop. In this case  $\delta = mk$ , and  $\psi/\theta = 1/k$ , or again of order  $m$  because  $mk$  is usually of order unity in size.

### 2.6.c. EXAMPLES OF PUPILS

The importance of stops and pupils is especially evident when auxiliary optics following the telescope are used to improve overall image quality. In both of the examples discussed here, one or more optical elements reimages the exit pupil of

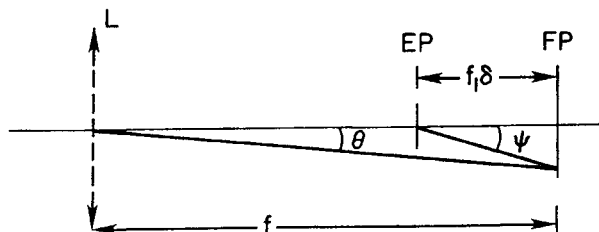


**Fig. 2.9.** Relation between incident and final chief ray angles,  $\theta$  and  $\psi$ , respectively, in two-mirror telescope. Here L is the lens of equivalent refractor, EP the exit pupil, FP the focal plane. See Eq. (2.6.4).

the telescope on to an optical element whose main function is improvement of the image quality. Generally there are additional optical requirements for these optical elements, but these are not relevant to our discussion of pupils.

The most dramatic example of the improvement of image quality was the “fix” of the spherical aberration (SA) present in the images produced by the Hubble Space Telescope (HST) when it was launched in 1990. We will discuss this aberration and the nature of the optical fix in detail in subsequent chapters; at this stage we consider only the role played by pupils in the fix.

The SA present in the HST images was attributed to a primary mirror that had been incorrectly figured. Although the mirror is of superb quality, its shape is less curved than that of the optical prescription, with the maximum difference of about  $2\mu$  at the edge of the mirror. The approach adopted to compensate for this error was to place a pair of mirrors (we will call them M1 and M2) into the converging beam near the telescope focus and to make M2 with a corresponding difference, but more curved rather than less. Each point on mirror M2 must be in one-to-one correspondence with a point on the primary, hence must be located at a pupil. The purpose of mirror M1 is to reimage the exit pupil of the telescope on to M2, that is, the exit pupil of the HST is the object for M1 with the image placed on M2.

Another example showing the importance of pupils occurs in the case of *adaptive optics*, the compensation in realtime of the degrading effects of the Earth’s atmosphere on starlight passing through it. (A discussion of the principles of adaptive optics follows in later chapters.) At this point we simply point out that the light reaching the primary mirror of a ground-based telescope is distorted by the atmosphere in a random way on a timescale of milliseconds. Although this mirror may be capable of producing a near-perfect image, to the remaining optics in the telescope it is as if the light from the primary is coming from a “rubber” mirror with everchanging shape on a small scale. The “fix” in this case is auxiliary optics that must reimage the telescope exit pupil on to a flexible mirror, sense and measure the distortion in the incoming light, and transmit the distortion to the flexible mirror in a reversed form to effect compensation.

These two examples are really quite similar. In both cases the exit pupil is reimaged on to a mirror that compensates for a distortion preceding it in the optical train. The major difference is that the correction is static in one case and dynamic in the other.

## 2.7. CONCLUDING REMARKS

The material in this chapter, based as it is on paraxial optics, is only an introduction to a much larger subject area. We have included topics deemed

essential for further discussion of telescopes and auxiliary instruments used with them, but left out topics such as principal planes, nodal points, and the methods of ray tracing. Any of the intermediate texts listed in the following bibliography should be consulted for an all-inclusive look into ray optics. A thorough presentation of the exact tracing of rays through an optical system is given by Welford (1986).

Our discussion of two-mirror telescopes is also only a beginning into an analysis of telescopes generally. We limited our presentation to an introduction of normalized parameters and their utility in describing the properties of two broad classes of two-mirror telescopes. In the following chapters we will go into much more detail, especially on aberrations and image characteristics of many types of telescopes within these classes, as well as for other types. Thorough discussions of the properties of telescopes are given by Wilson (1996) at an advanced level and by Rutten and van Venrooij (1988) at an intermediate level.

## BIBLIOGRAPHY

### *Intermediate-level texts in optics*

- Hecht, E. (1987). *Optics*, second edition, Reading, MA: Addison-Wesley.  
Jenkins, F. and White, H. (1976). *Fundamentals of Optics*, fourth edition, New York: McGraw-Hill.  
Longhurst, R. (1967). *Geometrical and Physical Optics*, second edition, New York: John Wiley.  
Pedrotti, F. and Pedrotti, L. (1993). *Introduction to Optics*, second edition, Englewood Cliffs, NJ: Prentice-Hall.

### *Advanced texts in optics*

- Born, M. and Wolf, E. (1980). *Principles of Optics*, sixth edition, Oxford: Pergamon.  
Ghatak, A. and Thyagarajan, K. (1978). *Contemporary Optics*, New York: Plenum.

### *Texts on telescope optics*

- Rutten, H. and van Venrooij, M. (1988). *Telescope Optics*, Richmond, VA: Willmann-Bell.  
Wilson, R. (1996). *Reflecting Telescope Optics I*, Berlin: Springer.

### *Discussion of ray-tracing in a form suitable for constructing a computer program*

- Welford, W. (1986). *Aberrations of the Symmetrical Optical System*, second edition, London: Academic Press.

A very powerful method in dealing with geometrical optics, the analysis of optical systems by tracing rays, is a principle ascribed to Fermat. For a single plane reflecting or refracting surface it states that the actual path that a light ray follows, from one point to another via the surface, is one for which the time required is a minimum. For this particular case, Fermat's Principle can be called the *principle of least time*.

Although the principle as stated here is correct for a single surface, it must be modified for application to a general optical system. In its modern form Fermat's Principle states that the actual path that a ray follows is such that the time of travel between two fixed points has a stationary value with respect to small changes of that path. In other words, the path of a ray from one point to another is such that the time taken has no more than an infinitesimal difference of second order from the time taken in traveling along other closely adjacent paths between the same points. Hence, to a first approximation, the travel time of the actual ray is equal to that along a closely adjacent path.

We first look at some of the consequences of this statement from a general point of view. The discussion involving calculus of variations can be skipped on a first reading, though results derived for the atmosphere are important for observations with ground-based telescopes. In subsequent sections we look at a number of other specifics that follow from this principle.

### 3.1. FERMAT'S PRINCIPLE IN GENERAL

The simplest case illustrating Fermat's Principle is shown in Fig. 3.1. A surface  $\Sigma$  lies between two points,  $P_0$  and  $P_1$ , with a ray joining these points consisting of straight line segments. The solid line is the actual ray path and the dashed line some other path. If the time of travel from  $P_0$  to  $P_1$  is denoted by  $\tau$ , then the condition that  $\tau$  have a stationary value for the actual path is

$$\partial\tau/\partial x = \partial\tau/\partial y = 0, \quad (3.1.1)$$

where  $x, y$  are the generalized coordinates of the point where the ray intersects the surface.

An equivalent statement of Fermat's Principle is obtained by replacing the words *time of travel* with *optical path length*. If  $dt$  is an infinitesimal time of travel, then  $cdt$  is the corresponding optical path length, where  $c$  is the velocity of light in vacuum. The *optical path length* (hereafter denoted by OPL) is expressed in terms of the geometrical path length and index of refraction as follows:

$$\begin{aligned} d(\text{OPL}) &= c dt = (c/v)v dt = n ds, \\ \text{OPL} &= c \int dt = \int n ds, \end{aligned} \quad (3.1.2)$$

where  $v$  is the speed of light in the medium of index  $n$ . The general statement of Fermat's Principle is either  $\delta\tau = 0$  or  $\delta(\text{OPL}) = 0$ , where  $n$  can be a function of all the coordinates that specify the position.

We now consider the two-dimensional (2D) case where the index of refraction  $n = n(y, z)$  and  $ds = \sqrt{dy^2 + dz^2}$ . Letting  $y' = dy/dz$ , Fermat's Principle gives

$$\delta \int_{P_0}^{P_1} n(y, z) \sqrt{1 + y'^2} dz = 0, \quad (3.1.3)$$

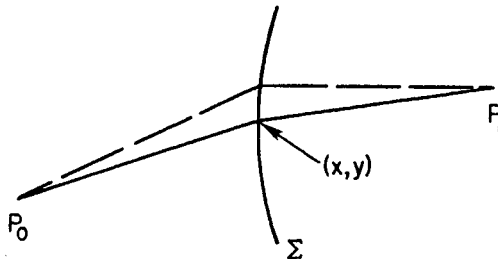


Fig. 3.1. Possible ray paths through interface between different optical media.

where  $ds$  has been replaced by  $dz\sqrt{(1+y'^2)}$ . Letting  $F(y, y', z)$  represent the integrand in Eq. (3.1.3) we get

$$\delta \int_{P_0}^{P_1} F(y, y', z) dz = \int_{P_0}^{P_1} \delta F(y, y', z) dz = 0, \quad (3.1.4)$$

where

$$\delta F = \frac{\partial F}{\partial y} \delta y + \frac{\partial F}{\partial y'} \delta y' = \frac{\partial F}{\partial y} \delta y + \frac{\partial F}{\partial y'} \frac{d}{dz} (\delta y).$$

Substituting for  $\delta F$  in Eq. (3.1.4) and integrating the term containing  $y'$  by parts, we get

$$\int_{P_0}^{P_1} \frac{\partial F}{\partial y} \delta y dz + \frac{\partial F}{\partial y'} \delta y \Big|_{P_0}^{P_1} - \int_{P_0}^{P_1} \frac{d}{dz} \left( \frac{\partial F}{\partial y'} \right) \delta y dz = 0. \quad (3.1.5)$$

The second term in Eq. (3.1.5) is zero because  $\delta y$  is zero at the endpoints. Therefore we can write Eq. (3.1.5) as

$$\int_{P_0}^{P_1} \left[ \frac{\partial F}{\partial y} - \frac{d}{dz} \left( \frac{\partial F}{\partial y'} \right) \right] \delta y dz = 0.$$

This expression must vanish for an arbitrary  $\delta y$  and therefore

$$\frac{\partial F}{\partial y} - \frac{d}{dz} \left( \frac{\partial F}{\partial y'} \right) = 0, \quad (3.1.6)$$

which is the equation required to satisfy Fermat's Principle.

We now take Eq. (3.1.6), replace  $F$  with the expression it represents, and carry out the differentiations indicated. As noted following Eq. (3.1.3) we have  $F = n(y, z)\sqrt{(1+y'^2)}$ . Noting that  $y'$  is not an explicit function of  $y$ , nor is  $n$  a function of  $y'$ , we get

$$\begin{aligned} & \sqrt{(1+y'^2)} \frac{\partial n}{\partial y} - \frac{d}{dz} \left[ \frac{ny'}{\sqrt{(1+y'^2)}} \right] \\ &= \sqrt{(1+y'^2)} \frac{\partial n}{\partial y} - n \frac{d}{dz} \left[ \frac{y'}{\sqrt{(1+y'^2)}} \right] - \frac{y'}{\sqrt{(1+y'^2)}} \frac{dn}{dz} = 0. \end{aligned} \quad (3.1.7)$$

Although Eq. (3.1.7) is a rather formidable equation in appearance, it is easily simplified after making some trigonometric substitutions. Figure 3.2 shows a

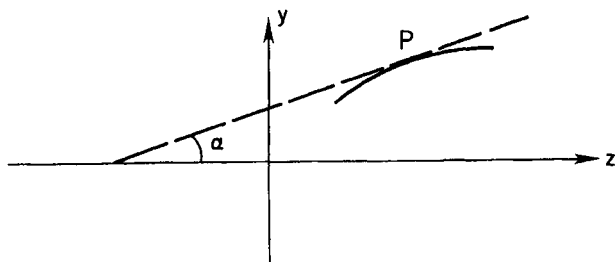


Fig. 3.2. Small segment of curved ray path in inhomogeneous medium. Dashed line is tangent to ray at point  $P$ .

segment of the ray path with the dashed line tangent to the path at point  $P$ . At this point

$$\begin{aligned} \tan \alpha &= \frac{dy}{dz} = y', & \sin \alpha &= \frac{dy}{ds} = \frac{y'}{\sqrt{(1+y'^2)}}, \\ \cos \alpha &= \frac{dz}{ds} = \frac{1}{\sqrt{(1+y'^2)}}, & \frac{d}{dz} \sin \alpha &= \cos \alpha \frac{d\alpha}{dz}. \end{aligned} \quad (3.1.8)$$

Using Eqs. (3.1.8) and noting that

$$\frac{dn}{dz} = \frac{\partial n}{\partial z} + y' \frac{\partial n}{\partial y'}$$

we write Eq. (3.1.7) as

$$\cos \alpha \frac{\partial n}{\partial y} - \sin \alpha \frac{\partial n}{\partial z} - n \cos \alpha \frac{d\alpha}{dz} = 0. \quad (3.1.9)$$

As a final item we note that the curvature  $\kappa$  of a path in space is defined as

$$\kappa = \frac{d\alpha}{ds} = \frac{d\alpha}{dz} \frac{dz}{ds} = \cos \alpha \frac{d\alpha}{dz}.$$

Substitution of this result into Eq. (3.1.9) gives

$$n\kappa = n \cos \alpha \frac{d\alpha}{dz} = \cos \alpha \frac{\partial n}{\partial y} - \sin \alpha \frac{\partial n}{\partial z}. \quad (3.1.10)$$

The result in Eq. (3.1.10) gives the local curvature of a light ray subject to Fermat's Principle in a medium in which the index of refraction is a smoothly varying function of position. Note that this relation applies to a ray in the  $yz$ -plane with  $n = n(y, z)$ .

As a special case of Eq. (3.1.10), assume that index  $n$  is constant. In this case the partial derivatives on the right side of Eq. (3.1.10) are zero and hence the curvature is zero. Thus the path of a light ray in a homogeneous medium is a straight line.

We now apply these results in turn to optical surfaces separating homogeneous media, such as air and glass, and to one inhomogeneous medium, the Earth's atmosphere.

### 3.2. FERMAT'S PRINCIPLE AND REFRACTING SURFACES

In this section we consider several examples of refracting surfaces and approach them from the point of view of Fermat's Principle. In doing this we will rederive some of the results of Chapter 2 as well as find some new ones. For all of the cases discussed we assume that homogeneous media are separated by a surface across which the index changes abruptly.

#### 3.2.a. LAWS OF REFRACTION AND REFLECTION

Fermat's Principle can be used to derive Snell's law at a plane interface where the index changes from  $n$  to  $n'$ , as shown in Fig. 3.3. For this situation the condition that the path is stationary is, from Eq. (3.1.2), given by

$$\delta \left[ n \int_{P_1}^{P_0} ds + n' \int_{P_0}^{P_2} ds \right] = 0,$$

which, upon evaluation of the integrals, gives

$$\delta \left\{ n \sqrt{(z_1^2 + y_0^2)} + n' \sqrt{[z_2^2 + (y_2 - y_0)^2]} \right\} = 0. \quad (3.2.1)$$

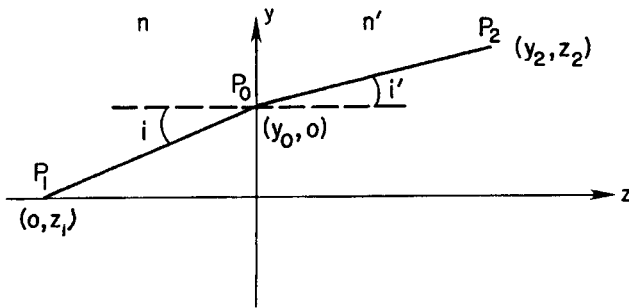


Fig. 3.3. Ray through plane interface between two homogeneous media with different indices of refraction.

This is, as expected, simply the sum of two optical lengths. Our variable is  $y_0$  and differentiating Eq. (3.2.1) gives

$$\left\{ n \frac{d}{dy_0} \sqrt{(z_1^2 + y_0^2)} + n' \frac{d}{dy_0} \sqrt{[z_2^2 + (y_2 - y_0)^2]} \right\} \delta y_0 = 0.$$

The expression in braces in this relation is independent of  $\delta y_0$ , and therefore we set the expression equal to zero. Doing the differentiation gives

$$n \frac{y_0}{\sqrt{(z_1^2 + y_0^2)}} - n' \frac{y_2 - y_0}{\sqrt{[z_2^2 + (y_2 - y_0)^2]}} = 0. \quad (3.2.2)$$

Examination of Fig. 3.3 shows that the factors multiplying  $n$  and  $n'$  are  $\sin i$  and  $\sin i'$ , respectively, and hence Eq. (3.2.2) is simply Snell's law of refraction,  $n \sin i = n' \sin i'$ . The law of reflection follows directly if we let  $n' = -n$ , in which case we also have  $i' = -i$ .

The nature of this stationary condition can be examined further by differentiating Eq. (3.2.2) with respect to  $y_0$  and looking at the sign of the result. Because the sign is positive, the path taken by the ray in going from one fixed point to another is such that its time of travel or OPL is a minimum.

### 3.2.b. SPHERICAL INTERFACE

Although we have already derived the paraxial equation for refraction at a spherical interface in Section 2.2, we will repeat the exercise using Fermat's Principle. The spherical surface separating two homogeneous media, along with conjugate points  $B$  and  $B'$ , is shown in Fig. 3.4. With due regard for signs according to the Cartesian convention, the optical length  $L$  from  $B$  to  $B'$  via point  $P$  is given by  $L = -nl + n'l'$ , where from the law of cosines

$$l = -\sqrt{R^2 + (R - s)^2 - 2R(R - s) \cos \phi},$$

$$l' = \sqrt{R^2 + (s' - R)^2 + 2R(s' - R) \cos \phi}.$$

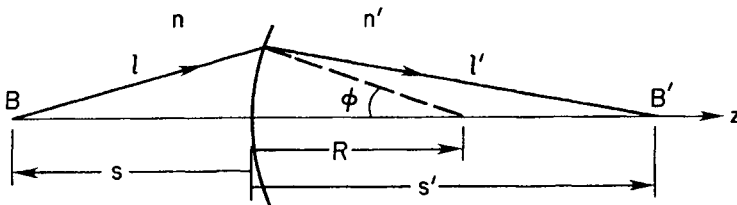


Fig. 3.4. Refraction at spherical interface.

Substituting  $l$  and  $l'$  into  $L$ , we have an expression in which  $\phi$  is the variable. We apply Fermat's Principle and find the stationary condition by setting  $dL/d\phi = 0$ . This gives

$$\frac{dL}{d\phi} = -\frac{nR(R-s)\sin\phi}{l} - \frac{n'R'(s'-R)\sin\phi}{l'} = 0. \quad (3.2.3)$$

In the paraxial limit  $l = s$  and  $l' = s'$ . Substitution of these into Eq. (3.2.3) immediately leads to Eq. (2.2.5).

### 3.2.c. FOCAL LENGTH OF THIN LENS

As an example of a slightly more complex system, we use Fermat's Principle to find the focal length of a thin lens of index  $n$ , with radii of curvature  $R_1$  and  $R_2$  as shown in Fig. 3.5.

To find the focal length we make use of the fact that Fermat's Principle must apply to every ray between two conjugate points of a focusing system. For example, in Fig. 3.4 we see that a ray from  $B$  to  $B'$  along the  $z$ -axis must have an OPL that is stationary with respect to closely adjacent paths. But each of these adjacent paths is itself stationary, hence the OPL is the same along all paths between two conjugate points, at least to a first approximation, provided the rays pass through the system. Stated differently, *the OPL (or time of travel) between two conjugates of a perfect focusing system is neither a minimum nor a maximum.*

Returning to the thin lens shown in Fig. 3.5, we find the OPL for each of two rays. For the ray coincident with the  $z$ -axis we get

$$L_0 = [BO_1] + n[O_1O_2] + f',$$

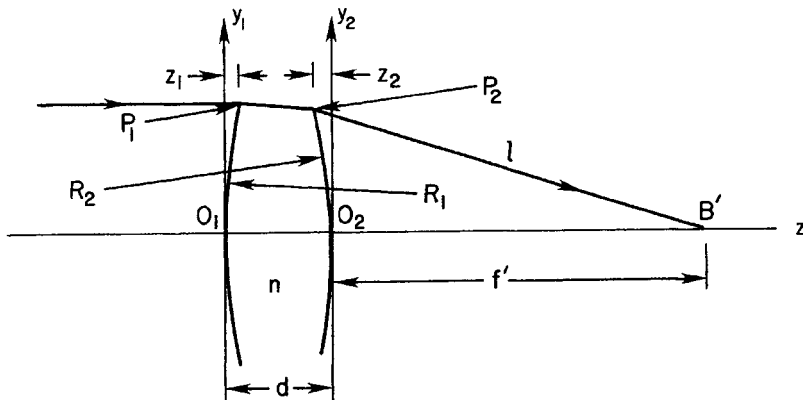


Fig. 3.5. Cross-section of thin lens (not to scale). By sign convention  $z_1 > 0$ ,  $z_2 < 0$ .

while for the ray at height  $y$  in the paraxial range

$$L_p = [BO_1] + z_1 + n[P_1P_2] - z_2 + l,$$

where  $z_2 < 0$  and  $l$  is measured from the  $y_2$  axis. Although the distance  $[BO_1]$  is infinite, this is of no consequence because on setting  $L_0$  equal to  $L_p$  this distance drops out, and we get

$$nd + f' = z_1 + n(d - z_1 + z_2) - z_2 + l. \quad (3.2.4)$$

In Eq. (3.2.4) we have substituted  $d = [O_1O_2]$ ,  $d - z_1 + z_2 = [P_1P_2]$ . Rearranging Eq. (3.2.4) leads to

$$l - f' = (n - 1)(z_1 - z_2). \quad (3.2.5)$$

The radii of curvature,  $R_1$  and  $R_2$ , are given by

$$\begin{aligned} R_1^2 &= y_1^2 + (R_1 - z_1)^2 = R_1^2 + y^2 - 2R_1z_1, \\ R_2^2 &= y_2^2 + (-R_2 + z_2)^2 = R_2^2 + y^2 - 2R_2z_2, \end{aligned}$$

where  $y_1 = y_2 = y$  for a thin lens in the paraxial range. In this approximation we get  $z_1 = y^2/2R_1$  and  $z_2 = y^2/2R_2$ .

From Fig. 3.5 we see that  $l^2 = y^2 + f'^2 = f'^2(1 + y^2/f'^2)$ . Taking the square root and using the binominal expansion gives  $l - f' = y^2/2f'$ . Taking these results, substituting for  $z_1$ ,  $z_2$ , and  $l - f'$  in Eq. (3.2.5), and canceling common factors gives

$$\frac{1}{f'} = (n - 1) \left( \frac{1}{R_1} - \frac{1}{R_2} \right),$$

a result already seen in Eq. (2.4.4). A similar approach can be used to find  $s$  and  $s'$  in terms of  $f'$ , an exercise left to the reader.

### 3.2.d. DISPERSING PRISM

As our final example in this section we consider a glass prism as shown in Fig. 3.6. Because  $n = n(\lambda)$  the angle of deviation  $\theta$  is also a function of  $\lambda$ , where  $\lambda$  is the wavelength of light. With rays incident as shown in Fig. 3.6, there is some wavelength whose rays in the prism follow paths parallel to the prism base. For these rays the diagram is symmetric about the vertical bisector of the prism, and hence  $s_1 = s_2 = s$ ,  $\varphi_1 = \varphi_2 = \varphi$ , and  $a_1 = a_2 = a$ .

Applying Fermat's Principle to this symmetric situation we get

$$2L \cos \varphi = nt, \quad (3.2.6)$$

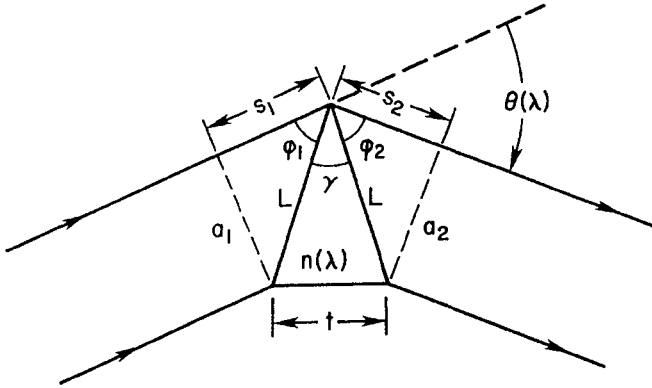


Fig. 3.6. Dispersing prism of base  $t$  and opposite angle  $\gamma$ .

where the left side of Eq. (3.2.6) is the OPL of the upper ray and the right side is the OPL of the lower ray in Fig. 3.6. We are interested in seeing how  $\theta$  changes with wavelength. Differentiating Eq. (3.2.6) with respect to wavelength gives

$$t \frac{dn}{d\lambda} = -2L \sin \varphi \frac{d\varphi}{d\lambda} = -2L \sin \varphi \frac{d\varphi}{d\theta} \frac{d\theta}{d\lambda}. \quad (3.2.7)$$

From Fig. 3.6 we see that  $L \sin \varphi = a$ ,  $\theta = \pi - \gamma - 2\varphi$ , from which we get  $d\varphi/d\theta = -1/2$ . Substituting into Eq. (3.2.7) we get

$$\frac{d\theta}{d\lambda} = \left( \frac{t}{a} \right) \frac{dn}{d\lambda}, \quad (3.2.8)$$

where  $t/a$  is the ratio of the base length to the beam width.

The index of refraction of most optical glasses can be expressed approximately in the form

$$n(\lambda) = A + (B/\lambda^2), \quad (3.2.9)$$

where  $A$  and  $B$  are constants. Differentiating Eq. (3.2.9) and combining with Eq. (3.2.8) we get

$$\frac{d\theta}{d\lambda} = -\left( \frac{2t}{a} \right) \left( \frac{B}{\lambda^3} \right). \quad (3.2.10)$$

The negative sign indicates that  $\theta$  decreases as  $\lambda$  increases, hence blue light is deviated more than red light. We also note that  $d\theta/d\lambda$ , *angular dispersion*, is numerically larger for shorter wavelengths.

## 3.3. WAVE INTERPRETATION OF FERMAT'S PRINCIPLE

Fermat's Principle is a statement about the behavior of light rays in terms of optical path length. The statement does not in any way make use of the fact that light is an electromagnetic wave capable of undergoing constructive and destructive interference. By treating light as a wave we can give a physical interpretation of Fermat's Principle in terms of destructive interference of waves

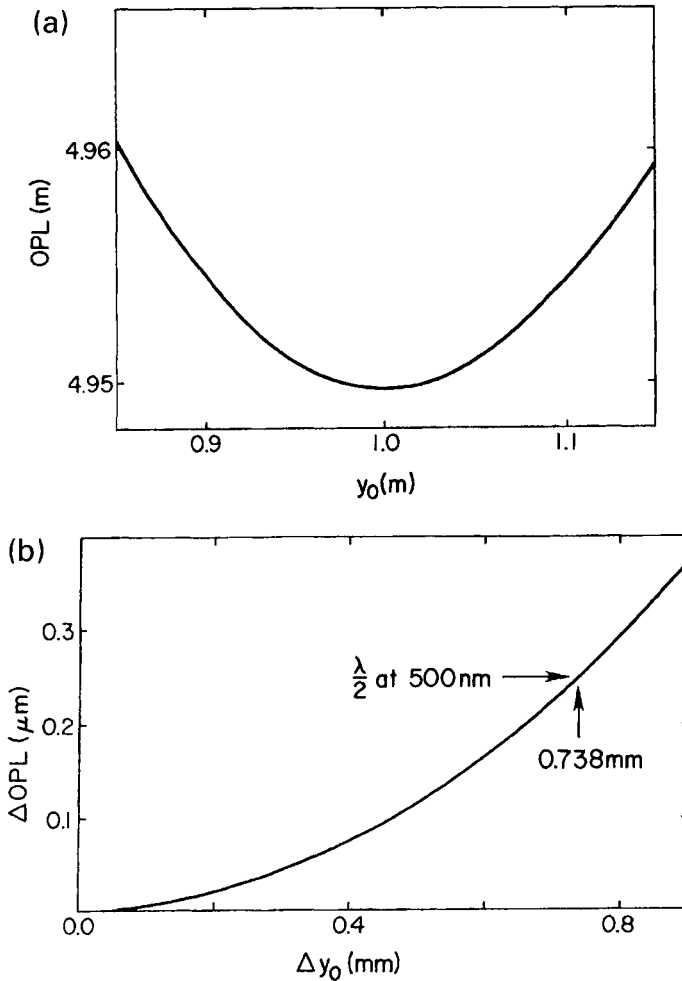


Fig. 3.7. (a) Optical path difference for ray in Fig. 3.3. See text, Section 3.3, for defined coordinates. (b) Greatly magnified view near minimum in (a).

following different paths. This is most easily done by means of a specific example.

If, in Fig. 3.3, we choose  $n = 1$ ,  $n' = \sqrt{5/2}$ , then the stationary path is that for which  $P_2$  is at  $(2, 2)$  when  $P_1$  is at  $(0, -1)$  and  $P_0$  is at  $(1, 0)$ . The optical path length between  $P_1$  and  $P_2$  is then a minimum. In order for another wave originating at  $P_1$  to reach  $P_2$  half a cycle after the wave following the minimum path, we need  $\Delta y_0$  of 1475 wavelengths for light of 500 nm, when the coordinates of the points are given in meters. One-half cycle difference for two waves corresponds to destructive interference.

Stated in another way, the extra path length introduced when  $y_0$  is changed by 1475 wavelengths (or 0.7375 mm) is only a half of a wavelength when the change is in the neighborhood of the stationary path. If, on the other hand, we choose  $P_0$  at  $(1.2, 0)$ , then the path from  $P_1$  to  $P_2$  is not a stationary one. In this case a half wavelength change in OPL is introduced when  $\Delta y_0$  is about 2.8 wavelengths. The variation in OPL as a function of  $y_0$  is shown in Fig. 3.7a,b.

Fermat's Principle can therefore be thought of as giving the path through which the highest transmission of light is possible. This path is the one that presents to the light waves the largest area without significant destructive interference for waves that pass through that area.

### 3.4. FERMAT'S PRINCIPLE AND REFLECTING SURFACES

The application of Fermat's Principle to a spherical refracting interface and thin lens in Section 3.2 gives results that apply in the paraxial domain. In these examples the surface shapes were specified (all spherical), with the result that the derived equations are strictly true only for paraxial rays. In this section on reflecting surfaces we adopt a different procedure and require that rays over the entire aperture satisfy Fermat's Principle. We then find the appropriate surface shape needed to satisfy this requirement.

#### 3.4.a. CONCAVE MIRROR, ONE CONJUGATE AT INFINITY

We first consider the concave mirror shown in Fig. 3.8. Parallel rays are incident from the left with all rays focused at a distance  $f$  from the mirror vertex. For convenience we let  $f$ ,  $l$ , and  $\Delta$  be positive quantities. Applying Fermat's Principle to a ray on the optical axis and a ray at height  $y$ , we see that equal OPLs require  $2f = l + (f - \Delta)$ , or  $l = f + \Delta$ .

From the geometry in Fig. 3.8 we see that

$$l^2 = y^2 + (f - \Delta)^2. \quad (3.4.1)$$

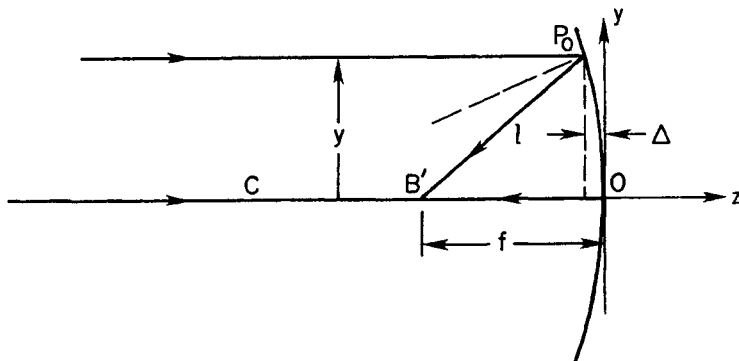


Fig. 3.8. Rays from distant point source incident on concave reflector, where  $l$  is the distance from  $P_0$  to  $B'$ . Image at  $B'$  is point for surface given by Eq. (3.4.3).

Eliminating  $l$  in Eq. (3.4.1) gives  $y^2 = 4f\Delta$ , which in terms of  $z$  is

$$y^2 = -4fz. \quad (3.4.2)$$

Equation (3.4.2) is the equation of a parabola whose vertex is at  $(0, 0)$ . The *paraboloid*, or paraboloidal surface of revolution, is obtained by rotating the parabola about the  $z$ -axis; its equation is found by replacing  $y^2$  by  $x^2 + y^2$ . Using Eq. (2.3.2) we can express  $f$  in terms of  $R$  which, upon applying the sign convention to  $R$ , gives

$$y^2 = 2Rz. \quad (3.4.3)$$

$R$  is the radius of curvature at the mirror vertex, and both  $R$  and  $z$  are negative in Fig. 3.8.

### 3.4.b. CONCAVE MIRROR, BOTH CONJUGATES FINITE

Figure 3.9 show a concave mirror with an object point at  $B$  and the corresponding image point at  $B'$ , both on the  $z$ -axis. Here we adopt the sign convention for  $s$  and  $s'$  at the outset, while choosing  $l$ ,  $l'$ , and  $\Delta$  as positive quantities. Given  $s$  and  $s' < 0$  in Fig. 3.9, the application of Fermat's Principle to the two rays leaving  $B$  gives

$$l + l' = -(s + s'),$$

$$l^2 = y^2 + (-s - \Delta)^2, \quad l'^2 = y^2 + (-s' - \Delta)^2.$$

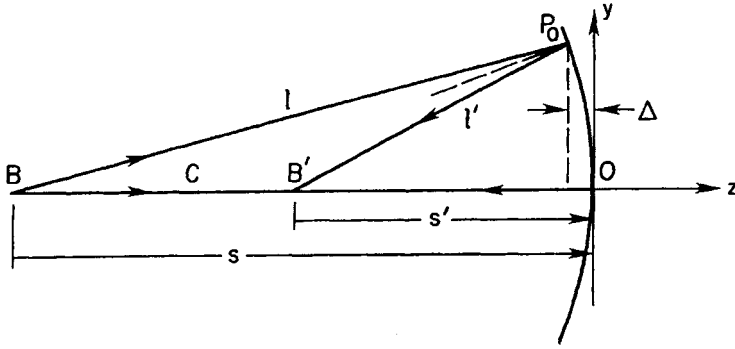


Fig. 3.9. Rays between conjugates at finite distances via concave reflector, where  $l(l')$  is the distance from  $P_0$  to  $B(B')$ . Imagery is perfect for surface given by Eq. (3.4.4).

Eliminating  $l$  and  $l'$  between these relations, and letting  $\Delta = -z$  as in Eq. (3.4.2), leads to the relation

$$y^2 - 4z \frac{ss'}{s+s'} + 4z^2 \frac{ss'}{(s+s')^2} = 0. \quad (3.4.4)$$

This is the equation for an ellipse with center  $(0, a)$ , with  $a$  and  $b$  the semimajor and semiminor axes, respectively. We can easily put Eq. (3.4.4) into the standard form of an ellipse equation if we choose  $2a = s + s'$ ,  $b^2 = ss'$ . The standard equation for an ellipse with center  $(0, a)$  is

$$\frac{(z-a)^2}{a^2} + \frac{y^2}{b^2} = 1,$$

which can be written as

$$y^2 - 2z \frac{b^2}{a} + z^2 \frac{b^2}{a^2} = 0. \quad (3.4.5)$$

The choice of  $a$  and  $b$  as given in the preceding follows directly from a comparison of Eqs. (3.4.4) and (3.4.5). It is not surprising that Fermat's Principle leads to an ellipse as the appropriate curve with the two conjugate points at the foci of the ellipse, considering the standard technique for drawing an ellipse with pencil, string, and two pins. A rotation of the ellipse about the  $z$ -axis gives an *ellipsoid*, with the surface equation given by Eq. (3.4.5) after replacing  $y^2$  by  $x^2 + y^2$ .

Note that the sphere is a special case of an ellipsoid in which  $s = s'$  and  $a = b$ . Note also that the parabola given by Eq. (3.4.2) is a special case of Eq. (3.4.4) in which  $s = \infty$  and  $s' = -f$ .

3.4.c. CONVEX MIRROR, BOTH CONJUGATES FINITE

Figure 3.10 shows a convex mirror with a virtual object point at  $B$  and the conjugate image point at  $B'$ , both on the  $z$ -axis. As with the ellipse, we adopt the sign convention for  $s$  and  $s'$  but choose  $l$ ,  $l'$ , and  $\Delta$  as positive quantities. The dashed arc in Fig. 3.10 is a circular arc whose center is at  $B$ . Applying Fermat's Principle to the two rays heading toward  $B$  gives

$$l + l' = 2s',$$

while the geometry of Fig. 3.10 gives

$$d^2 = y^2 + (-s - \Delta)^2, \quad l + d = s' - s, \quad l'^2 = y^2 + (s' + \Delta)^2.$$

Eliminating  $l$ ,  $l'$ , and  $d$  between these relations, and putting  $\Delta = -z$ , leads to

$$y^2 - 4z \frac{ss'}{s + s'} + 4z^2 \frac{ss'}{(s + s')^2} = 0, \tag{3.4.6}$$

an equation identical to Eq. (3.4.4). There is, however, an important difference between Eq. (3.4.4) and Eq. (3.4.6). In the former equation  $s$  and  $s'$  have the same sign because both conjugates are on the same side of the mirror vertex; in the latter equation  $s$  and  $s'$  have opposite signs. As is easily demonstrated, Eq. (3.4.6) is the equation of a hyperbola.

The standard equation for a hyperbola with a vertex at  $(0, 0)$  is

$$\frac{(z - a)^2}{a^2} - \frac{y^2}{b^2} = 1,$$

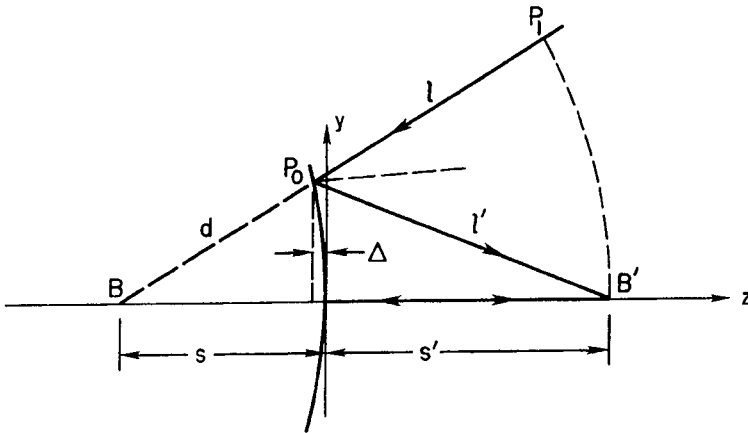


Fig. 3.10. Rays between conjugates at finite distances via convex reflector. Imagery is perfect for surface given by Eq. (3.4.6).

which can be rewritten as

$$y^2 + 2z \frac{b^2}{a} - z^2 \frac{b^2}{a^2} = 0. \quad (3.4.7)$$

Equations (3.4.6) and (3.4.7) agree if we choose  $b^2 = -ss'$ , and  $2a = s + s'$ . As before, the replacement of  $y^2$  by  $x^2 + y^2$  gives a *hyperboloid* of revolution about the  $z$ -axis.

The case of a convex mirror with one conjugate at infinity is left as an exercise for the reader. The appropriate surface for this situation is a paraboloid.

### 3.5. CONIC SECTIONS

Each of the surface cross sections derived in the preceding section is a conic section and it is therefore appropriate to find a single equation describing the family of such curves with the vertex at the origin. We proceed by working with Eq. (3.4.4) for an ellipse. From Eq. (2.3.1) we get

$$\frac{ss'}{s + s'} = \frac{R}{2}, \quad (3.5.1)$$

where this relation applies in the paraxial region, hence  $R$  is the vertex radius of curvature. For an ellipse the eccentricity  $e$  is defined as  $e = c/a$ , where  $c$  is the distance from one of the foci to the center of the ellipse and  $c^2 = a^2 - b^2$ . Substituting in terms of  $s$  and  $s'$  we get

$$1 - e^2 = \frac{4ss'}{(s + s')^2}, \quad e^2 = \frac{(s - s')^2}{(s + s')^2}. \quad (3.5.2)$$

Substituting Eqs. (3.5.1) and (3.5.2) into Eq. (3.4.4) gives

$$y^2 - 2Rz + (1 - e^2)z^2 = 0. \quad (3.5.3)$$

Although derived from the ellipse equation, the relation in Eq. (3.5.3) describes the family of conic sections, provided we choose  $e$  appropriately. In the literature one often sees a conic section described in terms of a *conic constant*  $K$ , where  $K = -e^2$ . In terms of both  $e$  and  $K$  the various conic sections are as follows:

oblate ellipsoid:	$e^2 < 0$	$K > 0$
sphere:	$e = 0$	$K = 0$
prolate ellipsoid:	$0 < e < 1$	$-1 < K < 0$
paraboloid:	$e = 1$	$K = -1$
hyperboloid:	$e > 1$	$K < -1$

In all of the discussion to follow, we use  $K$  to describe the conic sections. Rewriting Eq. (3.5.2) in terms of the magnification  $m$  by substituting Eq. (2.3.3) into Eq. (3.5.2) gives

$$K = -\frac{(m+1)^2}{(m-1)^2}. \quad (3.5.4)$$

Transforming Eq. (3.5.3) to get the equation for the surface of revolution gives

$$r^2 - 2Rz + (1+K)z^2 = 0, \quad (3.5.5)$$

where  $r^2 = x^2 + y^2$ .

At this point it is instructive to calculate  $R_{lc}$ , the *local radius of curvature* at a point  $(r, z)$  on the mirror surface. The relation for radius of curvature is

$$R_{lc} = (1 + z'^2)^{3/2} / z'',$$

where  $z' = dz/dr$ ,  $z'' = d^2z/dr^2$ . Solving Eq. (3.5.5) for  $z$  and carrying out the calculation gives

$$\begin{aligned} R_{lc} &= r[1 - K(r^2/R^2)]^{3/2} \\ &= R[1 - K(\varepsilon^2/16F^2)]^{3/2}, \end{aligned} \quad (3.5.6)$$

where  $F = |f|/D$  and  $r = \varepsilon D/2$ , with  $0 < \varepsilon < 1$ .

For  $K = 0$  we get  $R_{lc} = R$ , as expected. As we go through the family of conic surfaces from sphere to ellipsoid to paraboloid to hyperboloid, we see that  $R_{lc}$  gets progressively larger for a given  $r$  and  $R$ . Alternatively the *local curvature*,  $1/R_{lc}$ , gets progressively smaller. As the point on the surface approaches the vertex, hence  $r \rightarrow 0$ , we see that  $R_{lc} \rightarrow R$ . Near the vertex all of the surfaces have nearly the same shape and, in the paraxial approximation, are identical. We will return to a further discussion of Eq. (3.5.6) and its ramifications in the fabrication of large mirrors in Chapter 18.

In summary, then, we see that conic surfaces used as mirrors provide perfect imagery for a single pair of conjugates. A given conic mirror, however, will not strictly satisfy Fermat's Principle at any other pair of conjugates. As we will see, this failure to image a point into a point implies the presence of aberrations, a subject we explore in detail in subsequent chapters. In spite of this apparent limitation, the family of conic surfaces is the basis for most multi-mirror systems.

### 3.6. FERMAT'S PRINCIPLE AND THE ATMOSPHERE

In this section we consider some of the effects of the Earth's atmosphere, refraction and its variation with zenith angle and wavelength, and the effect of

time-varying index changes on the path of a light ray. Our discussion is only an introduction to further illustrate the utility of Fermat's Principle; more specifics on each of these topics will follow in subsequent chapters.

### 3.6.a. ATMOSPHERIC REFRACTION

Assume that the atmosphere is a flat, layered medium with the index  $n = n(z)$  only, hence the curvature of the atmosphere is neglected. In this case Eq. (3.1.10) becomes

$$nK = n \cos \alpha \frac{d\alpha}{dz} = -\sin \alpha \frac{dn}{dz}, \quad (3.6.1)$$

where the  $z$ -axis points toward the center of the Earth. The change in the index of the atmosphere from the top ( $n = 1$ ) to the surface ( $n = 1.00029$ ) is small, hence the path of a ray from a star is not deviated appreciably for  $\alpha$  not close to  $90^\circ$ . Integrating Eq. (3.6.1) with the assumption that  $\alpha$  is nearly constant, hence  $\cos \alpha$  and  $\sin \alpha$  brought out from the integral, gives

$$\delta\alpha = -\tan \alpha_0 \delta n = -(n - 1) \tan \alpha_0 \quad (3.6.2)$$

where  $\alpha_0$  is the angle of incidence at the top of the atmosphere, or *zenith angle*, and  $\delta n$  is the change in index.

For a ray passing downward through the atmosphere  $\delta n = (n - 1) > 0$ , and hence  $\delta\alpha < 0$ . Thus the angle the ray makes with the  $z$ -axis decreases as the ray proceeds down through the atmosphere, that is, the ray is bent "toward" the  $z$ -axis. That the effect is small is seen by taking, for example,  $\alpha_0 = 45^\circ$  and finding the ray deviation  $\delta\alpha = 0.00029$  radians or about 1 arc-min.

The index of refraction of the atmosphere is a function of wavelength, as shown by the entries in Table 3.1, hence the deviation  $\delta\alpha$  is not the same for different wavelengths. The parameter  $R_0$  in Table 3.1 is the *constant of refraction*, the index difference  $\delta n$  expressed in units of arc-seconds.

The change  $d(\delta\alpha)$  is the *differential atmospheric refraction*, with

$$d(\delta\alpha) = -\tan \alpha_0 d(\delta n) = -(n_2 - n_1) \tan \alpha_0 \quad (3.6.3)$$

and  $d(\delta n) = n_2 - n_1$ , the change in index between two wavelengths  $\lambda_2$  and  $\lambda_1$ . From the values in Table 3.1 we see that the index changes more rapidly at shorter wavelengths, hence differential refraction could adversely affect certain types of observations in the near ultraviolet at large zenith angle. As an example using the entries in Table 3.1,  $d(\delta\alpha)$  in arc-seconds is about  $1.38 \tan \alpha_0$  over the range from 320 to 400 nm, and  $2.48 \tan \alpha_0$  over the range from 320 to 550 nm. With  $\tan \alpha_0 \geq 1$ , for example, the visible image of a star centered on a small aperture could result in no ultraviolet light passing through the aperture.

Table 3.1

Index of Refraction of Atmosphere <sup>a</sup>		
$\lambda$ (nm)	$n - 1$	$R_0$ (arc-sec)
320	3.049E-4	62.86
400	2.982	61.48
550	2.929	60.38
700	2.907	59.93
1000	2.890	59.58

<sup>a</sup> Values of  $n$  from Allen (1973). Index given at  $T = 0^\circ\text{C}$ , pressure = 760 mm Hg, water vapor pressure = 4 mm Hg.

### 3.6.b. ATMOSPHERIC TURBULENCE

The assumption that  $n = n(z)$  neglects variations in index that are present in a turbulent atmosphere at constant height due primarily to temperature fluctuations. Consider a ray that enters the atmosphere from directly overhead, with the deviation of the ray from a vertical path denoted by  $\alpha$ . Assuming  $\alpha \ll 1$  we can write Eq. (3.1.10) as

$$n(\partial\alpha/\partial z) = \partial n/\partial y, \quad (3.6.4)$$

where the term in  $\sin \alpha$  is dropped because  $\alpha$  is small. Letting  $n = 1 + \delta n$ , Eq. (3.6.4) becomes (to first order)

$$\partial\alpha/\partial z = \partial(\delta n)/\partial y, \quad (3.6.5)$$

where  $\delta n$  is the fluctuation in the index of refraction from the local mean. In the general case there are corresponding equations in which  $x$  replaces  $y$ . Integrating Eq. (3.6.5) from the top of the atmosphere ( $z = 0$ ) through a distance  $s$  gives

$$\alpha_y(s) = \int_0^s [\partial(\delta n)/\partial y]_z dz. \quad (3.6.6)$$

The deviation given by Eq. (3.6.6) is, of course, a function of time, with random variations in time for  $\alpha_y$  and  $\alpha_x$ . Because  $\langle \delta n \rangle$  is zero, where  $\langle \rangle$  denotes an average over time, the time-averages of the deviations are also zero. The mean-square deviations, however, are not zero, and the net result is a ray that wanders randomly about a mean position.

The net effect of these variations leads to the phenomenon called *seeing*. In a small telescope the effect is seen as a star image in motion with excursions typically of a few arc-seconds. In a large telescope the cumulative effect of seeing is to give a blurred image with little or no motion of the image as a whole.

Although the approach using Fermat's Principle shows the origin of seeing effects, the statistical processes that lead to the effects described make it impractical to proceed further with this approach. Selected results based on a statistical approach to atmospheric turbulence are given in Chapter 16.

### 3.7. CONCLUDING REMARKS

#### 3.7.a. RAYS AND WAVEFRONTS

The application of Fermat's Principle to find conic surfaces that are perfect mirrors makes use of rays and optical path lengths. A different way of looking at what a focusing system does is in terms of wavefronts. A *wavefront* is simply a surface on which every point has the same optical path distance from a point source of light. In a homogeneous medium this surface is obviously a sphere whose center is the point object. In this same medium rays are radial lines directed outward, and at each point on a wavefront a ray is perpendicular to the wavefront. If a source is effectively at infinity, as for a star, then the resulting wavefront is plane.

Examples of wavefronts are shown in Fig. 3.11a,b, with a vertical chief ray at the center of each wavefront in this representation. The wavefront designated random is a plane wave plus point-by-point variations using a random number generator. This wavefront might, at least approximately, represent a plane wave after passing through a slightly turbulent atmosphere.

A perfect optical system that satisfies Fermat's Principle is one that converts a spherical wavefront centered on a point object (or plane wavefront for a distant object) to a spherical wavefront centered on the conjugate point image.

Conversely, if Fermat's Principle is not satisfied for all rays from a point object over a large aperture, then the wavefront converging toward the image is no longer spherical and the image has aberrations. The connection between ray and wavefront aberrations is established in the discussion in Chapter 5.

#### 3.7.b. HOW PERFECT IS "PERFECT"?

Fermat's Principle as used thus far is concerned only with rays and ignores the wave nature of light. Because of the wave character of light, no image is perfect in the sense that it is a point of infinitesimal size. The question to be addressed therefore, albeit not from a rigorous point of view here, is the minimum size of an image given an otherwise perfect optical system.

Consider an optical system  $L$  that is perfect according to Fermat's Principle, as shown schematically in Fig. 3.12. Light from two distant point sources,  $A$  and  $B$ ,

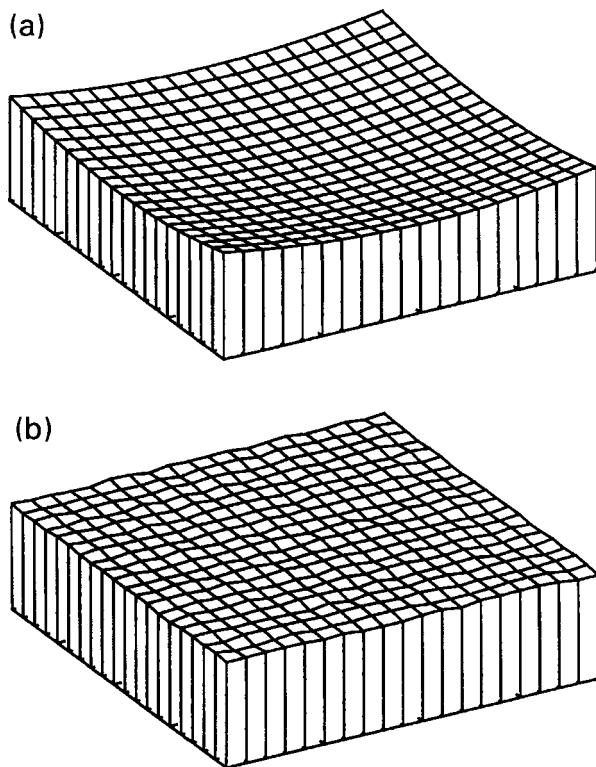
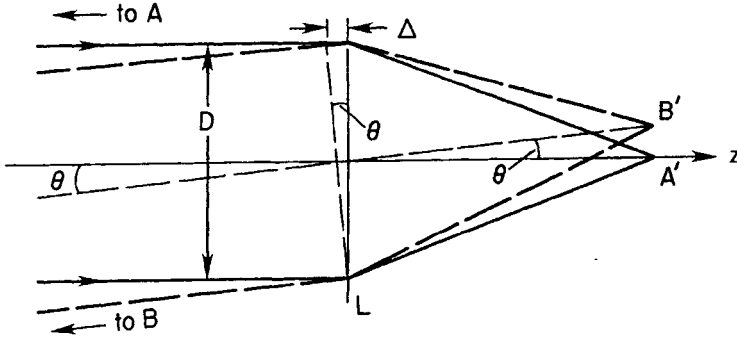


Fig. 3.11. Schematic diagrams of wavefronts: (a) spherical, (b) randomly distorted plane.

with angular separation  $\theta$ , fills the aperture of diameter  $D$ . According to wave theory, two image points cannot be resolved or separated if the difference in light-time travel of rays to them from opposite edges of the aperture is less than approximately one period of the wave. Equivalently, the points cannot be resolved if the *optical path difference*, or OPD, between these rays is less than approximately one wavelength. In Fig. 3.12 the OPD between these rays is  $\Delta$  with the resolution limit set by  $\Delta \approx \lambda$ . From the geometry we see that

$$\theta_{\min} \approx \lambda/D. \quad (3.7.1)$$

From the angular resolution limit in Eq. (3.7.1) we can infer that the individual images  $A'$  and  $B'$  must each have an angular diameter  $\theta \approx \lambda/D$ , as seen from  $L$ . If the angular diameter of each image was substantially smaller than  $\lambda/D$ , then the images would be resolved, contrary to the limit set by Eq. (3.7.1).



**Fig. 3.12.** Schematic of perfect optical system from which approximate diffraction limit is derived. See Eq. (3.7.1) and Section 3.7.

The reasoning used to arrive at Eq. (3.7.1) and an estimate of the minimum possible image size is not a rigorous procedure, nor does it tell how the light is distributed within the image. A more rigorous approach requires analysis using diffraction theory, a topic we consider in some detail in Chapter 10.

## REFERENCES

Allen, C. (1973). *Astrophysical Quantities*, third edition, Chap. 6, London: Athlone.

## BIBLIOGRAPHY

*Source of information on atmospheric refraction and seeing*

Stock, J. and Keller, G. (1960). *Stars and Stellar Systems I, Telescopes*, Chap. 9, Chicago: University of Chicago Press.

*Discussion of Fermat's Principle*

Born, M. and Wolf, E. (1980). *Principles of Optics*, sixth edition, Chap. 3, Oxford: Pergamon.

Hecht, E. (1987). *Optics*, second edition, Chap. 4, Reading, MA: Addison-Wesley.

Mahajan, V. (1998). *Optical Imaging and Aberrations, Part I, Ray Geometrical Optics*, Chap. 1, Bellingham, WA: SPIE Optical Engineering Press.

Thus far our discussion of optical systems has proceeded along two different lines. In Chapter 2 we developed the paraxial equations for spherical refracting and reflecting surfaces, and noted that in the paraxial limit there is a one-to-one correspondence between object and image point. In Chapter 3 we turned our attention to Fermat's Principle and reflecting surfaces of conic cross section. Our analysis led to the result that for a given pair of conjugate object and image points there is a conic surface that gives a perfect image, independent of the paraxial approximation.

In this chapter we begin to examine what happens when Fermat's Principle is not strictly satisfied in the range outside of the paraxial approximation. We will see that the geometrical image in this case is no longer a point but becomes a blur. An optical system that produces a blurred image, where the blur is in addition to the diffraction blur noted in Section 3.7, is a system with aberrations.

To illustrate the onset of aberrations we consider a very simple optical system, a single conic mirror. After calculating the aberrations of several such mirrors for selected object points, we introduce the topic of aberration compensation. By this we mean that the aberrations of one optical element can be offset, wholly or partially, by those of another element. The two systems considered in this chapter are the Schmidt camera and the family of Cassegrain telescopes. This discussion is only an introduction; a more complete description of aberrations and compensation follows in Chapter 5.

## 4.1. REFLECTING CONICS AND FOCAL LENGTH

We begin by calculating the focal length of a concave mirror or, more specifically, the distance from the mirror vertex to the point where a reflected ray from a distant object intersects the optical axis. Figure 4.1 shows a ray parallel to the optical axis striking a mirror at height  $r$ , where  $r$  is defined by Eq. (3.5.5). Contrary to our normal convention, the light from the object proceeds from right to left, a choice made for convenience. With this choice distances to the right of the mirror vertex measured along the  $z$ -axis are positive. We also take the angle  $\phi$  in Fig. 4.1 positive when  $r > 0$ .

From the geometry of Fig. 4.1 we see that  $f = z + z_0$ , where

$$z_0 = \frac{r}{\tan 2\phi} = \frac{r(1 - \tan^2 \phi)}{2 \tan \phi}. \quad (4.1.1)$$

From Fig. 4.1 we also note that  $\tan \phi$  is simply  $dz/dr$ , the negative of the slope of the normal to the mirror.

From Eq. (3.5.5) we find the relation

$$\frac{dz}{dr} = \frac{r}{R - (1 + K)z} = \tan \phi.$$

Substituting this into Eq. (4.1.1) gives

$$z_0 = \frac{r}{2} \left[ \frac{R - (1 + K)z}{r} - \frac{r}{R - (1 + K)z} \right]. \quad (4.1.2)$$

Putting Eq. (4.1.2) into  $f = z + z_0$  gives

$$f = \frac{R}{2} + \frac{(1 - K)z}{2} - \frac{r^2}{2(R - (1 + K)z)}. \quad (4.1.3)$$

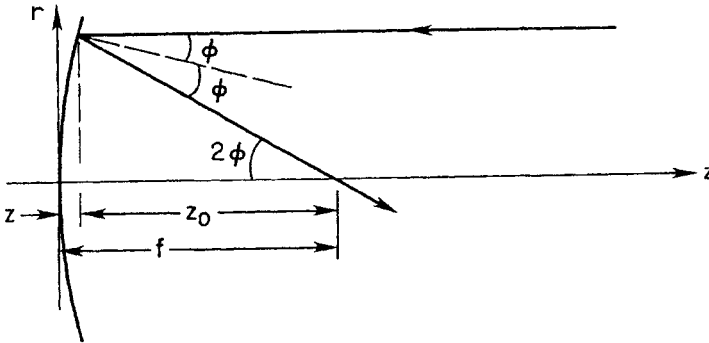


Fig. 4.1. Geometry of ray from distant object reflected from concave mirror.

Because the surface equation (3.5.5) is quadratic in  $z$ , the solution for  $z$  contains a square root, as will Eq. (4.1.3) when  $z$  is eliminated. We proceed, therefore, by expanding the square root as a power series in small quantities before substituting into Eq. (4.1.3). Solving Eq. (3.5.5) for  $z$  gives

$$\begin{aligned} z &= \frac{R}{1+K} \left[ 1 - \left( 1 - \frac{r^2}{R^2} (1+K) \right)^{1/2} \right] \\ &= \frac{r^2}{2R} + (1+K) \frac{r^4}{8R^3} + (1+K)^2 \frac{r^6}{16R^5} + \dots \end{aligned} \quad (4.1.4)$$

Substituting Eq. (4.1.4) into Eq. (4.1.3) gives

$$f = \frac{R}{2} - \frac{(1+K)r^2}{4R} - \frac{(1+K)(3+K)r^4}{16R^3} - \dots \quad (4.1.5)$$

Examination of Eq. (4.1.5) shows that  $f = R/2$  for  $K = -1$ , a paraboloid. Although higher power terms are not included in Eq. (4.1.5), this statement about a paraboloid is true when all terms are included. This is easily verified by setting  $K = -1$  prior to making the foregoing substitutions.

For a sphere or ellipsoid the conic constant  $K > -1$  and  $f < R/2$ , while for a hyperboloid  $f > R/2$ . As expected, Fermat's Principle is strictly satisfied, hence  $f$  is constant for any  $r$ , only for a paraboloid when the object is at infinity. For any other conic the change in focal length  $\Delta f$  as a function of  $r$  is

$$\Delta f = f(r) - f(\text{paraxial}) = -\frac{(1+K)r^2}{4R} - \frac{(1+K)(3+K)r^4}{16R^3} - \dots \quad (4.1.6)$$

Thus for any conic surface other than a paraboloid the image of a distant object on the optical axis is blurred. Examination of Eq. (4.1.6) shows that  $\Delta f$  is independent of the sign of  $r$ , hence the blur is symmetric about the  $z$ -axis. Note also that a change in the sign of  $R$  changes the sign of  $\Delta f$ , as it should.

## 4.2. SPHERICAL ABERRATION

We now examine in detail the nature of the aberration for the case of an object on the optical axis, an aberration called *spherical aberration*. Of particular interest is the size of the blur, measured perpendicular to the optical axis, at or near the paraxial focus.

### 4.2.a. TRANSVERSE AND LONGITUDINAL

We define the *transverse spherical aberration* (TSA), as the intersection of a ray from height  $r$  on the mirror with the paraxial focal plane, as shown in Fig. 4.2.

It is conventional to define the longitudinal spherical aberration (LSA), as the distance from the paraxial focal plane to the point where a ray from height  $r$  crosses the  $z$ -axis. In Fig. 4.2 we see that LSA is simply  $\Delta f$ . From similar triangles there we find

$$\text{TSA}/\text{LSA} = r/(f - z),$$

where both TSA and LSA are negative in Fig. 4.2. Using Eqs. (4.1.4)–(4.1.6), applying the binomial expansion, and retaining all terms through fifth order, gives

$$\text{TSA} = -(1 + K) \frac{r^3}{2R^2} - 3(1 + K)(3 + K) \frac{r^5}{8R^4} + \dots \quad (4.2.1)$$

Each term is designated according to the power of  $r$ . The first term is the third-order transverse spherical aberration (TSA3); the second term is fifth-order transverse spherical aberration (TSA5). For  $K = 0$ , a spherical surface, each term in Eq. (4.2.1) is negative for  $r > 0$ , and positive for  $r < 0$ . The sign of TSA indicates where a given ray crosses the paraxial focal plane, in accord with the sign convention established for distances measured perpendicular to the  $z$ -axis. Because of the presence of the factor  $(1 + K)$  in Eq. (4.2.1), the sign of TSA for a hyperboloid is opposite that for a sphere or ellipsoid. Note also that the sign of TSA is independent of the sign of  $R$ .

The relative size of the two terms in Eq. (4.2.1) for rays from the edge of the aperture is given by

$$\frac{\text{TSA5}}{\text{TSA3}} = \frac{3(3 + K)r^2}{4R^2} = \frac{3(3 + K)}{64F^2},$$

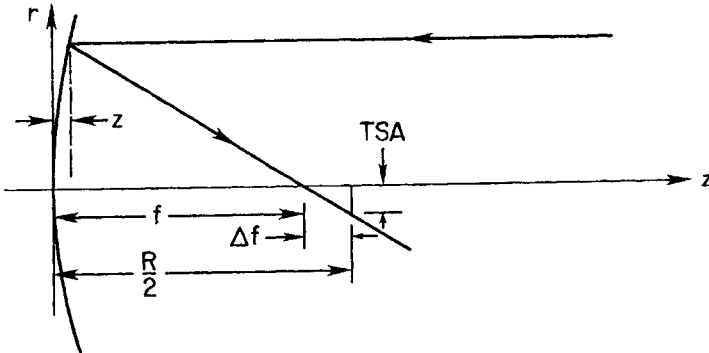


Fig. 4.2. Transverse spherical aberration (TSA) at paraxial focus. See Eqs. (4.1.6) and (4.2.1).

where  $F$  is the focal ratio. For a sphere TSA5 is 10% of TSA3 when  $F = 1.19$ . Thus it is sufficient to neglect the TSA5 term for all but very fast mirrors, that is, those with small focal ratios.

We can also find the spherical aberration for the case shown in Fig. 4.2 by working directly with surface equations, one for a paraboloid and one for a surface with conic constant  $K$ . From Eq. (4.1.4) we find the difference between the surfaces, through terms in  $r^4$ , given by

$$\Delta z = z_p - z(K) = -(1 + K) \frac{r^4}{8R^3} - \dots, \quad (4.2.2)$$

where the subscript  $p$  denotes the paraboloid. From Fig. 4.3 we see that the path difference between two rays, one incident on the paraboloid and one on the other surface at the same height, is approximately  $2 \Delta z$ , provided the angles  $\phi$  and  $\phi_p$  are small.

We also see from Fig. 4.3 that the directions of the reflected rays differ by  $2(\phi_p - \phi)$ , where  $\phi = dz/dr$ ,  $\phi_p = dz_p/dr$ , in the paraxial approximation. From Eq. (4.1.4) we find

$$2(\phi_p - \phi) = \frac{d}{dr}(2 \Delta z) = -(1 + K) \frac{r^3}{R^3}. \quad (4.2.3)$$

We now relate this difference in ray directions to TSA.

#### 4.2.b. ANGULAR

This difference in direction between the reflected rays is the *angular spherical aberration* (ASA). Because Eq. (4.2.3) is only taken to third order, it is appropriate to say ASA3 for the difference in direction given in Eq. (4.2.3).

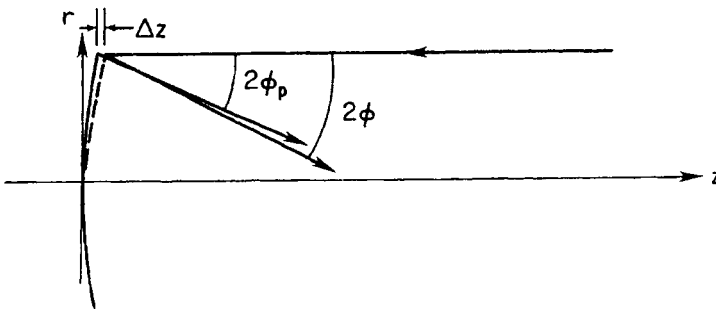


Fig. 4.3. Path difference between ray reflected from paraboloid (solid curve) and conic (dashed curve). Size of  $\Delta z$ , given in Eq. (4.2.2), is greatly exaggerated in the diagram.

From the geometry in Fig. 4.4 we see directly the relation between transverse and angular aberration, which is

$$\text{TSA3} = (R/2)(\text{ASA3}) = -(1 + K) \frac{r^3}{2R^2}, \quad (4.2.4)$$

where, as before, we assume the angle  $\phi_p$  is not too large. This result is the same as the first term in Eq. (4.2.1).

We need to review briefly the steps taken in arriving at Eq. (4.2.4) and the approximations used. In stating that the path difference between the two rays is  $2\Delta z$ , we replaced any cosine factors present in the exact difference by unity. In effect, we used the paraxial approximation in making this statement. The same approximation was made in writing the relation between TSA3 and ASA3 in Eq. (4.2.4). This approximation is quite good, even for a mirror as fast as  $f/2$ . In this case we find  $\tan \phi = 0.25$  and  $\cos \phi = 0.97$ , hence our third-order result is accurate to a few percent. If we wanted to use the same method to find the fifth-order term, we could not use the paraxial approximation but would need to retain higher power terms in the expansions of tangents and cosines of angles. But, as already noted, third-order aberration results suffice for reflecting surfaces in most optical systems.

The procedure followed to get the third-order result in Eq. (4.2.4) can be generalized to any pair of object and image conjugates. All that is needed is  $\Delta z$ , the difference between the reflecting surface that images that object without aberration and the actual surface, with the paraxial approximation used in the same way as in the preceding. The relations are

$$\text{ASA3} = \frac{d}{dr}(2\Delta z), \quad \text{TSA3} = s' \frac{d}{dr}(2\Delta z). \quad (4.2.5)$$

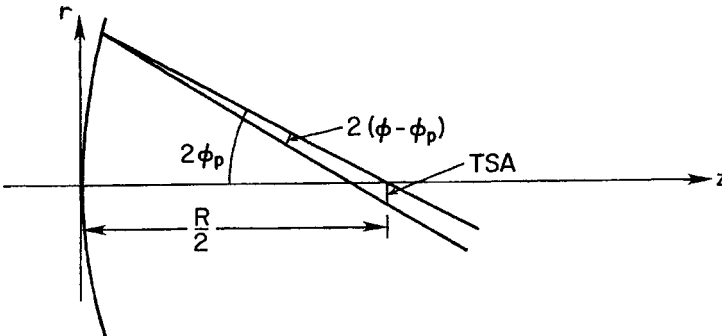


Fig. 4.4. Relation between TSA and angular difference between ray paths after reflection. See Eq. (4.2.3).

Equations (4.2.5) apply specifically to reflecting surfaces in air in which the mirror is oriented as shown in Fig. 4.1. In general the optical path difference, which includes the index of refraction, is required by Fermat's Principle and the calculation of  $\Delta z$ . The more general discussion of Eq. (4.2.5), including the index of refraction, is given in Chapter 5.

The importance of the procedure outlined in the paragraph preceding Eq. (4.2.5) lies in its utility when applied to optical systems with more than one surface. In Chapter 5 we develop the method by which  $\Delta z$  can be determined in a general way for any optical system with any object location. Once  $\Delta z$  is known, it is then a straightforward matter to calculate the angular and transverse aberrations.

#### 4.2.c. EXAMPLE: SPHERE WITH FINITE CONJUGATES

As an illustration of the utility of Eqs. (4.2.5) we consider an object point at a finite distance and an ellipsoid with the correct conic constant needed to form a perfect image. If a sphere is used in place of the ellipsoid, aberration is present in the image. Following the preceding prescription, we find the difference  $\Delta z$  between these two surfaces. From Eq. (4.1.4) we get

$$\Delta z = z_e - z_s = K_e r^4 / 8R^3,$$

through the terms of interest. Therefore Eqs. (4.2.5) give

$$\text{ASA3} = K_e (r^3 / R^3), \quad \text{TSA3} = K_e (r^3 / R^3) s', \quad (4.2.6)$$

where the range of  $K_e$  for the ellipsoid is  $-1 < K_e < 0$  for real conjugates. It is convenient to rewrite Eqs. (4.2.6) in terms of the transverse magnification  $m$ . Eliminating  $s$  between Eqs. (2.3.1) and (2.3.3) gives  $s'/R = (1 - m)/2$ . Substituting this and Eq. (3.5.4) for  $K$  we get

$$\text{ASA3} = - \left( \frac{m+1}{m-1} \right)^2 \frac{r^3}{R^3}, \quad (4.2.7a)$$

$$\text{TSA3} = + \frac{(m+1)^2}{m-1} \frac{r^3}{2R^2}. \quad (4.2.7b)$$

These relations give the spherical aberration of a sphere used at magnification  $m$ . Note that  $m < 0$  for real conjugates, hence TSA for a concave spherical mirror always has the same sign for a given  $r$ , independent of the sign of  $R$ . This sign is such that the focus for marginal rays, those rays reflected from the edge of the mirror, is closer to the vertex than the paraxial focus, as shown in Fig. 4.2. Note that the substitution of  $m = 0$  into Eqs. (4.2.7) gives the same ASA3 and TSA3 as when  $K = 0$  is substituted into Eqs. (4.2.3) and (4.2.4), as expected. As a final

comment, note that the spherical aberration is zero when  $m = -1$ . For this magnification  $s = s'$ , and the sphere is the perfect surface according to Fermat's Principle.

#### 4.2.d. DISTRIBUTION OF RAYS NEAR FOCUS

As given by the preceding relations, TSA is a measure of the image size of a point object at the paraxial focus. The distribution of rays near the paraxial focus is such that the image has a minimum size between paraxial focus and the focus for marginal rays. Here we consider the ray distribution as seen in cross section, both along and perpendicular to the optical axis.

A cross section of the image along the  $z$ -axis near paraxial focus is shown in Fig. 4.5 for a spherical mirror with  $m = 0$  and focal ratio  $F = 2$ . The paraxial focus is at the origin of the  $(r', z')$  coordinate frame. Each ray is drawn so that it

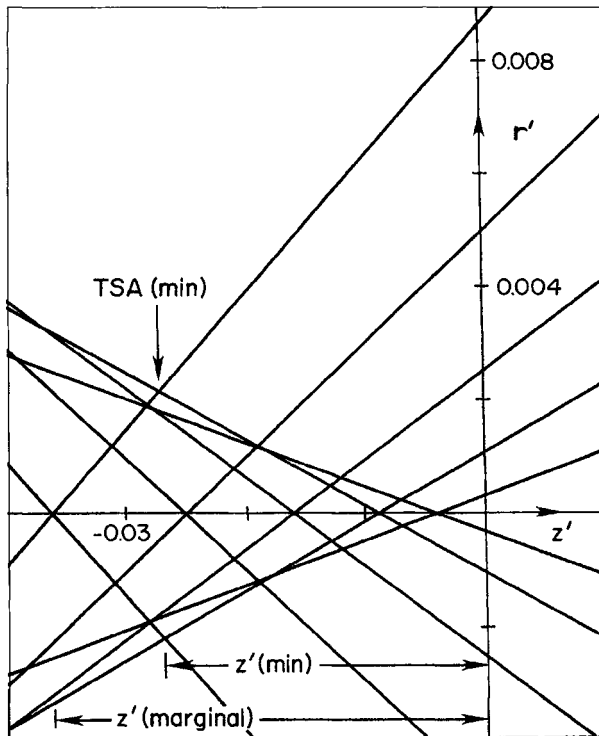


**Fig. 4.5.** Ray distribution near paraxial focus for image with spherical aberration. Paraxial focus is at  $(0, 0)$ . See Eq. (4.2.8) for definition of parameters.

crosses the  $z$ -axis at a distance  $LSA3$  (or  $\Delta f$ ) from the paraxial focus and intersects the paraxial focal plane at height  $TSA3$ . These coordinates are

$$r' = -r^3/2R^2, \quad \text{at } z' = 0, \quad (4.2.8a)$$

$$z' = -r^2/4R, \quad \text{at } r' = 0, \quad (4.2.8b)$$

where  $r' = TSA3$  from Eq. (4.2.4) and  $z' = \Delta f$  from Eq. (4.1.6). Note that the vertical scale in Fig. 4.5 is stretched relative to the horizontal scale. It is easy to see in Fig. 4.5 that the image width at the blur of minimum diameter is about four times smaller than  $TSA3$  at the paraxial focus. The image at its minimum size is called the *disk* or *circle of least confusion* (clc). The location of the clc,  $z'(clc)$ , is given by  $z'(clc) = 0.75 z'(\text{marginal})$ , hence  $r^2(clc) = 0.75 r^2(\text{marginal})$  from Eq. (4.2.8b). It follows that  $r(clc) = 0.866 r(\text{marginal})$ , a result we use in our analysis of a Schmidt camera in Section 4.4 of this chapter. Analytical calculations, such as those given by Welford (1986) support these graphical conclusions.

Image cross sections perpendicular to the optical axis, commonly called *spot diagrams*, are shown in Fig. 4.6. From a point source at infinity, a set of rays distributed uniformly over the aperture of this mirror is traced through the system. The cuts through the bundle of rays are shown equally spaced between the marginal focus on the left and the paraxial focus on the right. Note that the concentration of rays in the center of the image is somewhat smaller in the middle image in Fig. 4.6, even though the overall image diameter is larger than at the clc.

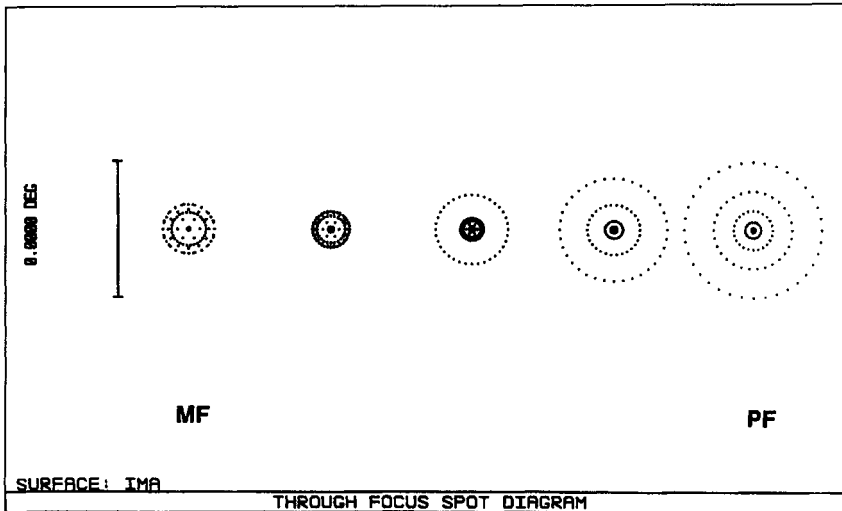


Fig. 4.6. Spot diagrams near paraxial focus for image with spherical aberration. Images are equally spaced between marginal focus (MF) at the left to paraxial focus (PF) at the right.

We show in Chapter 10 that this image, the one midway between paraxial and marginal focus, is the one with the minimum root-mean-square (rms) wavefront error.

From our discussion we see that the diameter of the circle of least confusion is  $|r^3/4R^2|$  when the object is at infinity. At the mirror this blur subtends an angle  $\alpha$  where

$$\alpha = r^3/2R^3 = 1/128F^3. \quad (4.2.9)$$

As the focal ratio  $F$  increases, the subtended angle  $\alpha$  decreases. A point is reached, however, where the image diameter no longer decreases but reaches the limit set by diffraction according to Eq. (3.7.1). The smallest  $F$  for which a spherical mirror used to image a distant object is approximately diffraction-limited is found by equating  $\alpha$  in Eq. (4.2.9) to  $\theta$  in Eq. (3.7.1). The result is  $D \approx 128\lambda F^3$ , in general, or  $D \approx 0.007F^3$ , for  $\lambda = 550$  nm. As examples, for green light, we find  $F \approx 11$  for  $D = 10$  cm, and  $F \approx 24$  for  $D = 1$  m. Thus, in spite of spherical aberration, a spherical mirror in collimated light is effectively diffraction-limited, provided the focal ratio is large enough.

An interesting exercise left to the reader is to take  $D \approx 128\lambda F^3$ , solve for  $\lambda$ , and substitute the result into Eq. (4.2.2). Setting  $K = 0$  we find that  $\Delta z$ , the difference between a paraboloid and a “diffraction-limited” sphere at the margins, is approximately  $\lambda/8$ . Hence the path difference between two marginal rays from the two mirrors is  $\approx \lambda/4$ . Alternatively, the wavefront emerging from the spherical mirror is no longer spherical but differs from the spherical wavefront emerging from the paraboloid by  $\lambda/4$  at the margin. Although this limit is found here in a special case, it turns out that this is a useful criterion for establishing when any optical system gives images that are approximately diffraction-limited.

### 4.3. REFLECTING CONICS AND FINITE OBJECT DISTANCE

The analysis in Section 4.1 leading to Eq. (4.1.6) and an expression for spherical aberration in Eq. (4.2.1) is restricted to an object at infinity. For completeness we extend this procedure and consider an object at a finite distance. We outline the method by which  $s'$  and TSA through fifth-order can be determined, and give the derived relations.

Consider a concave mirror with an object located on the optical axis at a finite distance  $s$ . The geometry of a ray intersecting a mirror at height  $r$  from the optical axis is shown in Fig. 4.7. From the triangles in Fig. 4.7 we get

$$\tan \alpha = \frac{r}{s-z}, \quad \tan \beta = \frac{r}{s'-z}, \quad \tan \phi = \frac{dz}{dr} = \frac{r}{R-(1+K)z}, \quad (4.3.1)$$

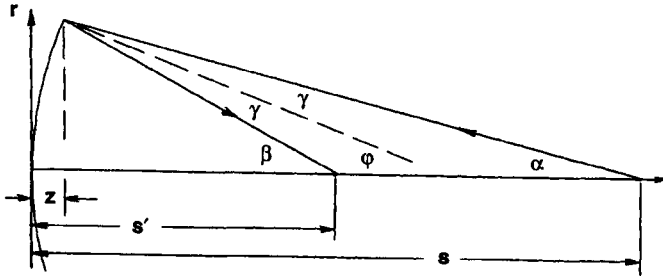


Fig. 4.7. Geometry of ray from point source at finite distance reflected from a concave mirror.

where  $\phi = \gamma + \alpha = \beta - \gamma$ . Solving for  $s'$  we find

$$s' - z = \frac{r}{\tan(2\phi - \alpha)} = r \frac{[1 + \tan \phi(2 \tan \alpha - \tan \phi)]}{2 \tan \phi - \tan \alpha(1 - \tan^2 \phi)}. \quad (4.3.2)$$

The procedure now is to take each  $\tan$  function in Eq. (4.3.2), expand it as a power series in  $r/R$ , and substitute for  $z$  with Eq. (4.1.4). After considerable algebra we find that the resulting lateral spherical aberration LSA or  $\Delta s'$  is given by

$$\begin{aligned} \Delta s' = s' - s'_0 = & -\frac{r^2}{4R}(m-1)^2 \left[ K + \left( \frac{m+1}{m-1} \right)^2 \right] \\ & \times \left\{ 1 + \frac{r^2}{4R^2} [K + 3 + 2m(K+1)] \right\}, \end{aligned} \quad (4.3.3)$$

where  $s'_0$  is the paraxial image distance.

We now proceed to the transverse spherical aberration. From Fig. 4.7 we see that  $\text{TSA} = \text{LSA} \tan \beta = r \Delta s' / (s' - z)$ . Using Eq. (4.3.3) and the expansion of Eq. (4.3.2) we find

$$\text{TSA} = -s'_0 \left( \frac{r}{R} \right)^3 \left[ K + \left( \frac{m+1}{m-1} \right)^2 \right] \left\{ 1 + \frac{3}{4} \left( \frac{r}{R} \right)^2 \left[ K - \left( \frac{m+3}{m-1} \right) \right] \right\}. \quad (4.3.4)$$

Equations (4.3.3) and (4.3.4) can be used as given, but when comparing results from these equations with those given by ray-tracing programs it is necessary to express  $r$  in terms of  $y$ , the height on the tangent plane to the mirror of the incident ray. The geometric relation between  $r$  and  $y$  follows from Fig. 4.7. Using the relation for  $\tan \alpha$  in Eqs. (4.3.1) and noting that  $\tan \alpha = y/s$ , we get

$$r = y \left( 1 - \frac{y^2}{2sR} \right) = y \left( 1 - \left( \frac{m}{m-1} \right) \frac{y^2}{R^2} \right). \quad (4.3.5)$$

Substituting Eq. (4.3.5) into Eq. (4.3.4) we find

$$\text{TSA} = -s'_0 \left(\frac{y}{R}\right)^3 \left[ K + \left(\frac{m+1}{m-1}\right)^2 \right] \left\{ 1 + \frac{3}{4} \left(\frac{y}{R}\right)^2 \left[ K - \left(\frac{5m+3}{m-1}\right) \right] \right\}, \tag{4.3.6}$$

where  $\text{TSA} = \text{TSA}_3 + \text{TSA}_5$ . Note that choosing  $K$  in Eq. (4.3.6) according to Eq. (3.5.4) gives zero TSA, as expected. It is left as an exercise for the reader to verify that Eq. (4.2.7b) follows from Eq. (4.3.6) with  $K = 0$ .

Comparing the third-order terms in Eqs. (4.3.4) and (4.3.6) we see that they are the same if  $r = y$ . In the paraxial approximation the height of a ray at the surface is always the same as its projection on the tangent plane to the surface. It turns out in general that all third-order aberrations can be expressed entirely in terms of paraxial (or first-order) parameters. This is not true for aberrations of higher order which are affected by the size of those of lower order. This effect is evident here in the fifth-order terms in Eqs. (4.3.4) and (4.3.6). Fortunately, third-order aberration results usually suffice when analyzing an optical system.

#### 4.4. OFF-AXIS ABERRATIONS

We now turn our attention briefly to off-axis aberrations, those aberrations present when the object point does not lie on the optical axis. In this section we want only to indicate the nature of these aberrations; a general discussion of this subject is the topic of the next chapter.

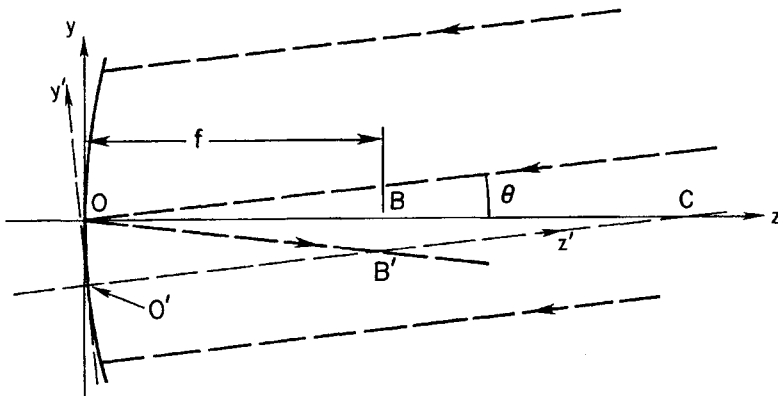


Fig. 4.8. Collimated beam at angle  $\theta$  with optical axis incident on paraboloid. Here  $O'$  is the origin of the rotated coordinate system; point  $C$  lies on both the  $z$  and  $z'$  axes.

To illustrate the source of off-axis aberrations we consider a special case, a paraboloid in collimated light. Figure 4.8 shows a cross section of a paraboloid with optical axis  $z$  and vertex at  $O$ . The image at  $B$  is, of course, a perfect one geometrically. The same paraboloid images a distant point object at angle  $\theta$  from the  $z$ -axis at point  $B'$ , where the distance  $BB'$  is approximately  $f\theta$ .

To determine the kinds of aberrations present in the image at  $B'$ , we find a system that takes the rays at angle  $\theta$  and forms a perfect image at  $B'$ . This system is obviously a paraboloid whose optical axis is parallel to the incident beam and passes through  $B'$ , with its vertex at distance  $f$  from  $B'$ . The coordinate system for this paraboloid is shown in Fig. 4.8; the optical axis is denoted by  $z'$  and the vertex is at  $O'$ . We then find the distance  $\Delta z$  between these two paraboloids in the  $yz$  plane and use Eq. (4.2.5) to find the third-order aberrations.

Omitting the details of these steps we find

$$\text{AA3} = 3a_1 \frac{y^2\theta}{R^2} + 2a_2 \frac{y\theta^2}{R} + a_3\theta^3, \quad (4.4.1)$$

where AA3 represents angular aberration to third-order.

The terms in Eq. (4.4.1) represent different aberrations: The first is *coma*, the second is *astigmatism*, and the last is *distortion*. The character of each aberration is quite different because of the different way in which each depends on  $y$  and  $\theta$ . Our following description of each aberration is limited to the  $yz$ -plane and is, therefore, incomplete. A complete description, based on rays over the entire aperture, is given in Chapter 5.

Coma is proportional to  $y^2\theta$  and hence is changed in sign when  $\theta$  changes sign. Coma is invariant to the sign of  $y$  and therefore rays from opposite sides of the mirror are on the same side of the central ray in the vicinity of the paraxial focus.

Astigmatism is proportional to  $y\theta^2$  and hence is unchanged by a sign change in  $\theta$ . A change in the sign of  $y$  changes the sign of the astigmatism and therefore rays from opposite sides of the mirror are on opposite sides of the central ray near paraxial focus.

Distortion is proportional to  $\theta^3$  and does not depend on  $y$ . Thus this aberration, if it is the only one present, does not affect the image quality, only its position. For a set of point objects equally spaced perpendicular to the optical axis, the set of images would not be equally spaced if distortion is present.

There is one final aberration that is present in Fig. 4.8 (it does not appear in Eq. (4.4.1)); the aberration is called *curvature of field*. Its character is most easily seen by noting that the transformation that takes the origin from  $O$  to  $O'$  is essentially one of a rotation about the center of curvature  $C$ . Thus the motion of point  $B$  in Fig. 4.8 to  $B'$  is along a circular arc whose center is  $C$ . The foci for different  $\theta$ , in the absence of other aberrations, are located on a curved surface, hence the name curvature of field.

At this stage five third-order aberrations have been identified: spherical aberration, coma, astigmatism, distortion, and curvature of field. The first of these is independent of field angle, but all others depend on some power of  $\theta$ . The first three aberrations in this list affect image quality, while the last two affect only image position.

From Eqs. (4.2.7b) and (4.4.1) we see that the transverse aberrations depend on aperture radius  $y$  (or  $r$ ) and field angle  $\theta$  according to the relation

$$\text{transverse aberration} \propto y^n \theta^m, \quad (4.4.2)$$

where  $n + m = 3$ . Hence each of these aberrations is called a third-order aberration. The main task in the analysis of the image quality in any optical system is the determination of how much of each of these aberrations is present, and then eliminating or reducing the amount of each by proper selection of system parameters.

## 4.5. ABERRATION COMPENSATION

In Section 3.7 we noted that a perfect optical system is one in which the wavefront emerging from the final surface is spherical. From the discussion in this chapter it is evident that there is a close relation between deviations from a spherical wavefront and the appearance of aberrations. Along any ray the actual wavefront may be behind or in front of the ideal wavefront, depending on whether that portion of the wavefront has been retarded or advanced.

Although the analysis so far has been limited to aberrations of a single mirror optical system, it should be evident that compensation of aberrations, wholly or in part, should be possible in systems with more than one surface. In terms of Fermat's Principle, exact compensation means that a wavefront advance introduced by one or more surfaces is canceled by an equal wavefront retardation introduced by other surfaces. As far as the final wavefront is concerned, it is only the net advance or retardation that determines the size of any image defect.

In this section we examine two systems, a Cassegrain telescope and a Schmidt camera, for each of which the net third-order spherical aberration is zero. Each system is composed of two optical elements chosen so that a wavefront advance due to one element is balanced by an equal retardation introduced by the other. The object point for each is a distant point source on the optical axis.

### 4.5.a. CASSEGRAIN TELESCOPE

The configuration of mirrors in a Cassegrain telescope is shown in Fig. 2.7a. Based on the discussion in Section 3.4, one pair of mirrors for which the spherical

aberration is zero is a paraboloidal primary and a hyperboloidal secondary. The former is the perfect mirror for a point object at infinity, while the latter is perfect for finite conjugate points on opposite sides of the mirror. From Eq. (3.5.4) we find the conic constants

$$K_1 = -1, \quad K_2 = -\frac{(m+1)^2}{(m-1)^2}, \quad (4.5.1)$$

where  $m$  is the magnification of the secondary. Choosing a value of  $\beta$  sets the normalized distance from the vertex of the primary to the final focal point. With the values of  $m$  and  $\beta$  chosen, the paraxial relations in Eqs. (2.5.1) are used to find the values of  $k$  and  $\rho$ . If, for example,  $m = 5$  and  $\beta = 0.2$ , then  $k = 0.2$ ,  $\rho = 0.25$ , and  $K_2 = -2.25$ . The telescope specification, specified so far only in terms of normalized parameters, is completed when the primary mirror diameter and focal length are chosen.

The paraboloid-hyperboloid combination specified in Eq. (4.5.1) is called a *classical Cassegrain*. We now show how this configuration can be changed into a different one by changing the conic constants of both the primary and secondary mirrors. This is done in a way that keeps the net third-order spherical aberration (SA3) zero, hence a change in  $K_1$  is accompanied by a change in  $K_2$  such that the wavefront advance at one mirror is equal to the wavefront retardation at the other, to third-order. Stated in terms of Fermat's Principle, the OPL from the object to the image along any ray does not change.

Starting with the classical Cassegrain configuration in Fig. 4.9, each surface is changed into a different conic by "bending" the original surface. If the new surfaces lie to the left of the original surfaces, as shown in Fig. 4.9, then the wavefront has been advanced at the primary and retarded at the secondary. The advance and retardation are  $2\Delta z_1$  and  $2\Delta z_2$ , where  $\Delta z_1$  and  $\Delta z_2$  are the surface differences at the primary and secondary, respectively. Using Eq. (4.1.4) each surface has  $z$  as follows:

$$\begin{aligned} z_1(\text{original}) &= \frac{y_1^2}{2R_1}, \\ z_1(\text{new}) &= \frac{y_1^2}{2R_1} + (1 + K_1) \frac{y_1^4}{8R_1^3}, \\ z_2(\text{original}) &= \frac{y_2^2}{2R_2} + \left[ 1 - \left( \frac{m+1}{m-1} \right)^2 \right] \frac{y_2^4}{8R_2^3}, \\ z_2(\text{new}) &= \frac{y_2^2}{2R_2} + (1 + K_2) \frac{y_2^4}{8R_2^3}. \end{aligned}$$

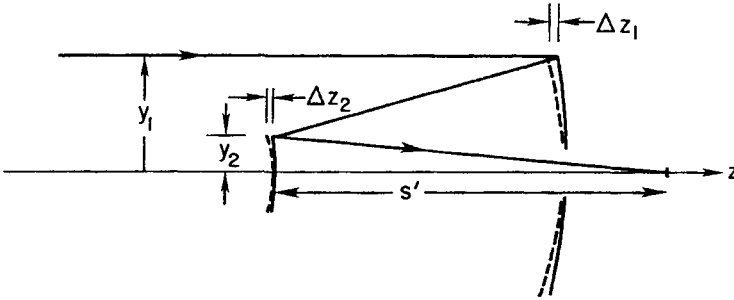


**Fig. 4.9.** Cassegrain telescope schematic. Classical Cassegrain has mirrors shown by solid curves; modified Cassegrain has mirrors shown by dashed curves. The  $R_1$ ,  $R_2$ ,  $m$ , and  $k$  are the same for both telescopes. Surface differences are given in Eqs. (4.5.2).

Therefore

$$2 \Delta z_1 = (1 + K_1) \frac{y_1^4}{4R_1^3}, \quad (4.5.2a)$$

$$2 \Delta z_2 = \left[ K_2 + \left( \frac{m+1}{m-1} \right)^2 \right] \frac{y_2^4}{4R_2^3}, \quad (4.5.2b)$$

where  $R_1$  and  $R_2$  are held constant. Applying the condition that the advance equals the retardation requires  $2 \Delta z_1 = 2 \Delta z_2$ . Note that this is equivalent to stating that the optical distance from object to image is unchanged, hence Fermat's Principle is satisfied for all rays from a distant point source.

Applying this condition gives

$$K_1 + 1 = \frac{y_2^4 R_1^3}{y_1^4 R_2^3} \left[ K_2 + \left( \frac{m+1}{m-1} \right)^2 \right] = \frac{k^4}{\rho^3} \left[ K_2 + \left( \frac{m+1}{m-1} \right)^2 \right]. \quad (4.5.3)$$

As an example, take the values of the paraxial parameters already given here for the classical Cassegrain and choose  $K_2 = 0$ . From Eq. (4.5.3) we get  $K_1 = -0.7696$ . This combination of an ellipsoidal primary and a spherical secondary is called a *Dall-Kirkham* telescope. Another possible choice is  $K_1 = -1.02$  and, from Eq. (4.5.3),  $K_2 = -2.4453$ . It turns out that this choice of conic constants gives a telescope called the *Ritchey-Chretien* telescope.

The solutions of Eq. (4.5.3) represent the family of Cassegrain telescopes for which SA3 of a distant point source is zero. For a given set of  $k$ ,  $m$ , and  $\rho$  there is an infinity of combinations of  $K_1$  and  $K_2$  that satisfy Eq. (4.5.3). In practice the choice of  $K_1$  and  $K_2$  from this set depends on other considerations, such as off-axis aberrations and the ease with which the mirrors can be made and tested. In the case of a Dall-Kirkham, for example, the separate mirrors are easily tested but

large coma results in a small usable field. On the other hand, the Ritchey–Chretien telescope has zero coma but hyperboloidal mirrors that are more difficult to make and test. Discussions of the aberrations of Cassegrain and other two-mirror telescopes are given in Chapter 6.

It is important to note here that Eq. (4.5.3) and the procedure used to derive it do not ensure that higher-order spherical aberration is also zero. Except for the two-mirror telescope with conic constants given by Eqs. (4.5.1), other two-mirror telescopes generally have higher-order spherical aberration.

4.5.b. SCHMIDT CAMERA

A Schmidt camera is composed of three elements: a concave spherical mirror, an aperture stop whose center is located at the center of curvature of the mirror, and a refracting plate in the plane of the stop, as shown schematically in Fig. 4.10. For the moment ignore the refracting plate and consider only the mirror and stop. Placement of the stop at the center of curvature gives a system that is effectively axis-free. Rays through the stop from an off-axis object point “see” an optical system, a portion of the spherical mirror, which is the same as that for rays from an on-axis point. In effect, any line through  $C$  from an off-axis point is equivalent to the  $z$ -axis. This axis-free character is, of course, true only for the sphere because of its constant curvature. Therefore the aberrations of an image of any object point, for this arrangement of mirror and stop, are just those of an on-axis image, namely, spherical aberration. Because of the rotational symmetry about point  $C$ , the image surface is spherical and curvature of field is present but, as already noted, this aberration does not affect image quality.

Because this very simple optical system is free of astigmatism and coma, it is the basis for cameras and telescopes that are designed for wide-field applications.

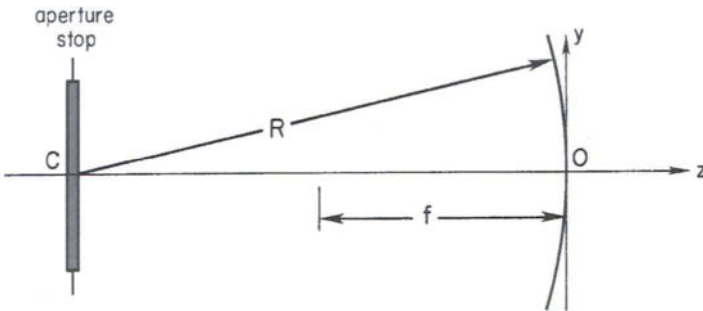


Fig. 4.10. Schmidt camera configuration. Center of curvature  $C$  of spherical mirror is at center of aperture stop. Surface figure on glass plate at stop is given by Eq. (4.5.5).

Note that freedom from these aberrations is true for objects at any point to the left of the stop in Fig. 4.10, not just for collimated beams from distant point sources.

The remaining optical element, the refracting plate or corrector, serves the function of correcting the spherical aberration due to the mirror, where the wavefront advance at the mirror is compensated by an equal wavefront retardation by the corrector. To find the required wavefront advance we take a distant object point, the only case considered here, and find  $\Delta z$  between the sphere and a reference paraboloid. The latter surface is, of course, the surface that would give a perfect on-axis image.

From Eq. (4.2.2) we find for  $K = 0$  that the wavefront advance at the mirror is

$$2 \Delta z = -r^4/4R^3. \quad (4.5.4)$$

Consider a plane-parallel plate of thickness  $t$  and index  $n$ . At any height  $y$  near one surface of this plate we remove a layer of air of thickness  $\tau$  and replace it with a layer of glass of optical thickness  $n\tau$ . The net change in optical path due to this change is  $(n - 1)\tau$  for a ray parallel to the  $z$ -axis. Because the light is "slowed down" in the glass, this optical path difference is the required retardation and

$$(n - 1)\tau = 2 \Delta z = -r^4/4R^3. \quad (4.5.5)$$

Defining  $\eta = r/r_0$  where  $r_0$  is the radius of the aperture stop, and noting that  $f = -R/2$ , gives

$$\tau = \frac{\eta^4 r_0^4}{32(n - 1)f^3} = \frac{f\eta^4}{512(n - 1)F^4}. \quad (4.5.6)$$

For an otherwise flat plate Eq. (4.5.6) defines the surface figure on one face required to correct the spherical aberration of the mirror. From the point of view of Fermat's Principle it does not matter whether the figured surface faces the mirror or the incident light. In either orientation rays at the edge of the aperture are retarded relative to those near the axis. Note also that Eq. (4.5.6) applies only to the case where the perfect reference surface is a paraboloid. For objects whose distance is not effectively at infinity the appropriate reference surface is an ellipsoid, but the procedure for finding  $\tau$  is the same.

We now consider how the corrector plate has caused the compensation of the spherical aberration of the mirror. Rays through the corrector near its center are essentially undeviated and hence are focused at the paraxial focal point of the mirror. Rays farther out on the corrector are deviated away from the  $z$ -axis because in cross section the corrector is a thin prism. If the effective prism angle is  $\gamma$ , as shown in Fig. 4.11, then the net ray deviation in the paraxial approximation is  $(n - 1)\gamma$ . Because of this deviation both the point at which the ray strikes the mirror and its angle of incidence are changed, and the reflected ray is directed toward the paraxial focus. From the center of the corrector outward the angle

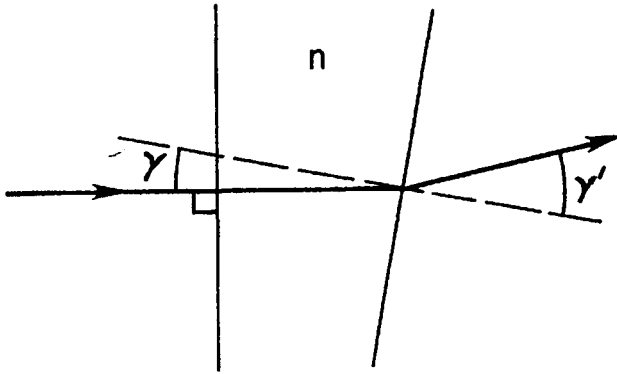


Fig. 4.11. Small section of corrector plate near edge, in cross section. Net ray deviation is  $(n - 1)\gamma$ .

increases as  $r^4$  and is a maximum at the edge; thus the marginal rays are deviated by the largest amount.

If the corrector had a constant index of refraction it would affect rays of any wavelength in the same way but, of course, this is not the case. Because  $n$  is not constant the deviation is also a function of wavelength. Denoting the deviation by  $\delta$ , a simple differentiation gives

$$d\delta/d\lambda = \gamma dn/d\lambda. \quad (4.5.7)$$

Thus rays of different wavelength are directed in slightly different directions with the effect largest at the edge of the corrector. A system corrected at one wavelength is no longer corrected at other wavelengths and the image now has the aberration called *chromatic spherical aberration*. This image defect is always present when the corrector is a single element, but it can be minimized by selecting a different focal point for the system.

Looking at Fig. 4.5 or 4.6 we see that the blur is smallest at the circle of least confusion. At this distance from the mirror neither the paraxial rays nor the marginal ones intersect the  $z$ -axis but, as noted following Eqs. (4.2.8), the rays from the zone at  $0.866r_0$  are in focus on the axis. It is also evident from Fig. 4.5 that the maximum deviation necessary to bring all rays to this same focus is less than that required to bring the marginal rays to the paraxial focus. The reference surface needed to minimize the overall ray deviation is a paraboloid whose focal point is at the circle of least confusion in Fig. 4.5, hence it has a radius of curvature different from the one used to derive Eq. (4.5.4).

The required change in  $R$  is  $2\Delta f$  where, from Eq. (4.2.8b), we find

$$z' = \Delta f = -(0.866r_0)^2/4R = -3r_0^2/16R,$$

hence

$$R' - R = 2 \Delta f = -3r_0^2/8R, \quad (4.5.8)$$

where  $R'$  is the radius of curvature of the modified paraboloid. Substituting Eq. (4.5.8) into Eq. (4.1.4) gives

$$z' - z = \frac{r^2}{2} \left( \frac{1}{R'} - \frac{1}{R} \right) \cong \frac{3r_0^2 r^2}{16R^3}. \quad (4.5.9)$$

With reference to the new paraboloid the wavefront advance at the spherical mirror is

$$2 \Delta z = \frac{3r_0^2 r^2}{8R^3} - \frac{r^4}{4R^3}. \quad (4.5.10)$$

Equating the wavefront advance and retardation gives the surface figure as

$$\tau = \frac{3r_0^2 r^2}{8(n-1)R^3} - \frac{r^4}{4(n-1)R^3} = \frac{f\eta^4}{512(n-1)F^4} \left( 1 - \frac{3}{2\eta^2} \right), \quad (4.5.11)$$

where  $\tau < 0$  over the entire corrector aperture. In contrast to the corrector whose profile is given by Eq. (4.5.6), this corrector is thickest at its center. Comparing Eq. (4.5.11) to Eq. (4.5.6) we also see that an additional term has been introduced into the surface figure, one that amounts to including a radius term. Rewriting Eq. (4.5.11) we get

$$\tau = \frac{r^2}{2R_c} - \frac{r^4}{4(n-1)R^3}, \quad (4.5.12)$$

where  $R_c$ , the radius of curvature of the modified corrector, is

$$R_c = \frac{4(n-1)R^3}{3r_0^2}. \quad (4.5.13)$$

Throughout the analysis leading to Eq. (4.5.12), we have carefully followed the sign conventions established in Chapter 2. From the diagram in Fig. 4.10 we see that  $R < 0$ , hence  $R_c < 0$  as well. In absolute terms  $\tau$  has its largest value when  $r = 0.866r_0$ , as is easily verified by setting  $d\tau/dr = 0$  and solving for  $r$ . The rays for which the deviation is a maximum are those for which  $d\tau/dr$  is largest in an absolute sense, which occurs at  $\eta = 0.5$  and  $\eta = 1$ . The shapes of the corrector profile and the emerging wavefront, greatly exaggerated, are shown in Fig. 4.12.

As a final item for the Schmidt camera we calculate the chromatic TSA present when the index  $n$  differs from the one used in the design profile. The starting point is the wavefront retardation of the corrector,  $(n' - 1)$ , where  $n'$  is the variable. The change in retardation as a function of a change in index is  $\tau \delta n$ , where  $\delta n = n' - n$  and  $n$  is the design index. Equivalently,  $\tau \delta n$  is the optical path

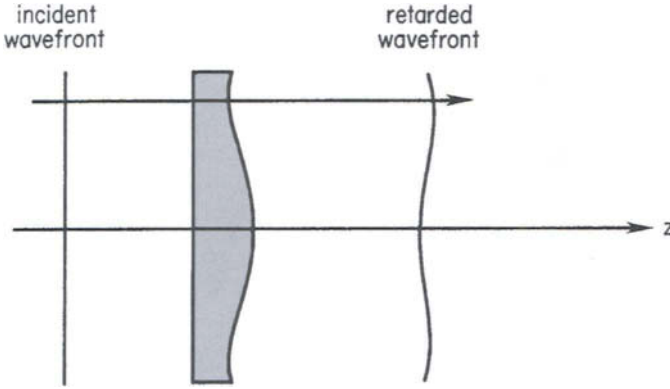


Fig. 4.12. Profiles, greatly exaggerated, of corrector and emerging wavefront. Ray shown at height  $\sqrt{3}/2$  of full aperture is undeviated.

difference (OPD) for index  $n'$ . Substitution of the OPD for  $2 \Delta z$  in Eq. (4.2.5) and setting  $s' = f$  gives the chromatic aberration. The result is

$$\text{TSA3} = f \frac{d}{dr} (\tau \delta n) = f \delta n \frac{d\tau}{dr} = \frac{f \eta^3 \delta n}{64(n-1)F^3} \left( 1 - \frac{3}{4\eta^2} \right). \tag{4.5.14}$$

Putting in  $\eta = 0.5$  or  $1$  gives the chromatic TSA for the rays that have the maximum deviation or largest effective prism angle. The two values of  $\eta$  give the same TSA value in magnitude and the result in absolute terms is

$$\text{TSA3} = \frac{f}{256F^3} \frac{\delta n}{n-1}, \tag{4.5.15}$$

which is effectively the radius of the chromatic image.

The prescription of the corrector profile required to correct the spherical aberration of a spherical mirror used in collimated light is correct through fourth-order terms in  $r$ . As noted in Eq. (4.2.1) there are higher-order terms in the expression for spherical aberration and Eq. (4.5.12) can be extended to eliminate their presence. The term in SA5 is significant for cameras of small focal ratio and is considered in Chapter 7. For further details on aberrations of fifth and higher order, the reader should consult the books by Bouwers (1946) and Linfoot (1955).

The introduction of the refracting corrector element gives an optical system with excellent image quality over a large field, with chromatic aberration setting the limit on the image quality. It should also be noted that the corrector does have an axis and therefore the camera is no longer axis-free. As a result there will be off-axis aberrations, though these aberrations are relatively small because the corrector is nearly a plane-parallel plate and is generally quite thin. For details on the magnitude of these off-axis effects the reader should consult an excellent

article by Bowen (1960). This article is also of interest in showing how the aberrations of a Schmidt camera can be calculated without recourse to Fermat's Principle.

The two systems treated in this section have only been examined in part. Our intent here has been to use Fermat's Principle as a tool to facilitate the analysis of optical systems and to demonstrate its power in the process, at least for on-axis aberrations. The full capability of this tool, including analysis of off-axis aberrations, will be evident after the treatment in the following chapter.

## REFERENCES

- Bowen, I. (1960). *Stars and Stellar Systems I, Telescopes*, Chap. 4, Chicago: University of Chicago Press.
- Welford, W. (1986). *Aberrations of the Symmetrical Optical System*, second edition, Chap. 6, New York: Academic Press.

## BIBLIOGRAPHY

### *Introduction to aberrations*

- Longhurst, R. (1967). *Geometrical and Physical Optics*, second edition, New York: John Wiley.
- Mahajan, V. (1998). *Optical Imaging and Aberrations, Part I, Ray Geometrical Optics*, Bellingham, WA: SPIE Optical Engineering Press.

### *Telescopes*

- Bowen, I. (1967). *Annual Review of Astronomy and Astrophysics*, **5**: 45, Palo Alto, CA: Annual Reviews.
- Gascoigne, S. (1973). *Appl. Opt.*, **12**: 1419.
- Learner, R. (1981). *Astronomy Through the Telescope*, Princeton, NJ: Van Nostrand-Reinhold.
- Meinel, A. (1960). *Stars and Stellar Systems I, Telescopes*, Chap. 3, Chicago: University of Chicago Press.
- Meinel, A. (1976). *Applied Optics and Optical Engineering*, vol. 5, Chap. 6, New York: Academic Press.
- Wetherell, W. and Rimmer, M. (1972). *Appl. Opt.*, **11**, 2817.
- Wilson, R. (1996). *Reflecting Telescope Optics I*, Berlin: Springer.

### *Schmidt Cameras*

- Bowers, A. (1946). *Achievements in Optics*, Chap. 1, Amsterdam: Elsevier.
- Bowen, I. (1960). *Stars and Stellar Systems I, Telescopes*, Chap. 4, Chicago: University of Chicago Press.
- Linfoot, E. (1955). *Recent Advances in Optics*, Chap. 4, London and New York: Oxford University Press.

At this point the stage is set for a general application of Fermat's Principle to a surface of revolution and the derivation of its aberrations. The theory of aberrations, generally called the Seidel theory, is a classical subject and has been treated in detail by many authors, including Born and Wolf (1980), and Welford (1986). Excellent introductions to the theory of aberrations are given by Longhurst (1967) and Mahajan (1998). The treatment here leads to nothing new, but the approach is one that leads to results that can be easily applied to optical systems of specific interest to astronomers, such as telescopes, cameras, and spectrometers. Rather than simply citing results derived from the Seidel theory, we start with Fermat's Principle and derive the desired relations in a systematic way. These aberration relations are then reduced to specific forms appropriate to given surface types, such as conic mirrors, spherical refracting surfaces, and aspheric plates as used in Schmidt cameras and telescopes.

### **5.1. APPLICATION TO SURFACE OF REVOLUTION**

A sketch of a general surface of revolution about the  $z$ -axis is shown in Fig. 5.1, with the origin of the coordinate system at the vertex of the surface. The homogeneous medium to the left of the surface has index  $n$ ; the medium to the right has index  $n'$ . The object and image points are at  $Q$  and  $Q'$ , respectively, and an arbitrary ray from  $Q$  intersects the surface at  $B(x, y, z)$ . Because the surface is

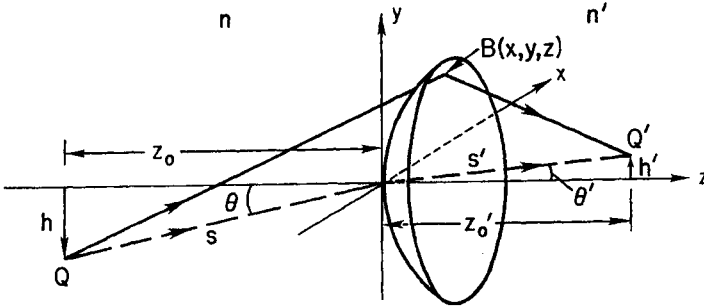


**Fig. 5.1.** Path of arbitrary ray through refracting surface. Points  $Q$  and  $Q'$  lie in the  $yz$  plane; point  $B$  is on the surface. The chief ray passes through the origin of the coordinate system.

symmetric about the  $z$ -axis, there is no loss of generality in placing  $Q$  and  $Q'$  in the  $yz$ -plane. The surface equation is a generalized form of Eq. (4.1.4) through fourth-power terms of  $r$  as follows:

$$\begin{aligned} z &= \frac{r^2}{2R} + (1 + K) \frac{r^4}{8R^3} + \frac{br^4}{8(n' - n)} \\ &= \frac{r^2}{2R} + \frac{r^4}{8} \left[ \frac{1 + K}{R^3} + \frac{b}{n' - n} \right] = \frac{r^2}{2R} + \frac{\alpha r^4}{8}. \end{aligned} \quad (5.1.1)$$

where  $\alpha$  represents the quantity in brackets, and  $r^2 = x^2 + y^2$ . The term in  $b$  explicitly includes the type of aspheric term required for corrector plates, one example of which is discussed in Section 4.5. The form of the  $b$  term in Eq. (5.1.1) is chosen to simplify its appearance in the aberration relations. In Fig. 5.1, the center of the aperture stop is located at the origin of the coordinate system. The case for an aperture stop displaced along the  $z$ -axis is considered later in this chapter.

Applying Eq. (3.1.2) to the ray shown in Fig. 5.1 gives

$$\text{OPL} = n[QB] + n'[BQ'], \quad (5.1.2)$$

where  $[QB]$  and  $[BQ']$  are the segments of the ray to the left and right of point  $B$ , respectively. From the geometry in Fig. 5.1 we have

$$\begin{aligned} [QB] &= [(y - h)^2 + (z_0 - z)^2 + x^2]^{1/2} \\ [BQ'] &= [(y - h')^2 + (z_0' - z)^2 + x^2]^{1/2}. \end{aligned} \quad (5.1.3)$$

The dashed line in Fig. 5.1 from  $Q$  to  $Q'$  passes through the center of the aperture stop and intersects the surface at its vertex. This line represents the chief ray through the system with angles  $\theta$  and  $\theta'$  with respect to the  $z$ -axis. The OPL measured along the chief ray is simply  $-ns + n's'$ , where  $s$  is negative and  $s'$  is positive by the sign convention.

The signs of other quantities in Fig. 5.1 are as follows:  $\theta$ ,  $\theta'$ ,  $h'$ , and  $z'_0$  are positive, and  $h$  and  $z_0$  are negative. The signs of  $\theta$  and  $\theta'$  are the same as those of  $i$  and  $i'$  in Fig. 2.1. With due regard for these signs, we have

$$\begin{aligned} h &= s \sin \theta, & z_0 &= s \cos \theta, & s^2 &= z_0^2 + h^2, \\ h' &= s' \sin \theta', & z'_0 &= s' \cos \theta', & s'^2 &= z_0'^2 + h'^2. \end{aligned} \quad (5.1.4)$$

Substituting the relations in the first line of Eq. (5.1.4) into  $[QB]$  gives

$$[QB] = -s \left[ 1 - \frac{2y}{s} \sin \theta + \frac{r^2}{s} \left( \frac{1}{s} - \frac{\cos \theta}{R} \right) + \frac{r^4}{4s^2} \left( \frac{1}{R^2} - \alpha s \cos \theta \right) \right]^{1/2}.$$

The relation for  $[BQ']$  is similar in form except that  $\theta'$  replaces  $\theta$ ,  $s'$  replaces  $s$ , and the leading minus sign is dropped. The expression for  $[QB]$  is now transformed by applying the binomial expansion and retaining all terms through fourth order, with the result

$$\begin{aligned} [QB] &= - \left\{ s - y \sin \theta + \frac{y^2}{2} \left( \frac{\cos^2 \theta}{s} - \frac{\cos \theta}{R} \right) + \frac{x^2}{2} \left( \frac{1}{s} - \frac{\cos \theta}{R} \right) \right. \\ &\quad + \frac{x^2 y}{2s} \sin \theta \left( \frac{1}{s} - \frac{\cos \theta}{R} \right) + \frac{y^3}{2s} \sin \theta \left( \frac{\cos^2 \theta}{s} - \frac{\cos \theta}{R} \right) \\ &\quad \left. + \frac{r^4}{8} \left[ \frac{1}{R^2} \left( \frac{1}{s} - \frac{(1+K) \cos \theta}{R} \right) - \frac{1}{s} \left( \frac{1}{s} - \frac{\cos \theta}{R} \right)^2 - \frac{b \cos \theta}{n' - n} \right] \right\}. \end{aligned}$$

A similar relation follows for  $[BQ']$  once the changes noted in the preceding are made. The substitution of these relations for  $[QB]$  and  $[BQ']$  into Eq. (5.1.2) then

gives the OPL for this general ray, as follows:

$$\begin{aligned}
 \text{OPL} = & (-ns + n's') - y(n' \sin \theta' - n \sin \theta) \\
 & + \frac{y^2}{2} \left[ \frac{n' \cos^2 \theta'}{s'} - \frac{n \cos^2 \theta}{s} - \frac{n' \cos \theta' - n \cos \theta}{R} \right] \\
 & + \frac{x^2}{2} \left[ \frac{n'}{s'} - \frac{n}{s} - \frac{n' \cos \theta' - n \cos \theta}{R} \right] \\
 & - \frac{x^2 y}{2} \left[ \frac{n \sin \theta}{s} \left( \frac{1}{s} - \frac{\cos \theta}{R} \right) - \frac{n' \sin \theta'}{s'} \left( \frac{1}{s'} - \frac{\cos \theta'}{R} \right) \right] \\
 & - \frac{y^3}{2} \left[ \frac{n \sin \theta}{s} \left( \frac{\cos^2 \theta}{s} - \frac{\cos \theta}{R} \right) - \frac{n' \sin \theta'}{s'} \left( \frac{\cos^2 \theta'}{s'} - \frac{\cos \theta'}{R} \right) \right] \\
 & + \frac{r^4}{8} \left[ \frac{1}{R^2} \left( \frac{n'}{s'} - \frac{n}{s} - \frac{(1+K)}{R} (n' \cos \theta' - n \cos \theta) \right) + \frac{n}{s} \left( \frac{1}{s} - \frac{\cos \theta}{R} \right)^2 \right. \\
 & \quad \left. - \frac{n'}{s'} \left( \frac{1}{s'} - \frac{\cos \theta'}{R} \right)^2 - \frac{b}{n' - n} (n' \cos \theta' - n \cos \theta) \right]. \quad (5.1.5)
 \end{aligned}$$

Although Eq. (5.1.5) is a formidable equation in appearance, the application of Fermat's Principle simplifies it considerably. We begin by noting that the first set of parentheses denotes the OPL for the chief ray. Because Fermat's Principle is concerned with optical path differences and stationary values, as given in Eq. (3.1.1), it is appropriate to remove this term by defining  $\Phi$  as the OPD between the general ray and the chief ray. Given this definition we have

$$\begin{aligned}
 \Phi &= \text{OPL} - \text{OPL}(\text{chief ray}) \\
 &= A_0 y + A_1 y^2 + A_1' x^2 + A_2 y^3 + A_2' x^2 y + A_3 r^4, \quad (5.1.6)
 \end{aligned}$$

where the  $A_i$ 's are the multiplying factors in Eq. (5.1.5). Applying Fermat's Principle in the form  $\delta(\text{OPL}) = 0$  to Eq. (5.1.6) gives

$$\frac{\partial}{\partial x}(\text{OPL}) = \frac{\partial \Phi}{\partial x} = 0, \quad \frac{\partial}{\partial y}(\text{OPL}) = \frac{\partial \Phi}{\partial y} = 0. \quad (5.1.7)$$

Equation (5.1.7) is satisfied for  $x = y = 0$  only if  $A_0 = 0$ , hence  $n' \sin \theta' = n \sin \theta$ , which is simply Snell's law for the chief ray.

Before proceeding to a detailed analysis of the various terms in Eq. (5.1.5) we look at each term in an approximate form. Consider first the terms in  $x^2$  and  $y^2$ . In

the paraxial approximation each cosine is replaced by one and the terms are zero by Eq. (2.2.5). In the next level of approximation each cosine is replaced by  $1 - \varphi^2/2$ , where  $\varphi$  is  $\theta$  or  $\theta'$ , and the terms are of the form  $x^2\varphi^2$  and  $y^2\varphi^2$ . Thus terms  $A_1y^2$  and  $A_1'x^2$  in Eq. (5.1.6) represent *astigmatism*, as noted in the discussion accompanying Eqs. (4.4.1) and (4.4.2). For the next two terms, those in  $x^2y$  and  $y^3$ , each cosine is replaced by one and each sine by its angle. The corresponding terms in Eq. (5.1.6),  $A_2y^3$  and  $A_2'x^2y$ , represent *coma*, with  $A_2 = A_2'$  in this level of approximation. The final term in Eq. (5.1.6), with all cosines replaced by one, is spherical aberration.

Returning to Eq. (5.1.5) we see that one or the other of the terms proportional to the square of the distance from the surface vertex can be made zero by a proper choice of  $s'$ . The term in  $y^2$  is zero if

$$\frac{n' \cos^2 \theta'}{s'_t} - \frac{n \cos^2 \theta}{s} = \frac{n' \cos \theta' - n \cos \theta}{R}, \quad (5.1.8)$$

where  $s'_t$  is the location of the *tangential astigmatic image*. As we will see, this image is a line image oriented perpendicular to the plane defined by the  $z$ -axis and the chief ray. Alternatively the term in  $x^2$  is zero if

$$\frac{n'}{s'_s} - \frac{n}{s} = \frac{n' \cos \theta' - n \cos \theta}{R}, \quad (5.1.9)$$

where  $s'_s$  is the location of the *sagittal astigmatic image*. This image is also a line but lying in the plane containing the  $z$ -axis and the chief ray. A sketch of these images as defined by selected rays is shown in Fig. 5.2. Note that  $s'_t = s'_s$  in the paraxial approximation where  $\cos \theta = \cos \theta' = 1$ , and both Eqs. (5.1.8) and (5.1.9) reduce to Eq. (2.2.5), as expected.

The separation between the two astigmatic images is found by solving Eqs. (5.1.8) and (5.1.9) for  $1/s'_t$  and  $1/s'_s$ , respectively, and taking the difference between the two expressions. The result is

$$\frac{\Delta s'}{s'_s s'_t} = \frac{\tan^2 \theta'}{n'} \left[ \frac{n' \cos \theta' - n \cos \theta}{R} + \frac{n}{s} \left( 1 - \frac{n^2}{n'^2} \right) \right],$$

where  $\Delta s' = s'_s - s'_t$ . To terms through  $\theta^2$  this expression reduces to

$$\frac{\Delta s'}{s'^2} = \frac{n^2 \theta^2}{n'} \left( \frac{1}{n' s'} - \frac{1}{n s} \right). \quad (5.1.10)$$

In Eq. (5.1.10)  $s'$  suffices to locate the image if  $\Delta s' \ll s'_s$  or  $s'_t$ . Note that the separation of the astigmatic images, and thus also the lengths of the line images, is proportional to  $\theta^2$ . Derivation of the image length follows in the next section.

At this point our analysis of Eq. (5.1.6) by means of Fermat's Principle has given Snell's law and the locations of the astigmatic images. In the next section

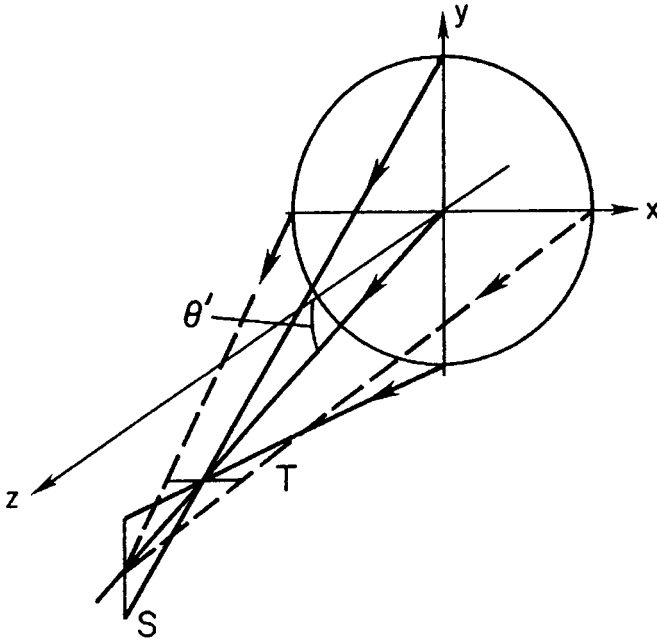


Fig. 5.2. Location and orientation of astigmatic line images. Tangential and sagittal images are denoted by  $T$  and  $S$ , respectively.

we use these results to evaluate the remaining coefficients in Eq. (5.1.6), which, if non-zero, determine the magnitude and type of aberration present in an image.

## 5.2. EVALUATION OF ABERRATION COEFFICIENTS

For an optical system that satisfies Eq. (5.1.7) for any  $(x, y)$  within the aperture, each of the coefficients in Eq. (5.1.6) must be zero and the system is perfect. If one or more of these coefficients is nonzero, then aberrations are present. Not surprisingly, the size of a given aberration is directly proportional to the corresponding coefficient in Eq. (5.1.6).

Before we evaluate each coefficient it is important to note that this analysis is limited to finding *third-order* angular and transverse aberrations only. As evident from the discussion following Eq. (5.1.7), this means retaining only those terms for which the sum of powers of  $\theta$  and  $r$ ,  $x$ , or  $y$  is not greater than four. Thus  $A_3$  is independent of  $\theta$ ,  $A_2$  and  $A'_2$  are each proportional to  $\theta$ , and  $A_1$  and  $A'_1$  are each proportional to  $\theta^2$ .

Using Snell's law and Eq. (2.2.5) to simplify the terms in Eq. (5.1.5) we get

$$A_3 = -\frac{1}{8} \left[ \frac{K}{R^3} (n' - n) + b \right] - \frac{n^2}{8} \left( \frac{1}{s} - \frac{1}{R} \right)^2 \left( \frac{1}{n's'} - \frac{1}{ns} \right), \quad (5.2.1)$$

$$A_2 = A'_2 = \theta \frac{n^2}{2} \left( \frac{1}{s} - \frac{1}{R} \right) \left( \frac{1}{n's'} - \frac{1}{ns} \right), \quad (5.2.2)$$

where the first term in brackets in Eq. (5.2.1) represents the contribution from the nonspherical part of the surface. Note that there is no term in Eq. (5.2.2) involving  $K$  or  $b$  and thus any nonspherical surface component does not contribute to the aberration associated with this coefficient, provided the aperture stop is at the surface as in Fig. 5.1. We will see later that this statement about Eq. (5.2.2) is not true when the aperture stop is displaced from the surface.

The evaluation of the remaining coefficients  $A_1$  and  $A'_1$  depends on the image distance chosen. For example, choosing  $s' = s'_s$  makes  $A'_1 = 0$ , and the coefficient  $A_1$  is evaluated by substituting  $s' = s'_s$  into  $A_1$  in Eq. (5.1.5). The result to second order in  $\theta$  is

$$A_1 = -\theta^2 \frac{n^2}{2} \left( \frac{1}{n's'} - \frac{1}{ns} \right). \quad (5.2.3)$$

If, on the other hand, the choice were  $s' = s'_t$ , then  $A_1 = 0$  and

$$A'_1 = \theta^2 \frac{n^2}{2} \left( \frac{1}{n's'} - \frac{1}{ns} \right), \quad (5.2.4)$$

hence  $A_1 = -A'_1$ . In either case terms involving  $K$  or  $b$  are absent but, as with  $A_2$ , they will be present when the aperture stop does not coincide with the surface.

The difference in sign between  $A_1$  and  $A'_1$  is a measure of the differences between the marginal rays at the ends of each of the line images. As seen in Fig. 5.2, the marginal rays in the  $yz$ -plane intersect the chief ray before reaching the sagittal image, while the marginal rays in the  $xz$ -plane reach the chief ray after passing through the tangential image. In terms of transverse aberrations at the two images, the magnitudes are the same but the signs are opposite.

Although the details are not given here, it is worth noting that choosing  $s'$  as the midpoint between the line images leads to the result that  $A_1 = -A'_1$  with each one-half as large as the values given in Eqs. (5.2.3) and (5.2.4). A look at Fig. 5.2 midway between the sagittal and tangential images shows that this result is expected. A series of spot diagrams for an image with astigmatism as its only aberration is shown in Fig. 5.3. As expected, the image blur midway between the line images is circular in cross section and the images outside of the region between the line images are elliptical in cross section.

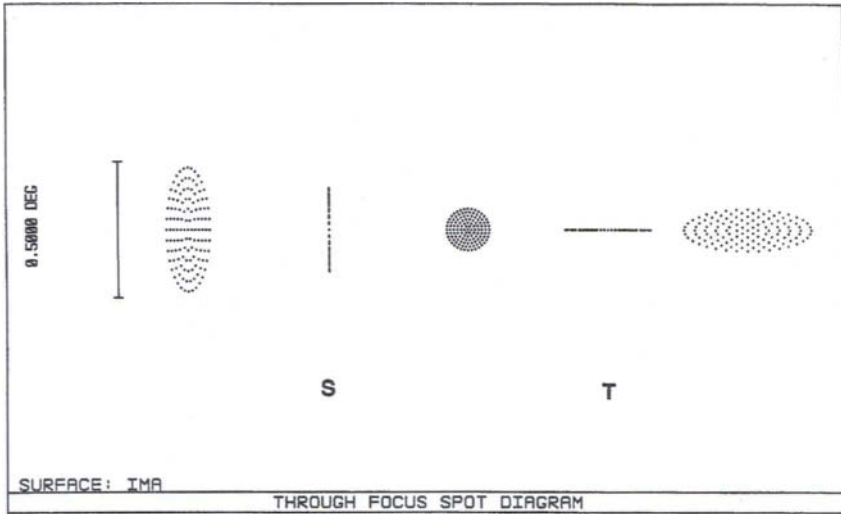


Fig. 5.3. Spot diagrams for image with astigmatism. The  $T$  and  $S$  images are to the right and left, respectively, of the astigmatic blur circle. Mirror has  $s = s' = R = 1000$  mm,  $y = 100$  mm.

Because of the close relationship between  $A_1$  and  $A'_1$ , it does not matter which  $s'$  is chosen to characterize the astigmatism present in an image. Our choice is  $s' = s'_s$  or  $A'_1 = 0$ , hence Eq. (5.2.3) is the relation used in subsequent discussions.

The direct way in which  $A_1$  is a measure of the astigmatism is seen in a comparison of Eqs. (5.2.3) and (5.1.10), from which it follows that

$$\Delta s'/s'^2 = -2A_1/n'. \quad (5.2.5)$$

Using Eq. (5.2.5) it is a simple matter to derive an expression for the transverse astigmatism at the sagittal image. Defining the transverse astigmatism (abbreviated TAS) as one-half the length of the line image, we find from the geometry of Fig. 5.2 that

$$\text{TAS} = -y(\Delta s'/s') = 2A_1 y s'/n', \quad (5.2.6)$$

where  $\text{TAS} < 0$  at the sagittal image in Fig. 5.2 when  $y > 0$ , as required by the sign convention. The diameter of the astigmatic blur circle midway between the line images is  $|\text{TAS}|$ . Using the mirror parameters given in Fig. 5.3, with  $\theta = 0.5^\circ$ , we get  $\Delta s' = -152 \mu\text{m}$  and  $\text{TAS} = -15 \mu\text{m}$  for the images shown.

The final coefficient to consider is  $A_0$ , which, from Eqs. (5.1.5) and (5.1.6), is

$$A_0 = -(n' \sin \theta' - n \sin \theta). \quad (5.2.7)$$

Instead of setting  $A_0 = 0$ , which defines the exact path of the chief ray, we follow the standard procedure of finding the angular difference in direction after refraction between the actual and paraxial chief rays for plane object and image surfaces. In the steps that follow, note that the usual statement for the paraxial approximation  $n'\theta' = n\theta$  is not sufficient. In order to preserve the exact direction from which the chief ray approaches the center of the stop, and the object and image surfaces as planes, it is necessary to express sines and tangents of angles through third order.

From Eqs. (5.1.4) we get  $\tan \theta = h/z_0$  and  $\tan \theta' = h'/z'_0$ . To third order

$$\theta = \frac{h}{z_0} - \frac{1}{3}\theta^3, \quad \theta' = \frac{h'}{z'_0} - \frac{1}{3}\theta'^3, \quad (5.2.8)$$

where  $\theta = \tan^{-1}(h/z_0)$ ,  $\theta' = \tan^{-1}(h'/z'_0)$ . We now expand Eq. (5.2.7) to third order, substitute Eqs. (5.2.8), and find

$$\begin{aligned} A_0 &= n \frac{h}{z_0} - n' \frac{h'}{z'_0} - n \frac{\theta^3}{2} \left(1 - \frac{n^2}{n'^2}\right), \\ &= -n \frac{\theta^3}{2} \left(1 - \frac{n^2}{n'^2}\right), \end{aligned} \quad (5.2.9)$$

where the first two terms cancel by Eq. (2.2.7). Note that  $s$  and  $s'$  in Eq. (2.2.7) are  $z_0$  and  $z'_0$  in the notation of this chapter. Note also that  $A_0 = 0$  for  $n' = -n$ , a reflecting surface.

At this point let us summarize our findings. We have relations for the aberration coefficients and, in the case of  $A_1$ , have its relationship to a transverse aberration. The next step is to find the connection between the remaining coefficients and their respective transverse aberrations. This is done by first establishing the connection between nonzero terms in Eq. (5.1.6) and deviations of the wavefront converging on the image point from the spherical shape produced by a perfect system.

### 5.3. RAY AND WAVEFRONT ABERRATIONS

An optical system free of aberrations takes light from an object point  $Q$ , for which the wavefront is a sphere with center at  $Q$ , and images it at the Gaussian image point  $Q'$ . The wavefront of the light converging toward  $Q'$  is a sphere whose center is at  $Q'$ , and the OPL along any ray through the system is constant. Thus  $\Phi$  in Eq. (5.1.6) is zero. This spherical wavefront is taken as our reference and designated  $\Sigma_r$ .

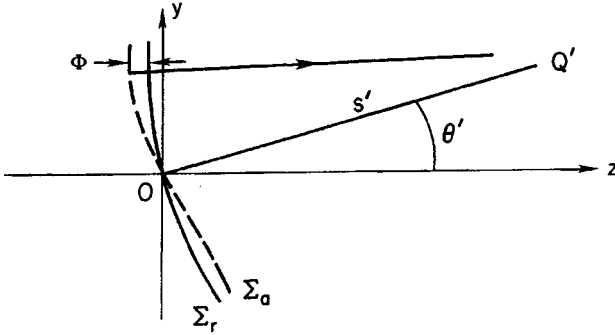


Fig. 5.4. Cross sections of reference and aberrant wavefronts,  $\Sigma_r$  and  $\Sigma_a$ , respectively. Radius of curvature of the reference wavefront is  $s'$ .

For a system with aberrations the wavefront converging toward  $Q'$  is no longer spherical and, depending on the sign of  $\Phi$ , is either advanced or retarded at each point on the wavefront. A schematic cross section of an aberrant wavefront designated  $\Sigma_a$ , is shown in Fig. 5.4, with it and the ideal wavefront  $\Sigma_r$  in contact at their centers where  $\Phi = 0$ . At any other point on the actual wavefront,  $\Phi$  is the OPD between  $\Sigma_r$  and  $\Sigma_a$ . The geometrical distance along any ray between the wavefronts is  $\Phi/n'$  and designating this distance as  $\Delta$  we have

$$\Delta = \frac{\Phi(x, y)}{n'} = \frac{1}{n'} [\Sigma_r(x, y) - \Sigma_a(x, y)]. \quad (5.3.1)$$

For the situation shown in Fig. 5.4 we have  $n' > 0$ , hence  $\Delta$  and  $\Phi$  have the same signs. When  $\Delta > 0$  the actual wavefront is retarded with respect to the reference wavefront; the actual wavefront is advanced when  $\Delta < 0$ .

Differentiating Eq. (5.3.1) gives

$$\frac{\partial \Delta}{\partial y} = \frac{1}{n'} \frac{\partial \Phi}{\partial y} = \frac{1}{n'} \left( \frac{\partial \Sigma_r}{\partial y} - \frac{\partial \Sigma_a}{\partial y} \right), \quad (5.3.2)$$

with a similar relation in which  $x$  replaces  $y$ . The quantity in parentheses in Eq. (5.3.2) is the difference in slopes between the reference and aberrant wavefronts in a slice parallel to the  $yz$ -plane. Because rays are perpendicular to wavefronts, this is also the difference between the slopes of the ray for a perfect system and the actual ray, each at point  $(x, y)$  on the respective wavefronts. Given this difference in slopes, there is a consequent transverse aberration in the  $y$ -direction at the image, as shown in Fig. 5.5. A similar result follows in the  $x$ -direction from Eq. (5.3.2) with  $x$  in place of  $y$ . From the geometry in Fig. 5.5 we get

$$TA_y = s' \frac{\partial \Delta}{\partial y} = \frac{s'}{n'} \frac{\partial \Phi}{\partial y}, \quad TA_x = s' \frac{\partial \Delta}{\partial x} = \frac{s'}{n'} \frac{\partial \Phi}{\partial x}, \quad (5.3.3)$$

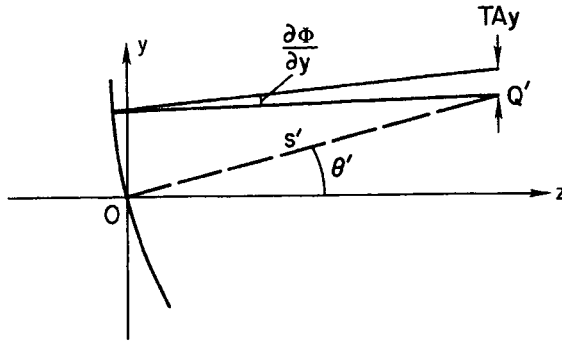


Fig. 5.5. Geometry of wavefront slope difference and transverse aberration in the image. See Eq. (5.3.3).

where the subscripts  $x$  and  $y$  on TA denote transverse aberrations in the  $x$ - and  $y$ -direction, respectively.

Substituting Eq. (5.1.6) into Eqs. (5.3.3) gives

$$TA_y = \frac{s'}{n'} [A_0 + 2A_1y + A_2(x^2 + 3y^2) + 4A_3yr^2], \tag{5.3.4}$$

$$TA_x = \frac{s'}{n'} [2A'_1x + 2A_2xy + 4A_3xr^2]. \tag{5.3.5}$$

We have now established the connection between the aberration coefficients and the geometrical transverse aberrations. The corresponding angular aberrations, denoted by AA, are given by

$$TA_y = s'AA_y, \quad TA_x = s'AA_x. \tag{5.3.6}$$

We now examine briefly the specific aberrations in Eq. (5.3.4) and relate each to the corresponding wavefront aberration.

The term with  $A_3$  is a measure of spherical aberration. As noted in the discussion following Eq. (4.3.6), we replace  $r$  with  $y$  for third-order aberrations. The resulting TSA3 changes sign when  $y$  changes sign, as shown clearly in Fig. 4.5. The corresponding wavefront aberration map is shown in Fig. 5.6, where the concave surface represents the advance of the spherically aberrant wavefront relative to the reference wavefront. The  $z$ -axis of the optical system in Fig. 5.6 is directed vertically upward and passes through the center of the diagram, origin  $O$  in Fig. 5.5 is at the center of the surface in Fig. 5.6, and the  $x$ -axis is to the right. Note that an unaberrated wavefront is a plane in this type of map, with the deviation from this plane proportional to  $\Delta$  of Eq. (5.3.1).

The term in Eq. (5.3.4) with  $A_1$  represents astigmatism, as discussed in the previous section, and the wavefront aberration map for the circular astigmatic blur in Fig. 5.3 is shown in Fig. 5.7. Note that this map shows a wavefront that is both

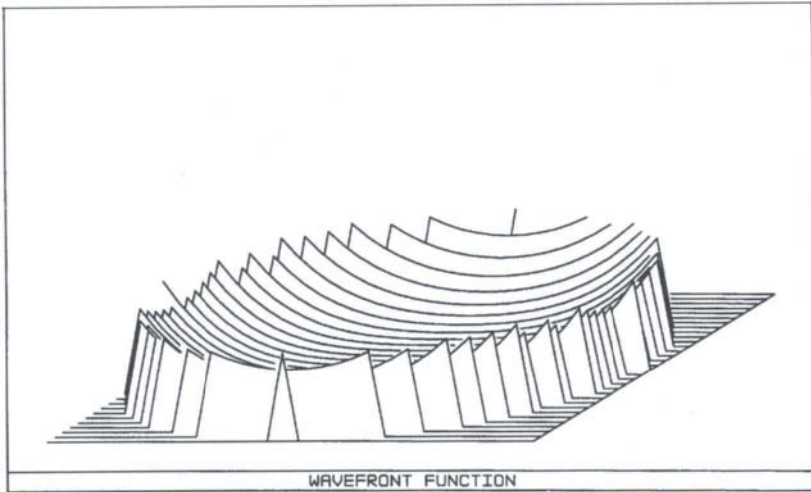


**Fig. 5.6.** Wavefront aberration map for image with spherical aberration. The image is located at the paraxial focus. See Figs. 4.5 and 4.6 for ray and spot diagrams.

advanced and retarded. The portion that is advanced is higher than the center, while the retarded part is lower. A useful exercise for the reader is to correlate the ray directions in Fig. 5.2 with the shape of the wavefront map in Fig. 5.7.

The coefficient  $A_2$  is a measure of coma. A sketch showing the asymmetric form of this aberration is given in Fig. 5.8. Note that the marginal rays on the

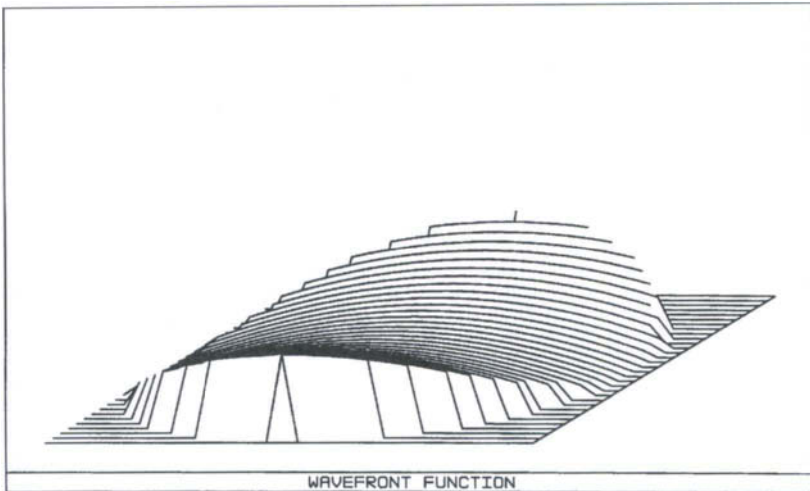


**Fig. 5.7.** Wavefront aberration map for the circular astigmatic image in Fig. 5.3.

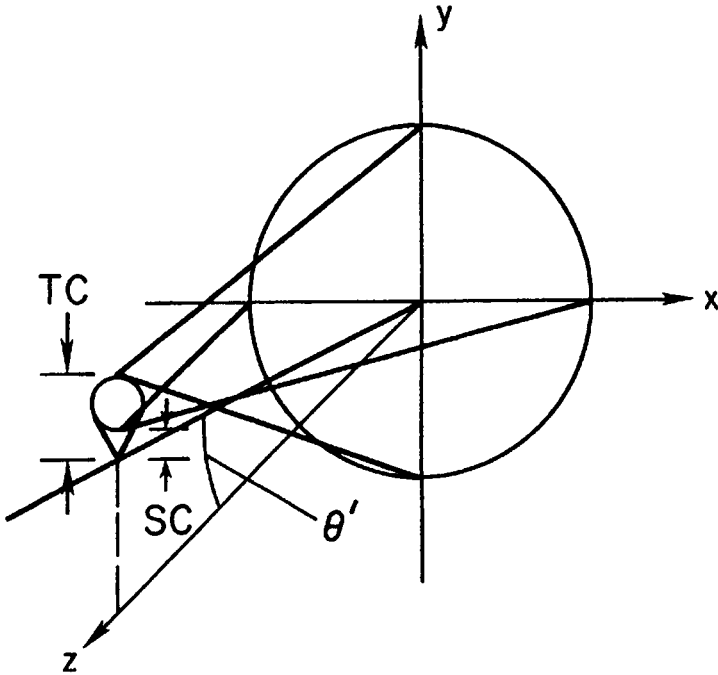
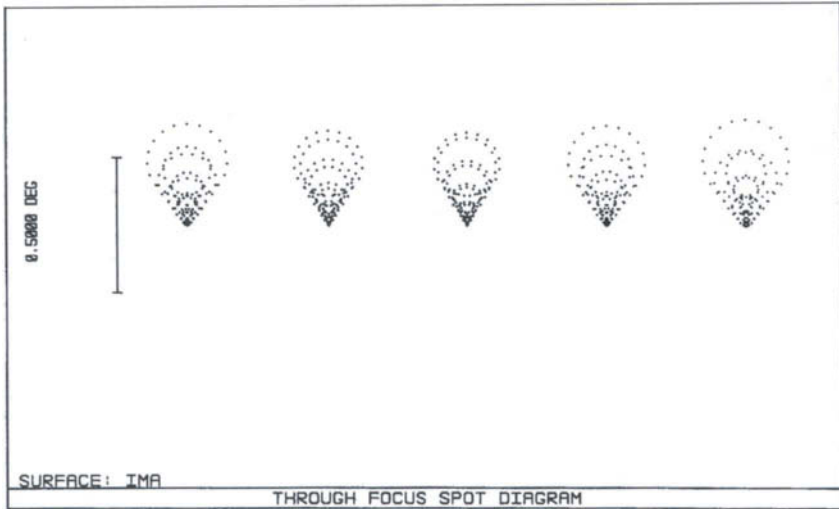


Fig. 5.8. Sketch of comatic image profile. Here TC and SC are tangential and sagittal coma, respectively.  $TC = 3 \cdot SC$ .

$y$ -axis meet at a point three times farther from the Gaussian image, compared with the corresponding point for the marginal rays on the  $x$ -axis. The source of this difference between the tangential and sagittal coma is evident by inspection of Eq. (5.3.4). Coma is fully specified by giving either transverse sagittal coma (TSC) or transverse tangential coma (TTC), with  $TTC = 3 \text{ TSC}$ .

The distribution of light rays over the comatic image is not uniform, there being a greater density of rays near the point of the comatic image. A spot diagram for a comatic image is shown in Fig. 5.9 with the chief ray at the point of the image. About 80% of the energy is within a distance equal to TSC from the Gaussian focus. Unlike the case of spherical aberration, a shift along the chief ray does not improve the image quality. The wavefront map for a comatic image is shown in Fig. 5.10. (For clarity the map in Fig. 5.10 is rotated by  $90^\circ$  relative to the spot diagram in Fig. 5.9, with the  $y$ -axis to the right.) In this case the asymmetry is clearly shown by the general downward slope from left to right in Fig. 5.10. A careful study of ray directions in Fig. 5.8 and slopes in Fig. 5.10 (suitably rotated) is suggested.



**Fig. 5.9.** Through-focus spot diagrams of image with coma.

The remaining coefficient  $A_0$  is a measure of distortion. If  $A_0$  is nonzero the effect is to displace the chief ray and change the position of the final image but not its quality. Any straight line in the object plane that does not pass through the  $z$ -axis is imaged as a curved line if distortion is present. Thus a square in the object plane centered on the  $z$ -axis will appear distorted in the image plane. If

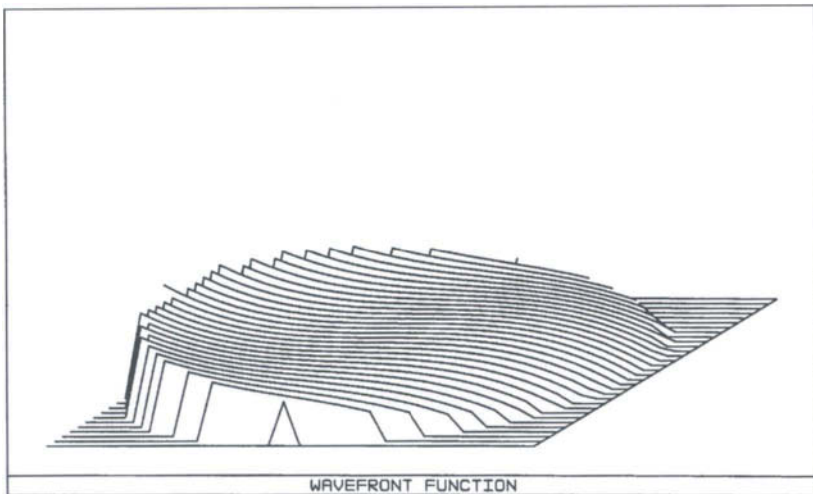


**Fig. 5.10.** Wavefront aberration map for the comatic image in Fig. 5.9. The map is rotated by  $90^\circ$  relative to the spot diagram in Fig. 5.9.

$A_0 > 0$  the reimaged square resembles a pincushion; if  $A_0 < 0$  the result is barrel distortion. See Born and Wolf (1980), or Welford (1986), for schematic diagrams of distortion.

For a mirror the paraxial equation is exact, and hence there is no distortion when the stop is at the surface. Distortion generally is present when the stop is displaced from the surface of a mirror.

Finally, we have not yet considered curvature of field, the final aberration noted in Section 4.4. Characteristics of this aberration are given in Section 5.7 of this chapter.

For more details on the nature of aberrations and wavefront maps, the reader should consult Born and Wolf (1980), and Welford (1986). An especially thorough discussion of aberrations is given by Mahajan (1998).

#### 5.4. SUMMARY OF ABERRATION RESULTS, STOP AT SURFACE

It is now appropriate to bring together all of the important results on aberrations and present them in a set of tables for convenient reference. Following are two tables of aberration coefficients, Table 5.1 for a general refracting surface and Table 5.2 for a reflecting surface. Because many of the applications considered in subsequent chapters involve single or multiple mirror systems, it is convenient to include a separate table for mirrors. The next two tables summarize the results for transverse aberrations, Table 5.3 for a general refracting surface and Table 5.4 for mirrors. Explanations and definitions are included as needed.

All of the results in this section apply specifically to the case where the aperture stop is at the surface. Because there are no optical surfaces either

**Table 5.1**

Aberration Coefficients for General Surface<sup>a,b</sup>

$$\begin{aligned}
 A_3 &= -\frac{1}{8} \left[ n^2 \left( \frac{1}{s} - \frac{1}{R} \right)^2 \left( \frac{1}{n's'} - \frac{1}{ns} \right) + \frac{K}{R^3} (n' - n) + b \right] \\
 A_2 &= \theta \frac{n^2}{2} \left( \frac{1}{s} - \frac{1}{R} \right) \left( \frac{1}{n's'} - \frac{1}{ns} \right) \\
 A_1 &= -\theta^2 \frac{n^2}{2} \left( \frac{1}{n's'} - \frac{1}{ns} \right) \\
 A_0 &= \theta^3 \frac{n}{2} \left( \frac{n^2}{n'^2} - 1 \right)
 \end{aligned}$$

<sup>a</sup> Entrance pupil is at surface.

<sup>b</sup> For a spherical refracting surface with no aspheric component, the last two terms in  $A_3$  are absent.

Table 5.2

Aberration Coefficients for Mirror Surface<sup>a,b</sup>

$$A_3 = \frac{n}{4R^3} \left[ K + \left( \frac{m+1}{m-1} \right)^2 \right] - \frac{b}{8}, \quad A_0 = 0$$

$$A_2 = -\frac{n\theta}{R^2} \left( \frac{m+1}{m-1} \right), \quad A_1 = \frac{n\theta^2}{R}$$

<sup>a</sup> Entrance pupil is at surface.<sup>b</sup> The following relations apply to a mirror:

$$\frac{1}{s} - \frac{1}{R} = \frac{1}{R} \left( \frac{m+1}{m-1} \right), \quad \frac{1}{n's'} - \frac{1}{ns} = -\frac{2}{nR}$$

Table 5.3

Transverse Aberrations for General Surface<sup>a,b</sup>

$$\text{TSA} = -\frac{1}{2} \left[ n^2 \left( \frac{1}{s} - \frac{1}{R} \right)^2 \left( \frac{1}{n's'} - \frac{1}{ns} \right) + \frac{K}{R^3} (n' - n) + b \right] \frac{y^3 s'}{n'}$$

$$\text{TSC} = \frac{n^2}{2} \left( \frac{1}{s} - \frac{1}{R} \right) \left( \frac{1}{n's'} - \frac{1}{ns} \right) \frac{y^2 \theta s'}{n'} = \frac{1}{3} \text{TTC}$$

$$\text{TAS} = -n^2 \left( \frac{1}{n's'} - \frac{1}{ns} \right) \frac{y \theta^2 s'}{n'}, \quad \Delta s' = -\frac{s'}{y} \text{TAS}$$

$$\text{TDI} = \frac{n}{2} \left( \frac{n^2}{n'^2} - 1 \right) \frac{\theta^3 s'}{n'}$$

<sup>a</sup> Entrance pupil is at surface.<sup>b</sup> Angular aberrations are given by the above relations with the final  $s'/n'$  divided out.

Table 5.4

Transverse Aberrations for Mirror Surface<sup>a</sup>

$$\text{TSA} = -\frac{y^3}{R^3} \left[ K + \left( \frac{m+1}{m-1} \right)^2 \right] s' + \frac{by^3}{2n} s'$$

$$\text{TSC} = \frac{y^2}{R^2} \left( \frac{m+1}{m-1} \right) \theta s' = \frac{1}{3} \text{TTC}$$

$$\text{TAS} = -\frac{2y}{R} \theta^2 s', \quad \text{TDI} = 0$$

<sup>a</sup> Entrance pupil is at surface.

preceding or following this surface, the entrance and exit pupils are also located at the surface.

#### 5.4.a. DEFINITIONS, CHARACTER OF ABERRATIONS

Measures of the transverse aberrations are taken from Eq. (5.3.4). For completeness a summary of the designations follows. Each aberration is designated by two letters: spherical aberration, SA; sagittal coma, SC; tangential coma, TC; astigmatism, AS; and distortion, DI. If the aberration is transverse, a prefix T is attached; if the aberration is angular, a prefix A is attached.

With these designations the transverse aberration expressions are:

$$\text{TSA} = \frac{4A_3y^3s'}{n'}, \quad \text{TSC} = \frac{A_2y^2s'}{n'}, \quad \text{TAS} = \frac{2A_1ys'}{n'}, \quad \text{TDI} = \frac{A_0s'}{n'}. \quad (5.4.1)$$

Note that TSC is simply one-third of the tangential coma, where the latter is based on the rays from the  $y$ -axis. All of the aberrations are computed using rays from the  $y$ -axis, with the full aberrations given by Eqs. (5.4.1) when the radius of the surface is substituted for  $y$ .

It is not necessary to use Eq. (5.3.5) to find transverse aberrations in the  $x$  direction because  $A'_1$  is zero, given our choice  $s' = s'_s$ , and the extent of the blur in the  $x$  direction is known from results of Eqs. (5.4.1). Thus all measures of transverse aberrations given in what follows are in the  $y$  direction, that is, measured in the plane defined by the chief ray and  $z$ -axis.

Results obtained by substituting from Tables 5.1 and 5.2 into Eqs. (5.4.1) are given in Tables 5.3 and 5.4. Although  $\Delta s'$  is actually a longitudinal aberration, its relation to TAS is included in Table 5.3 for completeness. All of the relations in Tables 5.1 and 5.2 include the sign convention and thus these equations give information about the character of the aberrations as well as their magnitudes. A brief summary of the relation between the sign of the aberration coefficient and image character follows, where the choice of sign is in accord with the figures illustrating each of the aberrations. With  $\theta > 0$ ,

- $A_3 < 0$ : marginal rays cross chief ray between surface and Gaussian focus,
- $A_2 > 0$ : coma flare is directed away from  $z$ -axis, or Gaussian focus between flare and axis,
- $A_1 < 0$ : tangential line image closer to surface than sagittal image, and
- $A_0 > 0$ : pincushion distortion.

For some purposes the sign of the aberration is of no consequence and the magnitude is all that matters. In terms of magnitudes, each of the aberrations has the following interpretation:

$$\begin{aligned}
 |TAS| &= \text{half-length of astigmatic line image} \\
 &= \text{diameter of astigmatic blur circle,} \\
 3|TSC| &= \text{length of comatic flare} \\
 &= 1.5 \times \text{width of comatic flare,} \\
 |TSA| &= \text{radius of blur at paraxial focus} \\
 &= 2 \times \text{diameter of circle of least confusion.}
 \end{aligned}$$

All of these results assume, of course, that only a single aberration is nonzero. If more than one aberration is present in an image, there is no simple way to characterize the blur character or dimensions.

Inspection of the entries in Tables 5.1 and 5.2 shows that the aberration coefficients are independent of the direction of incident light on a given surface. Reversing the direction of incident light is equivalent to taking Fig. 5.1 and reversing it left for right, thus changing the signs of  $n$ ,  $n'$ ,  $s$ ,  $s'$ ,  $R$ , and  $\theta$ . Thus the transverse aberrations are also the same for either direction of incident light. This result is expected because the direction of the incident light, left to right or vice versa, cannot change the character of the image.

#### 5.4.b. APLANATIC CONDITION AND OTHER EXAMPLES

We now examine the various terms in Tables 5.1 and 5.2 to find examples of surfaces that have specific aberration characteristics. For a spherical surface with  $b = 0$  the aberration coefficients  $A_1$  through  $A_3$  in Table 5.1 are zero when  $n's' = ns$ . For a mirror  $n' = -n$  and this condition is satisfied with  $s' = -s$ . Using the paraxial mirror equation (2.3.2) we find  $R = \infty$ , hence the surface is a plane mirror. This result is expected but not especially useful because a plane mirror has zero power.

For a spherical refracting surface the condition  $n's' = ns$ , together with the Gaussian equation (2.2.2) gives

$$ns = n's' = R(n + n'). \quad (5.4.2)$$

This defines the object and image positions for a so-called aplanatic sphere, where the term *aplanatic* means the system has zero spherical aberration and coma. A lens of this type is often used as the first element in high-power microscope objectives. It has also been used as an element near the focus of a Schmidt camera in a spectrograph to shorten the camera focal length, as noted by Bowen (1960). In this application its chromatic aberration is not a serious constraint in getting good image quality.

A paraboloid ( $K = -1$ ) in collimated light ( $m = 0$ ) has zero spherical aberration but nonzero coma and astigmatism. Thus this type of mirror, though perfect on-axis, has a limited field of view (FOV) when used as a telescope.

Further discussion of the image characteristics of a paraboloid is presented in Chapter 6.

For a conic mirror with  $b = 0$ , the condition for zero spherical aberration fixes  $K$  in terms of  $m$ . Setting  $A_3 = 0$  in Table 5.2 gives the relation in Eq. (3.5.4), a result used in Section 4.5 to establish the conic constant for the secondary mirror of a classical Cassegrain telescope. Note that such a mirror has coma and astigmatism.

From the entries in Table 5.2 we also see that a sphere ( $K = 0$ ) in a configuration with  $m = -1$ , thus  $s' = s = R$ , has zero spherical aberration and coma, hence is an aplanat.

As a final example we point out that a sphere in collimated light has nonzero aberrations both on- and off-axis. Although this would appear to limit the usefulness of a spherical mirror, our discussion in Chapter 4 shows that this is not the case when the aperture stop is separated from the mirror. This is our topic for the next section.

### 5.5. ABERRATIONS FOR DISPLACED STOP

We now determine the aberration coefficients for a single surface with the aperture stop displaced from the surface, as shown in Figs. 5.11 and 5.12. In Fig. 5.11 the stop defines the light bundle before refraction at the surface, and the entrance pupil coincides with the stop. In Fig. 5.12 the stop follows the surface and the entrance pupil, or image of the stop, is separate from the stop. In both figures the chief ray is directed toward the center of the pupil at angle  $\psi$  with the  $z$ -axis and intersects the surface at height  $L$ .

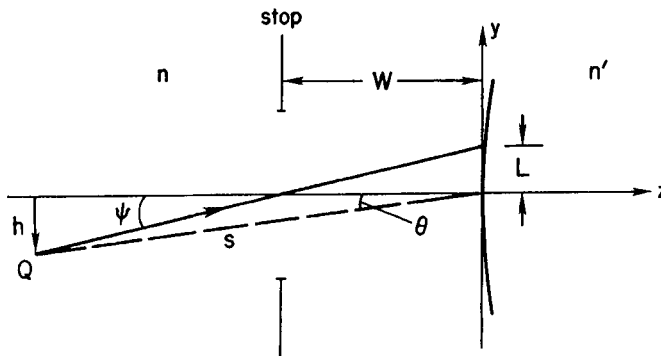


**Fig. 5.11.** Portion of Fig. 5.1 with aperture stop displaced from surface. The chief ray makes angle  $\psi$  with the  $z$ -axis and intersects the surface of height  $L$ . The entrance pupil is at the stop. The relation between parameters is given in Eq. (5.5.2). In this diagram  $W < 0$ ,  $L > 0$ ,  $\psi$  and  $\theta > 0$ .

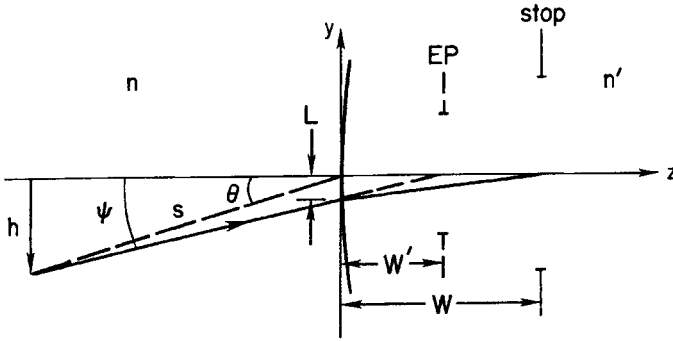


**Fig. 5.12.** Repeat of Fig. 5.11 with stop to right of surface. The stop is reimaged as the entrance pupil EP. Equation (5.5.2) applies when  $W'$  replaces  $W$ . In this diagram  $L < 0$ ,  $W$  and  $W' > 0$ .

Comparing these figures with Fig. 5.1 we see that an arbitrary ray that met the surface at  $(x, y)$  in Fig. 5.1 now meets the surface at  $(x, y + L)$ . Because a different portion of the surface refracts the light bundle from  $Q$  when the stop is displaced, it is expected that the image aberrations will differ from those derived for Fig. 5.1. An example of this difference was previously noted in Section 4.5, where the absence of coma and astigmatism for a sphere with stop at the center of curvature of the sphere was the basis for the Schmidt camera. These aberrations are not zero when the stop coincides with the surface, as is evident from Table 5.2. This one example illustrates the importance of the stop position in controlling or eliminating aberrations.

5.5.a. STOP-SHIFT RELATIONS

We now proceed to find the general aberration relations for a displaced stop. The procedure is simply one of putting  $y + L$  in place of  $y$  in Eq. (5.1.6). Collecting terms in various powers of  $x, y$ , or  $r$ , and dropping all constants independent of these variables, we get

$$\begin{aligned}
 \Phi &= y(A_0 + 2LA_1 + 3L^2A_2 + 4L^3A_3) \\
 &\quad + y^2(A_1 + 3LA_2 + 6L^2A_3) + x^2(A'_1 + LA'_2 + 2L^2A_3) \\
 &\quad + y^3(A_2 + 4LA_3) + x^2y(A'_2 + 4LA_3) + A_3r^4 \\
 &= B_0y + B_1y^2 + B'_1x^2 + B_2(x^2y + y^3) + B_3r^4,
 \end{aligned}
 \tag{5.5.1}$$

where  $A'_2 = A_2$  is used to combine the cubic terms.

Even before deriving the explicit form of the  $B_i$ , there are several important statements that follow from Eq. (5.5.1). These *stop-shift relations* are:

- (1)  $L$  does not appear in the  $r^4$ -term and thus the spherical aberration coefficient is independent of stop position.
- (2) If  $A_3 = 0$ , the coma coefficient  $B_2$  is independent of the stop position and the coma is that given in Section 5.4.
- (3) If both  $A_2$  and  $A_3$  are zero,  $B_1$  and  $B'_1$  are independent of the stop position, and reduce to  $A_1$  and  $A'_1$ , respectively.

The importance of these statements will become evident when specific systems are discussed in the chapters that follow. Although they are deduced here for a single surface, it turns out these statements also apply to a system made up of many surfaces.

### 5.5.b. ABERRATION COEFFICIENTS

The process required to evaluate each  $B_i$  is a straightforward one, though the algebra is a bit messy at times and therefore omitted in the discussion to follow. When the evaluation is more than simple substitution, as for astigmatism, a brief outline of the procedure is given.

To begin, we note the following relations, valid in the paraxial approximation, derived from the geometry in Fig. 5.11:

$$L = -W\psi, \quad \theta = \psi[1 - (W/s)], \quad (5.5.2)$$

where  $W$  is the distance from the surface to the entrance pupil, and both  $L$  and  $W$  are governed by the same sign convention as other distances. Figure 5.12 shows the geometry for the case where the stop follows the surface. In this case Eq. (5.5.2) applies if  $W$  is replaced by  $W'$ . A glance at Eq. (5.5.2) and Fig. 5.11 shows that, for a given  $\theta$ ,  $\psi$  increases in size as  $s$  approaches  $W$ . There will come a point where  $\psi$  is large enough to make the paraxial result in Eq. (5.5.2) invalid, and results derived using Eq. (5.5.2) will be incorrect. Unfortunately, no simple statement can be made about where this breakdown occurs, and one must check on a case-by-case basis as to the validity of results derived from third-order aberration theory. Exact ray-tracing is generally used to check the results.

A final point to be made is in the choice of parameters used in presenting the aberration coefficients. The choice made here is to eliminate  $L$  and  $\theta$ , and to give the results in terms of  $W$ , the entrance pupil position, and  $\psi$ , the chief ray angle.

With these preliminaries behind us, we proceed with the results; Table 5.5 gives the coefficients for a general surface, while Table 5.6 gives the results for a mirror. The spherical term  $B_3$  is taken from Tables 5.1 and 5.2 and is included here for completeness. The term  $B_2$  is derived from Eq. (5.5.1) and the entries in Tables 5.1 and 5.2 by direct substitution, while  $B_0$  follows from Eq. (5.5.1) and a procedure similar to that used in arriving at Eq. (5.2.9).

Table 5.5

General Aberration Coefficients, Centered Pupil<sup>a</sup>

$$\begin{aligned}
 B_3 &= -\frac{1}{8} \left[ \Gamma \left( \frac{1}{s} - \frac{1}{R} \right)^2 + \frac{K}{R^3} (n' - n) + b \right] \\
 B_2 &= \frac{(W\psi)}{2} \left[ \Gamma \left( \frac{1}{s} - \frac{1}{R} \right) \left( \frac{1}{W} - \frac{1}{R} \right) + \frac{K}{R^3} (n' - n) + b \right] \\
 B_1 &= -\frac{(W\psi)^2}{2} \left[ \Gamma \left( \frac{1}{W} - \frac{1}{R} \right)^2 + \frac{K}{R^3} (n' - n) + b \right] \\
 B_0 &= \frac{(W\psi)^3}{2} \left[ \Gamma \left( \frac{1}{W} - \frac{1}{R} \right) \left( \frac{1}{W} - \frac{1}{R} + \frac{1}{W} - \frac{1}{s} \right) + n \left( \frac{n^2}{n'^2} - 1 \right) \left( \frac{1}{W} - \frac{1}{R} \right) \left( \frac{1}{W} - \frac{1}{s} \right)^2 \right. \\
 &\quad \left. + \frac{K}{R^3} (n' - n) + b \right] \\
 \Gamma &= n^2 \left( \frac{1}{n's'} - \frac{1}{ns} \right)
 \end{aligned}$$

<sup>a</sup> Entrance pupil at distance  $W$  from surface.

The derivation of  $B_1$  is not one of direct substitution of the  $A_i$  but involves going through the steps analogous to those used in Sections 5.1 and 5.2. First we note that

$$B_1 = A_1 + 3L\Omega, \quad B'_1 = A'_1 + L\Omega, \quad (5.5.3)$$

where  $\Omega = A_2 + 2LA_3$ , and  $A_1$  and  $A'_1$  are the multiplying factors of  $y^2$  and  $x^2$ , respectively, in Eq. (5.1.5).

Table 5.6

Mirror Aberration Coefficients, Centered Pupil<sup>a</sup>

$$\begin{aligned}
 B_3 &= \frac{n}{4R^3} \left[ K + \left( \frac{m+1}{m-1} \right)^2 \right] - \frac{b}{8} \\
 B_2 &= -n \frac{(W\psi)}{R^2} \left[ \frac{K}{R} + \left( \frac{m+1}{m-1} \right) \left( \frac{1}{W} - \frac{1}{R} \right) \right] + \frac{b}{2} (W\psi) \\
 B_1 &= n \frac{(W\psi)^2}{R} \left[ \frac{K}{R^2} + \left( \frac{1}{W} - \frac{1}{R} \right)^2 \right] - \frac{b}{2} (W\psi)^2 \\
 B_0 &= -n (W\psi)^3 \left[ \frac{K}{R^3} + \frac{1}{R} \left( \frac{1}{W} - \frac{1}{R} \right) \left( \frac{1}{W} - \frac{1}{R} + \frac{1}{W} - \frac{1}{s} \right) \right] + \frac{b}{2} (W\psi)^3
 \end{aligned}$$

<sup>a</sup> Entrance pupil at distance  $W$  from surface.

The choice of  $B_1 = 0$  or  $B'_1 = 0$  locates the tangential or sagittal images, respectively. Corresponding to Eqs. (5.1.8) and (5.1.9) we find

$$\frac{n' \cos^2 \theta'}{s'_t} - \frac{n \cos^2 \theta}{s} = \frac{n' \cos \theta' - n \cos \theta}{R} - 6L\Omega, \quad (5.5.4)$$

$$\frac{n'}{s'_s} - \frac{n}{s} = \frac{n' \cos \theta' - n \cos \theta}{R} - 2L\Omega. \quad (5.5.5)$$

The relation analogous to Eq. (5.1.10), through terms in  $\theta^2$ , is

$$\frac{\Delta s'}{s'^2} = \left( \frac{\Delta s'}{s'^2} \right)_{w=0} - \frac{4L\Omega}{n'} \quad (5.5.6)$$

where the first term to the right of the equal sign is given in Eq. (5.1.10).

The next step is to choose an image at which to evaluate the astigmatism and, as in Section 5.2, the choice is the sagittal image. Solving Eq. (5.5.5) for  $s'_s$ , substituting the result into  $B_1$  in Eq. (5.5.3), and evaluating to second-order in  $\theta$ , gives

$$B_1 = A_1 + 2L\Omega = -\frac{n'}{2} \left( \frac{\Delta s'}{s'^2} \right)_{w=0} + 2L\Omega. \quad (5.5.7)$$

Note that  $A_1$  in the first part of Eq. (5.5.7) is the value at the sagittal image, hence different from  $A_1$  in Eq. (5.5.3). From a comparison of Eqs. (5.5.6) and (5.5.7) we find

$$\Delta s'/s'^2 = -2B_1/n', \quad (5.5.8)$$

a relation corresponding to Eq. (5.2.5). Thus  $B_1$  is a measure of the astigmatism when the entrance pupil is not at the surface. The entry for  $B_1$  in Table 5.5 is obtained by evaluation of Eq. (5.5.7).

The relations between the aberration coefficients and the transverse aberrations are similar to those given in Eqs. (5.4.1), but with  $B_i$  replacing  $A_i$ .

$$\begin{aligned} \text{TSA} &= \frac{4B_3 y^3 s'}{n'}, & \text{TSC} &= \frac{B_2 y^2 s'}{n'} = \frac{1}{3} \text{TTC}, \\ \text{TAS} &= \frac{2B_1 y s'}{n'}, & \text{TDI} &= \frac{B_0 s'}{n'}. \end{aligned} \quad (5.5.9)$$

The full aberration is obtained from Eq. (5.5.9) when  $y$  is replaced by the height at which a marginal ray from  $Q$  on the  $z$ -axis intersects the surface. Tables analogous to 5.3 and 5.4 are left to the reader.

## 5.5.c. EXAMPLES

At this point it is appropriate to illustrate the aberration relations with two examples. Our choices are a sphere and a paraboloid, each illuminated with collimated light, hence  $m = 0$ . We assume no aspheric component and set  $b = 0$ .

For the sphere we find  $A_3 = B_3 = n/4R^3$ , hence we expect that both  $B_2$  and  $B_1$  will depend on the stop position. Inspection of the coefficients in Table 5.6 shows that this is the case. When  $W = R$ , both  $B_2$  and  $B_1$  are zero; this stop position is the starting point for the Schmidt camera.

Taking a sphere in collimated light with an aspheric component, we find  $B_3 = 0$  when  $b = 2n/R^3$ . This aspheric component could be put directly on the mirror, but this does little good because now the mirror has nonzero coma independent of  $W$ . The solution, of course, is to put the aspheric component on another optical element located at  $W = R$ , as already shown in our discussion of the Schmidt camera. The discussion of how aberrations are calculated for systems with many surfaces is the topic of the next section.

Consider now the parabola with  $B_3 = 0$ . Setting  $m = 0$  and  $K = -1$  in  $B_2$  we see that the coma is independent of  $W$ . This is the expected result, based on the stop-shift relations following Eq. (5.5.1). Because coma is not zero the astigmatism coefficient depends on  $W$ , hence a proper choice of  $W$  will mean zero astigmatism. From  $B_1$  in Table 5.6 we see that this choice is  $W = R/2$ , hence the stop is at the focal surface.

## 5.6. ABERRATIONS FOR MULTISURFACE SYSTEMS

## 5.6.a. GENERAL FORMULATION

The real power of the approach to aberrations using Fermat's Principle is particularly evident when systems with many surfaces are analyzed. For any surface in such a system, say the  $i$ th one, the object and image are at  $Q_i$  and  $Q_i'$  located at distances  $s_i$  and  $s_i'$ , respectively, from the surface. Between the object and image the OPD between an arbitrary ray and the chief ray is given by Eq. (5.5.1), where  $W_i$  is the position of the entrance pupil for the surface. If this same ray is followed from the original object to the final image, then the OPD for the system is

$$\Phi_s = \Phi_1 + \Phi_2 + \cdots + \Phi_f = \Sigma\Phi_i, \quad (5.6.1)$$

where the subscript  $f$  denotes the last surface. Each term in Eq. (5.6.1) can be replaced by Eq. (5.5.1), with the appropriate  $(x, y)$  at each surface. Before making this substitution, note that a complete description of the aberrations according to

Eq. (5.4.1) is obtained from rays in the  $yz$ -plane only. Therefore we set  $x = 0$  in Eq. (5.5.1), and the system OPD for rays in the  $yz$ -plane is

$$\begin{aligned}\Phi_s &= \sum (B_{0i}y_i + B_{1i}y_i^2 + B_{2i}y_i^3 + B_{3i}y_i^4) \\ &= \sum_j \left( \sum_i B_{ji}y_i^{j+1} \right), \quad j = 0, 1, 2, 3,\end{aligned}\quad (5.6.2)$$

with the geometrical distance along an arbitrary ray between the actual and reference wavefronts at the final surface given by

$$\Delta = \Phi_s(y_i)/n'_f. \quad (5.6.3)$$

To find the transverse aberration at the final image, we proceed along the lines followed in going from Eq. (5.3.1) to Eq. (5.3.3), but do so with only one of the aberration terms, say the  $j$ th one. With reference to the last surface we get

$$\frac{\partial \Delta}{\partial y_f} = \frac{1}{n'_f} \frac{\partial \Phi_s}{\partial y_f} = \frac{1}{n'_f} (j+1) \sum_i B_{ji} y_i^j \frac{\partial y_i}{\partial y_f}. \quad (5.6.4)$$

The partial derivative in Eq. (5.6.4) is easily evaluated with the aid of Fig. 5.13, where two rays from an intermediate axial object point are shown passing through several surfaces. Because each  $Q_i$  is imaged to  $Q_i'$ , the ratio of the differential change in  $y_i$  to that of any other  $y$ , say the  $f$ th one, is simply the ratio  $y_i/y_f$ . Substituting this into Eq. (5.6.4) and multiplying by  $s'_f$ , we can write the  $j$ th transverse aberration in the  $y$ -direction as

$$\text{TA}_{jy} = \frac{s'_f}{n'_f} \frac{\partial \Phi_s}{\partial y_f} = \frac{s'_f}{n'_f} (j+1) \left[ \sum_i B_{ji} \left( \frac{y_i}{y_f} \right)^{j+1} \right] y_f^j \quad (5.6.5)$$

or

$$\text{TA}_{jy} = \frac{s'_f}{n'_f} (j+1) B_{js} y_f^j. \quad (5.6.6)$$

In Eq. (5.6.6) the representation of the sum in brackets in Eq. (5.6.5) is reduced to a single symbol, with the subscript  $s$  denoting a system aberration coefficient. Note the close correspondence between Eq. (5.6.6) and each of the terms containing  $y$  in Eq. (5.3.4).

Calculation of the transverse aberration using Eq. (5.6.6) is based on the marginal ray height at the last surface. In many cases it is convenient to express the transverse aberration in terms of the marginal ray height at some other surface, such as at the system entrance pupil. This is easily done by multiplying

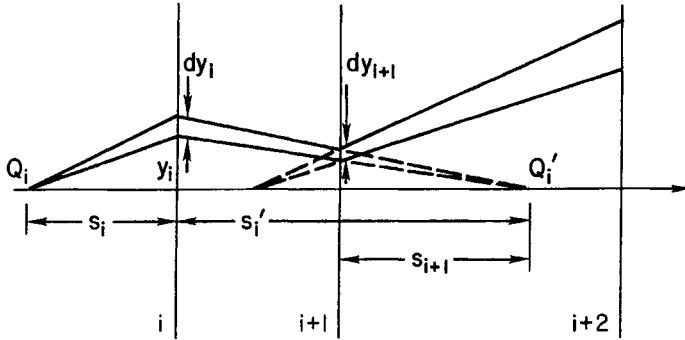


Fig. 5.13. Paths of two adjacent rays from  $Q_i$  through several surfaces, where  $Q_i$  is an intermediate axial object point. Differential heights  $dy_i \propto y_i$  at each surface.

and dividing Eq. (5.6.5) by the ray height at another surface, say the  $i$ th one, raised to the  $j + 1$  power. The results are

$$B_{js} = \sum_i B_{ji} \left( \frac{y_i}{y_i} \right)^{j+1}, \quad (5.6.7)$$

$$\text{TA}_{jy} = \frac{s'_j}{n'_j} \left( \frac{y_i}{y_f} \right) (j+1) B_{js} y_i^j. \quad (5.6.8)$$

Note that the terms in Eq. (5.6.7) depend on the choice of  $i$  but  $\text{TA}_{jy}$  is, of course, independent of this choice.

The formalism needed to calculate third-order aberrations for a multisurface system is now complete. The necessary aberration coefficients are in Tables 5.5 and 5.6, and it is simply a matter of computing each one surface-by-surface and substituting into Eqs. (5.6.7) and (5.6.8).

The relations given in Section 5.4 between the signs of the aberration coefficients and the character of an image also hold for the coefficients in Eq. (5.6.7) and the transverse aberrations in Eq. (5.6.8).

### 5.6.b. EXAMPLE: ABERRATION COEFFICIENTS OF TWO-MIRROR TELESCOPES

As an example of the procedure in Section 5.6.a, consider either the Cassegrain or Gregorian telescope shown in Fig. 2.7. We assume the stop is at the primary, thus its aberration coefficients can be taken from Table 5.2. Setting  $n = 1$ ,  $m = 0$ , and  $b = 0$  gives

$$B_{01} = 0, \quad B_{11} = \frac{\theta^2}{R_1}, \quad B_{21} = \frac{\theta}{R_1^2}, \quad B_{31} = \frac{1}{4R_1^3} (K_1 + 1). \quad (5.6.9)$$

For the secondary  $n = -1, b = 0$ , and  $\psi = -\theta$  (from the law of reflection  $i' = -i$ ). From Table 5.6 we get

$$\begin{aligned}
 B_{02} &= -(W\theta)^3 \left[ \frac{K_2}{R_2^3} + \frac{1}{R_2} \left( \frac{1}{W} - \frac{1}{R_2} \right) \left( \frac{1}{W} - \frac{1}{R_2} + \frac{1}{W} - \frac{1}{s_2} \right) \right], \\
 B_{12} &= -\frac{(W\theta)^2}{R_2} \left[ \frac{K_2}{R_2^2} + \left( \frac{1}{W} - \frac{1}{R_2} \right)^2 \right], \\
 B_{22} &= -\frac{(W\theta)}{R_2^2} \left[ \frac{K_2}{R_2} + \left( \frac{m+1}{m-1} \right) \left( \frac{1}{W} - \frac{1}{R_2} \right) \right], \\
 B_{32} &= -\frac{1}{4R_2^3} \left[ K_2 + \left( \frac{m+1}{m-1} \right)^2 \right].
 \end{aligned}
 \tag{5.6.10}$$

With  $y_i = y_1$ , the marginal ray height at the primary, we get

$$B_{js} = B_{j1} + B_{j2}(y_2/y_1)^{j+1}; \quad j = 0, 1, 2, 3,
 \tag{5.6.11}$$

where the subscripts 1, 2, and  $s$  on the  $B_j$  refer to the primary, secondary, and telescope, respectively.

In terms of the normalized parameters defined in Chapter 2 for a two-mirror telescope we have  $k = y_2/y_1, \rho = R_2/R_1$ , and  $W = (1 - k)f_1 = -(1 - k)R_1/2$ . For spherical aberration we then get

$$B_{3s} = \frac{1}{4R_1^3} \left\{ K_1 + 1 - \frac{k^4}{\rho^3} \left[ K_2 + \left( \frac{m+1}{m-1} \right)^2 \right] \right\}.
 \tag{5.6.12}$$

Note that spherical aberration is zero when the expression in braces is zero, a result previously given in Eq. (4.5.3). It was derived there by starting with a classical Cassegrain and "bending" the mirrors subject to the requirement that Fermat's Principle be satisfied.

Given Eq. (5.6.12) it is now a simple matter to find TSA3. Using Eqs. (2.5.3) and (2.5.7) we find  $s'_2 = m k f_1 = k f$ . Putting this and  $n'_2 = 1$  into Eq. (5.6.8) gives

$$\text{TSA3} = f \left( \frac{y_1}{R_1} \right)^3 \{ \quad \} = -\frac{f}{64F_1^3} \{ \quad \},
 \tag{5.6.13}$$

where the quantity in braces is that in Eq. (5.6.12), and  $F_1$  is the focal ratio of the primary mirror. Note that the sign of  $R_1$  makes the factor outside of the braces in Eqs. (5.6.12) and (5.6.13) negative.

Expressions for the other aberrations using Eqs. (5.6.9) through (5.6.11) are determined using the same procedure, but this development is left for Chapter 6 where the characteristics of telescopes are explored in detail.

## 5.7. CURVATURE OF FIELD

The remaining third-order aberration to be considered is that of curvature of field. As noted in Chapter 4 this aberration does not affect the image quality, but given the usual case of a flat detector can adversely affect the image definition over an extended field. For the Schmidt camera, for example, the focal surface has a radius of curvature equal to the camera focal length. Matching the detector to the focal surface requires either deforming it to the proper radius or using another optical element to “flatten” the field. The former method is used with most large Schmidt telescopes by bending photographic plates. The use of a field-flattener lens is discussed later in this section.

We now consider the situation shown in Fig. 5.14 where an optical surface whose vertex is at the origin of the  $(x, y, z)$  coordinate system images the curved object surface  $\Sigma$  into a curved image surface  $\Sigma'$ . The surfaces  $\Sigma$  and  $\Sigma'$  have radii of curvature  $r$  and  $r'$ , respectively, with the sign convention for each the same as for a surface radius of curvature, thus  $r > 0$  and  $r' < 0$  in Fig. 5.14. As a final definition, let  $\kappa$  denote the curvature of the image surface, with  $\kappa = 1/r'$ . It should be noted here that our sign convention for  $r$  and  $r'$  is opposite that of Born and Wolf (1980), but we choose to preserve its universal character.

The diagram in Fig. 5.14 can apply to any individual optical surface within a multi-surface system, where  $\Sigma$  is an intermediate object surface and  $\Sigma'$  its conjugate surface. In the discussion to follow we will not designate these surfaces with specific indices, but will include them at the end as needed.

The procedure is one of finding  $s'$  in terms of  $\theta'$  and applying a general relation between  $\kappa$  and  $s'$  to get the curvature of  $\Sigma'$ . A glance at Eqs. (5.5.4) and (5.5.5) shows that  $s'$  can contain only even powers of  $\theta$  and  $\theta'$  when expanded in a power

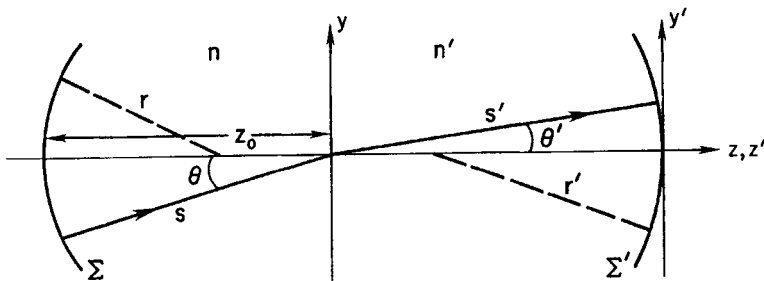


**Fig. 5.14.** Curved object surface  $\Sigma$  imaged to surface  $\Sigma'$ . The radii of curvature of the object and image surfaces are  $r$  and  $r'$ , respectively. The adopted sign convention has  $r > 0$  and  $r' < 0$  in the diagram.

series. Thus we can solve these equations for  $s'$  and, after substituting  $n\theta = n'\theta'$ , get  $s'$  through second order in the form

$$1/s' = a_0 + a_2\theta'^2. \quad (5.7.1)$$

With this form of  $s'$ , it can be shown that the curvature  $\kappa$  to zeroth order is given by

$$\kappa = -(a_0 + 2a_2), \quad (5.7.2)$$

hence  $\kappa$  is constant and to this approximation the image surface is a section of a sphere. (The relation between  $\kappa$  and  $s'$  in polar coordinates from which Eq. (5.7.2) is derived can be found in the *Mathematics Manual* by Merritt, 1962.)

### 5.7.a. PETZVAL SURFACE

We first determine the curvature of a special surface called the *Petzval surface*. This surface is the image surface in the special case where the astigmatism is zero, hence  $s'_s = s'_i = s'_p$ , where  $s'_p$  is the distance from the origin in Fig. 5.14 to the Petzval surface. We can find  $s'_p$  from either Eq. (5.5.4) or (5.5.5).

Given the condition that  $\Delta s' = 0$  in Eq. (5.5.8) we find  $2L\Omega = -A_1$  from Eq. (5.5.7). Substituting this into Eq. (5.5.5) gives

$$\frac{n'}{s'_p} = \frac{n}{s} + \frac{n' \cos \theta' - n \cos \theta}{R} + A_1. \quad (5.7.3)$$

To put Eq. (5.7.3) into the form required by Eq. (5.7.1) means the usual power series substitutions and using  $n\theta = n'\theta'$  to eliminate  $\theta$ . In addition to the angles that appear explicitly in Eq. (5.7.3), the distance  $s$  depends on  $\theta$ . The relation between  $s$  and  $\theta$  is found using the geometry in Fig. 5.15, where the sag  $u$  of  $\Sigma$  is

$$u = \frac{y^2}{2r} = \frac{s^2 \sin^2 \theta}{2r} = s \cos \theta - z_0,$$

and, solving for  $s$ , leads to

$$\frac{1}{s} = \frac{1}{z_0} - \frac{n'^2 \theta'^2}{2n^2} \left( \frac{1}{z_0} + \frac{1}{r} \right).$$

Substituting this result for  $s$  in Eq. (5.7.3) and collecting terms gives

$$\frac{1}{s'_p} = \frac{n}{n'z_0} + \frac{n' - n}{n'R} + \frac{\theta'^2}{2} \left[ \frac{(n' - n)^2}{n'nR} - \frac{n}{n'z_0} - \frac{n'}{nr} \right]. \quad (5.7.4)$$

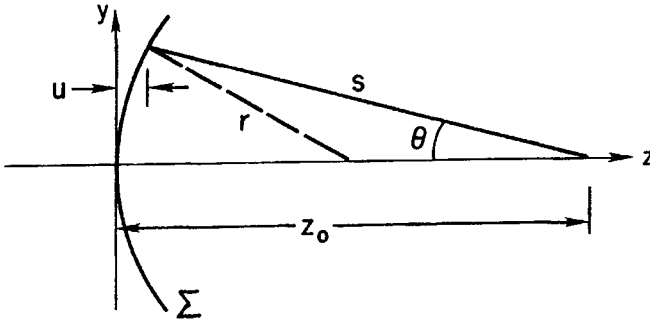


Fig. 5.15. Sag  $u$  of the object surface, with  $u = y^2/2r$ . See the discussion following Eq. (5.7.3).

Equation (5.7.4) is in the form shown in Eq. (5.7.1) and we now find  $\kappa = 1/r'$  from Eq. (5.7.2). The result is

$$\frac{1}{n'r'} - \frac{1}{nr} = -\left(\frac{n' - n}{n'nR}\right). \quad (5.7.5)$$

The importance of Eq. (5.7.5) lies in the fact that the curvature of the Petzval surface does not depend on the distances  $s$  and  $s'$ , nor on the position of the entrance pupil for this surface. This relation applies to each surface in a system and, given that  $n'r'$  for the  $i$ th surface is  $nr$  for the  $(i + 1)$ st surface, leads to a sum over all surfaces given by

$$\frac{1}{n'_f r'_f} - \frac{1}{n_1 r_1} = -\sum_i \left(\frac{n' - n}{n'nR}\right)_i, \quad (5.7.6)$$

where  $1$  and  $f$  refer to the first and last surfaces, respectively. For a flat object field, the most common situation, we get

$$\kappa_p = -n'_f \sum_i \left(\frac{n' - n}{n'nR}\right)_i. \quad (5.7.7)$$

Thus for any optical system for which the object field is flat, the Petzval surface is an invariant surface. If the system has astigmatism, each of the astigmatic image surfaces will have its own curvature. But, as we now show, there are definite relations between these curvatures, the amount of astigmatism, and the Petzval curvature.

## 5.7.b. CURVATURES OF ASTIGMATIC SURFACES

The procedure to find these curvature relations starts with the substitution of Eq. (5.2.5) into Eq. (5.5.6), giving

$$\frac{\Delta s'}{s'^2} = \frac{s'_s - s'_t}{s'_s s'_t} = -\frac{2}{n'}(A_1 + 2L\Omega).$$

Solving for  $2L\Omega$  and substituting into Eq. (5.5.5) gives

$$\frac{n'}{s'_s} = \frac{n}{s} + \frac{n' \cos \theta' - n \cos \theta}{R} + A_1 + \frac{n'}{2} \left( \frac{s'_s - s'_t}{s'_s s'_t} \right),$$

where we see by comparison with Eq. (5.7.3) that the first three terms to the right of the equals sign are simply  $n'/s'_p$ . With this substitution we get

$$2(s'_p - s'_s) = s'_s - s'_t, \quad (5.7.8)$$

where the factors in the denominator cancel because of their near equality. Equation (5.7.8) can also be written as

$$s'_p - s'_t = 3(s'_p - s'_s). \quad (5.7.9)$$

The geometric interpretation of Eq. (5.7.9) is a simple one; at a given height  $y$  the distance between the Petzval and tangential surfaces is three times the distance between the Petzval and sagittal surfaces, with the sagittal surface always between the other two. Because astigmatism is zero on-axis, the image surfaces are in contact where they intersect the  $z$ -axis.

Note that Eq. (5.7.9) holds for any surface in an optical system and does not depend on the object distance for that surface, nor does it depend on the entrance pupil location. Hence it must also hold for the final image surfaces of a system with many surfaces, and the relations to follow are taken at the final surfaces.

It is a simple matter to write Eqs. (5.7.8) and (5.7.9) in terms of surface curvatures. From the geometry in Fig. 5.16 we get

$$u_\alpha - u_\beta = s'_\alpha - s'_\beta \quad (5.7.10)$$

where  $u$  is the surface sag and  $\alpha$  and  $\beta$  denote any pair of image surfaces. We also see that  $u = y^2 \kappa / 2$  and thus

$$\kappa_\alpha - \kappa_\beta = \frac{2}{\theta^2} \left( \frac{s'_\alpha - s'_\beta}{s'^2} \right), \quad (5.7.11)$$

from which it follows using Eqs. (5.7.8) and (5.7.9) that

$$\kappa_s - \kappa_t = 2(\kappa_p - \kappa_s), \quad \kappa_p - \kappa_t = 3(\kappa_p - \kappa_s). \quad (5.7.12)$$

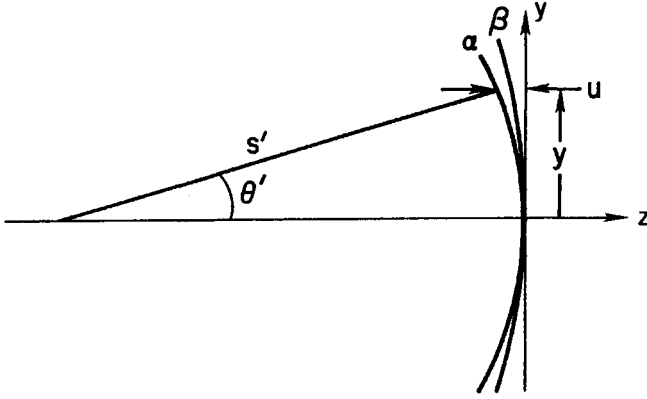


**Fig. 5.16.** Sags of image surfaces  $\alpha$  and  $\beta$ , where  $u_\alpha - u_\beta = s'_\alpha - s'_\beta$  in the paraxial approximation.

Choosing  $\alpha = s$  and  $\beta = t$  in Eq. (5.7.11) and substituting Eq. (5.5.8) we get

$$\kappa_s - \kappa_t = -4B_{1s}/n'\theta'^2, \quad (5.7.13)$$

where  $B_{1s}$  is the system astigmatism coefficient from Eq. (5.6.7) with  $t = f$ . Note that  $B_{1s}$  is referenced to the last surface in the system because  $\theta'$  is specified at the last surface.

It is now a simple matter to combine Eqs. (5.7.12) and (5.7.13) and solve for the curvatures of the individual surfaces. The results are given in Table 5.7. Included is an entry for the curvature  $\kappa_m$  of the surface midway between the  $S$ - and  $T$ -surfaces, that surface on which the astigmatic images are circular.

### 5.7.c. EXAMPLES

A few simple examples are now in order. Consider first a spherical mirror in collimated light, hence  $m = 0$ . From Table 5.6 we get

$$B_1 = \frac{n\theta^2}{R} \left(1 - \frac{W}{R}\right)^2,$$

where  $\psi = \theta$  from Eq. (5.5.2). For a single reflecting surface we have  $n' = -n$ ,  $\theta' = -\theta$ . Substituting into the entries in Table 5.7 leads to

$$\kappa_p = \frac{2}{R}, \quad \kappa_s = \frac{2}{R} - \frac{2}{R} \left(1 - \frac{W}{R}\right)^2, \quad \kappa_t = \frac{2}{R} - \frac{6}{R} \left(1 - \frac{W}{R}\right)^2. \quad (5.7.14)$$

For  $W = R$  each of the curvatures in Eq. (5.7.14) is  $2/R$ , as expected, because the astigmatism is zero. For  $W = 0$  we find  $\kappa_s = 0$ ,  $\kappa_t = -4/R$ . Thus the Petzval and

Table 5.7

Image Surface Curvatures

$$\begin{aligned} \kappa_p &= -n'_f \sum_i \left( \frac{n' - n}{n'nR} \right)_i \\ \kappa_s &= \kappa_p + \frac{2B_{1s}}{n'\theta'^2}, \quad \kappa_t = \kappa_p + \frac{6B_{1s}}{n'\theta'^2} \\ \kappa_m &= \frac{\kappa_s + \kappa_t}{2}, \quad B_{1s} = \sum_i B_{1i} \left( \frac{y_i}{y_f} \right)^2 \end{aligned}$$

tangential surfaces have opposite curvatures with a flat sagittal surface between them. Although collimated light was specified in the forementioned, note that these results hold for any object distance because  $B_1$  is independent of the magnification  $m$ .

As a second example consider a Schmidt camera. As already noted here and in Section 4.5, a spherical mirror with  $W = R$  has zero astigmatism but a curved image surface with curvature  $2/R$ . One way to flatten the image surface is to introduce another element whose astigmatism is zero, to a first approximation, and to choose its characteristics to make the Petzval curvature zero for the system. This is done with a thin lens located near the image surface, as shown in Fig. 5.17. The contribution of the corrector plate is ignored in the analysis to follow because  $R_c \gg R$  for any practical focal ratio, a result that is evident from Eq. (4.5.13).

The Petzval curvature for the mirror-lens combination, derived from the relation in Table 5.7, is

$$\kappa_p = \frac{2}{R} - \left( \frac{n - 1}{n} \right) \left( \frac{1}{R_1} - \frac{1}{R_2} \right) \tag{5.7.15}$$

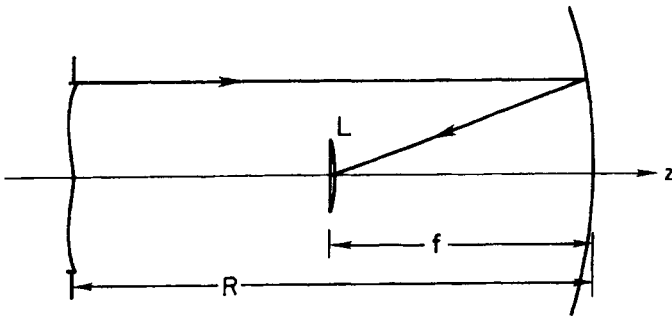


Fig. 5.17. Schmidt camera with lens  $L$  near focal surface to give zero Petzval curvature. See Eq. (5.7.15).

where  $R_1$  and  $R_2$  are the radii of curvature of the first and second surfaces, respectively, of the lens and the index  $n$  of the lens is positive. Setting  $R_2 = \infty$  gives a lens whose flat surface faces the image surface and, though this is not required, we make this choice for convenience. Therefore the Petzval surface is flat if

$$\frac{n-1}{nR_1} = \frac{2}{R}. \quad (5.7.16)$$

Because  $R$  of the mirror is negative, so also is  $R_1$ , hence the lens is plano-convex in cross section (thickest at the center) and has positive power. Though the combination now has a flat Petzval field, the thin lens may introduce some astigmatism. We show in Chapter 9 that the amount is small if the lens is close to the image surface.

Our final example is that of a two-mirror telescope, either Cassegrain or Gregorian. For light incident on the primary according to our usual convention we have  $n_1 = 1$ ,  $n_2 = -1$ . The Petzval curvature is then

$$\kappa_p = 2 \left( \frac{1}{R_2} - \frac{1}{R_1} \right) = \frac{2}{R_1} \left( \frac{1-\rho}{\rho} \right) \quad (5.7.17)$$

where  $\rho = R_2/R_1$ . For a Gregorian  $\rho < 0$  and  $\kappa_p$  is opposite in sign to that of  $R_1$ . Thus the Petzval surface for a Gregorian is convex as seen from the secondary. For a Cassegrain the Petzval surface is concave as seen from the secondary, provided  $\rho < 1$ . Discussion of the curvatures of the other astigmatic surfaces of two-mirror telescopes is left to Chapter 6.

## 5.8. ABERRATIONS FOR DECENTERED PUPIL

The aberration results given to this point are correct for an optical system in which all of the elements, including the aperture stop and pupils, are centered. By centered we mean there is a single axis, designated the  $z$ -axis, about which the system can be rotated without change, where the  $z$ -axis passes through the center of each element. If one or more of these elements is displaced laterally from the  $z$ -axis or rotated about a line perpendicular to the  $z$ -axis, the system is no longer rotationally symmetric and aberrations are introduced. The lateral displacement is commonly referred to as a *decenter* and the rotation as a *tilt*. Decenter and/or tilt of, for example, the secondary mirror in a two-mirror telescope is one important case of this loss of symmetry, and is discussed in Chapter 6.

5.8.a. GENERAL FORMULATION

In this section we find the aberration coefficients for a general surface with its associated pupil where the center of the pupil is displaced from the  $z$ -axis of the surface. A cross section of this situation is shown in Fig. 5.18 where the pupil is displaced in the  $y$ -direction by  $L'$ . The chief ray passes through the center of the pupil and makes angle  $\psi$  with the  $z$ -axis, the axis of symmetry of the surface. In the paraxial approximation we find the following relations from the geometry in Fig. 5.18:

$$L = L' - W\psi, \quad \theta = \psi \left( 1 - \frac{W}{s} \right) + \frac{L'}{s}, \quad (5.8.1)$$

where  $W$  is the distance from the surface to the entrance pupil, and the signs of each distance and angle are set by the sign convention (see caption to Fig. 5.18). The relations in Eq. (5.8.1) are a generalization of those in Eq. (5.5.2).

The procedure of finding the aberration coefficients is the same as that followed in Section 5.5, except that Eq. (5.8.1) is used instead of Eq. (5.5.2) when substituting into Eq. (5.5.1). The results of carrying out these substitutions for coma and astigmatism are given in Table 5.8 for a general surface and Table 5.9 for a mirror surface. Distortion is not included because the change in it is too small to be significant. The spherical aberration is independent of  $L'$ , hence  $B_3 = B_3$  (cen).

Examination of the entry for  $B_2$  in Table 5.8 shows that the part of the coma coefficient that results from the decentering is not dependent on the angle of the chief ray. Hence the effect of the decentering is to introduce constant coma over the entire image field, in addition to any angle-dependent coma that is present. The effect of the decentering on  $B_1$  is to introduce a constant term and a term that

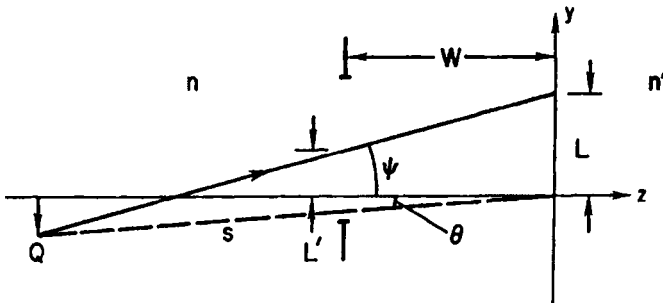


Fig. 5.18. Sketch of chief ray through center of stop displaced by  $L'$  from the  $z$ -axis of the surface. The relation between parameters is given in Eq. (5.8.1). In this diagram  $L$  and  $L' > 0$ ,  $\psi$  and  $\theta > 0$ .

Table 5.8

General Aberration Coefficients, Decentered Pupil<sup>a</sup>

$$\begin{aligned}
 B_2 &= B_2(\text{cen}) + \frac{L'}{2} \left[ \frac{\Gamma}{R} \left( \frac{1}{s} - \frac{1}{R} \right) - \frac{K}{R^3} (n' - n) - b \right] \\
 B_1 &= B_1(\text{cen}) - \frac{L'^2}{2} \left[ \frac{\Gamma}{R^2} + \frac{K}{R^3} (n' - n) + b \right] \\
 &\quad - L'(W\psi) \left[ \frac{\Gamma}{R} \left( \frac{1}{W} - \frac{1}{R} \right) - \frac{K}{R^3} (n' - n) - b \right] \\
 \Gamma &= n^2 \left( \frac{1}{n's'} - \frac{1}{ns} \right)
 \end{aligned}$$

<sup>a</sup>  $B_i(\text{cen})$  are entries in Table 5.5, with  $i = 1, 2$ .

Table 5.9

Mirror Aberration Coefficients, Decentered Pupil<sup>a</sup>

$$\begin{aligned}
 B_2 &= B_2(\text{cen}) + \frac{nL'}{R^3} \left[ K - \left( \frac{m+1}{m-1} \right) - \frac{bR^3}{2n} \right] \\
 B_1 &= B_1(\text{cen}) + nL'^2 \left( \frac{K+1}{R^3} - \frac{b}{2n} \right) \\
 &\quad + \frac{2nL'(W\psi)}{R^2} \left( \frac{1}{W} - \frac{K+1}{R} + \frac{bR^2}{2n} \right)
 \end{aligned}$$

<sup>a</sup>  $B_i(\text{cen})$  are entries in Table 5.6, with  $i = 1, 2$ .

depends linearly on the angle of the chief ray. Hence astigmatism is also present over the entire image field.

The calculation of the system aberration coefficients is carried out following the procedure in Section 5.6. In all cases of interest, it turns out that the effect of a decentered stop is much greater on coma than on astigmatism, hence the image surface curvatures are not significantly affected and the results of Table 5.7 can be used with  $B_{1s}(\text{cen})$ .

### 5.8.b. EXAMPLE: SCHMIDT CAMERA

At this point it is instructive to give an example of a system with decentered stop. The example discussed is that of a Schmidt camera in which the axis of the corrector plate is displaced from the mirror axis, as shown in Fig. 5.19. The aperture stop of the system is the corrector plate, with collimated light incident.

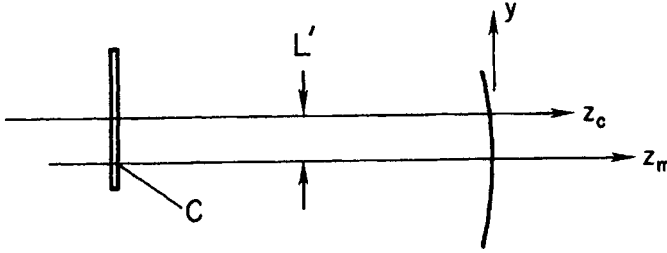


Fig. 5.19. Schmidt camera with axis of corrector  $z_c$  displaced from mirror axis  $z_m$  by  $L'$ .

Because  $W = 0$  for the corrector, its aberration coefficients from Table 5.5 are

$$B_1 = 0, \quad B_2 = 0, \quad B_3 = -b/8, \tag{5.8.2}$$

where  $R = \infty$  is the choice for the radius of curvature of the corrector. (For a corrector profile that minimizes chromatic aberration,  $R$  is finite as shown in Section 4.5. However, as we show in Chapter 7, the aberration coefficients are dominated by the term in  $b$ .)

The parameters for the spherical mirror are  $W = R$ ,  $m = 0$ ,  $b = 0$ , and  $n = 1$ , in which case  $B_1(\text{cen})$  and  $B_2(\text{cen})$  are zero. From Table 5.9 we then find

$$B_1 = \frac{L'^2}{R^3}, \quad B_2 = \frac{L'}{R^3}, \quad B_3 = \frac{1}{4R^3}. \tag{5.8.3}$$

With the ray heights at the corrector and mirror equal, the system aberration coefficients according to Eq. (5.6.7) are simply the sums of corresponding terms in Eqs. (5.8.2) and (5.8.3). Putting these sums into Eq. (5.6.6) and dividing by  $s'$  to get the angular aberration gives

$$\text{AAS} = \frac{1}{2F} \left( \frac{L'}{R} \right)^2, \quad \text{ATC} = \frac{3}{16F^2} \left( \frac{L'}{R} \right), \tag{5.8.4}$$

for the angular astigmatism and tangential coma, respectively. Spherical aberration is zero provided  $b = 2/R^3$ .

The relation for ATC in Eq. (5.8.4) can be used to find the largest permissible  $L'$  for a given ATC. If we choose a blur limit of 1 arc-sec, then the reader can verify that  $L'/R$ , expressed in arc-seconds, cannot exceed  $16F^2/3$ . The value of AAS for this value of  $L'/R$  is about 1000 times smaller and thus is negligible.

It is also instructive to take this same system and tilt the mirror with respect to the corrector, as shown in Fig. 5.20. From the geometry in Fig. 5.20 we see that  $L' = -\alpha R$  and  $\psi = \theta - \alpha$ , where  $\alpha$  is the tilt angle of the mirror and  $\psi$  is the angle of the chief ray relative to the mirror axis. The fact that  $\psi$  depends on  $\alpha$  is of no consequence here because  $B_1(\text{cen})$  and  $B_2(\text{cen})$  for the mirror are zero,

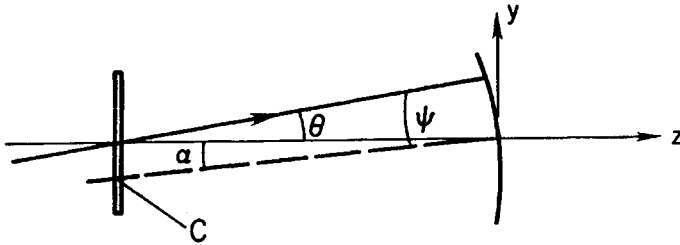


Fig. 5.20. Schmidt camera with axis of mirror, denoted by dashed line, tilted by angle  $\alpha$  with respect to the  $z$ -axis of the corrector.

independent of  $\psi$ . Hence Eqs. (5.8.2) through (5.8.4) are the same for this system, with  $\alpha$  replacing  $L'/R$ .

It is not surprising that the systems in Figs. 5.19 and 5.20 have the same aberrations because they are, in fact, equivalent. The tilt, in effect, has offset the center of curvature of the mirror by a distance  $L'$  from the center of the corrector and, because the sphere has no preferred axis, the systems are the same. Note that this equivalence between a tilt and decenter does not hold for any surface that has a unique axis.

Before leaving this system, it is worth examining Fig. 5.20 from the point of view of Fermat's Principle. For  $\theta = 0$ , rays through the upper half of the corrector are advanced at the mirror while those through the bottom half are retarded. Hence an asymmetry is introduced into the reflected wavefront and the dominant aberration in the image is coma.

### 5.8.c. EXAMPLE: EBERT-FASTIE MIRROR

As a final example we consider a single concave mirror in combination with an intermediate plane mirror, as shown in Fig. 5.21. The beam from a point object located off the  $z$ -axis is converted to a collimated beam by one side of mirror  $M$  and returned to the other side of  $M$  by the plane mirror. The final image, like the original object, is approximately one focal length from the tangent plane to  $M$ . This optical arrangement is a so-called *Ebert-Fastie* system and is best known in a type of grating spectrometer of that name. In the spectrometer a diffraction grating replaces the plane mirror. Here we examine the aberration characteristics with a plane mirror only; the details of this system as a spectrometer are left for Chapter 15.

The system shown in Fig. 5.21 has an entrance pupil decentered by  $L'_1$  at distance  $W_1$  from the concave mirror  $M$ . The plane mirror is located at the focal point of  $M$ , a choice made to preserve the symmetry above and below the  $z$ -axis in Fig. 5.21. For the incident beam  $m = m_1 = \infty$ ; for the final beam  $m = m_2 = 0$ .

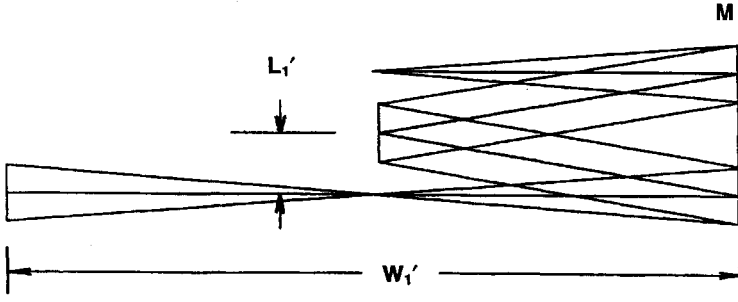


**Fig. 21.** Ebert-Fastie configuration with spherical mirror  $M$ . Entrance pupil is at distance  $W'_1$  from  $M$  and decentered by  $L'_1$ . See the discussion preceding Eq. (5.8.5).

We consider first a special case, that in which the chief ray through the center of the entrance pupil is parallel to the  $z$ -axis, hence  $\psi_1 = 0$ .

The entrance pupil is imaged by  $M$  and the plane mirror according to Eqs. (2.3.2) and (2.3.3). Applying those equations we find the entrance pupil for the second reflection from  $M$  located at distance  $L'_2$  above the  $z$ -axis and distance  $W_2$  from  $M$ , where

$$L'_2 = -L'_1 \left( \frac{W'_1}{W_1} \right), \quad \frac{1}{W'_1} = \frac{2}{R} - \frac{1}{W_1}, \quad W_2 = R - W'_1. \quad (5.8.5)$$

With the condition that  $\psi_1 = 0$  and, from the geometry in Fig. 5.21,  $\psi_2 = 2L'_1/R$ , we now find the aberration coefficients using Table 5.9. With  $b = 0$ , and  $B_1(\text{cen})$  and  $B_2(\text{cen})$  zero for the first reflection, we find for this first reflection that

$$B_{11} = \frac{L_1'^2}{R^3} (K + 1), \quad B_{21} = \frac{L_1'}{R^3} (K - 1) \quad (5.8.6)$$

Taking the entries from Tables 5.9 and 5.6, substituting Eqs. (5.8.5), and doing a bit of algebra, we find  $B_{12} = B_{11}$  and  $B_{22} = -B_{21}$  for  $\psi_1 = 0$ .

We now find the system coefficients using Eq. (5.6.7). Because the beam size does not change between reflections, the system coefficients are simply the sum of the surface coefficients. Therefore

$$B_{1s} = \frac{2L_1'^2}{R^3} (K + 1), \quad B_{2s} = 0. \quad (5.8.7)$$

Although the separate reflections have coma, their signs are opposite and the net coma is zero. This is not surprising, given the symmetry on opposite sides of the  $z$ -axis. On the other hand, we see that astigmatism is present except when  $K = -1$  and the mirror is a paraboloid. Thus a paraboloid, used as shown in Fig. 5.21, if free of third-order spherical aberration, coma, and astigmatism. Any optical system for which this is true is called an *anastigmat*.

Given this freedom from aberrations for the case with  $\psi_1 = 0$ , we now consider what happens for a paraboloid when  $\psi_1 \neq 0$ . The differences in this case are that  $B_1(\text{cen})$  and  $B_2(\text{cen})$  are not zero for the first reflection, and that the angle of the chief ray for the second reflection is  $\psi_2 = 2L'_1/R - (W_1/W'_1)\psi_1$ . With this result for  $\psi_2$ , and using Eqs. (5.8.5), we find

$$B_{2s} = -\frac{\psi_1}{R^2}(K + 1). \quad (5.8.8)$$

Thus the system has zero coma if the mirror is a paraboloid. Given this outcome we find the astigmatism only for  $K = -1$ . The result is

$$B_{11} = \frac{\psi_1^2}{R} \left( 1 - \frac{2W_1}{R} \right) + \frac{2L'_1\psi_1}{R^2} = -B_{12}, \quad (5.8.9)$$

hence the system astigmatism is also zero. There is no third-order spherical aberration, coma, or astigmatism over the field spanned by  $\psi_1$ . Although a paraboloid in this configuration is anastigmatic, there are higher-order aberrations that set the limit on image quality. Ray traces also show that the image surface is tilted and curved relative to the chief ray coming from the paraboloid.

It is worth noting here that a spherical mirror in this configuration used in a monochromator mode ( $\psi_1 = 0$ ) has both spherical aberration and astigmatism. This is not a serious problem provided the beam focal ratio is not too small. Further discussion of this mode is given in Chapter 15.

## 5.9. CONCLUDING REMARKS

All of the results needed to calculate the aberrations of a general centered optical system to third order are now in place. By centered we mean there is a single axis of symmetry passing through the vertices of all the optical surfaces. It is well to remember that these results are not exact, but for most systems used in optical astronomy they are sufficient. Exact image characteristics derived from ray-tracing can, of course, be used to supplement the third-order results.

A comparison of the form of the coefficients in this chapter with those in, for example, the book by Born and Wolf (1980), shows a significant difference in notation. The results given in Chapter 5 of their classic text are derived in terms of Seidel variables, while our results are given in terms of actual variables. Though the two approaches give the same final system aberrations, the representation we have chosen is more convenient to use in practice. A comparison of the Seidel results with those in this chapter is given in Appendix A.

With the availability of sophisticated computer ray-tracing programs, the reader may question the necessity of a detailed development of these analytical results. From the point of view of an optical designer starting from scratch to choose a suitable system for a particular application, the analytical results are preferred because one can usually determine rather quickly whether a given type of system is appropriate. Once a basic arrangement of optical elements has been selected, a computer can be used to optimize the system and check image characteristics.

Getting the required aberration relations has been a lengthy process. It would have been sufficient simply to present the final results without the derivations, but for the reader who is venturing into this field for the first time it is useful to see the source of the results. Discussions in subsequent chapters are directed toward finding the characteristics of systems, with the results provided here available for reference.

We also have the results needed to calculate the aberrations introduced when one or more of the optical elements in a system is decentered. The general treatment is complicated when more than one element is decentered, and we limit our following discussion to those cases in which one element is decentered.

There is one more topic of aberration theory, which is covered in a later chapter. In Chapter 14 we use Fermat's Principle as a starting point to derive the characteristics of diffraction grating surfaces. These results, when combined with those given here, will allow us to discuss the characteristics of a variety of spectrographic instruments.

## APPENDIX A: COMPARISON WITH SEIDEL THEORY

Some of the key results derived using Seidel theory are shown in the following table. Of the five Seidel coefficients for spherical aberration, coma, astigmatism, field curvature, and distortion, we present results for all but field curvature. The interested reader should consult Chapter 5 in the text by Born and Wolf (1980) for all of the results, including derivations.

Selected results from Table 5.5 in this chapter are in the left-hand column, with corresponding Seidel terms in the other columns. The quantities in square brackets represent the terms in brackets in Table 5.5.

Use Eqs. (5.5.9), (5.6.7), and (5.6.8) to calculate the transverse aberrations using the entries from Table 5.5.

Multiply each  $TA'$  by  $(s'/n'h)$  to get the transverse aberrations using the Seidel approach.

Aberration Coefficients		
<i>Table 5.5</i>	<i>Seidel Coefficient</i> <sup>1</sup>	<i>TA</i> <sup>1,2,3</sup>
$B_3 = -\frac{1}{8}[\Phi_3]$	$B = \frac{1}{2}h^4[\Phi_3]$	$B\rho^3$
$B_2 = \frac{W\psi}{2}[\Phi_2]$	$F = \frac{1}{2}Hh^3[\Phi_2]$	$-Fy_0\rho^2$
$B_1 = -\frac{(W\psi)^2}{2}[\Phi_1]$	$C = \frac{1}{2}H^2h^2[\Phi_1]$	$2Cy_0^2\rho$
$B_0 = \frac{(W\psi)^3}{2}[\Phi_0]$	$E = \frac{1}{2}H^3h[\Phi_0]$	$-Ey_0^3$

<sup>1</sup>  $h = -y/\rho$ ;  $Hy_0 = -W\psi$ . For multisurface systems the Seidel coefficients are computed for each surface and summed to get a single coefficient.

<sup>2</sup>  $TA'$  is the transverse aberration in Seidel coordinates.

<sup>3</sup>  $\rho$  is the height of the marginal ray at the pupil;  $y$  is the height of the marginal ray at the surface.

## REFERENCES

- Bowen, I. (1960). *Stars and Stellar Systems I, Telescopes*, Chap. 4, Chicago: University of Chicago Press.
- Merritt, F. (1962). *Mathematics Manual*, New York: McGraw-Hill.

## BIBLIOGRAPHY

### *Introduction to aberrations*

- Longhurst, R. (1967). *Geometrical and Physical Optics*, second edition, New York: John Wiley.
- Mahajan, V. (1998). *Optical Imaging and Aberrations, Part I. Ray Geometrical Optics*, Bellingham, WA: SPIE Optical Engineering Press.

### *Advanced theory of aberrations*

- Born, M. and Wolf, E. (1980). *Principles of Optics*, sixth edition, Oxford: Pergamon.
- Welford, W. (1986). *Aberrations of the Symmetrical Optical System*, second edition, London: Academic Press.

Reflecting telescopes and their associated instrumentation are the principal tools of the observational astronomer. In this chapter we consider the characteristics of the reflecting telescope in many of its various forms. Although refracting telescopes are still in use, they are relatively few in number and do not compete in light gathering power with the large reflectors. We choose to consider reflecting telescopes only.

In the discussions to follow we consider the various kinds of reflectors, their inherent aberrations for a distant object field, and their advantages and limitations. Because of the aberrations there are definite field limitations, which are noted for each type. The aberration calculations are based on the results of Chapter 5, with the results of the calculations presented in terms of angular measure as seen on the sky (or object field). These measures are given in both analytical and numerical form, with the latter given in units of arc-seconds. Although close attention is given to the sign convention in deriving the aberration formulas, the final angular results are given without regard for sign. The one exception to this is the field curvature for which the sign is essential.

In addition to giving the aberration characteristics of aligned two-mirror telescopes, we discuss the effect of misalignment between their mirrors. The trend in many of the recently designed large telescopes is to make them as short as possible, hence a “fast” primary mirror. Aberrations introduced by misalignments in such telescopes can be quite significant and much effort is devoted to keeping these aberrations within acceptable limits on a near realtime basis.

Descriptions of many of the types discussed here appear in the literature with references given at the end of the chapter. An especially complete treatment is given by Wilson (1996). In our discussion we cover a large number of telescope types with a common notation to facilitate comparison between them. In this chapter and succeeding ones our discussion assumes the reader has digested the main themes in the preceding chapters. If this is not the case, then, at a minimum, Section 2.5, Chapter 4, and Sections 5.4, 5.6, and 5.7 should be reviewed. Only pure mirror systems are considered in this chapter, including discussions of three- and four-mirror telescopes. Schmidt telescopes and systems with refracting corrector systems are the subjects of Chapters 7–9.

## 6.1. PARABOLOID

The single-mirror paraboloid is the simplest telescope that is free from spherical aberration, a result noted in Chapter 5. A paraboloid is almost always used with the aperture stop at the mirror and thus the aberrations and field curvatures can be taken directly from Tables 5.4 and 5.7. Results are given in Table 6.1, where  $y$  is the height of a marginal ray at the mirror and the telescope focal ratio  $F = |R/4y|$ .

From the transverse aberrations given in Table 6.1 we find a coma flare directed away from the center of the field ( $TSC > 0$ ), and a tangential astigmatic image lying closer to the mirror than the sagittal line image ( $TAS < 0$ ). For the angular aberrations, we divide each of the transverse aberrations by  $s'$  and drop any leading minus signs to get the results shown in Table 6.1. We choose this approach for the angular aberrations because it is usually their absolute size that is of primary concern.

Results for angular aberrations from Table 6.1 are shown in Fig. 6.1 for three focal ratios. The principal item to notice in Fig. 6.1 is the dominance of coma for

Table 6.1

Aberrations of Paraboloid Telescope

$TSC = -\frac{y^2}{R^2} \theta s'$	$TAS = -\frac{2y}{R} \theta^2 s'$
$ASC = \frac{y^2}{R^2} \theta = \frac{\theta}{16F^2}$	$AAS = \frac{2y}{R} \theta^2 = \frac{\theta^2}{2F}$
$\kappa_p = \frac{2}{R}$	$\kappa_m = -\frac{2}{R}$
	$u_m = \frac{f\theta^2}{2}$

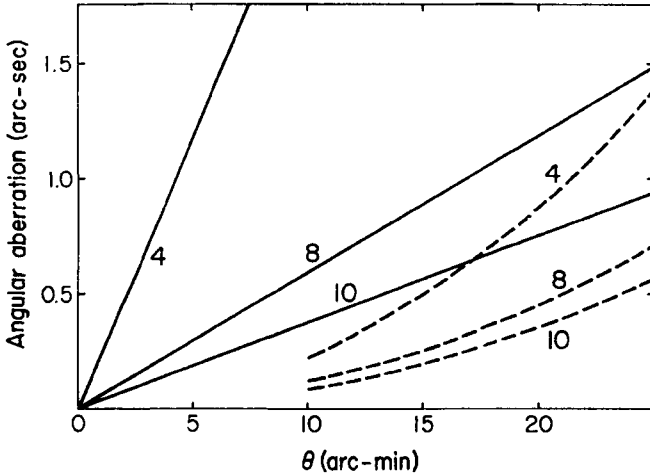


Fig. 6.1. Angular aberrations of paraboloid in collimated light at selected focal ratios. Solid lines: sagittal coma; dashed curves: astigmatism. Number on each curve is focal ratio. See Table 6.1.

small field angles, which sets the limit to the radius of the field over which the image quality can be considered “good.” By “good” we mean an angular blur size that is less than or equal to the blur given an otherwise perfect image by atmospheric distortion. In our discussions we take the typical blur due to atmospheric effects as 1 arc-sec.

A typical comatic image is shown in Fig. 5.9. Setting the total span of this image equal to the atmospheric blur, we can use Fig. 6.1 and the relation between tangential and sagittal coma to determine the limiting field radius for “good” images. The results are given in Table 6.2 for a blur of 1 arc-sec, from which it is clear that the paraboloid is limited to small fields, especially for small focal ratios.

Table 6.2

Limiting Field Radius for Good<sup>a</sup> Images: Paraboloid Telescope

$F$	$\theta$ (arc-min)
4	1.42
8	5.69
10	8.89

<sup>a</sup> Good defined as tangential coma that measures 1 arc-sec.

With coma as the aberration that limits the size of the field, the placement of the aperture stop at any other position does not improve the image quality. Coma is independent of stop position when spherical aberration is zero, as noted in Section 5.5, and reducing astigmatism has little effect on the overall blur size.

The remaining items in Table 6.1 are related to field curvature. Here  $\kappa_p$ ,  $\kappa_m$ , and  $u_m$  are, respectively, the Petzval curvature, median curvature, and sag of the median surface midway between the tangential and sagittal focal surfaces. Given the limiting field radii in Table 6.2, the reader can verify that for any practical focal length  $f$  the median image surface is essentially flat.

In summary, then, the paraboloid telescope is limited to small fields with coma setting the field limit. All other aberrations are negligible over this field.

## 6.2. TWO-MIRROR TELESCOPES

We introduced the topic of two-mirror telescopes in Chapter 2 with schematic diagrams of two types, Cassegrain and Gregorian, in Fig. 2.7, as well as a set of definitions of normalized parameters with which to describe any two-mirror telescope. Selected items from Section 2.5 and Table 2.1 are summarized in Table 6.3 for convenient reference.

It is instructive to study the relations between the normalized parameters in Table 6.3 because they define the bounds on the parameters for each of the possible telescope types. For all types we require that the final image is real.

If the primary is concave, hence  $f_1$  positive, the requirement of a real final image means  $mk > 0$ . If  $m$  and  $k$  are positive the telescope type is Cassegrain; if

Table 6.3

Normalized Parameters for Two-Mirror Telescopes

---

$k = y_2/y_1$ = ratio of ray heights at mirror margins
$\rho = R_2/R_1$ = ratio of mirror radii of curvature
$m = -s_2/s_1 = f/f_1$ = transverse magnification of secondary
$f_1\beta = D\eta$ = back focal distance, or distance from vertex of primary mirror to final focal point
$\beta$ and $\eta$ , back focal distance in units of $f_1$ and $D$ , respectively
$F_1 =  f_1 /D$ = primary mirror focal ratio
$W = (1 - k)f_1$ = distance from secondary to primary mirror = location of telescope entrance pupil relative to the secondary when the primary mirror is the aperture stop
$mkf_1$ = distance from secondary to focal surface
$F =  f /D$ = system focal ratio, where $f$ is telescope focal length

---

$$m = \frac{\rho}{\rho - k} \quad \rho = \frac{mk}{m - 1} \quad k = \frac{1 + \beta}{m + 1}$$


---

their signs are negative the telescope type is Gregorian. In both cases  $|k| < 1$  to ensure that some light reaches the primary.

If the primary is convex, hence  $f_1$  negative, then a real final image requires that  $mk$  is negative. In this case the secondary must be larger than the primary, hence  $k > 1$ , and  $m$  is negative. This type of telescope, with its concave secondary, is the so-called inverse Cassegrain.

The different combinations of  $m$ ,  $k$ , and  $\rho$  are summarized in Table 6.4. It is worth noting here that among the Cassegrains with concave secondary and the inverse Cassegrains are the so-called Couder and Schwarzschild designs that will be discussed later in this chapter. The Cassegrain with flat secondary is not included in the analysis and discussion to follow.

We now proceed to find the aberration relations for two-mirror telescopes using Eqs. (5.6.11) and the aberration coefficients of the primary and secondary in Eqs. (5.6.9) and (5.6.10). Before writing the system aberration coefficients,  $W$  is written in terms of the normalized parameters:  $W/R_2 = (k - 1)/2\rho$ , and  $W/s_2 = (k - 1)/k$ . With these substitutions, and after straightforward but tedious algebra, the two-mirror aberration coefficients given in Table 6.5 are found. Note that these coefficients apply to any pair of conic mirrors, including pairs for which the spherical aberration is not zero. It is worth noting that  $B_{3s}$  is the only aberration coefficient affected by the conic constant of the primary mirror. An error in  $K_1$ , such as for the Hubble Space Telescope, has no effect on the off-axis aberrations.

We can also use the condition for zero spherical aberration and rewrite the aberration coefficients in terms of  $K_1$ . Setting  $B_{3s}$  in Table 6.5 equal to zero we find, after more algebra, the results given in Table 6.6. These results are based on a choice of locating the aperture stop at the primary mirror. When spherical aberration is zero, coma is independent of the stop location; when both SA and coma are zero, astigmatism is independent of the stop position. We will comment further on these conditions when discussing specific types of telescopes.

Table 6.4

Parameter Combinations for Two-Mirror Telescopes<sup>a</sup>

$m$	$k$	$\rho$	Type	Secondary
$>1$	$>0$	$>0$	Cassegrain	convex
$=1$	$>0$	$\infty$	Cassegrain	flat
0 to 1	$>0$	$<0$	Cassegrain	concave
$<0$	$<0$	$<0$	Gregorian	concave
$<0$	$>1$	$>0$	Inverse Cassegrain	concave

<sup>a</sup>For  $m = 1$ ,  $k = (1 + \beta)/2$

Table 6.5

General Aberration Coefficients for Two-Mirror Telescopes

$$\begin{aligned}
 B_{3s} &= \frac{1}{4R_1^3} \left[ K_1 + 1 - \frac{(m-1)^3(1+\beta)}{m^3(m+1)} \left( K_2 + \left( \frac{m+1}{m-1} \right)^2 \right) \right] = -\frac{1}{32f_1^3} \left[ - \right] \\
 B_{2s} &= \frac{\theta}{m^2 R_1^2} \left[ 1 + \frac{(m-1)^3(m-\beta)}{2m(m+1)} \left( K_2 + \left( \frac{m+1}{m-1} \right)^2 \right) \right] = \frac{\theta}{4f^2} \left[ - \right] \\
 B_{1s} &= \frac{\theta^2}{mR_1} \left[ 1 + \frac{(m-1)(m-\beta)}{m(m+1)} \left( 1 - \frac{(m-1)^2(m-\beta)}{4m(1+\beta)} (K_2 + 1) \right) \right] = -\frac{\theta^2}{2f} \left[ - \right] \\
 B_{0s} &= \frac{\theta^3(m-\beta)(m^2-1)}{8m^3(1+\beta)^2} \left[ (m+\beta)(3m+\beta) + \left( \frac{m-1}{m+1} \right)^2 (m-\beta)^2 K_2 \right]
 \end{aligned}$$

The choice of parameters used in Tables 6.5 and 6.6 is arbitrary and different combinations may be more convenient, depending on the application. The advantage of expressing the system coefficients in terms of  $m$  and  $\beta$  is that certain important conclusions are more easily deduced.

Getting from the system coefficients in Tables 6.5 and 6.6 to the transverse aberrations requires substituting each  $B_s$  in turn into Eq. (5.6.8) where, as noted in Section 5.6,  $s'_2/n'_2 = kf$  and  $y_1/y_2 = 1/k$ . Take care to note that Eq. (5.6.8) gives tangential coma; our results are given for sagittal coma. To get the angular aberration as an angle projected on the sky, the transverse aberration is divided by  $f$  and any leading minus signs are dropped. Angular aberrations are given in Table 6.7, with quantities in brackets taken from Table 6.5 or 6.6.

Table 6.6

Aberration Coefficients for Two-Mirror Telescopes with  $B_{3s} = 0^a$ 

$$\begin{aligned}
 B_{2s} &= \frac{\theta}{m^2 R_1^2} \left[ 1 + \frac{m^2(m-\beta)}{2(1+\beta)} (K_1 + 1) \right] = \frac{\theta}{4f^2} \left[ - \right] \\
 B_{1s} &= \frac{\theta^2}{mR_1} \left[ \frac{m^2 + \beta}{m(1+\beta)} - \frac{m(m-\beta)^2}{4(1+\beta)^2} (K_1 + 1) \right] = -\frac{\theta^2}{2f} \left[ - \right] \\
 B_{0s} &= \frac{\theta^3(m-\beta)(m^2-1)}{4m^2(1+\beta)^2} \left[ m + 3\beta + \frac{m^2(m-\beta)^2}{2(1+\beta)(m^2-1)} (K_1 + 1) \right]
 \end{aligned}$$

<sup>a</sup> In terms of  $m$  and  $\beta$ , spherical aberration is zero according to the relation

$$K_1 + 1 = \frac{(m-1)^3(1+\beta)}{m^3(m+1)} \left( K_2 + \left( \frac{m+1}{m-1} \right)^2 \right).$$

Table 6.7

Angular Aberrations of Two-Mirror Telescopes<sup>a</sup>

$$\begin{aligned} \text{ASA} &= \frac{1}{8} \left( \frac{y_1}{f} \right)^3 \left[ - \right] = \frac{1}{64F_1^3} \left[ - \right] \\ \text{ASC} &= \frac{\theta}{4} \left( \frac{y_1}{f} \right)^2 \left[ - \right] = \frac{\theta}{16F^2} \left[ - \right] = \frac{1}{3} \text{ATC} \\ \text{AAS} &= \theta^2 \left( \frac{y_1}{f} \right) \left[ - \right] = \frac{\theta^2}{2F} \left[ - \right] \quad \text{ADI} \doteq B_{0s} \end{aligned}$$

<sup>a</sup> Terms in square brackets are taken from Table 6.5 or 6.6.

Before discussing the characteristics of specific telescope types we give the general relations for the image surface curvatures based on the results in Section 5.7. As noted following Eq. (5.7.13), the coefficient  $B_{1s}$  and the angle  $\theta'$  are referenced to the last surface in the system, hence the secondary mirror. The relation between this  $\theta'$  and the field angle  $\theta$  is derived by noting that the focal surface to secondary distance is  $k$  times smaller than  $f$ . Hence a point on the image surface, which subtends angle  $\theta$  on the sky, subtends angle  $\theta/k$  at the secondary.

The coefficient  $B_{1s}$  referenced to the secondary is calculated using the relation in Table 5.7. The relation between this result, denoted  $B_{1s}(\text{sec})$ , and that given in Table 6.5 or 6.6, denoted  $B_{1s}(\text{pri})$ , is  $k^2 B_{1s}(\text{sec}) = B_{1s}(\text{pri})$ . Therefore

$$\begin{aligned} B_{1s}(\text{sec})/\theta'^2 &= B_{1s}(\text{pri})/\theta^2, \\ \kappa_p &= \frac{2}{R_1} \left[ \frac{m(m - \beta) - (m + 1)}{m(1 + \beta)} \right], \\ \kappa_m &= \frac{2}{mR_1} \left[ \frac{(m^2 - 2)(m - \beta) + m(m + 1)}{m(1 + \beta)} - \frac{m(m - \beta)^2}{2(1 + \beta)^2} (K_1 + 1) \right]. \end{aligned} \quad (6.2.1)$$

With all of the necessary relations now in hand, we turn our attention to a discussion of the characteristics of specific two-mirror telescopes. The categories considered in greatest detail are the so-called classical telescopes, those for which the primary mirror is a paraboloid, and the aplanatic telescopes, those with zero coma. We also discuss less widely used types, such as the Dall-Kirkham with its spherical secondary, a two-mirror version with spherical primary mirror, and several variants of the aplanat.

## 6.2.a. CLASSICAL TYPE

This category of two-mirror telescopes is one for which  $K_1 = -1$ . The condition for zero spherical aberration then requires that the conic constant of the secondary is

$$K_2 = -\left(\frac{m+1}{m-1}\right)^2. \quad (6.2.2)$$

For the Cassegrain,  $m > 0$  and the secondary is a hyperboloid; for the Gregorian and inverse Cassegrain,  $m < 0$  and the secondary is a prolate ellipsoid.

With the substitution of  $K_1 = -1$  in Eq. (6.2.1) and the formulas in Tables 6.6 and 6.7, the aberration expressions are much simplified. For convenient reference, these relations are given in Table 6.8.

The first thing to note about the relations in Table 6.8 is that the coma is exactly the same as that of a paraboloid of the same focal ratio, as given in Table 6.1. Note also that this is true for either a Cassegrain or Gregorian, hence neither type has an advantage with respect to this aberration.

To evaluate the astigmatism, we note that  $\beta$  is typically a small positive number of the order of a few tenths, while  $|m|$  is typically ten or more times larger. A good measure of the astigmatism is thus obtained by setting  $\beta = 0$ , with the result that  $\text{AAS} = m\theta^2/2F$ . A comparison of this result with AAS in Table 6.1 shows that a classical telescope whose focus is at the primary mirror vertex has astigmatism  $|m|$  times larger than that of a paraboloid of the same  $F$ . As in the case of coma, there is no discriminant due to astigmatism between Cassegrain and Gregorian types.

The astigmatism for  $\beta = 0$  can also be written as  $\text{AAS} = \theta^2/2F_1$ . Thus the astigmatism in this case depends only on the focal ratio of the primary mirror. A comparison of the tangential coma blur size with the astigmatic blur diameter

Table 6.8

Aberrations of Classical Two-Mirror Telescopes

---


$$\begin{aligned} \text{ASC} &= \frac{\theta}{16F^2} \\ \text{AAS} &= \frac{\theta^2}{2F} \left[ \frac{m^2 + \beta}{m(1 + \beta)} \right] \\ \text{ADI} &= \frac{\theta^3(m - \beta)(m^2 - 1)(m + 3\beta)}{4m^2(1 + \beta)^2} \\ \kappa_m &= \frac{2}{R_1} \left[ \frac{(m^2 - 2)(m - \beta) + m(m + 1)}{m^2(1 + \beta)} \right] \end{aligned}$$


---

shows that coma is almost always the aberration that sets the limiting field size for good images, as the reader can verify by constructing a diagram similar to that of Fig. 6.1. Spot diagrams for an  $f/10$  Cassegrain with  $m = 4$  and  $\beta = 0.25$  are shown in Fig. 6.2. The images for a classical Gregorian are very similar.

Looking at the curvature of the median image surface in the case  $\beta = 0$ , we see that it is approximately  $2(m + 1)/R_1$ . This relation is not exact, but it illustrates three features of the image surface. First, the sign of  $\kappa_m$  is opposite for the Cassegrain and Gregorian types; the surface of best images for the Cassegrain (Gregorian) is concave (convex) as seen from the secondary. Second, the curvature is larger for the Cassegrain than for the Gregorian. And, third, the median image surface is more strongly curved for larger  $|m|$ . This, however, is rarely a limitation because the field covered is usually smaller in angle when  $m$  is larger.

In summary, the classical two-mirror telescope is limited to small fields with coma setting the field limit for good images. Compared to the paraboloid the astigmatism is larger, but for small fields this is rarely a limiting factor. With coma as the dominant aberration, and independent of the stop location when spherical aberration is zero, the location of the aperture stop could be changed, if necessary, without significantly changing the character of the images. Thus it is acceptable to locate the aperture stop at the secondary mirror, as is often done in infrared telescopes.

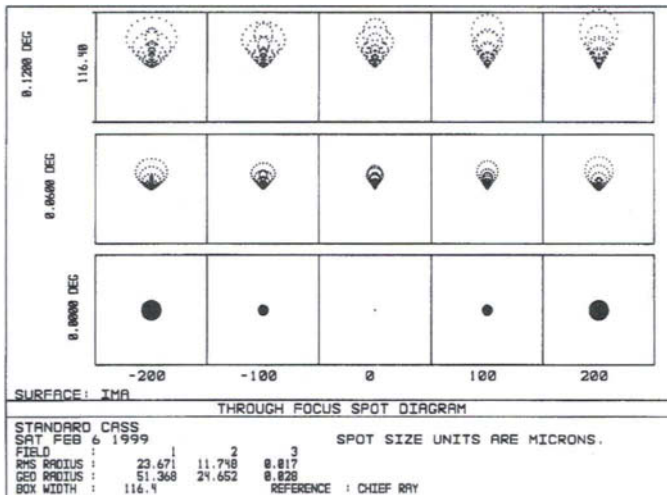


Fig. 6.2. Spot diagrams for 1.2-m  $f/10$  classical Cassegrain with  $m = 4$  and  $\beta = 0.25$ . Box width is 2 arc-sec.

Because of the small field size, distortion is typically a few thousandths of an arc-second and thus much smaller than the atmospheric blur. Compared to the asymmetry of a comatic image, as seen in Fig. 6.2, distortion is not important. The only differences between the Cassegrain and Gregorian of the classical type are the sign and magnitude of the image surface curvature but, given the relatively small usable fields, these differences are usually of little consequence.

### 6.2.b. APLANATIC TYPE

The classical telescope is clearly limited in field coverage by the presence of coma in the off-axis images. In this section we consider the category of telescopes for which, to third order, coma is zero. As noted in Section 5.4, any optical system in which both spherical aberration and coma are absent is called an aplanat. In recent years the *aplanatic Cassegrain* telescope, or *Ritchey-Chretien* as it is commonly called, has been the overwhelming choice of builders of large telescopes of 2-m aperture or larger, including the 2.4-m Hubble Space Telescope. Thus this class of telescope has been carefully studied and merits our close attention. An extensive article by Wetherell and Rimmer (1972) is an additional source of information on aplanatic telescopes, as is the text by Wilson (1996).

It should not be surprising that both spherical aberration and coma can be eliminated in a system with two conic mirrors. A glance at the condition for zero spherical aberration in Table 6.6 shows that there are two free parameters, the conic constants of the mirrors. One conic constant is chosen to make  $B_{2s}$  in Table 6.6 zero, after which the condition for zero spherical aberration sets the other. Thus we find that the conditions for an aplanatic telescope are

$$K_1 = -1 - \frac{2(1 + \beta)}{m^2(m - \beta)}, \quad (6.2.3)$$

$$K_2 = -\left(\frac{m + 1}{m - 1}\right)^2 - \frac{2m(m + 1)}{(m - \beta)(m - 1)^3}. \quad (6.2.4)$$

For the Ritchey-Chretien (RC) the primary is now a hyperboloid, as is the secondary. The conic constant for the secondary of the RC is more negative than for the classical Cassegrain. For the *aplanatic Gregorian* (AG) the primary is now an ellipsoid. The conic constant for the secondary of the AG is more negative than that of the classical Gregorian, provided  $|m| > 1$ , but the conic is still ellipsoidal.

In each case the two mirrors have been “bent” in the same direction in the manner shown in Fig. 4.10. However, the direction of deformation for the mirrors of the RC is opposite that for the AG, as the reader can easily verify.

Table 6.9

Aberrations of Aplanatic Two-Mirror Telescopes

$$\begin{aligned}
 \text{AAS} &= \frac{\theta^2}{2F} \left[ \frac{m(2m+1) + \beta}{2m(1+\beta)} \right] \\
 \text{ADI} &= \frac{\theta^3(m-\beta)}{4m^2(1+\beta)^2} [m(m^2-2) + (3m^2-2)] \\
 \kappa_m &= \frac{2}{R_1} \left[ \frac{(m+1)}{m^2(1+\beta)} (m^2 - \beta(m-1)) \right]
 \end{aligned}$$

Substitution of Eq. (6.2.3) into Eq. (6.2.1) and the coefficients in Table 6.6 gives the aberrations for the aplanatic telescopes, with the results given in Table 6.9.

As with the classical telescopes, we choose  $\beta = 0$  to determine the approximate magnitudes of the aberrations. The results are

$$\text{AAS} = \frac{\theta^2}{2F} \left( m + \frac{1}{2} \right), \quad \text{ADI} = \frac{\theta^3}{4} (m^2 - 2), \quad \kappa_m = \frac{2}{R_1} (m + 1). \quad (6.2.5)$$

Compared to the classical type at the same focal ratio, the astigmatism for the RC is larger while that of the AG is smaller. At a given  $R_1$ , the curvature of the median image surface is larger for the RC than for the AG, with the curvatures again of opposite sign. A comparison of  $\kappa_m$  with  $\kappa_p$  in Eq. (6.2.1) shows a median surface more strongly curved than the Petzval surface for the RC, but less strongly curved for the AG.

The distortion is the same for both types of aplanatic telescope, and is slightly less than for a classical type with  $\beta = 0$ . At the edge of the usable field of an aplanatic telescope the distortion is usually a few hundredths of an arc-second, and may need to be taken into account in certain types of observations.

Spot diagrams for an  $f/10$  RC telescope with  $m = 4$  and  $\beta = 0.25$  are shown in Fig. 6.3. Note that the field size shown in Fig. 6.3 is twice that of the classical Cassegrain in Fig. 6.2 and that at the edges of their respective fields the image quality of the RC is significantly better. Note also that the image blur due to astigmatism is symmetric and therefore the centers of the images can be located more accurately. Because both coma and spherical aberration are zero, the location of the stop does not affect the astigmatism.

In summary, the aplanatic two-mirror telescope has a field limit for good images set by astigmatism. Given the symmetric images and significantly larger field of the RC compared to the classical Cassegrain, it is not surprising that the RC has become the telescope of choice in Cassegrain telescopes. Further

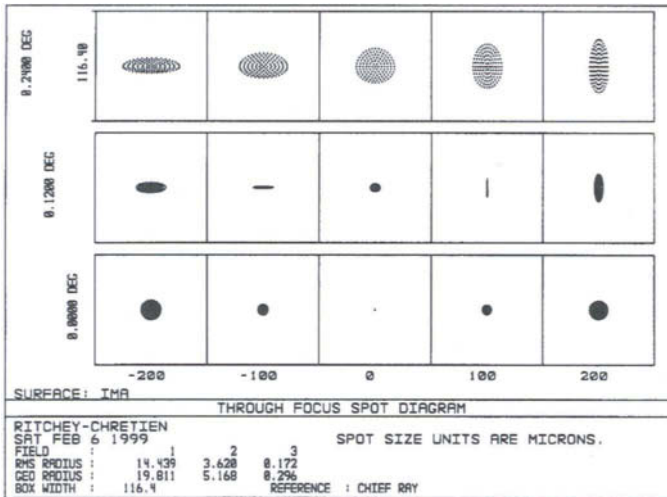


Fig. 6.3. Spot diagrams for 1.2-m  $f/10$  Ritchey-Chretien telescope with  $m = 4$  and  $\beta = 0.25$ . Box width is 2 arc-sec. Off-axis field angles are two times larger than in Fig. 6.2.

comparison of aplanatic and classical telescopes follows a brief discussion of other selected two-mirror telescope types.

### 6.2.c. OTHER TWO-MIRROR TELESCOPES

In addition to the classical and aplanatic two-mirror telescopes, there are other less common types that deserve comment. Because each of these types has one or more serious drawbacks, our discussion of each is brief. In this section we consider in turn the Dall-Kirkham, two-mirror with spherical primary, two kinds of anastigmatic telescopes, and a flat-field aplanat.

The Dall-Kirkham telescope is one in which the secondary is spherical ( $K_2 = 0$ ) and the primary is ellipsoidal, with the appropriate value of  $K_1$  found from the relation for zero spherical aberration in Table 6.6. It is straightforward to find the coma coefficient by setting  $K_2 = 0$  in  $B_{2s}$  of Table 6.5 and, for similar normalized parameters, compare its value with that of a classical Cassegrain. For  $\beta = 0$  the Dall-Kirkham has coma that is  $(m^2 + 1)/2$  times larger than that of the classical Cassegrain, hence the field of good images for the Dall-Kirkham is smaller by this same factor. All other aberrations are negligible over this field.

Although the Dall-Kirkham is severely limited in its field coverage, the mirrors are relatively easy to build and test, as discussed in Section 18.1, and several

telescopes of this type have been built. One other advantage of the Dall-Kirkham is that its on-axis image quality is relatively insensitive to misalignments between the mirrors, as compared to the classical and aplanatic types.

Another type of two-mirror telescope that has some attractive features is one with a spherical primary mirror (SP). The main advantages of the SP design are ease of fabrication and testing of large spherical mirrors, and the possibility of making very large segmented primaries by using a number of smaller spherical mirrors. Designs for SPs with primaries as large as 25 m in diameter have been proposed. Zero spherical aberration with an SP design requires a convex oblate ellipsoidal secondary ( $K > 0$ ) in the Cassegrain version and a concave hyperboloid ( $K < -1$ ) in the Gregorian version, as the reader can verify.

The drawbacks of SP designs are the large off-axis aberrations. This is easily verified by setting  $K_1 = 0$  in the coefficients in Table 6.6 and comparing the results with those found for a classical type with  $K_1 = -1$ . For  $\beta = 0$  these ratios, SP to classical, are  $(m^3 + 2)/2$  for coma and  $(m^2 + 4)/4$  for astigmatism. Choosing  $m = 4$  we find a coma ratio of 33 and an astigmatism ratio of 5. Relative to a classical Cassegrain the off-axis aberrations are indeed very large. The situation for off-axis aberrations is only slightly better for an SP Gregorian.

Given these characteristics, SP types are limited to very small fields or additional optical elements must be added to achieve a reasonable field size. If, for example, additional mirrors were added in the vicinity of the secondary, then the aberrations of the overall system could presumably be reduced to acceptable levels. But in this case it is no longer a two-mirror telescope.

The remaining two-mirror telescopes considered are variations of the aplanatic type, specifically those for which another aberration is corrected. Because the conic constants of the mirrors in an aplanat are chosen to give zero spherical aberration and coma, elimination of another aberration will put restrictions on the remaining normalized parameters. The available choices are easily found by setting each expression in Table 6.9 equal to zero in turn, with a specific combination of  $m$  and  $\beta$  now required. This combination, in turn, places restrictions on the remaining parameters.

The zero-distortion type is of little practical importance because distortion is quite small in two-mirror telescopes with small fields of view, and we will not discuss this type. The remaining choices are the zero-astigmatism type, or anastigmatic aplanat, and the flat-field aplanat.

For the anastigmatic aplanat the pertinent relations between the parameters are

$$\beta = -m(2m + 1), \quad k = 1 - 2m, \quad mk = m(1 - 2m). \quad (6.2.6)$$

The condition for a real final focus requires magnification in the range  $0 < m < 0.5$  when the primary is concave. For any  $m$  in this range, the secondary is also concave and the focal surface is located between the mirrors. This type of

telescope, the so-called *Couder*, therefore suffers from the problem that the focal surface is relatively inaccessible. For a reasonable choice of  $m$ , say 0.25, it also has a relatively large secondary obscuration compared to the Ritchey-Chretien. One final thing to note is that the telescope focal length, in general, is one-half the distance between the primary and secondary mirrors. A diagram of a Couder design is shown in Fig. 6.4.

Another type of anastigmatic aplanat is found if the primary is convex and  $k > 1$ . From Eq. (6.2.6) we find  $m < 0$ , hence there is a real final focus and the configuration is that of an inverse Cassegrain. For  $m$  in the range  $-0.5 < m < 0$ , the focal surface lies between the mirrors because  $\beta > 0$ . (Recall that  $\beta f_1$  is the back focal distance, as defined in Section 2.5, with the focus outside of the space between the mirrors when  $\beta f_1 > 0$ . For an inverse Cassegrain,  $f_1 < 0$  and the focus is outside of the mirrors when  $\beta < 0$ .) A sketch of this configuration with  $\beta > 0$  shows that a blocking plate must be centered in the incident beam to prevent the focal surface from seeing the incident light directly. This configuration also has the problem that a significant fraction of the incident light is reflected back through the hole in the secondary.

For  $m < -1$  some of the light reflected from the secondary passes outside the boundary of the primary, and if  $m$  is sufficiently negative a significant fraction reaches the focus. A feasible configuration of this type is one in which each mirror is a sphere. Substituting  $\beta = -m(2m + 1)$  into Eqs. (6.2.3) and (6.2.4), and setting  $K_1 = K_2 = 0$ , gives  $m = -(1 + \sqrt{5})/2$ . The resulting configuration is the *concentric Schwarzschild anastigmat*, with the mirrors and curved focal surface having the same center, as shown in Fig. 6.5. The reader can verify that the fraction of light vignetted by the primary is 0.2 for this telescope.

Because the secondary mirror is larger than the primary, and because of problems with vignetting and unwanted light reaching the focal surface, this configuration is not really practicable for a telescope. However, it has been used as the basis for cameras in spectrographs.

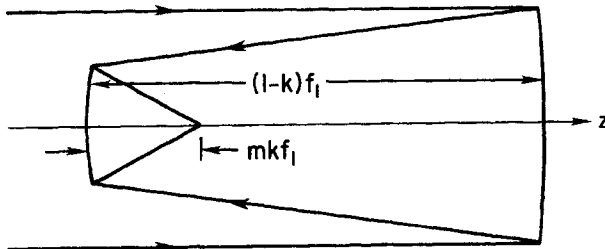


Fig. 6.4. Couder anastigmat with  $m = 0.25$  and  $k = 0.5$ .

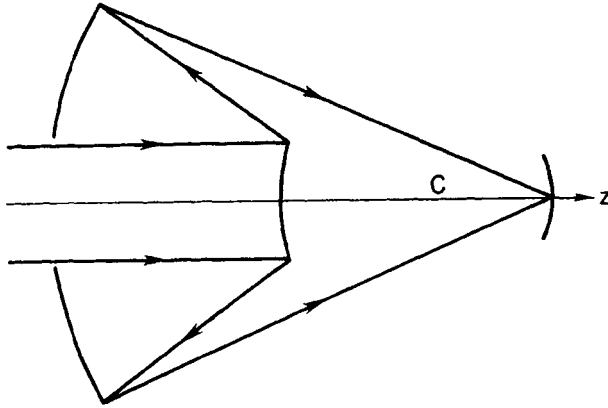


Fig. 6.5. Schwarzschild concentric anastigmat with  $C$  the center of curvature of surfaces. Parameters are  $m = -(1 + \sqrt{5})/2$  and  $k = 2 + \sqrt{5}$ .

The *flat-field aplanat* is defined by  $\kappa_m = 0$ , with the relations for selected parameters given by

$$\beta = \frac{m^2}{m-1}, \quad mk = \frac{m(m^2 + m - 1)}{m^2 - 1}. \quad (6.2.7)$$

An analysis of these relations leads to two possible types: Cassegrain with concave secondary and focus between the mirrors, and inverse Cassegrain. Each of these types suffers from the same problems of image inaccessibility and relatively large vignetting as the corresponding anastigmat.

And, finally, it is worth noting that a solution for a *flat-field anastigmat* can be found by equating the relations for  $\beta$  in Eqs. (6.2.6) and (6.2.7) and solving for  $m$ . The result of this exercise is  $m = \pm 1/\sqrt{2}$ . It is left for the reader to show that only the negative solution gives a configuration with a real final image. In this case the primary mirror is again convex with the secondary  $(1 + \sqrt{2})$  times larger in diameter than the primary, hence not practical as a telescope.

For more details on all of these variations of the aplanat, the reader should consult the article by Wetherell and Rimmer (1972). A thorough discussion of all the telescopes covered in this section is also given by Wilson (1996).

#### 6.2.d. COMPARISON OF CLASSICAL AND APLANATIC TYPES

From the discussion in the preceding sections it should be clear that a two-mirror classical or aplanatic telescope can be most easily tailored to meet the varied observing demands of astronomers. There is great flexibility in these designs to provide the required magnification and image surface accessibility

with generally acceptable vignetting of the incoming beam by the secondary mirror. Some of the shortcomings of these telescopes can be overcome with additional optical elements. Examples include flattening a curved focal surface or increasing the usable field size. These topics are discussed in Chapter 9.

It is therefore appropriate at this stage to take a specific set of parameters and show all of the characteristics of each type of classical and aplanatic telescope. The parameters chosen are characteristic of those for a typical two-mirror telescope with  $\beta = 0.25$  selected to give an accessible focal surface. Each telescope has the same primary mirror and overall focal ratio. A listing of these parameters, including the conic constants, is given in Table 6.10.

The important characteristics of each telescope type, using the parameters in Table 6.10, are given in Table 6.11. In addition to the angular aberrations, entries are included that provide a normalized measure of the size of each telescope type.

Table 6.10

Parameter for Two-Mirror Telescopes<sup>a</sup>

Parameter	CC	CG	RC	AG
$K_1$	-1.000	-1.000	-1.0417	-0.9632
$K_2$	-2.778	-0.360	-3.1728	-0.4052

<sup>a</sup>CC, Classical Cassegrain; CG, Classical Gregorian; RC, Ritchey-Chretien; AG, Aplanatic Gregorian;  $F_1 = 2.5$ ,  $|F| = 10$ ,  $\beta = 0.25$ ,  $|m| = 4$ .

Table 6.11

Characteristics of Two-Mirror Telescopes<sup>a,b</sup>

Parameter	CC	CG	RC	AG
$m$	4.00	-4.00	4.00	-4.00
$k$	0.25	-0.417	0.25	-0.417
$1 - k$	0.75	1.417	0.75	1.417
$mk$	1.000	1.667	1.000	1.667
ATC	2.03	2.03	0.00	0.00
AAS	0.92	0.92	1.03	0.80
ADI	0.079	0.061	0.075	0.056
$\kappa_m R_1$	7.25	-4.75	7.625	-5.175
$\kappa_p R_1$	4.00	-8.00	4.00	-8.00

<sup>a</sup>Parameters are those of telescopes in Table 6.10. Aberrations are given at a field angle of 18 arc-min in units of arc-seconds.

<sup>b</sup>Coma is given in terms of tangential coma.

From the results in Table 6.11 we can deduce the approximate field angle at which the dominant angular aberration is equal to the diameter of a star image blurred by atmospheric effects or “seeing.” If the blur diameter is 1 arc-sec, the field angle at which the aberration blur equals the “seeing” blur is about 9 arc-min for the classical telescopes dominated by coma, about 18 arc-min for the RC, and about 20 arc-min for the AG. Thus the field diameter is roughly a factor of two larger for the aplanatic type of telescope and the field area is 4 times larger.

From the astigmatic surface curvatures in Table 6.11 we find that, in absolute value, the median surfaces have greater curvature and the Petzval surfaces have smaller curvature for the Cassegrain types, as compared with the Gregorian types. The median surface curvature is also somewhat larger for the aplanatic type compared to its classical counterpart. Because  $R_1 < 0$ , the astigmatic surfaces as seen from the secondary are concave and convex for the Cassegrain and Gregorian types, respectively.

If aberrations were the only discriminant of the four telescope types in Table 6.11, the aplanatic Gregorian would emerge as the preferred choice. Other factors, however, strongly favor the RC and it is this type that has been the overwhelming choice for new large telescopes over the past three decades. The reasons for this choice are to be found in rows 2–4, Table 6.11.

Recall that  $k$  is the ratio of the secondary-to-primary diameter for an on-axis light bundle, and thus  $k^2$  is the minimum fractional area of the primary obscured by the secondary. The parameter  $(1 - k)$  is the separation of the primary and secondary in units of  $f_1$ , while  $mk$  is the distance from the secondary to the final focal surface in the same units.

Obstruction of the light by the secondary in the Gregorian is clearly larger than in the Cassegrain, hence the latter has the edge. Comparing values of  $(1 - k)$  for the Cassegrain and Gregorian types we find that the primary-secondary separation is almost 1.9 times larger for the Gregorian. We also find that the distance from the secondary to the focal surface is nearly 70% larger for the Gregorian. Thus for a given focal length and primary and final focal ratio, the physical length of the Gregorian is substantially greater.

This greater length has two very significant impacts on the choice of a telescope and the cost of an observatory facility. First, the cost of a building and dome needed to house the telescope is significantly greater for a larger telescope. For a large telescope the building costs are usually comparable to the cost of the telescope. Second, the cost of the Gregorian telescope itself is greater because the framework supporting the mirrors is longer and more massive. This framework must keep the mirrors in proper alignment if the image quality is to be held to the values given in Table 6.11. In Section 6.3 to follow we consider the effects of misalignment of the primary and secondary and show that significant aberrations can be introduced if the mirrors are not properly aligned.

The one feature of the Gregorian that might be important for certain types of observations is its real exit pupil. A physical stop located here will act to suppress stray light scattered from the support structure of the telescope. Unless this specific feature of the Gregorian is an essential one, the smaller and less expensive RC is preferred.

Given the preference for a Cassegrain telescope over a Gregorian, it is also instructive to compare the characteristics of Cassegrain telescopes with the same diameters, focal lengths, and back focal distances. We choose to make this comparison for RC telescopes, with the results shown in Table 6.12. Note especially the shorter overall telescope length, and thus the expected ease of mirror alignment when the primary mirror is “faster.” We also see that the astigmatism is somewhat larger for the faster primary mirror. In spite of the larger astigmatism at the same field angle, the advantages of a shorter telescope are substantial.

The choice between the Ritchey-Chretien and classical Cassegrain is not as clearcut as that between Cassegrain and Gregorian. For most large telescopes intended for stellar observations, the Ritchey-Chretien has been the favored type, although the classical Cassegrain was the choice for the Keck 10-m telescopes. The discussion in the following section indicates one possible reason for choosing the classical configuration.

### 6.2.e. HYBRID TYPES

To take advantage of the design flexibility of Cassegrain telescopes, many are provided with interchangeable secondaries with each primary-secondary

**Table 6.12**

Comparison of  $f/10$  Ritchey-Chretien Telescopes

Parameter	Ref <sup>a</sup>	RC <sub>1</sub>	RC <sub>2</sub>	RC <sub>3</sub>
$m$	4.00	6.00	7.00	8.00
$F_1$	2.50	1.67	1.43	1.25
$f_1/f_1(\text{ref})$	1.00	0.667	0.571	0.500
$\beta$	0.25	0.375	0.438	0.500
$k$	0.25	0.196	0.180	0.167
$mkf_1/f_1(\text{ref})$	1.000	0.786	0.719	0.667
AAS <sup>b</sup>	1.03	1.35	1.49	1.62
$\kappa_m R_1$	7.63	9.65	10.53	11.34

<sup>a</sup> Parameters of reference RC telescope in Tables 6.10 and 6.11.

<sup>b</sup> Astigmatism is given at a field angle of 18 arc-min in units of arc-seconds.

combination giving a different telescope focal length and focal ratio. With a secondary other than the one designed for the Cassegrain focus, the telescope focus is usually located at a different physical position. For a telescope in an equatorial mount plane mirrors redirect the light, with the final beam directed along the polar axis of the telescope to the so-called *Coude focus*. For a telescope in an altitude-azimuth (alt-az) mount a plane mirror directs the light along the altitude axis to the so-called *Nasmyth focus*. In both cases  $m$  and  $\beta$  are usually larger than at the Cassegrain focus.

For a classical telescope the conic constant of the secondary is given by Eq. (6.2.2) for each  $m$  selected, and the telescope is still of the classical type. The relations in Table 6.8 apply, with the normalized parameters for the Cassegrain replaced by the new values.

A Ritchey-Chretien primary in combination with a different secondary, on the other hand, is no longer aplanatic and the results in Table 6.9 do not apply. This type of telescope is not a Ritchey-Chretien and we choose to call it a *hybrid* telescope. The aberration coefficients given in Table 6.6 apply to hybrid telescopes, provided  $K_1$  for the original RC primary is used. Denoting the parameters for the RC as  $m_c$  and  $\beta_c$ , the conic constant of the primary is, according to Eq. (6.2.3), given by

$$K_1 = -1 - \frac{2(1 + \beta_c)}{m_c^2(m_c - \beta_c)}. \quad (6.2.8)$$

The conic constant of the secondary is set by the condition that the spherical aberration of the hybrid telescope is zero. Substituting  $K_1$  from Eq. (6.2.8) into the zero spherical aberration relation in Table 6.6 gives

$$K_2 = -\left(\frac{m+1}{m-1}\right)^2 - \frac{2m^3(m+1)}{(m-1)^3(1+\beta)} \frac{(1+\beta_c)}{m_c^2(m_c-\beta_c)}, \quad (6.2.9)$$

where  $m$  and  $\beta$  are parameters for the hybrid. Substituting  $K_1$  from Eq. (6.2.8) into the coma and astigmatism coefficients in Table 6.6 gives

$$B_{2s} = \frac{\theta}{4f^2} \left[ 1 - \left(\frac{m}{m_c}\right)^2 \left(\frac{m-\beta}{1+\beta}\right) \left(\frac{1+\beta_c}{m_c-\beta_c}\right) \right], \quad (6.2.10)$$

$$B_{1s} = -\frac{\theta^2}{2f} \left[ \frac{m^2 + \beta}{m(1+\beta)} + \frac{m}{2m_c^2} \left(\frac{m-\beta}{1+\beta}\right)^2 \left(\frac{1+\beta_c}{m_c-\beta_c}\right) \right], \quad (6.2.11)$$

where  $f$  is the focal length of the hybrid telescope.

It is evident from Eqs. (6.2.10) and (6.2.11) that the aberrations are different from those of the aplanatic telescope and that coma is not zero. A good measure

of the amounts of coma and astigmatism present is found by setting both  $\beta$  and  $\beta_c$  to zero, with the results

$$\text{ASC} = \frac{\theta}{16F^2} \left[ 1 - \left( \frac{m}{m_c} \right)^3 \right], \quad \text{AAS} = \frac{\theta^2}{2F} \left[ m + \frac{1}{2} \left( \frac{m}{m_c} \right)^3 \right]. \quad (6.2.12)$$

For typical values of  $m/m_c$ , three or more, the coma of the hybrid telescope is much larger than that of the classical type of the same focal ratio and, although the astigmatism is also larger, the size of the usable field is set by coma.

Dropping the one in the expression for ASC in Eq. (6.2.12), ignoring the minus sign, and substituting  $F = mF_1$ , we can write  $\text{ASC} = F\theta/16(m_cF_1)^3$ . For a given ASC at the edge of the usable field,  $F\theta$  and hence  $f\theta$  is a constant for a given RC primary. Because  $f\theta$  is the linear radius of this field at the hybrid focus, the larger the magnification of the hybrid secondary the smaller is the usable field in angular measure. Although the field size is smaller, the observations made at a Coude or Nasmyth focus are most often made on or near the axis where coma is not significant.

#### 6.2.f. AFOCAL TYPES

As a final class of two-mirror telescope we consider those that are *afocal*, hence the output beam is collimated and the final image is at infinity. One possible application of such a telescope is as a beam reducer, if the secondary mirror is smaller than the primary, or as a beam expander if the secondary is larger. An even more important application is as the input end of a three- or four-mirror telescope. In Section 6.4 of this chapter we discuss selected designs of three-mirror telescopes. In anticipation of that section, it is convenient to determine the characteristics of afocal two-mirror telescopes and include them with other two-mirror telescopes.

We begin by noting that an afocal telescope is one for which  $m$ , the magnification of the secondary mirror, is infinite. Thus we can take previously derived relations and have them apply after letting  $m \rightarrow \infty$ . Because  $\beta$ , the normalized back focal distance, also becomes infinite in this limit, it is convenient to express  $\beta$  in terms of  $m$  and  $k$  before taking this limit. Following this procedure for the aberration coefficients in Table 6.5, we get the results shown in Table 6.13. Also included is the Petzval curvature from Eq. (6.2.1).

Examination of the entries in Table 6.13 show that the obvious choices for conic constants are  $K_1 = -1$  and  $K_2 = -1$ , hence both mirrors are paraboloids. With these choices we see that the afocal two-mirror telescope is free of spherical aberration, coma, and astigmatism, and hence is an *anastigmatic aplanat*. We point out that the same conclusions can be reached by taking Eqs. (6.2.3) and

Table 6.13

General Aberration Coefficients for Afocal Two-Mirror Telescopes

$$\begin{aligned}
 B_{3s} &= \frac{1}{4R_1^3} [K_1 + 1 - k(K_2 + 1)] = -\frac{1}{32f_1^3} [-] \\
 B_{2s} &= \frac{\theta}{R_1^2} \left[ \frac{(1-k)}{2} (K_2 + 1) \right] = \frac{\theta}{4f_1^2} [-] \\
 B_{1s} &= -\frac{\theta^2}{R_1} \left[ \frac{(1-k)}{4k} (K_2 + 1) \right] = \frac{\theta^2}{2f_1} [-] \\
 B_{0s} &= \frac{\theta^3(1-k)}{8k^2} [(1+k)(3+k) + (1-k)^2 K_2] \\
 &= \frac{\theta^3(1-k)(1+3k)}{4k^2}, \text{ for } K_2 = -1 \\
 \kappa_p &= \frac{2}{R_1} \left( \frac{1-k}{k} \right)
 \end{aligned}$$

(6.2.4), and AAS from Table 6.9, and letting  $m \rightarrow \infty$ . Note that in the afocal limit there is no difference between the classical and aplanatic types.

We now determine some of the characteristics of pupils and chief ray directions. From Table 6.3 we see that  $mk$  is the normalized distance from the secondary to the focal point, while from Eq. (2.6.1) we find that the normalized distance from the exit pupil to the focal point is  $\delta$ . For an afocal telescope the ratio  $\delta/mk = 1$ , or  $\delta/m = k$ . Substituting this result into Eq. (2.6.3) we see that  $\Psi$ , the chief ray angle after reflection from the secondary, is given by  $\psi = \theta/k$ . With the aperture stop at the primary mirror, it is left as an exercise for the reader to show that the distance from the secondary mirror to the exit pupil of an afocal telescope is given by  $W' = -k(1-k)f_1$ . It is also straightforward to show that the diameter of the exit pupil is  $|kD|$ , where  $D$  is the diameter of the primary.

As a final comment about this type of telescope, we note that it follows from the stop-shift relations in Section 5.5 that the location of the aperture stop is arbitrary in this type of telescope. That is, spherical aberration, coma, and astigmatism are zero for any position of the aperture stop. This freedom to move the stop and make use of the stop-shift relations will help in the analysis of some of the three-mirror telescopes discussed in Section 6.4.

### 6.3. ALIGNMENT ERRORS IN TWO-MIRROR TELESCOPES

We now consider the consequences of an error in the position of the secondary mirror relative to the primary in a two-mirror telescope. This position error can be

a *decenter* and/or *tilt* of the secondary, either of which is a misalignment between the axes of the mirrors. The error can also be an axial displacement of the secondary toward or away from the primary, in which case the error is called *despace*. In the discussion to follow, aberrations introduced by misalignment are treated separately from those resulting from despace.

### 6.3.a. TILT OR DECENTER MISALIGNMENT

In analyzing the effect of misalignment, we begin by noting that the aperture stop of the telescope is the primary and the reference axis for the secondary is the axis through the vertex of the primary. We consider both coma and astigmatism in our general discussion of misalignment, but apply our results for astigmatism only to the case of the aplanatic telescope. For the classical telescope the astigmatism due to misalignment has little effect on the overall image quality and can generally be ignored.

A possible layout of a misaligned secondary is shown in Fig. 6.6, where the secondary is decentered by an amount  $l$  in the  $y$  direction and tilted through an angle  $\alpha$  about a line perpendicular to the plane of the diagram and tangent to the mirror at its vertex. In this particular case the displacement of the center of the stop from the axis of the secondary, its symmetry axis, is simply the sum of the separate displacements due to decenter and tilt. In the general case the displacements at the stop due to decenter and tilt are not colinear and must be combined by vector addition. We consider only the case shown in Fig. 6.6, however, because compensation of coma, specifically, due to misalignments, requires colinear displacements as shown in Fig. 6.6.

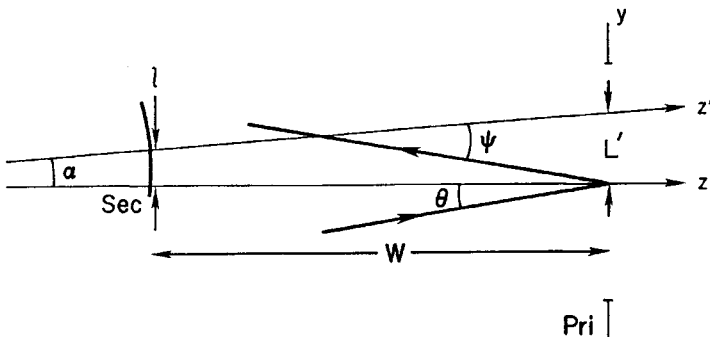


**Fig. 6.6.** Secondary (Sec) in two-mirror telescope decentered by  $l$  and tilted by angle  $\alpha$  with respect to axis of the primary (Pri). The relation between parameters is given in Eq. (6.3.1).

From the geometry of Fig. 6.6 we see that

$$L' = -(l + \alpha W), \quad \psi = -(\theta + \alpha), \quad (6.3.1)$$

where  $L'$  is the distance from the center of the stop to the axis of the secondary and  $\psi$  is the angle between the reflected chief ray and the secondary axis. Substitution of Eq. (6.3.1) into the coefficients in Tables 5.6 and 5.9 gives

$$\begin{aligned} B_{22} &= B_{22}(\text{sec}) + \frac{1}{R_2^2} \left[ \frac{l}{R_2} \left[ K_2 - \left( \frac{m+1}{m-1} \right) \right] - \alpha \left( \frac{m+1}{m-1} \right) \right], \\ &= B_{22}(\text{sec}) + B_{22}(\text{mis}), \end{aligned} \quad (6.3.2)$$

$$\begin{aligned} B_{12} &= B_{12}(\text{sec}) - \frac{1}{R_2} \left[ \left( \alpha + \frac{l}{R_2} \right)^2 + 2\theta \left( \alpha + \frac{l}{R_2} \right) \left( 1 - \frac{W}{R_2} \right) + K_2 \frac{l}{R_2} \left( \frac{l}{R_2} - \frac{2W\theta}{R_2} \right) \right] \\ &= B_{12}(\text{sec}) + B_{12}(\text{mis}) \end{aligned} \quad (6.3.3)$$

where  $n = -1$  for the secondary. The factors  $B_{22}(\text{sec})$  and  $B_{12}(\text{sec})$  are the coma and astigmatism coefficients, respectively, from Eq. (5.6.10) and are the coefficients for a properly aligned secondary. We are interested primarily in the effects of the terms in Eqs. (6.3.2) and (6.3.3) denoted by  $B_{i2}(\text{mis})$  with  $i = 1, 2$ .

We take Eqs. (6.3.2) and (6.3.3), substitute into Eq. (5.6.11), and get

$$B_{2s} = B_{2s}(\text{cen}) + k^3 B_{22}(\text{mis}), \quad (6.3.4)$$

$$B_{1s} = B_{1s}(\text{cen}) + k^2 B_{12}(\text{mis}), \quad (6.3.5)$$

where  $B_{is}(\text{cen})$  are the coefficients for an aligned telescope from Table 6.6. Note that Eqs. (6.3.4) and (6.3.5) apply specifically to the situation shown in Fig. 6.6, that is, along the  $y$ -axis. Generalization to an arbitrary point on the image is considered later in this section. A thorough discussion of the effects of alignment errors across the image field is given by Shack and Thompson (1980).

### 6.3.b. IMAGE SHIFT FROM MISALIGNED SECONDARY

In addition to the introduction of coma and astigmatism, a misaligned secondary will shift the image field perpendicular to the  $z$ -axis in Fig. 6.6. For tilt  $\alpha$  and no decenter, the chief ray from an on-axis object point is reflected from the secondary at angle  $2\alpha$  relative to the  $z$ -axis. Hence the transverse shift of the chief ray at the image is  $2\alpha mkf_1$ , a shift in the positive  $y$ -direction for a Cassegrain or Gregorian telescope with  $mk$  and  $\alpha > 0$ . For decenter  $l$  and no tilt, the on-axis chief ray emerges from the secondary at angle  $2\varphi$  relative to the  $z$ -axis, where  $\varphi = l/R_2$  is the slope of the surface normal at the point where the chief ray hits the secondary. The transverse shift of this chief ray at the image is

$2\phi mkf_1 = -l(m-1)$ . For  $l > 0$  this shift is in the negative  $y$ -direction for  $m > 0$  (Cassegrain) and in the positive  $y$ -direction for  $m < 0$  (Gregorian).

For a chief ray in the  $yz$ -plane making angle  $\theta_y$  with the  $z$ -axis, as shown in Fig. 6.6, the angular shift projected on the sky,  $\psi'$ , is given by

$$\psi' = \theta_y + 2k \left( \alpha + \frac{l}{R_2} \right) = \theta_y + 2k \left( \alpha - \frac{(m-1)l}{2k\bar{f}} \right). \quad (6.3.6)$$

The corresponding transverse shift is found from the product  $f\psi'$  or  $mf_1\psi'$ .

### 6.3.c. COMA FROM MISALIGNED SECONDARY

The amount of transverse coma introduced in a two-mirror telescope with a misaligned secondary is easily found by combining Eqs. (6.3.2) and (6.3.4), and substituting  $B_{2s}$  into Eq. (5.6.8). To get the angular coma as an angle projected on the sky, the transverse coma is then divided by the telescope focal length. The general result along the  $y$ -axis in Fig. 6.6 is

$$\text{ATC} = \text{ATC}(\text{cen}) - \frac{3(1+\beta)}{16F^2} \left[ \frac{l(m-1)^3}{f 2(1+\beta)} \left( K_2 - \frac{(m+1)}{(m-1)} \right) + \alpha(m-1) \right]. \quad (6.3.7)$$

The principal feature of Eq. (6.3.7) is that the coma due to misalignment is independent of the field angle  $\theta$ , hence it is *constant* over the field.

For an aplanatic telescope  $\text{ATC}(\text{cen}) = 0$  and, after substitution for  $K_2$  from Eq. (6.2.4), we get

$$\text{ATC} = -\frac{3(1+\beta)(m-1)}{16F^2} \left[ \alpha - \frac{l m}{f k} \left\{ 1 + \frac{1}{(m-\beta)(m-1)} \right\} \right]. \quad (6.3.8)$$

For a classical telescope we take  $\text{ATC}(\text{cen})$  from Table 6.8, substitute for  $K_2$  from Eq. (6.2.2), and find

$$\text{ATC} = \frac{3\theta_y}{16F^2} - \frac{3(1+\beta)(m-1)}{16F^2} \left[ \alpha - \frac{l m}{f k} \right]. \quad (6.3.9)$$

From Eqs. (6.3.8) and (6.3.9) it is apparent that coma due to misalignment can be made zero by a proper combination of tilt and decenter.

To illustrate the effects of misalignment, we take the set of telescopes whose parameters are given in Table 6.10 and evaluate the relations in Eqs. (6.3.8) and (6.3.9) for each type. Setting  $\theta = 0$  for the classical telescopes, and scaling the telescopes by choosing  $D = 3.6$  m, we get the results shown in Table 6.14 for  $l = 3$  mm and  $\alpha = 3$  arc-min. The entries in Table 6.14 retain the signs given by the relations in Eqs. (6.3.8) and (6.3.9).

Table 6.14

Angular Tangential Coma for Misaligned Secondary<sup>a,b</sup>

	CC	CG	RC	AG
ATC(dec)	1.93	1.93	2.10	2.02
ATC(tilt)	-1.27	2.11	-1.27	2.11

<sup>a</sup> Angular coma is given in units of arc-seconds. Parameters of telescopes are given in Table 6.10 with  $D = 3.6$  m.

<sup>b</sup>  $\alpha = 0.05^\circ = 3.0$  arc-min;  $l = 3$  mm =  $|f|/1.2E4$ .

From the results in Table 6.14 we see that the secondary in the chosen Gregorians is more sensitive to tilt than is the secondary in the Cassegrains. There is little difference between the coma introduced by decenter, although the aplanatic types have slightly larger values. Recall, however, that the Gregorian is significantly longer than the Cassegrain and hence the required tolerances are more easily met with a Cassegrain.

It is important to note that coma contributions due to the separate misalignments can be significantly larger in a telescope with a faster primary mirror. Taking the telescope labeled RC<sub>3</sub> in Table 6.12 we find, for the same tilt and decenter, that ATC(tilt) is 2.8 times larger and ATC(dec) is nearly 8 times larger than for the RC telescope in Table 6.14.

We return now to the aplanatic telescope. From Eq. (6.3.8) we find  $ATC = 0$  if

$$\alpha = \frac{l}{f} \frac{m}{k} \left\{ 1 + \frac{1}{(m - \beta)(m - 1)} \right\}. \quad (6.3.10)$$

For an RC telescope with  $m > 1$ , and  $k$  and  $f > 0$ , we see from Eq. (6.3.10) that  $\alpha$  and  $l$  have the same sign, while for an aplanatic Gregorian their signs are opposite. The importance of the result in Eq. (6.3.10) is that, even if the primary and secondary mirrors are not aligned, there is a tilt that compensates for decenter and gives an image free from coma due to misalignment.

Any combination of tilt and decenter is equivalent to a rotation of the secondary around an axis that is perpendicular to the axis of the primary and intersects it. For the particular combination of  $\alpha$  and  $l$  in Eq. (6.3.10) the intersection of these two axes is called the *neutral point*, and its location on the primary mirror axis depends on the type of telescope. Denoting  $d_{np}$  as the distance from the secondary mirror to the neutral point, we find from Eq. (6.3.10)

$$d_{np} = -kf_1 \left\{ 1 + \frac{1}{(m - \beta)(m - 1)} \right\}^{-1} = -\frac{l}{\alpha}. \quad (6.3.11)$$

The sign convention applies to  $d_{np}$  in Eq. (6.3.11). For a typical RC telescope  $\alpha$  and  $l$  have the same sign and the neutral point lies to the left of the secondary mirror in Fig. 6.6. For an aplanatic Gregorian the neutral point is to the right of the concave secondary. Because the quantity multiplying  $kf_1$  is less than unity, the neutral point is between the secondary mirror and the focal point of the primary for an aplanatic telescope. The existence of a neutral point can be used to advantage if the secondary is deliberately displaced to bring a different source on to a fixed detector as, for example, is done with many infrared telescopes.

We now turn our attention to a classical telescope and Eq. (6.3.9). The situation is more complicated than for an aplanatic telescope because the condition for zero coma from Eq. (6.3.9) has three independent parameters,  $\theta_y$ ,  $\alpha$ , and  $l$ . We choose, therefore, to find the combination of these parameters that makes ATC zero for an image on the axis of the primary mirror.

Setting  $\psi' = 0$  in Eq. (6.3.6), solving for  $\theta_y$ , and substituting for  $\theta_y$  in Eq. (6.3.9), we find

$$\text{ATC (on-axis)} = -\frac{3k}{16F^2} \left[ \alpha(m^2 + 1) - \frac{l}{kf}(m^3 - 1) \right]. \quad (6.3.12)$$

Setting Eq. (6.3.12) to zero and solving for  $\alpha$  we find

$$d_{np} = -kf_1 \left\{ \frac{m(m^2 + 1)}{m^3 - 1} \right\} = -\frac{l}{\alpha}. \quad (6.3.13)$$

The directions of the neutral point from the secondary mirror for classical telescopes are to the left and right, respectively, for the Cassegrain and Gregorian versions. Because the quantity in curly brackets in Eq. (6.3.13) is greater than unity, the distance to the neutral point is slightly larger than  $|kf_1|$ , the distance from the secondary to the focal point of the primary mirror.

It is worth noting that the condition for zero coma on the axis of the primary gives a different relation between  $\alpha$  and  $l$  than obtained by setting  $\theta_y = 0$  in Eq. (6.3.9) and finding the combination of tilt and decenter that then makes  $\text{ATC} = 0$  for an object point on the primary mirror axis. In this latter case the point of zero coma is shifted from the axis of the primary and the neutral point is at the focal point of the primary.

Representative combinations of  $\alpha$  and  $l$  that make coma zero are given in Table 6.15 for both types of Cassegrain telescopes. In all cases  $l = 3$  mm, with  $\theta_y$  chosen to represent the two cases discussed in the preceding.

As a final note, recall that Eqs. (6.3.4) and (6.3.9) apply along the  $y$ -axis as they are written. We can generalize Eq. (6.3.4) for a classical telescope and have it

Table 6.15

Zero Coma Combinations for Cassegrain Telescopes<sup>a,b</sup>

	$\alpha$ (arc-min)	$\theta$ (arc-min)	$\psi'$ (arc-min)
RC	4.99	not relevant	
CC (zero coma for image on primary mirror axis)	4.25	-1.26	0
CC (zero coma for object on primary mirror axis)	4.58	0	1.43

<sup>a</sup> Parameters of telescopes are given in Table 6.10 with  $D = 3.6$  m.<sup>b</sup>  $l = 3$  mm =  $|f|/1.2E4$ .

apply at an arbitrary image point for a tilt and decenter combination shown in Fig. 6.6. The result is

$$B_{2s}\mathbf{r} = \frac{\theta_x}{4f^2}\mathbf{i} + \frac{1}{4f^2}\left\{\theta_y - (1 + \beta)(m - 1)\left[\alpha - \frac{l m}{f k}\right]\right\}\mathbf{j}, \quad (6.3.14)$$

where  $\mathbf{i}$  and  $\mathbf{j}$  are unit vectors along the  $x$ - and  $y$ -axes, respectively. The magnitude of  $B_{2s}$  is found from the components in the usual way, while the direction of the coma flare is along the line from the image point to the point on the  $y$ -axis where the coma is zero.

#### 6.3.d. ASTIGMATISM FROM MISALIGNED SECONDARY

Misalignment of the mirrors in a two-mirror telescope also introduces astigmatism in addition to that already present, as shown by Eqs. (6.3.3) and (6.3.5). In this section we consider the nature of this added astigmatism and how it affects the inherent astigmatism already present.

In our analysis we consider only the situation where coma due to misalignment is zero. Applying this condition to Eq. (6.3.2) gives

$$\alpha = \frac{l}{R_2}\left[K_2\left(\frac{m-1}{m+1}\right) - 1\right]. \quad (6.3.15)$$

Substituting Eq. (6.3.15) into Eq. (6.3.3), expressing  $W$  and  $R_2$  in terms of normalized parameters, and rearranging terms, gives the astigmatism coefficient for the telescope as

$$B_{1s} = B_{1s}(\text{cen}) - \frac{1}{2f}\left(\frac{l}{f}\right)K_2\frac{(m-1)^3}{(1+\beta)}\left[\theta_y + \frac{l}{f}\frac{m}{2(m-\beta)(m-1)}\right]. \quad (6.3.16)$$

For a given decenter we see from Eq. (6.3.16) that the astigmatism due to misalignment is *linear* in the angle  $\theta_y$  over the field. The subscript is applied to this angle, as it is in our discussion of coma, because we are considering specifically the case shown in Fig. 6.6.

There is also a term in Eq. (6.3.16) that is constant over the field. In many instances this constant term is negligible compared to the linear term, especially near the edge of the usable field. Each case must be analyzed individually to determine whether the constant term can be ignored.

From this point on we consider only aplanatic telescopes. We do this because it is coma that largely determines the image quality in Cassegrain telescopes, as shown in Fig. 6.2. A change in the astigmatism due to mirror misalignment will have little noticeable effect on the usable field of a Cassegrain unless the values of  $\alpha$  and  $l$  are unreasonably large.

For aplanatic telescopes we get

$$B_{1s} = -\frac{\theta^2}{2f} \left[ \frac{m(2m+1) + \beta}{2m(1+\beta)} \right] - \frac{1}{2f} \left( \frac{1}{f} \right) K_2 \frac{(m-1)^3}{(1+\beta)} \left[ \theta_y + \frac{l}{f} \frac{m}{2(m-\beta)(m-1)} \right], \quad (6.3.17)$$

$$\text{AAS} = -\frac{\theta^2}{2F} \left[ \frac{m(2m+1) + \beta}{2m(1+\beta)} \right] - \frac{1}{2F} \left( \frac{1}{f} \right) K_2 \frac{(m-1)^3}{(1+\beta)} \left[ \theta_y + \frac{l}{f} \frac{m}{2(m-\beta)(m-1)} \right], \quad (6.3.18)$$

where we can write  $\theta^2 = \theta_x^2 + \theta_y^2$ .

We now evaluate Eq. (6.3.18) for the RC telescope in Table 6.10 with the tilt and decenter combination in Table 6.15. With  $\theta_x$  and  $\theta_y$  expressed in units of arc-min, Eq. (6.3.18) becomes

$$\text{AAS (arc-sec)} = -3.16\text{E-}3[\theta_x^2 + \theta_y^2 - 5.42\theta_y - 0.276]. \quad (6.3.19)$$

Note that the constant term contributes less than 0.001 arc-sec, a negligible amount. We now take a cut along the  $y$ -axis by setting  $\theta_x = 0$  and get the resulting AAS shown in Fig. 6.7. Also shown are AAS with  $l = 0$  and the linear AAS due solely to misalignment. From Fig. 6.7 and Eq. (6.3.19) we find  $\text{AAS} = 0$  at  $\theta_y = 0$  and  $\theta_y = 5.42$  arc-min. We also see from Fig. 6.7 that the effect of the addition of linear astigmatism is to shift the curve for aligned mirrors and to put the minimum in the curve at a point midway between the corrected points, that is, the shifted curve appears symmetric on either side of  $\theta_y = 2.71$  arc-min.

Through-focus spot diagrams at selected values of  $\theta_y$  are shown in Fig. 6.8 relative to a focal surface whose curvature is computed from the relation in Table 6.9. From Figs. 6.7 and 6.8 we see that AAS in the range  $0 < \theta_y < 5.42$  arc-min is of opposite sign to AAS outside of this range. In the range given, the sagittal

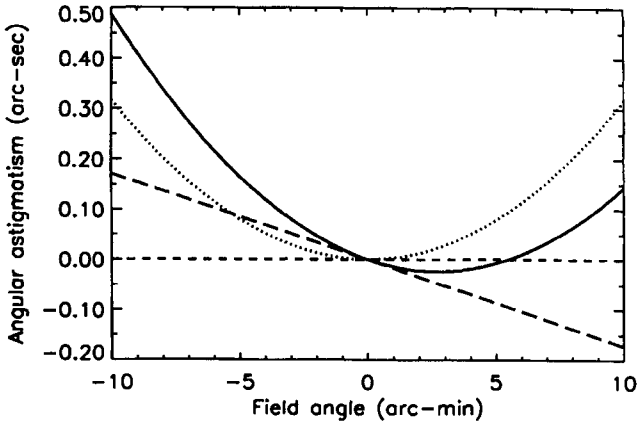


Fig. 6.7. Angular astigmatism (solid line) for Ritchey-Chretien telescope misaligned along  $y$ -axis. The AA is the sum of astigmatism for aligned telescope (dotted line) and linear astigmatism (long dashed line). Parameters of the telescope are given in Table 6.10; tilt and decenter parameters are given in Table 6.15. See the discussion following Eq. (6.3.18).

image (along the  $y$ -axis) is closer to the secondary mirror than the tangential image; outside of this range the sagittal image is farther from the secondary.

We also see in Fig. 6.8 that the astigmatic blur circles midway between the line images are displaced by differing amounts from the curved focal surface. This suggests that the proper curved focal surface for the misaligned case is both shifted and tilted relative to the focal surface for aligned mirrors. If the vertex of the aligned focal surface is offset by 45.5 mm (2.71 arc-min plus  $\psi'$  from Eq. (6.3.6) over the telescope scale of 0.0955 arc-min/mm), displaced by 0.18 mm in the  $-z$  direction, and tilted about the  $x$ -axis by  $0.79^\circ$ , the through-focus spot patterns are then those shown in Fig. 6.9. The symmetry of the blur circles on opposite sides of  $\theta_y = 2.71$  arc-min is now apparent.

We now take Eq. (6.3.19) and rewrite it as

$$\text{AAS (arc-sec)} = -3.16\text{E-}3[\theta_x^2 + (\theta_y - 2.71)^2 - 7.07]. \tag{6.3.20}$$

From Eq. (6.3.20) we see that AAS can be expressed in terms of  $\theta^2 = \theta_x^2 + \theta_y'^2$ , where  $\theta_y' = \theta_y - 2.71$ , and a constant term. When written in this form we see that the center of symmetry of the astigmatic patterns along the  $y$ -axis has shifted to  $\theta_y' = 0$ . Thus, for example, sagittal images far from the symmetry point will fall on lines through the symmetry point. Examples of this are shown in Fig. 6.9.

It is instructive to evaluate Eqs. (6.3.15) and (6.3.18) for the RC<sub>3</sub> telescope with its  $f/1.25$  primary in Table 6.12. For a decenter of 3 mm the tilt required to give zero coma is 14.0 arc-min and, in Eq. (6.3.20),  $\theta_y' = \theta_y - 9.84$  arc-min, the

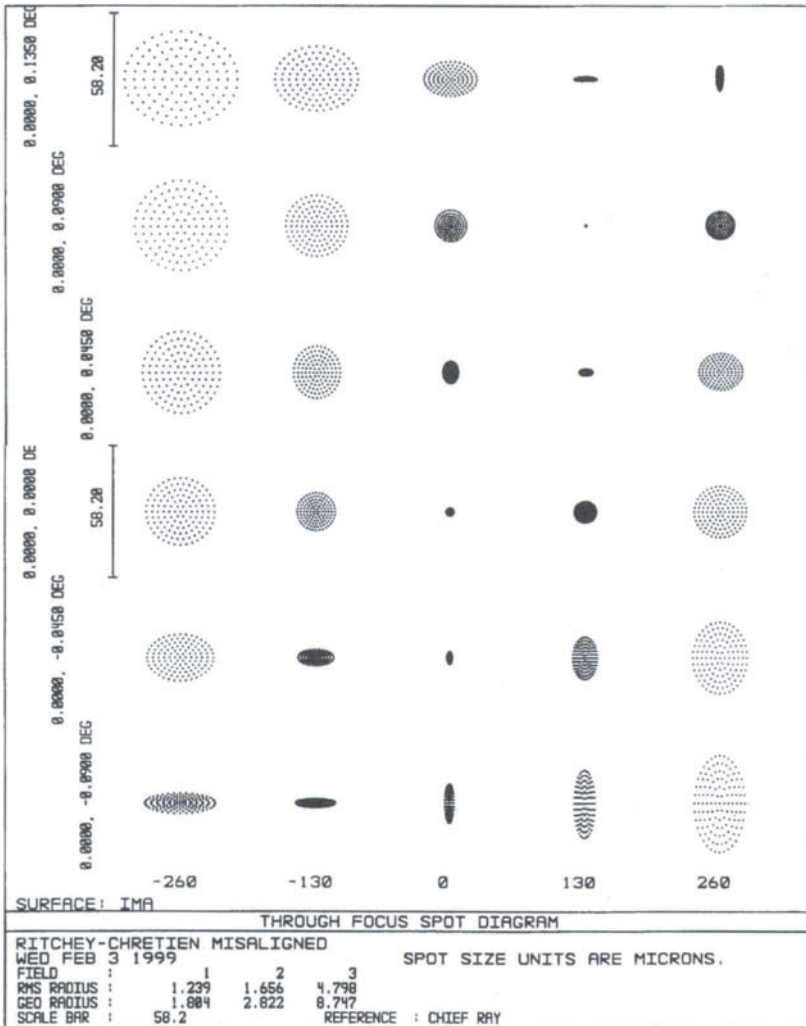


**Fig. 6.8.** Through-focus spot diagrams for misaligned Ritchey-Chretien telescope. Scale bar on upper left is 1 arc-sec long. See the caption of Fig. 6.7 for source of the parameters.

constant in square brackets is 96.8, and the multiplier is  $-4.96\text{E-}3$ . Astigmatism due to misalignment for this telescope is substantially larger.

It is clear from our discussion that correcting coma in an aplanatic telescope by a tilt and decenter combination satisfying Eq. (6.3.15) does affect the astigmatism, with the principal effect a decentered and tilted astigmatic focal surface. It is also evident from Fig. 6.7 that the effect of linear astigmatism leads to differences

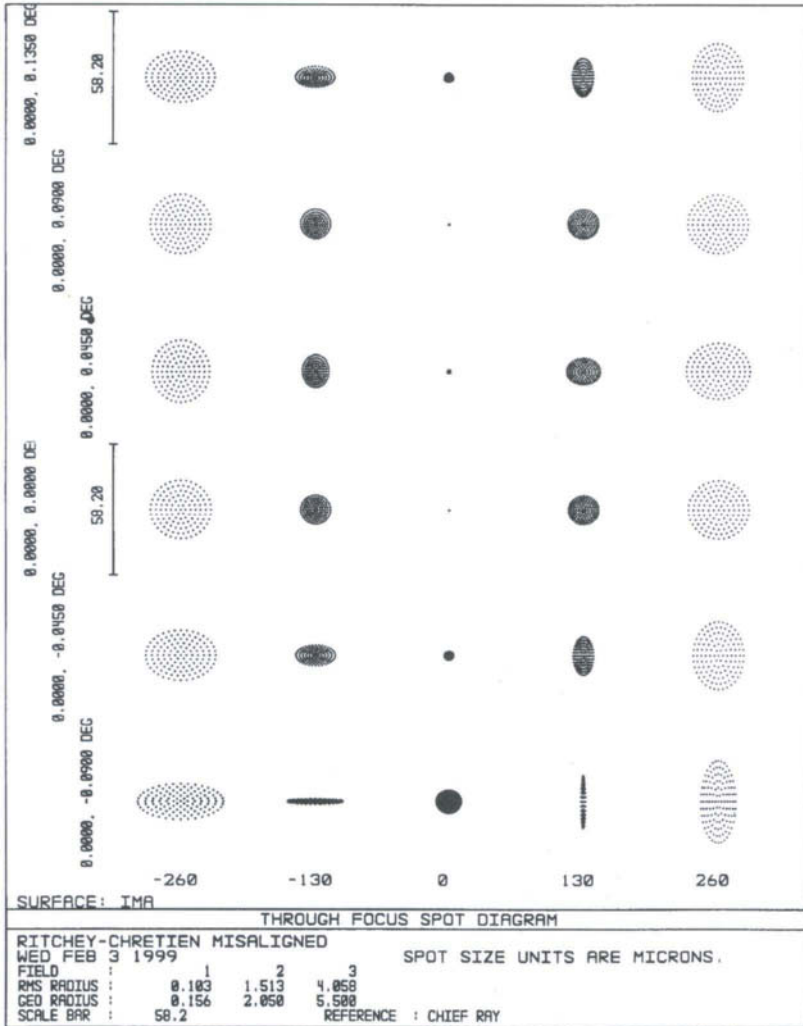


**Fig. 6.9.** Through-focus spot diagrams for misaligned Ritchey-Chretien telescope with shifted and tilted focal surface. Scale bar on upper left is 1 arc-sec long. See the discussion following Eq. (6.3.19).

that are largest at the edge of the usable field. McLeod (1996) describes how observations of the astigmatic images at the edge of the field can be used to find the tilt and decenter. It is then a straightforward procedure to reduce the values of  $\alpha$  and  $l$  while maintaining zero coma. These effects on astigmatism due to misalignment have also been discussed by Wilson and Delabre (1997) in connection with the ESO “New Technology Telescope” (NTT).

## 6.3.e. DESPACE ERROR

We now turn our attention to the aberrations that appear when the error in placement of the secondary is one of despace. If the secondary is not at its nominal design position, then spherical aberration and coma are introduced and images at all points in the image field are degraded. Although spherical aberration is larger than coma, results are given for both aberrations. Astigmatism is also introduced but its size is negligible by comparison.

The starting point for the calculation of spherical aberration resulting from despace is  $B_{3s}$  from Table 6.5 and ASA from Table 6.7, with the terms in square brackets in  $B_{3s}$  substituted into the relation for ASA. If  $m$  is expressed in terms of  $k$  and  $\rho$ , the only variable parameter remaining is  $k$ . The position of the secondary relative to the focal point of the primary is given by  $s_2 = -kf_1$ , hence a change in  $k$  means an axial shift of the secondary.

Taking the derivative of ASA with respect to  $k$ , and resubstituting for  $k$  and  $\rho$  in terms of  $m$ , we find

$$\frac{d}{dk}(\text{ASA}) = \frac{1}{16F^3} \left\{ m(m^2 - 1) - (m - 1)^3 \left[ K_2 + \left( \frac{m+1}{m-1} \right)^2 \right] \right\}. \quad (6.3.21)$$

If  $dk$  is the change in  $k$  starting from the position of the secondary where the spherical aberration is corrected, then  $d(\text{ASA})$  is the angular spherical aberration resulting from the despace, or simply ASA.

It is now a simple matter to evaluate this relation for different types of telescopes and determine the sensitivity to despace. Using the relations for  $K_2$  in Eqs. (6.2.2) and (6.2.4) for classical and aplanatic telescopes, respectively, the results are

$$\text{ASA (classical)} = \frac{m(m^2 - 1) ds_2}{16F^3 f_1}, \quad (6.3.22a)$$

$$\text{ASA (aplanatic)} = \frac{m(m^2 - 1)}{16F^3} \left[ 1 + \frac{2}{(m-1)(m-\beta)} \right] \frac{ds_2}{f_1}. \quad (6.3.22b)$$

A comparison of the relations in Eqs. (6.3.22) shows that aplanatic telescopes are somewhat more sensitive to despace error than are the classical type, though only by 10–15% for typical parameter values such as in Table 6.10. Comparing ASA for the aplanatic telescopes in Table 6.16 shows that the Ritchey-Chretien is more sensitive by a few percent to error in secondary position.

A final thing to note about Eqs. (6.3.22a,b) is that, to a good approximation, ASA is inversely proportional to the cube of primary mirror focal ratio. Hence a telescope with a “faster” primary is more sensitive to despace error. A similar

Table 6.16

Angular Aberrations for Despaced Secondary<sup>a,b</sup>

	RC	AG
ASA	0.912	0.846
ATC	0.252	0.174

<sup>a</sup>  $dk = ds_2/f_1 = 0.001$ .<sup>b</sup> Aberrations are given in units of arc-seconds, ATC is given at a field angle of 18 arc-min, and parameters of telescopes are given in Table 6.10.

conclusion was already noted here for secondary misalignments. In general, a telescope with a faster primary is more sensitive to alignment errors of any kind.

The calculation of coma introduced by a despaced secondary proceeds in a similar way. We start with the coma coefficient  $B_{2s}$  in Table 6.6 and ATC from Table 6.7, express all variables in terms of  $k$  and  $\rho$ , and differentiate with respect to  $k$ . The result for the aplanatic telescope is

$$\text{ATC} = \frac{3\theta}{16F^2} \left[ \frac{(2m^2 - 1)(m - \beta) + 2m(m + 1)}{(1 + \beta)} - \frac{1 + \beta}{m - \beta} \right] \frac{ds_2}{f_1}. \quad (6.3.23)$$

Corresponding results for other two-mirror telescopes are of little importance because the coma already present in the off-axis images is dominant over that introduced by despace.

A comparison of the relative sizes of ASA and ATC for aplanatic telescopes with despaced secondary is given in Table 6.16, with the parameters of the telescopes taken from Table 6.10.

#### 6.4. THREE-MIRROR TELESCOPES

With the addition of a third mirror to a reflecting system there are additional degrees of freedom to minimize or eliminate aberrations. It is possible, for example, to design systems free of third-order spherical aberration, coma, and astigmatism with flat image surfaces. Such three-mirror flat-field anastigmats can be found in a variety of practical configurations, unlike the case for two mirrors where there is only one possible configuration.

The general analysis of a three-mirror system in terms of aberration coefficients is considerably more complicated than that of a two-mirror system. Because of this complexity, we will only outline the procedure and apply it to

some relatively simple examples, those in which there is collimated light between the secondary and tertiary mirrors. Such three-mirror systems are generally referred to as *Paul-Baker* telescopes. For a discussion of the general approach to the design of three-mirror telescopes the reader should consult the article by Robb (1978). An especially thorough discussion of the many possible three-mirror configurations is given by Korsch (1991). The interested reader should also consult the text by Wilson (1996).

#### 6.4.a. GENERAL FORMULATION

Setting up the general relations that describe a three-mirror system is a straightforward extension of results given in Chapter 5. The system aberration coefficients, referenced to the primary, are

$$B_{js} = B_{j1} + B_{j2} \left( \frac{y_2}{y_1} \right)^{j+1} + B_{j3} \left( \frac{y_3}{y_1} \right)^{j+1}; \quad j = 0, 1, 2, 3, \quad (6.4.1)$$

where the subscripts 1, 2, and 3 refer to the primary, secondary, and tertiary mirrors, respectively. Note that Eq. (6.4.1) is simply an extension of Eq. (5.6.11). The other relation of interest is that for the Petzval curvature, which, from Table 5.7, is given by

$$\kappa_p = 2 \left( \frac{1}{R_1} - \frac{1}{R_2} + \frac{1}{R_3} \right). \quad (6.4.2)$$

The general procedure is now one of selecting the system configuration, mirror separations and radii of curvature, and adjusting the conic constants to eliminate third-order aberrations. This procedure is best carried out with optimization routines available in ray-tracing software. We will not pursue this general approach but instead discuss some special cases. In our analysis we will make use of some of the special properties of afocal two-mirror telescopes.

#### 6.4.b. EXAMPLE: PAUL-BAKER TYPE

The starting point for the Paul-Baker telescope, hereafter denoted PB, is a Cassegrain afocal telescope of the type discussed here in Section 2.f. The mirror pair consists of two paraboloids, a concave primary and a convex secondary, whose focal points coincide. This combination, shown in Fig. 6.10, converts an input beam of diameter  $D$  into a collimated output beam of diameter  $kD$ , where  $k = y_2/y_1 = f_2/f_1 = R_2/R_1$ . As shown in Section 2.f of this chapter this afocal reducer has zero spherical aberration, coma, and astigmatism.

## 6. Reflecting Telescopes

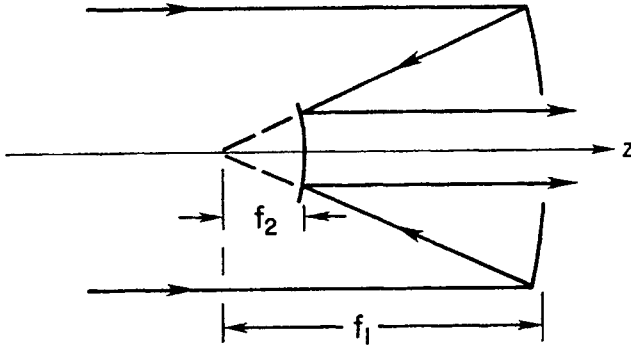


Fig. 6.10. Afocal beam reducer. Ratio of beam diameters  $= k = f_2/f_1$ .

We now add to the afocal reducer a concave spherical tertiary mirror whose center of curvature is at the vertex of the secondary mirror, as shown in Fig. 6.11. Note that the placement of the tertiary is similar to that of the spherical mirror in a Schmidt camera. Because we have added a spherical mirror in collimated light the system now has spherical aberration and, to compensate, the paraboloidal secondary is replaced by a sphere, which introduces spherical aberration of opposite sign. If  $R_3 = R_2$ , these two contributions of spherical aberration are equal in absolute magnitude and the system is again free of spherical aberration. It was first noted by Paul in 1935 that this system is also free of third-order coma and astigmatism with a focal surface whose curvature  $\kappa = 2/R_1$ .

The fact that this three-mirror system is free of third-order aberrations can be shown in two ways. The first way is to evaluate Eq. (6.4.1) for  $j = 1, 2, 3$  and

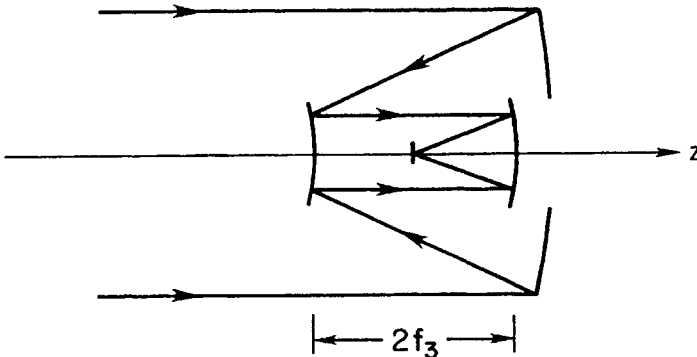


Fig. 6.11. Paul-Baker three-mirror telescope with focal length  $f = f_3/k$ .

show directly that  $B_{1s} = 0$ ,  $B_{2s} = 0$ . Substitutions needed in the  $j = 1, 2$  coefficients for the tertiary are

$$\psi_3 = \frac{\theta}{k}, \quad m_3 = 0, \quad \frac{W_3}{R_3} = 1 + \frac{R_2}{R_3} \left( \frac{1-k}{2} \right). \quad (6.4.3)$$

This method is straightforward but tedious and does little to show the elegance of the original Paul system and its variants.

A more insightful approach is to make use of the stop-shift relations and draw on our discussion of the Schmidt camera in Chapter 4. In our analysis of the afocal telescope given here in Section 2.f we pointed out that the third-order aberrations, though derived for the stop at the primary, are zero for any position of the aperture stop, a result that follows from the stop-shift relations in Chapter 5. Therefore let us place the aperture stop at the secondary. We now have a system in which the tertiary spherical mirror is illuminated with collimated light from a stop at its center of curvature, a combination optically similar to a Schmidt camera.

As noted in Chapter 4, a spherical mirror plus aperture stop at the center of curvature has no preferred axis and is free of coma and astigmatism. The spherical aberration of the mirror is eliminated by an aspheric plate located at the stop; the wavefront advance at the mirror is compensated by an equal wavefront retardation from the aspheric plate. Because this plate is located at the stop, it does not introduce coma or astigmatism.

Returning now to the PB system, the wavefront advance at the spherical tertiary mirror is compensated by an equal wavefront retardation introduced by changing the paraboloidal secondary to a sphere. But this change of the secondary is entirely equivalent to introducing an aspheric plate, as seen by comparing the  $r^4$  terms in Eq. (5.1.1). Hence no coma or astigmatism is introduced into the PB design by changing the conic constant of the secondary.

This conclusion is especially important because it means that the original Paul design with  $R_3 = R_2$  can be generalized to systems with  $R_3 \neq R_2$ , provided two conditions are met: (1) the center of curvature of the spherical tertiary is located at the vertex of the secondary; and (2) the conic constant of the secondary is chosen to give zero spherical aberration for the complete system.

The family of variants of the original Paul design is easily found by starting with the relation for spherical aberration obtained from Eq. (6.4.1). Substituting the spherical aberration coefficients for the secondary and tertiary mirrors from Table 5.6 into Eq. (6.4.1) gives

$$B_{3s} = k^4 \left( \frac{1}{4R_3^3} - \frac{K_2 + 1}{4R_2^3} - \frac{b}{8} \right), \quad (6.4.4)$$

where  $k = y_2/y_1 = y_3/y_1$ . The choice of parameters that makes  $B_{3s} = 0$  includes

$$K_2 = 0, \quad b = \frac{2}{R_2^3} \left[ \left( \frac{R_2}{R_3} \right)^3 - 1 \right], \quad (6.4.5a)$$

$$b = 0, \quad K_2 = -1 + \left( \frac{R_2}{R_3} \right)^3. \quad (6.4.5b)$$

These choices are, of course, equivalent through terms in  $r^4$  in Eq. (5.1.1), as substitution of Eqs. (6.4.5a) and (6.4.5b) in turn demonstrates. The first of these combinations can be described as an aspheric figure on a spherical mirror, the other as an ellipsoidal mirror. With either combination it is a straightforward exercise to verify directly that coma and astigmatism are zero, but with our use of the stop-shift relations it is not necessary to do so. For fast systems the solutions given by Eqs. (6.4.5a,b) must be supplemented by aspheric terms of higher order on the mirrors to control fifth and higher-order aberrations.

We now take the general Paul design and add the condition for zero Petzval curvature, an analysis first done by Baker (1969). Writing Eq. (6.4.2) in terms of  $k$  gives

$$\kappa_p = \frac{2}{R_1} \left[ 1 - \frac{1}{k} \left( 1 - \frac{R_2}{R_3} \right) \right]. \quad (6.4.6)$$

Setting  $\kappa_p = 0$  gives  $R_2/R_3 = 1 - k$ .

Additional relations for Paul-Baker telescopes are given in Table 6.17. Note in particular that the choice of the primary mirror focal ratio and any two from among the mirror separation ratio, obscuration ratio  $k$ , or  $R_3/R_2$  set the basic parameters of the telescope. Once these parameters are selected and a field size is chosen, the diameters of the secondary and tertiary mirrors and the effective obscuration ratio can be computed.

**Table 6.17**

General Relations for Paul-Baker Telescopes<sup>a</sup>

---

Mirror separation ratio:  $\frac{3-2}{1-2} = \frac{R_3}{R_2} \left( \frac{2k}{1-k} \right)$

Focal ratios and lengths:  $\frac{F}{F_1} = \frac{f}{f_1} = \frac{R_3}{R_2}$

Diameter of secondary:  $D_2 = D[k + 2F_1\theta(1-k)]$

Diameter of tertiary:  $D_3 = D[k + 2F_1\theta(1-k) + 4F\theta]$

Effective obscuration ratio:  $k'D = D_3 + 4kF\theta D$

---

<sup>a</sup> For flat-field Paul-Baker telescopes use  $\frac{R_3}{R_2} = \frac{1}{1-k}$ .

The first telescope of the PB type built is the CCD/transit instrument described by McGraw *et al.* (1982), and located at the Steward Observatory of the University of Arizona. This telescope has a 1.8-m  $f/2.2$  primary with  $k \approx 0.32$ , and near-diffraction-limited images over a  $1^\circ$  field of view. Because of the baffles required to prevent light reflected directly from the primary or tertiary from reaching the detector, the vignetting by the central obscuration is approximately 22%. For further details, the reader should consult the article by McGraw *et al.* (1982).

There are several examples of PB designs in the literature. One example is a PB telescope with an  $f/1$  primary and  $f/2$  final focal ratio, and excellent image quality over a  $1^\circ$  diameter field, by Angel, Woolf, and Epps (1982). In their design, aspheric terms are put on the secondary and tertiary mirrors. The nominal parameters of the design are  $k = 0.168$  and  $R_3/R_2 = 2$ , hence the mirror separation ratio from the relation in Table 6.17 is 0.808.

Willstrop (1984) has published designs of PB telescopes with curved focal surfaces and one with a flat focal plane. One particular design with a curved focal surface has a field of view of  $4^\circ$  diameter, with  $f/1.6$  for both the primary mirror and overall telescope. He chooses to place the focal surface at the vertex of the primary mirror, thus the mirror separation ratio = 2 and  $k = 0.5$ . By allowing higher-order aspherics on each of the three mirrors, Willstrop is able to achieve image diameters under 0.31 arc-sec over a  $4^\circ$  field. For further details the interested reader should study the articles by Willstrop.

Because of the excellent image quality achievable with the PB system, a more detailed look into the characteristics of a representative PB is in order. We choose a flat-field version with an  $f/1.575$  primary and  $k = 0.28$  covering a field of  $1.6^\circ$  diameter, as shown in Fig. 6.12, with surface parameters given in Table 6.18. With the addition of aspheric terms in  $y^6$  and  $y^8$  to the secondary and tertiary mirrors, and the application of an optimization algorithm in a raytrace package to these terms, the diameters of images range from about 0.25 arc-sec diameter near the center of the field to 0.5 arc-sec at the edge. No attempt was made to further improve the image quality by letting other parameters vary, although improvement is expected. If aspheric terms are added to all of the mirrors, then image diameters are 0.1 arc-sec or less over the entire flat field.

Given the excellent image quality that can be obtained with the Paul-Baker design, it is legitimate to wonder why more telescopes with this configuration have not been built. Factors that could be considered shortcomings for this type of telescope are: (1) limited volume available for instrumentation behind the focal surface; (2) relatively large vignetting because of baffles required to shield the tertiary mirror from extraneous light; (3) effect of additional optics, such as a filter or atmospheric dispersion corrector, on image quality; and (4) constraint on the overall focal length and focal ratio. We will discuss each of these briefly.

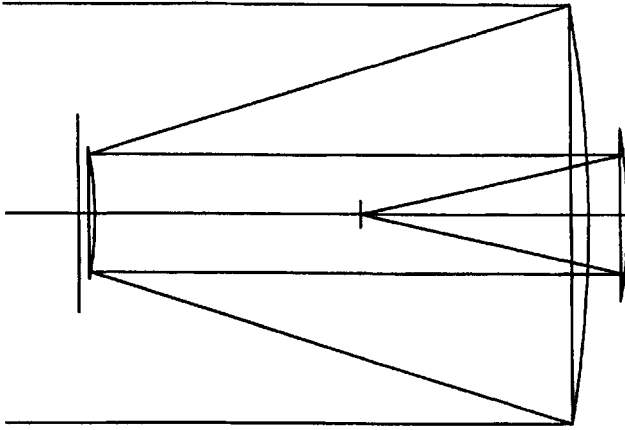


Fig. 6.12. Flat-field Paul-Baker telescope with  $f/2.19$  overall and field diameter of  $1.6^\circ$ . See Table 6.18 for the mirror parameters.

With the focal surface located midway between the secondary and tertiary mirrors, much of the volume behind the focal surface is taken up by light traveling to and from the secondary. Although there is enough space for detectors used for direct imagery, the same cannot be said for slit spectrographs. Using a telescope such as this for spectroscopy would require optical fibers feeding a bench spectrograph.

The focal surface is in the focal plane of the tertiary, hence this mirror must be shielded from starlight from sources outside of the nominal field-of-view (FOV). At a minimum this means a circular obstacle behind the secondary of the size shown in Fig. 6.12. The size of this obstacle is the diameter of the tertiary needed to accept all light from the primary within the FOV plus an annulus that excludes light from within the FOV from entering the telescope aperture and going directly to the tertiary. This diameter is given in Table 6.17 as  $k'D$ , along with the

Table 6.18

Parameters for Flat-Field Paul-Baker Telescope<sup>a</sup>

Surface	$R(\text{mm})$	$K$	Separation(mm)
Primary	-11025	-1	-3939
Secondary	-3087	-0.62675	4287.5
Tertiary	-4287.5	0	

<sup>a</sup>  $D = 3.5$  m,  $k = 0.28$ ,  $F_1 = 1.575$ ,  $F = 2.1875$ .

diameters of the secondary and tertiary mirrors. For  $k = 0.28$ ,  $F = 2.1875$ , and  $\theta = 0.8^\circ$ , the computed value of  $k' = 0.468$  and, at a minimum, the fraction of the incident light lost before reaching the primary is about 0.22.

There are two possible locations for additional optical elements, such as filters or an atmospheric dispersion corrector (ADC), one in the collimated light beam in the plane of the focal surface, the other in the convergent beam just before the focal plane. In the former location the beam diameter is about 1.2 m for a 3.5-m telescope. Making a filter or ADC of this size and holding it in position would be a formidable task. Such an element would also give additional vignetting of the converging beam from the primary and increase the fraction lost to about 0.31.

Thus any additional optics would likely be placed in the converging beam near the focal plane. A plane-parallel plate in this beam will shift the focus by an amount given by Eq. (2.4.5) and introduce both coma and spherical aberration. Using the aberration coefficients for such a plate from Eqs. (7.2.11) and (7.2.12), we find that the transverse aberrations of a glass plate of index  $n$  and thickness  $t$  are

$$\text{TSA} = \left( \frac{n^2 - 1}{2n^3} \right) \frac{t}{8F^3}, \quad \text{TTC} = 3\theta \left( \frac{n^2 - 1}{2n^3} \right) \frac{t}{4F^2}. \quad (6.4.7)$$

The blur introduced by a 6-mm plate of BK7 glass in our representative PB telescope is of the order of 0.2 arc-sec. Hence the monochromatic image quality at best focus is only slightly degraded.

A more serious consequence of introducing a plate into the converging beam is *longitudinal chromatic aberration* or LCA, the change in focus with wavelength. We can determine the approximate LCA by computing how  $\Delta$  in Eq. (2.4.5) changes with wavelength. The result for a plate of thickness  $t$  is

$$\frac{d\Delta}{d\lambda} = \frac{d\Delta}{dn} \frac{dn}{d\lambda} = \frac{t}{n^2} \frac{dn}{d\lambda}, \quad (6.4.8)$$

hence

$$\text{LCA} = \delta\Delta \cong \frac{t}{\langle n \rangle^2} \delta n, \quad (6.4.9)$$

where  $\delta\Delta$  is the change in focus for an index difference  $\delta n$  and average index  $\langle n \rangle$ . The blur size is a minimum at the midpoint between the extreme focus positions, with the blur diameter  $\cong \delta\Delta/2F$ . For a 6-mm BK7 plate transmitting from 400 to 700 nm, we find  $\delta n \cong 0.018$ ,  $\langle n \rangle \cong 1.52$ ,  $\text{LCA} = 47 \mu\text{m}$ , and a blur diameter projected on the sky of approximately 0.3 arc-sec. The combined effects of TSA and LCA over this wavelength range give an effective blur of about 0.4 arc-sec. Willstrop (1984) has designed an ADC for an  $f/1.6$  beam and points out the substantial amount of LCA that is an inevitable part of such a system.

The final limitation of the Paul-Baker telescope, at least in comparison with a two-mirror telescope, is the lack of freedom in choosing the final focal ratio. From Table 6.17 we see that  $F$  is tied to  $F_1$  by the choice of mirror radii. We also see that for the same field size the effective obscuration ratio  $k'$  increases as  $F$  and  $F_1$  increase, hence all proposed designs are based on a fast primary mirror with a final focal ratio that is significantly smaller than that for a typical Cassegrain.

Thus the Paul-Baker design, in spite of its excellent image quality over a field significantly larger than that of a Ritchey-Chretien telescope, has not been the choice for large telescope systems.

#### 6.4.c. OTHER THREE-MIRROR TELESCOPES

If the constraint of collimated light between the secondary and tertiary mirrors is removed, then many three-mirror telescope designs with excellent image quality are possible. In this section we present only a few such designs to illustrate some of these possibilities.

A design by Korsch (1972) has a slowly converging beam between the secondary and tertiary mirrors and a flat focal surface just outside of the space between the mirrors. The layout is shown in Fig. 6.13 for an  $f/3$  primary,  $f/4.5$  overall, and a field diameter of  $1.2^\circ$ , with the parameters given in Table 6.19. Note that each of the mirrors is hyperbolic in cross section. Image quality is excellent with 0.1 arc-sec diameters over the flat field. Although the focal surface is now easily accessible, the price paid is relatively large obscuration by the tertiary of the converging beam from the primary, with the fraction of light lost at about 0.35.

Another flat-field design by Korsch (1977) is shown in Fig. 6.14 with the system parameters scaled to a 3.5-m telescope given in Table 6.20. Image sizes over a  $1.5^\circ$  diameter field are at the 0.1 arc-sec level or less. This  $f/12$  design

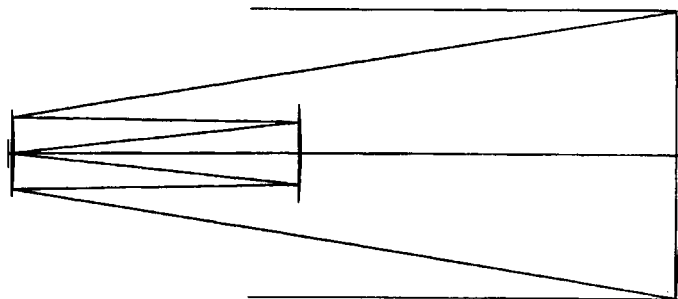


**Fig. 6.13.** Flat-field Korsch telescope with  $f/4.5$  overall and external focus of diameter  $1.2^\circ$ . See Table 6.19 for the mirror parameters.

Table 6.19

Parameters for Korsch Flat-Field Telescope<sup>a</sup>

Surface	$R(\text{mm})$	$K$	Separation(mm)
Primary	-21000	-1.26294	-7875
Secondary	-5833.3	-2.84322	3365.4
Tertiary	-8076.9	-1.40148	-3432.7
Image	$\infty$		

<sup>a</sup>  $D = 3.5 \text{ m}$ ,  $F_1 = 3.0$ ,  $F = 4.5$ .

features a fold mirror located at the exit pupil in the space between the primary and tertiary mirrors, thus giving a large accessible focal plane. Because of the fold mirror the center of the field is totally vignetted and a portion around the center is partially vignetted. Unlike the other three-mirror telescopes discussed, this design has a relatively large final focal ratio. Korsch points out that an advantage of this type of configuration is a focal surface free from stray light without an extensive system of baffles. This advantage is typical of what is called a 2-axis configuration.

The final example presented in this section is a design by Robb (1978), a flat-field  $f/5$  system with the focal plane located near the vertex of the primary, as shown in Fig. 6.15. Image diameters over a field spanning  $2^\circ$  are 0.2 arc-sec or smaller. The parameters given by Robb show that each of the mirrors is hyperbolic in cross section, with additional aspheric terms added to the primary and secondary. For the field size shown in Fig. 6.15 we see that the vignetting by the focal plane of the beam heading toward the tertiary is quite substantial.

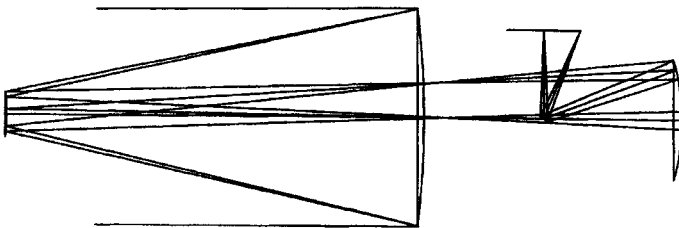
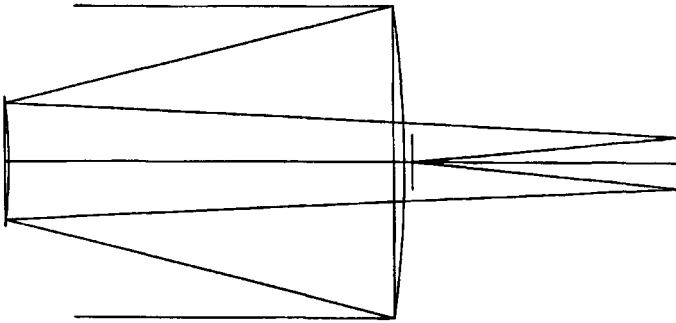


Fig. 6.14. Flat-field 2-axis Korsch telescope with  $f/12$  overall and external focus of diameter  $1.5^\circ$ . See Table 6.20 for the mirror parameters.

Table 6.20

Parameters for Korsch 2-Axis Flat-Field Telescope<sup>a</sup>

Surface	$R(\text{mm})$	$K$	Separation(mm)
Primary	-15400	-0.969825	-6483.4
Secondary	-2962.16	-1.739743	10481.3
Tertiary	-3620.02	-0.558565	-3573
Image	$\infty$		

<sup>a</sup>  $D = 3.5 \text{ m}$ ,  $F_1 = 2.2$ ,  $F = 12$ .Fig. 6.15. Flat-field Robb telescope with  $f/5$  overall and field diameter of  $2^\circ$ .

### 6.5. FOUR-MIRROR TELESCOPES

As astronomers push for telescopes larger than 10-m diameter, it is likely that conventional designs suitable for telescopes in the 4- to 8-m class will no longer be appropriate for what we will call giant telescopes. The principal reason for this is the expected change from monolithic primary mirrors, quite satisfactory for 8-m class telescopes, to segmented primaries such as in the 10-m Keck telescopes.

Segmented mirrors can, in principle, be made for any aspheric shape, but it seems likely that giant segmented primary mirrors will be spherical. Although the Keck mirrors are parabolic in cross section, and do the job quite well, polishing off-axis aspheric segments to the required accuracy is a nontrivial and costly task. The advantages of spherical segments include ease of polishing to the required accuracy and complete interchangeability of segments within the primary mirror array. These advantages, in turn, translate into lower cost.

Among the telescope systems considered so far in this chapter, the two-mirror telescope with spherical primary and zero overall spherical aberration has an

unacceptably small field because of large coma. For two-mirror telescopes, in general, two aberrations can be corrected with the proper choices of the conic constants on the mirrors, leading to the aplanatic designs with zero spherical aberration and coma discussed in Section 6.2. If, however, the primary mirror is spherical, then the remaining conic constant can, in general, be set to make only one aberration zero, specifically spherical aberration. Although two mirrors can be configured to correct for more than two aberrations, as in the anastigmat or flat-field aplanat discussed in Section 6.2, such designs are constrained to particular combinations of normalized parameters and are of limited usefulness.

With three mirrors it is possible, in general, to correct for three aberrations with the proper choices for the conic constants. For the three-mirror telescope designs based on the Paul-Schmidt concept the choices are a paraboloidal primary and spherical tertiary with the conic constant of the secondary tailored to the layout of the mirrors. If, in addition, a flat field is required, then the system parameters are again constrained to certain combinations. Other three-mirror designs are similarly limited to particular combinations of conic constants and system parameters when more than three aberrations are corrected. As with two-mirror telescopes, requiring a spherical primary in a three-mirror system removes one variable from the parameters available for correction of aberrations and leads to no practical designs.

It is for these reasons that we consider, at least briefly, some of the possibilities with four mirrors. In our analysis we will follow the excellent discussion on four-mirror telescopes by Wilson (1996), with an emphasis on the principles leading to practical designs of such systems with a spherical primary mirror. We will also consider only 2-axis designs, largely because of the problems with vignetting in single-axis systems.

### 6.5.a. EXAMPLES

As a starting point in an analysis leading to a practical four-mirror telescope we return to Table 6.13 and the aberration coefficients for afocal telescopes. The first three coefficients are zero when the mirrors are paraboloids, our starting point for the Paul-Baker designs. Consider instead choosing  $K_1 = 0$  and  $K_2 = -1$  for the afocal arrangement. From Table 6.13 we see that coma and astigmatism are still zero although, of course, spherical aberration is not zero. These results are expected because the coefficients were derived with the aperture stop at the primary mirror, and coma and astigmatism are independent of the conic constant when the pupil is at the surface. Thus the beam from this modified afocal system has zero coma and astigmatism, but large spherical aberration from mirror  $M_1$ . Given the nonzero spherical aberration, the exit pupil is fixed at a distance  $-k(1 - k)f_1$  relative to mirror  $M_2$ .

This afocal pair is now used as the feeder for a third mirror. Following the Paul-Schmidt concept, mirror  $M_3$  is spherical and its center of curvature coincides with the center of the exit pupil of the afocal feeder. Mirror  $M_3$ , in turn, reimages the exit pupil on to the fourth mirror of the system,  $M_4$ , where the conic constant  $K_4$  is chosen to zero the spherical aberration of the system. Because  $M_1$  is the source of most of the spherical aberration, the large wavefront advance at the primary will be compensated by an approximately equal wavefront retardation at  $M_4$ . Note that  $M_4$  will introduce some coma and astigmatism into the design, but adjusting  $K_4$  will not introduce additional amounts of these off-axis aberrations.

At this point we make the crucial observation that the mirror arrangement described in the preceding paragraph is possible only with a 2-axis system. Mirror  $M_3$  reimages the exit pupil back on itself when the pupil is a distance  $R_3$  from the mirror, but the light is intercepted by  $M_2$  and no light reaches the reimaged pupil. Hence the beam must be folded between mirrors  $M_2$  and  $M_3$ , with the obvious choice that the fold mirror be located where the beam is smallest, near the focal point of  $M_3$  where an intermediate image is formed. A layout of such a four-mirror configuration is shown in Fig. 6.16.

Following Wilson we will choose a 16-m telescope with an  $f/1.5$  primary and  $k = 0.25$ . We choose to set  $M_3$  at a distance 1.25 times farther from the secondary than is the primary. With the position of  $M_3$  established, its radius of curvature and the position of  $M_4$  are easily found. The final parameter to be set is the position of the final focus from which the radius of curvature of  $M_4$  can be found. For our example we choose the magnification of the intermediate image  $m_4 = -2$ . The nominal parameters for this telescope are given in Table 6.21 and can serve as the starting point for an optimization analysis. The value of  $F_3$  follows from the focal ratio relation in Table 6.17, with the overall  $F = |m_4|F_3$ .

The nominal value of  $K_4$  in Table 6.21 is found by substituting the spherical aberration coefficients for  $M_1$  and  $M_4$  from Table 5.2 into Eq. (5.6.7) and setting the sum to zero. This gives

$$K_4 = \frac{1}{k^4} \left( \frac{R_4}{R_1} \right)^3 - \left( \frac{m_4 + 1}{m_4 - 1} \right)^2, \quad (6.5.1)$$

or about  $-13.6$  for the parameters in Table 6.21. Thus mirror  $M_4$  is strongly hyperbolic, as expected.

The parameters allowed to vary in an optimization process include the conic constants and aspheric terms of sixth order and higher for  $M_3$  and  $M_4$ . In order to work on the coma and astigmatism introduced by  $M_4$ , the locations of these mirrors relative to the secondary are also allowed to vary. The radii of curvature of all the mirrors and the shapes of  $M_1$  and  $M_2$  are generally held constant. We will not give the detailed results of our analysis, but simply note that the final mirror is

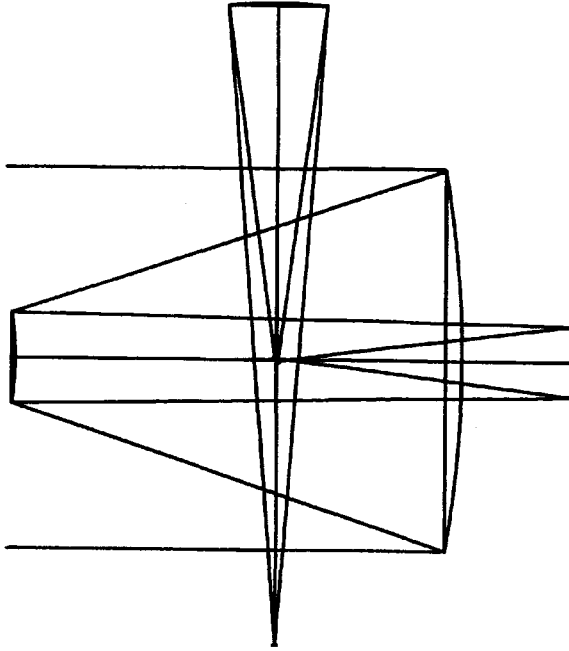


**Fig. 6.16.** A four-mirror 2-axis telescope configuration based on the Paul-Schmidt principle. See Table 6.21 for nominal parameters and discussion following Eq. (6.5.1).

**Table 6.21**

Nominal Parameters for Four-Mirror 2-Axis Telescope<sup>a</sup>

Surface	$R(\text{m})$	Separation(m)	$K$
Primary	-48		0
		-18	
Secondary	-12	22.5	-1
Tertiary	-27	-27	0
Fourth Image	18	27	-13.6

<sup>a</sup> $D = 16 \text{ m}$ ,  $F_1 = 1.5$ ,  $F_3 = 3.375$ ,  $F = 6.75$ . Signs of radii and separations apply to unfolded 1-axis telescope.

strongly hyperbolic and the tertiary is approximately parabolic. Image diameters are 0.2 arc-sec or less over a flat field of 18 arc-min diameter.

Wilson and Delabre (1997) have analyzed this type of system in great detail and point out that the secondary  $M_2$  can also be made spherical rather than parabolic. For their specific design with  $K_2 = 0$ , they find  $K_3 = -0.951$  and  $K_4 = -11.12$ . They point out that the second axis can be positioned favorably to coincide with the altitude axis of an alt-az mounting, and that two identical “Nasmyth-type” foci are possible. The reader should consult their papers for further details.

The design in Fig. 6.16 has collimated light between mirrors  $M_2$  and  $M_3$ , and an intermediate focus and fold mirror between  $M_3$  and  $M_4$ . Another possibility is a reversal of these roles, an intermediate focus and fold mirror between  $M_2$  and  $M_3$ , and collimated light between  $M_3$  and  $M_4$ . A layout of this type of configuration with an  $f/1.5$  primary is shown in Fig. 6.17. Wilson and Delabre have also examined this type of system in detail and find that excellent image quality is achievable over a 30 arc-min diameter field, comparable to that for the configuration in Fig. 6.16.

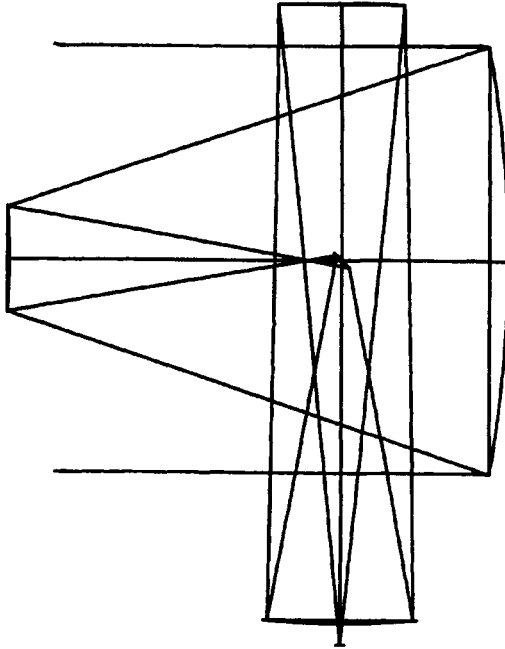


**Fig. 6.17.** A four-mirror 2-axis telescope configuration based on the Paul-Schmidt principle with intermediate focus between the secondary and tertiary mirrors.

These two examples will suffice to introduce the reader to possibilities for practical four-mirror telescopes with spherical primaries. Wilson (1966) discusses other four-mirror configurations; the interested reader should consult his text for specifics.

### 6.5.b. PUPIL ALIGNMENT

In Section 6.3 we discussed the consequences of a misaligned secondary mirror in a two-mirror telescope and showed that an error in its position (tilt, decenter, and/or despace) introduced aberrations. In this section we consider the consequences of a *misaligned pupil* and show that aberrations are again the result. In the case of a four-mirror telescope with its entrance pupil at  $M_1$ , the pupil is misaligned if the optics between mirrors  $M_1$  and  $M_4$  do not properly image the entrance pupil on to  $M_4$ . Pupil misalignment is, of course, a consequence of the incorrect placement of the optics between  $M_1$  and  $M_4$ , but our emphasis here is on the misalignment of the pupil, not on the error in location of preceding optics.

We assume that the error at the entrance pupil is entirely fixed third-order spherical aberration (SA3) and not a more complicated type of wavefront error, either static or dynamic. (Correction of dynamic wavefront error is discussed under the headings of active and adaptive optics.) The assumption that the error is entirely SA3 is often true in practice. The best known case is that of the error in the Hubble Space Telescope (HST) primary where an undetected error in an optical test fixture was propagated into a surface error on the mirror. Numerous other primary mirrors have also had residual errors of this type that went undetected until put into operation in telescopes. In the case of HST, the “fix” was put on an optical element at a reimaged entrance pupil and careful attention was paid to possible pupil misalignment. A discussion of HST in the context of this section follows our general analysis.

We begin by designating the entrance pupil by  $\Sigma_0$  and the exit pupil by  $\Sigma$ . We also assume that the pupil imaging optics has negligible spherical aberration, hence the amount of SA3 wavefront error added to the shape of the optic at  $\Sigma$  is equal in magnitude but opposite in sign to that present at  $\Sigma_0$ . The two effects we consider quantitatively are pupil magnification and pupil shear, with a brief qualitative discussion of pupil aberration. Our analysis of these effects parallels a detailed discussion of this topic by Meinel and Meinel (1992).

Let  $\Omega$  and  $\Omega'$  denote the magnitudes of the wavefront errors added at the exit pupil  $\Sigma$  and reimaged by the intermediate optics, respectively. The general forms of these errors for SA3 are

$$\Omega = Ay^4, \quad \Omega' = Ay'^4. \quad (6.5.2)$$

The difference between the wavefronts is the residual error  $\Delta\Omega$ . For an aligned pupil  $y' = y$  and there is no residual error.

*Pupil magnification* occurs when the reimaged entrance pupil has a different size than the wavefront error added at  $\Sigma$ . In this case  $y' = (1 + \varepsilon)y$  and the error is

$$\begin{aligned}\Delta\Omega_m &= Ay^4 - A(1 + \varepsilon)^4 y^4 = -4A\varepsilon y^4 \\ &= -4\varepsilon\Omega,\end{aligned}\tag{6.5.3}$$

plus terms in higher powers of  $\varepsilon$  that are negligible for  $\varepsilon \ll 1$ . The residual error in this case is spherical aberration. Note that the size of the residual error is proportional to the error at the entrance pupil. In a four-mirror telescope this effect is controlled by proper spacing of mirrors  $M_2$  and  $M_3$  with their as-built radii of curvature.

*Pupil shear* occurs when the reimaged entrance pupil is decentered on the exit pupil. In this case  $y' = y + \delta y$  and the residual error for pupil shear is

$$\begin{aligned}\Delta\Omega_s &= Ay^4 - A(y + \delta y)^4 = -4Ay^3 \delta y \\ &= -4\Omega(\delta y/y),\end{aligned}\tag{6.5.4}$$

plus terms in higher powers of  $\delta y$  that are negligible for  $\delta y \ll y$ . The residual error in this case has the form of coma, which we designate by CM3. Note that larger spherical aberration at the entrance pupil requires a tighter tolerance on pupil centering for the same coma residual. Coma due to pupil shear is constant across the image field.

As examples of the tolerance of pupil misalignment we consider two examples, the nominal four-mirror telescope in Fig. 6.16 and Table 6.21, and HST with the two-mirror correction system called Corrective Optics, Space Telescope Aberration Recovery (COSTAR).

From Table 6.21 we get  $R_1 = -48$  m and  $y_1 = 8$  m at the edge of the primary, giving a surface error of 9.26 mm or about  $1.463E4$  waves at a wavelength of 633 nm. Assuming an allowable surface error of six waves in Eqs. (6.5.3) and (6.5.4) we find the following approximate limits:  $|\varepsilon| < 1E-4$ ,  $|\delta y/y| < 1E-4$ . The first of these limits leads to the requirement that the ratio of the actual to the expected magnification differs from unity by no more than  $|\varepsilon|$ . The second limit gives a tolerance on pupil shear of  $0.0001y$  at mirror  $M_4$ , or about 0.2 mm. The residual error of six waves gives angular coma of about 0.3 arc-sec, a reasonable limit for a ground-based telescope. Given the tight tolerance on  $\delta y$  in a telescope of this size, active monitoring and control of pupil shear would be necessary.

Turning now to HST, the COSTAR system of two mirrors was an addition to the original telescope following the recognition that the HST primary had the wrong conic constant. The COSTAR mirrors  $M_1$  and  $M_2$  were designed to act much like mirrors  $M_3$  and  $M_4$  in a four-mirror telescope, with  $M_1$  reimaging the HST exit pupil on to  $M_2$ . In the case of HST, however, the COSTAR mirrors are small compared to the HST primary, with each mirror about 25 mm in diameter. The surface error at the edge of the HST primary is about 2.2  $\mu\text{m}$  or about 3.5

waves at  $\lambda = 633$  nm. The wavefront error, in turn, is about 7 waves. Given the requirement that the corrected HST should be diffraction-limited leads to an allowable residual wavefront error of about 0.2 waves. Putting these numbers into Eq. (6.5.4) gives a tolerance of  $\pm 90$   $\mu\text{m}$  for pupil shear. Because of this stringent requirement, mechanisms for aligning the mirrors were an essential part of the COSTAR package.

The two effects considered so far assume that the reimaged pupil is at the surface of the optical element correcting SA3 at the entrance pupil. If the reimaged pupil lies in front of or behind the correcting surface, then there is no longer a one-to-one correspondence between points on the entrance pupil and correcting surface. In this case rays from a single point on the entrance pupil land on an area on the correcting surface, a larger area for a wider field of view, and the best that can be done is to provide an average correction. Coma and astigmatism will also enter into the analysis when the projected entrance pupil is not at the correcting surface.

The discussion in this section is intended to illustrate the consequences of pupil misalignment when a wavefront error at the entrance pupil is corrected farther along in the optical train. We have considered only the simplest error to correct, that of SA3. If the primary mirror is segmented rather than monolithic, then piston or tilt errors of individual segments must also be considered. The interested reader should consult the article by Meinel and Meinel (1992) for a discussion of these effects.

## 6.6. CONCLUDING REMARKS

The discussion of the image characteristics in this chapter is based entirely on the geometric theory derived with the aid of Fermat's Principle, without taking into account the limit set by diffraction. Characteristics of images in the diffraction limit where geometric aberrations are negligible is discussed in detail in Chapter 10. The relations in this chapter are derived assuming the mirror surfaces are essentially perfect, thus the figure on the surface of each mirror is according to the prescription given by Eq. (5.1.1). Real mirrors are not perfect and polishing errors give rise to scattered light and image degradation. We discuss this topic in Chapter 18.

We have devoted most of our discussion to two-mirror telescopes because nearly all large reflectors are of this type. It should be evident, however, from our discussion of the Paul-Baker designs that families of three-mirror telescopes with excellent image characteristics can be found, given the additional free parameters with another mirror. Although many three-mirror designs have been published, they have common problems of image surface accessibility and larger vignetting

of the incident beam, compared to two-mirror telescopes. With careful attention given to these problems, however, practical three-mirror designs with excellent image characteristics can be found.

Although practical configurations of four-mirror telescopes have been proposed, none of these designs have yet been built. The push to build giant ground-based telescopes with moderate fields and excellent image quality makes this type of telescope a viable contender to more conventional designs.

Finally, there are innovative telescope designs not discussed here. One of these is the 9-m Hobby-Eberly telescope with a segmented spherical primary and a four-mirror, all-reflecting Gregorian corrector located at prime focus. The corrector removes the very large spherical aberration of the  $f/1.45$  primary. Another design not considered is the 6.5-m replacement for the Multiple-Mirror Telescope. This telescope has an  $f/5$  Cassegrain focus at which a field diameter of  $1^\circ$  is obtained with an all-refractive corrector located near the Cassegrain focus. Both of these telescopes are primarily used with fiber-fed spectrometers.

## REFERENCES

- Angel, R., Woolf, N., and Epps, H. (1982). *Proc. SPIE Int. Soc. Opt. Eng.*, **332**: 134.  
 Baker, J. (1969). *IEEE Trans. Aerosp. Electron. Syst.*, **5**: 261.  
 Korsch, D. (1972). *Appl. Opt.*, **11**: 2986.  
 Korsch, D. (1977). *Appl. Opt.*, **16**: 2074.  
 McGraw, J., Stockman, H., Angel, R., and Epps, H. (1982). *Proc. SPIE Int. Soc. Opt. Eng.*, **331**: 137.  
 McLeod, B. (1996). *Publ. Astron. Soc. Pac.*, **108**: 217.  
 Meinel, A. and Meinel, M. (1992). *SPIE Optical Engineering*, **31**: 2271.  
 Paul, M. (1935). *Rev. Opt.*, **14**: 169.  
 Robb, P. (1978). *Appl. Opt.*, **17**: 2677.  
 Shack, R. and Thompson, K. (1980). *Proc. SPIE Int. Soc. Opt. Eng.*, **251**: 146.  
 Wetherell, W. and Rimmer, M. (1972). *Appl. Opt.*, **11**: 2817.  
 Willstrop, R. (1984). *Mon. Not. R. Astr. Soc.*, **210**: 597.  
 Wilson, R. and Delabre, B. (1997). *Publ. Astron. Soc. Pac.*, **109**: 53.

## BIBLIOGRAPHY

- Bowen, I. (1967). *Annual Review of Astronomy and Astrophysics*, **5**: 45, Palo Alto, CA: Annual Reviews.  
 Gascoigne, S. (1973). *Appl. Opt.*, **12**: 1419.  
 Hewitt, A. (ed.). (1980). *Optical and Infrared Telescopes for the 1990s*, vols. 1 and 2, Tucson, AZ: Kitt Peak National Observatory.  
 Korsch, D. (1991). *Reflective Optics*, Boston, MA: Academic Press.  
 Mahajan, V. (1998). *Optical Imaging and Aberrations, Part I, Ray Geometrical Optics*, Bellingham, WA: SPIE Optical Engineering Press.

- Wetherell, W. and Rimmer, M. (1972). *Appl. Opt.*, **11**: 2817.  
Wilson, R. (1996). *Reflecting Telescope Optics I*, Berlin: Springer.

*Conference Proceedings*

- Ardeberg, A. (ed.). (1997). *Proc. SPIE Int. Soc. Opt. Eng.*, **2871**.  
Barr, L. (ed.). (1986). *Proc. SPIE Int. Soc. Opt. Eng.*, **628**.  
Barr, L. (ed.). (1990). *Proc. SPIE Int. Soc. Opt. Eng.*, **1236**.  
Stepp, L. (ed.). (1994). *Proc. SPIE Int. Soc. Opt. Eng.*, **2199**.  
Stepp, L. (ed.). (1998). *Proc. SPIE Int. Soc. Opt. Eng.*, **3352**.

Typical ground-based two-mirror telescopes without correctors have usable field diameters of a fraction of a degree. In Chapter 9 we show that larger fields are obtained with the addition of a corrector system to such telescopes, reaching about  $1^\circ$  at prime focus and up to  $3^\circ$  at Cassegrain focus. Still larger fields require a telescope of the Schmidt type, or one of the many members of the family of telescopes based on the principle of the Schmidt. This principle is basically one of using a corrector plate to compensate for the spherical aberration of the reflecting optics and locating the plate and aperture stop to give zero coma and astigmatism for the system, at least to third order.

In this chapter we consider in more detail the classical Schmidt system first introduced in Chapter 4, including solid and semisolid Schmidt systems in which all or part of the air between the optical surfaces is replaced by glass. We discuss derivatives of the Schmidt design, such as Schmidt-Cassegrain and Bouwers-Maksutov systems in Chapter 8.

The classical Schmidt is the choice for a wide-field telescope if an aperture of 1 m or more is required. The principal reasons are its relative simplicity, only two large optical elements, and the smaller chromatic aberration of the aspheric corrector compared to that of the corrector in other types. In smaller apertures the choices for a wide-field instrument are a folded Schmidt or one of the two-mirror types. Whether the intended use is as a spectrograph camera or a telescope for visual observation, the requirement of an accessible focal surface is of overriding importance in this case.

## 7.1. GENERAL SCHMIDT CONFIGURATION

The Schmidt camera in its usual configuration is a corrector plate located at the center of curvature of a spherical mirror, as shown in Fig. 4.10. This arrangement was discussed in Section 4.5, where it was introduced to illustrate the application of Fermat's Principle to cancel the on-axis aberration of the mirror in collimated light. The importance of locating the aperture stop at the center of curvature of the mirror to eliminate off-axis aberrations was also noted there.

In this section we extend these discussions and consider the Schmidt configuration in a more general way. This is done to show the range of possibilities for placement of the aperture stop and corrector.

Consider the system of spherical mirror, corrector plate, and aperture stop shown in Fig. 7.1, with the object surface at distance  $s$  to the left of the mirror. The corrector plate is located a distance  $d$  to the left of the mirror, and the aperture stop is distance  $g$  to the left of the corrector. The distances  $s$ ,  $d$ , and  $g$  in Fig. 7.1 are negative according to the sign convention. We choose  $n_o$  to denote the index of the medium for the rays incident on the mirror and reserve  $n$  and  $n'$  for the media before and after the aspheric correcting surface.

Defining  $k = y_2/y_1$ , the ratio of the beam height at the mirror to that at the corrector, we see from Fig. 7.1 that  $k = s/(s - d)$ .

The aberration coefficients for the corrector and mirror are found in Table 5.5 and Table 5.6, respectively, with only the  $b$  terms taken for the corrector. Substituting these results into Eq. (5.6.7) to get the system coefficients gives

$$B_{3s} = -\frac{1}{8} \left[ b - \frac{2n_o}{R^3} k^4 \left( \frac{m+1}{m-1} \right)^2 \right], \quad (7.1.1)$$

$$B_{2s} = \frac{\psi}{2} \left[ bg - \frac{2n_o}{R^2} k^3 \left( \frac{m+1}{m-1} \right) \left( 1 - \frac{W}{R} \right) \right], \quad (7.1.2)$$

$$B_{1s} = -\frac{\psi^2}{2} \left[ bg^2 - \frac{2n_o}{R} k^2 \left( 1 - \frac{W}{R} \right)^2 \right], \quad (7.1.3)$$

where  $W = d + g$ . From the system aberration coefficients, and the requirement that each be zero, we can determine what freedom, if any, there is in their locations.

Setting Eq. (7.1.1) to zero, putting the result for  $b$  into Eqs. (7.1.2) and (7.1.3), and setting each equal to zero gives the condition,

$$\frac{1}{R} \left( \frac{m+1}{m-1} \right) g = \frac{1}{k} \left( 1 - \frac{W}{R} \right). \quad (7.1.4)$$

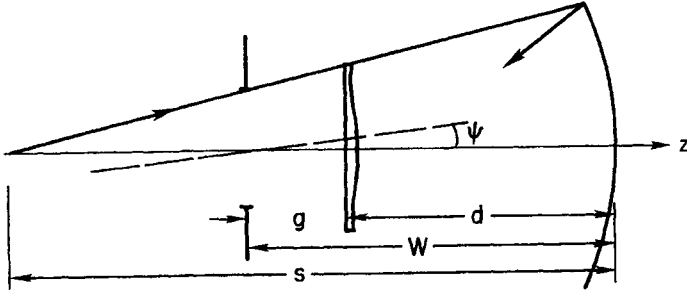


Fig. 7.1. Schmidt camera with stop at distance  $g$  from corrector and object at distance  $s$  from mirror.

Using the relation between  $R$  and  $m$  in Table 5.2 and substituting for  $W$  and  $k$  in terms of  $s$ ,  $d$ , and  $g$ , we find

$$g(R - s) = (s - d)(R - d - g).$$

Solving this equation for  $d$  gives two solutions:  $d = R$  and  $d = s - g$ . The first of these solutions places the corrector at the center of curvature of the mirror, the same location as in the earlier discussions. The second solution gives  $W = s$ , hence the stop is at the object surface. This result is untenable and is discarded because it violates the condition that  $\psi$  is small, as is evident by putting  $W = s$  into Eq. (5.5.2).

With  $d = R$ , hence  $W = R + g$ , we find  $k = -(m - 1)/(m + 1)$ , and therefore the aspheric factor is

$$b = \frac{2n_o}{R^3} \left( \frac{m - 1}{m + 1} \right)^2. \tag{7.1.5}$$

For collimated light  $m = 0$  and  $b = 2n_o/R^3$ , the result given in Section 5.5. For the configuration shown in Fig. 7.1,  $n_o = 1$ ,  $m < 0$  and  $|m| < 1$ . Thus the factor in parentheses in Eq. (7.1.5) is larger than one, and  $b$  for noncollimated light is larger than for collimated light.

The upshot of this analysis is that for either collimated or noncollimated light the corrector plate must be located at the center of curvature of the mirror, but the location of the stop is arbitrary, provided  $W/s$  is not close to unity. Note that if an optical system precedes the Schmidt camera, the stop is the exit pupil of the preceding system.

This result is important because in some configurations using a Schmidt camera the stop or pupil is necessarily displaced from the corrector. An example of this is a camera in a spectrograph where the pupil is usually at the prism or grating and different wavelengths leave the dispersing element in different directions. It is worth noting here that when the stop is displaced from the

corrector, the corrector is larger and its chromatic effects are also larger. To minimize the chromatic effects, therefore, the pupil should be at the corrector or as close as can be arranged. We discuss the relation between the pupil location and the chromatic effect in a following section.

## 7.2. CHARACTERISTICS OF ASPHERIC PLATE

The aspheric plate is obviously the key to a correctly configured Schmidt system and we now consider its aberration characteristics in some detail. In this section we consider the finite thickness of a real plate and its effect on the aberrations, and the effect of the radius term introduced in Section 4.5 to minimize the chromatic aberration of the plate. We also discuss chromatic aberration in more detail than in Section 4.5, and give relations for fifth-order spherical aberration of an aspheric plate and spherical mirror in collimated light.

The equation for an aspheric surface is given by an extension of Eq. (5.1.1), with  $K = -1$ , as follows:

$$z = \frac{r^2}{2R_c} + \frac{br^4}{8(n' - n)} + \frac{b'r^6}{16(n' - n)} = \frac{r^2}{2R_c} + Er^4 + Fr^6, \quad (7.2.1)$$

where the latter form in Eq. (7.2.1) is that usually used in ray-tracing programs. We include the terms in  $r^6$  in anticipation of the section on fifth-order spherical aberration.

The difference between setting  $K = -1$  versus  $K = 0$  is of no practical consequence for a refracting plate. If  $K = 0$  the added terms,  $r^4/8R_c^3$  and  $r^6/16R_c^5$ , are each several orders of magnitude smaller than the terms in  $b$  and  $b'$ , respectively, for any practical plate. For the corrector plate example in Section 7.3, the effect of these added terms is to change the thickness at the margin by less than 0.3 nm.

### 7.2.a. CHROMATIC ABERRATION

One approach to finding the chromatic properties of an aspheric plate is given in Section 4.5.b, where the analysis gives a relation for the minimum chromatic spherical aberration in Eq.(4.5.15). In this section we determine the chromatic properties in a more general way, including the effect of a stop displaced from the aspheric plate.

We first consider the Schmidt system shown in Fig. 4.10 with the aspheric figure on the surface facing the mirror. The plate of index  $n$  is located in air. For a plate of radius  $r_0$  the profile of the aspheric surface can be written as

$$(n - 1)z = \frac{1}{32f^3}(r^4 - ar_0^2r^2), \tag{7.2.2}$$

where  $f = -R/2$  and  $a$  is an arbitrary parameter. Note that this relation is simply Eq. (4.5.11) written with  $a/4$  replacing  $3/8$  in the term containing  $r_0^2$ .

For a ray parallel to the  $z$ -axis, the angle of deviation  $\delta$  at height  $r$  at the aspheric surface is given by  $\delta = i(n - 1)$ , as shown in Fig. 7.2. The angle of incidence  $i$  at the aspheric surface is  $i = -dz/dr$ , where  $dz/dr$  is the slope of the normal to the surface. Thus

$$\delta = -(n - 1) \frac{dz}{dr} = \frac{1}{16f^3}(ar_0^2r - 2r^3). \tag{7.2.3}$$

From Eq. (7.2.3) we see that  $\delta = 0$  when  $r = 0$  and  $r = r_0\sqrt{a/2}$ , where the latter value defines the radius of the neutral zone.

Inside the neutral zone the ray deviation is a maximum at the inflection zone, defined as that  $r$  for which  $d\delta/dr = 0$ , while outside the neutral zone  $r$  is a maximum at the edge of the plate. The characteristics of the aspheric surface at these zones, expressed in terms of  $a$ , are given in Table 7.1.

From the entries in Table 7.1 it is evident that the deviations at the inflection zone and edge have opposite signs for  $a < 2$ . As  $a$  increases from zero,  $\delta$  at the inflection zone increases while  $\delta$  at the edge decreases. The net deviation across the plate is a minimum when the values of  $\delta$  at these two radii are equal in magnitude. This is obtained with the choice  $a = 1.5$  and the resulting magnitude of  $\delta = r_0^3/32f^3$  at these radii. The neutral zone is then at  $r = r_0\sqrt{3}/2 = 0.866r_0$ .

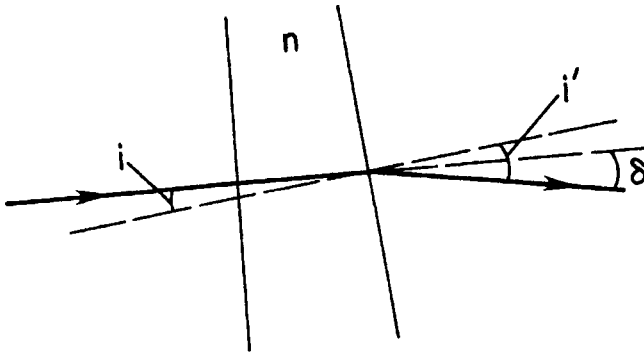


Fig. 7.2. Angle of deviation  $\delta$  at wedge-shaped section of aspheric plate.

Table 7.1

Deviations at Zones of Aspheric Plate		
Zone	Radius	Deviation
Inflection	$r_0 \left(\frac{a}{6}\right)^{1/2}$	$\frac{r_0^3}{4f^3} \left(\frac{a}{6}\right)^{3/2}$
Neutral	$r_0 \left(\frac{a}{2}\right)^{1/2}$	0
Edge	$r_0$	$\frac{r_0^3}{16f^3} (a - 2)$

Differentiating Eq. (7.2.1) and setting it equal to zero, substituting for  $r$  at the neutral zone, and solving for  $R_c$  gives

$$R_c = -\frac{8(n' - n)}{3br_0^2} = -\frac{1}{3Er_0^2}, \quad (7.2.4)$$

where  $n' = 1$  for the configuration in Fig. 4.10.

The sign of  $b$  depends only on the character of the plate. From Eq. (7.1.5) we see that  $b < 0$  for a plate in a Schmidt camera because  $n_o$  and  $R$  are always of opposite sign. As shown in Section 4.5.b and Fig. 4.11, a Schmidt plate has a “turned-up” edge. Conversely,  $b > 0$  for a plate with a “turned-down” edge. The sign of  $E$ , on the other hand, depends on whether the aspheric is on the first or second surface of the corrector, and on the direction of light through the plate. Note also from Eq. (7.2.4) that  $E$  and  $R_c$  always have opposite signs in order to place the neutral zone at the desired radius.

The chromatic blur is obtained by finding the variation of  $\delta$  with changing  $n$ . Using Eq. (7.2.3) we get

$$\frac{d\delta}{dn} = -\frac{dz}{dr} = \frac{\delta}{n - 1}. \quad (7.2.5)$$

Figure 7.3 shows two rays for different values of  $n$  leaving a point on the aspheric surface and intersecting the mirror a distance  $R d\delta$  apart. The point on the aspheric surface can, in effect, be considered an object point at distance  $R$  that is reimaged at the corrector. Hence the blur at the focal surface for these two rays is  $f d\delta$ . Substituting the values of  $\delta$  at the inflection zone and edge into Eq. (7.2.5) gives a blur diameter of  $2f d\delta$ . Hence

$$\text{CSA} = \frac{f}{128F^3} \left( \frac{dn}{n - 1} \right), \quad (7.2.6)$$

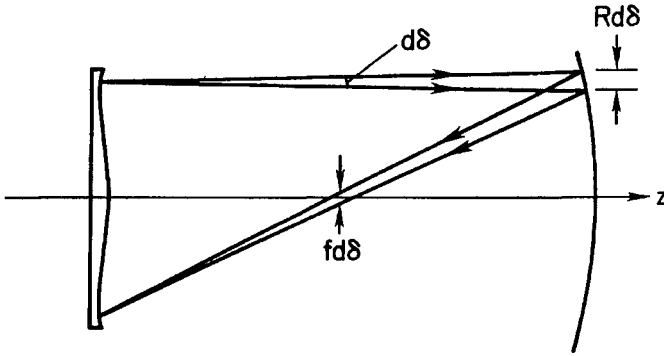


Fig. 7.3. Paths of rays of different wavelength through Schmidt camera. See Eqs. (7.2.5) and (7.2.6).

where CSA is the chromatic spherical aberration and  $F$  is the focal ratio of the mirror. This result is, as expected, equivalent to that given in Eq. (4.5.15).

The results so far are appropriate for a corrector with aperture stop at the plate. When the stop or pupil is displaced from the plate, as shown in Fig. 7.4, the radius of the plate must be larger by a factor  $\Gamma$  to accept all of the light without vignetting. If  $r_0$  is the radius of a collimated beam at the plate, then  $\Gamma = 1 + W\theta/r_0$ , and all of the results in Table 7.1 apply to the enlarged plate if  $r_0$  is replaced by  $\Gamma r_0$ .

The chromatic effects are again minimized by choosing  $a = 1.5$ , hence the neutral zone is at  $r = 0.866(\Gamma r_0)$ . The deviations at the inflection zone and edge are now larger by the factor  $\Gamma^3$ , as is the blur diameter in Eq. (7.2.6). It is clear from this result that the placement of the stop or pupil at the corrector is the preferred choice to minimize chromatic effects. As a final item note that the relations for  $R_c$  in Eq. (7.2.4) apply to a plate of radius  $\Gamma r_0$  with the substitution of  $\Gamma r_0$  for  $r_0$ .

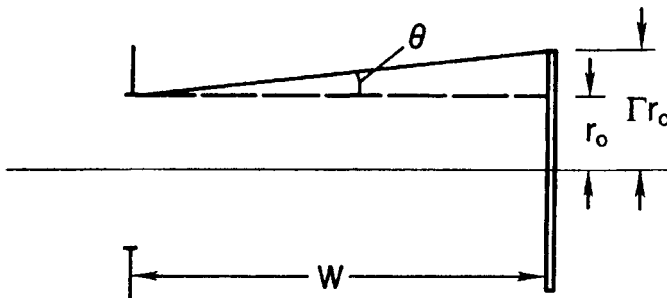


Fig. 7.4. Corrector size required to cover field when stop is displaced from plate.

## 7.2.b. ABERRATION COEFFICIENTS

We now determine the effect of the plate thickness and radius  $R_c$  on the aberration coefficients of a real plate in collimated light. Consider a plate of index  $n$  and thickness  $t$ , as shown in Fig. 7.5. Its first surface is plane and its second surface has a radius of curvature  $R_c$  and an aspheric term  $b$ , with the pupil for the plate located a distance  $W_1$  to the left of the first surface. The image of the pupil by the first surface is  $W_1'$  from this surface and  $W_2$  from the second surface. Because collimated light is incident on the plate, the beam heights at the two surfaces are equal.

The aberration coefficients for the first surface are zero when the light is collimated. The coefficients for the second surface from Table 5.5 are

$$\begin{aligned}
 B_{12} &= -\frac{\psi_2^2}{2} \Gamma_2 \left(1 - \frac{W_2}{R_c}\right)^2 - \frac{b}{2} (W_2 \psi_2)^2, \\
 B_{22} &= -\frac{\psi_2 \Gamma_2}{2 R_c} \left(1 - \frac{W_2}{R_c}\right) + \frac{b}{2} (W_2 \psi_2), \\
 B_{32} &= -\frac{\Gamma_2}{8 R_c^2} - \frac{b}{8}, \quad \Gamma_2 = -\frac{n^2(n-1)}{R_c},
 \end{aligned} \tag{7.2.7}$$

where

$$\psi_2 = \frac{\psi_1}{n} = \frac{\theta}{n}, \quad W_2 = W_1' - t = nW_1 - t. \tag{7.2.8}$$

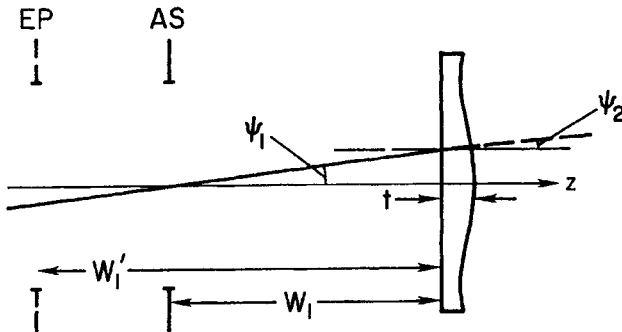


Fig. 7.5. Cross section of aspheric plate with stop AS and pupil EP. See Eq. (7.2.8).

Substituting Eq. (7.2.8) into Eqs. (7.2.7), and assuming that  $W_2 \ll R_c$  for all configurations using an aspheric plate, we find the following aberration coefficients for the corrector:

$$\begin{aligned} B_{1c} &= \frac{\theta^2(n-1)}{2R_c} - \frac{b\theta^2}{2} \left( W_1 - \frac{t}{n} \right)^2, \\ B_{2c} &= \frac{\theta n(n-1)}{2R_c^2} + \frac{b\theta}{2} \left( W_1 - \frac{t}{n} \right), \\ B_{3c} &= -\frac{b}{8} + \frac{n^2(n-1)}{8R_c^3}. \end{aligned} \quad (7.2.9)$$

Substituting Eq. (7.2.4) for one  $R_c$  in  $B_{3c}$  of Eqs. (7.2.9), we find that the right-hand term is of order  $(r_0/R_c)^2$  smaller than the first term. For any practical plate  $r_0 \ll R_c$  and the right-hand term in  $B_{3c}$  is negligible.

For the remaining coefficients in Eq. (7.2.9) we see that the contribution of the aspheric term in each is zero when  $W_1 = t/n$ . The remaining terms are simply those for a plano-convex lens in collimated light. If Eq. (7.2.4) is substituted into  $B_{1c}$  and  $B_{2c}$ , and  $W_1 - t/n$  is replaced by  $\varepsilon$ , the coefficient  $B_{1c}$  is dominated by the term in  $R_c$  when  $\varepsilon$  is small. For  $B_{2c}$ , on the other hand, the term in  $\varepsilon$  dominates when  $|\varepsilon| > r_0^2/R_c$ , hence the coma coefficient is sensitive to small changes in  $\varepsilon$ . This result can be used to minimize the effect of coma in a Schmidt system by adjusting the plate location.

Relations of a comparable form to those in Eq. (7.2.9) are obtained for an aspheric plate with its figured surface facing the incident light, with the principal change one of substituting  $W_1$  for  $W_1 - t/n$ . The comments in the previous paragraph on the dependence of  $B_{1c}$  and  $B_{2c}$  on small values of  $W_1$  hold without change.

If the incident light is coming from a source at a finite distance, then there is an additional contribution to each of the aberration coefficients from the plate thickness. These effects are easily derived with the aid of the geometry in Fig. 7.6 for a plane-parallel plate, with the coefficients for each surface taken from Table 5.1 with  $b = 0$  and  $R = \infty$ . When these relations are substituted into Eq. (5.6.7), an exercise left to the reader, we find for a plate  $p$

$$B_{1p} = \frac{\theta_1^2(n^2-1)t}{2n^3s_1^2}, \quad (7.2.10)$$

$$B_{2p} = -\frac{\theta_1(n^2-1)t}{2n^3s_1^3}, \quad (7.2.11)$$

$$B_{3p} = \frac{(n^2-1)t}{8n^3s_1^4}. \quad (7.2.12)$$

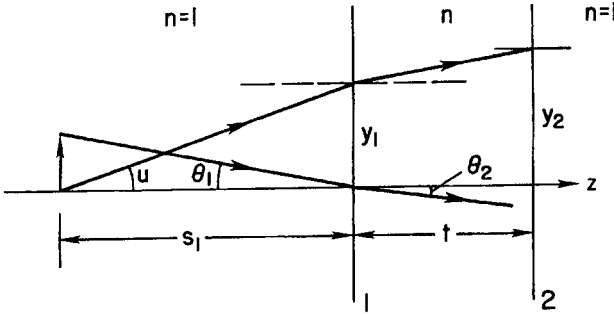


Fig. 7.6. Cross section of plane-parallel plate of index  $n$  in air.

The importance of these coefficients for an aspheric plate in noncollimated light depends on the specifics of a given configuration. In most configurations it turns out that their contributions are of little significance, with the details best left to computer ray-trace analysis.

Although the term in  $R_c$  in  $B_{3c}$  of Eq. (7.2.9) is negligible, the value of  $R_c$  does affect the optimum choice of  $b$  required to zero the third-order spherical aberration of the system. With the addition of a radius term the corrector becomes, in effect, a weak positive lens with an aspheric figure. The effect of the lens part of the corrector is to convert the incident collimated light into a slightly converging beam. Thus the marginal rays intersect the mirror at a slightly smaller distance from the mirror vertex, as compared to the case where the corrector has no radius term. Omitting the details of the derivation, the spherical aberration coefficient for a Schmidt system in collimated light is given by

$$B_{3s} = -\frac{b}{8} + \frac{n_o}{4R^3} \left[ 1 - \frac{3}{2} \left( \frac{r_0}{R} \right)^2 \right], \quad (7.2.13)$$

for the case where  $R_c$  is chosen according to Eq. (7.2.4). Setting  $B_{3s}$  equal to zero gives

$$b = \frac{2n_o}{R^3} \left[ 1 - \frac{3}{2} \left( \frac{r_0}{R} \right)^2 \right] = \frac{2n_o}{R^3} \left[ 1 - \frac{3}{32F^2} \right]. \quad (7.2.14)$$

For typical values of  $F$  the result is a reduction of 1 or 2% in the magnitude of  $b$  needed to cancel the spherical aberration of the mirror.

With the exception of the correction given by Eq. (7.2.14), the effects of the plate thickness and radius of curvature on the aberration coefficients of an aspheric plate are usually small compared to those of terms containing  $b$ . Therefore the usual approach to the analysis of a system that includes one or more aspheric plates is to include only terms in  $b$  and let this description serve as the starting point for a ray-trace analysis.

Table 7.2

Fifth-Order Spherical Aberration Results<sup>a</sup>

Surface	$B_5$	ASA5
Aspheric	$-\frac{b'}{16}$	$-\frac{3b'}{8}r^5$
Spherical mirror	$\frac{3n_o}{8R^3}$	$\frac{9n_o}{4}\left(\frac{r}{R}\right)^5$

<sup>a</sup>Results valid for collimated light only.ASA5 =  $6B_5r^5$ .

### 7.2.c. FIFTH-ORDER SPHERICAL ABERRATION

The prescription of a Schmidt corrector plate usually includes higher-order aberration terms. Fifth-order spherical aberration is the most significant of these terms and we give here, without derivation, the necessary relations for a spherical mirror and aspheric corrector in collimated light.

The fifth-order spherical aberration coefficients, denoted by  $B_5$ , are obtained after a lengthy analysis paralleling that in Chapter 5, but with  $\theta$  set equal to zero. The results of this analysis are given in Table 7.2, with the entry for ASA5 of the mirror derived from Eq. (4.2.1).

The calculation of the system aberration coefficient  $B_{5s}$  for the combined aspheric and spherical mirror is carried out using Eq. (5.6.7) with  $j = 5$ . Because the ray heights at the corrector and mirror are equal in a first approximation,  $B_{5s}$  is simply the sum of the coefficients in Table 7.2. Setting the sum equal to zero gives  $b' = 6n_o/R$ ; with this choice of  $b'$  the fifth-order spherical aberration of the system is zero.

### 7.3. SCHMIDT TELESCOPE EXAMPLE

We now apply the preceding results to an example of a 1-m Schmidt telescope with  $F = 2.5$ . The aspheric surface on the corrector plate faces the mirror; the plate material is  $\text{SiO}_2$  and its thickness is 10 mm at the vertex. The parameters  $R_c$ ,  $E$ , and  $F$  in Eq. (7.2.1) are calculated at  $\lambda = 548$  nm, at which wavelength the plate index is 1.460. Values of the telescope parameters are given in Table 7.3, with  $b$  given both for  $R_c = \infty$  and according to Eq. (7.2.14). The depth of the corrector at the neutral zone, calculated from Eq. (7.2.1), is 0.1534 mm.

Results from a ray-trace analysis are given in Table 7.4, with all aberrations given in angular terms in units of arc-seconds. Various combinations of

Table 7.3

Parameters of 1-m Schmidt Telescope<sup>a</sup>

$R = -5000$ mm	$r_0 = 500$ mm
$b = 2/R^3 = -1.60\text{E-}11$	$E = 4.34785\text{E-}12$
$b' = 6/R^5 = -1.92\text{E-}18$	$F = 2.6087\text{E-}19$
$R_c = -1/3Er_0^2 = -306\ 667$	
From Eq. (7.2.14)	
$b = -1.576\text{E-}11$	$E = 4.2826\text{E-}12$

<sup>a</sup> Values of  $E$  and  $F$  are computed using  $n = 1.46$ .

parameters from Table 7.3 are used to illustrate the effect of each of the parameters on the angular aberrations. Note that the on-axis angular aberrations of the mirror without corrector, given in arc-seconds, are  $ASA_3 = 206.3$ , and  $ASA_5 = 4.64$ , while the off-axis aberrations are zero in the third-order approximation.

Examination of the results in Table 7.4 clearly shows the improvement in the on-axis image quality when a fifth-order term is included in the aspheric and the third-order aspheric term is calculated from Eq. (7.2.14). We also see that there are small but nonzero off-axis aberrations that appear when the radius term is included on the corrector. These aberrations are a result of the terms in  $R_c$  in Eq. (7.2.9). The presence of these off-axis aberrations limits the field size, and ray traces of the final system in Table 7.4 gives an image blur diameter of about 1 arc-sec at a field angle of  $3.5^\circ$ .

Values for the angular chromatic spherical aberration, computed from Eq. (7.2.6), are shown in Table 7.5, where the indices are those of  $\text{SiO}_2$ . Because the index of refraction rises more steeply at shorter wavelengths, the chromatic blur increases rapidly for blue and ultraviolet wavelengths.

Table 7.4

Ray-Trace Results for 1-m Schmidt Telescope<sup>a,b</sup>

$-b$	$-b'$	System Parameters				
		$-R_c$	ASA3	ASA5	ATC	AAS
1.60E-11	0	$\infty$	<0.01	4.76	0.000	0.000
1.60E-11	0	306667 <sup>c</sup>	3.09	4.69	0.010	0.048
1.60E-11	1.92E-18	306667	3.09	0.02	0.010	0.048
1.576E-11	1.92E-18	306667 <sup>d</sup>	0.01	0.02	0.010	0.048

<sup>a</sup> Telescope scale = 82.5 arc-sec/mm or 12.1  $\mu\text{m}/\text{arc-sec}$ .<sup>b</sup> Ray traces at  $\lambda = 548$  nm with  $\theta = 1^\circ$ . Angular aberrations are given in arc-seconds.<sup>c</sup> Shift of 9.38 mm from paraxial focus; see  $\Delta f$  in Eq. (4.5.8).<sup>d</sup> Shift of 9.41 mm from paraxial focus.

Table 7.5

Image Diameters for 1-m Schmidt Telescope<sup>a</sup>

$\lambda$ (nm)	$n$	ACSA <sup>b</sup>
350	1.47689	3.78
400	1.47012	2.26
450	1.46577	1.24
548	1.46000	0.00
650	1.45650	0.79
700	1.45523	1.08

<sup>a</sup> Image diameters are given in arc-sec.<sup>b</sup> ACSA = angular chromatic spherical aberration.

From the results in Table 7.5 it is evident that a single corrector does not give good images at all wavelengths over an extended spectral range. One alternative is to have several correctors, each designed to give good images over a selected range of wavelengths. Although this option is practical for a small telescope or camera, it is not considered practical for a Schmidt telescope of the 1-m class.

A different alternative, suggested by Bowen (1960), is to design the corrector for a wavelength near the short end of the desired range and to use a flat glass plate of appropriate thickness to partially correct the chromatic aberration of the corrector at longer wavelengths. This plate, usually a filter to remove shorter wavelengths, is placed in the converging beam close to the focal surface. For details on this approach the reader should consult the reference by Bowen. A final alternative is to use an achromatic corrector made of two different glasses, the subject of the next section.

The Schmidt telescope example in this section is intended primarily to illustrate the application of the theory to the design of a wide-field telescope. The focal surface is curved and further refinement of the design might include the addition of a field-flattener lens, as discussed in Section 5.7. Such a lens will introduce spherical aberration over the entire field and coma near the edge of the field, hence the parameters of the corrector will have to be adjusted to get an optimum system. The process of optimization is best carried out with a computer ray-trace program and will not be pursued here. For a theoretical discussion of the aberrations of a field-flattened Schmidt camera the reader should consult the reference by Linfoot (1955).

A final point worth noting is the increasing importance of higher-order aberrations for smaller focal ratios. The importance of fifth-order spherical aberration is evident in our example, but in faster cameras it is necessary to consider the effects of still higher orders. In addition, fifth-order off-axis aberrations become important and attention must be given to their effects in the design of a fast camera.

## 7.4. ACHROMATIC SCHMIDT TELESCOPE

The wavelength range over which a Schmidt telescope with a single element corrector gives images of acceptable size is set by the dispersive characteristics of the corrector. This range can be extended by replacing the single-element plate with a two-element corrector, with each element a glass of different dispersive characteristics and plate parameters to make the combination achromatic. In this section we outline the procedure for making an achromatic corrector and apply the results to an example of a 1-m Schmidt telescope.

A cross section of a two-element corrector is shown in Fig. 7.7, with the plane surfaces of the elements in contact and the aspheric surfaces facing outward. The differential deviation for each element is given by Eq. (7.2.5), which can be written as

$$d\delta_1 = \delta_1/V_1, \quad d\delta_2 = \delta_2/V_2, \quad (7.4.1)$$

where

$$V_1 = \frac{\langle n_1 \rangle - 1}{n'_1 - n_1}, \quad V_2 = \frac{\langle n_2 \rangle - 1}{n'_2 - n_2}. \quad (7.4.2)$$

In Eq. (7.4.2)  $V$  is the *Abbe number* and  $\langle n \rangle$  is the mean of the indices in the denominator for each glass. The primed indices are taken at a shorter wavelength, by convention, hence  $V$  is positive.

The achromatic condition requires that  $d\delta_1 = -d\delta_2$ , hence a change in deviation with wavelength in one glass is compensated by a change of opposite sign in the other glass. Therefore

$$\delta_1/V_1 = -\delta_2/V_2. \quad (7.4.3)$$

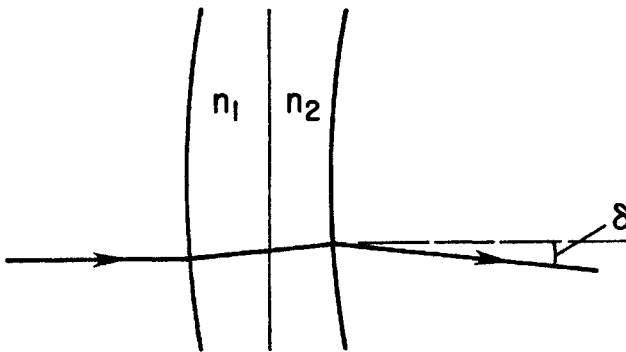


Fig. 7.7. Cross section of portion of achromatic corrector. The net deviation  $\delta$  is the sum of the deviations of individual elements.

Because the Abbe numbers are positive, the deviations of the two elements are opposite in sign and one plate has a “turned-up” edge, as for a normal Schmidt plate, while the other has a “turned-down” edge, as shown in Fig. 7.7.

Assuming that the deviation at the plane interface is negligible, the net deviation of the achromatic plate is

$$\delta = \delta_1 + \delta_2 = \delta_1 \left( \frac{V_1 - V_2}{V_1} \right). \quad (7.4.4)$$

Given that the achromatic plate is a replacement for a single plate, the deviation given by Eq. (7.4.4) must be the same as that in Eq. (7.2.3).

From Eqs. (7.4.3) and (7.4.4) we see that both  $\delta_1$  and  $\delta_2$  are larger than  $\delta$  in magnitude, hence each aspheric surface has a larger local slope than on the single plate at the same ray height. If the achromatic plate is oriented as shown in Fig. 7.7,  $\delta$  and  $\delta_1$  have opposite signs and from Eq. (7.4.4) we find  $V_1 < V_2$ . Thus the element with the turned-up edge is the one with the larger Abbe number, a result true for either orientation of the corrector.

It is evident from Eqs. (7.4.3) and (7.4.4) that the ratios  $\delta_1/\delta$  and  $\delta_2/\delta$  are independent of ray height  $r$  for a given set of glasses. Substituting Eq. (7.2.1) into Eq. (7.2.3) we see that each  $\delta$  has the form

$$\delta_i = -(n_i - 1)(c_i r + 4E_i r^3 + 6F_i r^5), \quad (7.4.5)$$

where  $c_i$  is the vertex curvature. If the ratio of one  $\delta$  to another is independent of  $r$ , then it follows that the ratios of corresponding plate parameters must also have a common value. Substituting Eq. (7.4.5) into Eq. (7.4.4) and applying this condition gives

$$\frac{c_1}{c} = \frac{E_1}{E} = \frac{F_1}{F} = \left( \frac{(n) - 1}{(n_1) - 1} \right) \left( \frac{V_1}{V_2 - V_1} \right), \quad (7.4.6)$$

where the unsubscripted parameters are those of the single element corrector. Note the reversed order of the factors in the difference of the Abbe numbers between Eqs. (7.4.4) and (7.4.6), a consequence of the sign difference between  $\delta$  and  $\delta_1$ . Using Eq. (7.4.3) we find

$$\frac{c_2}{c_1} = \frac{E_2}{E_1} = \frac{F_2}{F_1} = \frac{n'_1 - n_1}{n'_2 - n_2}. \quad (7.4.7)$$

All of the relations needed to specify an achromatic plate are now in hand, and their application is straightforward once a suitable pair of glasses is chosen.

We choose two glasses from the Schott catalog, UBK7 and LLF2, the former a crown glass and the latter a light flint. Both glasses have good internal transmittances in the near ultraviolet, with values of 0.85 and 0.74 at  $\lambda = 320$  nm for a 10-mm thickness of UBK7 and LLF2, respectively. The pair of chosen wavelengths at which to make the plate achromatic are 320 and

880 nm, with the indices at these wavelengths and Abbe numbers shown in Table 7.6.

Given the results in Table 7.6 and the discussion following Eq. (7.4.4), LLF2 and UBK7 are the glasses for elements 1 and 2, respectively, of the corrector shown in Fig. 7.7. The mean index  $\langle n \rangle$  in Table 7.6 is approximately the index at  $\lambda = 420$  nm for each glass. We use this wavelength to calculate the parameters of a single element  $\text{SiO}_2$  plate needed in Eq. (7.4.6).

The Schmidt telescope used in the following comparison is the same one used in the previous section, with Eqs. (7.4.6) and (7.4.7) used to calculate the parameters of the achromatic plate. The calculated parameters for both the single and achromatic plate are found in Table 7.7. The sags at the neutral zone for the LLF2 and UBK7 elements are 0.2765 and 0.4268 mm, respectively.

Ray traces of a 1-m Schmidt telescope with an achromatic plate specified by the parameters in Table 7.7 show a well-corrected system at 320 and 880 nm, with the blur diameter on-axis set primarily by residual fifth-order spherical aberration. The blur diameters for on-axis images over the range 320–1000 nm is shown by the solid curve in Fig. 7.8. Although the correction is excellent at the ends of the range shown, the image diameters in the blue and near ultraviolet are larger than desired.

The corrector as specified provides the proper correction at the chosen wavelengths, but gives too large a correction over much of the range. This is easily remedied by making the aspherics on each surface slightly weaker. The

**Table 7.6**

Indices and Abbé Numbers for UBK7 and LLF2<sup>a</sup>

	$n$ (320 nm)	$n$ (880 nm)	$n' - n$	$n - 1$	$V$
UBK7	1.54634	1.50935	0.03699	0.52784	14.27
LLF2	1.58789	1.53081	0.05708	0.55935	9.799

<sup>a</sup>Indices of refraction taken from Schott catalog.

**Table 7.7**

Parameters of Single and Achromatic Correctors

	$R_c$	$E$	$F$
$\text{SiO}_2^a$	-312067	4.2085E-12	2.5636E-19
LLF2	-170120	7.7201E-12	4.7026E-19
UBK7	-110240	1.1913E-11	7.2567E-19

<sup>a</sup>Parameters for  $\text{SiO}_2$  plate are similar to those in Table 7.3, but computed with  $n = 1.46810$ .

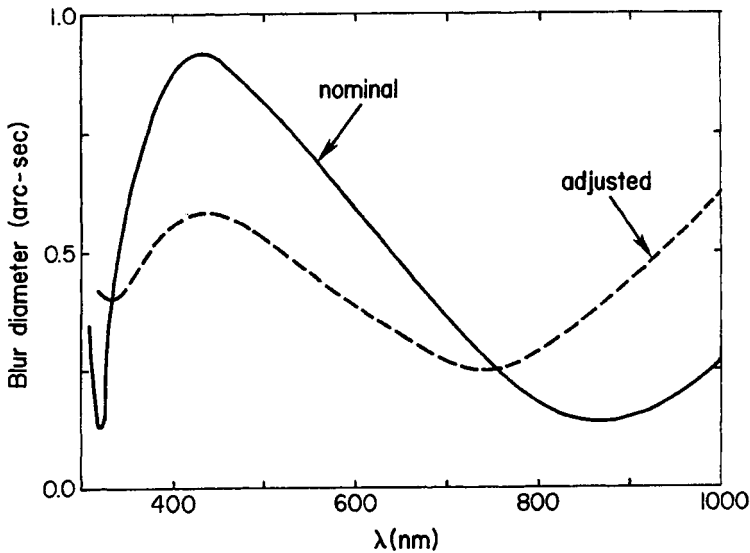


Fig. 7.8. Image diameters for  $f/2.5$  achromatic Schmidt camera. Solid curve: parameters in Table 7.7; dashed curve: parameters adjusted as noted in text, Section 7.4.

dashed curve in Fig. 7.8 shows the image diameters when the values of  $E$  and  $F$  for the elements of the achromatic plate in Table 7.7 are reduced by 0.25%, with the values of  $R_c$  increased by the same amount. The overall improvement in on-axis image quality over much of the range is evident from a comparison of the two curves.

The quality of the off-axis images is acceptable for the modified corrector, provided it is moved about 30 mm away from the mirror. This shift reduces the coma to near negligible levels and ray traces give symmetrical images of acceptable size over a field diameter of  $6^\circ$ . Spot patterns are shown in Fig. 7.9 at five wavelengths and three field angles, in addition to the images on axis.

As in the design of any Schmidt system, computer optimization is used to balance the various aberrations and find the best overall set of parameters. For a discussion of this process and the results found for an  $f/3.5$  achromatic Schmidt, the reader should consult the reference by Buchroeder (1972). Results for a Schmidt camera in an echelle spectrometer are given in the reference by Schroeder (1987).

In summary, the Schmidt telescope with an achromatic corrector has the advantage of an extended wavelength range over which good images are obtained. With the availability of several glasses that transmit well into the ultraviolet, the choice of an achromatic corrector over a standard one is a viable option.

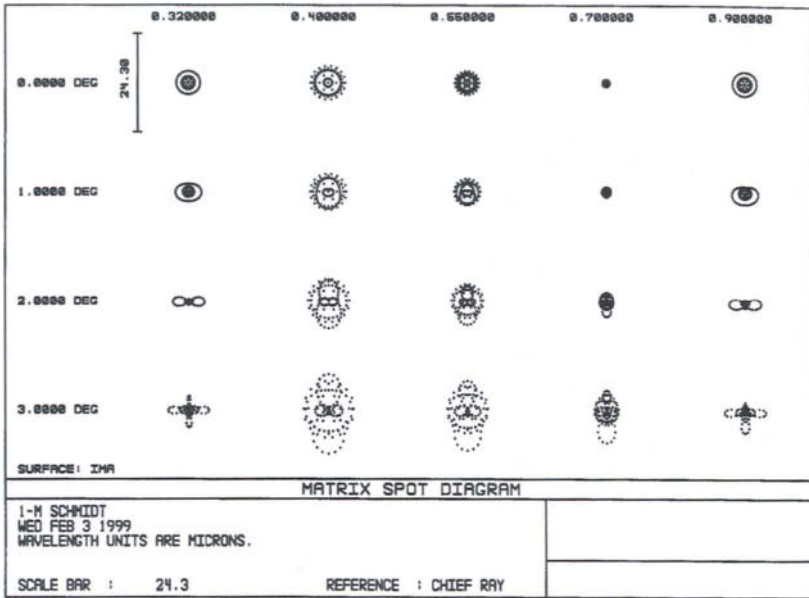


Fig. 7.9. Spot diagrams for 1-m/ $f/2.5$  achromatic Schmidt camera at selected wavelengths and field angles. Scale bar at the upper left is 2 arc-sec long. See Section 7.4 for the parameter values.

## 7.5. SOLID- AND SEMISOLID-SCHMIDT CAMERAS

A common use of the standard Schmidt camera is as the camera in a spectrograph. In this application different wavelengths are in focus at different places on the focal surface, and it is no longer necessary that the camera be strictly achromatic. It is therefore possible to modify the standard air-Schmidt to achieve improvements that are otherwise not possible.

One such modified Schmidt is the so-called solid-Schmidt, one in which the space between the corrector and mirror is filled with glass, as shown in Fig. 7.10. In this design the aspheric surface is on one end of the glass block and the mirror is on the other end. If the length of the block is equal to the radius of curvature of the mirror, then third-order off-axis aberrations are zero, just as for an air-Schmidt. The condition for zero spherical aberration and minimum chromatic aberration is given by Eq. (7.2.14), where  $n_0 = n$ , the index of the glass block. Compared to an air-Schmidt, the aspheric figure is  $n$  times stronger and the radius  $R_c$  is  $n$  times smaller.

From Fig. 7.10 we see that a chief ray entering the block at angle  $\theta$  makes angle  $\theta/n$  with the  $z$ -axis inside the block. Because this ray is reflected back on itself,

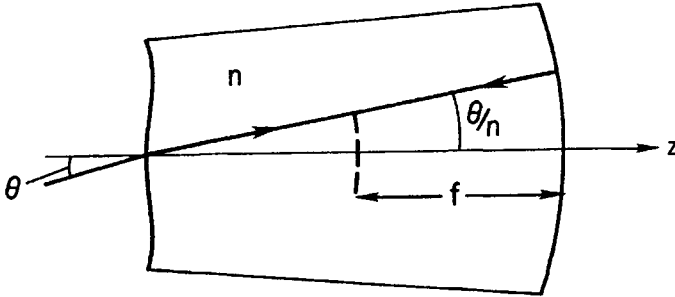


**Fig. 7.10.** Solid-Schmidt camera of index  $n$  and effective focal length  $f/n$ . The aspheric figure and mirror are on opposite ends of the block.

the height  $h$  of the corresponding image is  $f\theta/n$  from the  $z$ -axis. Thus the effective focal length  $f'$  of the solid-Schmidt is  $f/n$ , where  $f$  is the focal length of the equivalent air-Schmidt.

The reduction in focal length by a factor of  $n$  is significant for several reasons. First, the focal ratio is reduced by this factor and thus the “speed” of the camera is effectively larger by a factor of  $n^2$ . The term “speed” for a spectrograph is defined in Chapter 12; at this point it is sufficient to note that exposure time to a given level is inversely proportional to the speed. Second, the off-axis aberrations present in an optimized air-Schmidt camera are smaller by a factor of  $n^2$  in a solid-Schmidt. As a consequence, a solid camera will have comparable image quality at a field angle that is  $n$  times larger than that of an air-Schmidt of the same size. Alternatively, a solid-Schmidt will cover the same field as that of an air-Schmidt, where the former is  $n$  times shorter.

Given height  $h = f\theta/n$ , we find the variation of  $h$  with changing index is given by

$$dh = -\theta f \, dn/n^2. \quad (7.5.1)$$

If, for example, we take the values of  $n$  for  $\text{SiO}_2$  from Table 7.5 at 400 and 700 nm, and assume  $f = 500$  mm, then  $dh = 61 \mu\text{m}$  for a field angle of  $1^\circ$ . A lateral shift of this amount is not acceptable in direct imagery because a point source would be imaged as a short spectrum, with its length proportional to the field angle. In a spectrograph camera, on the other hand, each image of the slit is quasi-monochromatic and the lateral shift is simply an offset without additional blurring.

The effect of index  $n$  on the aberrations is most easily seen from an example. Ignore for the moment the aspheric term on the surface of the solid-Schmidt and

consider only the radius term. Because the stop is at the surface, the astigmatism coefficient is that given in Table 5.1. For  $s = \infty$  we find

$$A_1 = -\frac{\theta^2}{2} \left( \frac{n-1}{n^2 R_c} \right). \quad (7.5.2)$$

The corrector for the air-Schmidt, in the absence of the aspheric term, is a plano-convex lens of thickness  $d$ . The astigmatism coefficient of the lens is the sum of the surface coefficients.

With the convex surface facing the incident light, and the stop at this surface, we find that the astigmatism coefficient of the lens for  $d \ll R_c$  is given by

$$B_1 = -\frac{\theta^2}{2} \left( \frac{n-1}{R_c} \right). \quad (7.5.3)$$

In comparing Eqs. (7.5.2) and (7.5.3) it is important to note that Eq. (7.5.2) applies to the solid-Schmidt and  $R_c$  is  $n$  times smaller than in Eq. (7.5.3). Therefore  $A_1$  for the solid-Schmidt is  $n$  times smaller than  $B_1$  for the air-Schmidt. Substituting each of these coefficients into Eq. (5.6.6) we see that the transverse aberration for the solid-Schmidt is smaller by another factor of  $n$ . Hence the net reduction in the astigmatism due to the radius term on the corrector is smaller by a factor of  $n^2$ , as already stated here. The same factor is found in a comparison of the coma coefficients.

The fabrication of the solid-Schmidt is obviously difficult because the curved focal surface lies in the center of the block. To avoid the complication of preparing this surface in a hole in the block, an alternative is the so-called semisolid- or thick-mirror Schmidt. This camera is one in which glass fills the space between the focal surface and the mirror, with a conventional aspheric plate in front of the block, as shown in Fig. 7.11. Except for the curved focal surface, the face of the block toward the corrector is plane.

From Fig. 7.11 we see that the location of the corrector is such that the chief ray, after refraction at the surface of the block, appears to come from the center of

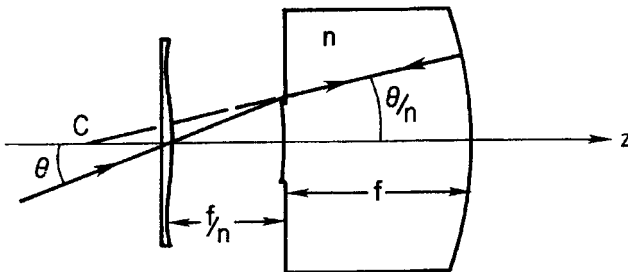


Fig. 7.11. Semisolid-Schmidt camera with center of curvature at  $C$ . Focal length  $= f/n$ .

curvature of the mirror. Because the refracted chief ray makes angle  $\theta/n$  with the  $z$ -axis, the distance from the axis to the image point is the same as that of the solid-Schmidt. Hence the focal length of the thick-mirror Schmidt is the same as that of the solid-Schmidt and all of the preceding comments also apply. The aspheric figure and radius  $R_c$  are also the same as those for the solid-Schmidt.

Ray traces of a solid-Schmidt and thick-mirror Schmidt, with a  $b'$  aspheric term added to control fifth-order spherical aberration, show very similar image characteristics. For  $F = 2.5$ , the focal ratio of the equivalent air-Schmidt, the image blur diameters are 1 arc-sec at a field angle of  $5^\circ$ . Compared with the  $f/2.5$  design example in Section 7.3, the field is about  $n$  times larger, as expected.

## REFERENCES

- Bowen, I. (1960). *Stars and Stellar Systems I, Telescopes*, Chap. 4, Chicago: University of Chicago Press.
- Buchroeder, R. (1972). *Appl. Opt.*, **11**: 2968.
- Linfoot, E. (1955). *Recent Advances in Optics*, Chap. 4, London and New York: Oxford University Press.
- Schroeder, D. (1987). in *Instrumentation for Ground-Based Astronomy*, Robinson, L. (ed.), p. 39, New York: Springer-Verlag.

## BIBLIOGRAPHY

- Bouwers, A. (1946). *Achievements in Optics*, Chap. 1, Amsterdam: Elsevier.
- Mahajan V. (1998). *Operating Imaging and Aberrations, Part I, Ray Geometrical Optics*, Chap. 6, Bellingham, WA: SPIE Optical Engineering Press.
- Wilson, R. (1996). *Reflecting Telescope Optics I*, Berlin: Springer.

In this chapter we discuss various derivatives of the Schmidt type of telescope, including Schmidt-Cassegrain, Baker-Schmidt, and Bouwers-Maksutov systems. Each of these is a type of *catadioptric* telescope in which a full-aperture refracting element provides the aberration correction needed to get good imagery over a wide field. Given this definition, the classical Schmidt telescope is also of this type.

The Schmidt-Cassegrain, as the name suggests, is a two-mirror system with an aspheric corrector in the collimated beam ahead of the primary mirror. Baker-Schmidt systems are a subclass of the Schmidt-Cassegrain with a flat focal surface, of which examples of two specific types are given. The Bouwers-Maksutov type is one in which the aspheric corrector is replaced by a meniscus lens with spherical surfaces. This type of corrector, in combination with one or two mirrors, is the basis for a wide variety of wide-field systems. The design parameters are given for selected examples of systems using a meniscus corrector.

### **8.1. SCHMIDT-CASSEGRAIN TELESCOPES**

The Schmidt-Cassegrain telescope, hereafter designated SC, is a two-mirror telescope with a corrector plate in the collimated beam, as shown in Fig. 8.1. Compared to an all-reflective Cassegrain, the principal differences are the addition of an aspheric plate to compensate for the spherical aberration of the

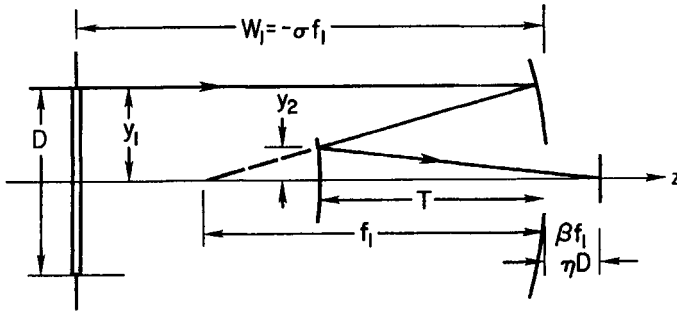


Fig. 8.1. Schematic of Schmidt-Cassegrain telescope with stop at corrector plate. Distance from stop to primary =  $\sigma f_1$ .

mirrors and the shift of the aperture stop from the primary to the corrector. With these changes there are additional free parameters available for the elimination of other aberrations, and a host of wide-field SC systems are possible.

In this section we outline the procedure by which the aberration characteristics of a general SC are found. Rather than exploring the features of the general SC, however, we choose to apply these results to a selected number of SC types to illustrate their basic features. The types considered include the flat-field anastigmat, the SC with spherical mirrors, and the “short” SC with the corrector approximately a distance  $f_1$  from the primary. For further details on these and other types of SC systems, the reader should consult the work by Linfoot (1955). A thorough discussion of a variety of Schmidt-Cassegrain systems is also given by Wilson (1996).

### 8.1.a. GENERAL PARAMETERS

The notation used in writing the aberration coefficients for each surface is the same as that used for two-mirror telescopes. The subscripts 1 and 2 refer to the primary and secondary mirrors, respectively, while the subscript  $c$  is used for the corrector. For a concave primary, the only type considered, the focal length  $f_1$  is positive.

The relative locations of the mirrors and focal surface of the SC are described in terms of the normalized parameters in Table 6.3 used for two-mirror telescopes. An additional normalized parameter introduced for the SC is  $\sigma$ , the location of the aspheric plate relative to the primary in units of the primary focal length. According to our sign convention, the distance  $W_1$  from the primary to the stop is negative and we therefore choose to define  $\sigma = -W_1/f_1$  to make  $\sigma$  positive.

Table 8.1

Aberration Coefficients for SC Primary

$$B_{11} = \frac{\theta^2}{R_1} \left[ \frac{\sigma^2}{4} K_1 + \left( 1 - \frac{\sigma}{2} \right)^2 \right]$$

$$B_{21} = \frac{\theta}{R_1^2} \left[ 1 - \frac{\sigma}{2} (K_1 + 1) \right]$$

$$B_{31} = \frac{K_1 + 1}{4R_1^3}$$

With the stop at the corrector, hence  $W_c = 0$ , the only nonzero aberration coefficient for the corrector is  $B_{3c} = -b/8$ . In writing this result we ignore the radius term added to minimize chromatic aberration.

For the primary mirror, the stop is at a distance  $W_1 = -\sigma f_1$ , the chief ray angle  $\psi_1$  is the field angle  $\theta$ , and the magnification  $m$  is zero. Substituting these results into the equations in Table 5.6 gives the coefficients for the primary, in the form shown in Table 8.1. Note that  $n = 1$  for the primary.

To find the aberration coefficients for the secondary, we first determine the location of the pupil for the secondary using the paraxial relations. As shown in Fig. 8.2, the primary images the stop at a distance  $W'_1 = f_1 \sigma / (1 - \sigma)$ , where  $W'_1$  is negative when  $\sigma > 1$ . The location of the pupil relative to the secondary is  $W_2 = W'_1 + T$ , where  $T = (1 - k)f_1$  is the separation between the primary and secondary.

To find the chief ray angle  $\psi_2$  for the secondary, we see from Fig. 8.2 that the chief ray is directed toward the center of pupil after reflection from the primary.

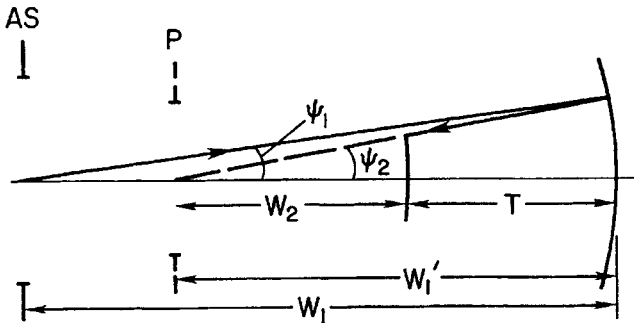


Fig. 8.2. Geometry of aperture stop AS, pupil P, and chief ray angles for Cassegrain telescope. See Eq. (8.1.1) and preceding discussion.

Table 8.2

Aberration Coefficients for SC Secondary

$$\begin{aligned}
 B_{12} &= -\frac{\theta^2(\sigma-1)^2}{\rho R_1} \left[ \left( \frac{W_2}{\rho R_1} \right)^2 K_2 + \left( 1 - \frac{W_2}{\rho R_1} \right)^2 \right] \\
 B_{22} &= \frac{\theta(\sigma-1)}{(\rho R_1)^2} \left[ \left( \frac{W_2}{\rho R_1} \right) K_2 + \left( \frac{m+1}{m-1} \right) \left( 1 - \frac{W_2}{\rho R_1} \right) \right] \\
 B_{32} &= -\frac{1}{4(\rho R_1)^3} \left[ K_2 + \left( \frac{m+1}{m-1} \right)^2 \right] \\
 \frac{W_2}{\rho R_1} &= \frac{1+k(\sigma-1)}{2\rho(\sigma-1)}
 \end{aligned}$$

Therefore  $W_1\psi_1 = W'_1\psi_2$ , where  $\psi_2$  is the chief ray angle for the secondary. Substituting for  $\psi_1$  and  $W'_1$  gives

$$\psi_2 = \theta(\sigma-1), \quad \frac{W_2}{f_1} = -\frac{1+k(\sigma-1)}{\sigma-1} = -\frac{2W_2}{R_1}. \quad (8.1.1)$$

The resulting aberration coefficients for the secondary, taken from Table 5.5, are shown in Table 8.2. Note that  $n = -1$  for the secondary and that  $R_2$  has been replaced by  $\rho R_1$  in writing these relations.

The system aberration coefficients are found by applying Eq. (5.6.11) to corresponding sets of surface coefficients. After substitution of Eqs. (8.1.1) into the coefficients in Table 8.2, and following some straightforward algebra, we get the system coefficients for a general SC given in Table 8.3. Also given in Table 8.3 is the curvature of the median astigmatic surface. The derivation of this curvature relation follows from the discussion preceding Eq. (6.2.2).

Before proceeding to apply these aberration results to selected examples, we develop some additional useful relations between the normalized parameters. From Section 2.5 we find  $\eta = \beta F_1 = \beta F/m$ , where  $\eta$  is the back focal distance in units of the telescope diameter  $D$ . Using the relations in Table 6.3 we write  $k$  in terms of  $\rho$ ,  $\eta$ , and  $F$ , with the result

$$k^2 F - kF(2\rho + 1) + \rho(F + \eta) = 0$$

Solving this relation for  $k$  we get

$$k = \rho + \frac{1}{2} - \left( \rho^2 + \frac{1}{4} - \frac{\rho\eta}{F} \right)^{1/2}, \quad (8.1.2)$$

where the minus sign in front of the radical is chosen to ensure that  $k < 1$ . From Eq. (8.1.2) we see that a specification of  $\rho$ ,  $\eta$ , and  $F$  sets the value of  $k$ , which in turn fixes the values of  $m$  and  $F_1$ . Note that  $k$  is independent of  $F$  when  $\eta = 0$ .

Table 8.3

Aberration Coefficients for General SC

$$\begin{aligned}
 B_{1s} &= \frac{\theta^2}{4R_1} (\Omega_2 \sigma^2 - 2\Omega_1 \sigma + \Omega_0) \\
 B_{2s} &= \frac{\theta}{2R_1^2} (\Omega_1 - \Omega_2 \sigma) \\
 B_{3s} &= \frac{\Omega_2}{4R_1^3} - \frac{b}{8} \\
 \Omega_0 &= 4 - \frac{k^2}{\rho^3} [(2\rho + 1 - k)^2 + (1 - k)^2 K_2] \\
 \Omega_1 &= 2 - \frac{k^2}{\rho^3} [(2\rho - k)(2\rho + 1 - k) - k(1 - k)K_2] \\
 \Omega_2 &= 1 + K_1 - \frac{k^2}{\rho^3} [(2\rho - k)^2 - k^2 K_2] \\
 \kappa_m &= \frac{2}{R_1} \left( \frac{1 - \rho}{\rho} \right) + \frac{1}{R_1} (\Omega_2 \sigma^2 - 2\Omega_1 \sigma + \Omega_0)
 \end{aligned}$$

It is also important to determine the sizes of the primary and secondary required to cover a given field without vignetting. If  $D$  is the diameter of the aperture stop, then from the geometry in Fig. 8.3 we find that  $D_1$ , the diameter of the primary, is given by

$$D_1 = D(1 + 2\theta\sigma F_1), \quad (8.1.3)$$

where  $\theta$  is the angular radius of the field.

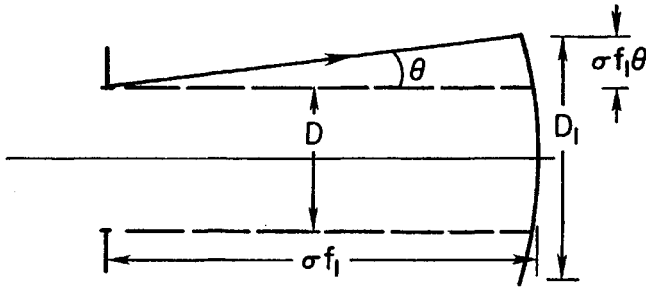


Fig. 8.3. Geometry showing primary mirror diameter needed to cover field of angular radius  $\theta$  without vignetting. See Eq. (8.1.3).

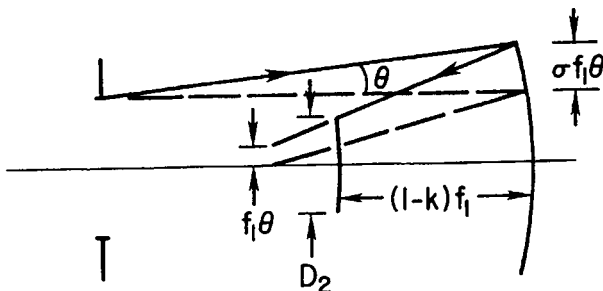


Fig. 8.4. Geometry of secondary mirror diameter needed to cover field of radius  $\theta$  without vignetting at outer edge. See Eq. (8.1.4).

To determine the size of the secondary, we use the geometry in Fig. 8.4. The diameter  $D_2$ , expressed in terms of the diameter of the corrector, is given by

$$D_2 = D[k + 2\theta F_1(k(\sigma - 1) + 1)]. \quad (8.1.4)$$

Note that Eqs. (8.1.3) and (8.1.4) with  $\sigma = 0$  apply to the two-mirror telescopes discussed in Chapter 6. Note also that  $D_1$  and  $D_2$  can be expressed in terms of  $\eta$  and  $F$  with the substitution  $F_1 = F(\rho - k)/\rho$ . We now apply the results in this section to some specific types of SC telescopes.

### 8.1.b. FLAT-FIELD ANASTIGMATIC SCHMIDT-CASSEGRAIN

An anastigmatic optical system, as noted in Section 5.8.c, is one with zero astigmatism, coma, and spherical aberration. The condition for a flat field for an anastigmat is zero Petzval curvature; the surface of best images is a plane. From Eq. (5.7.17) it follows that Petzval curvature is zero when  $\rho = 1$ . Setting  $\rho = 1$  also fixes  $m$  in terms of  $k$ . From Table 6.3 we get  $m = 1/(1 - k)$ .

Applying the anastigmatic condition to the aberration coefficients in Table 8.3 gives

$$\Omega_1 = \sigma\Omega_2, \quad \Omega_0 = \sigma\Omega_1, \quad bR_1^3 = 2\Omega_2. \quad (8.1.5)$$

The first step in the procedure for solving the relations in Eqs. (8.1.5) to find the system parameters is to calculate  $k$  from Eq. (8.1.2) for selected  $\eta$  and  $F$ . Substituting this value of  $k$  into  $\Omega_0 = \sigma\Omega_1$  gives a relation between  $\sigma$  and  $K_2$ , and one can be found after the other is specified. With  $\sigma$  and  $K_2$  now known,  $K_1$  is computed using  $\Omega_1 = \sigma\Omega_2$ . Finally, using the known values of the conic constants,  $b$  is calculated using the last relation in Eq. (8.1.5). Carrying out the first step for  $F = 3$  and selected values of  $\eta$ , we get the results shown in Table 8.4.

Table 8.4

Parameters of  $f/3$  Flat-Field Anastigmatic Schmidt-Cassegrain

$\eta$	$k$	$m$	$F_1$
-0.10	0.3672	1.580	1.899
-0.05	0.3745	1.599	1.876
0.00	0.3820	1.618	1.854
0.05	0.3894	1.638	1.832
0.10	0.3970	1.658	1.809

Note that  $\eta < 0$  places the focal plane between the primary and secondary mirrors.

Using the values of  $k$  from Table 8.4 we now find the characteristics of two specific systems, first analyzed by Baker (1940). The first is the so-called Baker A design with  $\sigma = 1$ ; the second is the Baker B design for which  $K_2 = 0$ . Baker also gave the results for two other flat-field systems; the Baker C design has  $K_1 = 0$  and the Baker D design is free of distortion. The parameters of the C design are little different from those of the B design, while those of the D design lie between those of the Baker A and B systems. For specifics on these other versions, see the reference by Linfoot (1955).

For the Baker A design, the solution of the relations in Eqs. (8.1.5) gives

$$K_1 = 1 + 2k, \quad K_2 = -1 + \frac{2(1+k)}{k^2}, \quad (8.1.6)$$

and for the Baker B

$$K_1 = \frac{k^2(1-k)^2}{4-k^2(3-k)^2}, \quad \sigma = \frac{4-k^2(3-k)^2}{2-k^2(2-k)(3-k)}. \quad (8.1.7)$$

Table 8.5 gives the parameters of the Baker A design, including the radius of the secondary needed to cover a field 0.1 radians in diameter. Table 8.6 gives the results for the Baker B design.

From the tabulated data in Tables 8.5 and 8.6 it is evident that there is a significant difference between the two designs. The mirrors in the Baker A design are strongly elliptical, while the primary in the other system differs only slightly from a sphere. The diameter of the secondary needed to cover the given field is about 15% smaller for the A version, hence there is about 30% less vignetting in this design. This difference is a direct consequence of the difference in lengths between the two designs, about a factor of two.

The most significant difference between the two designs is in the size of  $\Omega_2$ , which is approximately 3 times larger for the A version. As seen from Eqs.

8. Catadioptric Telescopes and Cameras

Table 8.5

Parameters of  $f/3$  Baker A Design<sup>a</sup>

$\eta$	$K_1$	$K_2$	$\Omega_2$	$D_2/D$	$m^3\Omega_2$
-0.10	1.7343	19.284	2.0245	0.557	7.99
-0.05	1.7491	18.597	2.0125	0.562	8.23
0.00	1.7639	17.944	2.0000	0.567	8.47
0.05	1.7789	17.322	1.9870	0.573	8.73
0.10	1.7940	16.729	1.9735	0.578	9.00

<sup>a</sup>Field radius  $\theta = 0.05$  radians.

Table 8.6

Parameters of  $f/3$  Baker B Design<sup>a</sup>

$\eta$	$K_1$	$\sigma$	$\Omega_2$	$D_2/D$	$m^3\Omega_2$
-0.10	0.01761	2.1581	0.6582	0.638	2.60
-0.05	0.01809	2.1644	0.6475	0.644	2.65
0.00	0.01858	2.1708	0.6366	0.650	2.70
0.05	0.01906	2.1775	0.6256	0.657	2.75
0.10	0.01954	2.1843	0.6146	0.663	2.80

<sup>a</sup>Field radius  $\theta = 0.05$  radians.

(8.1.5), this means that the aspheric term  $b$  is larger by this factor, as are the chromatic effects. This is most easily seen by noting that CSA in Eq. (7.2.6) is proportional to  $b$ , the aspheric parameter. By definition, CSA is proportional to the slope of the surface at the edge of a corrector configured for minimum chromatic aberration. Putting Eq. (7.2.4) into Eq. (7.2.1), setting  $r = r_0$ , and ignoring the term in  $b'$ , we find

$$\frac{dz}{dr} = \frac{br_0^3}{8(n' - n)}. \tag{8.1.8}$$

Hence larger  $b$  means larger CSA in direct proportion, and the chromatic aberration of the Baker A design is about 3 times that of the B design.

It is also important to compare the chromatic properties of each SC system with that of a standard Schmidt of the same final focal ratio. The ratio of the chromatic aberrations is simply the ratio of the corresponding  $b$  terms, hence

$$\frac{\text{CSA(SC)}}{\text{CSA(SS)}} = \frac{2\Omega_2 R^3}{R_1^3 2} = m^3\Omega_2, \tag{8.1.9}$$

where SS denotes a standard Schmidt and  $m$  is the magnification of the Schmidt-Cassegrain. Values of the relative chromatic aberration from Eq. (8.1.9) are found in the rightmost columns in Tables 8.5 and 8.6. It is evident from these results that a single element corrector in a Schmidt-Cassegrain as fast as  $f/3$  has chromatic aberration that is significantly larger than that of a standard Schmidt, especially for the Baker A version.

Ray traces of the Baker B system, with the addition of a  $b'$  aspheric parameter to control fifth-order spherical aberration, show acceptable images to a field radius of about  $3^\circ$  at the design wavelength. An acceptable image is defined as one for which the blur diameter is no larger than  $15\ \mu\text{m}$  for an overall focal length of 2700 mm. This diameter corresponds to an angular blur of about 1 arcsec for this focal length.

Ray traces of the Baker A design give acceptable on-axis images, as defined here, only with the addition of aspheric parameters of still higher order to the corrector plate profile. This is not surprising given that the spherical aberration of the pair of highly elliptical mirrors is significantly larger than for the Baker B mirror pair, especially SA5 and SA7. The field radius for acceptable images is less than one-half that of the Baker B design. Thus the A version, in spite of its shorter length and smaller vignetting by the secondary compared to the B version, is probably not a viable option as a wide-field telescope.

An analysis of the general solution of the relations in Eqs. (8.1.5) shows that the product  $\sigma\Omega_2$  decreases slowly as  $K_2$  decreases. As can be verified from  $\Omega_1$  in Table 8.3 together with the first of Eqs. (8.1.5), a change in  $K_2$  from 10 to zero gives a decrease in  $\sigma\Omega_2$  of roughly 30%. For this same decrease in  $K_2$ , the factor  $\Omega_2$  decreases by a bit over a factor of 2 while  $\sigma$  increases by about a factor of 1.6. Hence there is a tradeoff between chromatic aberration and vignetting of the secondary, with a reasonable balance achieved when the conic constants of the mirrors are near zero.

Compared to a standard Schmidt, the Baker B design has the advantages of a flat, focal surface, and a shorter length by about 40%. If these advantages more than outweigh the disadvantages of larger chromatic aberration and vignetting by the secondary of 40% or more, then this system is a viable alternative to the Schmidt. To be competitive with a standard Schmidt over a wide spectral range would, however, require an achromatic corrector of the type described in Section 7.4.

### 8.1.c. SCHMIDT-CASSEGRAIN WITH SPHERICAL MIRRORS

An alternative to the flat-field anastigmatic SC is the family in which both mirrors are spherical and the focal surface is curved. The analysis of this type of SC proceeds in a way very similar to that in the last section. Putting  $K_1 = K_2 = 0$

in the relations in Table 8.3, the system aberration factors take the following simplified form

$$\begin{aligned}\rho^3\Omega_0 &= 4\rho^3 - k^2(2\rho + 1 - k)^2, \\ \rho^3\Omega_1 &= 2\rho^3 - k^2(2\rho - k)(2\rho + 1 - k), \\ \rho^3\Omega_2 &= \rho^3 - k^2(2\rho - k)^2.\end{aligned}\quad (8.1.10)$$

If we require that the system be anastigmatic, then the relations in Eq. (8.1.5) apply. The only solution from these relations is  $2\rho = 1 + k$ . Substituting for  $\rho$  in Eqs. (8.1.10) gives  $\Omega_0 = 2\Omega_1 = 4\Omega_2$ , hence  $\sigma = 2$  by Eqs. (8.1.5). Writing  $\rho$  in terms of  $R_1$  and  $R_2$ , we find the relation  $R_2 - R_1 = (1 - k)f_1$ . Hence the two mirrors have a common center of curvature with the vertex of the corrector at this common point. This is the so-called *concentric Schmidt-Cassegrain*. Because the mirrors are concentric, so also is the Petzval surface, the focal surface when the astigmatism is zero.

Substituting  $2\rho = 1 + k$  into Eq. (8.1.2) we find

$$k = \frac{1 + \eta/F}{3 - \eta/F}. \quad (8.1.11)$$

The magnification of the secondary is  $m = (1 + k)/(1 - k)$  and the Petzval curvature from Eq. (5.7.17) is

$$\kappa_p = \frac{2}{R_1} \left( \frac{1 - k}{1 + k} \right) = \frac{1}{R_1} \left( 1 - \frac{\eta}{F} \right). \quad (8.1.12)$$

Parameters for several concentric SCs are given in Table 8.7. Comparison with the parameters for the Baker B systems in Table 8.6 shows that the chromatic spherical aberration of the concentric SC is approximately 2 times larger. Thus the simplification of having only spherical mirrors is offset by larger chromatic aberration and a curved focal surface.

Another system with only spherical mirrors is the *aplanatic spherical Schmidt-Cassegrain*, a system in which spherical aberration and coma are zero but astigmatism is not. In this case only the first and last of the relations in Eqs. (8.1.5) hold. With astigmatism not equal to zero, we choose to set  $\kappa_m$ , the curvature of the median image surface to zero. Combining the relations for  $B_{1s}$  and  $\kappa_m$  in Table 8.3, and setting  $\kappa_m = 0$ , gives

$$B_{1s} = -\frac{\theta^2}{2R_1} \left( \frac{1 - \rho}{\rho} \right), \quad (8.1.13)$$

hence

$$\text{AAS} = 2B_{1s,y} = \frac{m\theta^2}{4F} \left( \frac{1 - \rho}{\rho} \right). \quad (8.1.14)$$

Table 8.7

Parameters of  $f/3$  Schmidt-Cassegrains with Spherical Mirrors

Concentric Design ( $\sigma = 2$ )					
$\eta$	$k$	$\rho$	$m$	$\Omega_2$	$m^3\Omega_2$
-0.10	0.3187	0.6593	1.936	0.6457	4.69
0.00	0.3333	0.6667	2.000	0.6250	5.00
0.10	0.3483	0.6742	2.069	0.6041	5.35
Aplanatic Design ( $\rho = 0.95$ )					
$\eta$	$k$	$\sigma$	$m$	$\Omega_2$	$m^3\Omega_2$
-0.10	0.3618	2.198	1.615	0.6388	2.69
0.00	0.3765	2.214	1.657	0.6163	2.80
0.10	0.3913	2.231	1.700	0.5943	2.92

It is evident from Eq. (8.1.14) that it is necessary to have  $\rho$  (near one) to keep the astigmatism small. If, for example, we choose  $\rho = 0.95$ ,  $m = 1.7$ , and  $F = 3$ , then AAS is approximately 1 arc-sec when  $\theta = 1.5^\circ$ .

Table 8.7 gives the calculated parameters for several aplanatic SCs with spherical mirrors. Note that chromatic aberration, the main discriminant between the two spherical mirror designs, is significantly smaller for the aplanat. We also see that CSA for the aplanat and the Baker B design are comparable, a result that is not surprising given mirrors that are similar.

Ray traces of the aplanat in Table 8.6, with the addition of a  $b'$  parameter to control fifth-order spherical aberration, show that astigmatism limits the field diameter to about  $3^\circ$ , as compared with roughly twice this value for the Baker B design. Thus the Baker B system, with its substantially larger field, has a clear edge over the aplanat.

#### 8.1.d. COMPACT SCHMIDT-CASSEGRAIN WITH SPHERICAL PRIMARY

We have limited our discussion of the Schmidt-Cassegrain in the preceding sections to those designs that are possible alternatives to the standard Schmidt, that is, designs with wide field and relatively fast focal ratios. If these conditions are changed to smaller field, on the order of  $1^\circ$  in diameter, and Cassegrain focal ratios  $\approx 10$ , then a family of aplanatic SC designs is found with  $\sigma \approx 1$  and tolerable astigmatism. Although various combinations of  $K_1$  and  $K_2$  are possible, the usual choice is a spherical primary. With this choice the secondary is ellipsoidal and  $m \approx 5$ . Small telescopes of this type are available from several manufacturers and are popular choices among amateur astronomers.

The characteristics of "short" aplanatic SC telescopes of this type are found by applying the general theory given in the preceding. In this section we outline the approach and give results for a typical set of parameters. We consider only the case where the primary is spherical, hence  $K_1 = 0$ .

The aplanatic condition is zero coma and spherical aberration, hence  $B_{2s}$  and  $B_{3s}$  in Table 8.3 are set to zero. From the zero coma condition we find

$$K_2[1 + k(\sigma - 1)] = -\left(\frac{m}{m-1}\right)^3 + \left(\frac{m+1}{m-1}\right)\left[1 - k(\sigma - 1)\left(\frac{m+1}{m-1}\right)\right], \quad (8.1.15)$$

where  $\rho$  has been expressed in terms of  $m$  and  $k$  using the relations in Table 6.3. Putting the zero coma condition into the first equation in Table 8.3 we find

$$B_{1s} = \frac{\theta^2}{4R_1} \left[ \left(\frac{1+k}{k}\right)(2-\sigma) - \frac{2}{k} \left(\frac{m-1}{m}\right)^2 \left[1 - k(\sigma - 1)\left(\frac{m+1}{m-1}\right)\right] \right]. \quad (8.1.16)$$

There are an infinite number of possible combinations, but we are only interested in "short" versions and choose  $\sigma = 1$ . Equations (8.1.15) and (8.1.16) are now much simpler, but analysis of this special case will illustrate the general characteristics of this type of telescope.

Substituting  $\sigma = 1$  and expressing  $k$  in terms of  $m$  and  $\beta$  from Table 6.3 gives

$$B_{1s} = \frac{\theta^2}{4R_1} \left(\frac{m+1}{1+\beta}\right) \left[1 + \left(\frac{1+\beta}{m+1}\right) - 2\left(\frac{m-1}{m}\right)^2\right], \quad (8.1.17)$$

where  $\beta$  is the normalized back focal distance. As an example let  $m = 5$  and  $\beta = 0.2$ . From Eq. (8.1.15) we get  $K_2 = -0.4531$  ( $K_2$  is independent of  $\beta$ ) and from Eq. (8.1.17) we get  $B_{1s} = -0.40(\theta^2/4R_1)$ . Inserting  $B_{1s}$  into Eq. (5.6.6) and dividing by  $s'$  to get the angular aberration gives AAS = 0.39 arc-sec for  $\theta = 0.5^\circ$  and  $F_1 = 2$ . Thus, for the chosen parameters, the astigmatism is undetectable over a  $1^\circ$  field diameter with a ground-based telescope for practically all atmospheric conditions. It is worth noting that a choice of  $m = 4.5$ , with the other parameters unchanged, gives astigmatism that is about 10 times smaller at the same field angle. An increase in the field diameter to  $2^\circ$  is possible in this case.

For configurations with negligible astigmatism the field curvature is essentially Petzval curvature only. For  $m = 4.5$  and  $\beta = 0.2$  we find  $k = 0.218$  and  $\rho = 0.281$ . Thus the Petzval curvature is  $5.12/R_1$  and the focal surface is rather strongly curved. As Wilson notes, this curvature is of little consequence for visual use but would require a field flattening lens for photography to get the best image definition over a wide field.

It is left as an exercise for the reader to determine the chromatic properties of the corrector plate for a short SC. The result for  $m = 4.5$  is  $\Omega_2 = 0.80$  and  $m^3\Omega_2 = 73$ . Although this latter value is large compared to those in Tables 8.6 or 8.7, it should be noted that for the short SC the comparison is with a standard Schmidt whose focal ratio is of order 10, not 3 as in the tables cited. If, instead, we compare an  $f/9$  SC ( $f/2$  primary mirror for  $m = 4.5$ ) with an  $f/3$  Schmidt of the same diameter, then the ratio from Eq. (8.1.9) is 2.7. Thus the chromatic aberration due to a single corrector plate is tolerable in a short SC with  $m \approx 5$ .

### 8.1.e. CONCLUDING REMARKS

The SC designs discussed in the preceding sections are either anastigmats or aplanats with the stop located at the corrector plate. Because both spherical aberration and coma are zero in all of these designs, it follows from the discussion in Section 5.5 that both coma and astigmatism are independent of the stop position. Thus all of the results given, except the chromatic aberrations, are valid for an arbitrary stop position. If the stop is displaced from the corrector, the chromatic effects increase by the factor  $\Gamma^3$ , as described in Section 7.2. Given the already large chromatic effects in the SC compared to those of the standard Schmidt, it is evident that an SC with a stop displaced from the corrector is of limited usefulness.

Of all of the designs considered in this section, only the Baker B version can be considered a contender with a standard Schmidt in the 1-m class, and then only if the corrector plate is achromatic. The Baker B design has a flat field, a factor in its favor, but larger vignetting because of its larger central obscuration, a factor against it.

The short Schmidt-Cassegrain design, so popular with amateur astronomers, is really a competitor with two-mirror Cassegrain telescopes of the type discussed in Chapter 6 and not with Schmidt telescopes. With an accessible focal surface (a requirement for visual and photographic use) and excellent image quality (an aplanat with negligible astigmatism if properly designed), the compact Schmidt-Cassegrain is often the telescope of choice in apertures of 0.4 m or smaller.

## 8.2. CAMERAS WITH MENISCUS CORRECTORS

We now turn our attention to another type of wide-field camera, one in which the aspheric corrector is replaced by a meniscus lens. The purpose of the meniscus is the same as that of the corrector, to compensate for the spherical aberration of the following mirror(s). The theory of the meniscus corrector was developed independently by Bouwers (1946), Maksutov (1944), and Baker

(1940) with their names attached to various versions of meniscus cameras. In this section we consider a subset of the many types of meniscus cameras that have been described in the literature. The reader should consult the references at the end of the chapter, including the monograph by Maxwell (1972), for details on these and other designs. Another excellent discussion of cameras of this type is given by Wilson (1996).

### 8.2.a. CONCENTRIC MENISCUS CORRECTOR

A type of meniscus lens is one in which the two surfaces of the lens are concentric with the surface of a spherical mirror, as shown in Fig. 8.5. If an aperture stop is placed at the common center of curvature, as in a standard Schmidt, then the system has no unique axis and all off-axis aberrations are zero. The Petzval surface is also concentric with the other surfaces and the image surface is curved, as in a standard Schmidt. The characteristics of the images are determined entirely by the spherical aberration and any chromatic aberration introduced by the meniscus.

The complete analysis of the spherical aberration of the system shown in Fig. 8.5 involves the application of Eq. (5.6.7) with  $j = 3$  together with the corresponding coefficients from Tables 5.5 and 5.6. The result of this exercise, with all surfaces concentric, is a cubic equation involving the thickness and location of the meniscus. Although the solutions of this equation gives results in good agreement with those derived from ray traces, the form of the equation is quite complicated and gives little insight into the workings of the meniscus lens. It is more instructive to follow the approach by Bouwers and we choose to use his method.

The starting point in the Bouwers method is the assumption that the spherical aberration coefficient of the meniscus is that of a thin lens for which the source is at infinity. Although the derivation of this result is straightforward using the

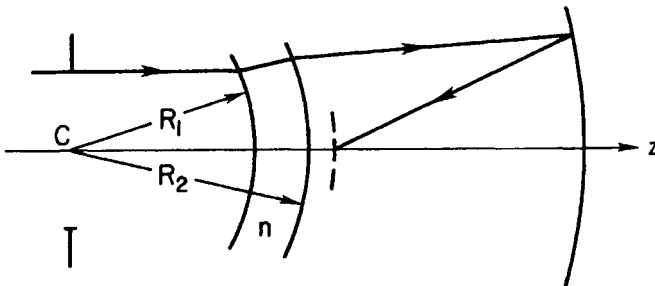


Fig. 8.5. Bouwers concentric camera with meniscus corrector. All surfaces are spherical with common center of curvature  $C$ .

results in Chapter 5, we take the expression given by Bouwers and convert it into the desired coefficient. The result is

$$B_{31} = -\frac{1}{8f^3} \left[ \left( \frac{n}{n-1} \right)^2 - \frac{f}{R_1} \left( \frac{2n+1}{n-1} \right) + \left( \frac{f}{R_1} \right)^2 \left( \frac{n+2}{n} \right) \right], \quad (8.2.1)$$

where  $f$  is the focal length of the lens and  $R_1$  is the radius of curvature of its first surface. For a concentric lens, as we show in what follows,  $f \gg R_1$  and to a good approximation

$$B_{31} = -\frac{1}{8f^3} \left[ \left( \frac{f}{R_1} \right)^2 \left( \frac{n+2}{n} \right) \right]. \quad (8.2.2)$$

The focal length of a thick lens is found by substituting  $P_1$  and  $P_2$  in Eq. (2.4.1) into Eq. (2.4.3), with the result

$$\frac{1}{f} = (n-1) \left( \frac{1}{R_1} - \frac{1}{R_2} \right) + \frac{d(n-1)^2}{n R_1 R_2}. \quad (8.2.3)$$

The condition for a concentric lens is  $d = R_1 - R_2$ , where  $d > 0$  and the radii are negative according to the sign convention. Rewriting Eq. (8.2.3) in terms of  $d$  we find that the focal length of a concentric lens is given by

$$\frac{1}{f} = -\frac{d}{R_1 R_2} \left( \frac{n-1}{n} \right). \quad (8.2.4)$$

Practical values of  $d$  are 10 or more times smaller than  $R_2$ , hence  $f$  is typically 30 times or more larger than  $R_1$ . Thus we are justified in taking Eq. (8.2.2) for the spherical aberration coefficient of the lens.

Note that the concentric meniscus lens has a large negative focal length and is therefore a weak diverging lens. Thus the lens is thicker at the margin than at the center, the same as that of an aspheric corrector without an added radius term, and the signs of the spherical aberration coefficients of the lens and aspheric plate are the same.

To find the system spherical aberration coefficient we simply add Eq. (8.2.2) to that of a spherical mirror in collimated light from Table 5.2. The result, after substitution of Eq. (8.2.4), is

$$B_{3s} = \frac{(n-1)(n+2)}{8n^2} \frac{d}{R_1^3 R_2} + \frac{1}{4R^3}, \quad (8.2.5)$$

where  $R$  is the radius of curvature of the mirror. Note that by adding the coefficients to get Eq. (8.2.5), we have ignored the divergence of the beam from the lens and taken the same ray heights at the mirror and lens. This is similar to

the procedure followed for the Schmidt telescope and is acceptable here in view of the other approximations made.

At this point we express  $d$ ,  $R_1$ , and  $R_2$  in terms of  $R$  as follows:

$$d = -\zeta R, \quad R_1 = \chi R, \quad R_2 = (\chi + \zeta)R,$$

where  $\chi$  and  $\zeta$  are positive. Setting Eq. (8.2.5) equal to zero, substituting in terms of  $R$ , and solving for  $\zeta$ , we find

$$\zeta = \chi^4 \left[ \frac{(n-1)(n+2)}{2n^2} - \chi^3 \right]^{-1}. \quad (8.2.6)$$

Taking  $n = 1.46$ , values of  $\zeta$  for a selected set of  $\chi$  values are found in Table 8.8. Note that  $\zeta$ , the normalized thickness of the meniscus, increases rapidly as the lens is placed farther from the stop.

The values of  $\chi$  and  $\zeta$  in Table 8.8 serve as the starting point for ray-trace analysis of the meniscus camera. Results from ray traces of a series of  $f/3$  systems with these nominal parameters are given in Table 8.8. In view of the approximations made in this approach by Bouwers, it is not surprising that the image quality is unacceptable for the calculated combinations of  $\chi$  and  $\zeta$ . Analysis of these images shows the presence of both residual third-order spherical aberration and a significant amount of fifth-order spherical aberration.

Acceptable image quality is achieved by holding  $\chi$  constant and adjusting  $\zeta$  to give the monochromatic image diameter its smallest possible value. The results found from this analysis for  $f/3$  systems are shown in Table 8.9. Note that for larger  $\chi$  the values of  $\zeta$  derived by this procedure are significantly larger than those from Eq. (8.2.6). By changing  $\zeta$  at a given  $\chi$ , third-order spherical aberration of an amount approximately equal in magnitude but opposite in sign to that of the fifth-order contribution for rays at the margin can be introduced. The

**Table 8.8**

Nominal Parameters for Concentric Meniscus Lens<sup>a</sup>

$\chi$	$\zeta$	Blur <sup>b</sup>
0.200	0.00438	3.2
0.225	0.00708	4.5
0.250	0.01092	8.7
0.275	0.01622	11.7
0.300	0.02339	15.4

<sup>a</sup> Values of  $\chi$  and  $\zeta$  derived from Eq. (8.2.5) with  $n = 1.46$ .

<sup>b</sup> Image diameter at best focus, in units of arc-seconds, for  $f/3$  systems.

Table 8.9

Parameters for Optimized Concentric Meniscus Cameras <sup>a</sup>				
$\chi$	$\zeta$	$f_c/R$	BFD/R	Blur <sup>b</sup>
0.200	0.0043	0.492	0.508	2.8
0.225	0.0076	0.489	0.511	2.0
0.250	0.0128	0.485	0.515	1.6
0.275	0.0209	0.481	0.519	1.2
0.300	0.0338	0.475	0.525	1.0

<sup>a</sup> Results derived from ray traces with  $\zeta$  adjusted to minimize image blur diameter;  $f_c$  = camera focal length; BFD = distance from mirror to focal surface.

<sup>b</sup> Image diameter at best focus, in units of arc-seconds, for  $f/3$  systems.

result is an image diameter that is significantly smaller. Hence a significant improvement is achieved by balancing the spherical aberration contributions.

Note also that the camera focal lengths decrease and the back focal lengths increase as the lens thickness increases. This is a consequence of the changing focal length of the concentric lens, as is evident from examination of Eq. (8.2.4).

Although the monochromatic image size is acceptable for a meniscus camera with a thick lens, such as for  $\chi \approx 0.3$ , the polychromatic image size is unacceptable. This is a consequence of the change in focal length of the lens with changing wavelength, or *longitudinal chromatic aberration*. From Eq. (8.2.4) we find that the focal length of the lens changes with index according to the relation

$$df/f = -dn/n(n-1). \quad (8.2.7)$$

Because the rays incident on the mirror appear to come from the focal point of the lens, a shift of this point translates into a shift of the camera focal point. Denoting the camera focal length by  $f_c$  and applying Eq. (2.5.5) we find  $df_c = -m^2 df$ , where  $m$  is approximately  $-f_c/f$ , the magnification due to the mirror.

Combining these results with Eqs. (8.2.4) and (8.2.7) we find

$$\frac{df_c}{f_c} \cong \frac{\zeta}{2\chi^2} \frac{dn}{n^2}, \quad (8.2.8)$$

where  $df_c$  is the axial shift of focus with changing index. For the balanced system with  $\chi = 0.275$ ,  $\zeta = 0.0209$ ,  $dn = 0.0018$ , and  $n = 1.46$ , Eq. (8.2.8) gives  $df_c/f_c = 0.000117$ . The diameter of the image over the range of wavelengths spanned by this change of index (510 to 590 nm for an SiO<sub>2</sub> lens) is nearly 9 arc-sec, a significant increase over the monochromatic diameter of 1.2 arc-sec.

Thus the concentric meniscus corrector lens is not a viable option because of longitudinal chromatic aberration.

There are two methods for reducing the chromatic aberration of the meniscus. One, proposed by Bouwers, is an achromatic meniscus made of two different glasses cemented together. In this case the cemented interface cannot be made concentric with the outer surfaces, and the system is no longer strictly concentric. If, however, the two glasses have the same index of refraction but different Abbe numbers, then the cemented lens is still very nearly concentric. This possibility is discussed by Wilson (1996). For further details the reader should also consult the references by Bouwers (1946) and Maxwell (1972).

A second method, first proposed by Maksutov (1944), is an achromatic meniscus corrector made of a single glass with  $f$  invariant to a change in index. To achieve this condition, however, it is necessary to depart from the concentric lens surfaces. We examine briefly the characteristics of this type of corrector in the next section.

### 8.2.b. MAKSUTOV ACHROMATIC CORRECTOR

The achromatic corrector proposed by Maksutov is one in which the focal length is invariant to a change in index. This condition is easily derived by taking  $f$  for a thick lens and setting  $df/dn = 0$ . Applying this condition to Eq. (8.2.3) we find

$$d = (R_1 - R_2) \left( \frac{n^2}{n^2 - 1} \right). \quad (8.2.9)$$

Relative to a concentric lens, we see from Eq. (8.2.9) that this lens is roughly 2 times thicker. Using Eq. (8.2.9) we can find the separation  $\Delta z$  between the centers of curvature of the surfaces of the meniscus, with the result

$$\Delta z = (R_1 - R_2) - d = -d/n^2, \quad (8.2.10)$$

where the minus sign indicates that the center of curvature of surface 2 is closer to the mirror than that of surface 1. It is evident from Eq. (8.2.10) that the surfaces of the meniscus are more nearly concentric for small  $d$ .

We are not going to discuss all of the details in the design of a Maksutov camera, but instead will illustrate the general characteristics with one example. For a mirror of radius of curvature  $R$  we take  $d = -0.02473 R$  as a constant and vary  $R_1, R_2$ , and the lens-mirror separation until spherical aberration of the marginal rays is balanced. The value of  $R_2$ , of course, is tied to that of  $R_1$  by Eq. (8.2.9). The axial position of the stop is then altered until coma is balanced, with the parameters of the final system shown in Table 8.10. Note that the stop is near the first surface of the meniscus lens.

Table 8.10

Parameters of a Maksutov Achromatic Camera<sup>a</sup>

	Distance from Mirror
Stop	0.5947 R
Surface 1 of lens	0.5914 R
Surface 2 of lens	0.5667 R
Image	0.5129 R

<sup>a</sup> Index  $n$  used in Eq. (8.2.8) is 1.46,  $d = 0.0248|R|$ ,  $R_1 = 0.2087 R$ ,  $R_2 = 0.2219 R$ .  
Radius of curvature of image surface = 0.538 R.

Ray traces for an  $f/3$  system with parameters given in Table 8.10 show an on-axis image whose angular diameter is about 3 arc-sec, and a slow increase in image size to 5 arc-sec at a field radius of  $2^\circ$ . This on-axis image diameter is about 10  $\mu\text{m}$  for a camera whose focal length is 750 mm. The chromatic effects of the corrector are much smaller than those of the concentric meniscus, as expected, with  $df_c$  some thirty times smaller than that given by Eq. (8.2.7). For an  $\text{SiO}_2$  corrector the on-axis image diameters on a fixed focal surface do not exceed 4 arc-sec over the wavelength range from 400–700 nm.

Although this system was not given a detailed optimization, it is evident that its image quality is quite satisfactory, provided the camera is not too large. Compared to the concentric meniscus camera, the Maksutov achromatic camera is clearly superior in its chromatic characteristics.

### 8.2.c. CONCLUDING REMARKS

The discussion of meniscus lens cameras in the preceding sections is only an introduction to cameras based on this type of corrector. Among other types are those in which the meniscus is split, with part of it preceding the aperture stop. In addition, the meniscus on either side of the stop may itself be split into two separate pieces of glass. There are also so-called hybrid systems in which an aspheric plate located at the stop is used in conjunction with a meniscus corrector and others in which an aspheric surface is put on one of the surfaces of the meniscus.

A widely used hybrid system is the Super-Schmidt or Baker-Nunn camera used for wide-field photography to record trails of meteors and artificial satellites. This type of camera has a double concentric meniscus, half on either side of the stop, with a doublet Schmidt plate at the stop. The light reflected from the mirror passes through the meniscus nearer the mirror a second time before coming to the

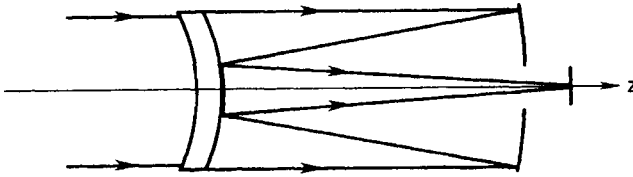


**Fig. 8.6.** Maksutov Cassegrain telescope with achromatic meniscus corrector. The secondary mirror shown is an aluminized circular area on the back face of the corrector.

curved focal surface. Because the design is based on the concentric principle, an angular field diameter of about  $50^\circ$  with good imagery is achieved.

A meniscus lens can also be used in place of an aspheric corrector in a Cassegrain camera, as shown schematically in Fig. 8.6. The secondary mirror in this type of system can be a separate mirror or a centered reflecting area on the back surface of the meniscus lens.

For more details on these and other meniscus lens systems, the reader should consult the references at the end of the chapter, with those by Bouwers (1946) and Maxwell (1972) a good introduction.

### 8.3. ALL-REFLECTING WIDE-FIELD SYSTEMS

The discussion in this chapter and the preceding one is intended to show the basic characteristics of so-called wide-field cameras and telescopes. It is evident from this discussion that there are many designs capable of good imagery over fields of several degrees, with chromatic effects generally setting the limit to the range of wavelengths that can be covered.

The principles used for these catadioptric designs also apply to all-reflecting wide-field systems. One obvious use of such a system is a space-based ultraviolet telescope. In these systems a reflecting aspheric corrector replaces the refracting plate and chromatic effects are absent. To separate the incident beam from the beam reflected from the corrector, the corrector axis is tilted by angle  $\theta$  relative to the mirror axis. The angle between the incident and reflected chief ray at the corrector is then  $2\theta$ .

The main complication of a tilted corrector is that its surface figure must be modified so that a collimated beam from the center of the field "sees" a circular profile on the corrector. This is achieved by placing an elliptical figure on the corrector with  $r^2$  in Eq. (7.2.1) given by  $r^2 = x^2 \cos^2 \theta + y^2$ , instead of  $r^2 = x^2 + y^2$ . The other change required is to replace  $z$  in Eq. (7.2.1) by  $z \cos \theta$ ; this ensures that the OPD introduced by the tilted corrector is the same as that of an untilted plate. An aspheric plate with an elliptical figure is obviously

more difficult to make than one with a circular figure, and no large systems of this type have been made. We do not discuss this type of system in detail here; the interested reader should consult the paper by Schroeder (1978).

## REFERENCES

- Baker, J. (1940). *Proc. Am. Philos. Soc.*, **82**: 339.
- Bouwer, A. (1946). *Achievements in Optics*, Chap. 1, Amsterdam: Elsevier.
- Linfoot, E. (1955). *Recent Advances in Optics*, Chap. 4, London and New York: Oxford University Press.
- Maksutov, D. (1944). *J. Opt. Soc. Am.*, **34**: 270.
- Maxwell, J. (1972). *Catadioptric Imaging Systems*, New York: American Elsevier.
- Schroeder, D. (1978). *Appl. Opt.*, **17**: 141.
- Wilson, R. (1996). *Reflecting Telescope Optics I*, Berlin: Springer.

Telescopes are often used for direct imaging without extra optics in the light beam, but there are many observations for which auxiliary optics are required. Examples of some types of observations that require additional optics are spectroscopy and photometry. In the case of photometry this is often no more than a field lens to reimage the exit pupil of the telescope onto a detector. For spectroscopy the extra optics may be as simple as a prism or diffraction grating placed in the light beam, or a separate spectrograph with many optical elements whose entrance aperture is at one of the telescope foci. The characteristics of spectrometers are discussed in Chapters 14 and 15.

Even for direct imaging, it may be important to enhance the characteristics of an existing telescope by adding optical elements to widen the field, flatten the image surface, compensate for atmospheric refraction, or reimage at a different focal ratio. For a new telescope it is now customary to include such optics in the early design stages and often to design the telescope with its auxiliary optics as a system in itself.

The kinds of auxiliary optics discussed in this chapter include field lenses and field flatteners, corrector systems for both prime and Cassegrain focus, focal reducers for Cassegrain telescopes, and atmospheric dispersion correctors. There is also a brief discussion of elements used in fiber optics. Attention is given to the aberration characteristics of these systems, with examples given for each type of system considered.

## 9.1. FIELD LENSES, FLATTENERS

A field lens is an element that is placed at or near an image plane in an optical system. One application for such a lens, as noted in Section 5.7, is that of flattening a curved image surface. Before discussing this application, and others, we consider the aberrations introduced when an object or image lies close to an optical surface.

### 9.1.a. ABERRATIONS

The aberration coefficients for a general surface are given in Table 5.5. For an object close to the surface, take  $\Gamma$  from Table 5.5, replace  $s'$  using Eq. (2.2.4), and let  $s \ll R$ . The result obtained is

$$\Gamma = \frac{n}{s} \left( \frac{n^2}{n'^2} - 1 \right). \quad (9.1.1)$$

Given the condition that  $s$  is small, the dominant terms in the coefficients in Table 5.5 are those containing the factor  $\Gamma$ . Taking only the dominant terms, putting the coefficients into Eq. (5.5.9), and letting  $s'/n' = s/n$ , gives

$$\begin{aligned} \text{TSA} &= -\frac{s}{2} \left( \frac{y}{s} \right)^3 \Lambda, & \text{TSC} &= \frac{s\psi}{2} \left( \frac{y}{s} \right)^2 \left( 1 - \frac{W}{R} \right) \Lambda, \\ \text{TAS} &= -s\psi^2 \left( \frac{y}{s} \right) \left( 1 - \frac{W}{R} \right)^2 \Lambda, & \Lambda &= \frac{n^2}{n'^2} - 1. \end{aligned} \quad (9.1.2)$$

Because  $y/s$  is finite for all  $s$ , each of the transverse aberrations in Eq. (9.1.2) goes to zero as  $s$  approaches zero and the image is free of aberrations in this limit. This result is not surprising because  $s' \rightarrow 0$  as  $s \rightarrow 0$ , and the image and object coincide when  $s = 0$ .

For a real lens placed at an image surface,  $s$  cannot be zero for both surfaces, but it is small enough for each surface so that its contributions are usually of little consequence.

### 9.1.b. FIELD-FLATTENED RITCHEY-CHRETIEN TELESCOPE

As an example, we consider a lens placed near the Cassegrain focus of a Ritchey-Chretien telescope, as shown in Fig. 9.1. The lens parameters are chosen so that the median astigmatic surface of the telescope-lens combination is flat, thus

$$\kappa_m(\text{RC}) + \kappa_m(\text{lens}) = 0. \quad (9.1.3)$$

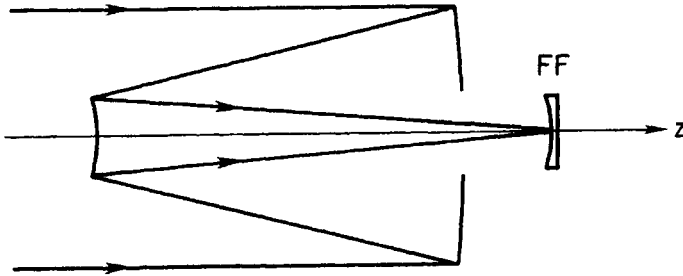


Fig. 9.1. Ritchey-Chretien telescope with field flattener lens FF. The lens parameters are given in Eq. (9.1.4).

The relation for the first term in Eq. (9.1.3) is given in Table 6.9. We find the second term by noting that a thin lens with  $s \approx 0$  has negligible aberrations according to Eq. (9.1.2), hence  $\kappa_m = \kappa_p$ .

The Petzval curvature of a lens is derived from the relation in Table 5.7, with the choice  $R_2 = \infty$  so that the distance between the flat image and lens can be made as small as desired. Substituting the derived result into Eq. (9.1.3) gives

$$(n - 1)/nR_l = \kappa_m(\text{RC}), \quad (9.1.4)$$

where  $R_l$  is the radius of curvature of the lens surface facing the secondary. Because  $\kappa_m$  for a Ritchey-Chretien is negative (the image surface is concave as seen from the secondary), the lens has  $R_l < 0$  and is plano-concave in cross section, as shown in Fig. 9.1.

Using the parameters of the RC telescope in Table 6.10 and letting  $R_1 = -6000$  gives  $R_l = -248$  for  $n = 1.46$ , the index of  $\text{SiO}_2$  at a wavelength of 548 nm. The aberrations of the telescope with and without the field flattener lens are given in Table 9.1, with the results taken from a computer ray-trace program.

Note that the field lens does change the system aberrations, but only slightly. Because the lens has zero astigmatism, the assumption that  $\kappa_m = \kappa_p$  for the lens is not quite true, and the image surface curvature is not zero. However, this assumption is a good first approximation, and a change of  $R_l$  to  $-260$  gives a flat image surface.

### 9.1.c. FIELD-FLATTENED SCHMIDT CAMERA

As a second example we consider a field-flattener lens placed near the curved focal surface of a Schmidt camera. In Section 5.7 we derived the condition for a flat Petzval surface for the combination of a spherical mirror and thin lens, with Eq. (5.7.16) giving the required condition for a plano-convex lens. The spherical

Table 9.1

Aberrations for Field-Flattened Ritchey-Chretien Telescope<sup>a,b</sup>

	Without lens	With lens	
		$R_1 = -248$	$R_1 = -260$
ASA	0.000	0.002	0.002
ATC	0.000	0.039	0.037
AAS	1.025	0.913	0.924
$\kappa_m R_1$	7.625	-0.393	-0.003
$f$	12000	12101	12096

<sup>a</sup> Lens: plano-concave shape; thickness at vertex = 6; back focal distance: = 0.43. Telescope:  $R_1 = -6000$ . Other parameters in Table 6.10.

<sup>b</sup> Aberrations are given at a field angle of 18 arc-min in units of arc-seconds.

aberration of the mirror alone is canceled by an aspheric plate with  $b$  chosen according to Eq. (7.1.5) with  $m = 0$ .

Choosing  $R = -1000$  and  $R_c = \infty$  gives  $b = -2.E-9$  and  $R_1 = -157.5$  for  $n = 1.46$ . The aberrations of the camera with and without the flattener lens are shown in Table 9.2, with  $F = 2.5$  for the camera without the lens. Note that the lens flattens the field, but introduces significant aberrations, especially coma and spherical aberration.

Table 9.2

Aberrations for Field-Flattened Schmidt Camera<sup>a,b</sup>

	Without lens	With lens	
		$W/R = 1.0$	$W/R = 0.979$
ASA	0.002	2.807	2.807
ATC	0.000	2.247	0.010
AAS	0.000	0.208	0.217
$\kappa_p R$	2.000	-0.0004	-0.0004
$f$	500.0	494.2	494.2

<sup>a</sup> Lens: plano-concave shape;  $R_1 = -157.5$ ; thickness at vertex = 5; back focal distance = -0.53. Mirror:  $R = -1000$ . Corrector:  $b = -2E-9$ ,  $R_c = \infty$ , thickness at vertex = 10.

<sup>b</sup> Aberrations are given at a field angle of 1° in units of arc-seconds.

The coma due to the field flattener lens can be largely removed by reducing the corrector-mirror separation by about 2%, but this displacement does not, of course, affect the spherical aberration. For this example it turns out that higher-order aberrations are not negligible. Fifth-order spherical aberration compensates in part for third order and the result from ray tracing is an on-axis blur diameter of about 1.4 arc-sec. This blur can be reduced to a negligible value by adding an aspheric term of higher order to the corrector, as noted in Section 7.2.

Comparing the effects of the flattener lens in these two examples, it is evident that the aberrations it introduces are significantly larger for the Schmidt camera. For spherical aberration this is entirely a consequence of the different focal ratios,  $F = 2.5$  for the camera and  $F = 10$  for the RC telescope, where  $y/s = 1/2F$  in Eq. (9.1.2). For astigmatism and coma the different pupil position for the lens is also a factor. For the RC telescope the pupil location is given by Eq. (2.6.1), from which we find  $W/R_1 \approx 15$ . For the Schmidt camera the mirror images the aperture stop back on itself and  $W/R_1 \approx 3$ . Substitution of these results into the relations in Eq. (9.1.2) accounts for the relative sizes of the aberrations introduced by the field lens.

In two other applications of a field lens its primary purpose is to reimagine the exit pupil of the telescope. For a photometer an aperture at the telescope focus passes the light of a single star and a field lens at the aperture images the telescope exit pupil on the photosensitive surface of a detector. If the star should wander in the aperture because of atmospheric effects, the effect is not seen by the detector because the reimaged exit pupil does not wander on its surface. Such a lens is often called a *Fabry lens*. When the instrument on a telescope is a spectrograph a lens is often placed at the entrance aperture so that the lens, in combination with the spectrometer collimator, reimages the exit pupil onto the grating or prism that follows the collimator in the spectrometer.

## 9.2. PRIME FOCUS CORRECTORS

A large Ritchey-Chretien telescope is generally equipped with interchangeable secondaries to provide a range of focal ratios, as noted in Section 6.2. The focal ratio at the Cassegrain focus is usually the smallest, typically 6 to 8, which for a 4-m telescope gives an image scale of about 7 arc-sec/mm. With this scale the typical blur diameter of a star image is often not well matched to the size of a detector resolution element, usually an individual pixel in a solid state detector. A better match between image and pixel size is achieved if the focal ratio is smaller, which in a Cassegrain configuration means a larger secondary and more obscuration. An alternative approach to getting a smaller focal ratio is to use

the primary mirror only, which, in combination with a corrector system, can provide a usable field at a focal ratio of 2 or 3.

### 9.2.a. ASPHERIC PLATES

The simplest prime focus corrector system is a single aspheric plate in the converging beam near the image surface, as shown in Fig. 9.2. The aperture stop is the primary mirror and the plate is distance  $g$  from the focus, hence  $W = f - g$  for the plate. The aberration coefficients for the primary are taken from Table 5.2, with  $m = 0$ , and the coefficients for the corrector are taken from Table 5.5, using only the terms in  $b$ . Substituting these results into Eq. (5.6.7) and choosing  $y_i = y_1$ , we get

$$\begin{aligned} B_{1s} &= -\frac{\theta^2}{2f} \left[ 1 + \frac{b(f-g)^2 g^2}{f} \right], \\ B_{2s} &= \frac{\theta}{4f^2} \left[ 1 - \frac{2b(f-g)g^3}{f} \right], \\ B_{3s} &= -\frac{1}{8f^3} \left[ \frac{K+1}{4} + \frac{bg^4}{f} \right], \end{aligned} \quad (9.2.1)$$

where  $\psi = -\theta$  and  $y_2/y_1 = g/f$  have been substituted. For a given  $K$  there are two free parameters,  $b$  and  $g$ , in Eqs. (9.2.1) and two of the coefficients can be set to zero. The dominant aberrations at small field angle, for any primary other than a paraboloid, are spherical aberration and coma. Setting these coefficients to zero gives

$$b = -\frac{(K+1)f}{4g^4}, \quad \frac{g}{f} = \left( \frac{K+1}{K-1} \right). \quad (9.2.2)$$

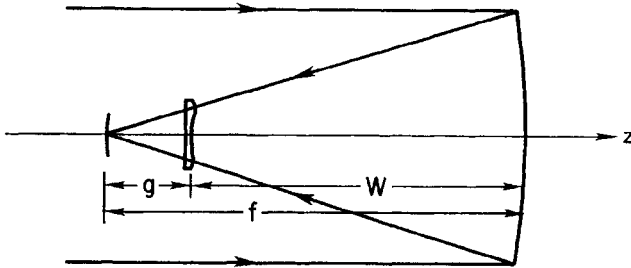


Fig. 9.2. Aspheric plate prime-focus corrector for hyperboloidal primary at distance  $g$  from the focal surface.

It is evident from Eqs. (9.2.2) that the location of the plate is set by the conic constant of the primary and this, in turn, sets the value of  $b$ . Because  $g$  and  $f$  are each positive, so is  $b$  for  $K < -1$ . Note also that the condition  $g > 0$  means that correction of both spherical aberration and coma with a single plate is not possible for an ellipsoidal primary.

Taking  $b$  from Eq. (9.2.2) and substituting into  $B_{1s}$  we find

$$\text{AAS} = 2B_{1s}y_1 = \frac{\theta^2}{2F} \left( \frac{K}{K+1} \right). \quad (9.2.3)$$

Comparing the astigmatism given by Eq. (9.2.3) with that of the primary only, we see that, depending on the value of  $K$ , the radius of the usable field is limited to a few arc-minutes. From Eq. (9.2.3) we also see that the larger is  $K$  for the hyperboloid in absolute terms, the smaller is the astigmatism at a given field angle and the larger is the usable field. A larger difference also means a greater distance between the plate and the focus, and a larger plate size, as seen from Eq. (9.2.2). As pointed out by Gascoigne (1973), these conclusions also hold for more complex corrector systems.

The final parameter of interest for this system is the curvature of the median image surface. Following the procedure in Section 6.2 we find

$$k^2 B_{1s}(\text{cor}) = B_{1s}(\text{pri}), \quad \theta = k\theta',$$

where  $k = g/f$ . Using these relations we get

$$\kappa_m = \frac{1}{f} \left( \frac{K-1}{K+1} \right) = \frac{1}{g}, \quad (9.2.4)$$

hence the focal surface of best images is strongly curved, and is concave as seen from the primary.

An example of these results applied to an  $f/3$  Ritchey-Chretien primary is shown in Table 9.3. The conic constant chosen is that for an RC telescope with  $m = 2.5$  and  $\beta = 0.25$  at the Cassegrain focus. The plate has a diameter-to-thickness ratio of 25 and its radius of curvature is chosen to give minimum chromatic effect. The radius of the plate  $r_0$  is chosen to cover a field radius of about  $0.12^\circ$ .

From the results in Table 9.3 we see that the coma and spherical aberration of the primary have been largely but not entirely eliminated. The size of the residuals depends on plate thickness and orientation. Although ASA for the example in Table 9.3 can be reduced to zero either by moving the plate closer to the primary or adjusting the value of  $b$ , ray-trace results show that spherical aberration and coma of higher order are not negligible. These aberrations are reduced to negligible levels by including a fifth-order aspheric coefficient  $b'$  and adjusting the aspheric parameters and plate position, details that are omitted here.

**Table 9.3**  
 Characteristics of a Prime Focus Corrector<sup>a,b</sup>

	Without plate	With plate	
		theory	actual <sup>c</sup>
ASA	21.221	0.000	0.850
ATC	7.500	0.000	0.057
AAS	0.105	0.696	0.707
$\kappa_m f$	1.000	12.25	12.20

<sup>a</sup> Primary: diameter = 4.0 m;  $f = 12.0$  m;  $K = -1.17778$ .  
 Plate:  $b = 5.792E-10$ ;  $R = -52800$  mm;  $r_0 = 200$  mm,  
 $n = 1.46$ ; thickness = 16 mm;  $g = 0.08163f$ ;  $W = 11,000$   
 mm.

<sup>b</sup> Aberrations are given at a field angle of  $0.1^\circ$  in units of arc-seconds.

<sup>c</sup> Values in "actual" columns are from ray-trace program.

This example illustrates a general procedure in the design of any system in which one or more of the elements is an aspheric plate. The procedure is one of taking only the aspheric terms in the aberration coefficients to get a first-order design and using computer analysis to refine the design. In this way one reduces the effort required in the theoretical analysis leading to the original design and uses the computer to help arrive at the final design.

Although the single-plate corrector makes the prime focus of a Ritchey-Chretien primary usable, the surface of best images is sufficiently curved so that a field flattener lens is also needed. The sag of the image surface at a field angle of 6 arc-min is about  $220 \mu\text{m}$ . This sag, in combination with blur already present in the off-axis image, gives an unacceptably large blur on a flat detector in focus on the on-axis image. Wilson (1971) gives spot patterns for an aspheric plate-field flattener combination for the ESO 3.6-m telescope, with acceptable image quality over a field diameter of about  $0.25^\circ$ .

Before going on to other prime-focus correctors, it is worth noting that a single plate will not improve the images of a paraboloidal primary. Putting a corrector in the beam will, for example, introduce spherical aberration and astigmatism of unacceptable amounts if  $b$  is chosen to eliminate coma. The verification of this statement using Eqs. (9.2.1) is left as an exercise for the reader.

Getting a larger and flatter image field at prime focus requires more complex correctors, of which many are discussed in the literature. Here we consider briefly a few of these, but without the detail given to the single-plate corrector. One kind of system that has been explored in detail is a set of corrector plates in series in the converging beam, as shown in Fig. 9.3 for three plates. Taking the aberration

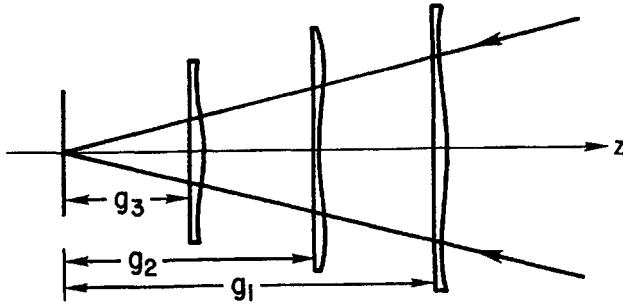


Fig. 9.3. Schematic of three-plate prime focus corrector.

coefficients for the mirror from Table 5.2 and those for the correctors from Table 5.5, it is a straightforward step to the system coefficients. The results are

$$\begin{aligned}
 B_{1s} &= -\frac{\theta^2}{2} \left( \frac{1}{f} + \Sigma b_i W_i^2 k_i^2 \right), \\
 B_{2s} &= \frac{\theta}{2} \left( \frac{1}{2f^2} - \Sigma b_i W_i k_i^3 \right), \\
 B_{3s} &= -\frac{1}{8} \left( \frac{K+1}{4f^3} + \Sigma b_i k_i^4 \right),
 \end{aligned}
 \tag{9.2.5}$$

where the  $i$ th corrector is a distance  $W_i$  from the primary,  $g_i$  from the image surface, and  $k_i = g_i/f$ .

For two plates there are four free parameters,  $b_1, g_1, b_2, g_2$ , and each of the coefficients in Eq. (9.2.5) can be made zero for a hyperboloidal primary. In this case the signs of the aspheric coefficients are opposite, with  $b > 0$  for the plate nearer the primary. For the same primary mirror parameters as in Table 9.3, ray-trace analysis of a two-plate corrector shows that the field of acceptable images is about two times larger in diameter than that of a single-plate system. The curvature of the median image surface is about 10 times smaller for the two-plate system, though its curvature is significant over the larger field. As noted by Gascoigne (1973), a paraboloid with a two-plate corrector has image blurs and surface characteristics comparable to those of a hyperboloid with a single-plate corrector.

The design for a three-plate corrector, first proposed by Meinel (1953), has been described in the literature and the reader should consult the references at the end of the chapter for details. The field is larger than that achieved with the two-plate corrector by about a factor of two but, as noted by Wilson, the complete corrector set is not easy to manufacture because of the several large aspheric surfaces required. Wilson points out that the optical performance of the three-

plate corrector system is no better than that of three-lens systems with spherical surfaces, a type we consider briefly in the next section.

### 9.2.b. WYNNE TRIPLETS

An alternative approach to prime focus correctors is to use lenses with spherical surfaces, such as the Wynne corrector for a hyperboloidal primary shown in Fig. 9.4. Designs of this type give fields of good images up to 50 arc-min in diameter for an  $f/2.7$  mirror and a somewhat larger field for a slower primary. The major advantages of this type, compared to the multiplate type, are ease of fabrication, flatter fields, and more compact size. For the corrector shown in Fig. 9.4 the length  $L$  is approximately  $0.06f$ , less than that of aspheric plate systems, and hence the diameters of the separate lenses are less than those of the aspheric plates.

Wynne has also shown that a three-lens corrector with a paraboloidal primary gives fields of comparable size and image quality. A schematic of this type of corrector, given by Wynne for an  $f/3.25$  primary, is shown in Fig. 9.5. The correctors shown in Figs. 9.4 and 9.5 are drawn to the same scale for ease of comparison. Although the general forms of the corresponding lenses in the two correctors are similar, there are obvious differences in shape and spacing. The interested reader should consult the papers by Wynne (1972, 1974) for further details on these types of correctors.

An excellent summary of the characteristics of prime focus lens correctors, including spot patterns, is given by Wilson (1996). He also compares the chromatic properties of three-plate aspheric systems with Wynne three-lens systems and notes that the latter have somewhat better image quality over an extended wavelength range.

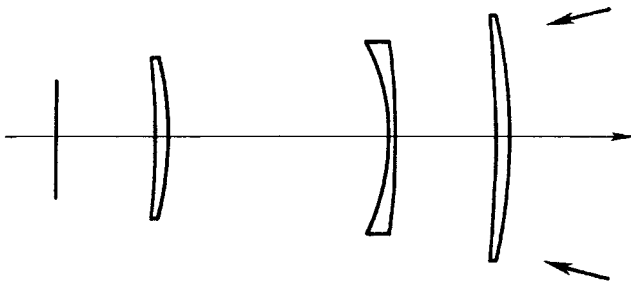
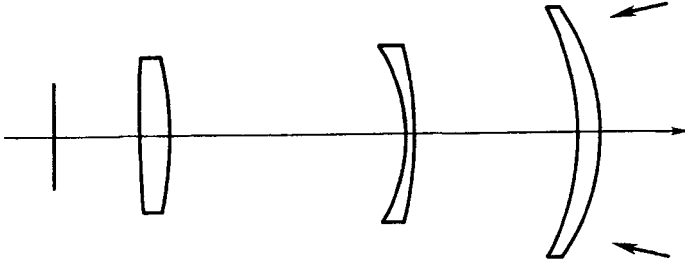


Fig. 9.4. Wynne triplet corrector for prime focus of hyperboloidal primary. See the article by Wynne (1972) for characteristics of the lens elements for an  $f/3.25$  primary.



**Fig. 9.5.** Wynne triplet corrector for prime focus of paraboloidal primary. See the article by Wynne (1974) for characteristics of the lens elements for an  $f/3.25$  primary.

### 9.3. CASSEGRAIN FOCUS CORRECTORS

Of the common two-mirror telescopes discussed in Chapter 6, the Ritchey-Chretien type has the largest field at the Cassegrain focus. To third order, the only significant aberrations are astigmatism and field curvature. It was first shown by Gascoigne that the placement of an aspheric plate in the Cassegrain beam removes the astigmatism without introducing a significant amount of coma and spherical aberration. This plate also reduces the field curvature because, as noted in Section 6.2, the median image surface is more strongly curved than the Petzval surface. In this section we discuss the characteristics of this type of corrector for the Cassegrain focus.

#### 9.3.a. ASPHERIC PLATE

A diagram of an RC telescope with aspheric plate in the Cassegrain beam is shown in Fig. 9.6, with the plate located a distance  $g$  from the focus and  $W$  from the telescope exit pupil. The aberration coefficients of the system, referenced to the primary, are

$$\begin{aligned}
 B_{3s} &= -\frac{b}{8} \left(\frac{g}{f}\right)^4, & B_{2s} &= \frac{b}{2} \left(\frac{g}{f}\right)^3 (W\psi), \\
 B_{1s} &= -\frac{\theta^2}{2f} \left[ \frac{m(2m+1) + \beta}{2m(1+\beta)} \right] - \frac{b}{2} \left(\frac{g}{f}\right)^2 (W\psi)^2,
 \end{aligned}
 \tag{9.3.1}$$

where the astigmatism coefficient for the telescope is taken from Table 6.6, with Eq. (6.2.3) substituted for  $(K_1 + 1)$ .

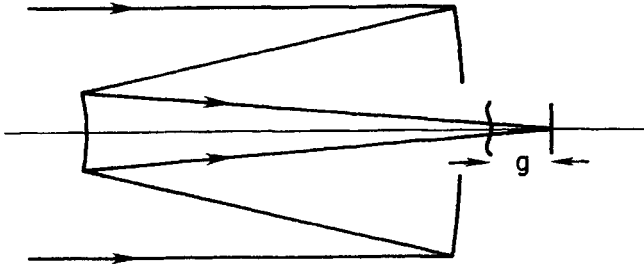


Fig. 9.6. Aspheric corrector for Cassegrain focus of Ritchey-Chretien telescope. The aspheric figure is similar to that of a Schmidt plate.

To evaluate the coefficients we first express  $W$  and  $\psi$  in terms of the telescope parameters and plate location. The location of the telescope pupil is given by Eq. (2.6.1), and  $W = g - f_1\delta$ , where  $W$  is negative for the plate. The relation between  $\psi$  and  $\theta$ , given by Eq. (2.6.4), is  $\psi = \theta(m/\delta)$ . In terms of the telescope parameters we get

$$W\psi = -f\theta \left[ 1 - \frac{g}{f} \frac{m^2 + \beta}{m(1 + \beta)} \right]. \quad (9.3.2)$$

A good first approximation to zero astigmatism is obtained by assuming that  $g/f \ll 1$ , substituting  $W\psi = -f\theta$  into Eq. (9.3.1), and setting  $B_{1s} = 0$ . The relation found is

$$bfg^2 = -\frac{m(2m + 1) + \beta}{2m(1 + \beta)} = -\Lambda. \quad (9.3.3)$$

This is one relation between  $b$  and  $g$ , with the other relation found by requiring that the coma at a given field angle does not exceed a specified amount. Substituting Eq. (9.3.3) into  $B_{2s}$  and  $B_{3s}$  we find the following angular aberrations:

$$\text{ATC} = \frac{3\theta\Lambda}{8F^2} \left( \frac{g}{f} \right), \quad \text{ASA} = \frac{\Lambda}{16F^3} \left( \frac{g}{f} \right)^2. \quad (9.3.4)$$

As an example we take the parameters for the RC telescope in Table 6.10 and, from Eq. (9.3.3), find  $\Lambda = 3.625$ . Assuming that  $\text{ATC} = 0.25$  arc-sec at  $\theta = 0.3^\circ$ , we find from Eqs. (9.3.4) that  $g/f = 0.01703$  and  $\text{ASA} = 0.014$  arc-sec. Putting this value of  $g/f$  into  $W\psi$  in Eq. (9.3.2), and substituting  $W\psi$  into Eq. (9.3.1), we get better values for the off-axis aberrations. The results in arc-seconds are  $\text{ATC} = 0.236$  and  $\text{AAS} = 0.056$ , and all of the aberrations are clearly at a tolerable level.

The one remaining calculation is that of finding  $b$  using Eq. (9.3.3). Because  $b < 0$ , the plate has the shape of a Schmidt plate. With a radius added to the plate to minimize chromatic aberration, from Eq. (7.2.4), a ray-trace analysis of the plate in this example shows that the image diameters are 1 arc-sec or less over a field diameter of about  $1.2^\circ$ . Through-focus spot diagrams at  $\lambda = 550$  nm and spot patterns at best focus for several wavelengths are shown in Figs. 9.7 and 9.8, respectively. It is instructive to compare the spot patterns for an uncorrected RC telescope in Fig. 6.3 with those in Fig. 9.7. Note especially the significantly larger field for the corrected RC and the presence of coma in its images. A close look at the off-axis images in Fig. 9.8 shows a lateral displacement away from the center of the field as the wavelength increases. This effect is a consequence of the plate thickness, in this case 10 mm, and will not degrade image quality under normal seeing conditions.

Because the plate in this example is in an  $f/10$  beam, higher-order aberrations are negligible. The curvature of the median image surface found from ray traces is  $\kappa_m = 4.69/R_1$ , a value about 10% larger than the Petzval curvature calculated from ray tracing.

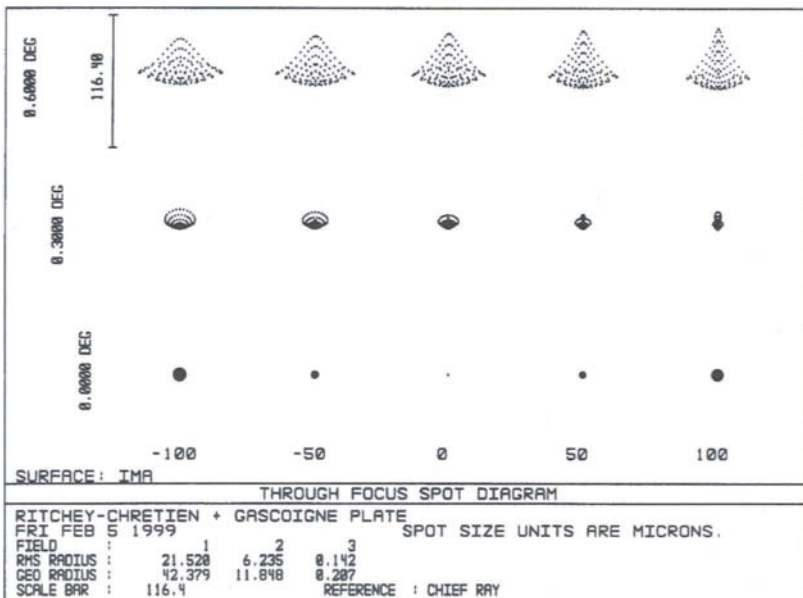


**Fig. 9.7.** Through-focus spot diagrams at  $\lambda = 550$  nm for system shown in Fig. 9.6. Scale bar on the upper left is 2 arc-sec long. See the discussion following Eqs. (9.3.4).

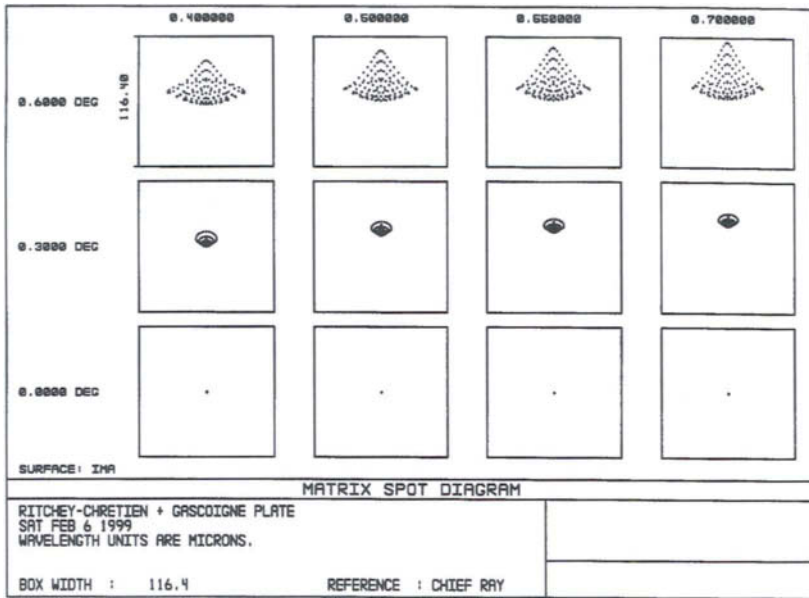


**Fig. 9.8.** Spot diagrams at selected wavelengths for system shown in Fig. 9.6. Box width is 2 arc-sec. See the discussion following Eqs. (9.3.4).

### 9.3.b. MODIFIED RITCHY-CHRETIEN TELESCOPE

The effectiveness of an aspheric plate in the Cassegrain beam suggests that still larger fields are possible if the telescope plus plate are designed as a system. In this case the conic constants of the primary and secondary are also adjustable parameters, and all of the aberrations can be made zero. Examples of such designs are the 1.0- and 2.5-m telescopes described by Bowen and Vaughan (1973) and located at Las Campanas Observatory in Chile. The design of the 1.0-m telescope has the additional feature of a flat Petzval field, thus the need for bending a photographic plate or arranging arrays of CCD detectors to match a curved median image surface is avoided. Well-corrected fields over  $2^\circ$  in diameter are achieved with these designs.

The first step in the procedure for designing a flat-field Ritchey-Chretien to cover a wide field is to specify zero Petzval curvature for the telescope. Thus  $\rho = 1$ , as is evident from Eq. (5.7.17). This condition, in turn, requires that

$$m^2 - 1 = m(1 + \beta). \quad (9.3.5)$$

Substitution of Eq. (9.3.5) into Eqs. (6.2.3) and (6.2.4) gives the conic constants of the mirrors, and all of the telescope parameters are now specified. If, for

example, we choose  $\beta = 0.2$ , then  $m = 1.7762$ ,  $K_1 = -1.4912$ ,  $K_2 = -26.905$ , and  $k = 0.4338$ . From these results we see that the mirrors, especially the secondary, are strongly hyperbolic and that the obscuration of the secondary is larger than that of the typical RC telescope.

The next step in the design is simply one of substituting  $m$ ,  $\beta$ , and a choice of  $g$  into Eq. (9.3.3) and finding a first-order solution for  $b$ . The telescope parameters and the values of  $b$  and  $g$  are then the starting point for computer optimization of the complete system, telescope plus corrector plate.

#### 9.4. CASSEGRAIN FOCAL REDUCERS

A focal reducer is an optical system whose function is to change the focal ratio of a telescope. It is most often used at the Cassegrain focus to reduce the focal ratio so that a given field can be placed on a detector of smaller area. In this section we discuss the general characteristics of focal reducers used at the Cassegrain focus. With the exception of a Schmidt camera example for a Ritchey-Chretien telescope, we omit the details of specific designs.

##### 9.4.a. GENERAL CONFIGURATION

A schematic of a Cassegrain focal reducer is shown in Fig. 9.9. Its components include a field lens at the Cassegrain focus to image the exit pupil of the telescope onto the aperture stop of the focal reducer, a collimator to render the light parallel, and a camera. Other optical elements, such as a grating or filter, can be put in the space between the collimator and camera. Because such elements are located in a collimated beam, they introduce no additional aberrations.

The diameters of the focal reducer components depend on the field to be covered. If the angular radius of the field on the sky is  $\theta$ , then the diameter of the field lens is  $2f\theta$ , where  $f$  is the telescope focal length. The diagram in Fig. 9.10

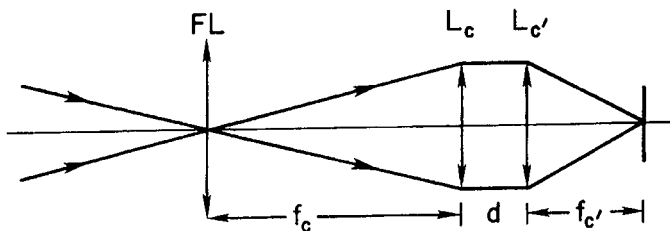
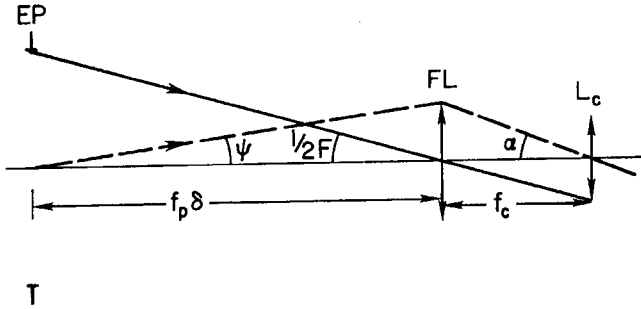


Fig. 9.9. Schematic of focal reducer where  $c$  and  $c'$  denote collimator and camera, respectively, and FL is the field lens at the telescope focus.



**Fig. 9.10.** Schematic of focal reducer in relation to telescope exit pupil EP. See text, Section 9.4, for definitions of symbols.

shows the chief ray from the center of the telescope exit pupil for an object at the edge of the field. Assuming the aperture stop of the focal reducer is at the collimator lens, the angle  $\alpha$  at which this chief ray enters the collimator is given by

$$\alpha f_c = \psi f_p \delta = f \theta, \quad (9.4.1)$$

where  $f_c$  is the focal length of the collimator,  $f_p$  is the focal length of the primary, and Eq. (2.6.4) is substituted to eliminate  $\psi$ .

We also see from Fig. 9.9 that  $D_c$ , the diameter of the collimator lens, is  $f_c/F$ . Therefore

$$\alpha/\theta = f/f_c = D/D_c. \quad (9.4.2)$$

For a real lens pair the stop is often located in the space between the lenses, but the distance  $d$  in Fig. 9.9 is usually small compared to  $f_c$  and, to a good approximation, the stop is effectively at the collimator. If  $d$  is small, the diameters of the collimator and camera lens are nearly equal, and Eq. (9.4.2) can be used to find the diameter of either.

For a given  $D$  and  $\theta$ , we see from Eq. (9.4.2) that a smaller  $D_c$  implies a larger  $\alpha$ . A larger value of  $\alpha$ , in turn, generally means that the design of the lenses in the focal reducer is more difficult. We also see that the size of the focal reducer scales directly with the size of the telescope for a given  $\alpha$  and  $\theta$ .

The focal length of the telescope-focal reducer combination is  $f$  of the telescope times the magnification of the focal reducer. The reader can verify that the magnification of the focal reducer is the ratio of the camera to collimator focal lengths or focal ratios, hence  $f$  of the combination is the diameter  $D$  of the telescope times the focal ratio of the camera.

As an example, let  $\theta = 0.5^\circ$ ,  $\alpha = 20^\circ$ , and  $D = 1$  m. Substituting these values into Eq. (9.4.2) gives  $D_c = 25$  mm, and a well-designed commercial camera lens

is appropriate for the camera lens of the focal reducer. If  $F = 10$  for the telescope, then  $f_c = 250$  mm is the focal length of the collimator, and the constraints on its design are relatively modest compared to those on the camera lens. With the same telescope magnification and angles, but  $D = 4$  m, the dimensions of the lenses are  $4\times$  larger and their design and mounting is a more difficult problem.

#### 9.4.b. TYPES OF FOCAL REDUCERS

A variety of focal reducer types have been analyzed by a number of investigators, with a good summary of these given by Wilson (1971). His paper includes examples of multilens systems that convert an  $f/8$  telescope beam to  $f/3$  with good image quality of a field  $0.9^\circ$  in diameter. The main difficulty with lens systems, as noted by Wilson, is the chromatic aberration over an extended wavelength range.

Catadioptric systems have the advantage of smaller chromatic aberration but the disadvantage of obstruction due either to the detector or one of the mirrors. Wilson describes briefly some catadioptric systems that have been proposed for focal reducers, such as the standard Schmidt, Bouwers-Maksutov, and Schmidt-Cassegrain cameras, where each is used with a field lens to reimagine the telescope exit pupil. The text by Wilson (1996) should be consulted for further details and references.

Meinel, Meinel and Wang (1985) have described a four-mirror focal reducer for the Nasmyth focus of a large telescope with good imagery over a field radius of 8 arc-min. Their paper should be consulted for details.

#### 9.4.c. EXAMPLE: SCHMIDT CAMERA

To illustrate the approach to the design of a focal reducer, we consider a Schmidt camera modified for the required conditions. The basic configuration adopted, field lens plus camera, is shown in Fig. 9.11. The field lens images the telescope exit pupil on the aspheric plate with the chief ray shown entering the camera at angle  $\psi$ , where  $\psi/\theta = f/d$  for a telescope of focal length  $f$  with field angle  $\theta$ . We assume a Ritchey-Chretien telescope and adjust the camera parameters to eliminate the astigmatism present at the RC focal surface.

The RC telescope is free of coma and spherical aberration, while the aspheric plate has no coma and astigmatism when it is at a pupil. Thus the coma of the system is that of the mirror only, with the coma coefficient given in Table 5.6. Setting this coefficient to zero gives

$$\frac{W}{R} = \left[ 1 - K \left( \frac{m-1}{m+1} \right) \right]^{-1}, \quad (9.4.3)$$

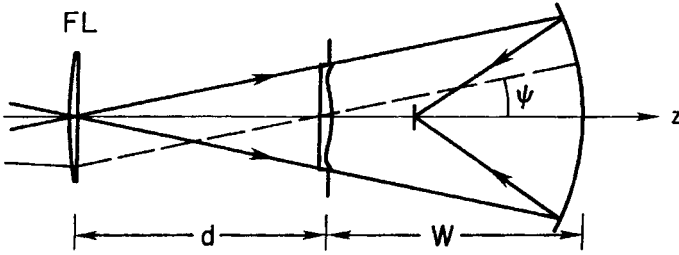


Fig. 9.11. Schematic of Schmidt focal reducer. See text, Section 9.4, for discussion.

where  $K$  is the conic constant of the mirror. As we will show shortly,  $K$  must be chosen nonzero to eliminate the telescope astigmatism.

The system spherical aberration is that of the aspheric plate and mirror, while the astigmatism is that of the telescope and focal reducer mirror. Taking the appropriate coefficients for the corrector and mirror from Tables 5.5 and 5.6, and the telescope astigmatism from Table 6.6, we get

$$B_{1s} = B_1(\text{RC}) + \frac{n\psi^2}{R} \left(\frac{y_4}{y_1}\right)^2 \left[ \left(\frac{W}{R}\right)^2 K + \left(1 - \frac{W}{R}\right)^2 \right], \quad (9.4.4)$$

$$B_{3s} = -\frac{b}{8} \left(\frac{y_3}{y_4}\right)^4 + \frac{n}{4R^3} \left[ K + \left(\frac{m+1}{m-1}\right)^2 \right], \quad (9.4.5)$$

where the subscripts 1, 3, and 4 refer to the telescope primary, aspheric plate, and camera mirror, respectively, and  $n = 1$  for the mirror. In writing these system coefficients we assume the field lens and aspheric plate thickness and radius do not contribute to the aberrations.

The terms in Eqs. (9.4.4) and (9.4.5) are simplified by noting that  $y_3/y_4 = d/s$ ,  $y_4/y_1 = s/f$ , and  $\psi = \theta(f/d)$ , where  $s$  is the distance from the field lens to the camera mirror.

The procedure is now one of substituting Eq. (9.4.3) into Eq. (9.4.4), setting Eq. (9.4.4) to zero, and solving for  $K$  in terms of  $B_1(\text{RC})$ . Letting  $B_1(\text{RC}) = -\theta^2\Gamma/2f$ , where  $\Gamma$  is the quantity in brackets in AAS in Table 6.9, the result is

$$K = \frac{\Gamma R}{2f} \left(\frac{m+1}{m-1}\right)^2 \left(1 - \frac{\Gamma R}{2f}\right)^{-1}. \quad (9.4.6)$$

The value of  $K$  from Eq. (9.4.6) is substituted into Eq. (9.4.3) to find  $W/R$ , which, in turn, is used to find the ratio  $d/s$ . In terms of the camera parameters we find

$$\frac{d}{s} = 1 - \frac{W}{s} = 1 - \frac{W}{R} \left(\frac{2m}{m-1}\right). \quad (9.4.7)$$

Values derived from Eqs. (9.4.6) and (9.4.7) are substituted into Eq. (9.4.5), which is solved for  $b$  after setting  $B_{3s}$  to zero.

All of the relations needed to specify the Schmidt focal reducer (SFR) are now in hand. For the telescope we take the design parameters of the 1.5-m  $f/8$  telescope shown in Table 9.4. For the SFR we assume a final focal ratio of 2.67, hence  $m = -1/3$  for the camera, with  $s = -2000$  mm and  $R = -1000$  mm.

With these parameters we find  $\Gamma = 2.67$ ,  $K = -0.025$ ,  $W = 1.053R$ ,  $d/s = 0.4737$ ,  $b = -8.937E-9$  for an  $\text{SiO}_2$  corrector at  $\lambda = 500$  nm. A listing of all the SFR parameters, including the field lens, is shown in Table 9.5.

Ray traces of the system with the nominal SFR parameters given in Table 9.5 show an image diameter of about 1 arc-sec at a field angle of  $0.5^\circ$  and wavelength of 500 nm. With a 2-mm change in the corrector location and a 10% increase in the focal length of the field lens, the image diameter is reduced to approximately 0.25 arcsec at the same field angle and wavelength. Over the range from 320 to 1000 nm, the image diameter is 0.5 arcsec or smaller at the edge of the field, hence the broadband image quality is satisfactory. The image surface is curved with a radius of curvature of  $-950$  mm.

Although this type of camera would appear to be an obvious choice for a focal reducer, it has several disadvantages. One problem is its curved focal surface, but a field flattener lens can be added to remove this curvature. A much more serious problem is the location of the focal surface inside the camera. It is not possible to locate large detector systems such as cooled solid-state arrays at an internal focus without vignetting most of the light before it reaches the mirror. One way of getting an external focus is a folded Schmidt camera with a tilted plane mirror between the corrector and sphere, as shown in Fig. 15.7, and the detector behind a hole in the plane mirror. The size of the hole and the position of the detector determine the amount of vignetting, and for a large field this is significant. Schmidt-Cassegrain cameras of the type described in Chapter 8, modified to reimage an object surface at a finite distance, also have an external focus, but vignetting by the camera's secondary mirror can be a shortcoming of this type of focal reducer. An example of a Schmidt-Cassegrain focal reducer with field-flattening optics is described by Opal and Booth (1990).

**Table 9.4**

Parameters of 1.5-m Ritchey-Chretien Telescope

Overall:	$m = 2.667$ ,	$k = 0.3273$ ,	$\beta = 0.2$
	$f = 12.0$ m,	$F = 8$	
Primary:	$R_1 = -9000$ mm,	$K_1 = -1.1368$	
Secondary:	$R_2 = -4712.7$ mm,	$K_2 = -6.5524$	

Table 9.5

Parameters of Schmidt Focal Reducer		
Overall:	$m = -0.333,$	$s = -2000 \text{ mm}$
Mirror:	$R = -1000 \text{ mm},$ $W = 1.053R \text{ (nominal)}$ $= 1.055R \text{ (optimized)}$	$K = -0.025$
Corrector:	$b = -8.937\text{E-}9,$ $R_c = -35\ 320 \text{ mm},$	$E = 2.416\text{E-}9$ thickness = 10 mm
Field Lens:	plano-convex, $R_2 = -380 \text{ mm (nominal)}$ $= -420 \text{ mm (optimized)}$	thickness = 18 mm
Lens and corrector material: $\text{SiO}_2$		

## 9.5. ATMOSPHERIC DISPERSION CORRECTORS

We now turn our attention to a different type of corrector, one that compensates for the *dispersion* of the Earth's atmosphere. This effect, discussed in Section 3.6.a under the name of *differential atmospheric refraction*, is a consequence of the wavelength-dependent index of refraction of the atmosphere. A curve of the differential refraction at  $45^\circ$  zenith angle over the wavelength range 340–1000 nm is shown in Fig. 9.12. This curve is based on a relation from Allen for the atmospheric conditions given in Table 3.1. The scale on the vertical axis in Fig. 9.12 is set to zero at  $\lambda = 435 \text{ nm}$ , a choice approximately centered in the range shown. For other zenith angles the scale is simply expanded or contracted according to Eq. (3.6.3).

The device that compensates for this effect is called an *atmospheric dispersion corrector* or ADC. In the absence of an ADC the image of a star with a ground-based telescope is a short, vertical spectrum, especially noticeable if the angle between the telescope axis and zenith is large. With an ideal ADC this same image shows no dispersion at any zenith angle, as well as no large displacement from a nominal position on the detector. Thus there are two basic requirements for an ADC: (1) variable dispersion to compensate that of the atmosphere at a given zenith angle; and (2) zero-deviation at some mean wavelength, denoted by  $\lambda_0$ , within the range of interest for all zenith angles.

The first of these requirements suggests counterrotating prisms with dispersion a maximum (minimum) when the apex angles of the prisms are in the same (opposite) directions. Two prisms are sufficient to satisfy this requirement, but they cannot satisfy the zero-deviation condition unless each prism by itself is a zero-deviation unit, a pair of prisms with different dispersions and oppositely directed apex angles. Thus an ADC is a set of four prisms paired to satisfy the

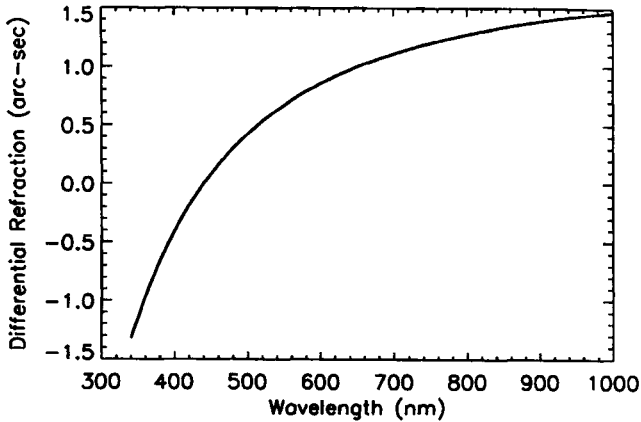


Fig. 9.12. Differential atmospheric refraction at a  $45^\circ$  zenith angle. See Table 3.1 for the atmospheric conditions and Section 3.6 for discussion.

given requirements. Because the required dispersion is small, each prism in an ADC can be considered “thin” and the paraxial approximation is adequate for the analysis. Schematic diagrams of an ADC, with angles exaggerated for clarity and the doublet pairs separated, are shown in Fig. 9.13. The dispersion of the ADC is a maximum in Fig. 9.13a and zero in Fig. 9.13b.

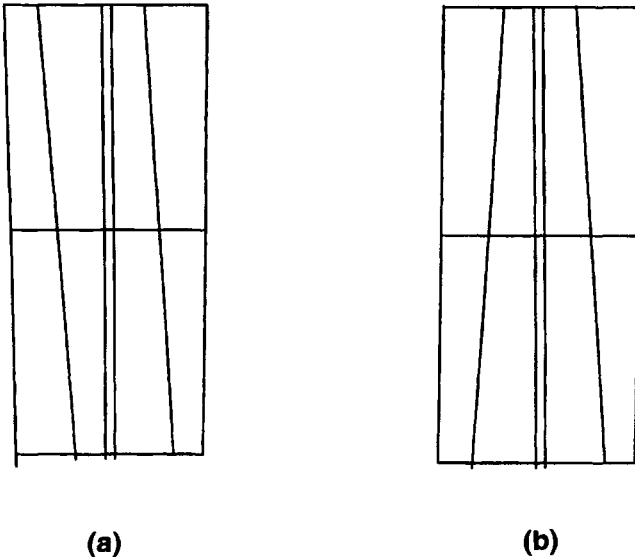


Fig. 9.13. Schematic diagrams of atmospheric dispersion correctors: (a) maximum dispersion, (b) zero dispersion. Angles are exaggerated for clarity.

For a single thin prism of index  $n$  the deviation  $\delta = (n - 1)\gamma$ , as shown in Fig. 4.12. The condition for zero deviation for a pair of prisms is

$$(n_1 - 1)\gamma_1 = (n_2 - 1)\gamma_2, \quad (9.5.1)$$

where both apex angles are taken positive. The prisms in each doublet in Fig. 9.13 are cemented, both for mechanical stability and ease of handling and for maximum light transmission.

From Eq. (9.5.1) we see that the choice of two glasses with the same indices of refraction at  $\lambda_0$  gives equal apex angles and plane-parallel opposite faces. In this case light of one wavelength is neither deviated nor displaced laterally, hence the pointing of the telescope is unaffected by inclusion of the ADC in the light beam. In practice it is difficult to find suitable glasses to satisfy this condition. The usual approach, and the one followed here, is to take glasses with adequate transmission in the near ultraviolet and a large difference in dispersive powers, and to accept a small amount of lateral displacement at the detector.

#### 9.5.a. EXAMPLE: ADC IN COLLIMATED LIGHT

As an example we consider the glasses UBK7 and LLF6 from the Schott catalog. We choose the wavelength of zero deviation  $\lambda_0 = 435$  nm and find the indices  $n(\text{UBK7}) = 1.52675$  and  $n(\text{LLF6}) = 1.54559$ . Given these indices we use Eq. (9.5.1) to find the ratio of the prism angles. The selection of the individual prism angles depends on the telescope and configuration in which the ADC is used; for this example we choose  $1.506^\circ$  and  $1.454^\circ$  for the UBK7 and LLF6 prisms, respectively. These angles are the same as those used by Wynne (1984) in the design of an ADC for the 4.2-m William Herschel telescope.

Our chosen layout of each of the doublet prisms in Fig. 9.13a,b is UBK7 on the left, facing the incident light, with the interface between the prism pairs perpendicular to the axis of a telescope. To ensure maximum light transmission, the doublet prisms are placed in contact, with an oil film between them to allow rotation of one relative to the other. Each individual prism is given a central thickness of 10 mm and collimated light incident on the ADC is focused by a perfect thin lens with  $f = 1000$  mm following the ADC.

Results of ray traces for selected wavelengths are shown in Fig. 9.14 for the ADC configuration in Fig. 9.13a. Note that the wavelengths are spaced at constant intervals of 70 nm, with decreasing dispersion as the wavelength increases, similar to that of the atmosphere as shown in Fig. 9.12. Not shown in Fig. 9.14 is the lateral displacement for  $\lambda_0$  of about 0.5 mm, a consequence of the wedge angle of  $0.052^\circ$  for each half of the ADC. If the configuration of the ADC is changed to that of Fig. 9.13b, then all wavelengths are superposed at  $\lambda_0$  in Fig. 9.14 and the lateral displacement is nearly zero.

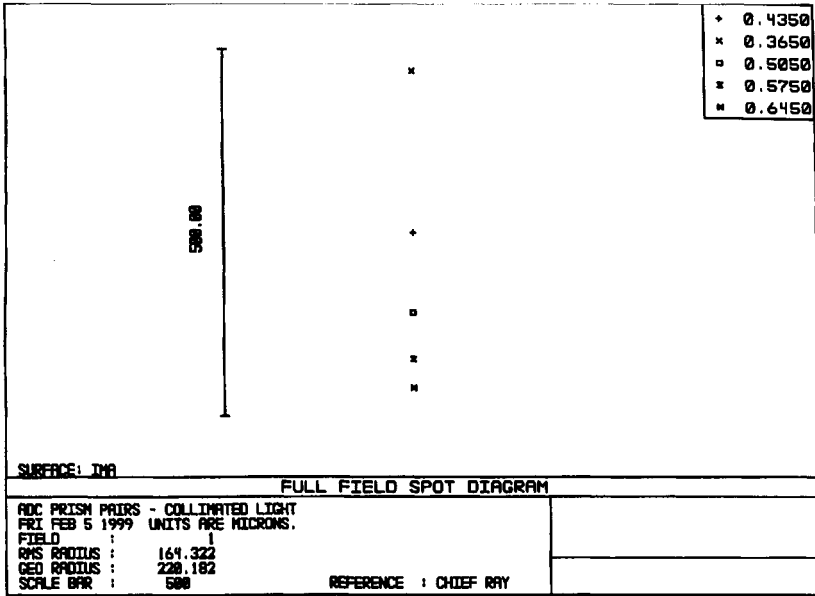


Fig. 9.14. Ray traces of wavelengths at 70 nm intervals of collimated light through ADC shown in Fig. 9.13(a). Glasses are UBK7 and LLF6. See the text for prism parameters and discussion.

The example here is simply to illustrate how an ADC is configured and to give dispersion results for typical glasses and angles. In practice, an ADC is designed to match a particular telescope such that maximum dispersion is obtained at the maximum desired zenith angle. At smaller zenith angles the two separate doublet prisms are rotated in opposite directions to reduce the net dispersion but maintain a vertical direction for this dispersion. The net dispersion is simply the vector sum of the separate dispersions of the individual prism pairs. As an example, if each pair is rotated 45° from the configuration for maximum dispersion, the net dispersion is reduced by a factor of  $\sqrt{2}$ .

9.5.b. EXAMPLE: ADC IN CONVERGENT LIGHT

The preceding example with collimated light illustrates the principles of an ADC without the complications of aberrations. Most often, however, an ADC is located in a convergent beam as, for example, in a Cassegrain telescope. In this case aberrations are introduced by the prisms and a more detailed analysis of the telescope plus ADC is required to ensure that image quality over the desired field is not seriously degraded. An example of such a detailed analysis is given by

Wynne and Worswick (1986) for the  $f/11$  Cassegrain beam of the William Herschel telescope; the interested reader should consult their paper.

Here we are interested in the aberrations introduced by the ADC without the added complication of telescope aberrations. We take the same UBK7-LLF6 combination as in the previous example and locate the incident face of this ADC in a converging  $f/4$  beam 500 mm from focus. Ray traces with the orientation of the ADC prism pairs at maximum dispersion give the spot patterns shown in Fig. 9.15 for three field angles and four wavelengths. Figure 9.16 shows spot patterns for the configuration of minimum dispersion.

There are several features of interest in Figs. 9.15 and 9.16, and we consider them in turn. First, and most obvious, is the variation of image size with wavelength, hence a chromatic focal error. Second, asymmetry due to coma is evident at off-axis field positions for both configurations. The final feature worth noting is that on-axis images are symmetric in the case of minimum dispersion but slightly comatic in the configuration for maximum dispersion. The source of these asymmetries is discussed in the following section.

The chromatic focal error is most clearly seen in through-focus spot diagrams, as shown in Fig. 9.17 at zero field angle for the ADC set for maximum dispersion. As shown by Wynne and Worswick, this error is eliminated by

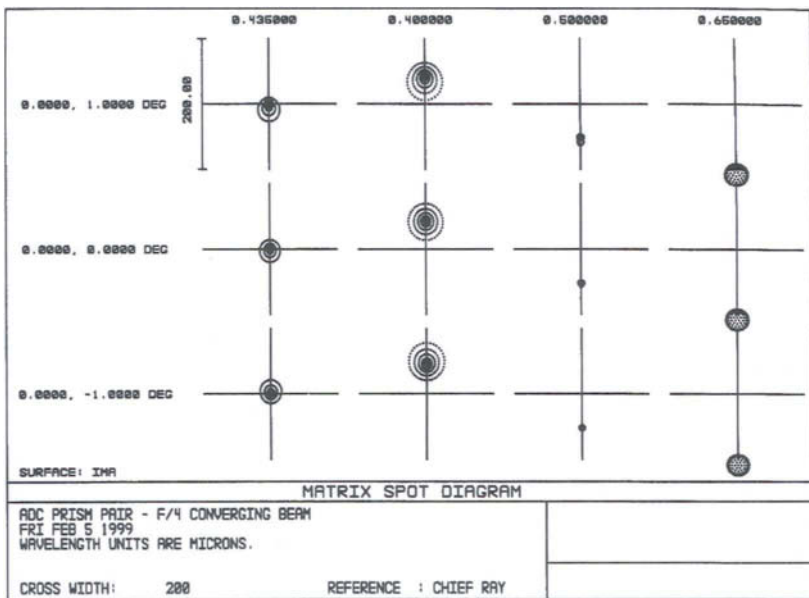
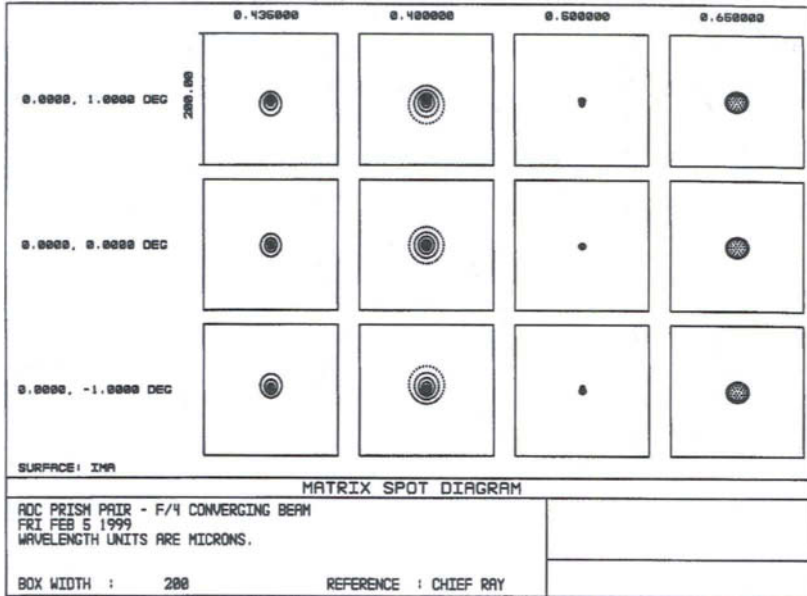


Fig. 9.15. Spot diagrams for selected wavelengths and field angles of  $f/4$  beam through ADC with maximum dispersion. See the text for prism parameters and discussion.



**Fig. 9.16.** Spot diagrams for selected wavelengths and field angles of  $f/4$  beam through ADC with minimum dispersion. See the text for prism parameters and discussion.

putting a slight curvature on the interface between the zero-deviation units. For this example, putting a radius of curvature of 5 m on each of the oiled contact surfaces gives the through-focus patterns shown in Fig. 9.18. The first prism pair of the ADC is a weak converging lens and the second is a weak diverging lens. Because of the power added to each half of the ADC, a refocus of about 1 mm is also required.

It is also worth comparing the linear dispersions at the detector for these two examples. The angular dispersion of the ADC is constant, but the linear dispersion is directly proportional to the effective lever arm, 1000 mm in the first example and 500 mm in the second.

### 9.5.c. ABERRATIONS OF PRISMS IN CONVERGING BEAM

We now consider the aberrations introduced when prisms are placed in a converging beam and examine, in turn, a single prism, a doublet prism, and a complete ADC at different dispersion orientations. For either a single prism or prism combinations, the effects due to thickness and angles can be separated as

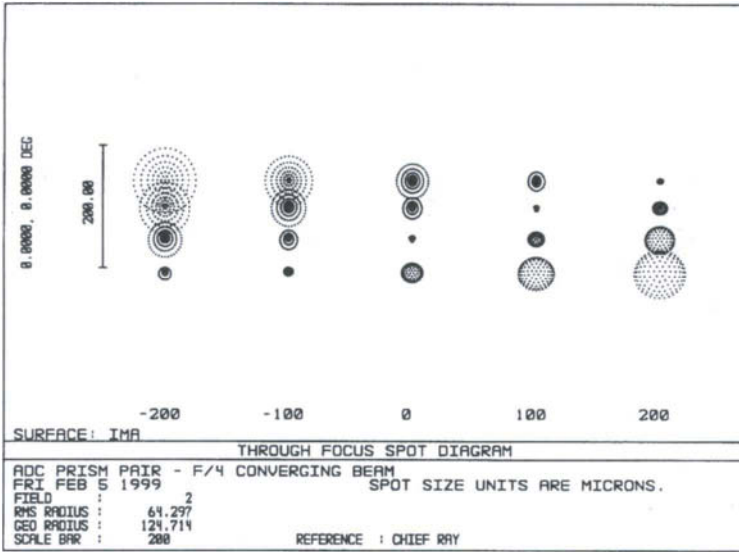


**Fig. 9.17.** Chromatic focal error for ADC in  $f/4$  beam set for maximum dispersion. All of the prism faces are plane. Wavelengths from top to bottom are 400, 435, 500, and 650 nm.

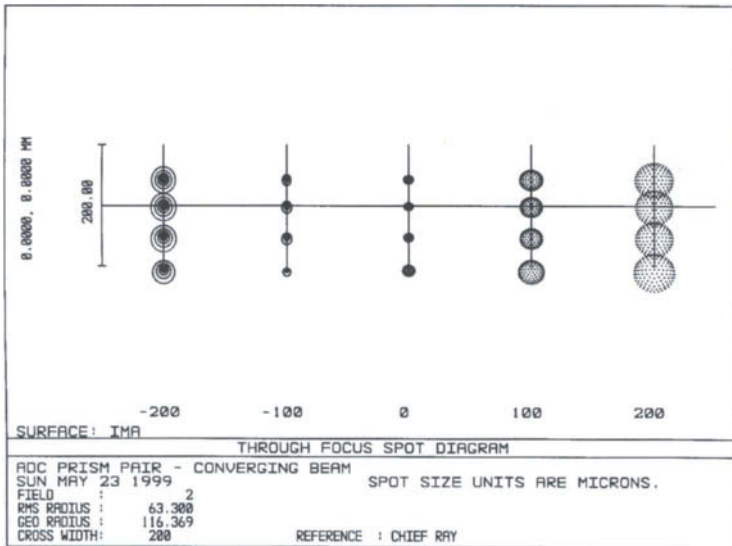


**Fig. 9.18.** Through-focus spot diagrams for ADC in  $f/4$  beam. The surfaces between the front and back pairs of the ADC have a radius of curvature of 5 m. Wavelengths from top to bottom are 400, 435, 500, and 650 nm.

any prism is essentially a plane-parallel plate plus a thin wedge. The effect due to the thickness is considered first.

The aberration coefficients for a plane-parallel plate of thickness  $t$  and index  $n$  are given in Eqs. (7.2.10)–(7.2.12), with  $\theta_1$  the angle of the chief ray at the first surface. Substituting these relations into Eq. (5.4.1) gives the results in Table 9.6, transverse aberrations for a plate in a converging beam. It is evident from the results in Table 9.6 that the aberrations are more significant for thicker plates (and multiple prisms as in an ADC) and faster beams.

The aberrations of a single thin wedge are derived in Section 15.6 and we take the important results from that discussion. Note that the coefficients for a wedge given in Eqs. (15.6.5) and (15.6.6) are simply the sum of the surface coefficients because the wedge is thin and the beam size is the same at both surfaces. Note also that these coefficients are expressed in terms of  $\varepsilon$  and  $\gamma$ , where the angle of incidence at the wedge of angle  $\gamma$  is  $\theta_1 = \varepsilon\gamma$ .

We substitute the coefficients in Eqs. (15.6.6) and (15.6.5) into Eq. (5.4.1) to get transverse coma and astigmatism, with these relations given in Table 9.7. Note that the relation for coma in Table 9.7 is independent of  $\varepsilon$ , hence it does not depend on the orientation of the wedge. Astigmatism, on the other hand, does depend on the wedge orientation.

The procedure used to find the aberration coefficients for a single prism is easily extended to that of a cemented double prism. As with a single prism, the pertinent coefficients are those of coma and astigmatism from Table 5.1, now written for each of the three surfaces. Because the wedge pair is thin, the sum of the surface coefficients is the coefficient for the wedge. We outline this procedure for coma.

**Table 9.6**

Transverse Aberrations of Plane-Parallel  
Plate in Converging Beam

$$\text{TSA} = 4A_{3p}y^3s' = \frac{(n^2 - 1)}{16n^3F^3} \left(\frac{t}{s}\right)s'$$

$$\text{TTC} = 3A_{2p}y^2s' = -\theta_1 \frac{3(n^2 - 1)}{8n^3F^2} \left(\frac{t}{s}\right)s'$$

$$\text{TAS} = 2A_{1p}ys' = \theta_1^2 \frac{(n^2 - 1)}{2n^3F} \left(\frac{t}{s}\right)s'$$

Table Symbols:  $t$  = thickness of plate of index  $n$ ;  $s' \cong s$ ;  $F = s/2y$  = focal ratio of converging beam.

Table 9.7

Transverse Aberrations of Single Thin Prism in Converging Beam

$$\text{TTC} = 3A_{2w}y^2s' = -\gamma \frac{3(n^2 - 1)}{8nF^2} s'$$

$$\text{TAS} = 2A_{1w}ys' = -\gamma^2 \frac{(n^2 - 1)}{2F} \left(1 - \frac{2\epsilon}{n}\right) s'$$

Table Symbols:  $\gamma$  = angle of wedge; angle of incidence =  $\epsilon\gamma$ ;  $F = s/2\gamma$  = focal ratio of converging beam;  $s'$  = distance from prism to focus.

Let the indices of refraction and wedge angles for the first and second prisms be denoted by  $n_1, \gamma_1$ , and  $n_2, \gamma_2$ , respectively, and let the surfaces in order be numbered 1 through 3. The coma coefficient for the prism pair in air is

$$A_2(\text{pair}) = \frac{\theta_1}{2s_1^2} \left(\frac{1 - n_1^2}{n_1^2}\right) + \frac{n_1\theta_2}{2s_2^2} \left(\frac{n_1^2 - n_2^2}{n_2^2}\right) + \frac{n_2\theta}{2s_3^2} (n_2^2 - 1), \quad (9.5.2)$$

where  $s_2 = n_1s_1$  and  $s_3 = n_2s_1$ . Although Eq. (9.5.2) can be evaluated for an arbitrary angle of incidence at the first surface and an arbitrary prism pair, we consider only the special case where  $\theta_1 = \gamma_1 - \gamma_2$ ,  $\theta_2 = -(n_2/n_1)\gamma_2$ ,  $\theta_3 = 0$ , and Eq. (9.5.1) applies. The prism described by these restrictions is the first half of the ADC shown in Fig. 9.13a,b. Evaluating Eq. (9.5.2) with these conditions gives the coma coefficient for a zero-deviation doublet prism as

$$A_{2z} = -\frac{\gamma_2(n_2 - n_1)(n_2 - 1)}{2n_1n_2s_1^2}, \quad (9.5.3)$$

where the subscript  $z$  denotes zero-deviation. Following the same procedure for the astigmatism gives

$$A_{1z} = \frac{\gamma_2^2(n_2 - n_1)(n_2 - 1)}{n_1(n_1 - 1)s_1} \quad (9.5.4)$$

Evaluation of Eq. (9.5.2) for an arbitrary angle of incidence gives Eq. (9.5.3) for any angle within the range over which the paraxial approximation is valid. A similar analysis for astigmatism gives a relation in which the dependence on the orientation of the prism pair is a factor. It turns out on further analysis that this dependence is only a minor factor for the range of angles likely to be encountered for an ADC in a typical telescope, hence Eq. (9.5.4) is acceptable as a measure of the astigmatism coefficient for all small angles of incidence.

Following the usual procedure of substituting the aberration coefficients into Eq. (5.4.1) we get the transverse aberrations for a zero-deviation doublet prism in Table 9.8. It is worth noting again that the contributions of coma and astigmatism given in Table 9.8 for a single doublet prism are constant over the field and do not include the prism thickness.

We are now in a position to determine coma and astigmatism for a full ADC. Consider first the coma due to the prism effect. When the dispersions add, as in the configuration in Fig. 9.13a, the comas of the pairs add and the resultant is twice that given in Table 9.8. When the configuration is that shown in Fig. 9.13b the comas of the pairs have opposite signs and the coma due to the wedge effect is zero. At other dispersions the coma is reduced from its maximum value by an amount equal to the fractional reduction in the dispersion.

For astigmatism due to the prism effect the aberration is a maximum when the configurations are as shown in Fig. 9.13a,b, and is zero when the prism pairs are at right angles with respect to one another.

#### 9.5.d. DISCUSSION OF ABERRATION RESULTS

For actual thin prisms, such as those used in the preceding examples, the net aberrations are simply the sum due to both thickness and wedge effect. For an ADC configured as in Fig. 9.13a, the net transverse coma is the sum of TTC from Table 9.6 and 2 TTC from Table 9.8. A similar sum gives the net astigmatism for an ADC in this configuration.

We now calculate the various transverse aberrations at  $\lambda = 435 \text{ nm}$  and  $\theta = 1^\circ$  for the ADC giving the spot patterns shown in Fig. 9.15. All of the following results are given in microns. For a total central thickness of 40 mm we find

**Table 9.8**

Transverse Aberrations of Zero-Deviation  
Doublet Prism<sup>a</sup> in Converging Beam

$$\text{TTC} = 3A_{22}y^2s' = -\gamma_2 \frac{3(n_2 - n_1)(n_2 - 1)}{8n_1n_2F^2} s'$$

$$\text{TAS} = 2A_{12}ys' = \gamma_2^2 \frac{(n_2 - n_1)(n_2 - 1)}{n_1(n_1 - 1)F} s'$$

<sup>a</sup> zero-deviation condition:

$$(n_1 - 1)\gamma_1 = (n_2 - 1)\gamma_2.$$

Table Symbols:  $F = s/2y$  = focal ratio of converging beam;  $s'$  = distance from prism to focus. Angular aberration subtended on sky =  $\text{TA}/f$ ,  $f$  = telescope focal length.

TSA = 14.6, TTC = -6.0, TAS = 0.6; for the wedge effect we get TTC = -2.6 and TAS = 2.0. The only difference for the spot patterns in Fig. 9.16 is that TTC = 0 for the wedge effect.

From these numbers we see that coma due to thickness is more significant than that due to the wedge effect. We can use the signs and relative sizes of the coma numbers to account for the differences between positive and negative  $\theta$  seen in Figs. 9.15 and 9.16. We also see that spherical aberration is a factor in this  $f/4$  beam, but that astigmatism is relatively unimportant.

The sizes of the computed aberrations suggest that the example ADC could be used in a beam faster than  $f/4$  without undue image degradation. This is not the case, however, because the elimination of the chromatic focal error by putting a radius of curvature at the oiled contact introduces a significant amount of spherical aberration, as is evident from the images at best focus in Fig. 9.18. Because of this curvature factor, the use of an ADC with plane outer faces in a converging beam is limited to beams no faster than  $f/5$  or  $f/6$ , with detailed analysis based on ray traces required over the entire range of wavelengths to ensure adequate image quality.

#### 9.5.e. EXAMPLE: ADC IN RITCHEY-CHRETIEN TELESCOPE

The previous examples illustrate the principles of an ADC in a collimated beam and a converging beam, but do not relate the characteristics of an ADC, angles and locations in the beams, to the correction of atmospheric dispersion. Doing the latter requires selecting a telescope and maximum zenith angle at which atmosphere refraction is corrected. We choose a 3.6-m RC telescope with the parameters given in Table 6.10, but with  $F_1 = 1.5$  and  $F = 6$ , and a maximum zenith angle  $\alpha_0 = 68.2^\circ$  ( $\tan \alpha_0 = 2.5$ ). We again use UBK7 and LLF6 glasses.

With the needed parameters in hand, we proceed to match an ADC to the chosen telescope. From Fig. 9.12 we get a differential atmospheric refraction of 1.40 arc-sec between 400 and 650 nm when the zenith angle is  $45^\circ$ . Scaling this to the maximum zenith angle by using Eq. (3.6.3) gives a maximum difference in refraction of 3.5 arc-sec between 400 and 650 nm. The telescope in this example has a focal length  $f = 21.4$  m and a scale of  $105 \mu\text{m}/\text{arc-sec}$ . Thus the ADC in the Cassegrain beam must give a maximum separation at the focal surface of about  $366 \mu\text{m}$  between these wavelengths to compensate for the atmospheric dispersion.

Our previous example, located 500 mm from focus, gives a separation of  $150 \mu\text{m}$  between 400 and 650 nm. Increasing this by the required factor of 2.44 means either: (a) an increase in the prism angles by this factor with no change in distance from focus, (b) an increase in distance from focus by this factor with no change in angles, or (c) some combination of the two. Choosing between these

options requires analysis of image quality over the desired field, an exercise not done here.

For this example we choose option (b) and place the first surface of our example ADC at 1220 mm from the nominal telescope focus. Because the ADC is farther from focus, hence larger in diameter, we give each prism a central thickness of 20 mm. From ray traces we find that a radius of curvature of 15 m at the interface between the doublet prisms eliminates the chromatic focal error. The resulting spot patterns at three field angles and four wavelengths are shown in Fig. 9.19. Spot patterns for the telescope without an ADC are roughly comparable to those for  $\lambda = 500$  nm. Although the images with an ADC are larger than those of a bare telescope, the latter is restricted to small zenith angles or narrowband filters to achieve comparable image quality.

9.5.f. CONCLUDING REMARKS

For faster beams, such as at prime focus, spherical aberration and coma due to the thickness of the prisms makes the images unacceptably large. Wynne (1986) has pointed out that it is possible to design an acceptable ADC if each equivalent

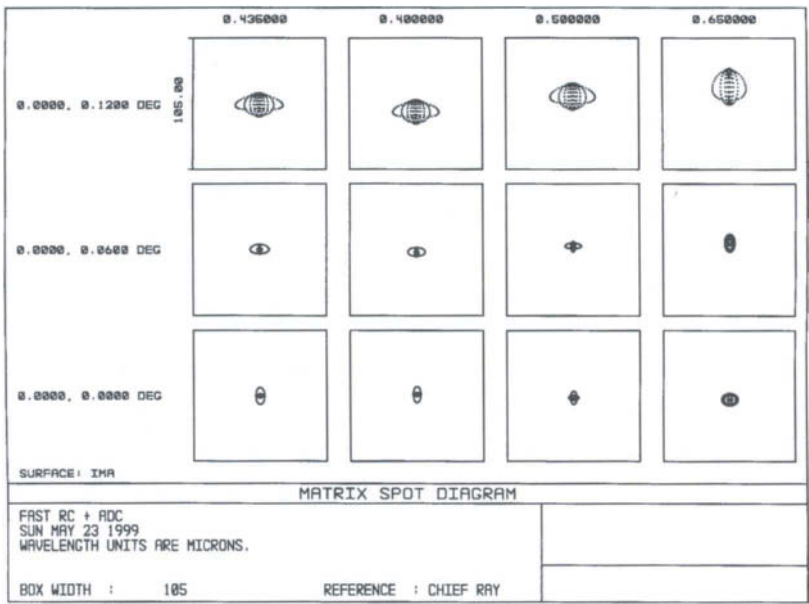


Fig. 9.19. Spot diagrams for selected wavelengths and field angles for a 3.6-m RC telescope with an ADC in the  $f/6$  Cassegrain beam. Box width is 1 arc-sec. See the text for discussion.

plane-parallel plate is replaced by a meniscus lens. Except for the wedge added to make each lens a prism, the curved surfaces of these lenses have a common center of curvature at the on-axis focus of the telescope. The interested reader should consult the article by Wynne for further details. A design of an ADC in an  $f/1.6$  beam in a wide-field 3-mirror telescope has been given by Willstrop (1987).

Finally, it is important to note that the differential dispersion produced by an ADC is not generally a mirror image of that due to the atmosphere. As a consequence the exact compensation at a pair of wavelengths may leave residual dispersions at other wavelengths. Wynne and Worswick show that the residual dispersion for the UBK7-LLF6 combination is approximately 0.4 arc-sec for a zenith angle  $\alpha_0 = 71.6^\circ$ . This residual scales as the tangent of the zenith angle and is 0.13 arc-sec at  $\alpha_0 = 45^\circ$ .

## 9.6. FIBER OPTICS

With the development of high-efficiency optical fibers to pipe light from one point in space to another, astronomers have found a tool that is revolutionizing spectroscopy. Individual fibers placed on stellar sources at a telescope focal surface have their opposite ends aligned along the slit of a spectrometer, and the result is *multiple-object spectroscopy* (MOS). By this means, the observing efficiency of a telescope is increased dramatically. In this section we outline the characteristics of optical fibers, especially those of importance to astronomers. Our discussion follows an excellent review article by Barden (1995).

The type of fiber most often used is a multimode, stepped-index fiber. This kind of fiber consists of a high index of refraction glass core surrounded by a sheath of a lower index glass called a cladding. Core diameters used in MOS are generally in the range of 50 to 500  $\mu\text{m}$ , and the thickness of the cladding is typically about one-tenth that of the core. Light is guided through the core by total internal reflection that takes place at the interface between the core and cladding. A plastic outer coating called a buffer protects the glass fiber. A common way of giving the size of a fiber is core/cladding/buffer in  $\mu\text{m}$ , such as 200/220/240. Characteristics of particular interest in MOS are spectral transmittance, focal ratio degradation, and image scrambling. We now consider each of these in turn.

Transmission as a function of wavelength depends in large part on the OH content of the fiber core. Fibers with high OH content, so-called wet fibers, have poor transmittance in the red and near-infrared but are good transmitters in the near-ultraviolet. Dry fibers with low OH content have excellent transmittance in the 1–2  $\mu\text{m}$  range, but are not suitable for wavelengths shorter than about 500 nm. It has been found that hydrogen-doped dry fibers have good transmittance from

the infrared and to wavelengths as short as 400 nm. Typical fiber lengths required with large telescopes are in the 20-m range. The total transmittance over this length, including a reflection loss of 4% at each end, is about 90% for a dry fiber at 1  $\mu\text{m}$ . Curves of transmittance as a function of wavelength can be found in the cited article by Barden.

The transfer of the light from a star at the focus of a telescope via a fiber to a spectrometer is most efficient if the output focal ratio from the fiber ( $F_{\text{out}}$ ) is equal to the input focal ratio at the telescope focus ( $F_{\text{in}}$ ). It turns out that all fibers tend to increase the cone angle of the output beam compared to the input beam, that is,  $F_{\text{out}} < F_{\text{in}}$ , an effect called *focal ratio degradation* (FRD). This degradation depends on several factors, including mechanical stresses induced by bending that deforms the cylindrical shape of the fiber. An excellent review of FRD, including a discussion of the mechanisms responsible for FRD, is given by Ramsey (1988).

Extensive measurements of FRD on a variety of fibers show that faster input focal ratios are more nearly preserved than slower ones. Figure 9.20 shows typical results for  $F_{\text{out}}$  plotted as a function of  $F_{\text{in}}$ . Each curve indicates the fraction of light collected by the collimator of a spectrometer for different input focal ratios. It is clear from the results in Fig. 9.20 that the normal design of a spectrometer with  $F_{\text{col}} = F_{\text{tel}}$  is not appropriate for a fiber-fed spectrometer. The options are to increase the diameter of the collimator to capture most of the light from the fiber or live with substantially less dispersed light because of light loss at the

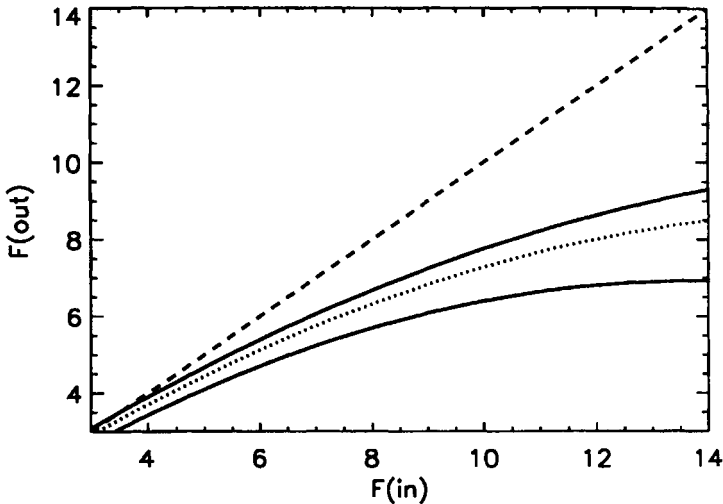


**Fig. 9.20.** Representative curves for focal ratio degradation (FRD).  $F(\text{in})$  is the beam focal ratio at a fiber input;  $F(\text{out})$  is the focal ratio of the emerging beam for different fractions collected at that focal ratio. Fraction collected: Lowest curve, 1.0; Dot-dot curve, 0.95; Upper solid curve, 0.90.

collimator. As pointed out by Ramsey, either represents a loss for spectroscopy. A full discussion of the effect of FRD on resolution-throughput products is found in Section 12.3.

The final characteristic we consider is that of *image scrambling*, the mixing of the input light both radially and azimuthally by a fiber to produce a uniform output beam. In effect, the output from a fiber has no memory of the distribution of light on the input end of the fiber. This is especially important for spectrometers used to measure wavelengths to very high precision, as in the search for planets and other faint stellar companions from measures of changing radial velocities. The interested reader should consult the excellent review by Heacox (1995).

This section is a brief introduction to a large topic. The work in this field is well covered in conference proceedings edited by Barden (1988) and cited at the end of this chapter.

## REFERENCES

- Barden, S. (1995). *Proc. SPIE Int. Soc. Opt. Eng.*, **2476**: 2.  
 Bowen, I. And Vaughan, A. (1973). *Appl. Opt.*, **12**: 1430.  
 Gascoigne, S. (1973). *Appl. Opt.*, **12**: 1419.  
 Meinel, A., Meinel, M. and Wang, Y. (1985). *Appl. Opt.*, **24**: 2751.  
 Ramsey, L. (1988). In *Fiber Optics in Astronomy*, Barden, S. (ed.), Astron. Soc. Pac. Conf. Series **3**, 26.  
 Wilson, R. (1971). *ESO/CERN Conference on Large Telescope Design*, p. 131, Geneva: European Southern Observatory.  
 Wynne, C. (1972). *Progress in Optics*, vol. 10, Chap. 4, Amsterdam: North-Holland.  
 Wynne, C. (1974). *Mon. Not. R. Astron. Soc.*, **167**: 189.  
 Wynne, C. (1984). *The Observatory*, **104**: 140.  
 Wynne, C. (1986). *The Observatory*, **106**: 163.  
 Wynne, C. and Worswick, S. (1986). *Mon. Not. R. Astron. Soc.*, **220**: 657.

## BIBLIOGRAPHY

- Barden, S. (ed.). (1988). *Fiber Optics in Astronomy*, Astron. Soc. Pac. Conf. Series, **3**.  
 Barden, S. (ed.). (1995). *Proc. SPIE Int. Soc. Opt. Eng.*, **2476**.  
 Heacox, W. (1995). *Proc. SPIE Int. Soc. Opt. Eng.*, **2476**: 204.  
 Meinel, A. (1953). *Astrophys. J.*, **118**: 335.  
 Opal, C. and Booth, J. (1995). *Proc. SPIE Int. Soc. Opt. Eng.*, **1235**: 263.  
 Willstrop, R. (1987). *Mon. Not. R. Astron. Soc.*, **225**: 187.  
 Wilson, R. (1996). *Reflecting Telescope Optics I*, Berlin: Springer.

The discussion of telescopes and their aberrations in previous chapters is entirely from the point of view of geometric optics. This approach is one in which the ray is a well-defined entity, with the wavelength in the geometric optics limit effectively zero. The paths of rays through an optical system are governed by Fermat's principle and aberrations occur when rays do not pass through the paraxial image point. An aberration-free image in the geometric optics limit is, according to Fermat's principle, a true point image. It was pointed out in Section 3.7, however, that the wave nature of light sets the image size for an otherwise perfect or diffraction-limited optical system, with the analysis there intended only to give an estimate of the size of the diffraction image.

In this chapter and the next the emphasis is on the character of the perfect image from the point of view of diffraction theory. Because no optical system is strictly perfect, we also consider the effect of the aberrations of a nearly perfect optical system on the diffraction image. Our analysis proceeds along two lines. In this chapter the starting point is Huygens' principle and the superposition of waves from points on a wavefront. In the following chapter the analysis is in terms of transfer functions, with application to the imaging capability of the Hubble Space Telescope (HST) expected before its launch.

As part of our discussion of the near-perfect image, we generalize our representation of its characteristics in terms of transverse aberrations and introduce orthogonal aberrations in terms of Zernike polynomials. With this representation we find that giving image quality in terms of root mean square (rms) wavefront error is especially informative. Our discussion includes a

comparison between image size for the near-perfect image found by diffraction theory and that from geometric aberration theory as given in Chapter 5.

Before discussing the nature of a perfect image as formed by a telescope with a circular or annular aperture, we discuss Huygens' principle and its extension by Fresnel. This principle is the basis for diffraction theory and the Fresnel-Kirchhoff diffraction integral. We first apply this theory to a rectangular aperture. The mathematics is a bit simpler in this case and the results, although of interest in their own right, are especially useful in situations where the rectangular aperture reduces to a narrow slit, as in many types of spectrometers.

Our analysis is limited to the special case of Fraunhofer diffraction and parallels that given in most optics texts, such as those by Hecht (1987) or Born and Wolf (1980), with the notation basically that of the latter authors.

## 10.1. HUYGENS-FRESNEL PRINCIPLE

The initial statement of Huygens' principle was made in an attempt to understand the laws of reflection, refraction, and the propagation of light. He started with the assumption that light was a wave and could be described in terms of wavefronts. From the point of view of Fermat's principle, a wavefront is a surface on which every point has the same optical path distance from a point source of light. Viewed as a wave, a wavefront is a surface on which every point has the same phase. Huygens postulated that at a given time each point on a primary wavefront acts as a source of secondary spherical wavelets, and that the envelope of these wavelets at a slightly later time is the new primary wavefront. He further stated that these secondary wavelets propagate with a speed and frequency equal to that of the primary wave.

This statement suffices to account for the laws of reflection and refraction, and the approximately straightline propagation of light through large apertures, but it fails to account for diffraction, the deviations from exact straightline propagation of light. Fresnel extended Huygens' principle by assuming that the secondary wavelets interfere with one another according to the principle of superposition. His statement postulated that each unobstructed point on a wavefront is a source of spherical wavelets, and that the amplitude of the wave at any point ahead of the wavefront is the superposition of all of these wavelets. In adding these wavelets it is necessary to include the amplitude and phase of each wavelet. The Huygens-Fresnel principle was put on a firm theoretical basis by Kirchhoff and expressed as an integral derived from the wave equation. Details of the derivation of the Fresnel-Kirchhoff diffraction integral can be found in Born and Wolf (1980) or any intermediate optics text.

For our purposes we are interested only in the special case of *Fraunhofer diffraction*, that in which the source of light and the field point of interest are effectively at infinity relative to the aperture. In practice this is accomplished in a lab by collimating the light from a point source, passing that light through an aperture, and observing the diffraction pattern in the focal plane of a lens following the diffracting aperture. Thus the image of a star formed by a telescope or, equivalently, the converging spherical wave diffracted by the exit pupil of the telescope, is a Fraunhofer diffraction pattern.

10.1.a. FRAUNHOFER DIFFRACTION: RECTANGULAR APERTURE

The layout for a rectangular aperture is shown in Fig. 10.1, with a spherical wavefront  $W$  of radius of curvature  $R$  emerging from the aperture of sides  $2a$  and  $2b$ . An arbitrary point  $Q$  on the spherical wavefront has coordinates  $(\xi, \eta, \zeta)$ , with the origin of this coordinate system at the center of the rectangle. An arbitrary field point  $P$  has coordinates  $(x, y, z)$  with the origin  $O$  of this system at distance  $R$  along the  $\zeta$  axis. The wave amplitude  $U$  at point  $P$  is the sum of all amplitude contributions from each area  $dS$  on the wavefront. For all cases of interest we assume the dimensions of the rectangle and the distance of point  $P$  from the origin of its coordinate system are small compared to  $R$ . When these conditions are satisfied, the sum of the contributions from each  $dS$  is a simple scalar sum given by

$$U(P) = C \int_w \exp [ik(s - R)]dS, \tag{10.1.1}$$

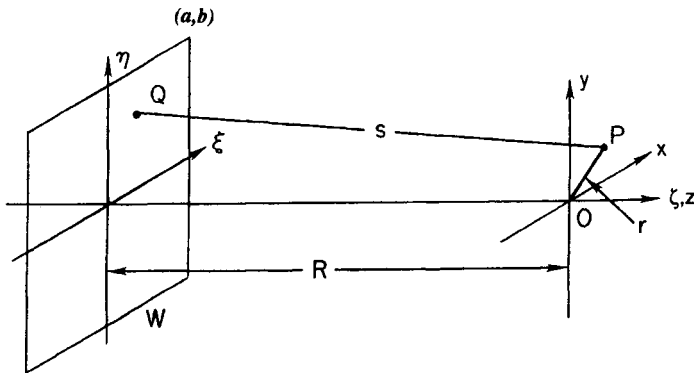


Fig. 10.1. Coordinate frames at exit pupil  $(\xi, \eta, \zeta)$  of rectangular aperture and image surface  $(x, y, z)$  of optical system.  $W$  is a spherical wavefront of radius  $R$  centered at  $O$ . See Eq. (10.1.1).

where  $k = 2\pi/\lambda$ ,  $s$  is the distance from  $Q$  to  $P$ ,  $C$  is a constant proportional to the amplitude at  $Q$ , and the integration is over the unobstructed wavefront.

As noted in the foregoing, the center of curvature of the wavefront is at point  $O$ . For this particular point  $P$  we have  $s = R$  for all points  $Q$  on the wavefront, hence all waves are in phase at  $O$ . Therefore the argument in Eq. (10.1.1) is zero and the integral gives the area of the rectangle. Because all waves are in phase at  $O$ , the amplitude  $U(O)$  is a maximum. For any other  $P$  the path and phase differences are  $(s - R)$  and  $k(s - R)$ , respectively, and the amplitude at  $P$  is less than that at  $O$ .

Expressing  $s$  in terms of the coordinates of  $Q$  and  $P$ , relative to the origin at  $O$ , we get

$$\begin{aligned} s^2 &= (\xi - x)^2 + (\eta - y)^2 + (\zeta - z)^2, \\ &= R^2 - 2(x\xi + y\eta + z\zeta), \end{aligned} \quad (10.1.2)$$

where all squared terms in  $x, y$ , and  $z$  are negligible. With  $s$  nearly equal to  $R$ , given our assumption about distances in the preceding, we have  $s^2 - R^2 = (s - R)(s + R) \cong 2R(s - R)$ . Substituting this relation into Eq. (10.1.2) gives

$$\begin{aligned} s - R &= -\frac{x\xi + y\eta + z\zeta}{R} \\ &= -\frac{x\xi + y\eta}{R} + z\left(1 - \frac{\xi^2 + \eta^2}{2R^2}\right). \end{aligned} \quad (10.1.3)$$

At this point we define  $p = x/R$ ,  $q = y/R$ , where  $p$  and  $q$  are the direction cosines of a line from the center of the rectangle to  $P$ . Setting  $z = 0$  to limit our analysis to the paraxial focal plane, we substitute the remaining terms into Eq. (10.1.1) and get

$$\begin{aligned} U(P) &= C \int_{-a}^a \int_{-b}^b \exp(-ik(p\xi + q\eta)) d\xi d\eta \\ &= C \int_{-a}^a \exp(-ikp\xi) d\xi \int_{-b}^b \exp(-ikq\eta) d\eta. \end{aligned} \quad (10.1.4)$$

Evaluating the integral we get

$$U(P) = CA \left( \frac{\sin kpa}{kpa} \right) \left( \frac{\sin kqb}{kqb} \right) = CA \left( \frac{\sin v_x}{v_x} \right) \left( \frac{\sin v_y}{v_y} \right), \quad (10.1.5)$$

where  $A = 4ab$  is the area of the rectangular aperture, and  $v_x$  and  $v_y$  are dimensionless variables.

The intensity at point  $P$  of an image is the absolute square of the time-averaged amplitude of the electromagnetic wave at  $P$ , while the *point spread*

function (PSF) at  $P$  is the intensity normalized to unity at the point where the intensity is a maximum. Denoting the intensity at the center of the image by  $I_0$ , and the PSF at point  $P$  by  $i(P)$ , we get

$$i(P) = \frac{i(P)}{I_0} = \left( \frac{\sin v_x}{v_x} \right)^2 \left( \frac{\sin v_y}{v_y} \right)^2, \quad (10.1.6)$$

where  $I_0 = C^2 A^2$ .

A two-dimensional (2D) surface plot of  $i(P)$  for a square aperture is shown in Fig. 10.2, with  $i(P) > 0.1$  removed to enhance the secondary peaks. A semilog plot of the function  $X = (\sin v_x/v_x)^2$  is shown in Fig. 10.3. Note that the function  $X$  is zero when  $v_x = \pm n\pi$ , where  $n$  is any nonzero integer. Hence the plot in Fig. 10.3 of  $X$  versus  $v_x/\pi$  shows the minima at integer values.

Of particular interest is the minimum with  $n = 1$  adjacent to the principal maximum. At this minimum  $v_x = \pi = (2\pi/\lambda) pa$ , hence

$$p_1 = x_1/R = \lambda/2a. \quad (10.1.7)$$

From Eq. (10.1.7) we see that the linear distance between minima on opposite sides of the main peak is  $2x_1$ . We also find that the *full-width-half-maximum* (FWHM) of the principal peak is approximately  $0.9x_1$ . The corresponding angular distances are  $2p_1$  and  $0.9p_1$ , where the latter is the angle subtended by the FWHM at the aperture.

The importance of Eq. (10.1.7) in angular terms cannot be overemphasized. *For a point source, the angular FWHM in a given direction is approximately the wavelength divided by the width of the aperture in that direction.* The larger is the width, the smaller is the angular size. The only difference between apertures of

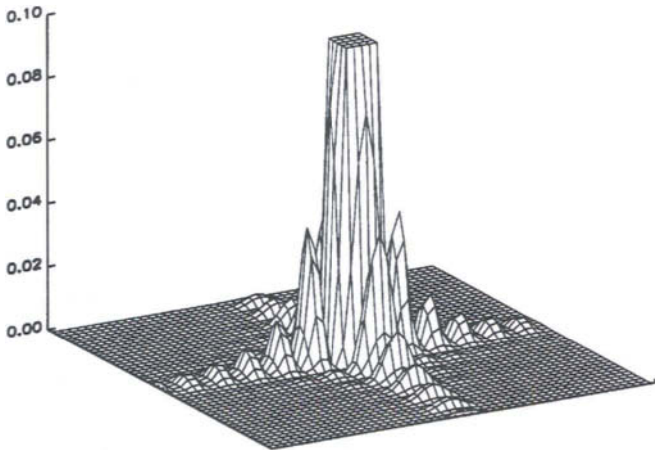


Fig. 10.2. Surface plot of  $i(P) < 0.1$  for a square aperture.

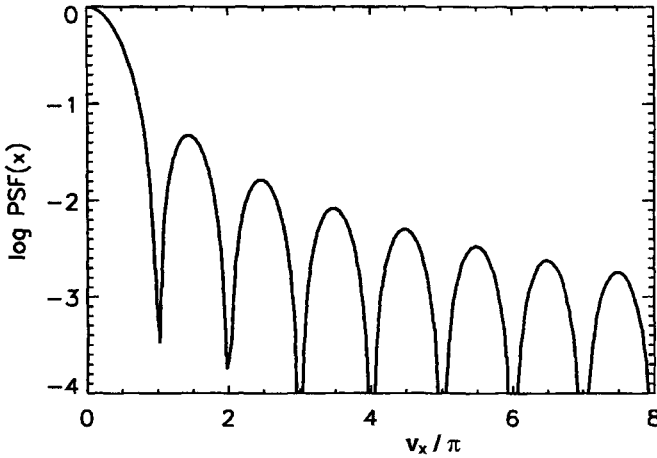


Fig. 10.3. Slice of  $i(P)$  for a square aperture along the  $x$ -axis.

different shape is the numerical factor of order unity that multiples wavelength/width.

The decrease in the PSF in the wings of the diffraction pattern beyond a few bright fringes is best described in terms of a *locally smoothed* PSF. Across a fringe the average value of  $\sin^2 v = 0.5$ , hence along the  $x$ -axis

$$\langle i(P) \rangle_x = \frac{1}{2\langle v_x \rangle^2} = \frac{1}{2\pi^2} \left( \frac{\lambda}{2a} \right)^2 \frac{1}{p^2}, \tag{10.1.8}$$

with a similar relation along the  $y$ -axis. In the case of a square aperture of side  $2a$ , the average PSF along the diagonal of the diffraction pattern  $x = \pm y$  is

$$\langle i(P) \rangle_{x=y} = \frac{1}{4\langle v \rangle^4} = \frac{1}{4\pi^4} \left( \frac{\lambda}{2a} \right)^4 \frac{1}{p^4}. \tag{10.1.9}$$

For a circular or annular aperture the decrease in the PSF is proportional to  $1/\alpha^3$ , where  $\alpha$  is the field angle. It is an interesting exercise to compare the average PSF in the wings of an image for a circular aperture, given in Eq. (10.2.12), with that of a square aperture, and consider the possible advantages of using the latter in the search for faint stellar companions.

The enclosed energy EE is defined as the fraction of the total energy E within an area of sides  $(2x, 2y)$  centered on the PSF, where E is proportional to the

integral of  $i(P)$  over the entire receiving plane. In terms of dimensionless variables we have

$$EE = \int_{-v_{x0}}^{v_{x0}} \int_{-v_{y0}}^{v_{y0}} i(P) dv_x dv_y / \iint_{-\infty}^{\infty} i(P) dv_x dv_y. \quad (10.1.10)$$

For a square aperture of side  $2a$  we take a square area of side  $2x$  at the PSF. To find EE for the principal maximum we have  $x = x_1$ ,  $v_{x0} = v_{y0} = \pi$ . Substituting for  $i(P)$  from Eq. (10.1.6) and evaluating Eq. (10.1.10) at these limits, we find  $EE = 0.815$  for the principal maximum. Within a square enclosing the FWHM we get  $EE = 0.52$ .

The final item of interest for a rectangular aperture is the case where  $a \ll b$ , hence a narrow slit in the  $y$  direction. In the limiting case where the slit is effectively infinite in length, it is appropriate to consider the distant source as a line rather than a point and the wavefront  $W$  in Fig. 10.1 as cylindrical. As a result there is no dependence on  $y$  and the resulting diffraction pattern is the  $x$ -part only of Eq. (10.1.6). The pattern consists of a series of bright and dark fringes parallel to the source and slit.

## 10.2. PERFECT IMAGE: CIRCULAR APERTURE

We now apply the Fresnel-Kirchhoff diffraction integral to the case of a circular aperture with a central obscuration, as is the usual case for a telescope. Our analysis is done for an annular aperture with an obscuration of diameter  $\epsilon D$ , from which results for a clear aperture follow with  $\epsilon$  set to zero.

As shown in the previous section, the characteristics of the image of a point source object formed by a perfect optical system are completely described by the point spread function (PSF) and quantities derivable from it. One of the quantities derived from the PSF is the encircled energy fraction (EE); for a circular or annular aperture this is the fraction of the total energy in the image within a circle of a given radius centered on the PSF. The intensity in units of flux per unit area at a point on the image is directly proportional to the PSF, while the average intensity over a centered portion of an image depends on both the PSF and EE. Derivation of each of these items in this section parallels that for the rectangular aperture.

### 10.2.a. POINT SPREAD FUNCTION

Consider the exit pupil of an optical system with radius  $a$ , as shown in Fig. 10.4, with a spherical wavefront  $W$  of radius of curvature  $R$  emerging from the

pupil. As in Fig. 10.1, an arbitrary point  $Q$  on the wavefront in Fig. 10.4 has coordinates  $(\xi, \eta, \zeta)$  and is a distance  $\rho a$  from the  $z$ -axis at angle  $\varphi$  with the  $\xi$  axis. For an annular aperture with central obscuration of radius  $\varepsilon a$ ,  $\rho$  is in the range  $\varepsilon$  to 1. An arbitrary field point  $P$  is a distance  $r$  from the  $z$ -axis at angle  $\psi$  with the  $x$  axis. Relative to the origin at  $O$ , the coordinates for points  $Q$  and  $P$  are

$$\begin{aligned}\xi &= a\rho \cos \varphi, & x &= r \cos \psi, \\ \eta &= a\rho \sin \varphi, & y &= r \sin \psi, \\ \zeta &= -\sqrt{(R^2 - a^2\rho^2)}.\end{aligned}\quad (10.2.1)$$

For all systems of interest we assume the distances  $z$ ,  $r$ , and  $a$  are small compared to  $R$ . When these conditions are satisfied, the sum of the contributions from each  $dS$  on the wavefront is given by Eq. (10.1.1), where the distance  $s$  from  $Q$  to  $P$  is given by Eq. (10.1.2).

Substituting Eqs. (10.2.1) into Eq. (10.1.2) gives

$$s - R = -\frac{a\rho r}{R} \cos(\varphi - \psi) + z \left[ 1 - \frac{1}{2} \left( \frac{a\rho}{R} \right)^2 \right], \quad (10.2.2)$$

where  $\zeta$  in Eqs. (10.2.1) is transformed by the binomial expansion. Following Born and Wolf, we define dimensionless variables  $u$  and  $v$  in the form

$$u = \frac{2\pi}{\lambda} \left( \frac{a}{R} \right)^2 z, \quad v = \frac{2\pi}{\lambda} \left( \frac{a}{R} \right) r. \quad (10.2.3)$$

Substituting Eqs. (10.2.3) into Eq. (10.2.2) gives

$$k(s - R) = -v\rho \cos(\varphi - \psi) - \frac{u\rho^2}{2} + u \left( \frac{R}{a} \right)^2. \quad (10.2.4)$$

The introduction of these dimensionless variables is made for convenience in relations involving aberrations to follow in subsequent sections.

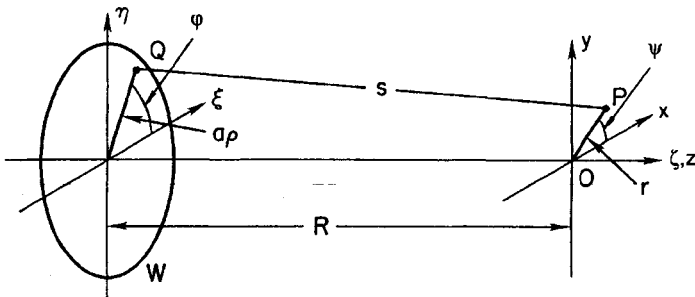


**Fig. 10.4.** Coordinate frames at exit pupil  $(\xi, \eta, \zeta)$  of circular aperture and image surface  $(x, y, z)$  of optical system.  $W$  is a spherical wavefront of radius  $R$  centered at  $O$ . See Eq. (10.2.1).

At this point we set  $u = 0$  and evaluate  $U(P)$  in the paraxial focal plane. Noting that the area element  $dS = a^2 \rho d\rho d\varphi$ , the amplitude in the paraxial focal plane is given by substituting Eq. (10.2.4) with  $u = 0$  into Eq. (10.1.1). The result is

$$U(P) = Ca^2 \int_0^{2\pi} \int_\epsilon^1 \exp[-iv\rho \cos(\varphi - \psi)] \rho d\rho d\varphi. \quad (10.2.5)$$

To carry out the integration over  $\varphi$  we note that  $U(P)$  is independent of  $\psi$  because the system is symmetric about the  $z$  axis. Therefore we can choose any convenient value for  $\psi$ ; we choose  $\psi = \pi$ . Carrying out the integration over  $\varphi$  involves substituting the integral representation of  $J_0$ , the Bessel function of order zero, with the result

$$U(P) = 2\pi a^2 C \int_\epsilon^1 J_0(v\rho) \rho d\rho = \frac{2\pi a^2 C}{v^2} \int_\epsilon^1 d[v\rho J_1(v\rho)]. \quad (10.2.6)$$

The second step in Eq. (10.2.6) follows after substituting one of the recurrence relations for Bessel functions found in tables of mathematical functions (see, e.g., "Tables of Integrals and Other Mathematical Data" by Dwight (1961)). Integration of Eq. (10.2.6) gives

$$U(P) = \pi a^2 C \left[ \frac{2J_1(v)}{v} - \epsilon^2 \frac{2J_1(\epsilon v)}{\epsilon v} \right], \quad (10.2.7)$$

where  $J_1$  is a Bessel function of order one. The ratio  $2J_1(w)/w$  approaches one as  $w$  approaches zero, hence  $U(O) = \pi a^2 C(1 - \epsilon^2)$ .

Using this result, we write the PSF at point  $P$  as

$$i(P) = \frac{I(P)}{I_0} = \frac{1}{(1 - \epsilon^2)^2} \left[ \frac{2J_1(v)}{v} - \epsilon^2 \frac{2J_1(\epsilon v)}{\epsilon v} \right]^2, \quad (10.2.8)$$

where  $I(P) = |U(P)|^2$  and  $i(P) = \text{PSF}$ . It is convenient to represent the intensity in this form to facilitate comparison of intensity profiles for apertures with different central obscurations. As examples, semilog plots of PSFs are shown in Fig. 10.5 for  $\epsilon = 0$ , a clear aperture, and  $\epsilon = 0.33$ , the obscuration of the Hubble Space Telescope. Note that the ordinate in Fig. 10.5 is  $v/\pi$ . A 2D surface plot of  $i(P)$  for a clear aperture is shown in Fig. 10.6, with  $i(P) > 0.1$  removed to enhance the rings around the main peak.

The PSF given by Eq. (10.2.8) and shown in Figs. 10.5 and 10.6 is in the paraxial focal plane and characterizes the so-called *Airy pattern*. The intensity is a maximum at the paraxial image point at  $v = 0$ , and the pattern is a central bright disk, the Airy disk, surrounded by concentric bright and dark rings. For a clear aperture the peak intensity of successive bright rings decreases monotonically as  $v$  increases; for an obstructed aperture the intensity of successive bright rings decreases in a cyclic manner, depending on the specific value of  $\epsilon$ .

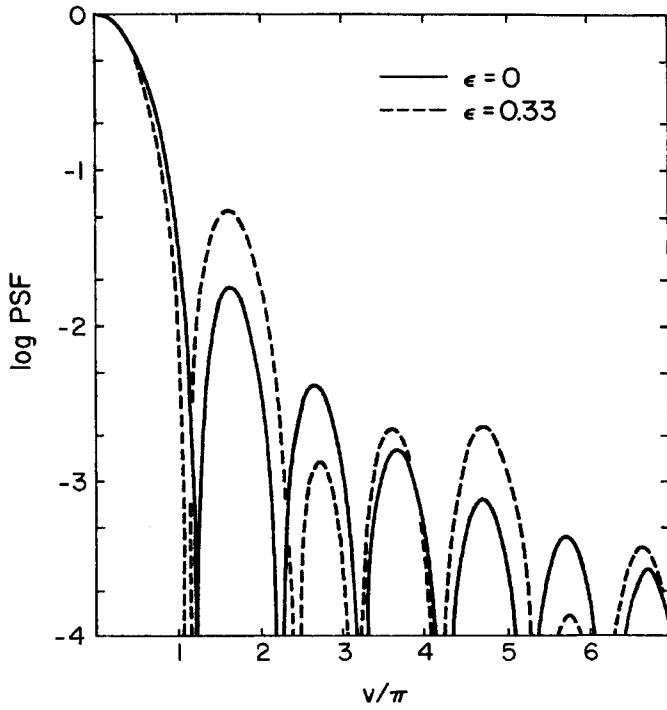


Fig. 10.5. Point spread function of perfect image for obscuration ratios  $\varepsilon = 0$  (solid line) and  $\varepsilon = 0.33$  (dashed line).

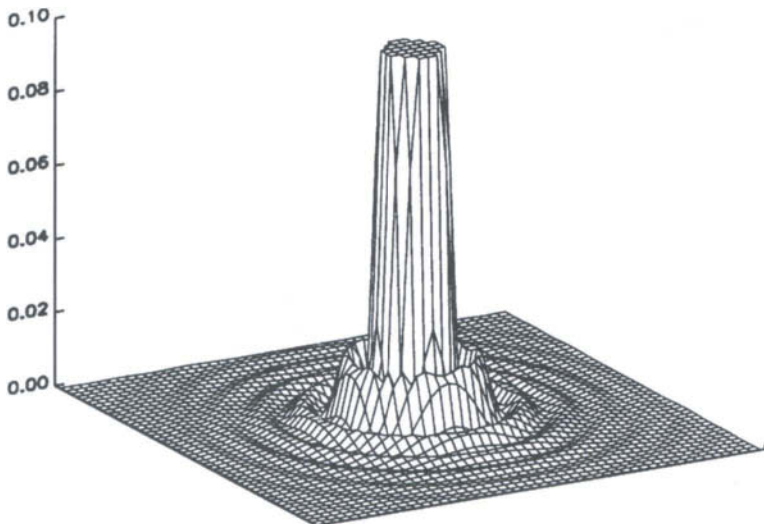


Fig. 10.6. Surface plot of  $i(P) < 0.1$  for a circular aperture with  $\varepsilon = 0$ .

The radii of the dark rings in the Airy pattern are found by setting  $i(P) = 0$ . Radii for the first three dark rings are given in Table 10.1 for several values of  $\varepsilon$ . Note that the radius of the first dark ring, which encloses the Airy disk, decreases as  $\varepsilon$  increases, while the radius of the second dark ring is a maximum near  $\varepsilon = 0.3$  and decreases for larger obscurations.

One important descriptor of the Airy pattern is the radius of the first dark ring. Substituting  $v_1$  from Table 10.1 with  $\varepsilon = 0$  into Eqs. (10.2.3) gives

$$r_1 = 1.22\lambda F, \quad \alpha_1 = \frac{r_1}{f} = 1.22 \frac{\lambda}{D}, \quad (10.2.9)$$

where  $r_1$  and  $\alpha_1$  are the linear and angular radii, respectively, of the Airy disk,  $f$  is the system focal length,  $D$  is the diameter of the entrance pupil, and  $F$  is the focal ratio. Substituting  $f/D$  for  $R/2a$  assumes the point source object is effectively at infinity, and replaces exit pupil distances with those of the entrance pupil. This substitution also defines the angular radius of the first dark ring as an angle projected on the sky. For other values of  $\varepsilon$ , the factor 1.22 in Eq. (10.2.9) is replaced by the corresponding numerical factor in the  $w_1$  column in Table 10.1.

For a distant point source, the variable  $v$  is related to the system parameters and a dimensionless radius  $w$  by the relations

$$v = w\pi = \frac{\pi r}{\lambda F} = \frac{\pi D\alpha}{\lambda}, \quad (10.2.10)$$

where  $r$  and  $\alpha$  are linear and angular radii, respectively. The radii  $w$  for the first and second dark rings, and the radius at which  $i(P) = 0.5$  are shown in Fig. 10.7 for a range of  $\varepsilon$ .

**Table 10.1**

Radii of Dark Rings in Airy Pattern<sup>a,b</sup>

$\varepsilon$	$w_1$	$w_2$	$w_3$
0.00	1.220	2.233	3.238
0.10	1.205	2.269	3.182
0.20	1.167	2.357	3.087
0.33	1.098	2.424	3.137
0.40	1.058	2.388	3.300
0.50	1.000	2.286	3.491
0.60	0.947	2.170	3.389

<sup>a</sup> Subscript on  $w$  is the number of the dark ring starting at the innermost ring.

<sup>b</sup>  $w = v/\pi$ .

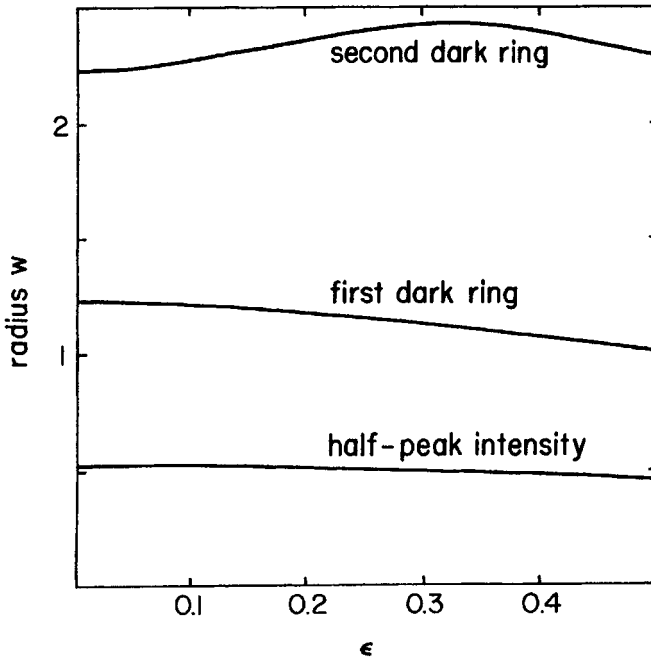


**Fig. 10.7.** Dimensionless radii at first two dark rings and one-half of peak intensity as a function of obscuration ratio. Linear radius =  $w\lambda F$ ; angular radius =  $w\lambda/D$ .

### 10.2.b. AVERAGE PSF IN AIRY WINGS

The description of the PSF in the wings of the Airy pattern beyond a few bright rings is derived by using the following asymptotic relation for the function  $J_n$ :

$$J_n(\beta) = \left(\frac{2}{\pi\beta}\right)^{1/2} \cos\left(\beta - \frac{n\pi}{2} - \frac{\pi}{4}\right). \quad (10.2.11)$$

This approximation is good to 1% or better for  $\beta > 15$ . Choosing  $n = 1$  and  $\beta = v$  or  $\epsilon v$ , as appropriate, Eq. (10.2.8) becomes

$$i(P) = \frac{1}{\pi(1 - \epsilon^2)^2} \left(\frac{2}{v}\right)^3 \left[ \cos\left(v - \frac{3\pi}{4}\right) - \sqrt{\epsilon} \cos\left(\epsilon v - \frac{3\pi}{4}\right) \right]^2.$$

Squaring and expanding the factor in brackets, we find a locally smoothed PSF by setting each of the  $\cos^2$  terms to one-half and the cross term to zero, with the result

$$\langle i(P) \rangle = \frac{4(1 + \varepsilon)}{\pi(1 - \varepsilon^2)^2} \frac{1}{v^3} = \frac{4(1 + \varepsilon)}{\pi^4(1 - \varepsilon^2)^2} \left(\frac{\lambda}{D}\right)^3 \frac{1}{\alpha^3}, \quad (10.2.12)$$

where  $\alpha$  is the field angle in radians. The quantity  $\langle i(P) \rangle$  is a good measure of the average intensity over one or two Airy rings in the range where the asymptotic relation for  $J_1$  is a good approximation. For  $\varepsilon = 0.33$ , for example, Eq. (10.2.12) is valid beyond the tenth bright ring.

From Eq. (10.2.12) we see that the average intensity in the wings of the Airy pattern is larger for larger values of  $\varepsilon$ . It is apparent that the effect of the central obscuration is to transfer some of the energy from the disk and nearest bright rings into the wings. A quantitative measure for the fraction of the energy in the wings of the Airy pattern is developed in the following section.

### 10.2.c. ENCIRCLED ENERGY

The encircled energy EE is defined as the fraction of the total energy  $E$  in the image enclosed within a circle of radius  $r$  centered on the PSF peak. Following Born and Wolf we have

$$EE = \frac{1}{E} \int_0^{2\pi} \int_0^{r_0} I(P)r \, dr \, d\psi \quad (10.2.13)$$

$$= \frac{1 - \varepsilon^2}{2I_0} \int_0^{v_0} I(P)v \, dv, \quad (10.2.14)$$

where  $v_0$  is a dimensionless radius, and  $I(P)$  is given by Eq. (10.2.8). The transformation of Eq. (10.2.13) into Eq. (10.2.14) follows from substitution of  $v$  for  $r$  using Eq. (10.2.3), and substitution of  $I_0$  for  $E$  according to

$$I_0 = C^2 A^2 = \frac{EA}{\lambda^2 f^2} = \frac{\pi E(1 - \varepsilon^2)}{4\lambda^2 F^2}, \quad (10.2.15)$$

where  $C$  is the constant in Eq. (10.1.1),  $A = \pi a^2(1 - \varepsilon^2)$  is the area of the annular aperture,  $f$  is the focal length, and  $F$  is the focal ratio. Further discussion of Eq. (10.2.15) follows in the next section.

We first evaluate Eq. (10.2.14) for the clear aperture, and find

$$\begin{aligned} EE(v_0) &= 2 \int_0^{v_0} \left( \frac{J_1(v)}{v} \right)^2 v \, dv \\ &= - \int_0^{v_0} d[J_0^2(v) + J_1^2(v)] \\ &= 1 - J_0^2(v_0) - J_1^2(v_0). \end{aligned} \quad (10.2.16)$$

The intermediate step in Eq. (10.2.16) follows after substitution of a recurrence relation. When  $v_0$  is taken at a dark ring,  $J_1(v_0)$  is zero and the fraction of the energy outside the dark ring is given by  $J_0^2(v_0)$ .

Following the same procedure for the obstructed aperture, Eq. (10.2.14) becomes

$$\begin{aligned} EE(v_0) &= \frac{1}{1 - \varepsilon^2} \left[ 1 - J_0^2(v_0) - J_1^2(v_0) + \varepsilon^2(1 - J_0^2(\varepsilon v_0) - J_1^2(\varepsilon v_0)) \right. \\ &\quad \left. - 2\varepsilon \int_0^{v_0} J_1(\varepsilon v) \frac{2J_1(v)}{v} \, dv \right]. \end{aligned} \quad (10.2.17)$$

Results derived from these relations for EE are shown in Fig. 10.8 for  $\varepsilon = 0$  and  $\varepsilon = 0.33$ . Encircled energy values within each of the first three dark rings are given in Table 10.2, with data for the first two dark rings plotted in Fig. 10.9. Also shown in Fig. 10.9 are EEs within the radii at which the intensity is one-half of the peak.

Examination of the results in Table 10.2 and Fig. 10.9 shows that there is a significant transfer of energy from the Airy disk to the first bright ring with increasing  $\varepsilon$ . We also see that EE in the disk and first bright ring combined decreases very slowly as  $\varepsilon$  increases from zero to 0.35. From Fig. 10.9 it is also evident that noticeable energy transfer to the second bright ring begins when  $\varepsilon$  is approximately equal to 0.4.

Returning to Eq. (10.2.17), we note that the value of the integral in this relation is equal to  $\varepsilon \pm \delta$  for  $v_0 \gg 1$ , with  $\delta \ll \varepsilon$ . As an example, with  $\varepsilon = 0.33$  we find  $\delta < 0.01$  for  $v_0 > 15$ . Therefore a good approximation to EE for large  $v_0$  is found by substituting  $\varepsilon$  for the integral in Eq. (10.2.17), and Eq. (10.2.11) for  $J_0$  and  $J_1$ .

Combining the terms involving the Bessel functions, we find

$$J_0^2(\beta) + J_1^2(\beta) = 2/\pi\beta,$$

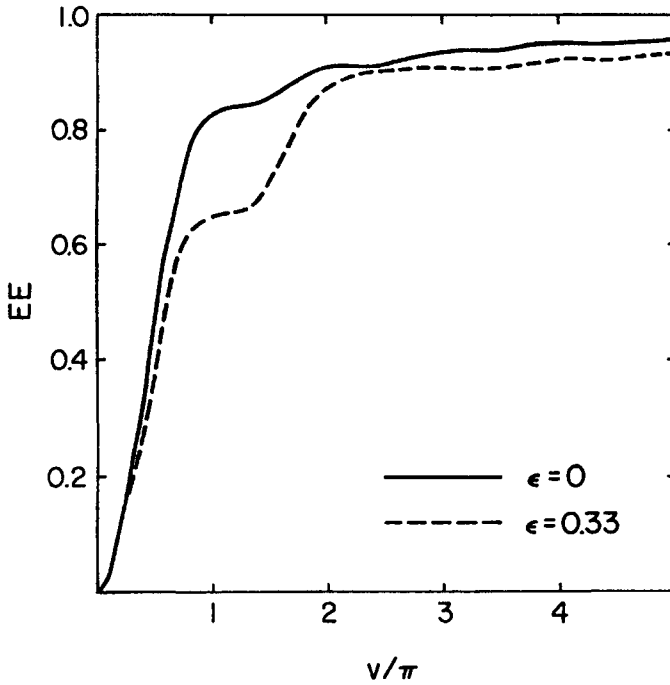


**Fig. 10.8.** Encircled energy fraction for obscuration ratios  $\epsilon = 0$  (solid line) and  $\epsilon = 0.33$  (dashed line), for perfect image.

**Table 10.2**

Encircled Energy Fraction within Airy  
Dark Rings<sup>a</sup>

$\epsilon$	EE <sub>1</sub>	EE <sub>2</sub>	EE <sub>3</sub>
0.00	0.838	0.910	0.938
0.10	0.818	0.906	0.925
0.20	0.764	0.900	0.908
0.33	0.654	0.898	0.904
0.40	0.584	0.885	0.903
0.50	0.479	0.829	0.901
0.60	0.372	0.717	0.873

<sup>a</sup>Subscript on EE is number of dark ring starting at innermost ring.

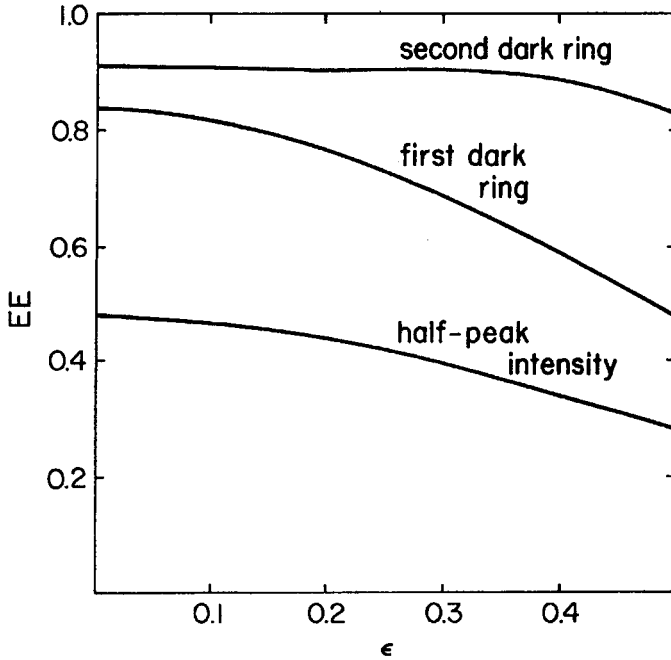


Fig. 10.9. Encircled energy fraction within first and second dark rings and within one-half of peak intensity. Results are given as a function of obscuration ratio.

where  $\beta$  is either  $v_0$  or  $\epsilon v_0$ . Therefore

$$EE(v_0 \gg 1) = 1 - \frac{2}{\pi(1 - \epsilon)v_0} = 1 - \frac{2\lambda}{\pi^2(1 - \epsilon)D\alpha}, \quad (10.2.18)$$

$$OE(v_0 \gg 1) = 1 - EE(v_0 \gg 1).$$

where OE is the fraction of the energy outside radius  $v_0$ . Examination of Eq. (10.2.18) shows that the larger  $\epsilon$ , the larger is the fraction of the energy outside a given large radius.

#### 10.2.d. IRRADIANCE AND INTENSITY

The PSF defined in Section 10.2.a is a dimensionless measure of the intensity or irradiance of the Airy pattern, but it is also necessary to give physical units to the PSF. In this section we give relations for the irradiance and intensity at the center of the Airy pattern and discuss the average irradiance over the Airy disk.

The terms intensity and irradiance are often interchanged in usage. The definition of *irradiance* is the *energy incident on a surface per unit area per unit time*, with units watts/m<sup>2</sup> (W/m<sup>2</sup>). Physicists commonly use the word *intensity* for the flow of *energy per unit area per unit time* through a surface. Astronomers, however, generally follow the definition that intensity is the *energy per unit time in a certain direction per unit solid angle*, with units watts/steradian (W/sr). We follow this latter usage of intensity. The symbol  $I$  is often used to represent both intensity and irradiance, and we follow this convention. The interested reader should consult the reference by Mahajan (1998) for a thorough discussion of the radiometry of imaging.

The relation given in Eq. (10.2.15) is derived by Born and Wolf (1980). Replacing the energy  $E$  in Eq. (10.2.15) by the energy per unit time, or *flux*  $\mathcal{F}$ , we have the irradiance  $I_0$  at the peak of the PSF as

$$I_0 = \frac{\mathcal{F} \pi D^2 (1 - \varepsilon^2)}{4\lambda^2 f^2} = \frac{\pi \mathcal{F} (1 - \varepsilon^2)}{4\lambda^2 F^2}. \quad (10.2.19)$$

It is instructive to compute the peak irradiance for a specific case. Consider a perfect Hubble Space Telescope (HST) with  $D = 2.4$  m,  $F = 24$ ,  $\varepsilon = 0.33$ , and area  $A = 4.03$  m<sup>2</sup>. Taking the canonical value for the photon flux as 1E4 photons/(sec cm<sup>2</sup> nm) for a zero-magnitude star at  $\lambda = 550$  nm, we get  $\mathcal{F} = 4.03\text{E}8$  photons/(sec nm) = 1.46E-10 W/nm, for the photon and energy flux per nm in the image of the HST with unit transmittance. Substituting the given values into Eq. (10.2.19), we find  $I_0 = 1.63\text{E}18$  photons/(sec m<sup>2</sup> nm) = 0.59 W/(m<sup>2</sup> nm) = 5.9E-13 W/(μm<sup>2</sup> nm), for a zero-magnitude star.

Another quantity of interest is the average irradiance over the Airy disk, that part of the image enclosed by the first dark ring. The average irradiance  $\langle I(\text{disk}) \rangle$  is the flux in the disk divided by its area, and is given by

$$\langle I(\text{disk}) \rangle = \frac{\sigma \mathcal{F}}{\pi r_1^2} = \frac{\sigma \mathcal{F}}{\pi \gamma^2 (1.22\lambda F)^2}, \quad (10.2.20)$$

where  $\sigma$  is the fraction of the total flux in the Airy disk,  $r_1$  is the radius of the Airy disk, and  $\gamma$  is a numerical factor such that  $1.22\gamma = \omega_1$  from Table 10.1 for an annular aperture. The value of  $\sigma$  also depends on  $\varepsilon$ , as noted in the discussion of encircled energy in the previous section.

Dividing Eq. (10.2.20) by Eq. (10.2.19), we get

$$\frac{\langle I(\text{disk}) \rangle}{I_0} = \frac{4\sigma}{(1.22\pi\gamma)^2 (1 - \varepsilon^2)} = 0.272 \frac{\sigma}{\gamma^2 (1 - \varepsilon^2)}. \quad (10.2.21)$$

Taking  $\varepsilon = 0$  and  $\varepsilon = 0.33$ , we use the results in Table 10.1 and find  $\gamma = 1$  and  $\gamma = 0.9$ , respectively, and from Table 10.2 we get  $\sigma = 0.838$  and  $\sigma = 0.654$ , respectively. Putting these values into Eq. (10.2.21) gives  $\langle I(\text{disk}) \rangle / I_0 = 0.228$

and 0.246 for the apertures with  $\varepsilon = 0$  and  $\varepsilon = 0.33$ , respectively, hence a smaller Airy disk roughly compensates for the smaller encircled energy fraction.

For another example assume a passband of 100 nm centered at  $\lambda = 550$  nm, and a star of apparent magnitude 25 imaged by HST. In this case we find a photon flux of 4.03 photons/sec passing through the HST aperture and 2.63 photons/sec on the Airy disk. Assuming a reflectance of 0.9 for the primary and secondary HST mirrors, a more accurate flux value is approximately 2.1 photons/sec for a star of apparent magnitude 25 at the  $f/24$  focus of HST. The detected photon flux, of course, depends on the efficiency of the optics and detector in a reimaging camera.

As a final item we note that Born and Wolf also define  $I_0 = EA/\lambda^2$ , hence units are those of intensity rather than irradiance. In this case the integral in Eq. (10.2.13) is over the solid angle subtended by the image at the aperture instead of the area of the image.

#### 10.2.e. RESOLUTION LIMIT

A telescope is often used at or near its *angular limit of resolution*, the minimum angular separation between two point sources of approximately equal brightness which can be seen as two separate images, or *just resolved*. Following the criterion first put forth by Lord Rayleigh, we say two stars of equal brightness are just resolved when the peak of one Airy disk falls on the first dark ring of the other Airy disk. Therefore the angular limit of resolution is

$$(\Delta\theta)_{\min} = 1.22\gamma\lambda/D, \quad (10.2.22)$$

where  $1.22\gamma = \omega_1$  from Table 10.1 to account for the decreasing diameter of the Airy disk with increasing obscuration.

At the point midway between the PSF peaks, the normalized intensity of the sum is  $2i(\omega_1/2)$  and ranges from about 0.74 at  $\varepsilon = 0$  to 0.81 at  $\varepsilon = 0.33$ . A detector with several pixels spanning an Airy disk will easily resolve the separate images in this case and the condition of “just resolved” is somewhat smaller than given in Eq. (10.2.22). The actual limit of resolution in practice depends on the brightness ratio of the stars and the characteristics of the detector. The convention adopted for convenience, however, does not consider these details and Eq. (10.2.22) gives the accepted limit.

### 10.3. THE NEAR PERFECT IMAGE

An image is perfect if the wavefront emerging from the exit pupil is spherical; if there are any deviations of the wavefront from a sphere the result is a less-than-perfect image. These wavefront deviations may be due to the presence of

geometric aberrations of the type discussed in Chapter 5, but also arise from random variations in optical surface quality as a result of the polishing process. Each of these wavefront deviations is characterized by a different scale at the exit pupil. Geometric aberrations vary slowly across the aperture and are specified in functional form, while random variations occur on a much shorter scale and are usually treated with statistical models.

Wavefront errors may also arise if the shape or orientation of the wavefront changes with time, where such time-dependent errors may be regular or random, and on a slow or fast time-scale. An example of a slow, regular time-dependent error is the change in focus of a Cassegrain telescope due to temperature changes. The error could be eliminated by periodically adjusting the secondary mirror and refocusing the telescope. Correction of slow time-dependent errors comes under the heading of *active optics*. An example of a rapid, random time-dependent error is the oscillation of an image centroid about its mean position due to atmospheric effects. Correction of rapid fluctuations in the shape of a wavefront is done with *adaptive optics*. These latter types of errors are also best treated with a statistical approach, with an introduction to this approach given in the next chapter.

In this section we consider geometric aberrations and their effects on image quality. Our discussion is only an introduction to a large subject matter, and the interested reader should consult some of the references listed at the end of the chapter for more extensive discussions.

### 10.3.a. DIFFRACTION INTEGRAL WITH ABERRATIONS

A cross section of a wavefront with aberrations and the reference sphere are shown in Fig. 5.3, where  $\Delta$ , as given in Eq. (5.3.1), is the geometrical path difference between the wavefront and reference sphere. In the notation of Fig. 10.1 the center of curvature  $O$  of the reference sphere is the location of the Gaussian image for a perfect system. The coordinate systems used to locate points on the wavefront and near the image are given in Eq. (10.2.1) for a circular aperture.

To include aberrations in the diffraction integral given in Eq. (10.1.1), we substitute  $(s - R + \Phi)$  for  $(s - R)$ , where  $\Phi$  is the optical path difference between the aberrated wavefront and reference sphere. If we consider only third-order aberrations, then from Eq. (5.5.1) we get

$$\Phi = B_0 y + B_1 y^2 + B_1' x^2 + B_2 y(x^2 + y^2) + B_3(x^2 + y^2)^2. \quad (10.3.1)$$

We choose, as in Chapter 5, to describe the astigmatism at the sagittal image, hence  $B_1' = 0$ . To make the notation in  $\Phi$  consistent with that used in this chapter

for a circular aperture, we replace  $x$  and  $y$  in Eq. (10.3.1) by  $\xi$  and  $\eta$ , respectively, using Eq. (10.2.1). The result is

$$\begin{aligned}\Phi &= B_0 a \rho \sin \varphi + B_1 a^2 \rho^2 \sin^2 \varphi + B_2 a^3 \rho^3 \sin \varphi + B_3 a^4 \rho^4 \\ &= \lambda(a_{11} \rho \sin \varphi + a_{22} \rho^2 \sin^2 \varphi + a_{31} \rho^3 \sin \varphi + a_{40} \rho^4),\end{aligned}\quad (10.3.2)$$

where the  $a$  coefficients include the radius of the exit pupil and are dimensionless. Note that the dimensions of  $\Phi$  are included in the wavelength  $\lambda$  in Eq. (10.3.2). The factors in Eq. (10.3.2) represent, in turn, distortion, astigmatism, coma, and spherical aberration, as follows:

$$\lambda a_{11} = B_0 a, \quad \lambda a_{22} = B_1 a^2, \quad \lambda a_{31} = B_2 a^3, \quad \lambda a_{40} = B_3 a^4, \quad (10.3.3)$$

with each corresponding  $a$  coefficient giving the amount of aberration in units of waves.

Note that the subscripts on the  $a$  coefficients are changed from those in the previous line with the first subscript the power of  $\rho$  and the second the power of  $\sin \varphi$ . This is done to bring our notation in line with that commonly used as, for example, by Mahajan (1998). It is also important to note that Eq. (10.3.2) is the optical path difference in a simplified case, that in which the incident chief ray is in the  $yz$  plane, as shown in Fig. 5.1. If we had chosen the  $xz$  plane instead, Eq. (10.3.2) would have  $\cos \varphi$  rather than  $\sin \varphi$ .

The diffraction integral for a circular exit pupil, including aberrations, is found by substituting the sum of Eq. (10.2.4) and  $k$  times Eq. (10.3.2) for  $k(s - R)$  in Eq. (10.1.1). The result is

$$U(P) = Ca^2 \int_0^{2\pi} \int_\epsilon^1 \exp [i(k\Phi - v\rho \cos(\varphi - \psi) - u\rho^2/2)] \rho \, d\rho \, d\varphi. \quad (10.3.4)$$

Note that the term  $u(R/a)^2$  in Eq. (10.2.4) is not included in Eq. (10.3.4). This term does not depend on the variables of integration, is removed from the integral, and does not appear in  $|U(P)|^2$ .

A complete analysis of Eq. (10.3.4) is beyond the scope of our treatment. For such an analysis the interested reader should consult the references by Born and Wolf (1980), Mahajan (1991, 1998), and Wetherell (1980) given at the end of this chapter. We do present selected results after discussing the effect of aberrations on peak intensity.

### 10.3.b. PEAK INTENSITY AND AVERAGE WAVEFRONT ERROR

Before discussing specific aberrations, it is important to show the relation between the peak intensity and the average wavefront error. We take point  $P$  at the center of the reference sphere, hence  $u = v = 0$ , and assume the aberrations are

small. Given that  $i(P) = |U(P)|^2$  is normalized to unity for a perfect image, we find

$$\begin{aligned} i(0) &= \frac{1}{\pi^2(1-\varepsilon^2)^2} \left| \int_0^{2\pi} \int_\varepsilon^1 \exp(ik\Phi)\rho \, d\rho \, d\varphi \right|^2 \\ &= C_0^2 \left| \int_0^{2\pi} \int_\varepsilon^1 [1 + ik\Phi + (ik\Phi)^2/2 + \dots] \rho \, d\rho \, d\varphi \right|^2, \end{aligned} \quad (10.3.5)$$

where  $C_0 = 1/\pi(1-\varepsilon^2)$ . We now define  $\langle \Phi^n \rangle$  as the average of the  $n$ th power of  $\Phi$ , where

$$\langle \Phi^n \rangle = C_0 \int_0^{2\pi} \int_\varepsilon^1 \Phi^n \rho \, d\rho \, d\varphi. \quad (10.3.6)$$

Neglecting all factors in  $k\Phi$  higher than second power in Eq. (10.3.5), we can write the approximate intensity at the center of the reference sphere as

$$\begin{aligned} i'(0) &= |1 + ik\langle \Phi \rangle - k^2\langle \Phi^2 \rangle/2|^2 \\ &= 1 - k^2[\langle \Phi^2 \rangle - \langle \Phi \rangle^2] = 1 - k^2\omega^2, \end{aligned} \quad (10.3.7)$$

where  $i'$  is used to indicate that this is an approximation to  $I$ . The parameter  $\omega$  is the root-mean-square (rms) or *rms wavefront error* given by

$$\omega = [\langle \Phi^2 \rangle - \langle \Phi \rangle^2]^{1/2}. \quad (10.3.8)$$

The rms wavefront error is a useful parameter for characterizing a high-quality optical system because its value can be calculated once the type and magnitude of aberrations are known. We see from Eq. (10.3.7) that the normalized intensity at the location of the nominal focal point is independent of the type of aberration, with the decrease from unity proportional to  $\omega^2$  in this approximation.

In the presence of aberrations, the normalized intensity  $i'(0)$  is often used as one measure of image quality. This normalized intensity, by convention, is called the *Strehl intensity* or *Strehl ratio*. A common convention is to consider a system as *diffraction-limited* if the *Strehl ratio* is greater than or equal to 0.8. Given this convention we find that  $\omega = 0.0712\lambda \cong \lambda/14$  for a system that is just diffraction-limited.

The Strehl ratio given by Eq. (10.3.7) is an approximation to the normalized peak intensity valid for small  $\omega$ . It was shown by Mahajan (1983) that a better approximation for the Strehl ratio  $S$  is given by

$$S = i'(0) = \exp(-k^2\omega^2). \quad (10.3.9)$$

A comparison between  $i(0)$  calculated directly from Eq. (10.3.5) with  $S$  from Eq. (10.3.9) shows that the latter agrees with the former with an error of less than 10% for  $S$  greater than 0.3. This limit corresponds approximately to  $\omega = \lambda/5.7$ .

**Table 10.3**  
Classical Aberrations and RMS Wavefront Errors<sup>a,b</sup>

Aberration		RMS Wavefront Error
Spherical	$a_{40}\rho^4$	$\frac{ a_{40} }{3\sqrt{5}}(4 - \varepsilon^2 - 6\varepsilon^4 - \varepsilon^6 + 4\varepsilon^8)^{1/2}$
Coma	$a_{31}\rho^3 \sin \varphi$	$\frac{ a_{31} }{\sqrt{8}}(1 + \varepsilon^2 + \varepsilon^4 + \varepsilon^6)^{1/2}$
Asigmatism	$a_{22}\rho^2 \sin^2 \varphi$	$\frac{ a_{22} }{4}(1 + \varepsilon^4)^{1/2}$
Defocus	$a_{20}\rho^2$	$\frac{ a_{20} }{2\sqrt{3}}(1 - \varepsilon^2)$
Distortion	$a_{11}\rho \sin \varphi$	$\frac{ a_{11} }{2}(1 + \varepsilon^2)^{1/2}$

<sup>a</sup> RMS error is given in units of wavelength. For linear measure, multiply by the wavelength.

<sup>b</sup> Error for astigmatism is given at sagittal focus; other errors given at paraxial focus.

### 10.3.c. CLASSICAL ABERRATIONS AND WAVEFRONT ERROR

The classical third-order aberrations are those given in Eq. (10.3.2). Substituting each in turn into Eq. (10.3.6), it is a straightforward matter to calculate the rms wavefront error for each, with the results given in Table 10.3. These expressions for  $\omega$  are appropriate for the specific image locations used to derive the aberration coefficients in Chapter 5: at the nominal paraxial or Gaussian focus for spherical aberration, coma, and distortion, and at the sagittal image for astigmatism. Note an additional aberration in Table 10.3, that of pure defocus.

Numerical calculations of  $i(P)$  using Eq. (10.3.4) including focus shift show that the Strehl ratio is not a maximum at these image locations. In the presence of spherical aberration only, for example, the “best” image is not at the paraxial focus but between the paraxial and marginal foci, as a glance at Fig. 4.5 shows. The distance between these two foci is  $2F$  TSA, where  $F = s'/2a$  and TSA is given in Eqs. (5.5.9). After substituting for  $B_3$  from Eqs. (10.3.3) we get the separation between the paraxial and marginal foci as  $16\lambda a_{40} F^2$ .

Calculations with  $\varepsilon = 0$  show that  $i(0)$  is largest at a point half way between these two foci and the corresponding rms wavefront error is a minimum at this point. The dependence of  $\omega$  and peak intensity on focus shift for  $\varepsilon = 0$  is shown in Fig. 10.10; in this case the value of  $\omega$  at the paraxial focus is 4 times larger than at the point where the peak intensity is a maximum.

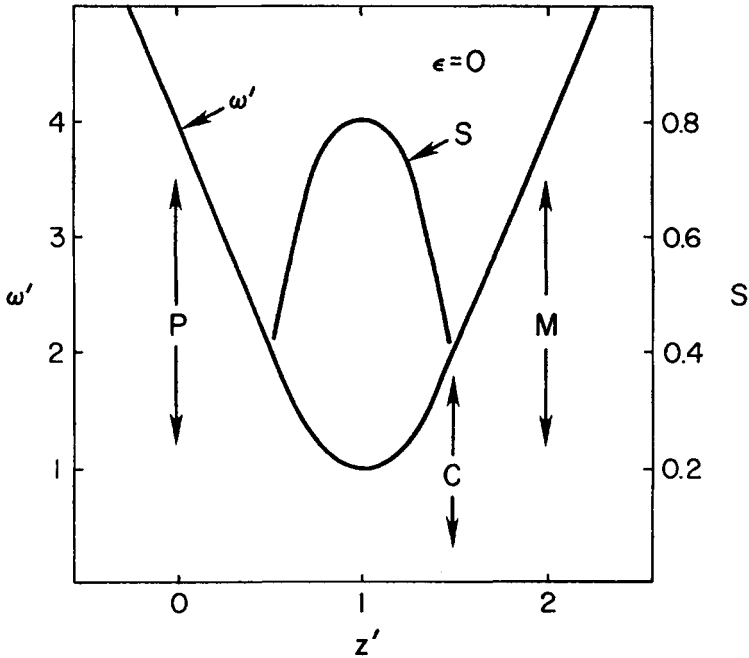


**Fig. 10.10.** Normalized rms wavefront error  $\omega'$  and Strehl ratio  $S$  for image with spherical aberration as a function of image surface location.  $S$  is given for  $\omega' = 1$ ,  $\omega = 0.075\lambda$  at  $z' = 1$ . The normalized focus shift is  $z'$ . P, paraxial focus; M, marginal focus; C, circle of least confusion.

Following a similar procedure, it turns out that a system with astigmatism has a minimum  $\omega$  and maximum  $i(0)$  at a point half way between the sagittal and tangential line images for any value of  $\epsilon$ . The distance between the line images is  $2F$  TAS, where TAS is given in Eqs. (5.5.9). After substituting  $B_1$  from Eqs. (10.3.3) we find the separation between the line images as  $8\lambda a_{22} F^2$ . The dependence of  $\omega$  and peak intensity on focus shift is shown in Fig. 10.11 for an astigmatic image. For a clear aperture the value of  $\omega$  at either line image is about 20% larger than at the midway point.

For both spherical aberration and astigmatism, the point of maximum  $i(0)$  is on the axis defined by  $v = 0$ . For coma and distortion  $i(0)$  is a maximum for a point displaced transversely from the paraxial image point and  $v$  is not zero. For a single aberration, the point at which the peak intensity is a maximum is called the *diffraction focus*. Table 10.4 gives the shifts from the foci specified in Table 10.3 to the diffraction focus for each of the classical aberrations. In the following section we outline the procedure by which these shifts are calculated.

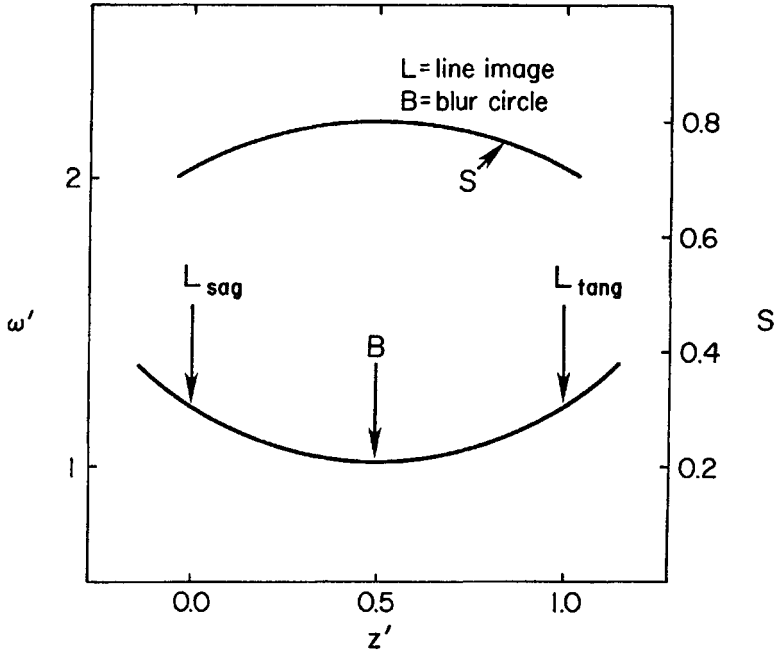


**Fig. 10.11.** Normalized rms wavefront error  $\omega'$  and Strehl ratio  $S$  for astigmatic image as a function of image surface location, with  $z' = 0, 1$  at line images.  $S$  is given for  $\omega' = 1, \omega = 0.075\lambda$  at blur circle  $B$ . The normalized focus shift is  $z'$ .

**Table 10.4**

Coordinate Shifts to Diffraction Focus<sup>a</sup>

Aberration	Along	
	y-axis	z-axis
Spherical	0	$8a_{40}\lambda(1 + \epsilon^2)F^2$
Coma	$\frac{4a_{31}\lambda F}{3} \left( \frac{1 + \epsilon^2 + \epsilon^4}{1 + \epsilon^2} \right)$	0
Astigmatism	0	$4a_{22}\lambda F^2$
Defocus	0	$8a_{20}\lambda F^2$
Distortion (tilt)	$2a_{11}\lambda F$	0

<sup>a</sup> For starting point of shift for each aberration, see Table 10.3.

## 10.3.d. ORTHOGONAL ABERRATIONS AND ZERNIKE POLYNOMIALS

As seen from Table 10.4, the location of the diffraction focus depends on the type and magnitude of aberration present. Because of this dependence, it is appropriate to restructure the classical aberration terms and include explicitly the required image shift to place the diffraction focus at  $u = v = 0$ . These modified terms are called orthogonal aberrations, with the polynomials in  $\rho$  and  $\varphi$  called *Zernike polynomials*. A list of Zernike polynomials needed for third-order aberrations of an unobstructed circular aperture is given in Table 10.5. Note the presence of both sin and cos factors in Table 10.5, hence the representation of coma and astigmatism of arbitrary orientation in an  $xy$  coordinate frame is possible. Table 10.6 lists the third-order orthogonal aberration terms for an annular aperture, along with expressions for the rms wavefront errors at the diffraction focus. For a detailed discussion of the properties of the orthogonal aberrations, including derivations, consult the references by both Mahajan and Born and Wolf.

The importance of representing the total aberration of a system as the sum of orthogonal aberrations is that each term in the sum is optimally chosen to give a minimum rms error over the exit pupil. In addition, the mean square error (MSE) of the total aberration is the sum of the MSE of the individual orthogonal aberrations. Thus it is straightforward to find the overall rms wavefront error once the separate  $a_{nm}$  in Eq. (10.3.3) are known.

Choosing an orthogonal aberration in an optimal way is done by adding one or more classical aberrations. We note, for example, that the spherical aberration terms in Tables 10.5 and 10.6 show a term in  $\rho^2$ , a focus shift term, added to that of  $\rho^4$ . A focus shift term is also evident in the entry for astigmatism in Table 10.6. In the case of coma, the added term is proportional to  $\rho \sin \varphi$ , which is effectively a tilt. We also see constant terms in the entries for spherical aberration and focus

**Table 10.5**  
Zernike Polynomials for Circular Aperture

Term	$Z(\rho, \varphi)$	Descriptor
0	1	constant
1	$\rho \cos \varphi$	$x$ -tilt
2	$\rho \sin \varphi$	$y$ -tilt
3	$2\rho^2 - 1$	focus shift
4	$\rho^2 \cos 2\varphi$	$x$ - or $y$ -astigmatism
5	$\rho^2 \sin 2\varphi$	$45^\circ$ -astigmatism
6	$(3\rho^2 - 2)\rho \cos \varphi$	$x$ -coma
7	$(3\rho^2 - 2)\rho \sin \varphi$	$y$ -coma
8	$6\rho^4 - 6\rho^2 + 1$	spherical

Table 10.6

Orthogonal Aberrations and RMS Wavefront Errors<sup>a</sup>

Orthogonal Aberration	RMS Wavefront Error
Spherical:	
$a_{40} \left[ \rho^4 - (1 + \varepsilon^2)\rho^2 + \frac{1}{6}(1 + 4\varepsilon^2 + \varepsilon^4) \right]$	$\frac{ a_{40} }{6\sqrt{5}}(1 - \varepsilon^2)^2$
Coma:	
$a_{31} \left[ \rho^3 - \frac{2(1 + \varepsilon^2 + \varepsilon^4)}{3(1 + \varepsilon^2)}\rho \right] \sin \varphi$	$\frac{ a_{31} (1 - \varepsilon^2)(1 + 4\varepsilon^2 + \varepsilon^4)^{1/2}}{6\sqrt{2}(1 + \varepsilon^2)^{1/2}}$
Astigmatism:	
$a_{22} \left[ \rho^2 \left( \sin^2 \varphi - \frac{1}{2} \right) \right]$	$\frac{ a_{22} }{2\sqrt{6}}(1 + \varepsilon^2 + \varepsilon^4)^{1/2}$
Defocus:	
$a_{20} \left[ \rho^2 - \frac{1}{2}(1 + \varepsilon^2) \right]$	$\frac{ a_{20} }{2\sqrt{3}}(1 - \varepsilon^2)$
Distortion: $a_{11}\rho \sin \varphi$	$\frac{ a_{11} }{2}(1 + \varepsilon^2)^{1/2}$

<sup>a</sup>Each expression is given in units of wavelength. For linear measure, multiply by wavelength.

in Tables 10.5 and 10.6. These constant terms are chosen to make the average wavefront error  $\langle \Phi \rangle = 0$  for these aberrations, without changing the rms error. The proof that adding a constant term to  $\Phi$  does not change the rms error is left as an exercise for the reader.

We now outline the procedure by which an orthogonal aberration is constructed, taking as an example spherical aberration for a clear aperture. The starting point is to write the wavefront error as classical spherical plus a variable focus shift,

$$\Phi = \lambda a_{40}(\rho^4 - \alpha \rho^2). \tag{10.3.10}$$

Substituting Eq. (10.3.10) into Eq. (10.3.6) with  $\varepsilon = 0$  gives

$$\begin{aligned} \langle \Phi \rangle &= \lambda a_{40} \left( \frac{1}{3} - \frac{\alpha}{2} \right), & \langle \Phi^2 \rangle &= (\lambda a_{40})^2 \left( \frac{1}{5} - \frac{\alpha}{2} + \frac{\alpha^2}{3} \right), \\ \omega^2 &= (\lambda a_{40})^2 \left( \frac{4}{45} - \frac{\alpha}{6} + \frac{\alpha^2}{12} \right). \end{aligned} \tag{10.3.11}$$

Setting the derivative of  $\omega^2$  with respect to  $\alpha$  equal to zero and solving for  $\alpha$  gives  $\alpha = 1$ ,  $\Phi = \lambda a_{40}(\rho^4 - \rho^2)$ , and  $\omega^2(\min) = (\lambda a_{40})^2/180$ . The relation between  $\alpha$  and the linear focus shift is found by noting that  $k$  times the term in  $\alpha$  in Eq.

(10.3.10) equals  $-u\rho^2/2$  in Eq. (10.3.4), hence  $\alpha = \Delta z/(8\lambda a_{40}F^2)$  where  $\Delta z$  is the shift from paraxial focus. The constant term added to  $\Phi$  is  $-\langle\Phi\rangle$  with  $\alpha = 1$ . This general procedure can be used to verify the entries in Tables 10.4 and 10.6, starting with the classical aberrations in Table 10.3.

### 10.3.e. EXAMPLES

As illustrations of the effects of aberrations on the PSF, we take two examples: a perfect image subject to defocus and an image with spherical aberration at the diffraction focus. The results were obtained by numerical integration of Eq. (10.3.4) and apply to an unobstructed aperture.

Figure 10.12 shows image profiles for the disk and the first two bright rings of an image with different amounts of defocus. Note that the ring structure, clearly visible for  $a_{20} = 0.25$  or  $\omega \cong \lambda/14$ , is essentially absent when  $a_{20} > 0.5$ . The effect of defocus is clearly one of transferring energy from the disk to the nearby rings and filling in the dark rings. Though not shown in Fig. 10.12, the intensity  $i(0) = 0$  when  $a_{20} = 1$ . In general, the peak intensity is zero for an image with pure defocus when  $|a_{20}| = 1/(1 - \varepsilon^2)$ . Surface plots of defocused PSFs are shown in Figs. 10.13 and 10.14 for  $a_{20} = 0.25$  and 0.75, respectively.

Figure 10.15 shows image profiles for an image at the diffraction focus with different amounts of spherical aberration. In this case the separate rings remain relatively well-defined, but the energy within them grows at the expense of the

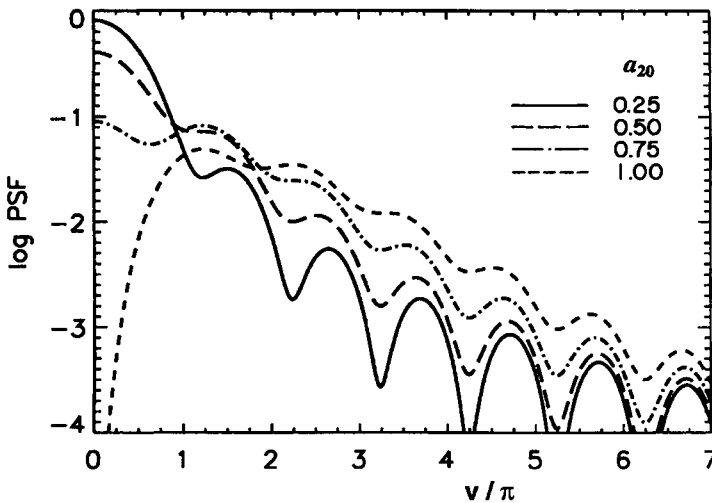


Fig. 10.12. Point spread function of perfect image with defocus. The aperture is unobstructed and the shift from diffraction focus  $= 8a_{20}\lambda F^2$ . See Fig. 10.5 for PSF of perfect image.

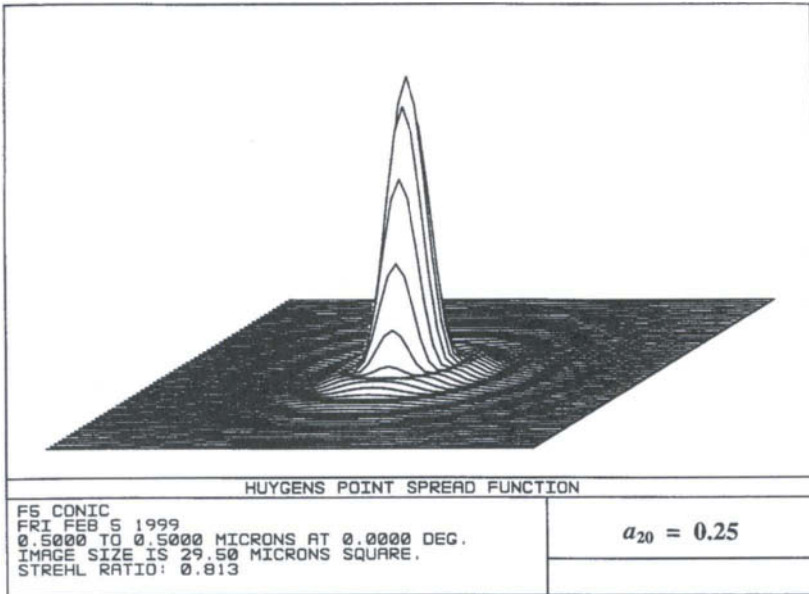


Fig. 10.13. Surface plot of perfect image with defocus;  $a_{20} = 0.25$ .

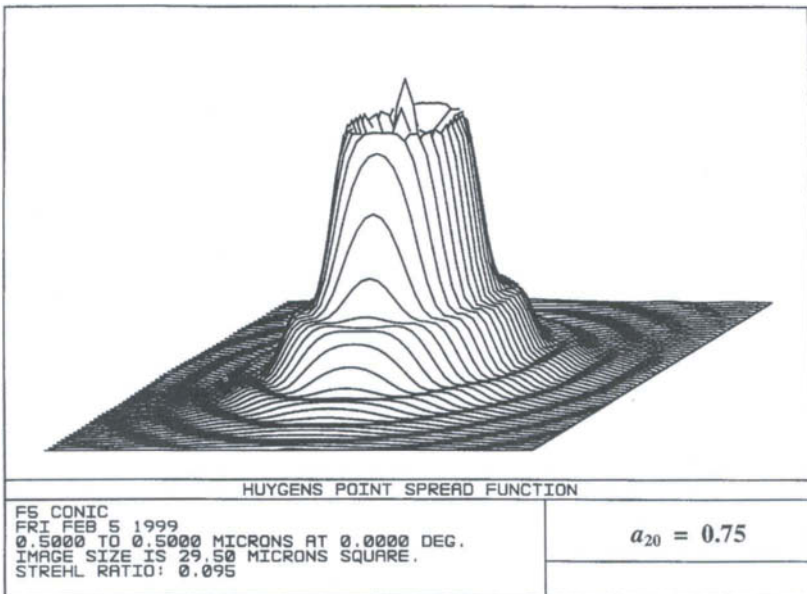


Fig. 10.14. Surface plot of perfect image with defocus;  $a_{20} = 0.75$ .

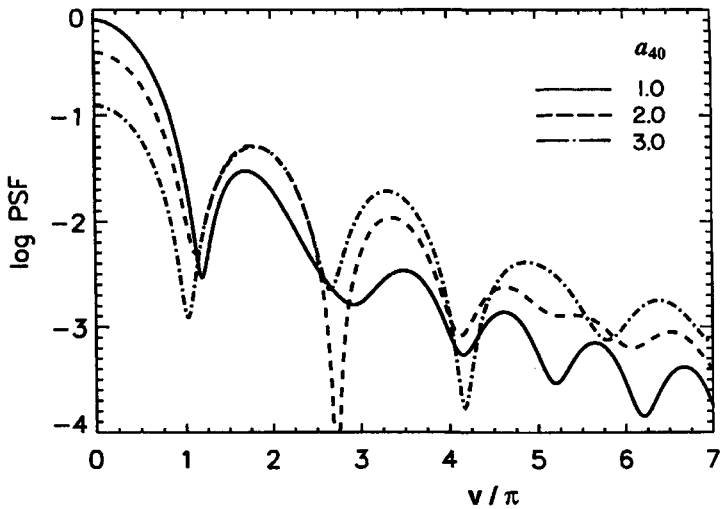


Fig. 10.15. Point spread function of image with spherical aberration at diffraction focus. The aperture is unobstructed. See Fig. 10.5 for PSF of perfect image.

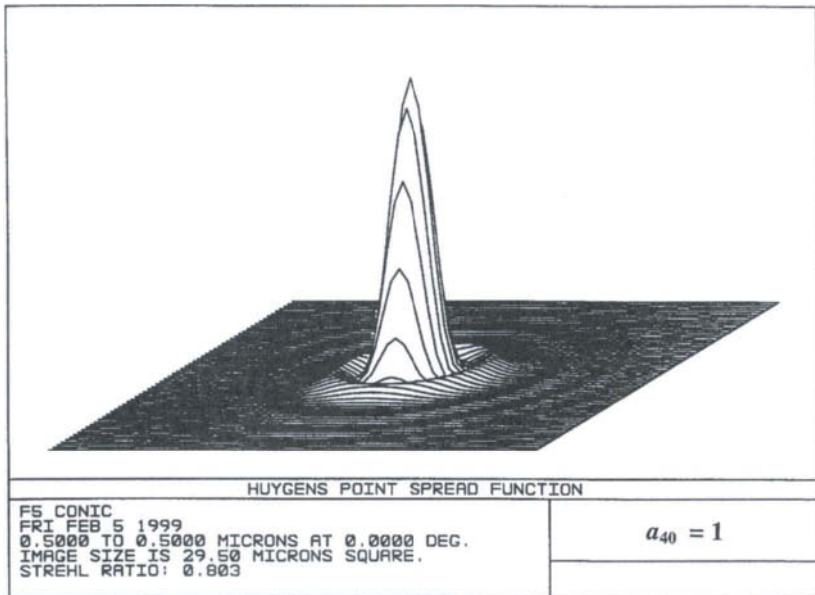


Fig. 10.16. Surface plot of spherically aberrant image at diffraction focus;  $a_{40} = 1$ .

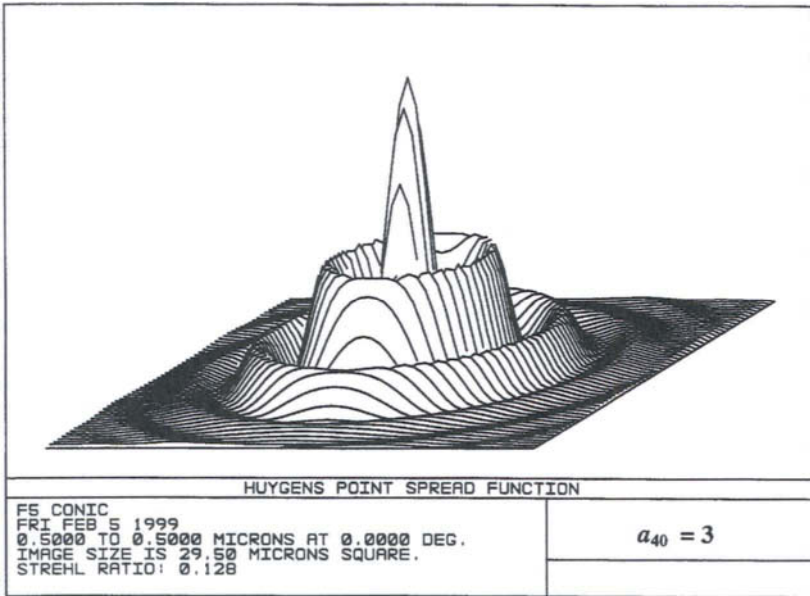


Fig. 10.17. Surface plot of spherically aberrant image at diffraction focus;  $a_{40} = 3$ .

Table 10.7

EE and  $\omega$  for Images with Aberrations

Fig. 10.12			Fig. 10.15		
$a_{20}$	EE <sub>1</sub>	$\omega$	$a_{40}$	EE <sub>1</sub>	$\omega$
0.25	0.733	0.072	1.0	0.668	0.075
0.50	0.490	0.144	2.0	0.324	0.149
0.75	0.248	0.217	3.0	0.094	0.224
1.00	0.105	0.289	4.0	0.068	0.298

disk. Surface plots of spherically aberrant PSFs are shown in Figs. 10.16 and 10.17 for  $a_{40} = 1$  and 3, respectively.

The rms wavefront errors and encircled energy in the Airy disk for the profiles in Figs. 10.12 and 10.15 are given in Table 10.7. The results for EE<sub>1</sub> were obtained by numerical integration of Eq. (10.2.13). It is evident from these entries that encircled energy fraction within the Airy disk drops dramatically with increasing rms wavefront error.

#### 10.4. COMPARISON: GEOMETRIC ABERRATIONS AND THE DIFFRACTION LIMIT

It is important to compare aberrations as computed from geometric optics, as done in Chapter 5, with those found using diffraction optics, as done in this chapter. We make this comparison in terms of angular aberrations because these are especially significant for telescopes. Our discussion is intended to give the reader an idea of when geometric aberration calculations are sufficient and when it is necessary to use diffraction theory for accurate results.

The relations for geometric angular aberrations are given in Table 10.8 in terms of the two sets of coefficients used to characterize aberrations. Coefficients for two-mirror telescopes found in Tables 6.5 and 6.6, for example, can be substituted for  $B_{n-1}$  in Table 10.8 to give the corresponding  $a_{nm}$  for the classical aberrations. These values of  $a_{nm}$  can, in turn, be used to find the rms wavefront errors from Table 10.3.

As an example of this procedure we take the Ritchey-Chretien design for the Hubble Space Telescope. The principal aberration for nonzero field angles is astigmatism, with the angular astigmatism according to geometric theory given in Table 6.9. Substituting the values of  $m$  and  $\beta$  in Table 11.2 into AAS in Table 6.9 gives  $\text{AAS} = \Gamma\theta^2/2F = 2B_1a$ , where  $\Gamma = 8.609$ ,  $B_1$  is the astigmatism coefficient,  $\theta$  is the field angle, and  $a$  is the radius of the aperture stop.

From Eq. (10.3.3) or Table 10.8 we get  $\lambda a_{22} = B_1a^2$ , hence  $a_{22} = \Gamma\theta^2 D/8\lambda F$ . We now find the rms wavefront error at the diffraction focus of the astigmatic image by substituting  $\varepsilon = 0.33$  and  $a_{22}$  into  $\omega$  for astigmatism in Table 10.6. The result, with  $\theta$  expressed in arc-minutes, is

$$\begin{aligned}\omega_{\text{HST}}(\mu\text{m}) &= 0.00197\theta^2 \text{ (arc-min)}, \\ \omega_{\text{HST}} \text{ (waves)} &= 0.00197\theta^2 \text{ (arc-min)}/\lambda(\mu\text{m}).\end{aligned}\tag{10.4.1}$$

Choosing  $\omega < \lambda/14$ , we find from Eq. (10.4.1) that HST is diffraction-limited for  $\theta < 4.8$  arc-min at 633 nm with smaller  $\theta$  at shorter wavelengths. Thus, for example, an instrument aperture at 3.6 arc-min off-axis is illuminated by images

**Table 10.8**  
Geometric Angular Aberrations

Spherical	$\text{ASA} = 4B_3a^3 = 4\lambda a_{40}/a$ = angular diameter at diffraction focus
Coma	$\text{ATC} = 3B_2a^2 = 3\lambda a_{31}/a$ = angular length of coma flare
Astigmatism	$\text{AAS} = 2B_1a = 2\lambda a_{22}/a$ = angular diameter at diffraction focus

that are diffraction-limited for visible and near ultraviolet wavelengths. For an aperture at larger field angles, on the other hand, the residual astigmatism of the HST must be corrected by the optics following the aperture.

If we approach the angular size of an image from the point of view of diffraction theory, then an image that is diffraction-limited has an approximate diameter for the Airy disk of  $2.44\lambda/D$  or  $1.22\lambda/a$  for a clear aperture. Contrary to predictions from geometric optics, an image cannot be smaller than that given by diffraction theory. It is instructive to take the top four entries for wavefront error in Table 10.3, set  $\varepsilon = 0$ , equate each to  $\omega/\lambda = 1/14$ , and solve for  $a_{nm}$ . The result is  $|a_{nm}| \approx 0.25$  for each of these coefficients, hence the maximum optical difference  $\Phi \approx \lambda/4$  for each aberration. This corresponds to the result given in Section 4.2 and is often called *Rayleigh's quarter-wavelength criterion* for the amount of aberration that is tolerable in an imaging system.

If we apply the same procedure to the orthogonal aberrations in Table 10.6, with  $\varepsilon$  set to zero, we get  $|a_{40}| \approx 0.96$ ,  $|a_{31}| \approx 0.60$ ,  $|a_{22}| \approx 0.35$ , and  $|a_{20}| \approx 0.25$ . Not surprisingly, the balancing of a classical aberration with a focus shift for spherical aberration and astigmatism, and a tilt for coma, gives a somewhat larger tolerance on the corresponding coefficients.

We now compare the size of the Airy disk with a geometrical image whose size is computed using the tolerance on  $a_{40}$ . Substituting  $a_{40} = 0.25$  into ASA in Table 10.8 we get  $ASA = \lambda/a = 2\lambda/D$ , and the geometric blur size is comparable to the diameter of the Airy disk. For values of  $a_{40}$  comparable to the tolerance limit or smaller, diffraction calculations are necessary, while for substantially larger values of  $a_{40}$ , the geometric blur size is an accurate measure of the image size.

It should be evident, therefore, that diffraction theory is required when the aberrations are small and the separate rms wavefront errors are comparable to the diffraction limit. If any one aberration has an rms error substantially larger than  $\lambda/14$ , then geometric aberration analysis is adequate. Fortunately, ray-tracing programs can easily do both types of calculations, thus facilitating the choice of the theory appropriate for the task.

## 10.5. DIFFRACTION INTEGRALS AND FOURIER THEORY

The starting point for our discussion of diffraction, including aberrations, is Eq. (10.1.1). We applied this to rectangular and annular apertures, and derived expressions in closed form for the point spread function and encircled energy fraction for aberration-free images. There is, of course, no limit placed on the shape of the aperture, for example, a spider structure supporting a secondary mirror in a Cassegrain telescope added to an annular aperture. With such an

addition Eq. (10.1.1) is still easily solved in closed form for a perfect image, as illustrated in Eq. (10.5.1) to follow. The solution of the diffraction integral for more complicated apertures is best done using the formalism of Fourier theory, a subject area we introduce here and discuss briefly.

### 10.5.a. APERTURE FUNCTION

Writing Eq. (10.1.1) with explicit reference to the coordinates of the aperture and image plane we get

$$U(x, y) = C \iint_{-\infty}^{\infty} A(\xi, \eta) \exp [ik(p\xi + q\eta)] d\xi d\eta, \quad (10.5.1)$$

where  $p$  and  $q$  are functions of  $x$  and  $y$ , respectively, and  $A(\xi, \eta)$  is the amplitude distribution in the aperture or *aperture function*. Aberrations can be incorporated by including a term of the form  $\exp(ik\Phi)$  in  $A(\xi, \eta)$ . Although the limits of integration extend over an infinite plane,  $A(\xi, \eta)$  is nonzero only over the aperture.

With the diffraction integral rewritten as Eq. (10.5.1), we have an integral in the form of a 2D Fourier integral or Fourier transform. We state, without proof, that *the amplitude distribution in the Fraunhofer diffraction pattern is the Fourier transform of the aperture function*. Conversely, from Fourier theory, *there is an inverse transform such that the amplitude distribution in the aperture (or pupil) of an optical system is the Fourier transform of the amplitude in the image plane*. Thus there is a Fourier transform pair connecting the aperture and the Fraunhofer image plane.

### 10.5.b. EXAMPLE: SPIDER IN CASSEGRAIN TELESCOPE

The entrance pupil of most two-mirror telescopes is an annulus plus a four-legged spider structure, as shown in Fig. 10.18. Therefore the aperture function is a clear aperture of radius  $a$ , a central obscuration of radius  $\varepsilon a$ , and two bars of length  $2a$  (one along  $\xi$  and one along  $\eta$ ) less two bars of length  $2\varepsilon a$ . Each obscuration is given a minus sign because it subtracts from the clear aperture. With this aperture function Eq. (10.5.1) becomes

$$U(P) = \text{Eq. (10.2.5)} - C \int_{-b}^b \exp(-i\beta)d\eta \left\{ \int_{-a}^{-\varepsilon a} \exp(-i\gamma)d\xi + \int_{\varepsilon a}^a \exp(-i\gamma)d\xi \right\} \\ - C \int_{-b}^b \exp(-i\gamma)d\xi \left\{ \int_{-a}^{-\varepsilon a} \exp(-i\beta)d\eta + \int_{\varepsilon a}^a \exp(-i\beta)d\eta \right\}, \quad (10.5.2)$$

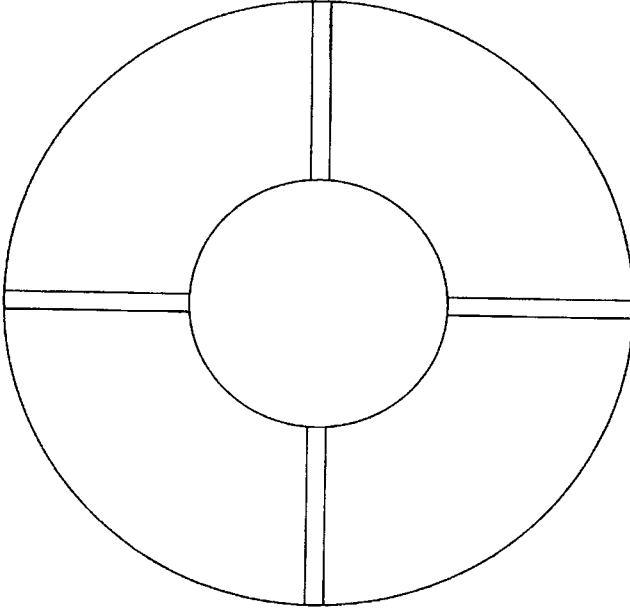


**Fig. 10.18.** Entrance pupil of typical two-mirror telescope with spider structure. See the text for discussion.

where  $\gamma = kp\xi$  and  $\beta = kq\eta$ . The integral on the first line of Eq. (10.5.2) is the horizontal part of the spider; the integral on the second line is the vertical part. Evaluating these integrals we get

$$U(P) = \text{Eq. (10.2.7)} - 4ab(1 - \varepsilon)C \left[ \frac{\sin(kqb)}{kqb} \frac{\sin(kpd/2)}{kpd/2} \cos\left(kp\left(\frac{1 + \varepsilon}{2}\right)a\right) + \frac{\sin(kpb)}{kpb} \frac{\sin(kqd/2)}{kqd/2} \cos\left(kq\left(\frac{1 + \varepsilon}{2}\right)a\right) \right], \quad (10.5.3)$$

where  $d = (1 - \varepsilon)a$  is the length of each of the four bars in the spider and  $2b$  is the width of each bar. Note that part of the argument of the cosine is the distance from the center of the aperture to the midpoint of each of the bars,  $(1 + \varepsilon)a/2$ .

With  $U(P)$  from Eq. (10.5.3), it is now straightforward to find  $I(P) = |U(P)|^2$ . The amplitude at the peak  $I_0 = |U(O)|^2$ , where  $U(O) = C[\pi a^2(1 - \varepsilon^2) - 8ab(1 - \varepsilon)] = C$  times the area of the open aperture.

## 10.5.c. ARRAY THEOREM

The spider in the previous section consists of two pairs of bars with each bar displaced from the center of the aperture. As noted following Eq. (10.5.3), the amount of this displacement from the center is explicitly part of  $U(P)$ . If each cosine in Eq. (10.5.3) is written in terms of complex exponentials using Euler's relations, then each bar has a factor representing its displacement in either the positive or negative direction along one of the axes. This association between displacement and a complex exponential suggests a closer look at identical multiple apertures or multiple obstacles within some larger aperture.

Consider a large screen containing  $N$  identical apertures with the designated center of each at  $(\xi_j, \eta_j)$  in the  $(\xi, \eta)$  coordinate frame. Let  $(\xi', \eta')$  be the local coordinates of each aperture relative to its center, hence  $\xi = \xi_j + \xi'$ ,  $\eta = \eta_j + \eta'$ . With this aperture Eq. (10.5.1) becomes

$$U(P) = C \sum_{j=1}^N \iint_{-\infty}^{\infty} A(\xi', \eta') \exp \left[ ik(p(\xi_j + \xi') + q(\eta_j + \eta')) \right] d\xi' d\eta' \quad (10.5.4)$$

where  $A(\xi', \eta')$  is the aperture function for a single hole.

Factoring  $\exp [ik(p\xi_j + q\eta_j)]$  from each integral in Eq. (10.5.4) we get

$$U(P) = C \iint_{-\infty}^{\infty} A(\xi', \eta') \exp [ik(p\xi' + q\eta')] d\xi' d\eta' \times \sum_{j=1}^N \exp [ik(p\xi_j + q\eta_j)], \quad (10.5.5)$$

where each term in the sum locates the center of one of the  $N$  apertures.

Equation (10.5.5) is a statement of the *array theorem*: the amplitude at point  $P$  in the Fraunhofer diffraction pattern of an array of identical apertures (or obstacles) is the Fourier transform of an individual aperture function times a function representing the positions of the aperture centers in the diffracting screen.

In our example of a spider on an annular aperture there are two aperture functions, a horizontal bar of length  $(1 - \epsilon)a$  and width  $2b$  and a vertical one of the same dimensions, with each displaced by  $\pm(1 + \epsilon)a/2$  along its long dimension. The net result is the pattern shown in Fig. 10.18. The reader can verify that applying Eq. (10.5.5) to this example gives  $U(P)$  in Eq. (10.5.3). Another example showing the utility of the array theorem is that of the HST pupil, the pupil shown in Fig. 10.18 plus three circular pads near the outer edge of the primary. The HST pupil, with coordinates and dimensions, and  $U(P)$  calculated from Eq. (10.5.5) are found in a paper by Schroeder and Golimowski (1996).

The array theorem is useful in any case where there are multiple diffracting apertures or obstacles. We make use of the array theorem in discussing telescope arrays in Chapter 18.

#### 10.5.d. CONCLUDING REMARKS

The reciprocal nature of the integrals in a Fourier transform pair is a mathematical consequence of the fact that the propagation of light through an optical system is reversible. The utility of Eq. (10.5.1) and its inverse transform were strikingly evident when the first aberrated images from HST were examined. An amplitude distribution derived from the observed PSF could be used to find the aberration part of the aperture function. Conversely, a host of aberration functions could be inserted into Eq. (10.5.1) and the computed  $I(P)$  for each compared to the observed PSF. These calculations led the way to recognition of the significant spherical aberration in the HST primary. We give some of the quantitative results from this analysis in Chapter 11.

We also see Fourier transform pairs occurring in our discussion of transfer functions, the first topic of Chapter 11. The proofs of these statements, along with extensive discussions of the connection between Fourier theory and optics, can be found in many intermediate optics texts, for example, by Hecht (1987). The text by Gaskill (1978) is also a useful source of information on Fourier optics.

## REFERENCES

- Born, M. and Wolf, E. (1980). *Principles of Optics*, sixth edition, Chaps. 8 and 9, Oxford: Pergamon.
- Dwight, H. (1961). *Tables of Integrals and Other Mathematical Data*, fourth edition, New York: Macmillan.
- Mahajan, V. (1983). *Appl. Opt.*, **22**: 3035.
- Mahajan, V. (1991). *Aberration Theory Made Simple*, SPIE Tutorial Text TT6, Bellingham, WA: SPIE Optical Engineering Press.
- Mahajan, V. (1998). *Optical Imaging and Aberrations, Part I, Ray Geometrical Optics*, Chap. 2, Bellingham, WA: SPIE Optical Engineering Press.
- Schroeder, D. and Golimowski, D. (1996). *Publ. Astron. Soc. Pac.*, **108**: 510.
- Wetherell, W. (1980). *Applied Optics and Optical Engineering*, vol. 8, Chap. 6, New York: Academic Press.

## BIBLIOGRAPHY

*Principles of diffraction theory*

Hecht, E. (1987). *Optics*, second edition, Reading, MA: Addison-Wesley.

Longhurst, R. (1967). *Geometrical and Physical Optics*, second edition, New York: John Wiley.

Pedrotti, F. and Pedrotti, L. (1993). *Introduction to Optics*, second edition, Englewood, NJ: Prentice Hall.

*Aberrations for systems with annular pupils*

Mahajan, V. (1981). *J. Opt. Soc. Am.*, **71**: 75.

Mahajan, V. (1982). *J. Opt. Soc. Am.*, **72**: 1258.

*Perfect point spread function*

Stoltzmann, D. (1983). *Applied Optics and Optical Engineering*, vol. 9, Chap. 4, New York: Academic Press.

*Fourier Transforms*

Gaskill, J. (1978). *Linear Systems, Fourier Transforms, and Optics*, New York: John Wiley.

Goodman, J. (1968). *Introduction to Fourier Optics*, New York: McGraw-Hill.

The results in the preceding chapter provide a complete description of the characteristics of a perfect or near-perfect image of a distant point object. The response of an optical system to a set of point objects or, more generally, an arbitrary intensity distribution was not considered in that analysis. Clearly this response depends on factors in addition to the PSF such as, for example, blurring due to image motion or detector pixel size. Factors such as these are most easily included by using the theory of transfer functions to describe the system response and image characteristics.

### **11.1. TRANSFER FUNCTIONS AND IMAGE CHARACTERISTICS**

This approach to image analysis makes use of a complex function called the *optical transfer function* or OTF, with the real part of the OTF called the *modulation transfer function* or MTF. One advantage of this approach is that each independent component of a complete system, from the atmosphere to the detector, has its own OTF, and the system OTF is the product of the separate OTFs. This separation also applies to different types of wavefront error, with separate OTFs for geometric aberrations, random wavefront errors, and blurring due to image motion. The response of the system to an incident wavefront is determined by the system OTF comprising all these factors.

In this section, following a discussion of basic concepts, we draw upon results derived from the theory of transfer functions and show how they are used to determine image characteristics. For derivations and discussion of the theory, the reader should consult references given at the end of the chapter.

### 11.1.a. DEFINITION OF THE TRANSFER FUNCTION

The concept of the transfer function is most easily seen by assuming a specific object intensity distribution. Consider a set of equally spaced line sources whose intensity in a direction perpendicular to the lines varies sinusoidally, as shown in Fig. 11.1(a). Two parameters that describe this source are the spacing between the lines and the contrast. We let  $p_0$  denote the spacing, or spatial period, where  $\nu_0 = 1/p_0$  is the spatial frequency in cycles per unit length. The contrast  $C_o$  of the object, in the notation of Fig. 11.1(a), is defined as

$$C_o = \frac{I_{\max} - I_{\min}}{I_{\max} + I_{\min}}, \quad (11.1.1)$$

where  $C_o$  is assumed independent of  $\nu_0$ .

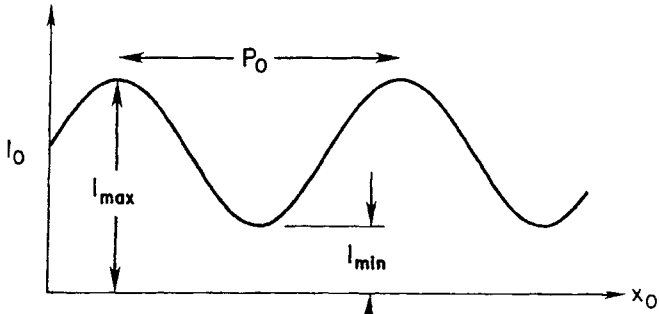
Assuming an optical system of constant magnification, the image of this object is also a sinusoidal intensity distribution, as shown in Fig. 11.1(b). Because each object point is imaged as a blur given by the PSF (or line spread function in one dimension), the image intensity is the superposition of all the individual spread functions. This addition of intensities assumes the illumination is incoherent.

We let  $p$  and  $\nu$  denote the spatial period and frequency, respectively, at the image surface. The contrast  $C_i$  in the image is defined according to Eq. (11.1.1), with maximum and minimum intensities substituted. For a system with magnification  $m$ , we have  $p = p_0 m$  and  $\nu = \nu_0/m$ . If the object distance is infinite, the spatial period and frequency of the object become angular period and frequency, with corresponding angular units. The image can also be described in angular terms in this case.

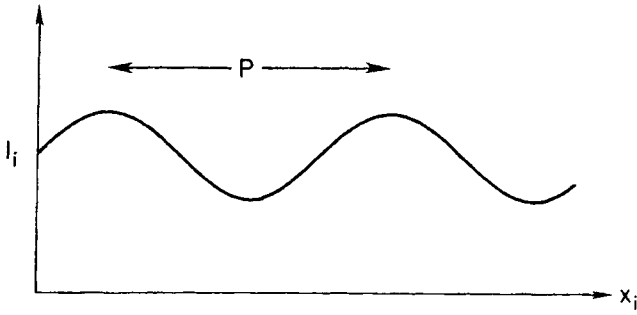
The *modulation transfer function*  $T$  is a measure of the change in contrast between the object and image, defined as

$$T(\nu) = \frac{C_i}{C_o} = \frac{\text{contrast in image at } \nu}{\text{contrast in object}}. \quad (11.1.2)$$

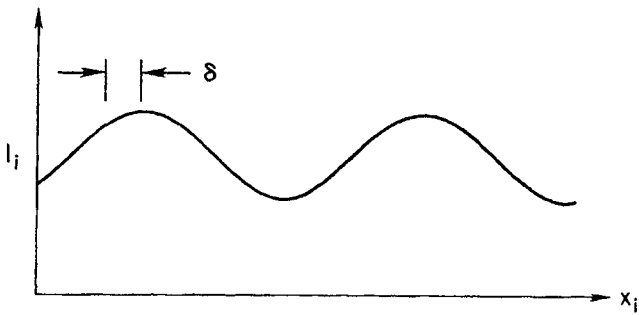
Given that each object point is imaged as a blur described by the point or line spread function, we expect  $T(\nu) < 1$  for all spatial frequencies. We also expect to find that  $T(\nu) \rightarrow 1$  as  $\nu \rightarrow 0$  and  $T(\nu) \rightarrow 0$  as  $\nu$  approaches the resolution limit set by the width of the PSF. The spatial frequency at which contrast in a perfect image goes to zero is called the *cutoff frequency*  $\nu_c$ . All information at frequencies higher than the cutoff frequency is lost.



(a)



(b)



(c)

**Fig. 11.1.** (a) Object sine wave intensity; (b) image intensity profile, unshifted; and (c) image intensity profile, shifted.

To determine the approximate cutoff frequency we apply the Rayleigh criterion of resolution to diffraction-limited images whose profiles are given by Eq. (10.2.8). As given in Section 10.2.e, this criterion states that two images of equal intensity are just resolved when the peak of one coincides with the first minimum of the other. For annular apertures Eq. (10.2.22) gives the angular limit of resolution as  $1.22\lambda/D$ , or approximately  $\lambda/D$ . The sum of two profiles like that in Fig. 10.5 at this separation gives an intensity midway between the peaks of approximately 0.8 that of either peak, and the peaks are “just resolved.” For a rectangular or square aperture, the corresponding angular separation of peaks of equal brightness that are just resolved is  $\lambda/b$ , where  $b$  is the aperture dimension parallel to the line joining the peaks of the PSFs. The intensity midway between the peaks is again approximately 0.8 that of either peak.

For an object at infinity, the angle  $\lambda/D$  corresponds to a linear separation of  $f\lambda/D$  at the image surface, or a spatial frequency of  $1/\lambda F$ . A rigorous derivation shows that the cutoff frequency  $\nu_c = 1/\lambda F$ , in linear units, with a corresponding cutoff frequency in angular units of  $D/\lambda$ . A good introduction to the theory of transfer functions, including derivation of the cutoff frequency, is given by Smith (1963). It is convenient to define the *normalized spatial frequency*  $\nu_n$  as

$$\nu_n = \nu/\nu_c = \nu_0/\nu_{0c}, \quad (11.1.3)$$

where the range of this parameter is zero to one. Comparisons of different optical systems, or the same system at different wavelengths, are most often made in normalized units.

In addition to reduced contrast, the intensity pattern may also be shifted laterally on the image surface, as shown in Fig. 11.1.c. This shift occurs if asymmetric aberrations, such as coma, are present. If the linear shift on the image surface is  $\delta$ , the phase transfer function  $\Phi_p$  is defined as

$$\Phi_p = 2\pi\delta/p. \quad (11.1.4)$$

A combination of Eqs. (11.1.2) and (11.1.4) leads to the definition of the complex *optical transfer function*  $Y(\nu)$  as

$$Y(\nu) = T(\nu) \exp[i\Phi_p(\nu)], \quad (11.1.5)$$

where each independent component of a system has its own  $Y(\nu)$ . The two mirrors of a Cassegrain telescope, for example, are considered a single component because the image quality is determined by the mirror combination.

Given these definitions it is possible, in principle, to determine the response of a system to any object intensity distribution. From the theory of Fourier analysis, one finds that any such distribution can be synthesized by some combination of sinusoidal functions of different frequencies. The transformation of each harmonic component of the object into the corresponding harmonic part of the image is determined by  $Y$  at that frequency.

An alternative method of finding the OTF is by calculating the autocorrelation of the pupil or aperture function. The pupil function for a perfect system is the transmittance, usually constant, within the boundaries of the exit pupil and is zero outside. For a system with aberrations, the pupil function is complex and includes aberrations, as noted in Section 10.5. The autocorrelation integral is essentially one that gives the area of overlap between two pupil functions, with one shifted relative to the other by an amount proportional to the spatial frequency. The reader should consult the references by both Born and Wolf and by Wetherell cited throughout this book for discussion of this approach to calculating the OTF.

The discussion in this section is intended as an introduction to the basic characteristics of the transfer function. We now turn our attention to the relation between the transfer function and image characteristics for the important case where the PSF is symmetric about the system axis.

### 11.1.b. POINT SPREAD FUNCTION AND ENCIRCLED ENERGY

The relations between image characteristics and the transfer function are derived using the theory of Fourier transforms. Given a PSF computed by the methods described in Section 10.2, the OTF is defined as the Fourier transform of the PSF. Because the PSF and OTF are a Fourier transform pair, the former can be calculated if the latter is known. For our purposes, we consider only the case where the phase transfer function  $\Phi_p$  is zero and the OTF reduces to the MTF. This limitation rules out the treatment of asymmetric aberrations such as coma.

In rectangular coordinates the MTF is given by

$$T(v_x, v_y) = A \iint_{-\infty}^{\infty} i(x, y) \exp [-2\pi i(v_x x + v_y y)] dx dy, \quad (11.1.6)$$

where  $v_x = v \cos \gamma$ ,  $v_y = v \sin \gamma$ ,  $x$  and  $y$  are given in Eq. (10.2.1), and  $A$  is a normalization factor chosen to give  $T = 1$  at  $v = 0$ .

In polar coordinates the corresponding relation to Eq. (11.1.6) is

$$T(v, \gamma) = \int_0^{2\pi} \int_0^{\infty} i(r, \psi) \exp [-2\pi i v r \cos (\psi - \gamma)] r dr d\psi, \quad (11.1.7)$$

where  $\gamma$  can be assigned any convenient value for the special but important case where the PSF is symmetric about the system axis. Letting  $\gamma = \pi$ , the integration over  $\psi$  in Eq. (11.1.7) is one of substituting the integral form of  $J_0$ , as done with Eq. (10.2.6).

Given a symmetric PSF and a circular aperture with a central obscuration, the methods of Fourier transforms give the following relations between the PSF, EE, and MTF:

$$T(v) = \frac{\pi^2(1 - \varepsilon^2)D^2}{2\lambda^2} \int_0^\infty i(\alpha) J_0(2\pi v\alpha) \alpha \, d\alpha, \quad (11.1.8)$$

$$\text{PSF}(\alpha) = \frac{8\lambda^2}{(1 - \varepsilon^2)D^2} \int_0^{v_c} T(v) J_0(2\pi v\alpha) v \, dv, \quad (11.1.9)$$

$$\text{EE}(\alpha) = 2\pi\alpha \int_0^{v_c} T(v) J_1(2\pi v\alpha) dv, \quad (11.1.10)$$

where  $v$  is the frequency in angular units,  $\alpha$  is the angular radius of the image, and  $J_0$  and  $J_1$  are Bessel functions. Because  $v$  is given in angular units, the cutoff frequency  $v_c$  in these units is  $D/\lambda$ . Equations (11.1.8)–(11.1.10) can be written in linear units by substituting  $fv$  (linear) for  $v$  (angular) and  $r$  for  $\alpha$ , where  $r = f\alpha$ . The factors outside the integrals in Eqs. (11.1.8)–(11.1.10) are normalization factors, with  $T(0) = 1$  and  $\text{PSF}(0) = 1$  for a perfect image, and  $\text{EE}(\infty) = 1$ .

Note the reciprocal relationship between Eqs. (11.1.8) and (11.1.9). Given the point spread function  $i(\alpha)$  we can find  $T(v)$  or, conversely, given  $T(v)$  we can compute  $i(\alpha)$ .

For ease of calculation and comparison of results for different systems or wavelengths, it is useful to rewrite these relations in terms of the normalized frequency  $v_n$ . The results are

$$T(v_n) = \frac{\pi^2(1 - \varepsilon^2)}{2} \int_0^\infty i(w) J_0(2\pi v_n w) w \, dw, \quad (11.1.11)$$

$$\text{PSF}(w) = \frac{8}{(1 - \varepsilon^2)} \int_0^1 T(v_n) J_0(2\pi v_n w) v_n \, dv_n, \quad (11.1.12)$$

$$\text{EE}(w) = 2\pi w \int_0^1 T(v_n) J_1(2\pi v_n w) dv_n, \quad (11.1.13)$$

where  $w = \alpha D/\lambda = \alpha v_c$ . Comparing the argument of each Bessel function with Eq. (10.2.10), we see that  $w\pi = v$ , the dimensionless parameter used in Section 10.2.

For calculations of PSF and EE, all that is needed is the MTF. The general expression for the MTF of a perfect circular pupil with a central obscuration, taken from Appendix B of the reference by Wetherell (1980), is given in slightly modified form in Table 11.1. For a clear circular aperture the factors  $B$  and  $C$  are zero. Substituting  $2A/\pi$  from Table 11.1 into Eq. (11.1.12), it is a simple calculation to verify that  $\text{PSF}(0) = 1$  for a clear aperture, as required by normalization.

Table 11.1

Modulation Transfer Function for Perfect Lens with Central Obscuration

---


$$T(v_n) = \frac{2}{\pi} \frac{(A + B + C)}{(1 - \varepsilon^2)}$$

$$A = [\cos^{-1} v_n - v_n(1 - v_n^2)^{1/2}], \quad 0 \leq v_n \leq 1$$

$$B = \varepsilon^2 \left\{ \cos^{-1} \left( \frac{v_n}{\varepsilon} \right) - \left( \frac{v_n}{\varepsilon} \right) \left[ 1 - \left( \frac{v_n}{\varepsilon} \right)^2 \right]^{1/2} \right\}, \quad \begin{array}{l} 0 \leq v_n \leq \varepsilon \\ v_n > \varepsilon \end{array}$$

$$= 0,$$

$$C = -\pi \varepsilon^2, \quad 0 \leq v_n \leq (1 - \varepsilon)/2$$

$$= -\pi \varepsilon^2 + \left\{ \varepsilon \sin \chi + \frac{\chi}{2} (1 + \varepsilon^2) - (1 - \varepsilon^2) \tan^{-1} \left[ \frac{(1 + \varepsilon)}{(1 - \varepsilon)} \tan \frac{\chi}{2} \right] \right\}, \quad (1 - \varepsilon) \leq 2v_n \leq (1 + \varepsilon)$$

$$= 0, \quad 2v_n > (1 + \varepsilon)$$

$$\chi = \cos^{-1} \left( \frac{1 + \varepsilon^2 - 4v_n^2}{2\varepsilon} \right)$$


---

Modulation transfer functions for selected values of  $\varepsilon$  are shown in Fig. 11.2. The main effect of a larger central obscuration is a decrease in the MTF in the middle of the frequency range. This is expected because the effect of the obscuration on the PSF is to put more energy into the first bright ring of the Airy pattern, and the contrast in the image of an extended object is reduced because of the larger fraction of energy in this ring. For spatial frequencies near the cutoff frequency, on the other hand, the MTF is slightly larger when the pupil has an obscuration. This is also expected because the FWHM of the Airy disk is smaller for larger  $\varepsilon$ , and the “sharper” peak implies a smaller limit of resolution according to the Rayleigh criterion.

When  $T(v_n)$  from Table 11.1 is substituted into Eqs. (11.1.12) and (11.1.13), and the equations are integrated numerically, results like those shown in Figs. 10.5 and 10.8 are obtained. For a perfect image it is obviously easier to use Eqs. (10.2.8) and (10.2.17) to find the PSF and EE, respectively, but in the presence of aberrations it is usually easier to use the MTF approach.

The calculation of MTFs in the presence of symmetrical aberrations is done by either evaluating the autocorrelation integral, with the aberrations included in the pupil function, or integrating Eq. (11.1.11) with  $i(w)$  for the aberrated image from Eq. (10.3.4). For images with defocus computed from Eq. (10.3.4), as shown in Figs. 10.12–10.14, the MTF curves are shown in Fig. 11.3. For a spherically aberrated image, as shown in Figs. 10.15–10.16, MTF curves at selected foci are shown in Fig. 11.4.

11. Transfer Functions; Hubble Space Telescope

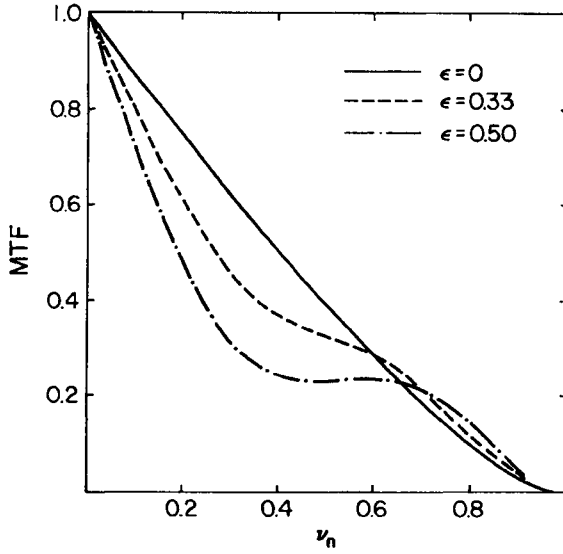


Fig. 11.2. Normalized modulation transfer function for several obscuration ratios calculated from relations in Table 11.1.

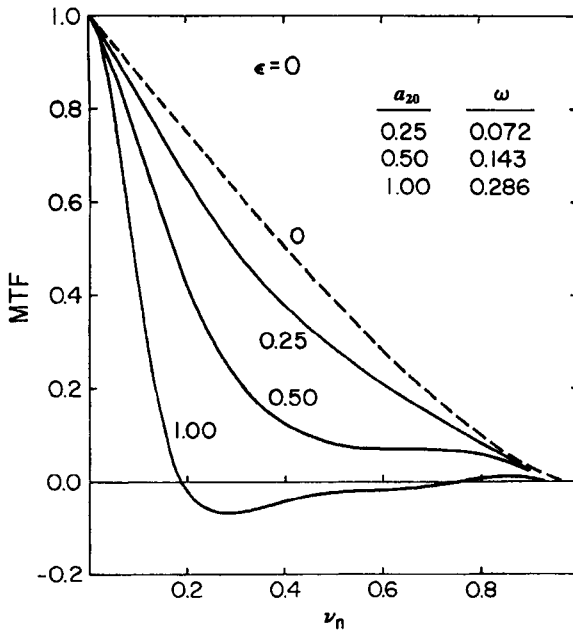


Fig. 11.3. Modulation transfer functions for perfect system ( $\epsilon = 0$ ) with defocus calculated from Eq. (11.1.11). The rms wavefront error  $\omega$  is given in units of waves.

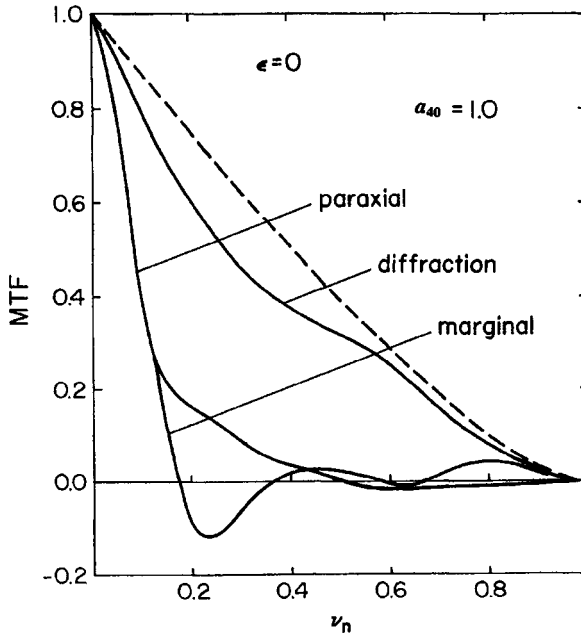


Fig. 11.4. Modulation transfer functions for unobstructed system ( $\varepsilon = 0$ ) with spherical aberration calculated from Eq. (11.1.11). Curves are given for paraxial, diffraction, and marginal foci.

### 11.1.c. MODULATION TRANSFER FUNCTIONS FOR OTHER WAVEFRONT ERRORS

In addition to wavefront errors due to classical aberrations, often called figure errors, we noted in the preceding that random errors on a finer scale due to the polishing process may also be present. Another source of image degradation is motion of an image due to effects from outside the optical system. Each of these nonfigure error contributions can be modeled with a factor in the MTF that is a statistical average of the effect. In this section we give an overview of some of these MTF models and their effects on the PSF and EE.

The proscribed way of including additional, independent MTF factors is to write the system MTF as a product of independent factors in the form

$$T = T_d T_f T_r T_p, \quad (11.1.14)$$

where  $T$  is the system MTF,  $T_d$  is the MTF for a perfect system, as given in Table 11.1, and the remaining factors are *degradation functions*. The subscripts  $f$ ,  $r$ , and  $p$  denote, in turn, contributions due to figure, random, and pointing errors. It is at this point where the advantage of Fourier transforms and the transfer function approach is most evident. If a degradation of the wavefront can be described

mathematically, then its MTF can be computed and included in the system MTF by a simple multiplication, provided this degradation is independent of all others. Complex wavefront degradation can therefore be reduced to a relatively simple set of separate contributions.

In considering random errors on a wavefront, we assume that all figure errors have been subtracted from the wavefront map at the exit pupil. Figure error is usually taken to be those components with spatial frequencies less than 5 cycles/radius over the pupil. We also assume that the remaining wavefront errors of higher spatial frequency are distributed in a random fashion over the residual wavefront. The choice for the upper limit to the spatial frequency depends on the size of the spatial period selected. For the 2.4-m primary mirror of the Hubble Space Telescope, a spatial period of 1 mm corresponds to a spatial frequency of 1200 cycles/radius. Random error in this middle range of spatial frequencies is often termed *ripple*.

A statistical analysis of this type of error has been made by O'Neill (1963). The result of this analysis is an MTF degradation factor in the midfrequency range of the form

$$T_m = \exp \{-k^2 \omega_m^2 [1 - c(v_n)]\}, \quad (11.1.15)$$

where  $k = 2\pi/\lambda$ ,  $\omega_m$  is the rms random wavefront error for midfrequencies, and  $c(v_n)$  is the normalized autocorrelation function of the residual pupil function. The characteristics of  $c(v_n)$  are such that  $c(0) = 1$  and  $c(v_n) \rightarrow 0$  for a large shift of the residual wavefront in the autocorrelation integral. If the function  $c(v_n)$  is modeled as a Gaussian of the form  $c(v_n) = \exp(-4v_n^2/l^2)$ , as given by Wetherell (1980), the degradation function  $T_m$  has the form shown in Fig. 11.5. The parameter  $l$  is the *normalized correlation length* and is a measure of the structure on the wavefront. To a rough approximation, the spatial period of the dominant structure is  $1/l$  cycles/diameter. For discussion of other forms of  $c(v_n)$  and comparison with measured results, the reader should consult the reference by Wetherell cited here.

Wavefront errors with high spatial frequencies, those larger than ones associated with ripple, are ascribed to microstructure on an optical surface, and often called *microripple*. The degradation function for high-frequency microripple follows directly from Eq. (11.1.15) if we let  $l \rightarrow 0$  in the autocorrelation function. In this limit

$$T_h = \exp(-k^2 \omega_h^2) \quad (11.1.16)$$

at all spatial frequencies except  $v_n = 0$ , where  $\omega_h$  is the rms wavefront error due to microripple. The product of Eqs. (11.1.15) and (11.1.16) is the degradation function  $T_r$  in Eq. (11.1.14).

Degradation of an image due to random motion has been discussed by several authors, including Mahajan (1978) and Wetherell (1980). The starting assumption

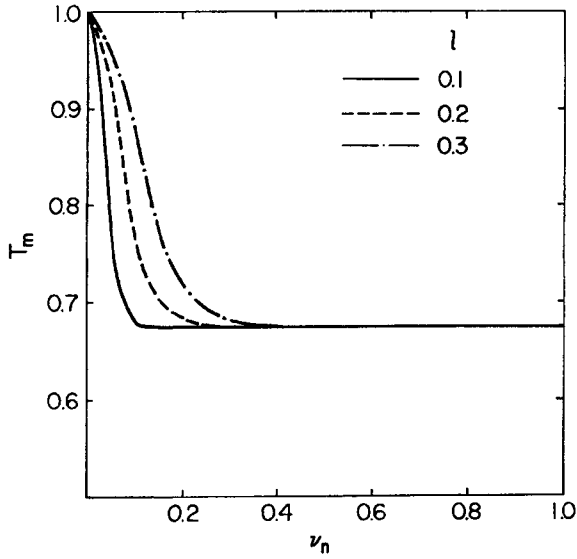


**Fig. 11.5.** Midfrequency degradation factor  $T_m$  with Gaussian correlation factor calculated from Eq. (11.1.15). The rms ripple error is 0.1 waves;  $l$  is the normalized correlation length.

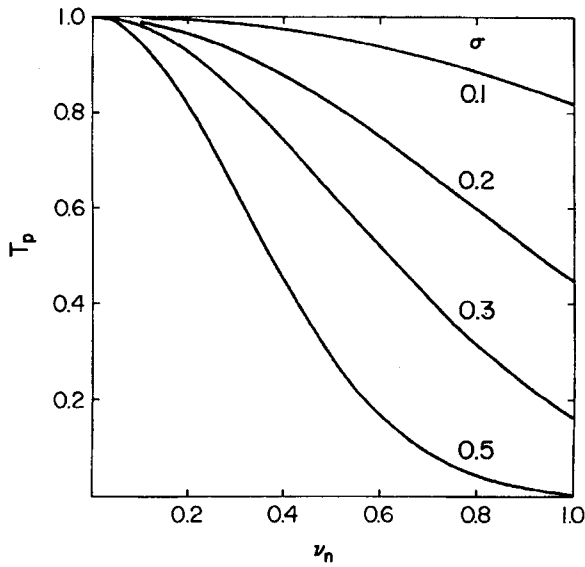


**Fig. 11.6.** Pointing degradation factor  $T_p$  for several normalized rms pointing errors calculated from Eq. (11.1.18).

of this analysis is an image motion that is rotationally symmetric and described by the unnormalized probability function

$$P(r) = \exp(-\alpha^2/2\sigma'^2), \quad (11.1.17)$$

where  $\sigma'$  is the standard deviation and  $\alpha$  is radius of the excursion of the image from the mean position, both in angular units. If we normalize  $\sigma'$  by multiplying by the cutoff frequency  $D/\lambda$ , then the pointing degradation function, as shown by Mahajan, is

$$T_p(v_n) = \exp(-2\pi^2\sigma^2 v_n^2). \quad (11.1.18)$$

Because  $T_p$  decreases as  $v_n$  increases, it is evident that the effect of this degradation function is to depress the MTF more at higher spatial frequencies. Figure 11.6 shows the pointing degradation function for several values of  $\sigma$ . For an otherwise perfect system, the product of curves in Figs. 11.2 and 11.6 gives the system MTF with random pointing error.

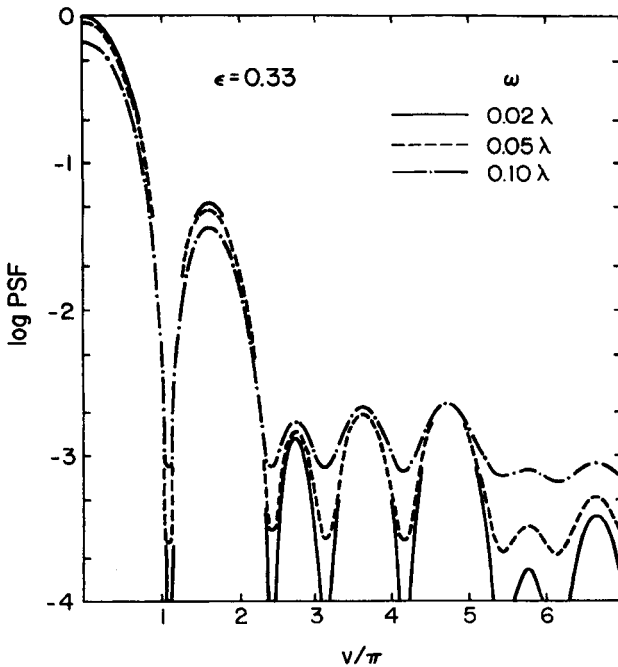


Fig. 11.7. Point spread function for obstructed system ( $\epsilon = 0.33$ ) with rms midfrequency error  $\omega$  and  $l = 0.04$ . Results are calculated from Eq. (11.1.12).

## 11.1.d. EXAMPLES

We now illustrate the results of the previous section by giving examples of PSFs and EEs calculated from Eqs. (11.1.12) and (11.1.13) with different degradation factors multiplying  $T_d$ , the diffraction MTF. All of the results given are for  $\epsilon = 0.33$ , the obscuration ratio of the HST, with zero figure error. A more complete discussion of the expected image characteristics of HST, with all factors taken together, follows in the next section.

Figures 11.7 and 11.8 show PSF and EE for a pupil wavefront with random error of the type described by Eq. (11.1.15), for three values of  $\omega$ . The approximate correlation length assumed for these calculations is 0.04 cycles/diameter. Relative to the PSF for a perfect system, given in Fig. 10.5, the effect of this error is to depress the disk and inner ring and raise the outer rings. The Strehl intensity is given by Eq. (10.3.9). The transfer of energy outward from the center of the Airy pattern is clearly shown in Fig. 11.8. Taking values of EE at the right-hand side of Fig. 11.8, we see that nearly five times as much energy is outside the fourth bright ring when  $\omega = 0.1\lambda$ , compared to a perfect image.

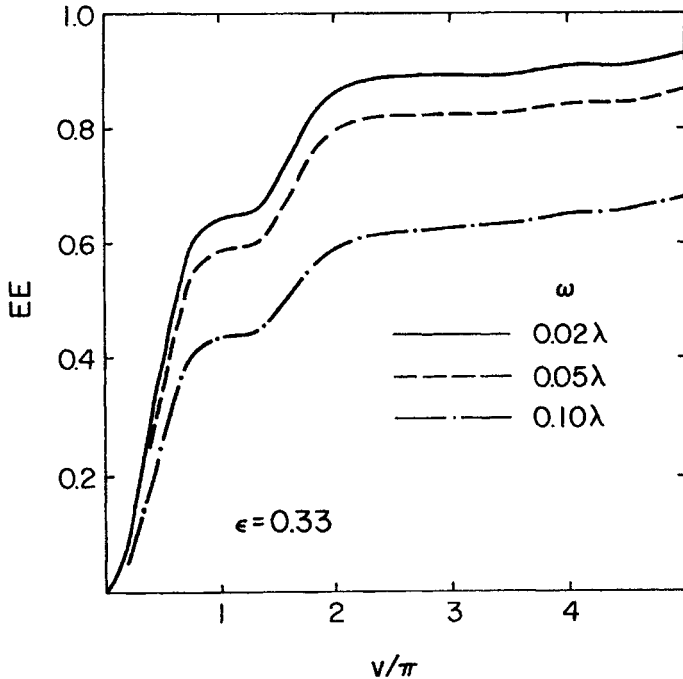
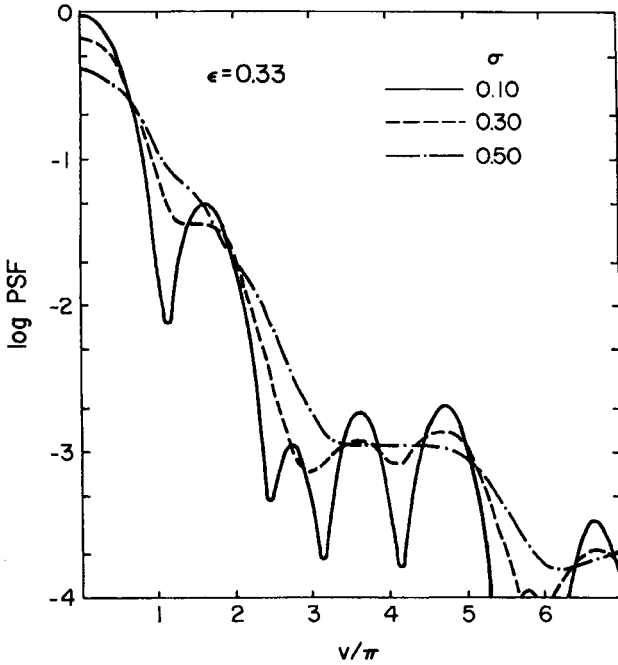


Fig. 11.8. Encircled energy fraction for obstructed system ( $\epsilon = 0.33$ ) with rms midfrequency error  $\omega$  and  $l = 0.04$ . Results are calculated from Eq. (11.1.13).

11. Transfer Functions; Hubble Space Telescope



**Fig. 11.9.** Point spread function for perfect system ( $\epsilon = 0.33$ ) with pointing error. The  $\sigma$  is the normalized rms Gaussian error. Results are calculated from Eq. (11.1.12).

When high-frequency microripple is present, as described by Eq. (11.1.16), the effect is to depress the PSF by the factor  $T_h$  at all image radii. This occurs because  $T_h$  is independent of spatial frequency, hence it can be taken out of the integral in Eq. (11.1.12). The effect of microripple on EE is similar, for the same reason. In theory, therefore, the energy scattered by microripple error disappears; in practice the energy is scattered at angles large compared to the Airy disk diameter.

Figures 11.9 and 11.10 show PSF and EE for a perfect system with pointing error described by Eq. (11.1.18), for three values of  $\sigma$ . The effect of increased pointing error is clearly one of reducing the Strehl intensity, smoothing the PSF pattern, and distributing a given fraction of the encircled energy over a larger area. For the values of  $\sigma$  shown, the redistribution of energy takes place largely between the disk and first bright ring. With specific reference to HST, the curve with  $\sigma = 0.1$  corresponds to an rms pointing error  $\sigma'$  on the sky of 0.005 arc-sec, at  $\lambda = 580$  nm, with  $\sigma' = \sigma(\lambda/D)$ . Because  $\sigma$  is inversely proportional to  $\lambda$  for a given  $\sigma'$ , the curve with  $\sigma = 0.3$  corresponds to the same pointing error at  $\lambda = 190$  nm. As expected, a given pointing error on the sky has a greater effect on a “sharper” image.

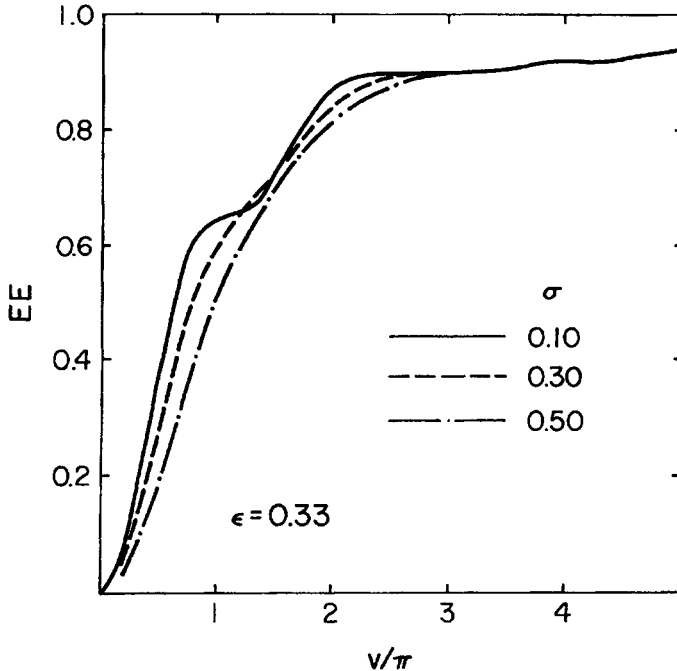


Fig. 11.10. Encircled energy fraction for perfect system ( $\epsilon = 0.33$ ) with pointing error. The  $\sigma$  is the normalized rms Gaussian error. Results are calculated from Eq. (11.1.13).

With these examples it should be clear that the MTF approach is a powerful technique, especially when errors other than figure errors are present. We conclude our introduction to the MTF approach in Section 11.4 following a discussion of the Hubble Space Telescope.

## 11.2. HUBBLE SPACE TELESCOPE, PRELAUNCH EXPECTATIONS

NOTE: *This section on the Hubble Space Telescope is essentially unchanged from the version that appeared in the 1st edition of this book. What was presented there, and is repeated here, represented the best estimates of the expected optical performance of HST following its launch. As is well known, HST did not perform up to expectations because of a primary mirror with the wrong conic constant. As is also well known, HST was given an optical "fix" that corrected for the spherical aberration introduced by the primary and the performance was restored, or nearly so, to that of prelaunch expectations. With this fix the results given here are again valid, hence the reason for leaving this section largely unchanged. A discussion of the postlaunch reality of HST follows in Section 11.3.*

The HST will be the first large astronomical observatory in space with a resolution capability an order of magnitude better than is possible with ground-based telescopes in the visible and near ultraviolet. This unique facility will enable astronomers to make observations not possible from the ground and obtain data needed to answer many fundamental astronomical questions. Given this promise, a brief description of HST and the expected image characteristics is in order.

### 11.2.a. BASIC CONFIGURATION

The HST is a 2.4-m Cassegrain telescope of the Ritchey-Chretien type, with the nominal parameters given in Table 11.2. The performance goals set by NASA at the start of the project include spectral coverage from 115 nm to the far infrared, with diffraction-limited performance at visible wavelengths. Analysis of the completed system shows that HST is expected to meet or exceed the stated goal of  $\lambda/20$  rms wavefront error at  $\lambda = 633$  nm on the axis of the  $f/24$  focal surface.

The complete observatory includes the following complement of instruments: wide-field/planetary camera (WFPC), faint object camera (FOC), faint object spectrograph (FOS), high-resolution spectrograph (HRS), and high speed photometer (HSP). The fine guidance system (FGS) of the telescope will also be used for astrometric observations. For details on these instruments and their observing modes, the reader should consult the references at the end of the chapter, especially the *Instrument Handbook* distributed by the Space Telescope Science Institute.

### 11.2.b. ON-AXIS IMAGE CHARACTERISTICS

In this section we describe the expected on-axis image characteristics at the  $f/24$  focal surface. All of the results presented assume the mirrors are clean with no scattering due to dust.

**Table 11.2**

Nominal Design Parameters of Hubble Space Telescope

Primary:	$D = 2400$ mm, $R_1 = -11040$ mm, $f/2.30$ $K_1 = -1.0022985$
Secondary:	$R_2 = -1358$ mm, $K_2 = -1.496$
Overall:	$m = 10.435$ , $\beta = 0.2717$ , $k = 0.1112$ , $f/24$ , obscuration ratio $\epsilon = 0.33$ scale = 3.58 arc-sec/mm = 279 $\mu\text{m}/\text{arc-sec}$

Analysis of HST performance proceeds along the lines described in the previous section. Each independent component is described by an MTF degradation function, and the product of these functions and the diffraction MTF is used as the basis of calculations of the image characteristics. Contributors to  $T_f$  in Eq. (11.1.14) include the aberrations of the mirrors, misalignments of the mirrors, thermal changes in orbit, ground-to-orbit changes, and errors of the optical system used to measure the wavefront in orbit. The errors that remain after figure errors are removed from the wavefront map are used to calculate  $T_m$  in the form given in Eq. (11.1.15). Surface errors derived from measurements on small parts of the mirrors are modeled as high-frequency errors in the form given in Eq. (11.1.16). The product of these functions, to which the figure error is the largest contributor, gives the system degradation function in the absence of pointing error. This combination leads to an overall rms system wavefront error of approximately  $\lambda/21$  at a wavelength of 633 nm.

The product of the system degradation function with the diffraction MTF and the pointing degradation factor given in Eq. (11.1.18) gives the rotationally symmetric system MTF used in Eqs. (11.1.12) and (11.1.13). All of the following results are derived from calculations using these relations, with a nominal rms pointing error of 0.007 arc-sec assigned to image motion.

Figures 11.11 and 11.12 show PSFs at a number of wavelengths, with EE for each of these wavelengths shown in Figs. 11.13 and 11.14. It is evident from these curves that the PSFs show progressive degradation at shorter wavelengths. The ring structure in the Airy pattern, clearly seen in the visible and infrared wavelengths, is absent at the shortest wavelengths. This is a result both of pointing error and nonfigure contributors to the degradation function. We also see that the level of the PSF decreases in the ultraviolet, a consequence of the mid- and high-frequency components in the degradation function.

The Strehl ratio  $S$  and the FWHM of the image peak are shown in Fig. 11.15. The most notable feature of the FWHM curve is the limiting core diameter of about 0.023 arc-sec at the shortest wavelengths. Figure 11.16 shows the peak intensity  $I_0$  as a function of wavelength, normalized to unity at  $\lambda = 633$  nm, assuming equal flux at each wavelength. The intensity at the peak is given by Eq. (10.2.19) with  $S$  included for a degraded image. Therefore

$$\frac{I_0(\lambda)}{I_0(633)} = \frac{S_\lambda}{S_{633}} \left( \frac{633}{\lambda} \right)^2, \quad (11.2.1)$$

wher  $\lambda$  is in nanometers and  $S$  is given in Fig. 11.15. Also shown in Fig. 11.16 is the average intensity over an area enclosing 60% of the total energy. These results are derived using Eq. (10.2.20) with  $\eta = 0.6$  and image radii taken from Figs. 11.13 and 11.14. The curves in Fig. 11.16 would show a  $\lambda^{-2}$  dependence for a perfect image; the actual curves show a peak in the ultraviolet.

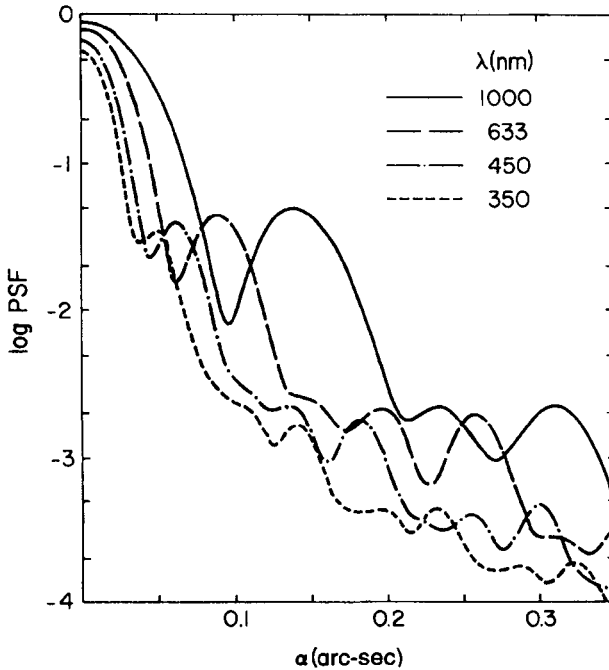


**Fig. 11.11.** Predicted PSFs for Hubble Space Telescope (HST). The rms wavefront error is  $\lambda/21$  at 633 nm; the rms pointing error is 0.007 arc-sec.

Extension of PSF calculations to larger image radii than those shown in Figs. 11.11 and 11.12 shows that the average intensity far from the Airy disk falls off as  $\alpha^{-3}$ , as for a perfect image. However, the intensity level is higher than that of a perfect image by an amount that depends on the wavelength. Comparing the average PSF at a radius of 1 arc-sec calculated from Eq. (11.1.12) with that given by Eq. (10.2.12), we get the results shown in Fig. 11.17. The increasing spread between the curves in Fig. 11.17 at shorter wavelengths is largely a consequence of the mid- and high-frequency factors in the degradation function. As noted in Section 11.1, the effect of these factors is to transfer energy from the inner region of the Airy pattern to the wings.

These characteristics for the HST images are based on extensive modeling and represent the best estimate of what can be expected once HST is in orbit. Predictions of the effect on the PSF and EE from dust on the mirrors have been made, with the results predicting some additional fraction of light scattered into the image wings. This fraction is uncertain because it is sensitive to the size distribution among the dust particles. Definitive image characteristics will only be known after extensive observations in space.

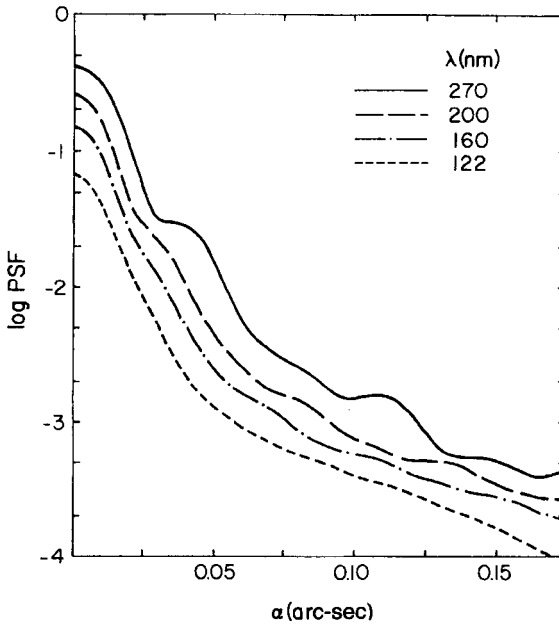


Fig. 11.12. Predicted PSFs for HST. The wavefront and pointing errors are given in the caption of Fig. 11.11.

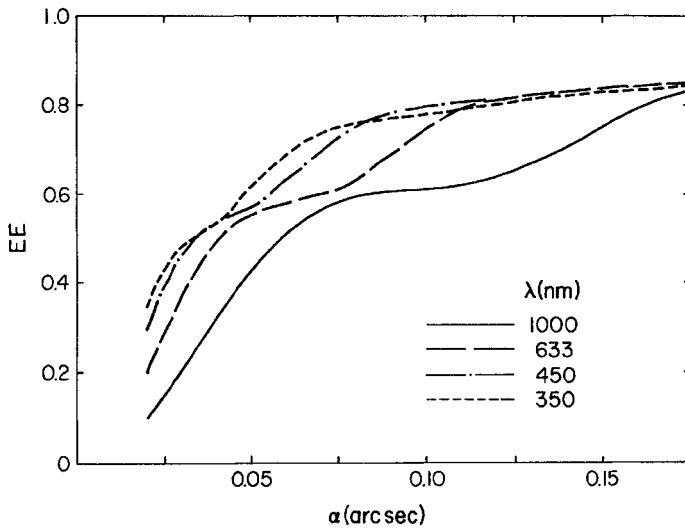


Fig. 11.13. Predicted EEs for HST. The wavefront and pointing errors are given in the caption of Fig. 11.11.

11. Transfer Functions; Hubble Space Telescope

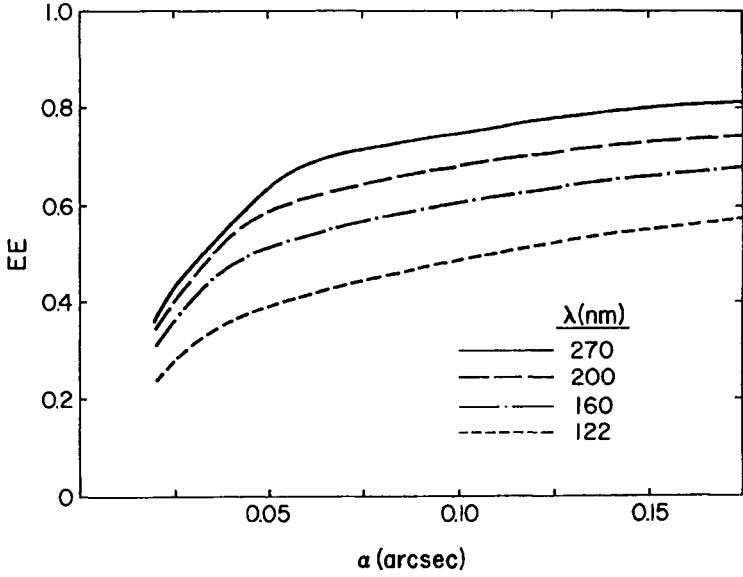


Fig. 11.14. Predicted EEs for HST. The wavefront and pointing errors are given in the caption of Fig. 11.11.

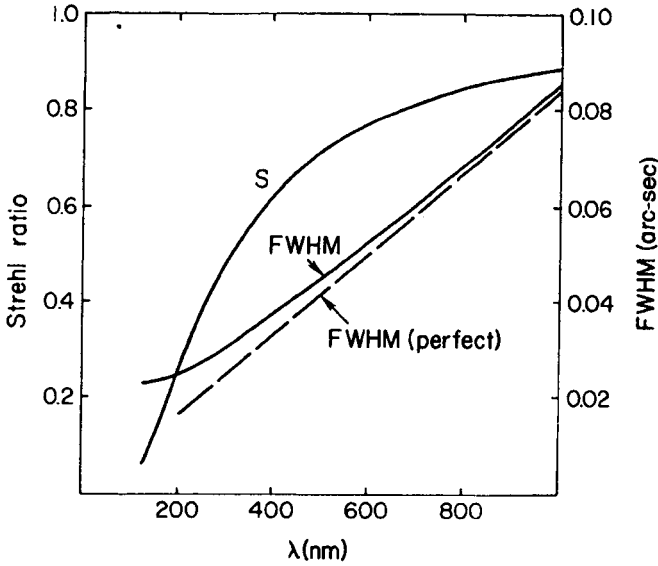


Fig. 11.15. Predicted Strehl ratio and FWHM for HST. The wavefront and pointing errors are given in the caption of Fig. 11.11.

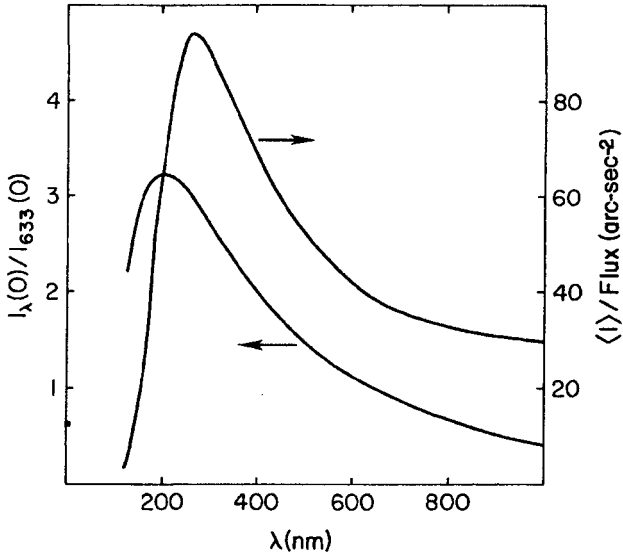


Fig. 11.16. Peak intensity of HST normalized to unity at 633 nm and average intensity per unit flux on area enclosing 60% of the encircled energy.

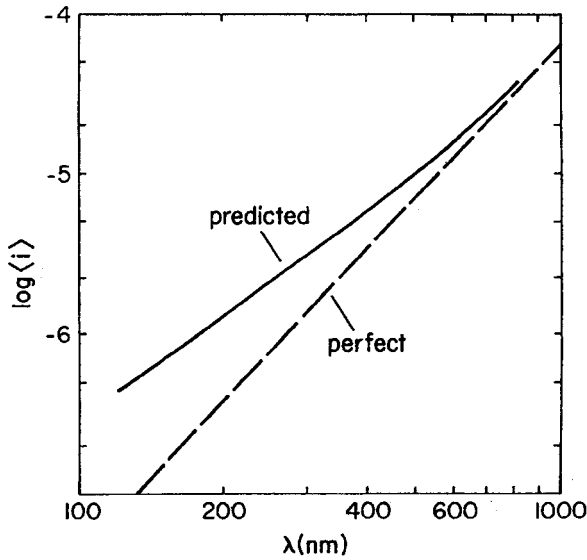


Fig. 11.17. Predicted average PSF for HST at 1 arc-sec from image peak. The wavefront and pointing errors are given in the caption of Fig. 11.11.

NOTE: *The material in Section 11.2.c of the 1st edition has been incorporated into Section 10.4 of this edition. The preceding paragraph appeared in Section 11.3 of the 1st edition and is now located where it properly belongs. A discussion related directly to the last sentence of the preceding paragraph follows.*

### 11.3. HUBBLE SPACE TELESCOPE, POSTLAUNCH REALITY

Contrary to the predicted diffraction-limited performance, actual images taken with HST shortly after launch were seriously deficient in quality, even after repeated attempts to improve the quality by refocusing the telescope. After careful analysis of the characteristics of the images obtained during the weeks following launch, it became clear that the image degradation was a consequence of significant spherical aberration introduced by the primary mirror. The error in the primary is essentially one of an incorrect conic constant, a consequence of errors in the null mirror/lens system used in the manufacture of the primary. An interested reader can learn more about the detailed characteristics of these aberrated images and the null system in a paper by Burrows (see Burrows, 1991).

For our purposes the details of the analysis leading to the identification of spherical aberration due to the primary as the cause for the poor images is unimportant. Rather, we take this as given and use both the geometric and diffraction theory of aberrations to determine the consequences of the spherical aberration on the image.

The starting point for our analysis is the spherical aberration coefficient  $B_3$  for a Cassegrain telescope from Table 6.5. Using the nominal parameters of HST from Table 11.2 we find  $B_3 = 0$ , as expected. If the conic constant  $K_1$  is changed to  $K'_1$ , the change in  $B_3$  is

$$\delta B_3 = \frac{K'_1 - K_1}{4R_1^3} = \frac{\delta K_1}{4R_1^3}, \quad (11.3.1)$$

hence

$$\lambda a_{40} = \delta B_3 a^4 = \frac{\delta K_1}{4} \left( \frac{a}{R_1} \right)^3 a = -\frac{\delta K_1}{256F_1^3} a. \quad (11.3.2)$$

The first part of Eq. (11.3.2) is taken from Table 10.8.

Analysis of the aberrated images gave  $K'_1 = -1.0140 \pm 0.0005$ , hence a change  $\delta K_1 = -0.0117$ . Substituting  $\delta K_1$  and parameters from Table 11.2 into Eq. (11.3.2) gives  $\lambda a_{40} = 4.51 \mu\text{m}$  as the magnitude of the wavefront error at the edge of the HST primary, hence a surface error of  $2.25 \mu\text{m}$ . With  $\delta B_3 > 0$ , the marginal focus lies farther from the secondary mirror than the paraxial focus.

This is expected from a primary that is “flatter,” that is, with a more negative conic constant.

Given the wavefront error  $\lambda a_{40} = 4.51 \mu\text{m}$  and  $\epsilon = 0.33$ , we find the rms wavefront error and blur diameter at diffraction focus and distances from paraxial focus as follows,

$$\begin{aligned} \omega &= 0.30 \mu\text{m} = 0.42 \text{ waves at } \lambda = 633 \text{ nm,} \\ \text{angular diameter at diffraction focus} &= 4\lambda a_{40}/a = 3.1 \text{ arc-sec,} \\ \text{paraxial focus} \rightarrow \text{marginal focus} &= 16\lambda a_{40}F^2 = 41.6 \text{ mm,} \\ \text{paraxial focus} \rightarrow \text{diffraction focus} &= 8\lambda a_{40}F^2(1 + \epsilon^2) = 23.1 \text{ mm,} \end{aligned}$$

with the necessary relations taken from Table 10.6, Table 10.8, Section 10.3.c, and Table 10.4, in turn. The overall system is clearly far from diffraction-limited.

We first examine the images as seen in spot diagrams. Figure 11.18 shows spot patterns at equal separations, starting with paraxial focus at the left and ending with marginal focus at the right. Note that the smallest overall image is at the circle of least confusion, as expected for large spherical aberration, with a diameter of approximately 1.6 arc-sec.

From the point of view of diffraction theory, the optimum image location is not the circle of least confusion, but at diffraction focus where the rms wavefront

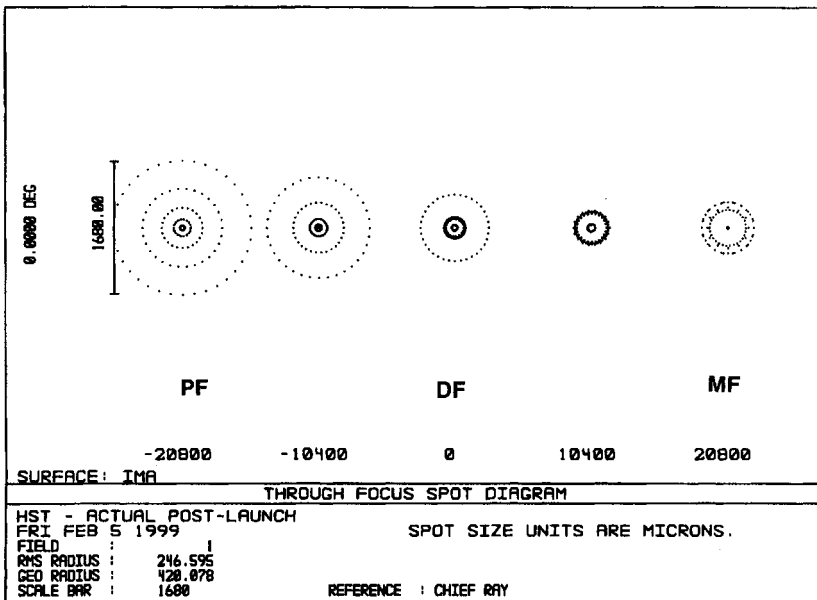


Fig. 11.18. Spot diagrams for the aberrant on-axis image of HST following launch. Paraxial focus (PF); diffraction focus (DF); marginal focus (MF). The scale bar on the left is 6 arc-sec long.

error is a minimum. Calculations of the encircled energy fraction show that, within an image radius of 0.5 arc-sec at  $\lambda = 633$  nm, EE is about 0.65 for diffraction focus versus approximately 0.4 for the circle of least confusion.

Although the choice of the optimum focus as diffraction focus seems evident, further considerations led to setting the focus at that position giving the maximum encircled energy fraction in 0.1 arc-sec radius at  $\lambda = 486$  nm. This setting is nearly 10 mm removed from diffraction focus and in the direction of paraxial focus. Curves of EE for the chosen focus and diffraction focus are shown in Fig. 11.19 for  $\lambda = 633$  nm. These curves were computed using Eq. (10.1.10) with  $i(P)$  calculated from Eq. (10.3.4). From Fig. 11.19 we see that EE is 0.15 within 0.1 arc-sec radius at the chosen focus.

Cross sections of  $i(P)$  at  $\lambda = 633$  nm for these two foci are shown in Fig. 11.20. Note the relatively sharp central peaks present in Fig. 11.20, with the peak at the chosen focus noticeably wider than the one at diffraction focus. Note that the first few rings surrounding the main peak at the chosen focus are also more widely spaced than those for diffraction focus. These results are understandable because the main contributions to the main peak for an image near paraxial focus come from the inner part of the annular aperture. Because the width of the contributing annulus is narrower, the diffraction peak is broader.

Conversely, the light from the outer part of the annulus, where the wavefront error is larger, is primarily responsible for the broad but faint plateau of light in which the main peak is centered. From geometric considerations, the radius of the spot pattern at the chosen focus is about 2.2 arc-sec, while the diffraction PSF in Fig. 11.20 shows a falloff in intensity starting at approximately 1.5 arc-sec.

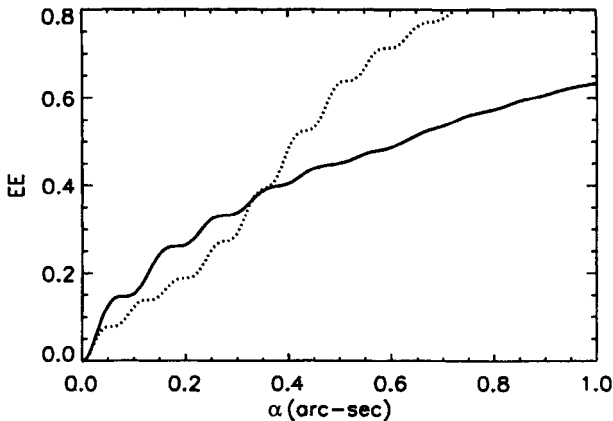


Fig. 11.19. Encircled energy curves for aberrant HST image at two focal positions: maximum encircled energy at 0.1 arc-sec (solid); diffraction focus (dashed).

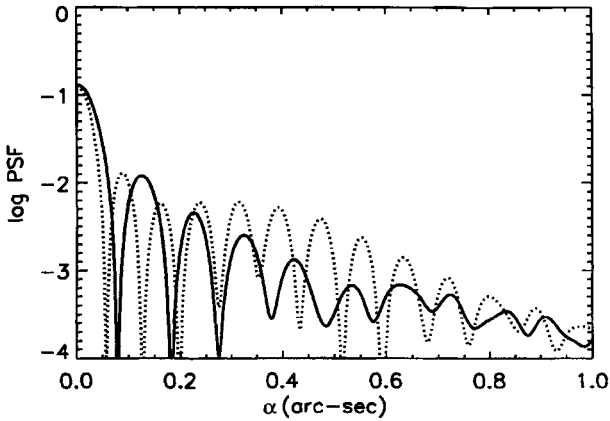


Fig. 11.20. The PSFs for aberrant HST image at two focal positions: maximum encircled energy at 0.1 arc-sec (solid); diffraction focus (dashed).

Because of the dramatic difference between the expected encircled energy fractions in Fig. 11.13 and those in Fig. 11.19, the performance of HST and its suite of instruments was severely compromised. In the months following the launch, a set of possible optical “fixes” of the spherical aberration was studied. The chosen solution has been discussed briefly in Sections 2.6.c and 6.5.b, namely, that of the addition of two mirrors following the HST secondary. The first of these two mirrors reimaged the entrance pupil (primary mirror) of HST onto the second mirror, where the optical correction was made. In effect, the surface error at the primary,  $(B_3/2)(\rho a)^4$  from Eq. (11.3.1) for a ray at radius  $\rho a$  on the primary is put on the second mirror, but with opposite sign, at radius  $\rho r_4$ . With this correction, rays through the aberrant telescope and the two-mirror add-on again satisfy Fermat’s Principle and spherical aberration is eliminated.

The implementation of this solution was specific to each of four instruments on HST. A separate pair of mirrors was configured for each of three axial instruments, the FOC, FOS, and HRS, and mounted in a separate module called COSTAR (for Corrective Optics, Space Telescope Aberration Recovery). With COSTAR in place in HST, each pair of mirrors was positioned ahead of the focal surface and redirected an incident beam in the proper direction. Thus the light entering the apertures of the spectrographs or camera was free of spherical aberration and the full capabilities of these instruments could be realized.

• In the case of WFPC, the radial instrument, implementation of the fix required modifying the original optical design slightly to ensure that the reimaged pupil was exactly on the secondary mirror of the instrument cameras. Because of the potentially serious problems due to pupil shear from a decentered pupil, discussed

in Section 6.5.b, WFPC2 was limited to four cameras rather than eight as in the original WFPC. Fortunately, the installation of COSTAR and WFPC2 in orbit was spectacularly successful and HST has realized its original promise.

#### 11.4. CONCLUDING REMARKS

The theory, as presented in Chapters 10 and 11, is an introduction to the main features of the diffraction theory of aberrations, but for many systems this is sufficient for design purposes. Relations for orthogonal aberrations of higher order have been derived and these are used in designing optical systems of the highest precision. The reader should consult the literature for information on these refinements.

The discussion in Section 11.1 leading up to Eq. (11.1.6) was general, but the derivation of Eqs. (11.1.8) through (11.1.13) required a symmetric aperture function and PSF. Returning to the general case, we outline the approach for an arbitrary aperture function.

The starting point for an arbitrary aperture function is Eq. (10.5.1) with  $A(\xi, \eta)$  including a term  $\exp(ik\Phi)$  for aberrations. The optical path difference  $\Phi$  usually covers figure errors of the type in Eq. (10.3.2), but may include a detailed map of other wavefront errors, as in the case of a mirror map for HST. With the aperture function specified, the solution of Eq. (10.5.1) gives  $U(P)$ , the Fourier transform of the aberrant aperture function, and  $i(P) = |U(P)|^2 / |U(O)|^2$ .

The next step is to compute the Fourier transform of  $i(P)$  according to Eq. (11.1.6) and find the transfer function  $T(v_x, v_y)$ . At this point mid- or high-frequency errors or pointing jitter can be incorporated by multiplying  $T$  by the appropriate degradation functions to get the overall system transfer function  $T_s$ . The final step to find the PSF is to take the Fourier transform of  $T_s$ .

Imaging characteristics of diffraction-limited telescopes at visible wavelengths were of little more than academic interest prior to the start of the space age, with images from large ground-based telescopes dominated by seeing. Fortunately the diffraction theory of aberrations discussed in Chapter 10 was well established at the time when thoughts turned to designing a space observatory as large as HST.

Diffraction theory, along with that of transfer functions, is now essential in the design of large ground-based telescopes. In Chapter 16 we use these theories to examine the effects of atmospheric turbulence on image quality and the potential gains from applying techniques of adaptive optics. In Chapter 18 we use transfer functions to represent some of the characteristics of large mirrors and their effects on image quality.

**REFERENCES**

- Mahajan, V. (1978). *Appl. Opt.*, **17**: 3329.  
O'Neill, E. (1963). *Introduction to Statistical Optics*, Reading, MA: Addison-Wesley.  
Smith, F. (1963). *Appl. Opt.*, **2**: 335.  
Wetherell, W. (1980). *Applied Optics and Optical Engineering*, vol. 8, Chap. 6, New York: Academic Press.

**BIBLIOGRAPHY***Fourier Optics*

- Goodman, J. (1968). *Introduction to Fourier Optics*, New York: McGraw-Hill.  
Hecht, E. (1987). *Optics*, second edition, Chap. 11, Reading, MA: Addison-Wesley.  
Steward, E. (1983). *Fourier Optics: An Introduction*, New York: John Wiley.

*Hubble Space Telescope*

- Burrows, C. (1991). *The First Year of HST Observations*, Kinney, A. and Blades, J. (eds.), p. 96, Baltimore, MD: Space Telescope Science Institute.  
*Instrument Handbooks*. Published periodically by the Space Telescope Science Institute, Baltimore, MD.  
*The Space Telescope Observatory* (1982). NASA CP-2244, NASA, Washington, DC.  
Schroeder, D. (1985). *Advances in Space Research: Astronomy from Space*, **5**: (3), 157.

Spectral analysis of celestial objects is probably the most important means for learning about the physics of these sources, with a large fraction of telescope time used to get spectral data. In this chapter we begin to consider the characteristics of spectrometers used with telescopes to get this data.

We use the term *spectrometer* in our discussion to refer to any of several types of spectroscopic instruments. A *spectrograph* is an instrument in which many spectral elements are recorded simultaneously with an area detector having many resolution elements. A *monochromator* is an instrument in which single spectral elements are recorded sequentially in time by a detector with a single resolution element. Many of the results that follow apply to either type of instrument, but if there is a difference the distinction is noted.

A simple method of getting spectral information is imaging with filters, broad- or narrowband filters placed in the beam ahead of the telescope focal surface and a detector. This technique is usually called *filter photometry*. For point sources the result is one piece of spectral information per image for each source in the field, while for extended objects there is one piece of spectral information for each resolution element on a 2D detector.

More detailed spectral information is obtained if the light is sent through a dispersing element, such as a prism or diffraction grating. In this case a spectrum is obtained for each source whose light passes through the disperser, with the number of pieces of spectral information per source determined by the mode in

which the disperser is used. In the so-called *slitless spectroscopy* mode a prism or grating acts as a dispersing filter and gives a spectrum for each source in the field. For *slit spectroscopy*, when the disperser is part of a slit spectrometer, a spectrum is obtained for each source whose light passes through the slit.

Two other spectroscopic modes used extensively in astronomy are *multiple object spectroscopy* (MOS) and *integral field spectroscopy* (IFS). When used with a grating spectrometer, each of these modes uses optical fibers to transfer light from a 2D focal surface of a telescope to the one-dimensional (1D) spectrometer slit. The difference between the modes is the arrangement of the fibers on the 2D focal surface. For MOS each fiber is set on a single source within a group of stars or galaxies, while for IFS the fibers are tightly packed in order to get spectra over an area of an extended source.

In succeeding sections we present the basic principles that govern the operation of all spectrometric devices and define such terms as limit of resolution, spectral resolving power, etendue, and luminosity. We also discuss in more detail the characteristics of the various modes noted here. Another source of information about the principles of spectrometry is the excellent book by Meaburn (1976).

## 12.1. INTRODUCTION AND DEFINITIONS

Each type of spectrometer is denoted by the kind of dispersing element that is used, hence prism, grating, or Fabry–Perot spectrometer. The dispersing element is usually located between auxiliary optics that collimate the light beam from the telescope and focus the dispersed light onto a detector. Exceptions to this type of arrangement are noted in the following sections, with representative examples discussed in Chapter 15.

The one type of spectrometer that does not have a dispersing element is the so-called Fourier transform spectrometer. This instrument is basically a Michelson interferometer whose output is an interferogram from which spectral information is derived by Fourier analysis. Because the Fourier spectrometer is not a dispersive device, the definitions in the following sections that include dispersion do not apply to this type of spectrometer. An introduction to Fourier spectrometers is provided in Section 13.6.

### 12.1.a. ANGULAR AND LINEAR DISPERSION

Each type of dispersing element is characterized by its *angular dispersion*, defined as  $d\beta/d\lambda$ , where  $d\beta$  is the angular difference between two rays of wavelength difference  $d\lambda$  emerging from the disperser. This is shown schematically in

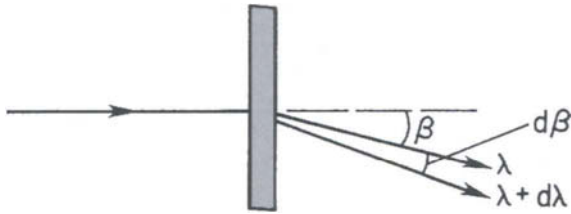


Fig. 12.1. Schematic of dispersive element. Angular dispersion  $A = d\beta/d\lambda$ .

Fig. 12.1 for a single ray incident on the dispersive element. Relations for angular dispersion of different dispersive elements are given in Chapter 13.

The angular dispersion is clearly a parameter associated with the dispersive element, independent of the configuration in which it is used. When the element is part of an optical system, the characteristics of both are combined to define the *linear dispersion*,  $dl/d\lambda$ , where  $dl$  is the linear separation on a focal surface between two rays of wavelength difference  $d\lambda$ .

If collimated light is incident on the disperser, then the linear dispersion is given by

$$dl/d\lambda = f \, d\beta/d\lambda = fA \quad (12.1.1)$$

where  $f$  is the focal length of the optics following the dispersive element, and  $A$  is the angular dispersion. This case is shown in Fig. 12.2.

If a convergent beam of light is incident on the disperser, the linear dispersion is

$$dl/d\lambda = s \, d\beta/d\lambda = sA \quad (12.1.2)$$

where  $s$  is the distance from the disperser to the focal surface. This case is shown in Fig. 12.3.

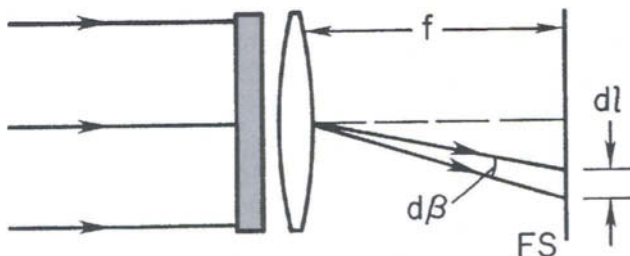
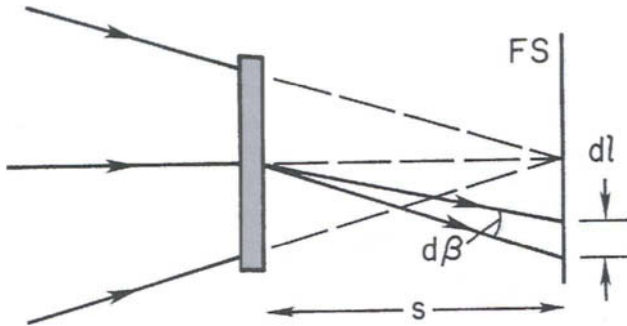


Fig. 12.2. Spectrum in focus on focal surface FS. Linear dispersion  $= f \, d\beta/d\lambda$ .



**Fig. 12.3.** Spectrum in focus on focal surface FS with convergent light incident on disperser. Linear dispersion =  $s d\beta/d\lambda$ .

#### 12.1.1.b. SPECTROMETER MODES; PLATE FACTOR

Spectrometer configurations to which Eq. (12.1.1) applies include both the slit spectrometer and a slitless mode where a prism or grating is placed in front of a telescope. In the case of a slit spectrometer a separate collimator provides a collimated beam to the dispersing element and  $f$  is the focal length of the camera optics. Fabry–Perot spectrometers also have separate collimator and camera optics. The type of slitless mode noted here is often called the *objective mode*; in this case  $f$  is the focal length of the telescope.

Configurations to which Eq. (12.1.2) applies include the slitless mode where a disperser, usually a grating or grism, is placed in a converging telescope beam ahead of the focal surface, either prime or Cassegrain. The *grism* is a combination of a grating and prism, with the grating as the main dispersing element. This type of slitless mode has been called the *nonobjective mode* by Hoag (see Hoag and Schroeder (1970)). Equation (12.1.2) also applies to the so-called Monk-Gillieson spectrometer, in which a mirror preceding the grating is both collimator and camera.

For any of the spectrometer modes noted here it is convenient to define  $P$ , the reciprocal linear dispersion or *plate factor*, where

$$P = (fA)^{-1}, \quad (12.1.3a)$$

$$P = (sA)^{-1}, \quad (12.1.3b)$$

for the modes in Figs. 12.2 and 12.3, respectively. The units of  $P$  are usually given as Angstroms per millimeter or nanometer per millimeter.

## 12.2. SLIT SPECTROMETERS

A general layout of a slit spectrometer in the most commonly used arrangement is shown in Fig. 12.4. Elements of the spectrometer include an entrance slit of width  $w$  and height  $h$  at the telescope focus, collimator and camera optics to reimage the entrance slit, and a disperser whose angular dispersion is  $A$ . Collimator and camera optics have focal lengths  $f_1$  and  $f_2$ , respectively, with a reimaged slit of width  $w'$  and height  $h'$  at the camera focus.

The entrance slit subtends angles  $\phi$  and  $\phi'$  on the sky and  $\delta\alpha$  and  $\delta\alpha'$  at the collimator, where  $\phi = w/f$ ,  $\phi' = h/f$ ,  $\delta\alpha = w/f_1$ , and  $\delta\alpha' = h/f_1$ . The collimated beam incident on the disperser has diameter  $d_1$ , with the direction of dispersion parallel to the slit width, or in the plane of the diagram in Fig. 12.4.

The size of the projected slit image depends upon  $f_1, f_2$ , and the characteristics of the disperser. Figure 12.5 shows the collimator and camera represented by equivalent thin lenses, with an object of length  $l$  subtending an angle  $\gamma$  at the collimator and its image of length  $l'$  subtending an angle  $\gamma'$  at the camera. For a system with no dispersing element between the lenses,  $\gamma' = \gamma$  and  $l' = l(f_2/f_1)$ . Because a system without a disperser is rotationally symmetric about the  $z$ -axis, these relations are true for any orientation of the object.

If a dispersing element is placed between the lenses, rotational symmetry about the  $z$ -axis is lost and the equality of the subtended angles is not necessarily preserved for different orientations of the object. In the direction perpendicular to the dispersion the beam passing through the disperser is unchanged, and  $\gamma' = \gamma$  holds as before. This is not the case in the direction along the dispersion, where it is necessary to take  $\gamma' = r\gamma$  to account for possible magnification effects due to the disperser. In terms of the subtended angles in Fig. 12.4 we have  $r = d\beta/d\alpha$ .

The parameter  $r$ , called the *anamorphic magnification*, depends on the type and orientation of the dispersing element. At this point we note, without derivation, that  $r = d_1/d_2$ , the ratio of the beam widths at the collimator and camera. This relation is derived in what follows and the form of  $r$  in terms of the parameters of a specific disperser is given in Chapter 13.

Applying these results to the slit dimensions in Fig. 12.4 gives

$$w' = rw(f_2/f_1) = r\phi DF_2, \quad (12.2.1a)$$

$$h' = h(f_2/f_1) = \phi' DF_2, \quad (12.2.1b)$$

where  $F_2 = f_2/d_1$ . This definition of the camera focal ratio in terms of the collimator beam diameter is made to ensure that  $F_2$  can be used in a meaningful way when discussing irradiance of detector pixels in Section 12.2. Note that the relations in Eq. (12.2.1a,b) also follow directly by substitution into Eq. (2.2.10) with  $n' = n$ .

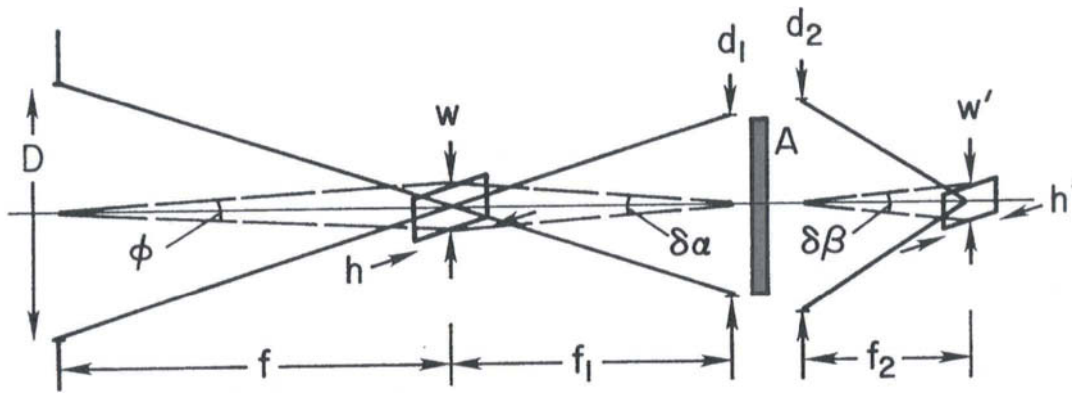


Fig. 12.4. Schematic layout of slit spectrometer with dispersing element of angular dispersion  $A$ . See text, Section 12.2, for definitions of parameters.

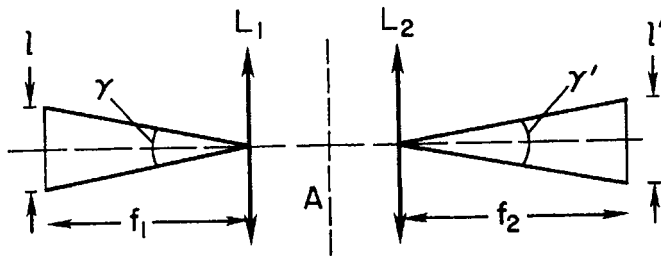


Fig. 12.5. Transverse magnification  $|m| = l'/l = f_2/f_1$  in direction perpendicular to dispersion. In the direction parallel to dispersion  $|m| = r(f_2/f_1)$ , where  $r$  is the anamorphic factor.

The relation in Eq. (12.2.1a) is important in establishing the proper value of  $F_2$  for a detector whose pixel size  $\Delta$  is correctly matched to  $w'$ . If we take a correct match to be one in which two pixels cover the width  $w'$ , then  $2\Delta = r\phi DF_2$ . If, for example, we choose  $\Delta = 20 \mu\text{m}$ ,  $\phi = 1$  arc-sec, and  $D = 4$  m, then from Eq. (12.2.1a) we find  $rF_2 = 2$ .

This match between pixel size and projected slit width is based on the Nyquist criterion for discrete sampling, discussed in detail in Chapter 16. For our purposes here we simply state that a minimum of two samples per resolution element are required for unambiguous resolution of images that are just resolved according to the Rayleigh criterion. We adopt a similar definition for limit of resolution and spectral resolving power in the following sections.

From Eq. (12.2.1a) we also see that a constant  $w'$  for a given angular slit width implies  $rDF_2 = \text{constant}$ . Thus a spectrometer on a larger telescope requires a camera with a smaller focal ratio, if the ratio  $w'/\phi$  is to remain constant.

### 12.2.a. LIMIT OF RESOLUTION AND SPECTRAL PURITY

Consider a spectrometer entrance slit of width  $w$  illuminated by light of two monochromatic wavelengths  $\lambda$  and  $\lambda + \Delta\lambda$ . The slit image in each wavelength has width  $w'$  and, from Eq. (12.1.1), the separation between the centers of the images is  $\Delta l = f_2 A \Delta\lambda$ . We define the *limit of resolution*  $\delta\lambda$  as the wavelength difference for which  $\Delta l = w'$ , hence the spectral images are on the verge of being resolved with a detector satisfying the Nyquist criterion. The analog to limit of resolution for a monochromator with exit slit of width  $w'$  observing a continuous light source is the *spectral purity*.

Putting this condition on  $\Delta l$  into Eq. (12.2.1a), and using Eqs. (12.1.1) and (12.1.3a), gives

$$\delta\lambda = \left(\frac{d\lambda}{d\lambda}\right)\Delta l = Pw' = \frac{r\phi}{A} \frac{D}{d_1}, \quad (12.2.2)$$

where from Fig. 12.4 we find  $f_1/d_1 = f/D$ .

For a given telescope diameter and angle on the sky, it is evident from Eq. (12.2.2) that the key factors that determine the limit of resolution are the angular dispersion and collimator beam diameter. We also see that putting a given spectrometer on a larger telescope gives a larger  $\delta\lambda$  for the same angle on the sky. In order to maintain the same limit of resolution or spectral purity with a given type of spectrometer on a larger telescope it is necessary to keep  $\phi D/d_1$  constant, hence a larger spectrometer for the same angle on the sky.

For a Monk-Gillieson slit spectrometer, usually configured as a monochromator and shown schematically in Fig. 12.6, the relations in Eqs. (12.2.1) apply if  $f_1$  and  $f_2$  are replaced by  $s_1$  and  $s_2$ . Combining Eqs. (12.1.3b) and (12.2.1a), we find the spectral purity is given by Eq. (12.2.2), provided  $d_1/r$  is replaced by  $d_2$ , where  $d_2$  is the beam size at the disperser. Hence for this spectrometer the spectral purity is set by the angular dispersion and beam size at the disperser, for a given  $\phi$  and  $D$ .

It is important to note here that the definition of limit of resolution is a geometric one that does not take into account the limit on image size set by diffraction. The limit of resolution cannot be smaller than  $\delta\lambda_0$ , the limit set by diffraction, where this limit depends on the angular dispersion, collimator beam diameter, and wavelength. The expression for  $\delta\lambda_0$  is derived in a later section.

### 12.2.b. SPECTRAL RESOLVING POWER

The *spectral resolving power*  $\mathcal{R}$ , a dimensionless measure of the limit of resolution, is defined as  $\mathcal{R} = \lambda/\delta\lambda$ , hence

$$\mathcal{R} = \frac{\lambda}{\delta\lambda} = \frac{\lambda A}{r\phi} \frac{d_1}{D}. \quad (12.2.3)$$

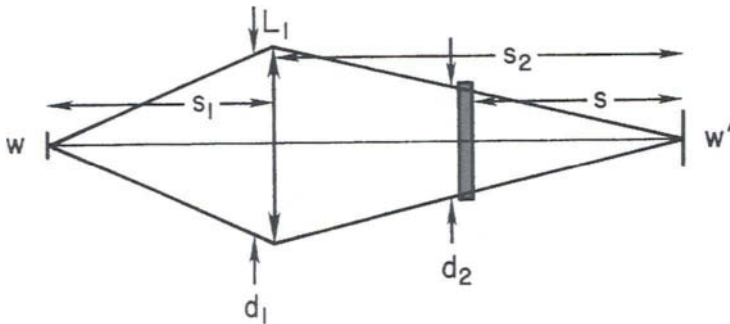


**Fig. 12.6.** Schematic of Monk-Gillieson spectrometer in direction parallel to dispersion, with dispersing element in convergent light.

It is clear from Eq. (12.2.3) that a larger telescope requires a larger beam diameter for a given type of disperser, if the resolving power is to be kept constant. Because  $\delta\lambda = \delta\lambda_0$  at the limit set by diffraction, there is also a largest possible spectral resolving power  $\mathcal{R}_0$ , although in most applications in astronomy the resolving power given by Eq. (12.2.3) is considerably smaller than  $\mathcal{R}_0$ .

12.2.c. FLUX, LUMINOSITY, AND ETENDUE

We now seek a relation for the energy flux transmitted by the telescope-spectrometer combination, with this relation expressed in terms of the system parameters. This analysis leads to a quantity called the *etendue*, a quantity whose importance in the analysis of spectrometric instruments was first emphasized by Jacquinot (1954). A second and related quantity introduced is the *luminosity*, defined as the product of the etendue and net transmittance of the optics.

The derivation of etendue given here makes use of basic photometric definitions given by Born and Wolf (1980). Consider a small, uniformly radiating surface element of area  $dS$  and photometric brightness  $B$ , as shown in Fig. 12.7. The flux  $d\mathcal{F}$  radiated into a small cone of solid angle  $d\Omega$  in a direction  $\theta$  from the normal to  $dS$  is given by

$$d\mathcal{F} = I d\Omega = B \cos \theta dS d\Omega, \tag{12.2.4}$$

where  $I$  is the intensity or flux per unit solid angle in the direction  $\theta$ . For a spectrometer we take  $dS$  as the area of the entrance slit.

The flux passing through the entrance pupil of the spectrometer, taken at the collimator, is the integral of Eq. (12.2.4) over the aperture of the pupil. For the annular cone shown in Fig. 12.8, the solid angle between  $\theta$  and  $\theta + d\theta$  is given by  $d\Omega = 2\pi \sin \theta d\theta$ , and therefore

$$\mathcal{F} = 2\pi B dS \int_0^{\theta_m} \cos \theta \sin \theta d\theta = BU, \tag{12.2.5}$$

$$U = \pi \sin^2 \theta_m dS, \tag{12.2.6}$$

where  $\tan \theta_m = d_1/2f_1$ ,  $U$  is the etendue, and  $dS = wh$ .

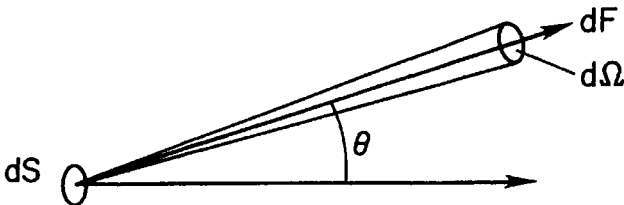


Fig. 12.7. Surface element of area  $dS$  and brightness  $B$  radiating into solid angle  $d\Omega$ . See Eq. (12.2.4).

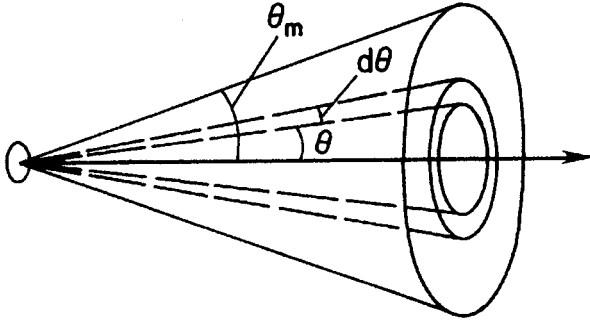


Fig. 12.8. Flux entering spectrometer entrance pupil. See Eq. (12.2.5).

Assuming  $\theta_m$  is small we can replace  $\sin \theta_m$  by  $\theta_m$ . Substituting for  $w$ ,  $h$ , and  $\theta_m$  in terms of the telescope and spectrometer parameters gives

$$U = \frac{\pi d_1^2}{4} \delta\alpha \delta\alpha' = \frac{\pi D^2}{4} \phi\phi' = S\Omega. \quad (12.2.7)$$

In this form we see that  $U$  is the product of the collimator (telescope) area  $S$  and the solid angle  $\Omega$  subtended by the slit at the collimator (or by the slit on the sky).

It is also instructive to write  $U = \pi w\theta_m \cdot h\theta_m$ . When written in this form, we see from the discussion following Eq. (2.2.10) that  $U/\pi$  is the product of two Lagrange invariants with  $n = 1$ . Because the Lagrange invariant is unchanged through an optical system, the etendue is also a constant of the system. Assuming  $n = 1$  for the space surrounding the image, we can write  $U$  for the image as

$$U = \frac{\pi d_1 d_2}{4} \delta\beta \delta\beta', \quad (12.2.8)$$

where  $\delta\beta$  and  $\delta\beta'$  are the angles subtended by the projected slit at the camera, as shown in Fig. 12.4. Given  $\delta\beta = r \delta\alpha$  and  $\delta\beta' = \delta\alpha'$ , equating Eqs. (12.2.7) and (12.2.8) gives the anamorphic magnification  $r = d_1/d_2$ , as stated here.

Taking  $\tau$  as the transmittance of the telescope-spectrometer combination, the luminosity  $\mathcal{L}$  of the system is given by

$$\mathcal{L} = \tau U = \tau S\Omega. \quad (12.2.9)$$

If  $\mathcal{F}_i$  is the monochromatic flux incident on the telescope, the flux  $\mathcal{F}$  in the projected image of the slit is

$$\mathcal{F} = \tau \mathcal{F}_i = \tau B U = B' U. \quad (12.2.10)$$

From Eq. (12.2.10) we see that the brightness  $B'$  of the image is less than the source brightness  $B$  by the factor  $\tau$ . It is worth emphasizing that Eq. (12.2.10) is restricted to the case where  $n = 1$  for the image space. If the image space index is

$n$ , as it is in solid or semisolid cameras, then  $B' = \tau n^2 B$ . As shown in Section 7.5, the focal length of solid cameras is  $n$  times smaller than that of the equivalent air camera, and therefore  $\delta\beta$  and  $\delta\beta'$  in Eq. (12.2.8) are each  $n$  times smaller. Thus the image area is  $n^2$  smaller, and the relation between  $\mathcal{F}$  and  $\mathcal{F}_i$  in Eq. (12.2.10) is unchanged, as must be true for conservation of energy.

#### 12.2.d. LUMINOSITY-RESOLUTION PRODUCT

The importance of the concepts of etendue and luminosity in evaluating spectrometer performance is particularly evident in the product of either with the spectral resolving power. Taking the product of Eqs. (12.2.3) and (12.2.7) gives the *luminosity-resolution product* as

$$\mathcal{L}\mathcal{R} = (\tau\pi/4)(D\phi')(\lambda A d_2), \quad (12.2.11)$$

where  $d_2$  has replaced  $d_1/r$  and the factors in the right-hand parentheses are specific to the spectrometer. For stellar sources  $\phi'$  is the diameter of the seeing disk, whereas for extended sources  $\phi'$  is the angular height of the entrance slit.

For constant  $\phi'$  the product  $\mathcal{L}\mathcal{R}$  is a constant for a given telescope-spectrometer combination. Increasing this product for a given telescope requires either a larger spectrometer beam diameter or a disperser with higher angular dispersion. Note that the width of the entrance slit does not appear in Eq. (12.2.11), hence higher resolving power implies lower luminosity, and conversely, as the slit width is changed. Meaburn has evaluated the  $\mathcal{L}\mathcal{R}$  product for a variety of spectrometers, including prism, grating, and Fabry-Perot instruments. We evaluate this product for a selected set of instruments in Chapter 13.

If Eq. (12.2.11) is multiplied by  $B$ , the source brightness, the result is a *flux-resolution product*  $\mathcal{F}\mathcal{R}$ . This product is more useful than Eq. (12.2.11) when  $\phi'$  is not a constant. The relation for  $B$  at the entrance slit depends on the source. We assume

$$B \text{ (extended source)} = \text{constant}, \quad (12.2.12a)$$

$$B \text{ (stellar source)} = C'/\phi'^2, \quad (12.2.12b)$$

where  $C'$  is a constant. For simplicity we assume that the stellar image is square and uniformly illuminated.

For extended sources the  $\mathcal{L}\mathcal{R}$  and  $\mathcal{F}\mathcal{R}$  products increase as  $\phi'$  increases, but the brightness  $B'$  of the image is unchanged. If the image covers many detector elements, the exposure time to a given signal level is also the same.

For stellar sources we get

$$\mathcal{F}\mathcal{R} = \tau C(D/\phi')(\lambda A d_2), \quad (12.2.13)$$

where  $C = \pi C'/4$ . When the star image overfills the entrance slit,  $\phi < \phi'$  and better seeing (smaller  $\phi'$ ) means a larger  $\mathcal{F}\mathcal{R}$  product. When the star image is entirely within the slit,  $\mathcal{F}$  is constant and  $\mathcal{R}$  is inversely proportional to  $\phi'$ .

A reevaluation and extension of the luminosity-resolution product has been done by Vaughn (1994). He points out that a single  $\mathcal{L}\mathcal{R}$  number may not accurately describe a given system, and that field-dependent factors should be taken into account. The interested reader should consult his paper.

### 12.2.e. SPECTROMETER SPEED AND PIXEL IRRADIANCE

The exposure time required to record a spectrum depends on the rate at which energy in a given spectral band is collected in a given area on the detector. For a spectrometer the *irradiance*  $E$  of an image is defined as the spectral flux received at the detector per unit area. Taking the flux  $\mathcal{F}$  as the flux per unit wavelength interval, the spectral flux in width  $w'$  is  $\mathcal{F} \delta\lambda$  with  $\delta\lambda = w'P$  from Eq. (12.2.2). Therefore the irradiance  $E$  is given by

$$E = \mathcal{F} \delta\lambda/w'h' = \mathcal{F}P/h', \quad (12.2.14)$$

where  $P$  is the plate factor. This relation for  $E$  is identical to one for a quantity Bowen (1952) called *speed*. It is obvious that greater speed or irradiance means shorter exposure times.

Taking  $B$  from Eqs. (12.2.12), we find  $\mathcal{F}$  from Eqs. (12.2.7) and (12.2.10). The results are

$$\mathcal{F} \text{ (extended)} = C\tau D^2 \phi \phi', \quad (12.2.15)$$

$$\mathcal{F} \text{ (stellar)} = C\tau D^2 (\phi/\phi'), \quad (12.2.16)$$

where  $C = \pi C'/4$  and  $\phi = \phi'$  if the stellar source is entirely within the slit. Substituting  $\mathcal{F}$  into Eq. (12.2.13) and using Eqs. (12.2.1) and (12.2.2) gives

$$E_e = \frac{C\tau \delta\lambda}{rF_2^2} = \frac{C\tau w'P}{rF_2^2}, \quad (12.2.17)$$

$$E_s = \frac{C\tau \delta\lambda}{r(F_2\phi')^2} = \frac{C\tau\phi DP}{F_2\phi'^2}, \quad \text{(slit-limited)} \quad (12.2.18)$$

$$E_s = \frac{C\tau \delta\lambda}{r(F_2\phi')^2} = \frac{C\tau D^2 Pr}{w'}, \quad \text{(seeing-limited)} \quad (12.2.19)$$

where  $E_e$  and  $E_s$  denote extended source and star, respectively.

It is also important to give relations for *pixel irradiance*, defined as the spectral flux per pixel. Given the definition of irradiance in Eq. (12.2.14), the pixel irradiance is simply  $E \Delta^2$ , where  $\Delta^2$  is the area of a single square pixel. As noted

following Eqs. (12.2.1), the proper match between pixel size and projected slit width is  $2\Delta = w'$ . If more than two pixels spans  $w'$  the spectral image is oversampled, the pixel irradiance is smaller than in the properly matched case, and the limit of resolution is set by  $w'$ . If fewer than two pixels spans the projected slit, the image is undersampled and the limit of resolution is set by the detector.

For stellar spectra in the slit-limited case, it is evident from Eq. (12.2.18) that better seeing means greater speed, in part because more light passes through the slit and in part because the image height  $h'$  is shorter. In the seeing-limited case all of the light passes through the slit and, given  $w' \propto \phi'$ , speed increases only in inverse proportion to improved seeing. For extended sources it is evident from Eq. (12.2.17) that seeing has no effect on speed.

It is important to note the dependence of speed on telescope diameter and camera focal ratio. For extended sources we see that speed is independent of diameter, and greater speed requires a faster camera. In the seeing-limited case for stellar sources, the speed is proportional to the telescope area. For stellar sources in the slit-limited case, the most usual situation with spectrometers on large telescopes, the speed is proportional to diameter and inversely proportional to the camera focal ratio.

It was pointed out by Bowen that scaling the size of a spectrometer in direct proportion to the telescope diameter does not change the speed, at the same limit of resolution. This is easily shown by noting that  $\mathcal{F}/w'h'$  is independent of  $D$ . Hence an increase in speed can only be achieved by using a spectrometer camera with a smaller focal ratio. This is one of the major reasons why much effort has gone into the design and construction of fast cameras.

In our preceding discussion we have assumed a stellar image with uniform brightness, rather than a more realistic one with a bright center and fainter surrounding halo. The results found using a realistic profile are essentially the same as those of the foregoing, and little is gained by introducing this refinement. For further discussion of spectrometer speed, the reader should consult the reference by Bowen (1952).

#### 12.2.f. CONCLUDING REMARKS

We have already noted here that many spectroscopic observations of stellar sources, especially with large telescopes, are made in the slit-limited mode with the star image wider than the slit. Compensation for atmospheric seeing with adaptive optics makes it possible to obtain higher spectral resolving power without losing an undue amount of light at the slit. Taking full advantage of such techniques requires, of course, careful attention to detector pixel size.

In the absence of adaptive optics techniques it is possible to recover much of the light intercepted by the slit jaws with so-called image slicers. Such a device, in

effect, slices the image into several strips and places these end- to-end along the length of the slit. For an excellent discussion of the principles of image slicers and their practical realization, the reader should consult the reference by Hunten (1974).

### 12.3. FIBER-FED SPECTROMETERS

The relations derived for slit spectrometers in the previous section are generally applicable to fiber-fed spectrometers, but only after one important difference is factored into the equations. This difference is that of *focal ratio degradation* (FRD), a factor discussed in Section 9.6. In our following discussion we assume that the output end of the fiber is positioned at the entrance slit of a spectrometer and that the slit width is the same as for the spectrometer without the fiber.

Consider first an existing slit spectrometer built to match a given telescope. The beam from the telescope fills the collimator, as shown in Fig. 12.4, and  $F_1 = f_1/d_1 = F = f/D$ . When a fiber is introduced, the effect of FRD is to expand the beam, hence  $F_1 < F$ , and lose light directly at the overfilled collimator. To avoid this light loss, a spectrometer with a larger  $d_1$  and smaller  $F_1$  can be built. Assuming the projected slit width  $w'$  is to remain constant, this requires a smaller  $F_2$ , hence a faster camera and generally a more difficult design.

It is important to note that this larger spectrometer, built specifically to recover lost light, does not have a larger spectral resolving power, as might be expected from Eq. (12.2.3). Given  $d_1 = f_1/F_1$  and  $D = f/F$ , we can rewrite Eq. (12.2.3) as

$$\mathcal{R} = \left(\frac{F_1}{F}\right) \frac{\lambda A}{r\phi} \frac{d_1}{D} = \frac{\lambda A}{r\phi} \frac{f_1}{f}. \quad (12.3.1)$$

This relation shows clearly that holding  $f_1$  constant and increasing  $d_1$  does not increase  $\mathcal{R}$ .

The etendue of the telescope is unchanged by the introduction of a fiber, hence  $U$  given in Eq. (12.2.7) is unchanged. It is left to the reader to take Eqs. (12.2.7) and (12.3.1) and form the different resolution products given in Section 12.2 for the slit spectrometer. The outcome of this exercise is that the luminosity-resolution and flux-resolution products can only decrease when a fiber is introduced.

This decrease in efficiency of a fiber-fed spectrometer for a single source is more than regained when multiple fibers are used. Individual fibers on sources on a telescope focal surface are deployed side-by-side along a spectrometer slit and the spectra of many sources are obtained simultaneously. With dozens of fibers so

arrayed, the gain in observing efficiency is significant. We discuss some of the optical characteristics of fiber-fed spectrometers in Chapter 15.

#### 12.4. SLITLESS SPECTROMETERS

Based on the discussions in Section 12.2, the relations for slitless spectrometers are easily found. The major differences for the slitless mode are: (1) the image size of a stellar source is set by atmospheric seeing or diffraction rather than a slit; (2) the anamorphic magnification is one in all practical configurations; and (3) the diameter  $d_1$  is the beam size at the dispersing element.

Thus the relations in Section 12.2 apply to slitless configurations if  $\phi$  is replaced by  $\phi'$  and  $r$  is set equal to one. With these changes the limit of resolution is given by

$$\delta\lambda = \frac{\phi'}{A} \frac{D}{d_1} = \frac{\phi'}{A} \frac{f}{s'}, \quad (12.4.1)$$

where  $f$  is the telescope focal length and  $d_1$  is the diameter of the dispersing element. In the objective mode, as shown in Fig. 12.2,  $s = f$  and  $d_1 = D$ . The irradiance of an image with spectral band  $\delta\lambda$  is given by Eq. (12.2.19).

#### 12.5. SPECTROMETERS IN DIFFRACTION LIMIT

We noted in Section 12.2 that the relation for the limit of resolution did not take into account the limit on image size set by diffraction. In this section we determine the form of the spectrometric parameters in the case where a stellar image in the focal plane of a diffraction-limited telescope is the effective entrance aperture for a perfect spectrometer.

One important characteristic of a perfect image from a telescope with an annular aperture is the radius of the first dark Airy ring, given by Eq. (10.2.9) for a clear aperture. This radius, in angular units, is also the limit of resolution according to the Rayleigh criterion, as given by Eq. (10.2.22). We now assume the effective width and height of the entrance aperture are equal to this radius, hence

$$w = h = 1.22\gamma\lambda F, \quad (12.5.1)$$

where  $1.22\gamma = \omega_1$  from Table 10.1. Substituting Eq. (12.5.1) in Eqs. (12.2.1) gives

$$w' = 1.22\gamma r \lambda F_2 \cong r \lambda F_2, \quad (12.5.2a)$$

$$h' = 1.22\gamma \lambda F_2 \cong \lambda F_2. \quad (12.5.2b)$$

From this point on we take the approximate relations given in Eq. (12.5.2a,b). We now apply the relations in Section 12.2 to find the spectrometric parameters for a diffraction-limited telescope-spectrometer system. The relation in Eq. (12.5.2a) can be used to find  $rF_2$  for a detector whose pixel size  $\Delta$  is matched to  $w'$ . Assuming  $2\Delta = w'$ , as done following Eq. (12.2.1), we find  $rF_2 = 80$  for a pixel size of  $20\ \mu\text{m}$  with  $\lambda = 500\ \text{nm}$ . It is evident from this value of  $rF_2$  that a spectrometer on a diffraction-limited telescope has no need for a Schmidt-type camera in the visible or near-infrared spectral regions.

Following the procedure in Section 12.2.a we take  $\Delta l = w'$  as the separation between two monochromatic images that are resolved by the Rayleigh criterion. The difference in wavelength between these two images, according to Eq. (12.1.1), is given by  $\delta\lambda_0 = \Delta l / f_2 A$ . Therefore

$$\delta\lambda_0 = \frac{r\lambda F_2}{f_2 A} = \frac{r\lambda}{Ad_1} = \frac{\lambda}{Ad_2}, \quad (12.5.3)$$

$$\mathcal{R}_0 = \frac{\lambda}{\delta\lambda_0} = \frac{Ad_1}{r} = Ad_2. \quad (12.5.4)$$

Note that the changes in Eqs. (12.2.2) and (12.2.3) to get the relations for the diffraction-limited case are simply a substitution of  $\lambda$  for  $\phi D$ . Following this procedure, and noting that  $\phi' = \phi$ , we can transform the remaining parameters in Section 12.2 into their diffraction-limited counterparts. The results are

$$U_0 = \frac{\pi}{4} \lambda^2, \quad (12.5.5)$$

$$(\mathcal{L}\mathcal{R})_0 = \tau \frac{\pi}{4} \lambda^2 Ad_2, \quad (12.5.6)$$

$$(\mathcal{F}\mathcal{R})_0 = C\tau D^2 Ad_2, \quad (12.5.7)$$

$$E_{s0} = \frac{C\tau D^2 \delta\lambda_0}{r(\lambda F_2)^2} = \frac{C\tau D^2 P}{\lambda F_2}. \quad (12.5.8)$$

The relations in Eqs. (12.5.5)–(12.5.8) apply only to stellar sources, with Eq. (12.5.8) the counterpart of Eq. (12.2.19).

It is possible to make various comparisons between the relations for diffraction-limited and seeing-limited cases, and we give two such comparisons. Taking the ratio of Eqs. (12.5.7) and (12.2.13) gives

$$\frac{(\mathcal{F}\mathcal{R})_0}{\mathcal{F}\mathcal{R}} = \frac{\tau_0 D_0^2 \phi'}{\tau \lambda D}, \quad (12.5.9)$$

where the parameters with subscript 0 refer to the diffraction-limited system. Consider the 2.4-m Hubble Space Telescope and a ground-based 8-m telescope. Taking  $\tau_0 = \tau$ ,  $\phi' = 0.5\ \text{arc-sec}$ , and  $\lambda = 500\ \text{nm}$ , gives an  $\mathcal{F}\mathcal{R}$  ratio of 3.6. A complete analysis of the detectability of a faint source must take into account the

sky background and detector characteristics; we defer this discussion including signal-to-noise ratio (SNR) to Chapter 16.

From Eqs. (12.2.3) and (12.5.4) we find the ratio of the resolving powers  $\mathcal{R}/\mathcal{R}_0 = \lambda/\phi D$ . For visible wavelengths and excellent seeing conditions, say 0.5 arc-sec, and  $D > 1$  m, we find that  $\mathcal{R}$  is small compared to  $\mathcal{R}_0$ . Thus the resolution at visible wavelengths at which spectrometers on ground-based telescopes are often used is well below the resolution that is theoretically possible. At infrared wavelengths, where  $\lambda$  is larger and seeing is typically better, it is possible that  $\mathcal{R}$  can approach  $\mathcal{R}_0$ .

## REFERENCES

- Bowen, I. (1952). *Astrophys. J.*, **116**: 1.  
 Hoag, A. and Schroeder, D. (1970). *Publ. Astron. Soc. Pac.*, **82**: 1141.  
 Jacquinet, P. (1954). *J. Opt. Soc. Am.*, **44**: 761.  
 Vaughnn, D. (1994). *Proc. SPIE Int. Soc. Opt. Eng.*, **2198**: 31.

## BIBLIOGRAPHY

- Born, M. and Wolf, E. (1980). *Principles of Optics*, sixth edition, Oxford: Pergamon.  
 Bowen, I. (1962). *Stars and Stellar Systems II, Astronomical Techniques*, Chap. 2, Chicago: Univ. of Chicago Press.  
 Hecht, E. (1987). *Optics*, second edition, Reading, MA: Addison-Wesley.  
 Hunten, D. (1974). *Methods of Experimental Physics: Astrophysics*, vol. 12, Part A: "Optical and Infrared," Chap. 4, New York: Academic Press.  
 James, J. and Sternberg, R. (1969). *The Design of Optical Spectrometers*, London: Chapman & Hall.  
 Meaburn, J. (1976). *Detection and Spectrometry of Faint Light*, Dordrecht, Netherlands: Reidel.  
 Schroeder, D. (1974). *Methods of Experimental Physics: Astrophysics*, vol. 12, Part A: "Optical and Infrared," Chap. 10, New York: Academic Press.

We now turn our attention to specific dispersing elements, discussing in turn the prism, diffraction grating, and Fabry-Perot interferometer. We give expressions for the angular dispersion and resolving power for each of these, and point out other characteristics that are important in their application. Finally, we also discuss the characteristics of the Fourier spectrometer.

### 13.1. DISPERSING PRISM

The angular dispersion  $A$  of a prism used at minimum deviation is derived in Section 3.2. A dispersing prism is generally used at or near minimum deviation, defined as that orientation at which  $\theta$  in Fig. 3.6 is a minimum and rays inside the prism are parallel to the base. From Eq. (3.2.8) we have

$$A = \frac{d\beta}{d\lambda} = \frac{t}{a} \frac{dn}{d\lambda}, \quad (13.1.1)$$

where  $t$  is the base length,  $a$  the beam width into and out of the prism, and  $dn/d\lambda$  the rate of change of index with wavelength. Because  $a$  is the same on either side of the prism, there is no anamorphic magnification and  $r = 1$ .

Substituting  $A$  into Eq. (12.4.4), and noting that  $d_2 = a$ , gives the limiting spectral resolution of a single prism as

$$\mathcal{R}_0 = t \, dn/d\lambda. \quad (13.1.2)$$

If there are  $k$  identical prisms in series, then Eqs. (13.1.1) and (13.1.2) are each multiplied by  $k$ .

Dispersion curves for three glasses selected from the Schott glass catalog are shown in Fig. 13.1. The form of these curves is typical of those for all transparent glasses, with  $dn/d\lambda$  going approximately as the inverse cube of the wavelength. Taking UBK7 at  $\lambda = 500$  nm, as an example, we find  $dn/d\lambda = 0.066 \mu\text{m}^{-1}$ , and thus  $\mathcal{R}_0 \cong 10,000$  for  $t = 150$  mm. This base length corresponds to a beam diameter of about 100 mm for a  $60^\circ$  prism or about 1400 mm for a  $6^\circ$  prism.

Prisms are often used in the objective mode on Schmidt telescopes in the 1-m class to obtain spectra suitable for classification. In this configuration  $\lambda/\phi D$  is approximately 0.1 and therefore  $\mathcal{R} \cong 1000$  for a UBK7 prism whose base is

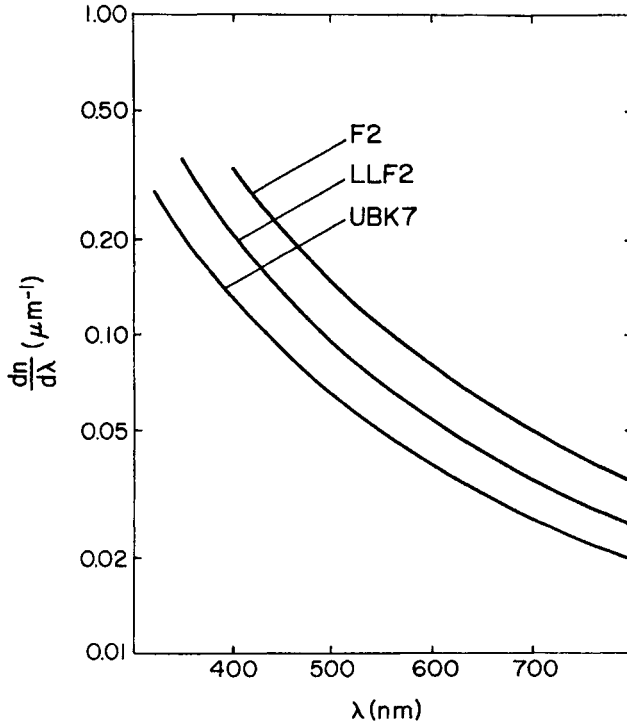


Fig. 13.1. Dispersion curves for three glasses from Schott glass catalog.

150 mm. This resolution is sufficient for this mode where the plate factor  $P$  is typically about  $150 \text{ \AA/mm}$ .

As we show in Section 13.2, the resolution of a prism is low compared to what is possible with a grating large enough to accept the same beam diameter. For this reason, prisms are little used as primary dispersing elements in slit spectrometers, having been largely replaced by gratings. Prisms are, however, often used as cross-dispersers in spectrometers that use gratings for the primary dispersion. For the objective mode, a prism is more efficient than a grating, for reasons made clear when we discuss grating efficiency.

### 13.2. DIFFRACTION GRATING; BASIC RELATIONS

The diffraction grating is the primary dispersing element in most astronomical spectrometers, where it has the advantage of significantly larger spectral resolving power than a prism of comparable size. A grating is also versatile in the spectral formats it can provide and can be quite efficient over a reasonable spectral range, though usually not as efficient as a prism. We discuss these and other characteristics of gratings in this section and the following one. A number of additional references that discuss gratings are given at the end of the chapter; the excellent book by Loewen and Popov (1997) is especially recommended.

#### 13.2.a. GRATING EQUATION

The starting point for our discussion of gratings is the well-known grating equation, the derivation of which is found in any introductory optics text. For the usual case of a chief ray in the  $xz$ -plane, with the grating grooves parallel to the  $y$  axis in the  $yz$ -plane, the grating equation is

$$m\lambda = \sigma(\sin \beta \pm \sin \alpha), \quad (13.2.1)$$

where  $m$  is the order number,  $\sigma$  is the distance between successive, equally spaced grooves or slits, and  $\alpha$  and  $\beta$  are angles of incidence and diffraction, respectively, measured from the normal to the grating surface. The parameter  $\sigma$  is also called the grating constant. The plus sign in Eq. (13.2.1) applies to a reflection grating; the minus sign to a transmission grating. We derive the general form of this equation from the point of view of Fermat's Principle in Chapter 14.

Schematics of grating cross sections are shown in Fig. 13.2 for both a reflection and a transmission grating. The plane defined by the incident ray and normal to the grating surface is in the plane of the paper in Fig. 13.2, with the grating grooves perpendicular to this plane. The angles  $\alpha$  and  $\beta$  are governed by the same sign convention as that given for  $i$  and  $i'$  in Chapter 2. For a reflection

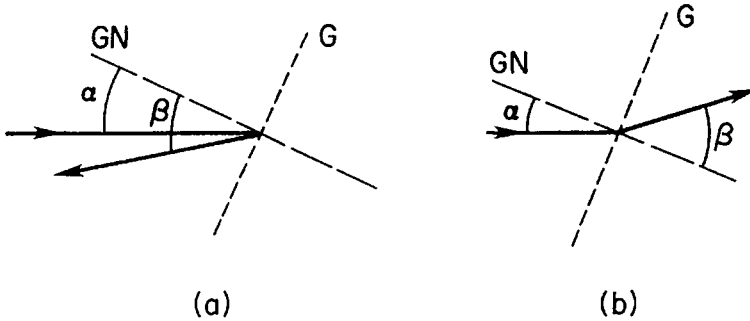


**Fig. 13.2.** Schematic showing angles of incidence  $\alpha$  and diffraction  $\beta$  for (a) reflection grating and (b) transmission grating. See the discussion following Eq. (13.2.1) for sign convention.

grating  $\alpha$  and  $\beta$  have the same signs if they are on the same side of the grating normal, while for a transmission grating they have the same signs if the diffracted ray crosses the normal at the point of diffraction. In each of the diagrams in Fig. 13.2,  $\alpha$  and  $\beta$  have the same signs. Note that  $m = 0$  for a reflection grating when  $\alpha = -\beta$ , while for a transmission grating this condition holds when  $\alpha = \beta$ .

### 13.2.b. ANGULAR DISPERSION

The angular dispersion follows directly from Eq. (13.2.1) by holding  $\alpha$  constant and differentiating with respect to  $\lambda$ , with the result

$$A = \frac{d\beta}{d\lambda} = \frac{m}{\sigma \cos \beta}, \quad (13.2.2a)$$

or

$$A = \frac{\sin \beta + \sin \alpha}{\lambda \cos \beta}. \quad (13.2.2b)$$

Unless otherwise noted, the following discussion refers to reflection gratings, hence the plus sign in Eq. (13.2.2b).

From Eq. (13.2.2a) we see that angular dispersion in a given order  $m$  is a function of  $\sigma$  and  $\beta$ . When looked at from the point of view of this equation, changing  $A$  means choosing a grating with a different grating constant and/or using the grating at a different angle of diffraction.

We see from Eq. (13.2.2b) that  $A$ , at a given wavelength, is set entirely by the angles  $\alpha$  and  $\beta$ , independent of  $m$  and  $\sigma$ . Thus a given angular dispersion can be obtained with many combinations of  $m$  and  $\sigma$ , provided the angles at the grating are unchanged and  $m/\sigma$  is constant. Recognition of this fact led to the

development of coarsely ruled reflection gratings specifically designed to achieve high angular dispersion by making  $\alpha$  and  $\beta$  large, typically about  $60^\circ$ . Such gratings, called *echelles*, have groove densities in the range of 300 to 30 per mm with values of  $m$  in the range of 10 to 100 for visible light. On the other hand, typical first- or second-order gratings have groove densities in the range 300 to 1200 per mm. Low-order gratings are often called *echelettes* to distinguish them from echelles. A typical echelle and an echelette grating used in first order are compared in a later section.

### 13.2.c. ANAMORPHIC MAGNIFICATION

The relation for anamorphic magnification is derived from Eq. (13.2.1) by holding  $\lambda$  constant and finding the change in  $\beta$  for a change in  $\alpha$ . The result is  $\cos \beta d\beta + \cos \alpha d\alpha = 0$ , and it follows that

$$r = \frac{|d\beta|}{|d\alpha|} = \frac{\cos \alpha}{\cos \beta} = \frac{d_1}{d_2}. \quad (13.2.3)$$

The relation between the beam widths and angles is derived from the geometry in Fig. 13.3, with  $d_1 / \cos \alpha = d_2 / \cos \beta$ .

Because  $r$  is in the denominator of the resolving power given in Eq. (12.2.3), it is clear that the choice  $r < 1$ , hence  $\beta < \alpha$ , gives higher resolution. This condition, in turn, means that the grating normal is more nearly in the direction of the camera than of the collimator. If the grating is to accept all of the light from the collimator, it follows that  $W = d_1 / \cos \alpha$  is required, where  $W$  is the width of

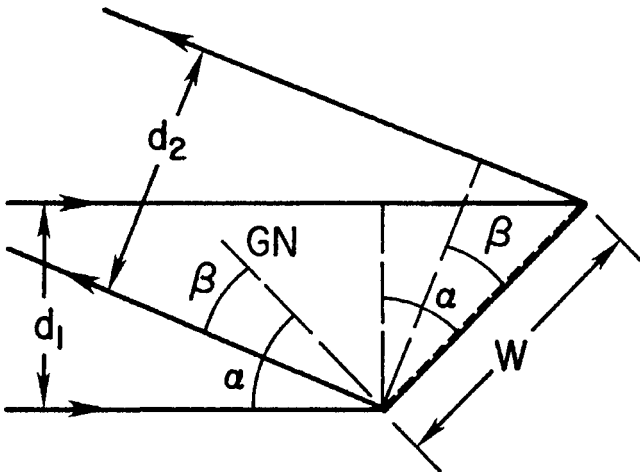


Fig. 13.3. Change in beam width due to anamorphic magnification of grating. See Eq. (13.2.3).

the grating. In the direction parallel to the grating grooves, the height of the grating is given by  $H = d_1$ .

For a typical echelette the value of  $r$  is not far from unity and has little effect on the spectral resolving power. In the case of an echelle the value of  $r$  has a significant effect on the resolving power, as our example to follow demonstrates.

### 13.2.d. SPECTRAL RESOLVING POWER

Substituting Eq. (13.2.2a) into Eq. (12.4.4) gives the spectral resolving power in the diffraction limit as

$$\mathcal{R}_0 = \frac{md_2}{\sigma \cos \beta} = \frac{mW}{\sigma} = mN, \quad (13.2.4a)$$

where  $N$  is the total number of grooves in the grating width  $W$ . The relation between  $W$ ,  $d_2$ , and  $\beta$  is shown in Fig. 13.3. Writing Eq. (13.2.4a) in terms of angles, we get

$$\mathcal{R}_0 = \frac{W}{\lambda} (\sin \beta + \sin \alpha). \quad (13.2.4b)$$

From Eq. (13.2.4b) we see that  $\mathcal{R}_0$  is directly proportional to the grating width for a given pair of angles. Using the geometry in Fig. 13.3, we also see that the numerator in Eq. (13.2.4b) has a simple geometric interpretation; it is the total path difference between the marginal rays spanning the grating width, and  $\mathcal{R}_0$  is the number of wavelengths in this path difference.

The resolving power for the seeing-limited case is obtained by replacing  $\lambda$  in Eq. (13.2.4b) by  $\phi D$ , and is

$$\mathcal{R} = \frac{W}{\phi D} (\sin \beta + \sin \alpha). \quad (13.2.5)$$

Given that  $\mathcal{R} \propto W/D$ , it is evident from this relation why there has been a concerted effort to produce larger reflection gratings and echelles, as the size of telescopes has increased.

For ease of reference, the important grating relations are brought together in Table 13.1.

### 13.2.e. FREE SPECTRAL RANGE

For a given pair of  $\alpha$  and  $\beta$ , the grating equation is satisfied for all wavelengths for which  $m$  is an integer. Thus there are two wavelengths in successive orders,

Table 13.1

General Equations for Reflection Gratings

$$\begin{aligned}
 m\lambda &= \sigma(\sin \beta + \sin \alpha) \\
 A &= \frac{d\beta}{d\lambda} = \frac{m}{\sigma \cos \beta} = \frac{\sin \beta + \sin \alpha}{\lambda \cos \beta} \\
 \mathcal{R}_0 &= \frac{W(\sin \beta + \sin \alpha)}{\lambda} \\
 \mathcal{R} &= \frac{W(\sin \beta + \sin \alpha)}{\phi D}
 \end{aligned}$$

$\lambda$  and  $\lambda'$ , for which we have  $m\lambda' = (m+1)\lambda$ . The wavelength difference  $\Delta\lambda = \lambda' - \lambda$  is called the *free spectral range*, where

$$\Delta\lambda = \lambda' - \lambda = \lambda/m. \quad (13.2.6)$$

The two wavelengths are diffracted in the same direction and confusion is the result unless one is rejected by a filter or they are separated with a cross-disperser. Both techniques are used to eliminate the wavelength overlap, with a cross-disperser most often used when  $m$  is large and a filter when  $m$  is small.

### 13.3. ECHELLES

Echelles are diffraction gratings with relatively large groove spacings used in high order at large angles of incidence and diffraction. It is evident from Eq. (13.2.2b) that angular dispersion is larger for large angles  $\alpha$  and  $\beta$ , hence a given pair of spectral lines is more widely separated in the camera focal plane. This means, in turn, that the resolving power is larger for a given grating width, as is evident from Eqs. (13.2.4b) and (13.2.5). Because an echelle is used in high orders, the free spectral range is small compared to that of an echelette, as shown by Eq. (13.2.6). The resulting spectrum, therefore, is typically one of many orders.

#### 13.3.a. COMPARISON OF GRATING AND ECHELLE

As illustration of the relations in Section 13.2, we now consider two specific gratings, an echelle and an echelette, and give their characteristics at a wavelength near 500 nm. The reflection gratings chosen are assigned the following parameters:

13. Dispersing Elements and Systems

	$m$	$1/\sigma$ (mm)	$\delta$ ( $^\circ$ )
Echelette	1	1200	17.5
Echelle	45	79	63.5
$\alpha = \delta + \theta, \quad \beta = \delta - \theta, \quad \theta > 0$ if $\alpha > \beta$			

The reader can verify for each that the grating equation is satisfied for a wavelength near 500 nm when  $\theta = 0$ . The parameters chosen are typical of those for a first-order grating and echelle.

The angle  $\delta$ , the so-called *blaze angle*, is introduced here because it is one of the key grating parameters; its significance is discussed fully in Section 13.4. At this point we simply note that  $\delta$  is the angle between the plane of the grating and the plane of a single groove. We also note that grating efficiency is a maximum when  $\alpha$  and  $\beta$  are chosen as given, relative to the blaze angle. A sketch of the geometry showing the relation between these angles is shown in Fig. 13.4.

It is useful at this point to write the relations in Table 13.1 for the special case where  $\theta = 0$ , hence  $\alpha = \beta = \delta$ . This defines the so-called *Littrow configuration*, for which we get the results given in Table 13.2. Although the strict Littrow configuration is not a practical one for a reflection grating, the angle  $\theta$  is small in most grating spectrometers. Thus the relations in Table 13.2 are useful for calculating good first approximations to the true values, and comparisons of different gratings is easily made.

For our chosen grating and echelle,  $\mathcal{R}$  and  $\mathcal{R}_0$  in the Littrow mode are 6.36 times larger for the echelle, at the same  $d_1$  and  $\lambda$ . It is conventional to describe an echelle by its *R-value*, where  $R = \tan \delta$ . For our example we have chosen an R-2 echelle. It is also worth noting that  $W$  is 2.14 times larger for the echelle in the Littrow configuration, as compared with the echelette.

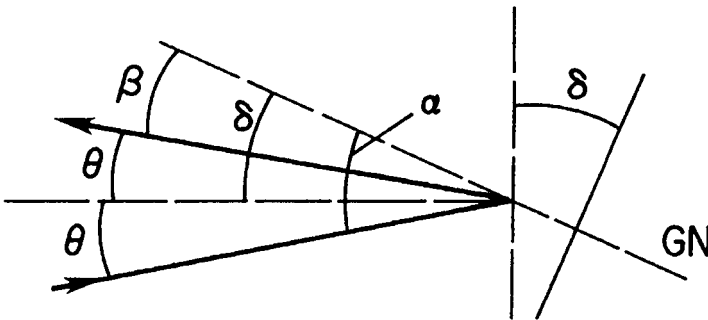


Fig. 13.4. Relation between blaze angle  $\delta$ , grating normal GN, and angles of incidence and diffraction.

**Table 13.2**  
Equations for Reflection Gratings in Littrow Configuration<sup>a</sup>

$$\begin{aligned}
 m\lambda &= 2\sigma \sin \delta \\
 A &= \frac{d\beta}{d\lambda} = \frac{m}{\sigma \cos \delta} = \frac{2 \tan \delta}{\lambda} \\
 \mathcal{R}_0 &= \frac{2W \sin \delta}{\lambda} = \frac{2d_1 \tan \delta}{\lambda} \\
 \mathcal{R} &= \frac{2d_1 \tan \delta}{\phi D}
 \end{aligned}$$

<sup>a</sup>  $\alpha = \beta = \delta$ .

Values derived from relations in Table 13.1 are given in Table 13.3 for our example grating and echelle, with  $d_1 = 100$  mm,  $\phi = 1$  arc-sec, and  $D = 4$  m. From the entries in Table 13.3 we see that  $\mathcal{R}$  of the grating changes very little with changing  $\theta$ , while for the echelle the change is proportionately much larger. The trend in the values of  $W/d_1$  follows a similar pattern.

Compared to  $\mathcal{R}_0$  of the UBK7 prism given in Section 13.1, we see also from Table 13.3 that the grating and echelle have values that are 12.5 and 80 times larger. These increases in resolution potential and achievable resolving power for a given slit width are obviously significant.

**Table 13.3**  
Characteristics of Typical Grating and Echelle<sup>a</sup>

	Resolution in Littrow configuration			
	Grating		Echelle	
$\mathcal{R}_0$	1.3E5		8.0E5	
$\mathcal{R}$	3.1E3		2.0E4	
$\theta(^{\circ})$	Parameters in non-Littrow configuration			
	Grating		Echelle	
	$\phi D \mathcal{R} / d_1$	$W / d_1$	$\phi D \mathcal{R} / d_1$	$W / d_1$
0	0.630	1.05	4.01	2.24
2	0.637	1.06	4.31	2.41
4	0.644	1.07	4.67	2.61
6	0.652	1.09	5.08	2.86

<sup>a</sup> Parameters of grating and echelle are given in text:  $d_1 = 100$ ;  $\phi = 1$  arc-sec; and  $D = 4$  m.

The increase in resolution  $\mathcal{R}$  with increasing positive  $\theta$ , and thus  $\alpha > \beta$ , is a result that merits further comment. This result is a bit surprising at first glance because the angular dispersion, according to Eq. (13.2.2a), decreases with increasing  $\theta$ . At the same time, however, the anamorphic magnification  $r$  decreases at a faster rate. Hence  $\mathcal{R}$ , which is proportional to  $A/r$ , has the behavior as already noted. We discuss the consequences of this further in terms of the  $\mathcal{L}\mathcal{R}$  product in a later section.

### 13.3.b. IMMERSSED ECHELLE

Among the various possibilities for increasing the resolving power, a topic we discuss in the following section, another way of increasing  $\mathcal{R}$  is to immerse the ruled surface of the echelle in a material of index  $n$ . An example of an *immersed echelle* is shown in Fig. 13.5 where a prism is used to couple the incident light beam to the echelle. As shown in Section 14.1, the grating equation for an immersed grating is

$$m\lambda = n\sigma(\sin\beta + \sin\alpha). \quad (13.3.1)$$

The angular dispersion within the material of index  $n$  is given by

$$A = \frac{m}{n\sigma \cos\beta} = \frac{\sin\beta + \sin\alpha}{\lambda \cos\beta}. \quad (13.3.2)$$

For an echelle with a given blaze angle  $\delta$ , we see from Eq. (13.3.1) that the order  $m$  for an immersed echelle is  $n$  times larger than for the same echelle in air. From Eq. (13.3.2) we see that the angular dispersion within the prism is independent of the index  $n$ . However, the diffracted light emerging from the prism is deviated an additional amount. For the case shown in Fig. 13.5, with diffracted rays at near normal incidence on the prism face, an angular difference of  $\delta\beta$  within the prism is increased to  $n\delta\beta$  upon emergence. Thus  $A$  following the prism is  $n$  times  $A$  within the prism.

As a consequence of these comments on  $m$  and  $A$ , Eq. (13.2.4a) is correct as written, but Eqs. (13.2.4b) and (13.2.5) must be multiplied by  $n$ , hence  $\mathcal{R}_0$  is  $n$  times larger for an immersed echelle in the configuration shown in Fig. 13.5, compared to the same echelle in air.

Dekker has shown that, for a given beam size, an additional gain is possible if the angle of incidence at the prism is large rather than near zero. The effect on the beam is one of anamorphic magnification of the incident beam. The interested reader should consult the article by Dekker (1987) for details.

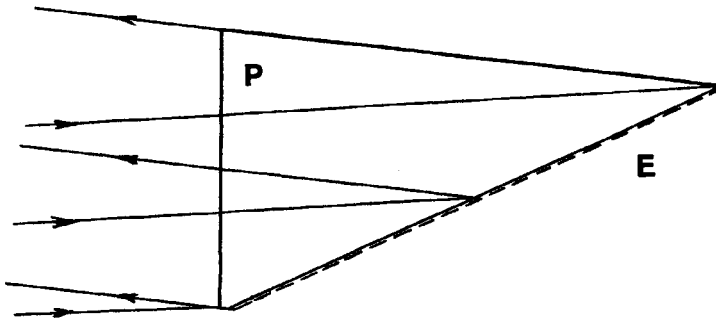


Fig. 13.5. An immersed echelle with a prism to couple the incident light beam to the echelle.

### 13.3.c. COMMENTS ON LARGER RESOLVING POWER

One of the consequences of the relations for resolving power in Tables 13.1 and 13.2, given  $\mathcal{R} \propto d_1/D$ , is the requirement for larger gratings and echelles on larger telescopes, simply to keep the resolving power constant. Not surprisingly, there is continual pressure to increase  $\mathcal{R}$ , even for larger telescopes, as demands are felt for more detailed spectroscopic study of astronomical sources.

The available parameters for increasing  $\mathcal{R}$  of an echelle on a telescope of a given  $D$  are larger beam size, larger R-value, narrower entrance slit, and immersion of the diffracting surface. A consequence of the first two factors is larger echelles, but practical limits exist on the maximum size that can be produced by the standard method of ruling with a diamond. The largest available ruled width  $W$  for a single echelle is about 400 mm, giving an unvignetted beam diameter of about 140 mm for  $\alpha = 69.5^\circ$  at an R-2 echelle. If some vignetting is acceptable at the ends of this echelle, then beam diameters of up to 200 mm are possible. For still larger beams it is necessary to use a mosaic of echelles, a topic we discuss further in Section 13.4.b.

A consequence of a narrower entrance slit is loss of light, unless seeing quality is improved by adaptive optics or active control of the thermal environment in the immediate vicinity of the telescope. The final factor, that of immersion of the ruled surface, requires a prism of excellent optical quality. This is especially important because the beam passes through the prism twice.

## 13.4. GRATING EFFICIENCY

The absolute efficiency of a grating is defined as the fraction of the energy at a given wavelength incident on the grating directed into a given diffracted order,

where the fraction of energy diffracted into a given order is determined by the so-called blaze function. In this section we examine the characteristics of the grating blaze function.

An exact treatment of grating efficiency is carried out by applying Maxwell's equations of electromagnetic theory to the interaction of light with a grating surface. For our purposes the exact theory is beyond the scope of our treatment and a scalar approximation is used instead. The polarization of the incident light is ignored in the scalar theory, but the results obtained from it are a good first approximation to the exact results. Important differences between the two approaches are noted. For a discussion of the exact theory, the reader should consult the references given at the end of the chapter. An especially thorough discussion of the results derived from the exact theory are found in the book by Loewen and Popov (1997). A good introduction to the results of scalar theory can be found in a handbook published by Milton Roy (1994).

13.4.a. BLAZE FUNCTION

Consider a reflection grating consisting of a number  $N$  of equally spaced facets, or grooves, of width  $b$  with center-to-center spacing  $\sigma$ , as shown in Fig. 13.6. For a beam of collimated light incident at angle  $\alpha$ , the normalized intensity of the diffracted wave is

$$i(\alpha, \beta) = IF \cdot BF = \left( \frac{\sin Nv'}{N \sin v'} \right)^2 \cdot \left( \frac{\sin v}{v} \right)^2, \tag{13.4.1}$$

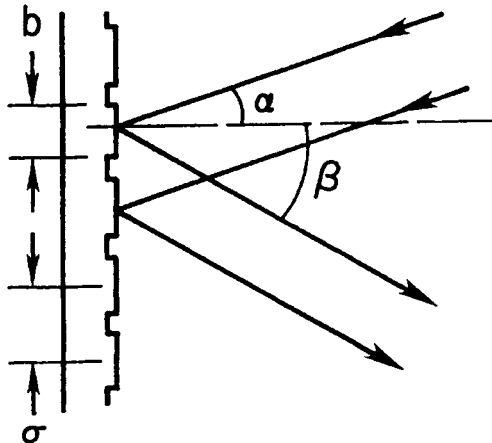


Fig. 13.6. Schematic of unblazed reflection grating with groove width  $b$  and separation  $\sigma$ .

where  $2v'$  is the phase difference between the centers of adjacent grooves and  $v$  is the phase difference between the center and edge of one groove. Equation (13.4.1) is composed of two parts, an *interference function* IF and a *blaze function* BF, with each function having a maximum value of unity. The derivation of Eq. (13.4.1) is found in any introductory optics text.

The relations for the phase differences are

$$2v' = \frac{2\pi\sigma}{\lambda} (\sin \beta + \sin \alpha), \quad (13.4.2)$$

$$v = \frac{\pi b}{\lambda} (\sin \beta + \sin \alpha). \quad (13.4.3)$$

Note that Eq. (13.4.2) is  $k$  times the path difference between rays from successive grooves. The interference function is a maximum when  $v' = m\pi$ , where  $m$  is an integer. Substituting  $v' = m\pi$  in Eq. (13.4.2) gives the grating equation (13.2.1).

The blaze function BF is the normalized intensity of a single slit diffraction pattern and is a maximum when  $v = 0$ , hence  $\alpha = -\beta$ , corresponding to  $m = 0$  in the grating equation. The derivation of this diffraction pattern is found in Section 10.1. As noted there, the first minimum in this pattern occurs at  $v = \pi$ . We also find that  $\text{BF} = 0.405$  when  $v = \pi/2$  and that the angular width at this intensity level is  $\lambda/b$ .

A sketch of the intensity pattern for a single wavelength is shown in Fig. 13.7, where it is evident that the pattern is simply the interference function IF modulated by the blaze function BF. From Fig. 13.7 we see that this grating directs most of the light to zero order and thus the efficiency in any other order is low.

In order to increase the efficiency in a dispersed order it is necessary, in effect, to move the blaze function along the axis in Fig. 13.7 until its peak coincides with an interference maximum in the dispersed order. This is done by tilting each facet

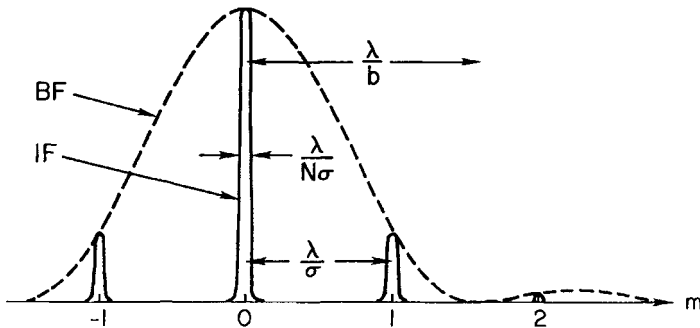


Fig. 13.7. Intensity pattern of single diffracted wavelength for grating in Fig. 13.6. BF, blaze function; IF, interference factor.

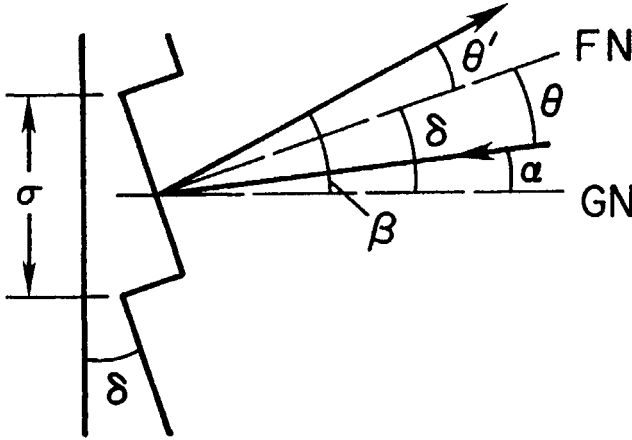


Fig. 13.8. Reflection grating of Fig. 13.6 with tilted facets to shift blaze function BF by angle  $2\delta$ . FN, facet normal; GN, grating normal.

of the grating by an angle  $\delta$  relative to the surface, as shown in Fig. 13.8. For a tilted groove the phase difference from center to edge is

$$\begin{aligned}
 v &= \frac{\pi\sigma \cos \delta}{\lambda} (\sin \theta - \sin \theta') \\
 &= \frac{\pi\sigma \cos \delta}{\lambda} [\sin(\beta - \delta) + \sin(\alpha - \delta)], \tag{13.4.4}
 \end{aligned}$$

where the width  $b = \sigma \cos \delta$  for a groove profile with right angle corners.

The shifted blaze function BF is a maximum when  $v = 0$ , and from Eq. (13.4.4) we get  $\alpha + \beta = 2\delta$  at the blaze peak. From Fig. 13.8 we get  $\alpha = \delta + \theta$  and  $\beta = \delta - \theta'$ , where  $\theta' = \theta$  at the peak of the blaze function. The wavelength at the peak of the blaze is called the *blaze wavelength*  $\lambda_b$ . At this wavelength Eqs. (13.2.1) and (13.2.2b) become

$$m\lambda_b = 2\sigma \sin \delta \cos \theta, \tag{13.4.5}$$

$$A = \frac{2 \sin \delta \cos \theta}{\lambda_b \cos \beta_b}. \tag{13.4.6}$$

The net effect of “blazing” a grating is to get maximum efficiency in the same direction in which light would be reflected by specular reflection in the absence of diffraction. Note that in a Littrow configuration  $\alpha = \beta = \delta$ , and the light returns on itself. The groove profile for a transmission grating is similar to that shown in Fig. 13.8, where each facet is a long narrow prism. In this case the blaze peak is in the direction in which light would be refracted in the absence of diffraction.

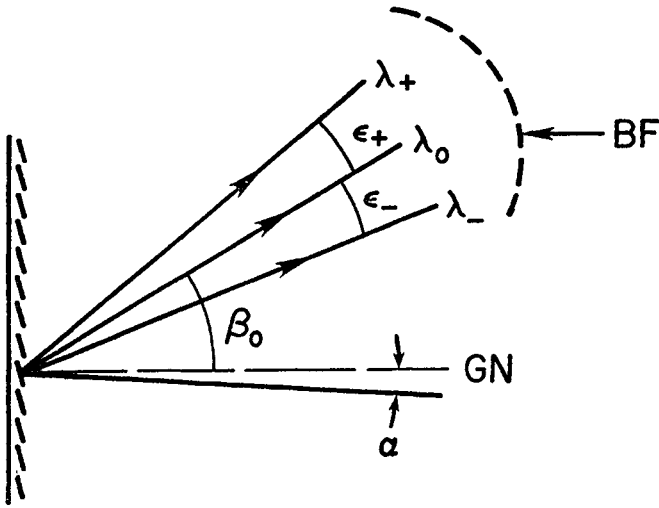


Fig. 13.9. Schematic of blaze function envelope with blaze peak at  $\lambda = \lambda_b$ . See Eq. (13.4.7).

The diffracted efficiency for a wavelength not at the blaze peak is determined by the value of BF for that wavelength in the diffracted direction. Figure 13.9 shows two wavelengths,  $\lambda_+$  and  $\lambda_-$ , on opposite sides of  $\lambda_b$ . The grating equation for these two wavelengths is

$$\begin{aligned} m\lambda_{\pm} &= \sigma \sin \alpha + \sigma \sin (\beta_b \pm \varepsilon_{\pm}) \\ &= m\lambda_b - \sigma \sin \beta_b (1 - \cos \varepsilon_{\pm}) \pm \sigma \cos \beta_b \sin \varepsilon_{\pm}, \end{aligned} \quad (13.4.7)$$

where  $\beta_b$  is the diffraction angle at the blaze peak.

We now choose  $\varepsilon_{\pm}$  as that pair of angles for which  $\text{BF} = 0.405$ , noting again that the width of a monochromatic single-slit diffraction peak between these points is  $\lambda/b$ . For a grating groove  $b = \sigma \cos \delta$  and therefore  $\varepsilon_{\pm} = \lambda_{\pm}/2\sigma \cos \delta$ . This relation for  $\varepsilon_{\pm}$  is accurate only in the small-angle approximation, but for most gratings of interest this accuracy is sufficient.

Assuming  $\varepsilon_{\pm}$  is small and  $\cos \beta_b \cong \cos \delta$ , we drop the middle term in Eq. (13.4.7) and find the wavelength limits

$$\lambda_{\pm} = \frac{m\lambda_b}{m \mp \frac{1}{2}}, \quad (13.4.8)$$

$$\lambda_+ - \lambda_- = \frac{m\lambda_b}{m^2 - \frac{1}{4}} = \frac{\lambda_b}{m}, \quad \text{for large } m. \quad (13.4.9)$$

In first order,  $\lambda_+ = 2\lambda_b$  and  $\lambda_- = 2\lambda_b/3$ . The asymmetry in these wavelengths about the peak is expected because the blaze function is broader for the longer wavelength.

The overall blaze function for wavelengths from  $\lambda_-$  to  $\lambda_+$  in first order is shown in Fig. 13.10. The values of  $\nu$  used to calculate BF at other wavelengths are given by  $\nu = m\pi(\lambda_b - \lambda)/\lambda$ . At the wavelengths  $\lambda_{\pm}$  given by Eq. (13.4.8), the reader can verify that  $\nu = \pm\pi/2$ , as expected. Published efficiency curves of first-order gratings with  $\sigma$  greater than a few wavelengths are similar to the curve in Fig. 13.10, though there is a difference between different polarizations of light. As examples, see efficiency curves in the reference by Loewen and Popov (1997).

For an echelle with large  $m$ , the asymmetry in the wavelengths given by Eq. (13.4.8) is much smaller and can usually be ignored. The blaze function spanning many echelle orders has the form shown in Fig. 13.11 for the Littrow configuration. The width of each peak in the scalloped curve is given by Eq. (13.4.9).

One important feature of the efficiency curve in Fig. 13.11 is that each peak covers one free spectral range of the echelle spectrum, as is seen by comparing

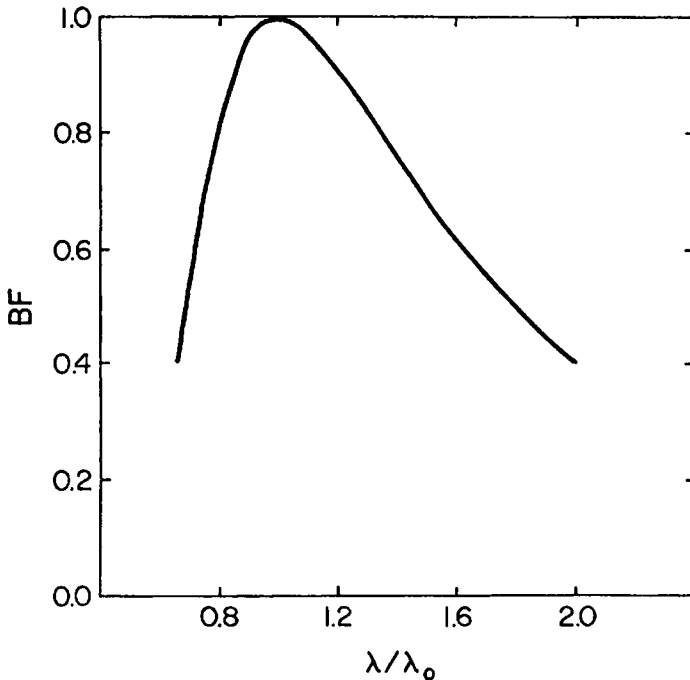


Fig. 13.10. Blaze function of grating with  $m = 1$ . See Eq. (13.4.8) and following discussion.

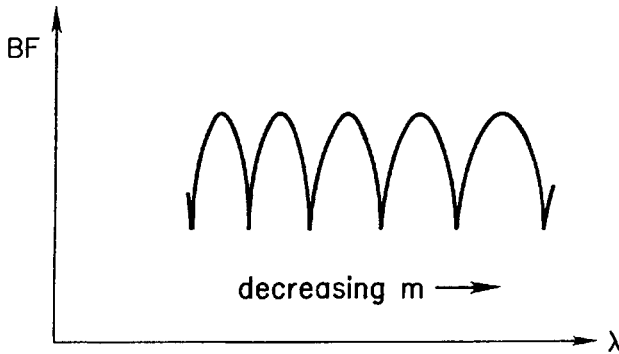


Fig. 13.11. Blaze function for echelle with  $m \gg 1$  in Littrow configuration. See Eq. (13.4.9).

Eqs. (13.2.6) and (13.4.9). Hence each wavelength over an extended range is diffracted with an efficiency no less than 40% that of the blaze wavelength.

When an echelle with rectangular grooves is illuminated at an angle  $\alpha > \delta$ , part of the width of each facet is not used and the effective groove width is less than  $\sigma \cos \delta$ . From the geometry in Fig. 13.12 we find that the effective groove width  $b'$  is

$$b' = \sigma \cos \alpha / \cos \theta. \quad (13.4.10)$$

Because the groove width is smaller, the angular width of the blaze function is larger. At the same time, according to Eq. (13.2.2a), the angular dispersion is smaller and one free spectral range has a smaller angular spread. Combining these two effects we find that the fraction of BF spanned by one free spectral range is a factor  $\cos \alpha / \cos \beta$  smaller than in the Littrow mode. Thus variation in the blaze

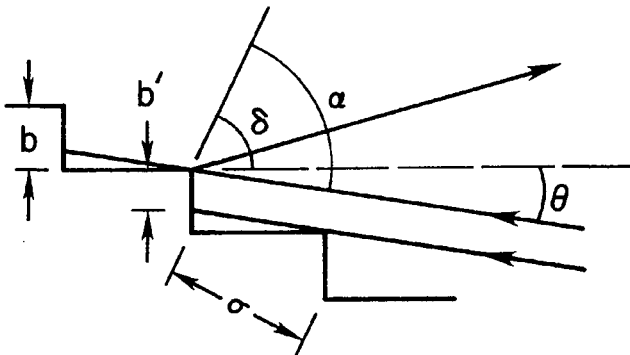


Fig. 13.12. Cross section of echelle showing effective facet width  $b'$  for  $\alpha > \delta$ . See Eq. (13.4.10).

function across a free spectral range is less pronounced when  $\alpha > \beta$  than in the Littrow mode.

At the same time, however, the efficiency at the peak is reduced because some light at the blaze peak is now diffracted into neighboring orders. As shown by Bottema (1986), the peak efficiency is reduced by a factor of  $\cos \alpha / \cos \beta$ . The net result of all these effects is a broader, but lower, efficiency profile. Profiles of a single blaze peak are shown in Fig. 13.13 for  $\theta = 0$  and  $\theta = 5^\circ$ , at a blaze angle of  $63.5^\circ$ . Examination of these curves shows that the efficiency at the ends of a free spectral range is somewhat higher at  $\theta = 5^\circ$  than at  $\theta = 0^\circ$ . The average efficiency across the range, however, decreases as  $\theta$  increases from zero.

The effects of groove shadowing for  $\alpha > \beta$  are present for all gratings with rectangular grooves, but are much less significant for gratings with small blaze angle. For our examples in Section 13.3,  $\cos \alpha / \cos \beta$  for  $\theta = 5^\circ$  is 0.95 for the grating and 0.70 for the echelle.

When light is incident on an echelle at an angle  $\alpha < \beta$ , each facet is fully illuminated but a fraction of the light is sent back in the general direction of the collimator. The effective groove width is again given by Eq. (13.4.10), as is evident from Fig. 13.12 when the arrows on the rays are reversed. Thus the blaze

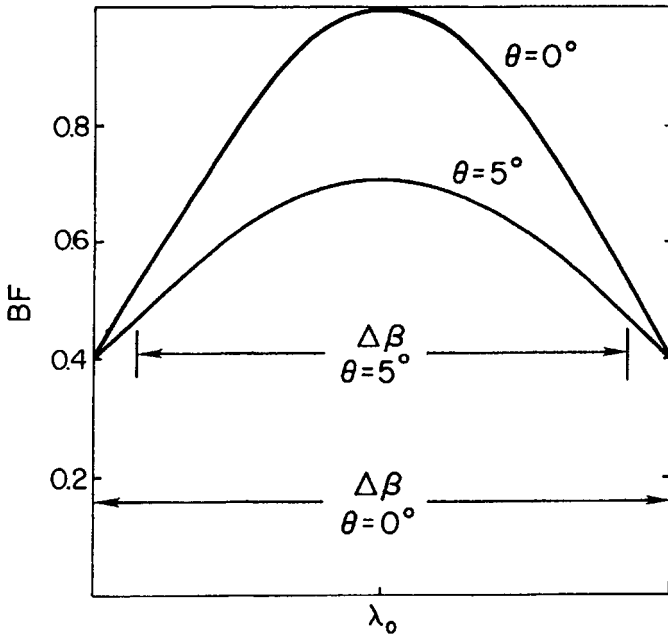


Fig. 13.13. Blaze function for single echelle order at two values of  $\theta$ . Angular width of the free spectral range is  $\Delta\beta$ . See the discussion following Eq. (13.4.10).

peak is again broadened. In this case, however, the angular dispersion is larger for increasing  $\beta$  and one free spectral range spans the same portion of the blaze peak. The peak efficiency in this case is reduced by the factor  $\cos \beta / \cos \alpha$ .

A final point to be made on grating efficiency is the extent to which polarization effects are important. Let  $P$  and  $S$  represent the diffracted efficiency for light polarized parallel and perpendicular, respectively, to the length of the grating grooves. We define fractional polarization as  $|P - S| / (P + S)$ . The size of this fraction is determined by the size of  $\lambda/b$ , hence the effect is smaller for a grating with larger grooves. Unpublished measurements at  $\lambda = 480$  nm on an echelle with 79 grooves/mm and  $\tan \delta = 2$  give a fractional polarization of 0.02, where  $\lambda/b = 0.085$ . Thus the curves in Figs. 13.11 and 13.13 are valid for either plane of polarization, to a good approximation. For a full discussion of grating efficiency consult the reference by Loewen and Popov (1997).

#### 13.4.b. RESOLUTION PRODUCTS

The luminosity-resolution product for a grating at the blaze peak follows from a substitution of  $A$  from Eq. (13.4.6) into Eq. (12.2.11). The result, given in terms of  $d_1$ , is

$$\mathcal{LR} = \tau \frac{\pi D \phi' d_1}{2} \frac{\sin \delta \cos \theta}{\cos(\delta + \theta)}. \quad (13.4.11)$$

Another useful product in assessing spectrometer capability at the blaze peak is found by substituting  $A$  from Eq. (13.4.6) into Eq. (12.2.3), with the result

$$\mathcal{R}\phi = \frac{2d_1}{D} \frac{\sin \delta \cos \theta}{\cos \alpha} = \frac{2W}{D} \sin \delta \cos \theta. \quad (13.4.12)$$

For a grating with a small blaze angle, these products are essentially constant over a range of  $\theta$  of many degrees. With our grating example in Section 13.3,  $\mathcal{LR}$  changes by less than 6% when  $\theta$  is changed from 0 to 10°. For a typical grating, therefore, it is sufficient to set  $\theta = 0$  in Eqs. (13.4.11) and (13.4.12).

For an echelle with a large blaze angle, on the other hand, the dependence of  $\mathcal{LR}$  on  $\theta$  is an important one. Over the range of  $\theta$  in Table 13.3,  $\mathcal{LR}$  changes by about 27% for our echelle example, assuming  $d_1$  remains constant. The size of this change indicates that a closer look at this product for echelles is in order.

It appears from Eq. (13.4.11) that  $\mathcal{LR}$  can be made as large as desired for a given  $d_1$  by choosing  $\alpha = \delta + \theta$  near  $\pi/2$ . This is not feasible in practice, however, because the width  $W$  needed to collect all the light is larger than the width of any practical grating. An additional complication at these large angles is that the diffracted beam width  $d_2$  is significantly greater than  $d_1$  because of anamorphic magnification. This extended width makes the design of cameras

**Table 13.4**  
Relative Beam Widths for Echelles<sup>a,b</sup>

tan $\delta$	$\theta = 5^\circ$		$\theta = 0$	
	$W/d_1$	$d_2/d_1$	$W/d_1$	$d_2/d_1$
2.0	2.72	1.42	2.24	1.00
2.4	3.30	1.53	2.60	1.00
2.8	3.95	1.65	2.97	1.00
3.2	4.68	1.78	3.35	1.00
3.6	5.48	1.92	3.74	1.00
4.0	6.36	2.08	4.12	1.00

$$^a \alpha = \delta + \theta, \beta = \delta - \theta.$$

$$^b W/d_1 = 1/\cos \alpha, d_2/d_1 = \cos \beta/\cos \alpha.$$

more difficult at the small focal ratios usually required. As an illustration of these comments, data on beam widths for a set of representative blaze angles and  $\theta = 0$  and  $5^\circ$  are given in Table 13.4. Given the state of grating technology and camera design for large systems, spectrometer designs with  $W/d_1 < 4$  are the only reasonable choices for getting large  $\mathcal{LR}$ . Hence R-4 echelles should be used very near Littrow.

Most large, commercially available, R-2 echelles have a width-to-length ratio of two. From the data in Tables 13.3 and 13.4, we see that  $W/d_1 > 2$ , hence a beam unvignetted by the echelle can cover its width but not its length. This is illustrated in Fig. 13.14, where  $W_c$  is the projected echelle width seen from the collimator and  $H$  is the height of the grooves. In terms of  $W$ , height  $H = W/2$  and  $W_c = W \cos \alpha$ .

Given this width-to-length ratio, the designer of an echelle spectrometer using a single echelle has three options:

- (1) Choose  $d_1 = W_c$ , hence no vignetting at the echelle.
- (2) Choose  $d_1 > W_c$ , but not larger than  $H$ , and accept some vignetting.
- (3) Choose  $\alpha < \beta$  in a way to make  $d_1 = H = W_c$ .

In options (1) and (2), we assume  $\alpha$  is larger than  $\beta$ .

Option (1) is acceptable, but does not make full use of the echelle surface. Option (3) has the same  $\mathcal{LR}$  as option (1), but is constrained to  $\cos \alpha = 0.5$ , hence  $\alpha < \beta$  for an R-2 echelle. As noted in the previous section, the variation in efficiency across a free spectral range is larger when  $\alpha < \beta$ , hence (1) is preferable even though its  $\mathcal{LR}$  is the same.

Option (2) is a tradeoff between larger  $d_1$  than (1) and smaller  $\tau$  due to vignetting. A larger  $d_1$  translates into a wider entrance slit for the same projected slit width  $w'$ , a result that follows from Eq. (12.2.1a) written as  $w' = rDf_2\phi/d_1$ .

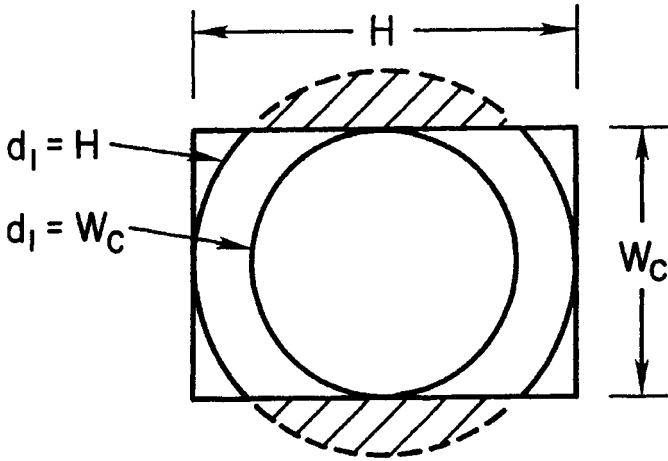


Fig. 13.14. Overfilling of echelle to increase  $\mathcal{LR}$  product. See Section 13.4.b.

A full analysis shows that the gain in light at the entrance slit more than offsets the light loss at the echelle, up to the point where  $d_1 = H$ . For angle  $\theta = 5^\circ$  the net gain amounts to about 17%.

It is important to note that another option available in the design of an echelle spectrometer is a mosaic of echelles, as done for HIRES, the High Resolution Echelle Spectrometer for the Keck 10-m telescope. This instrument, described by Vogt et al. (1994), has a beam diameter of 305 mm and a  $1 \times 3$  mosaic of  $305 \times 405$  mm R-2.8 echelles with an effective  $W \cong 1220$  mm. Given  $\tan \delta = 2.8$  and  $\theta = 5^\circ$  we find  $\cos \alpha = 0.253$  and  $W_c \cong 310$  mm, a bit larger than the beam diameter. In this case the echelle as seen from the collimator is approximately square and the only vignetting is at the gaps in the mosaic.

All of the relevant numbers needed to compute  $\mathcal{R}\phi$  for HIRES according to Eq. (13.4.12) are available in the preceding paragraph. It is left as an exercise to the reader to show that  $\mathcal{R}\phi \cong 0.225$  or, in units of arc-sec,  $\mathcal{R}\phi \cong 46,000$  arc-sec. We use this result in an example when discussing design considerations for grating and echelle spectrometers in Chapter 15.

### 13.4.c. SURFACE HOLOGRAPHIC GRATINGS

In the preceding sections we have discussed efficiency as it applies to classically ruled gratings with triangular groove shape. Another type of grating available is the *surface holographic grating*, produced by recording interference fringes from two expanded laser beams in a photosensitive material. This type of grating has a different groove shape than the ruled type, with efficiency a

sensitive function of groove shape and number of grooves/mm. As pointed out by Loewen and Popov (1997), a disadvantage of the surface holographic grating is that its groove shape cannot be easily controlled.

Although these gratings are competitive with ruled gratings when used in first order, they have not been made at the groove densities characteristic of echelles. First-order gratings are typically used at spectral resolutions of  $1E3$  to  $1E4$ , and in this range either type of grating can be used. For high resolution in the range  $3E4$  to  $1E5$ , the echelle is clearly superior for broad spectral coverage. Further information on holographic gratings is found in the references at the end of this chapter.

#### 13.4.d. VOLUME-PHASE HOLOGRAPHIC GRATINGS

A type of grating that shows promise for low and moderate resolution is the *volume-phase (VP) holographic grating*. In this type of grating the periodic diffracting structure arises from modulation of the index of refraction within the depth of the grating material. Light scattered from layers within a VP grating interferes constructively when the Bragg diffraction condition is satisfied. Details about the Bragg condition for different grating configurations are given in a paper by Barden et al. (1998).

One particular characteristic of a VP grating that makes it an attractive alternative to a ruled grating is its predicted efficiency approaching 100%, in both planes of polarization, for layer densities of 600 per mm or higher. Measurements on unpolarized light for a 6001/mm VP transmission grating give an absolute peak efficiency of about 80%, including reflective losses, and an overall efficiency greater than 55% from 450–900 nm. The blaze peak and blaze envelope of such a grating can be tuned by rotating the grating.

The technology of these gratings is in the development stage, but the work done to date indicates that VP gratings are likely to become viable options in the design of low-order grating spectrometers. This is especially true if VP gratings can be made in the sizes 300–400 mm needed for large telescopes. For a thorough review of the potential of VP gratings, see the paper by Barden et al. (1998).

### 13.5. FABRY-PEROT INTERFEROMETER

The Fabry-Perot spectrometer is an important instrument for astronomical observations that require very high spectral resolution of limited spectral ranges and/or large angular fields at moderate resolution. As we show, the Fabry-Perot is superior to a grating or echelle instrument in these cases. Although the Fabry-Perot was first used in astronomy as a scanning device with a single element

detector, it is now often used in the imaging mode. Both the scanning and imaging Fabry-Perot spectrometer modes are discussed in this section.

Our discussion of the Fabry-Perot is relatively brief, with results given without derivation. The basic theory of the Fabry-Perot can be found in any optics text, and extensive discussions of its application in astronomy are given by Roesler (1974) and by Meaburn (1976). Although relations for the Fabry-Perot are often given in terms of wavenumber, the reciprocal of the wavelength, we choose to give all results in terms of wavelength.

### 13.5.a. BASIC RELATIONS

A schematic diagram of a Fabry-Perot spectrometer is shown in Fig. 13.15. For a Fabry-Perot with material of index  $n$  between interferometer plates of separation  $d$ , the normalized intensity of the transmitted light at angle  $\alpha$  is given by

$$i_t = \frac{I_t}{I_i} = \left( \frac{T}{1-R} \right)^2 \left[ 1 + \frac{4R}{(1-R)^2} \sin^2 \left( \frac{\delta}{2} \right) \right]^{-1}, \quad (13.5.1)$$

where  $T$  and  $R$  are the fractions of the incident energy transmitted and reflected at each surface and  $\delta$ , the phase difference between successive transmitted beams, is

$$\delta = \frac{2\pi}{\lambda} 2nd \cos \alpha. \quad (13.5.2)$$

The reciprocal of the quantity in square brackets in Eq. (13.5.1) is the *Airy function*. This function is a maximum when  $\delta = 2m\pi$ , hence wavelengths are transmitted with maximum intensity when

$$m\lambda = 2nd \cos \alpha, \quad (13.5.3)$$

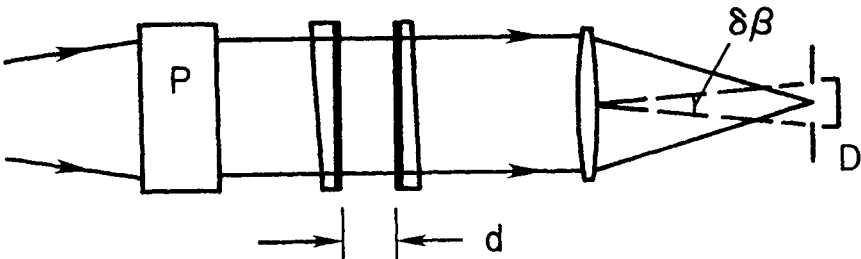


Fig. 13.15. Schematic of Fabry-Perot spectrometer. P, prefilter-collimator combination; D, detector.

where  $m$  is an integer order number. Because the Fabry-Perot is axially symmetric, the pattern in the focal plane of a camera for a broad monochromatic source is a set of concentric rings with each ring a separate order.

The normalized intensity in Eq. (13.5.1) is one if  $T + R = 1$  and  $m$  is an integer. More generally we have  $A + T + R = 1$ , where  $A$  is the fraction of the incident energy absorbed at each surface. It is left to the reader to show that the ratio  $i_t(\text{max})/i_t(\text{min})$  is independent of  $A$ .

The free spectral range  $\Delta\lambda$  is found by the same procedure used in Section 13.2.e, with a similar result,

$$\Delta\lambda = \lambda/m = \lambda^2/2nd \cos \alpha \cong \lambda^2/2nd. \quad (13.5.4)$$

Because  $m$  is usually large, a filter or predisperser is required to eliminate all unwanted orders. Given that  $\alpha$  is generally a small angle, we assume  $\cos \alpha = 1$  in the relations to follow, unless otherwise noted.

The limit of resolution or spectral purity is determined by the characteristics of the Airy function, and the result is

$$\delta\lambda = \Delta\lambda/N = \lambda^2/2Nnd, \quad (13.5.5)$$

where  $N$  is called the *finesse*. The *finesse* depends on the plate quality and the reflectance of the coatings. With perfectly flat and parallel reflecting surfaces the *reflective finesse*  $N_R = \pi\sqrt{R}/(1 - R)$ . For plates of high quality with multilayer coatings, a typical effective value of  $N$  is in the range 30–50.

From Eq. (13.5.5) the spectral resolving power is

$$\mathcal{R} = \frac{\lambda}{\delta\lambda} = \frac{N\lambda}{\Delta\lambda} = \frac{2Nnd}{\lambda}. \quad (13.5.6)$$

With the basic relations in hand, we now consider the different modes in which the Fabry-Perot is used.

### 13.5.b. SCANNING FABRY-PEROT

In one mode of operation a circular aperture isolates the central order and a single channel device, such as a photomultiplier, is the detector. Scanning of the Fabry-Perot is accomplished by changing either  $n$  or  $d$  in Eq. (13.5.3), with the scan rate set by the desired SNR in the output signal. The index  $n$  is changed by changing the pressure of the gas between the plates, while  $d$  is changed with piezoelectric actuators between the plates. A scan across one free spectral range is accomplished by changing the optical distance between the plates by  $\lambda/2$ . A good discussion of the piezoelectric scan method is given by Atherton (1987).

The optical layout of a scanning Fabry–Perot is generally similar to that shown in Fig. 9.9 for a focal reducer. The components include a field lens at the telescope focus to reimage the telescope exit pupil at the interferometer, a collimator preceding the interferometer, and a camera. The relation between the angle  $\alpha$  at which the chief ray enters the collimator and the angle  $\theta$  on the sky is, from Eq. (9.4.1),

$$\alpha f_c = f \theta, \quad (13.5.7)$$

where  $f_c$  and  $f$  are the focal lengths of the collimator and telescope, respectively.

The angular diameter  $\delta\beta$  of an axial hole that accepts all of the light in the full width at half-maximum (FWHM) of the central order is given by

$$\delta\beta = (8/\mathcal{R})^{1/2}. \quad (13.5.8)$$

Substituting Eq. (13.5.8) into Eq. (12.2.8) gives the etendue for a circular hole as

$$U = \frac{\pi d_1^2}{4} \frac{\pi(\delta\beta)^2}{4} = \frac{\pi d_1^2}{4} \frac{2\pi}{\mathcal{R}}, \quad (13.5.9)$$

where the anamorphic magnification is one, hence  $d_2 = d_1$ . Therefore the luminosity-resolution product for the Fabry–Perot is given by

$$\mathcal{L}\mathcal{R} = 2\pi\tau \cdot \pi d_1^2/4. \quad (13.5.10)$$

The transmittance  $\tau$  is the product of the transmittance  $\tau_0$  of the optical elements and the average of the Airy function over the FWHM of the central order, where the latter factor is about 0.8.

### 13.5.c. IMAGING FABRY–PEROT

An imaging Fabry–Perot differs from the scanning Fabry–Perot primarily at the detector end; a high efficiency area detector such as a CCD replaces the single channel axial detector. In effect, a single channel device has been converted into a multichannel one. The two systems are similar optically, with each having a field lens, collimator, and camera, in addition to the required filters to isolate the desired orders. Because of the detector the mode of operation is somewhat different. For the imaging Fabry–Perot the wavelength range of interest is typically scanned by making discrete changes in  $d$ , with the time spent at each setting determined by the desired SNR in the output signal.

The outputs of the 2D detector give what is called a *data cube*. This cube consists of two dimensions of spatial information and one of spectral information. It is important to note that the transmitted wavelengths for a single slice of this cube follow Eq. (13.5.3), which we write as

$$\lambda = \lambda_0 \cos \alpha, \quad (13.5.11)$$

where  $\lambda_0$  is the wavelength transmitted along the optical axis. Thus a surface of constant wavelength in the data cube is a curved surface intersecting many slices of the cube.

As an example of an imaging Fabry-Perot we take an  $f/8$ , 4-m telescope, and a Fabry-Perot system with 60-mm diameter plates,  $f/8$  collimator,  $f/2$  camera, and a CCD with 20- $\mu\text{m}$  pixels. The reader can verify that the scale at the telescope is approximately 160  $\mu\text{m}$  per arc-sec, hence two detector pixels span one arc-sec on the sky. Assuming the CCD is 1000 pixels on a side, the area on the sky is approximately 8 arc-min. If the Fabry-Perot is configured to give a resolving power of  $1\text{E}4$  on an extended source covering this area, the corresponding velocity resolution on the source is  $c/\mathcal{R}$  or 30 km/sec.

For further discussions of imaging Fabry-Perot systems the reader should consult the papers by Bland et al. (1990) and Reynolds et al. (1990).

#### 13.5.d. COMPARISON OF ECHELLE AND FABRY-PEROT

We now compare  $\mathcal{LR}$  for the Fabry-Perot with that for a typical echelle spectrometer. In Section 12.2 we find  $d_1 \delta\alpha' = D\phi'$  for any slit spectrometer and, after substitution into Eq. (13.4.11) and division into Eq. (13.5.10), we get

$$\mathcal{LR} \frac{(FP)}{(E)} = \frac{\tau_{FP}}{\tau_E} \left( \frac{d_{FP}}{d_E} \right)^2 \frac{\pi}{\delta\alpha' \tan \delta}, \quad (13.5.12)$$

with the echelle in the Littrow configuration. Note that  $\delta\alpha'$ , the angle subtended by the slit length at the collimator, is  $D/d_1$  times larger than the angular length  $\phi'$  projected on the sky.

For a well-defined projected slit, assume the largest practical  $\delta\alpha'$  is about  $1^\circ$ . Assuming  $\tan \delta = 2$ , the ratio in Eq. (13.5.11) is about 100 for the same transmittances and beam diameters in each instrument. If we assume the largest echelle beam is two times that of the largest Fabry-Perot beam, the  $\mathcal{LR}$  ratio is reduced to 25, still substantially larger for the Fabry-Perot. The value of  $\delta\alpha'$  assumed here is obviously appropriate for a large extended source. If  $D = 4\text{ m}$  and  $d_1 = 200\text{ mm}$ , the corresponding angle on the sky is 180 arc-sec. For smaller values of  $\delta\alpha'$ , the ratio  $\mathcal{LR}$  is even more in favor of the Fabry-Perot.

We now compare a scanning Fabry-Perot and echelle for a stellar source, with each spectrometer on a 4-m telescope. We assume beam diameters are 100 and 200 mm, respectively, for the Fabry-Perot and echelle, and the stellar seeing disk is one arc-sec. For an entrance slit width equal to the seeing disk diameter, the resolving power of the echelle is  $4\text{E}4$  in the Littrow configuration and about 20% larger for  $\theta = 5^\circ$ . This resolving power is far below the limit of  $1.6\text{E}6$  and the echelle could be used to get higher resolving power, say ten times higher, but only at the expense of luminosity.

For the Fabry-Perot we assume  $\mathcal{R} = 4E5$ , a resolving power appropriate for the observation of narrow spectral lines, for example. With this  $\mathcal{R}$  we find  $\delta\beta = 15$  arc-min, which projects to about 23 arc-sec on the sky. Light loss at the entrance aperture is not a problem with this telescope- spectrometer combination and the system is far from any reasonable seeing limit. It is important to note that for  $\lambda = 500$  nm and  $N = 40$  the free spectral range of the Fabry-Perot for this resolving power is only 0.05 nm, compared to 5 or 10 nm for an echelle in this same wavelength range.

These examples illustrate the kinds of observations for which the Fabry-Perot is especially well-suited, very high spectral resolving power on sources of small angular size or moderate to high resolving power for sources of large angular size.

Although the Fabry-Perot clearly has an advantage over an echelle system in terms of the  $\mathcal{LR}$  product, there are other considerations as well. One feature already noted here is the small free spectral range of the Fabry-Perot compared to the echelle. This, together with the area coverage of either a scanning or imaging system, makes the Fabry-Perot especially suited to studies of individual spectral lines of extended, emission line sources such as gaseous nebulae. Echelle spectrometers, on the other hand, are most often used in a mode in which the flux in all spectral elements over a wide wavelength range is recorded simultaneously. Thus the echelle is well suited to the study of stars and near stellar sources.

In summary, Fabry-Perot and echelle spectrometers are best viewed as complementary high-resolution spectral analyzers of celestial sources.

## 13.6. FOURIER TRANSFORM SPECTROMETER

Although a Fourier transform spectrometer (FTS), is not a dispersing system in the sense defined in Section 12.1, it gives an output from which the spectrum can be derived. Because the FTS is used to get spectral data, especially in the infrared, a brief discussion of its characteristics is in order. Results are given without derivation; for discussions of the theory of the FTS the reader should consult the references at the end of the chapter.

An FTS is basically a scanning Michelson interferometer with collimated light as the input, as shown schematically in Fig. 13.16. The input beam is divided by a beamsplitter with approximately one-half going to each of the mirrors A and B. The light reflected from the mirrors is again divided by the beamsplitter, with approximately one-half of the original beam recombined and sent to the single channel detector D.

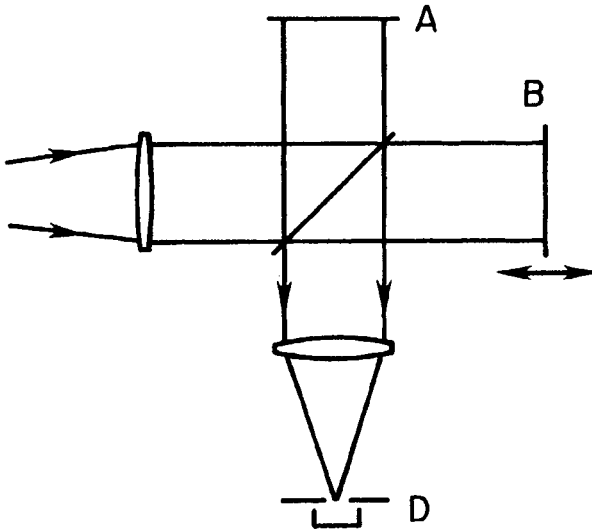


Fig. 13.16. Schematic of Fourier transform spectrometer. A, fixed mirror; B, movable mirror; D, detector.

### 13.6.a. BASIC RELATIONS

For a collimated monochromatic beam the on-axis intensity at D is determined by the path difference between the two arms of the interferometer. Let  $x_a$  and  $x_b$  denote the respective distances from the center of the beamsplitter to the center of each mirror. The OPD between the recombined axial beams, assuming  $n = 1$ , is  $2(x_b - x_a) = 2\Delta x$ , and the phase difference is  $2k\Delta x$ , where  $k = 2\pi/\lambda$ . Note that Eqs. (13.5.2) and (13.5.3) for the Fabry–Perot apply to off-axis beams in the Michelson if  $d$  is replaced by  $\Delta x$ .

The fraction  $T(k, \Delta x)$  of the incident beam in the output beam is given by

$$T(k, \Delta x) = \frac{1}{2}[1 + \cos(2k\Delta x)]. \quad (13.6.1)$$

If the beams from the two arms are in phase [ $\cos(2k\Delta x) = 1$ ] we have  $T = 1$ ; if the beams are  $\pi$  out of phase [ $\cos(2k\Delta x) = -1$ ] then  $T = 0$ . The relation in Eq. (13.6.1) is a direct consequence of two-beam interference.

Given an incident beam whose spectrum is  $I(k)$ , the flux  $\mathcal{F}$  in the output beam is

$$\begin{aligned} \mathcal{F}(\Delta x) &= C \int I(k)T(k, \Delta x)dk \\ &= \text{constant} + \frac{C}{2} \int I(k) \cos(2k\Delta x)dk, \end{aligned} \quad (13.6.2)$$

where  $C$  is a constant. The output  $\mathcal{F}(\Delta x)$  for all  $\Delta x$  from a minimum value, usually zero, to the maximum value is called the interferogram. The integral in the second line of Eq. (13.6.2) is the Fourier cosine transform of the spectrum. From the theory of Fourier transforms, the transform of the recorded flux  $\mathcal{F}(\Delta x)$  is the spectrum.

The spectral resolving power  $\mathcal{R}_0$  achievable with the FTS is directly proportional to the maximum  $\Delta x$  in the scan producing the interferogram, and is given by

$$\mathcal{R}_0 = \frac{\lambda}{\delta\lambda_0} = \frac{4 \Delta x(\text{max})}{\lambda}. \quad (13.6.3)$$

If, for example,  $\Delta x(\text{max}) = 10$  cm, then  $\mathcal{R}_0 = 4E5$  at  $\lambda = 1000$  nm. As in the case of a diffraction grating or Fabry-Perot,  $\mathcal{R}_0$  is the maximum path difference divided by the number of wavelengths in this distance.

Because Eq. (13.5.3) applies to both the Michelson and Fabry-Perot interferometers, the relations for  $\delta\beta$ ,  $U$ , and  $\mathcal{LR}$  in Eqs. (13.5.8)–(13.5.10) also apply to an FTS. As a consequence, the resolution achieved in practice is smaller than given in Eq. (13.6.3) by about a factor of two, when the angular diameter of the exit aperture is set according to Eq. (13.5.8).

### 13.6.b. COMPARISONS AND COMMENTS

Given the similarities between an FTS and a Fabry-Perot spectrometer and the discussion in the preceding section, it is evident that the FTS is also well-suited to observations requiring high spectral resolving power. An advantage of an FTS is that, unlike a scanning Fabry-Perot, all of the light in the passband of interest is being recorded all of the time in an FTS. Bland et al. (1990) has pointed out that this advantage is less significant for detectors with lower read noise. Based on Eq. (13.5.12) and the following discussion, it is also clear that an FTS has a significant  $\mathcal{LR}$  advantage over an echelle. Thus the etendue advantage of an FTS over an echelle is maintained at high resolution.

A disadvantage of an FTS is the extreme care that must be taken to produce a uniform scan. The value of  $\Delta x$  in Eq. (13.6.1) must be known to a small fraction of a wavelength to ensure that the transform of the flux in Eq. (13.6.2) gives a meaningful result. Stringent mechanical requirements on the scan mechanism and rigidity of the interferometer base are alleviated somewhat by using cube corners in place of the mirrors shown in Fig. 13.16.

It is also possible to construct an imaging FTS by placing an area detector in the focal plane of a camera lens. An example of an imaging FTS operating at moderate resolution in the near infrared is described by Simons et al. (1994). Another variant of the FTS is a nonscanning system in which the mirrors A and B

in Fig. 13.16 are replaced by diffraction gratings, with each tilted with respect to the axial ray incident upon it. This type of interferometer produces a Fizeau fringe pattern at the detector. For a discussion of its features the reader should consult the paper by Harlander and Roesler (1990).

### 13.7. CONCLUDING REMARKS

The dispersive devices discussed in this chapter range from the simple prism to elegant interferometric devices such as the Fabry-Perot and Michelson spectrometers. Most of the discussion, however, is given to diffraction gratings and their dispersive characteristics. This emphasis on gratings is simply a reflection of the fact that most of the spectral data on astronomical sources has been obtained with grating instruments. The versatility of grating spectrometers, especially their adaptability to observing multiple sources simultaneously, make them the choice for a wide range of observing programs.

A quick look at the tables of contents of proceedings from recent conferences on astronomical instrumentation suggests that diffraction grating spectrometers will continue as the most common type of spectrographic instrumentation. Following an analysis of grating aberrations and a brief discussion of concave gratings in Chapter 14, we complete our discussion of spectrographic instruments with a thorough look at plane grating spectrometers in Chapter 15.

### REFERENCES

- Bottema, M. (1980). *Proc. SPIE Int. Soc. Opt. Eng.*, **240**: 171.  
*Diffraction Grating Handbook* (1994). Rochester, NY: Milton Roy.  
*Optical Glass* (1980). Duryea, PA: Schott Optical Glass.

### BIBLIOGRAPHY

#### *Diffraction Gratings*

- Barden, S., Arns, J., and Colburn, W. (1998). *Proc. SPIE Int. Soc. Opt. Eng.*, **3355**: 866.  
 Dekker, H. (1987). in *Instrumentation for Ground-Based Astronomy*, Robinson, L. (ed.), p. 183, New York: Springer-Verlag.  
 Hutley, M. (1982). *Diffraction Gratings*, New York: Academic Press.  
 Loewen, E. and Popov, E. (1997). *Diffraction Gratings and Applications*, New York: Marcel Dekker.  
 Loewen, E. (1983). *Applied Optics and Optical Engineering*, vol. 9, Chap. 2, New York: Academic Press.  
 Maystre, D. (1984). *Progress in Optics*, vol. 21, Chap. 1, Amsterdam: North-Holland.

Richardson, D. (1969). *Applied Optics and Optical Engineering*, vol. 5, Chap. 2, New York: Academic Press.

Stroke, G. (1963). *Progress in Optics*, vol. 2, Chap. 1, Amsterdam: North-Holland.

Vogt, S., Allen, S., Bigelow, B., Bresee, L., Brown, B., Cantrall, T., Conrad, A., Couture, M., Delaney, C., Epps, H., Hilyard, D., Hilyard, D., Horn, E., Jern, N., Kanto, D., Keane, M., Kibrick, R., Lewis, J., Osborne, C., Osborne, J., Pardeilhan, G., Pfister, T., Ricketts, T., Robinson, L., Stover, R., Tucker, D., Ward, J., and Wei, M. (1994). *Proc. SPIE Int. Soc. Opt. Eng.*, **2198**: 362.

#### *Fabry-Perot Spectroscopy*

Atherton, P. (1987). in *Instrumentation for Ground-Based Astronomy*, Robinson L. (ed.), p. 124, New York: Springer-Verlag.

Bland, J., Tully, R., and Cecil, G. (1990). *Proc. SPIE Int. Opt. Eng.*, **1235**: 590.

Meaburn, J. (1976). *Detection and Spectrometry of Faint Light*, Dordrecht, Netherlands: Reidel.

Reynolds, R., Roesler, F., Scherb, F., and Harlander, J. (1990). *Proc. SPIE Int. Soc. Opt. Eng.*, **1235**: 610.

Roesler, F. (1974). *Methods of Experimental Physics: Astrophysics*, vol. 12, Part A: "Optical and Infrared," Chap. 12, New York: Academic Press.

Vaughan, A. (1967). *Annual Reviews of Astronomy and Astrophysics*, **5**: 139. Palo Alto, CA: Annual Reviews.

#### *Fourier Transform Spectroscopy*

Connes, P. (1970). *Annual Review of Astronomy and Astrophysics*, **8**: 209. Palo Alto, CA: Annual Reviews.

Harlander, J. and Roesler, F. (1990). *Proc. SPIE Int. Soc. Opt. Eng.*, **1235**: 622.

Ridgeway, S. and Brault, J. (1984). *Annual Review of Astronomy and Astrophysics*, **22**: 291. Palo Alto, CA: Annual Reviews.

Schnopper, H. and Thompson, R. (1974). *Methods of Experimental Physics: Astrophysics*, vol. 12, Part A: "Optical and Infrared," Chap. 11, New York: Academic Press.

Simons, D., Clark, C., Smith, S., Kerr, J., Massey, S., and Maillard, J. (1994). *Proc. SPIE Int. Soc. Opt. Eng.*, **2198**: 185.

Most astronomical spectrometers use a grating or echelle as the primary dispersing element. As noted in Chapter 13, this choice is made for reasons of flexibility in choice of spectrum format and resolution to match modern detectors, and the ability to get broad spectral coverage at good efficiency. In this chapter we discuss the limitations on grating performance from the point of view of geometrical optics, both for the grating itself and for selected concave grating instruments.

The limitations of a grating spectrometer are determined by two principal factors—the aberrations due to the collimator and camera optics, and the aberrations introduced by the grating. Grating aberrations are determined by the type of grating surface, whether it is plane or spherical, and the focal ratio of the incident beam. In most spectrometers the incident light is collimated, but there are systems in which the incident light is a convergent beam.

In this chapter we use Fermat's Principle to derive the aberrations of a grating surface, either reflecting or refracting. By combining these results with the aberrations of the other optics in a spectrometer, we can determine overall spectrometer performance. This system analysis is given for concave grating spectrometers in this chapter and plane grating instruments in the following chapter.

The approach followed in deriving the grating aberrations is similar to those used by Beutler (1945), Namioka (1959), and Welford (1965). Each uses a

different notation and the reader should note these differences when comparing results given by different authors. Our approach parallels that given in Chapter 5 for a general refracting surface, with those results modified to include the grating characteristics.

### 14.1. APPLICATION OF FERMAT'S PRINCIPLE TO GRATING SURFACE

Although a plane reflection grating is the element of choice in most grating spectrometers, we choose to set up a more general case in order to derive the general grating equation. After showing that this equation for a transmission grating is similar to that for a reflection grating, we carry out subsequent derivations of aberrations for the reflection case only. During this discussion it will become evident why plane gratings are preferred over spherical gratings for most applications.

A sketch of a grating surface is shown in Fig. 14.1, with the origin of the coordinate system at the vertex of the surface. The grating grooves are taken parallel to the  $y$ -axis, with the separation between adjacent grooves, measured perpendicular to the  $yz$ -plane, given by  $\sigma$ . The medium in front of the surface has

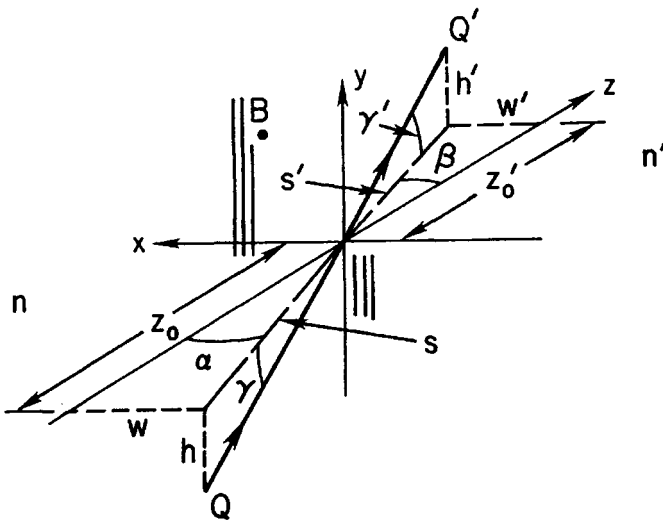


**Fig. 14.1.** Coordinate system for grating with center at origin and rulings parallel to  $y$  axis. The  $Q$  and  $Q'$  are object and image points, respectively; point  $B$  is on the grating surface.

index  $n$ ; the medium on the other side has index  $n'$ . The object and image points are at  $Q$  and  $Q'$ , respectively, and an arbitrary ray from  $Q$  intersects the grating surface at  $B(x, y, z)$ . The equation of the surface is given by Eq. (5.1.1) with  $K$  and  $b$  each set equal to zero. With this simplification we restrict our analysis to plane or spherical grating surfaces.

Unlike the situation in Chapter 5, the grating surface is not rotationally symmetric about the  $z$ -axis. Thus we locate  $Q$ , as shown in Fig. 14.1, distances  $h$  and  $w$  from the  $xz$ - and  $yz$ -planes, respectively. The chief ray from  $Q$  to the origin of the coordinate system makes angle  $\gamma$  with the  $xz$ -plane, and its projection on the  $xz$ -plane makes angle  $\alpha$  with the  $z$ -axis. The image point  $Q'$  and the refracted chief ray are defined in a similar way with primed quantities, except that  $\beta$  is used as the counterpart of  $\alpha$ .

It is important to note here that most spectrometers used on telescopes have  $\gamma = 0$  at the center of the entrance slit. This type of spectrometer is the so-called *in-plane* design in which the incident and diffracted chief ray are in the  $xz$ -plane. For an in-plane spectrometer with a long slit there is a range of  $\gamma$  and, as we show here, the result is spectral line curvature. If  $\gamma$  is not zero at the slit center, then the spectrometer is an *off-plane* design. In this case the spectral lines from a long slit source are both tilted and curved. The origin of these effects is discussed in what follows.

Proceeding now with Fermat's Principle applied to the arbitrary ray shown in Fig. 14.1, we write the optical path length OPL between  $Q$  and  $Q'$  as

$$\text{OPL} = n[QB] + n'[BQ'] \pm (m\lambda/\sigma)x, \quad (14.1.1)$$

where Fermat's Principle is satisfied when  $\delta(\text{OPL}) = 0$  for any change in  $B$  on the surface. The wavelength  $\lambda$  in Eq. (14.1.1) is the vacuum wavelength. To maintain consistency with the sign convention on angles, the plus sign on the right-hand term is applied to transmission gratings, and the minus sign to reflection gratings.

The first two terms in Eq. (14.1.1) are the same as those in Eq. (5.1.2); the additional term is what makes the surface a grating. This is most easily seen by assuming  $x$  changes by  $\sigma$ , a step from one groove to an adjacent one. Because of this change in  $x$  there is an accompanying  $\delta(\text{OPL}) = m\lambda$ , and a corresponding phase difference of  $2\pi m$  between the two points. If  $m$  is an integer, diffracted rays from these points are in phase and the effective change in OPL is zero. Thus these two rays interfere constructively at the image. Note that this conclusion is based on the assumption that the sum of the first two terms is the same for both rays, as required by Fermat's Principle for a nongrating surface.

The procedure from this point on is similar to that carried out in Chapter 5. The line segments in Eq. (14.1.1) are written in terms of the parameters in Fig.

14.1 and each, in turn, is expanded in powers of  $x$  and  $y$ . From the geometry in Fig. 14.1 we find

$$\begin{aligned} [QB] &= [(x-w)^2 + (y-h)^2 + (z_0-z)^2]^{1/2}, \\ [BQ'] &= [(x-w')^2 + (y-h')^2 + (z'_0-z)^2]^{1/2}, \end{aligned} \quad (14.1.2)$$

where

$$\begin{aligned} w &= s \sin \alpha, & h &= s \tan \gamma, & z_0 &= s \cos \alpha, \\ w' &= s' \sin \beta, & h' &= s' \tan \gamma', & z'_0 &= s' \cos \beta. \end{aligned} \quad (14.1.3)$$

The distances  $s$  and  $s'$  in Eqs. (14.1.3) are measured along the projections of  $[QB]$  and  $[BQ']$  on the  $xz$ -plane, respectively. The usual sign conventions apply to all parameters, with all angles in Fig. 14.1 positive,  $s$ ,  $w$ ,  $h$ , and  $z_0$  negative, and the primed distances positive.

#### 14.1.a. GENERAL GRATING EQUATION

To derive the grating equation we need only the linear terms in the expansion of Eq. (14.1.1). Substituting Eqs. (14.1.3) into Eqs. (14.1.2), we find that the OPL can be written as

$$\begin{aligned} \text{OPL} &= n's' - ns + y(n \sin \gamma - n' \sin \gamma') \\ &\quad + x[n \cos \gamma \sin \alpha - n' \cos \gamma' \sin \beta \pm (m\lambda/\sigma)] \\ &\quad + \text{terms in higher powers of } x \text{ and } y. \end{aligned} \quad (14.1.4)$$

Terms in higher power lead to aberrations and their forms are given in a subsequent section.

Taking the partial derivatives of OPL with respect to  $y$  and  $x$  and setting each equal to zero gives

$$n \sin \gamma = n' \sin \gamma', \quad (14.1.5)$$

$$m\lambda = \pm \sigma (n' \cos \gamma' \sin \beta - n \cos \gamma \sin \alpha). \quad (14.1.6)$$

These equations are the grating counterpart of Snell's law for a general surface of revolution. Equation (14.1.5) applies in the  $yz$ -plane and is simply Snell's law, while Eq. (14.1.6) is the grating equation.

For a reflection grating  $n' = -n$ , hence  $\gamma' = -\gamma$  and, choosing the minus sign in Eq. (14.1.6), we get

$$m\lambda = n\sigma \cos \gamma (\sin \beta + \sin \alpha), \quad (14.1.7)$$

where  $n > 0$  for light incident in the  $+z$  direction. Note that  $\beta$  is a function of  $\gamma$  for constant  $\alpha$  and  $\lambda$ , hence the image of a long straight slit parallel to the  $y$ -axis is curved. The details of this curvature are discussed in the next section.

For a transmission grating surface we choose  $\gamma = 0$  and the plus sign in Eq. (14.1.6), and get  $m\lambda = (n' \sin \beta - n \sin \alpha)$ . Applying this relation at the grating surface and Snell's law at the other gives, assuming plane parallel surfaces,

$$m\lambda = n\sigma(\sin \beta - \sin \alpha), \quad (14.1.8)$$

where  $\alpha$  is the angle of incidence at the first surface,  $\beta$  is the angle of diffraction following the second surface, and  $n$  is the index of the medium, usually air, in which the grating is located. The index  $n$  is positive for light directed in the  $+z$  direction. Note that the index of the blank is absent from Eq. (14.1.8). Thus the transmission grating is, in effect, a diffracting element of negligible thickness.

There is also an element called a grism in which a transmission grating is put on one surface of a prism. The relation in Eq. (14.1.8) applies to the grating if the combination is treated as a prism in contact with a grating of negligible thickness.

#### 14.1.1.b. SPECTRUM LINE CURVATURE AND TILT

The curvature of the image of a straight slit is a consequence of the dependence of  $\beta$  on  $\gamma$  noted following Eq. (14.1.7). At constant  $\alpha$  and  $\lambda$  we get

$$\frac{d\beta}{d\gamma} = \frac{\sin \gamma (\sin \alpha + \sin \beta)}{\cos \gamma \cos \beta} = \lambda A \tan \gamma, \quad (14.1.9)$$

where  $A$  is the angular dispersion of the grating for  $\gamma = 0$ . For small  $\gamma$  the total change in  $\beta$  between  $\gamma = 0$  and some largest  $\gamma_0$  is found by integrating Eq. (14.1.9) between these limits. The result, expressed as  $\Delta\beta$ , is

$$\Delta\beta = (\gamma_0^2/2)\lambda A. \quad (14.1.10)$$

Note that  $\Delta\beta > 0$ , hence the change in  $\beta$  is toward longer wavelengths. In the camera focal plane, as shown in Fig. 14.2, the linear displacement from a straight image is  $f_2 \Delta\beta$ , where

$$f_2 \Delta\beta = \frac{\lambda A}{2f_2} (f_2 \gamma_0)^2 = \frac{(f_2 \gamma_0)^2}{2\rho}, \quad (14.1.11)$$

where  $\rho = f_2/\lambda A$  is the radius of curvature of the image.

The slope at a point on the curved image, relative to a straight image, is  $d\beta/d\gamma$  as given in Eq. (14.1.9). Hence a short entrance slit for which  $\gamma$  is not zero at the center is imaged as a tilted, though nearly straight, line. This assumes, of course, that the entrance slit is not tilted out of the  $yz$ -plane. Line tilt of this type is present in all off-plane spectrometer designs.

Note that line curvature and tilt are present even if the grating and spectrometer are otherwise free of aberrations. If the instrument has large astigmatism,

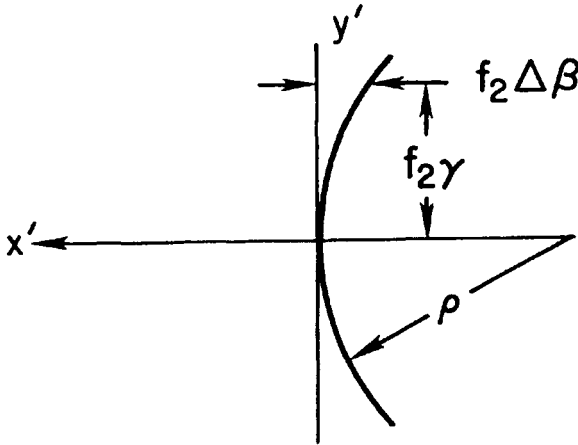


Fig. 14.2. Spectrum line curvature in spectrometer focal plane with radius of curvature  $\rho$ . See Eq. (14.1.10).

this curvature is superposed on any curvature of the astigmatic image. The reader can consult the reference by Welford (1965) for details on this combination.

It is also important to note that curvature and tilt are larger for an echelle than for a typical grating of small blaze angle, in direct proportion to the angular dispersion. This factor is an important one to take into account in the design of any spectrometer, but especially so for an echelle instrument.

## 14.2. GRATING ABERRATIONS

The aberrations of a grating are found from the higher-order terms in Eq. (14.1.4). In the general case, these terms contain factors depending on  $\sin \gamma$  and  $\sin \gamma'$  to various powers. Most spectrometers, however, are of the in-plane design and we choose to set  $\gamma$  and  $\gamma'$  to zero. The factors left out of the aberration coefficients with this choice are of order  $\gamma^2$  and  $\gamma'^2$  smaller than those that remain.

Another simplification results if we consider only the case of a reflection grating. This is sufficient because the aberration coefficients for a plane reflection grating also apply to a transmission grating, given the discussion leading to Eq. (14.1.8).

We also give only the squared and cubed terms in the OPL expansion, thus the only aberration coefficients we derive are those of astigmatism and coma. Spherical aberration, which comes from the fourth-power terms, is negligible in most cases. If it is significant for a specific grating type, its value is given in our discussion for that type.

Following our discussion in Section 5.1, we define  $\Phi$  as the optical path difference between the general and chief rays, and find

$$\begin{aligned} \Phi &= -\frac{nx^2}{2} \left[ \frac{\cos^2 \beta}{s'} + \frac{\cos^2 \alpha}{s} - \frac{\cos \beta + \cos \alpha}{R} \right] \\ &\quad - \frac{ny^2}{2} \left[ \frac{1}{s'} + \frac{1}{s} - \frac{\cos \beta + \cos \alpha}{R} \right] \\ &\quad - \frac{nx^3}{2} \left[ \frac{\sin \beta}{s'} \left( \frac{\cos^2 \beta}{s'} - \frac{\cos \beta}{R} \right) + \frac{\sin \alpha}{s} \left( \frac{\cos^2 \alpha}{s} - \frac{\cos \alpha}{R} \right) \right] \\ &\quad - \frac{nxy^2}{2} \left[ \frac{\sin \beta}{s'} \left( \frac{1}{s'} - \frac{\cos \beta}{R} \right) + \frac{\sin \alpha}{s} \left( \frac{1}{s} - \frac{\cos \alpha}{R} \right) \right] \\ &= A_1 x^2 + A_1' y^2 + A_2 x^3 + A_2' xy^2. \end{aligned} \quad (14.2.1)$$

Note that Eq. (14.2.1) does not contain the linear terms from Eq. (14.1.4); these are zero from the grating equation.

A comparison of terms in Eq. (14.2.1) with corresponding ones in Eq. (5.1.5) shows that they are the same provided  $x$  and  $y$  are interchanged,  $\theta$  and  $\theta'$  are replaced by  $\alpha$  and  $\beta$ , respectively, and  $n'$  is replaced by  $-n$ . Note that the chief ray in Fig. 5.1 is in the  $yz$ -plane while the chief ray in Fig. 14.1 is in the  $xz$ -plane. Because of this correspondence we can use many of the results derived in Chapter 5. One important difference in the results to follow is that the small angle approximation is not applied, except in selected cases.

The locations of the astigmatic images are found by setting either  $A_1$  or  $A_1'$  in Eq. (14.2.1) to zero. Setting  $A_1 = 0$  gives

$$\frac{\cos^2 \beta}{s_t'} + \frac{\cos^2 \alpha}{s} = \frac{\cos \beta + \cos \alpha}{R}, \quad (14.2.2)$$

where  $s_t'$  is the location of the tangential astigmatic image. This is a line image perpendicular to the  $xz$ -plane, hence parallel to the grating grooves, as shown in Fig. 14.3. The detector must be located at this image, if grating astigmatism is not to degrade the spectral resolution. For a plane transmission grating the right side of Eq. (14.2.2) is zero and the plus on the left side is changed to a minus.

Setting  $A_1'$  to zero gives  $s_s'$ , the location of the sagittal astigmatic image. Taking this expression and Eq. (14.2.2) we find that the separation  $\Delta s'$  between the astigmatic images is

$$\begin{aligned} \frac{\Delta s'}{s_s' s_t'} &= \left[ \frac{\sin^2 \beta (\cos \beta + \cos \alpha)}{R \cos^2 \beta} + \frac{\sin^2 \alpha - \sin^2 \beta}{s \cos^2 \beta} \right] \\ &= -\frac{2A_1'}{n} = \frac{2A_1'}{n'}, \end{aligned} \quad (14.2.3)$$

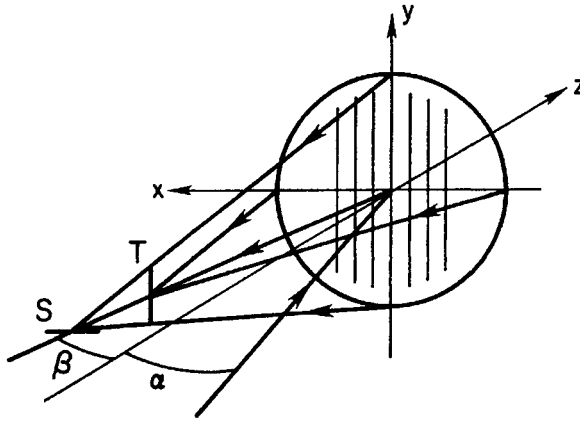


Fig. 14.3. Tangential (T) and sagittal (S) astigmatic images. Maximum spectral resolution is achieved with the detector at the T image.

where the relation between  $\Delta s'$  and  $A'_1$  is the grating counterpart of Eq. (5.2.5) and follows by substituting  $s'_t$  for  $s'$  in  $A'_1$ . The analog to Eq. (5.2.6) for the transverse astigmatism is

$$\text{TAS} = y(\Delta s'/s'_t) = 2A'_1 y s'_t/n', \tag{14.2.4}$$

where the total length of the tangential image is  $2 |\text{TAS}|$ . The length of the line image, in units of the grating groove length, is

$$|\text{TAS}|/y = 2A'_1 s'_t/n'. \tag{14.2.5}$$

We now return to Eq. (14.2.2) and select several combinations of  $s'_t$  and  $s$  that satisfy that equation. Commonly used names are given for each combination, or mounting as it is usually called, with results given in Table 14.1.

Table 14.1  
Grating Mountings

Grating	$s$	$s'_t$	Name
Concave	$R \cos \alpha$	$R \cos \beta$	Rowland
Concave	$\infty$	$\frac{R \cos^2 \beta}{\cos \beta + \cos \alpha}$	Wadsworth
Plane	$\infty$	$\infty$	
Plane	$s$	$\pm s \left( \frac{\cos^2 \beta}{\cos^2 \alpha} \right)$	Monk-Gillieson

The characteristics of each mounting in Table 14.1 are easily described in terms of the object and image locations. For the *Rowland mounting* the entrance slit and image lie on the Rowland circle, a circle of diameter  $R$  tangent to the concave grating at its vertex. The grating in the *Wadsworth mounting* is illuminated with collimated light and the curved focal surface is roughly a distance  $R/2$  from the grating vertex. A convergent or divergent light bundle is incident on the grating in the *Monk-Gillieson mounting*. The object and image lie on opposite sides of a reflection grating, and the minus sign in Table 14.1 applies. For a transmission grating the plus sign in Table 14.1 applies and object and image are on the same side.

We get the transverse astigmatism for each mounting in Table 14.1 by substituting  $R$ ,  $s$ , and  $s'_i$  into Eqs. (14.2.3) and (14.2.4). The results are given in Table 14.2, where TAS is expressed in units of grating groove length. There is no entry for a plane grating in collimated light because its  $A'_1$  is zero.

From the entries in Table 14.2 we see that astigmatism is zero for the Rowland mounting only when  $\alpha = \beta = 0$ , corresponding to the zero order. The Wadsworth mounting has zero astigmatism on the grating normal and small astigmatism over a limited range on either side. For the Monk-Gillieson mounting, the astigmatism is zero when  $\beta = \pm\alpha$ , where the minus sign gives the zero order for a plane reflection grating and the plus sign is the zero order for a transmission grating. For either plane grating in this mounting, therefore, there is a direction in which astigmatism is zero at a diffracted wavelength given by  $m\lambda = 2\sigma \sin \beta$ .

The coefficients  $A_2$  and  $A'_2$  in Eq. (14.2.1), with  $-n'$  substituted for  $n$ , are

$$A_2 = \frac{n'}{2} \left( \frac{\cos^2 \alpha}{s} - \frac{\cos \alpha}{R} \right) \left( \frac{\sin \alpha}{s} - \frac{\sin \beta}{s'} \right), \quad (14.2.6)$$

$$A'_2 = \frac{n'}{2} \left[ \frac{\sin \beta}{s'} \left( \frac{1}{s'} - \frac{\cos \beta}{R} \right) + \frac{\sin \alpha}{s} \left( \frac{1}{s} - \frac{\cos \alpha}{R} \right) \right], \quad (14.2.7)$$

**Table 14.2**

Astigmatism of Grating Mountings

Rowland:	$\frac{\text{TAS}}{y} = \sin^2 \beta + \sin^2 \alpha \left( \frac{\cos \beta}{\cos \alpha} \right)$
Wadsworth:	$\frac{\text{TAS}}{y} = \sin^2 \beta$
Monk-Gillieson:	$\frac{\text{TAS}}{y} = \frac{\sin^2 \beta - \sin^2 \alpha}{\cos^2 \alpha}$
	$A'_1 = \frac{n'}{2s'_i} \frac{\text{TAS}}{y}$

where Eq. (14.2.2) is used to simplify (14.2.6). Relations analogous to Eqs. (5.3.4) and (5.3.5) for these coefficients are

$$TA_x = \frac{s'_t}{n'}(3A_2x^2 + A'_2y^2), \quad TA_y = \frac{s'_t}{n'}2A_2xy,$$

where TA denotes the transverse aberration. The expressions for the transverse tangential and sagittal coma are

$$TTC = 3A_2x^2s'_t/n', \quad TSC = A'_2y^2s'_t/n'. \quad (14.2.8)$$

With reference to Fig. 5.8 with  $x$  and  $y$  interchanged, the relations in Eqs. (14.2.8) give the coma in the direction parallel to the  $x$ -axis. If coma is present, its effect is to degrade the spectral resolution.

We now evaluate Eq. (14.2.6) for each of the grating mountings in Table 14.1. It turns out that  $A'_2$  is comparable in size to  $A_2$  and we give its value only for the one mounting in which  $A_2 = 0$ . The results are shown in Table 14.3.

From the entries in Table 14.3 we see that TTC for the Rowland mounting is zero and TSC is small because  $A'_2$  goes as the cube of factors that are usually small. Coma is zero for the Rowland mounting only in the zero order. The Wadsworth mounting has zero coma on the grating normal and small coma over a limited range on either side. For the Monk-Gillieson mounting the plus and minus signs apply to reflection and transmission gratings, respectively, and coma is zero only in zero order.

Spherical aberration is negligible in all practical configurations of the Rowland and Monk-Gillieson mountings. The spherical aberration coefficient for the Wadsworth mounting on the grating normal is given by

$$A_3 = \frac{n}{8R^3} \cos^2 \alpha (1 + \cos \alpha), \quad (14.2.9)$$

with the transverse spherical aberration given by Eq. (5.4.1). Its size, to a good approximation, is the same as that of a sphere in collimated light.

**Table 14.3**

Coma of Grating Mountings

Rowland:	$A_2 = 0$ $A'_2 = \frac{n'}{2R^2} (\sin \beta \tan^2 \beta + \sin \alpha \tan^2 \alpha)$
Wadsworth:	$A_2 = \frac{n' \sin \beta}{2R^2} \left[ \frac{\cos \alpha (\cos \beta + \cos \alpha)}{\cos^2 \beta} \right]$
Monk-Gillieson:	$A_2 = \pm \frac{n' \cos^2 \alpha}{2s^2} \left[ \sin \alpha \pm \sin \beta \left( \frac{\cos^2 \alpha}{\cos^2 \beta} \right) \right]$

Table 14.4

Tangential Image Surface Curvatures

Rowland:	$\kappa_t = -2/R$
Wadsworth:	$\kappa_t = -(2/R)\left(1 + \frac{3}{2}\cos\alpha\right)$
Monk-Gillieson:	$\kappa_t = \pm(3\cos^2\alpha)/s$

The aberration coefficients for the concave grating mountings are derived assuming the pupil is at the grating. Given the limited sizes of concave gratings, this is the only practical way of using the grating. A plane grating has no preferred axis and the aberration coefficients are independent of the pupil location.

For each of the grating mountings, we now determine the curvature of the image surface on which the tangential astigmatic images are located. This is easily done by applying Eqs. (5.7.1) and (5.7.2) to the relations for  $s'_t$  in Table 14.1. The curvatures obtained are given in Table 14.4, where the plus and minus signs for the Monk-Gillieson mounting apply to the reflection and transmission cases, respectively.

Note that the curvature for the Rowland mounting is exact because the images lie on the Rowland circle. For the other mountings in Table 14.4 the curvatures are only approximations to the exact curvatures, though the relations given are adequate for most configurations of these mountings. The image surface for each mounting is concave as seen from the grating.

All of the aberration relations needed for analysis of the different mountings are now in hand. The plane grating in collimated light has no aberrations, and aberration analysis of spectrometers with this mounting is reduced to considering the collimator and camera optics and any anamorphic magnification of the grating. The rest of this chapter is a discussion of the characteristics of selected concave grating spectrometers. Discussion of the characteristics of plane grating instruments follows in Chapter 15.

### 14.3. CONCAVE GRATING MOUNTINGS

In this section we look further at the characteristics of the two concave grating mountings introduced in the previous section. Although these mountings are little used, if at all, for stellar spectroscopy with ground-based telescopes, they are often used for ultraviolet spectroscopy from space. In this spectral region they are practical alternatives to plane grating spectrometers. For information on other

concave grating mountings, such as the Seya-Namioka monochromator (see Namioka, 1959), the references should be consulted.

#### 14.3.a. ROWLAND MOUNTING

The Rowland mounting was probably the first type of grating spectrometer used for astronomical spectroscopy. A schematic diagram of a Rowland mounting is shown in Fig. 14.4. Although it was adequate for recording solar spectra, it was a failure in stellar spectroscopy, primarily because of its astigmatism. As an example of the size of the astigmatism, we take  $\lambda = 500$  nm for a first-order grating with 600 grooves/mm and a diameter of 100 mm. From the relation in Table 14.2 we get  $TAS/y = 0.090$  for  $\alpha = 0$  and  $TAS/y = 0.045$  for  $\alpha = \beta$ , hence image lengths are 9 and 4.5 mm, respectively, for a point source at the entrance slit.

Note that these lengths depend only on the grating size and are independent of the output beam focal ratio. Given these image lengths, the speed of a Rowland spectrometer is much less than that of a stigmatic spectrometer at the same camera focal ratio because the light is spread over a significantly larger area.

Rowland spectrometers are used in the extreme ultraviolet where reflection efficiencies are low and the number of optical surfaces must be kept to an absolute minimum. In this spectral range both near-normal and grazing incidence mountings are used. Because of the shorter wavelengths, astigmatism is tolerable for near-normal mountings. For the grating example in the foregoing text, the

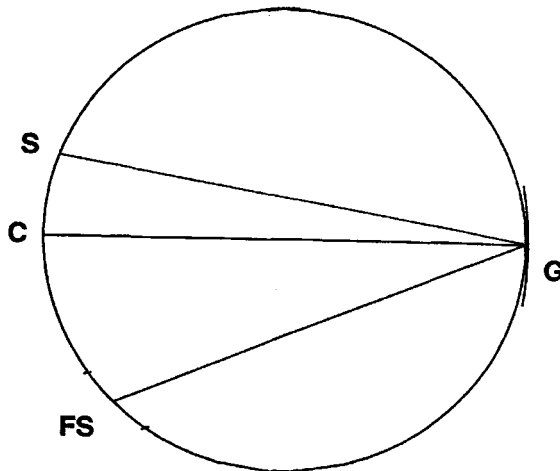


Fig. 14.4. Schematic of Rowland mounting; S, entrance slit; G, concave grating; C, center of curvature of grating; FS, focal surface.

astigmatism is smaller by a factor of 25 at  $\lambda = 100$  nm for the same grating diameter. A comparison of different Rowland mountings suitable as spectrometers in the ultraviolet has been given by Namioka (1961).

Grazing incidence spectrometers based on the Rowland circle are used at still shorter wavelengths, and their large astigmatism is reduced by using ellipsoidal and toroidal concave gratings. For further discussion of grazing incidence instruments, the reader should consult the references at the end of the chapter.

#### 14.3.b. WADSWORTH MOUNTING

The Wadsworth mounting was a successful replacement for the Rowland mounting in the early days of stellar spectroscopy, primarily because it has significantly smaller astigmatism. With the same grating parameters as in the preceding, the Wadsworth can be made stigmatic at  $\lambda = 500$  nm by choosing  $\sin \alpha = 0.3$ . At wavelengths of 400 and 600 nm we find that  $TAS/y$  is 0.0036, and the image length is 0.36 mm for the same grating diameter. This image length increases for wavelengths farther from the stigmatic wavelength, roughly as the square of the wavelength difference.

Comparing the astigmatic image lengths of the Wadsworth and Rowland mountings, it is evident that any decrease in transmittance of the Wadsworth due to additional optical elements is more than compensated by its greater speed. This advantage of the Wadsworth over the Rowland mounting holds at shorter wavelengths, provided high-efficiency reflecting films are available.

With  $\sin \alpha = 0.3$ , it is straightforward to calculate the transverse coma and spherical aberration. Using  $A_2$  from Table 14.3 and Eqs. (14.2.8) we find  $TTC = 0.175(d/F) \sin \beta$ , where  $d$  is the grating diameter and  $F$  is the grating focal ratio. With  $d = 100$  mm, as in the preceding, and  $F = 10$ , we find the magnitude of  $TTC = 0.1$  mm at 400 and 600 nm. Because coma is proportional to  $\sin \beta$ , its size is linearly dependent on the difference between the actual and corrected wavelengths.

Using Eqs. (14.2.9) and (5.4.1) we find that  $TSA = 0.014d/F$ , hence for our chosen  $d$  and  $F$  we get  $TSA = 14$   $\mu$ m. Compared to the size of the coma, it is evident that spherical aberration is negligible over most of the spectral region centered on 500 nm.

Because the grating in the Wadsworth mounting has collimated light incident, a separate collimator is required. A schematic diagram of a Wadsworth spectrometer is shown in Fig. 14.5, with a flat fold mirror in series with an on-axis collimator mirror. In a correctly designed system for a Cassegrain telescope, the fold mirror is entirely inside the shadow of the secondary and does not vignette the collimated beam.

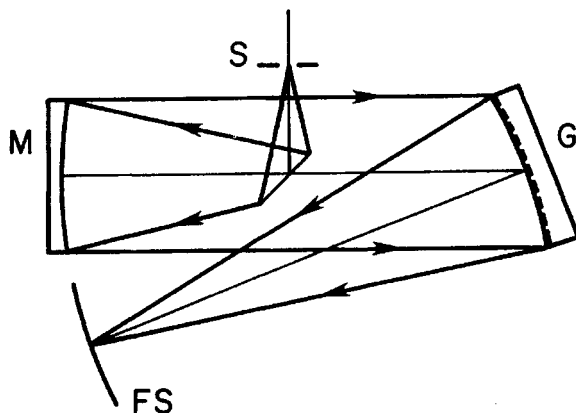


**Fig. 14.5.** Schematic of Wadsworth spectrometer; S, entrance slit; M, collimator; G, concave grating; FS, focal surface.

The collimator has no off-axis aberrations in this arrangement and spherical aberration is also zero if the mirror is a paraboloid. If the mirror is spherical, its spherical aberration adds to that of the grating. Other possible collimators include an off-axis parabolic mirror and a tilted concave mirror. The former is free of aberrations on-axis, while the latter has off-axis aberrations. The optical properties of a tilted spherical collimator and a concave grating have been calculated by Namioka (1959) and Seya and Namioka (1967), and these references can be consulted for details. They consider both collimated and noncollimated light incident on the grating.

#### 14.3.c. INVERSE WADSWORTH MOUNTING

In the standard Wadsworth mounting the grating is both the disperser and camera. In the inverse Wadsworth mounting the slit is at the focus of the grating, which is both the disperser and collimator, and a separate camera is required. The general aberration relations, not given here, are derived using the procedure already provided here. From these relations it turns out that coma and astigmatism are smallest at a given wavelength when  $\alpha$  is zero. This is not surprising from the point of view of Fermat's Principle; compared to the standard Wadsworth, whose aberrations are zero on the grating normal, the light rays are simply reversed in direction.

Assume a camera of focal length  $f$  that is aberration-free, and a concave grating for which the collimator focal ratio is  $F$ . The transverse aberrations of the inverse Wadsworth at  $\alpha = 0$  are given by

$$\begin{aligned} \text{TAS} &= \frac{f}{2F} \left[ \frac{\sin^2 \beta \sin^2(\beta/2)}{\cos^2 \beta} \right], \\ \text{TTC} &= \frac{3f}{16F^2} \left[ \frac{\sin \beta \sin^2(\beta/2)}{\cos^2 \beta} \right], \end{aligned} \quad (14.3.1)$$

where the total length of the tangential astigmatic image is  $2 \text{TAS}$ . Given  $\sin \beta = m\lambda/\sigma$  when  $\alpha = 0$ , we see that coma and astigmatism increase roughly proportional to the cube and fourth power of the wavelength, respectively.

With  $F = 10$ ,  $f = 1000$  mm, and the same 600 groove/mm grating as used previously here, the reader can verify that the image length and TTC are approximately 0.22 mm and 14  $\mu\text{m}$ , respectively, at a wavelength of 500 nm. Compared to a standard Wadsworth of the same focal length, the average coma and astigmatism are significantly less in the visible and ultraviolet spectral regions. The spherical aberration coefficient of the inverse Wadsworth is the same as that of a standard Wadsworth.

From the forementioned aberration relations, we see there is freedom to choose a shorter camera focal length and thereby reduce the transverse aberrations. A Schmidt camera, with its corrector plate close to the grating, is a practical choice for a fast camera in an inverse Wadsworth. Both the incident and diffracted light from the grating pass through the corrector in this arrangement and, with the stop at the grating, the corrector size is essentially the same as that of the grating.

#### 14.3.d. CONCLUDING REMARKS

From our discussion on concave grating mountings, it is evident that there are useful configurations, especially for short wavelengths, in which aberrations are tolerable. None of these mountings, however, has found favor on ground-based telescopes. One reason is that, except for the inverse Wadsworth, there is little freedom in the choice of camera focal ratios and match of projected slit to pixel size.

Another shortcoming of the concave grating is its efficiency relative to that of the plane grating. A concave grating ruled by conventional methods has lower overall efficiency than a plane grating because grooves near one side of the concave grating have a different effective blaze angle than those near the other side. To overcome this defect, at least in part, concave gratings with bipartite and tripartite rulings have been made. For more information about these types of

rulings and concave gratings in general, including holographic concave gratings, the reader should consult the reference by Loewen and Popov (1997).

## REFERENCES

- Beutler, H. (1945). *J. Opt. Soc. Am.*, **35**: 311.  
Loewen, E. and Popov, E. (1997). *Diffraction Gratings and Applications*, New York: Marcel Dekker.  
Namioka, T. (1959). *J. Opt. Soc. Am.*, **49**: 446.  
Welford, W. (1965). *Progress in Optics*, vol. 4, Chap. 6, Amsterdam: North-Holland.

## BIBLIOGRAPHY

### *Seya-Namioka monochromator*

Namioka, T. (1959). *J. Opt. Soc. Am.*, **49**: 951.

### *Concave grating mountings*

James, J. and Sternberg, R. (1969). *The Design of Optical Spectrometers*, London: Chapman & Hall.

Meltzer, R. (1969). *Applied Optics and Optical Engineering*, vol. 5, Chap. 3, New York: Academic Press.

Namioka, T. (1961). *Space Astrophysics*, p. 228. New York: McGraw-Hill.

### *Wadsworth mounting*

Seya, M. and Namioka, T. (1967). *Sci. Light*, **16**: 158.

Plane grating spectrometers have distinct advantages over concave grating instruments and have been the almost universal choice for large telescopes. Spectrometers in which the grating is illuminated by collimated light have only the aberrations of the collimator and camera degrading the spectrum quality. With careful attention to the design of these optical subsystems, aberrations can be reduced to an insignificant level. In addition, the freedom to choose collimator and camera focal ratios independently to get a desirable match between projected slit and pixel size is a significant advantage.

Other important advantages of plane gratings are the wide range of sizes, groove densities, and blaze angles available as standard items. The selection makes it possible to design and build systems, either fiber-fed or with a standard slit, suited to almost any observing program. For high resolution, large echelles are especially suited to configurations in which many orders are arranged to cover a convenient 2D format. For low spectral resolution, transmission gratings and grisms used in a nonobjective mode are well-suited for survey programs.

In this chapter we emphasize the design principles of plane grating spectrometers and cite examples of existing instruments for many of the configurations discussed. For a full range of design possibilities the interested reader should consult any of the conference proceedings cited at the end of the chapter.

## 15.1. ALL-REFLECTING SPECTROMETERS

We first consider plane grating spectrometers with mirror optics to collimate and focus the dispersed light. Instruments of this type, such as the Czerny-Turner and Ebert-Fastie designs, are used in laboratories and have been used as astronomical spectrometers. The major disadvantage of the designs discussed in this section is the lack of freedom to choose the camera focal ratio independently of the collimator focal ratio. In spite of this lack of flexibility, the characteristics of these designs merit some discussion.

## 15.1.a. CZERNY-TURNER MOUNTING

The *Czerny-Turner* design is a widely used laboratory spectrometer suited for either the monochromator or spectrograph mode. This design is also used for astronomical spectrometers, for example, the main spectrograph at the McMath solar telescope at Kitt Peak National Observatory, Arizona is of this type. We discuss the characteristics of both modes of operation, starting with the monochromator mode.

The optical layout for a Czerny-Turner mounting (CZ), is shown in Fig. 15.1. The spherical collimator and camera mirrors are  $M_1$  and  $M_2$ , respectively,  $G$  is the grating, and the entrance and exit slits are at  $Q$  and  $Q'$ , respectively. The axis of each mirror is tilted with respect to its incident chief ray, and thus each has both on- and off-axis aberrations.

To ensure that the tangential fan of rays incident on the grating is strictly collimated, the slit at  $Q$  is at the tangential focus of the collimator. The consequence of this choice is that the distance from the camera vertex to  $Q'$  is

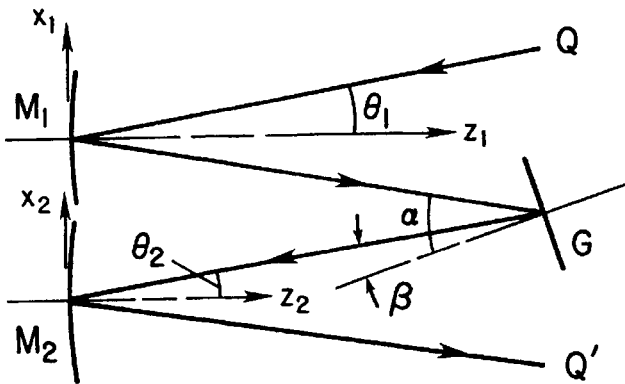


Fig. 15.1. Optical arrangement of Czerny-Turner mounting;  $M_1$ , collimator;  $G$ , grating;  $M_2$ , camera;  $Q(Q')$ , entrance (exit) slit. Dispersion direction is in the plane of diagram.

independent of the grating angles and separation between the grating and each mirror. The spectrum is scanned by rotating the grating about an axis along its central groove.

The aberrations of the CZ mounting are easily found using the results in Chapter 5. In the monochromator mode, the position of the stop is of no consequence because the beam location at the camera is always the same. Thus we can take the coefficients for each mirror from Table 5.2, where the magnification  $m$  is infinite for the collimator and zero for the camera. One change is needed in these coefficients before writing the system coefficients. The coefficient  $A_1$  denotes the astigmatism at the sagittal image, but for a grating instrument we require the astigmatism at the tangential image. Hence we take  $A'_1$  instead of  $A_1$  where, as seen in Eqs. (5.2.3) and (5.2.4), these coefficients have opposite signs. This sign change has no effect on the final relations that give the length of the astigmatic image.

With this change we take the coefficients from Table 5.2 and substitute them into Eq. (5.6.7) to get the system coefficients. The results are

$$A_{1s} = \frac{\theta_1^2}{R_1} + \frac{\theta_2^2}{R_2} \left( \frac{y_2}{y_1} \right)^2, \quad (15.1.1)$$

$$A_{2s} = \frac{\theta_1}{R_1^2} - \frac{\theta_2}{R_2^2} \left( \frac{x_2}{x_1} \right)^3, \quad (15.1.2)$$

where  $y_1 = y_2$ ,  $n_1 = n_2 = -1$  from Fig. 15.1, and subscripts 1 and 2 refer to collimator and camera mirrors, respectively.

Because  $R_1$  and  $R_2$  have the same sign, the astigmatisms of the two mirrors add to give the system astigmatism. A similar result is found for the spherical aberration of the system. With a proper choice of angles, however, the coma coefficient can be made zero.

The relation between  $x_1$  and  $x_2$  is derived from the geometry in Fig. 15.1. If  $x$  is the coordinate of a marginal ray at the grating, then  $x_1 \cos \theta_1 = x \cos \alpha$  and  $x_2 \cos \theta_2 = x \cos \beta$ . Putting these results into Eq. (15.1.2), and setting  $A_{2s} = 0$ , gives

$$\frac{\theta_2}{\theta_1} = \left( \frac{R_2}{R_1} \right)^2 \left( \frac{\cos \alpha_0}{\cos \beta_0} \right)^3 \left( \frac{\cos \theta_2}{\cos \theta_1} \right)^3. \quad (15.1.3)$$

The relation in Eq. (15.1.3) is an approximation to the exact third-order equation in which the left side is the ratio of the sines of the angles. As we will show, it is necessary to have  $\theta_1$  and  $\theta_2$  small in order to keep the astigmatism small. For most purposes, therefore, the paraxial approximation is adequate and  $\cos \theta$  factors can be replaced by one.

Note that a choice of  $\theta_1$  and  $\theta_2$  to satisfy Eq. (15.1.3) is possible for any set of grating angles, but once chosen there is a small residual coma at other

wavelengths. This residual, a result of wavelength-dependent anamorphic magnification, has been called subsidiary coma by Welford (1965). The size of the subsidiary coma is given in an example to follow.

Putting Eq. (15.1.3) into Eq. (15.1.1), with factors in  $\cos \alpha_0$  and  $\cos \beta_0$  retained, we find

$$A_{1s} = \frac{\theta_1^2}{R_1} \left[ 1 + \left( \frac{R_2}{R_1} \right)^3 \left( \frac{\cos \alpha_0}{\cos \beta_0} \right)^6 \right]. \quad (15.1.4)$$

The transverse aberrations are found by substituting the system coefficients into Eq. (5.5.9). The results are given in Table 15.1, with  $d_1$  and  $F_1$  denoting the collimator diameter and focal ratio, respectively.

The relations in Table 15.1 describe a spectrometer in which the coma is zero at one wavelength and negligible over an extended range of wavelengths. It is useful at this point to give the characteristics of a representative example, that of an  $f/10$  spectrometer with  $f_1 = 1$  m and  $R_1 = R_2 = 2$  m. We choose  $\alpha - \beta = 8^\circ$  and  $\theta_1 = 3^\circ$  to provide clearance between the optical elements and beams. With a 600 groove/mm grating used in first order, and choosing zero coma at  $\lambda_0 = 500$  nm, we find  $\theta_2 = 2.814^\circ$ .

With these parameters we find that the image length is 0.52 mm at the zero-coma wavelength and  $TSA = 31 \mu\text{m}$ . At  $\pm 200$  nm from the corrected wavelength, the transverse coma is  $2.6 \mu\text{m}$  and the length of the astigmatic image is unchanged. For all practical purposes over this range, coma is negligible, astigmatism is constant, and spherical aberration determines the spectral resolution. With a plate factor of 1.67 nm/mm, the resolution at the minimum width of the spherical aberration blur is 0.026 nm.

Table 15.1

Transverse Aberrations of Czerny-Turner  
Monochromator<sup>a</sup>

$$\begin{aligned} \text{TAS} &= \frac{\theta_1^2 d_1}{2} \left( \frac{R_2}{R_1} \right) \left[ 1 + \left( \frac{R_2}{R_1} \right)^3 \left( \frac{\cos \alpha_0}{\cos \beta_0} \right)^6 \right] \\ \text{TTC} &= \frac{3\theta_1 d_1}{16F_1} \left( \frac{R_2}{R_1} \right) \left[ 1 - \left( \frac{\cos \alpha_0}{\cos \beta_0} \frac{\cos \beta}{\cos \alpha} \right)^3 \right] \\ \text{TSA} &= \frac{d_1}{64F_1^2} \left( \frac{R_2}{R_1} \right) \left[ 1 + \left( \frac{R_1}{R_2} \right)^3 \right] \end{aligned}$$

<sup>a</sup> Angle  $\theta_2$  is chosen to give zero coma at  $\lambda = \lambda_0$ . All  $\cos \theta_1$  and  $\cos \theta_2$  factors are omitted. Length of astigmatic image is  $2 \cdot \text{TAS}$ .

From this example it is evident that a CZ monochromator gives good spectral resolution, provided the focal ratios of the camera and collimator are sufficiently large. An instrument of this type is suitable for stellar sources, but its astigmatism limits its usefulness for extended sources if spatial resolution along the slit is required. The angle corresponding to the image length projected on the sky can be calculated using Eq. (12.2.1b).

We now consider the CZ in the spectrograph mode, with the grating and camera mirror shown schematically in Fig. 15.2. The  $z$ -axis of the mirror is the normal to the mirror at its center, with the angle of the chief diffracted ray measured with respect to this axis. An arbitrary chief ray makes angle  $\theta_2$  with the axis, with  $\theta_{20}$  used for the chief ray at the mirror center.

The effective position of a pupil centered on the  $z$ -axis is shown in Fig. 15.2 as a distance  $W'$  from the mirror vertex. Denoting the grating-mirror separation measured parallel to the  $z$ -axis by  $W$  we find, in the paraxial approximation,  $W'\theta_2 = W(\theta_2 - \theta_{20})$ .

The aberration coefficients for the camera mirror are now found by substitution of  $W'$  for  $W$  and  $\theta_2$  for  $\psi$  in the relations in Table 5.6. Combining these with the coefficients of the collimator gives

$$B_{1s} = \frac{\theta_1^2}{R_1} + \frac{1}{R_2} \left[ \theta_2 - \frac{W}{R_2} (\theta_2 - \theta_{20}) \right]^2, \tag{15.1.5}$$

$$B_{2s} = \frac{\theta_1}{R_1^2} - \frac{1}{R_2^2} \left[ \theta_2 - \frac{W}{R_2} (\theta_2 - \theta_{20}) \right], \tag{15.1.6}$$

where the paraxial approximation is used for all angles. This approximation is quite adequate for calculating the image aberrations in the spectrograph mode, and is used in the discussion and example that follow.

Examination of Eqs. (15.1.5) and (15.1.6) shows that the coefficients are independent of  $\theta_2$  when  $W = R_2$ . The transverse aberrations of the spectrograph are then given by the relations in Table 15.1. An instrument with this choice of  $W$

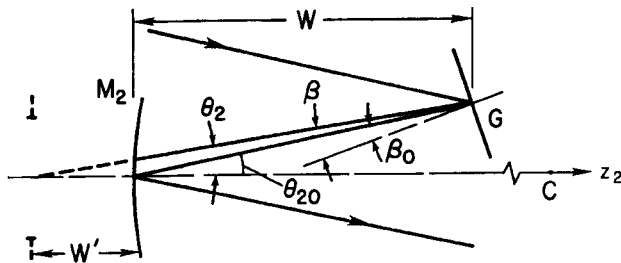


Fig. 15.2. Diffraction and camera angles for Czerny-Turner spectrograph. C, center of curvature of mirror  $M_2$ ;  $W'$ , distance of apparent stop from  $M_2$  with grating as stop.

has been described by Willstrop (1965). The principal disadvantages of a spectrograph with this  $W$  are its longer length and curved focal surface.

Returning to the geometry of the chief rays in Fig. 15.2, we see that  $\beta - \beta_0 = -(\theta_2 - \theta_{20})$ . In the paraxial approximation to the grating equation we find  $\beta - \beta_0 = m(\lambda - \lambda_0)/\sigma$ . With this substitution in Eqs. (15.1.5) and (15.1.6), the system coefficients are expressed in terms of the wavelength difference with respect to the wavelength at the center. The transverse aberrations, given in this form, are shown in Table 15.2, where  $\theta_{20}$  is chosen to give zero coma.

The relations in Table 15.2 show that the coma is linearly proportional to the wavelength difference, while the astigmatism depends on this difference in a more complicated way. As an example, we take the same grating and mirror parameters used for the monochromator, with  $\lambda_0 = 500$  nm and  $W/R_2 = 0.5$ . The coma for  $\Delta\lambda = \pm 50$  nm is 28  $\mu\text{m}$ , and the image lengths are 0.41, 0.53, and 0.73 mm at  $\lambda = 550, 500,$  and 450 nm, respectively. The results obtained from ray traces are within a few percent of these values and justify the approximations used.

Unlike the monochromator mode, neither the coma nor astigmatism are constant, and both the coma and spherical aberration determine the spectral resolution. Nevertheless, the CZ mounting is practical in the spectrograph mode, provided a modest spectral range is covered.

The final item of interest for the spectrograph mode is the curvature of the tangential focal surface, found using the geometry in Fig. 15.3. The line  $O'C$  passes through the center of the grating, which is the stop, and the center of curvature  $C$  of the mirror. A chief ray that makes angle  $\theta_2$  with the line  $OC$  makes angle  $\psi$  with the line  $O'C$ . Because all rays from the grating are parallel, an imaginary ray reflected at  $O'$  from an extension of the mirror makes angle  $\theta' = -\psi$  with the line  $O'C$ .

Relative to the line  $O'C$ , which is effectively a  $z$ -axis of the mirror, the astigmatism coefficient is  $B_1$  in Table 5.6. This coefficient cannot be used to find the transverse astigmatism because the actual mirror is not centered at  $O'$ , but it

**Table 15.2**

Transverse Aberrations of Czerny-Turner Spectrograph<sup>a</sup>

$$\begin{aligned} \text{TAS} &= \frac{d_1}{2} \left( \frac{R_2}{R_1} \right) \left\{ \theta_1^2 + \left( \frac{R_1}{R_2} \right) \left[ \theta_{20} + \left( 1 - \frac{W}{R_2} \right) \frac{m}{\sigma} (\lambda - \lambda_0) \right]^2 \right\} \\ \text{TTC} &= \frac{3d_1}{16F_1} \left( \frac{R_1}{R_2} \right) \left( 1 - \frac{W}{R_2} \right) \frac{m}{\sigma} (\lambda - \lambda_0) \end{aligned}$$

<sup>a</sup> Angle  $\theta_{20}$  is chosen to give zero coma at  $\lambda = \lambda_0$ .

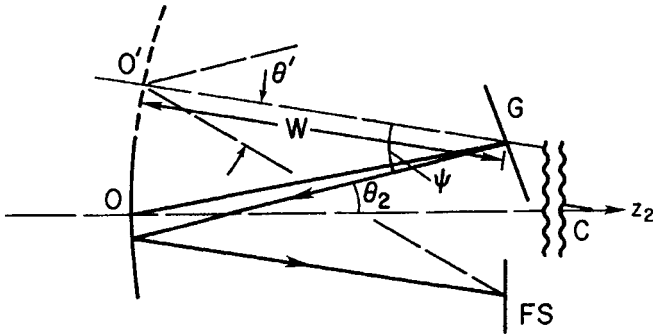


Fig. 15.3. Geometry for finding orientation and curvature of focal surface for Czerny-Turner spectrograph.

can be used to find the image surface curvature. Substituting  $B_1$  in  $\kappa_t$  in Table 5.7, and noting that  $\theta' = \psi$ , we find

$$\kappa_t = \frac{2}{R_2} - \frac{6}{R_2} \left(1 - \frac{W}{R_2}\right)^2, \quad (15.1.7)$$

where  $W$  is the distance  $OG$  in Fig. 15.3. The center of curvature of the image surface is on the line  $OC$ , and a flat image surface is perpendicular to this line.

Setting  $\kappa_t = 0$  gives the condition for a flat image surface as  $W/R_2 = 1 \pm 1/\sqrt{3}$ , with the minus sign a more convenient choice. With this value for  $W/R_2$ , the coma measures for the preceding example are increased by about 15%, but this is a small price to pay for the convenience of a flat field.

The monochromator and spectrograph modes of the Czerny-Turner design have been thoroughly analyzed in far more detail than given here. Higher-order aberrations and detailed ray trace analyses lead to refinements of the relations given here, and the interested reader should consult the references at the end of the chapter for more information. Included in these references are treatments of off-plane designs and instruments with curved slits for achieving the highest possible spectral resolution of broad sources. These treatments are not included here because for astronomical applications the in-plane design with a short slit is best suited to observations of point sources.

#### 15.1.b. EBERT-FASTIE MOUNTING

The Czerny-Turner design can be considered a generalized version of the *Ebert-Fastie* design. In the Ebert-Fastie mounting, hereafter denoted EF, a single spherical mirror serves as both collimator and camera, thus eliminating the need for alignment of separate mirrors. This mounting is almost always used in the

monochromator mode with the grating generally located at the paraxial focal point of the spherical mirror. Figure 15.1 applies to the EF mounting if the  $z$ -axes are redrawn to intersect at the common center of curvature for mirrors  $M_1$  and  $M_2$ . If the incident and emergent chief rays to and from the mirror are parallel in this redrawn diagram, the angle  $\alpha - \beta$  is nearly equal to  $2(\theta_1 + \theta_2)$ .

An analysis of the aberrations of an EF mirror with an intermediate plane mirror is given in Section 5.8, where we show that this configuration is an anastigmat if the mirror is a paraboloid. For a spherical mirror both spherical and astigmatism are present, though these do not seriously degrade the spectral resolution if the beam focal ratio is in the range  $f/10$  or slower. Coma is zero for the all-mirror system in Section 5.8, but the replacement of the plane mirror with a grating introduces subsidiary coma as noted following Eq. (15.1.3).

The aberrations of the Ebert-Fastie monochromator are given in Table 15.1 with  $R_1 = R_2$ . References on this mounting are listed at the end of the chapter.

### 15.1.c. MONK-GILLIESON MOUNTING

We now consider briefly the *Monk-Gillieson* mounting in which a plane grating is illuminated with a convergent light bundle. In this mounting the grating contributes to the system aberrations, but with proper arrangement of the optical elements these aberrations can be made zero at one wavelength. At other wavelengths, coma and astigmatism are present in amounts directly proportional to the wavelength difference with the corrected wavelength. Because of these wavelength-dependent aberrations, this mounting is best suited to the monochromator mode.

A schematic layout of a Monk-Gillieson monochromator, hereafter called MG, is shown in Fig. 15.4. The entrance and exit slits are at  $Q$  and  $Q'$ , respectively,

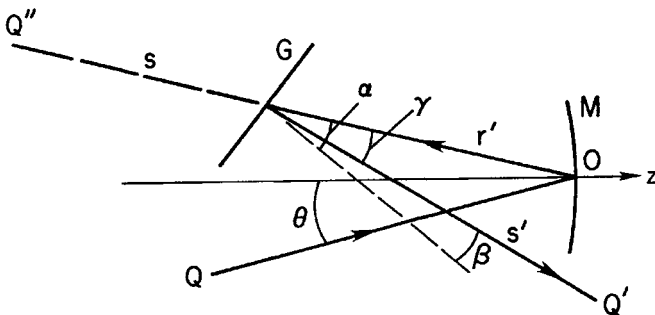


Fig. 15.4. Optical arrangement of Monk-Gillieson mounting.  $Q(Q')$ , entrance (exit) slit;  $M$ , spherical mirror;  $G$ , plane grating.

and  $M$  is a spherical mirror. If the grating  $G$  were absent, point  $Q$  would be imaged at  $Q''$ . The distances from the grating vertex to  $Q'$  and  $Q''$ , respectively, are  $s'$  and  $s$ , where  $s'$  refers to the tangential astigmatic image. The distance from the mirror vertex  $O$  to  $Q''$  is  $r = s + r'$ .

In the discussion that follows, all angles are assumed small enough so the paraxial approximation applies, hence the grating equation is  $m\lambda = n\sigma(\beta + \alpha)$ , where  $n = -1$  for the layout in Fig. 15.4. We also define  $\gamma = \alpha - \beta$ , and note that  $s' = -s$  in this approximation. In terms of these parameters, we find the system aberration coefficients by the usual method, and use Eqs. (5.4.1) to find the transverse coma and astigmatism. Omitting the details here, we find

$$\text{TTC} = \frac{3s'}{8F_2^2} \frac{m}{\sigma} |\lambda - \lambda_0|, \quad (15.1.8)$$

$$\text{TAS} = \frac{\theta_0 d}{|M + 1|} \frac{m}{\sigma} |\lambda - \lambda_0|, \quad (15.1.9)$$

where  $d$  is the beam diameter at the grating,  $F_2$  is the grating beam focal ratio, and  $\lambda_0$  is the wavelength at which both coma and astigmatism are zero. Here  $M$  is used for the magnification of the mirror to avoid confusion with the order number  $m$ .

The aberration coefficients used to construct Eqs. (15.1.8) and (15.1.9) contain the angles  $\theta$  and  $\gamma$ . Setting these coefficients to zero at the same wavelength  $\lambda_0$  gives

$$\theta_0 = -\frac{m\lambda_0}{\sigma} \frac{sR}{r^2(M + 1)}, \quad \gamma_0 = -\frac{2\theta_0}{M + 1}. \quad (15.1.10)$$

For the layout shown in Fig. 15.4,  $s$  and  $R < 0$ , and  $M < -1$ ; therefore  $\gamma_0$  and  $\theta_0$  have the same sign and are positive when  $m > 0$ . Given that the aberrations in Eqs. (15.1.8) and (15.1.9) are proportional to  $m$ , the only practical choice is  $m = 1$ .

Both aberrations increase linearly with the wavelength difference. Because astigmatism depends on  $\theta_0$ , its value is also proportional to  $\lambda_0$ . The spectral resolution is set by the size of TTC at any wavelength. It is convenient to define the *spectral coma*  $\delta\lambda_c$  as the spectral width of an image, where

$$\delta\lambda_c = \text{TTC} \cdot P, \quad (15.1.11)$$

and the plate factor  $P = \sigma/ms'$  for small  $\beta$ . Multiplying Eq. (15.1.8) by  $P$ , we see that the spectral coma depends only on the focal ratio of the beam at the grating for a given wavelength difference.

As an example we take a 600 groove/mm grating in first order, with  $QO = 500$  mm and  $M = -2$  for the mirror. We assume a beam diameter of

50 mm at the mirror, hence  $F_2 = 20$ , and place the grating to give  $s' = 545$  mm. Choosing  $\lambda_0 = 320$  nm gives angles  $\theta_0 = 3.6^\circ$  and  $\gamma_0 = 7.2^\circ$ , and at  $\pm 100$  nm from the corrected wavelength we find  $TTC = 31 \mu\text{m}$ ,  $\delta\lambda_c = 0.095$  nm and an image length of 0.2 mm. Ray traces of this system show that the actual  $\lambda_0$  is about 10% smaller and, with this correction, the spectral coma and astigmatism from the ray traces agree with the calculated values. The difference in  $\lambda_0$  is a consequence of the paraxial approximation.

Unlike the Czerny-Turner monochromator, the grating in the Monk-Gillieson cannot be rotated about an axis on its face and maintain focus at a fixed exit slit. From Table 14.1 we see that  $s'_t$  is a function of  $\alpha$  and  $\beta$  for a given  $s$ . Noting that both  $\alpha$  and  $\beta$  are variables in the scanning mode, with  $d\alpha = d\beta$ , we find in the paraxial approximation

$$ds'_t = -2s\gamma_0 d\alpha = -s\gamma_0(m d\lambda/\sigma), \quad (15.1.12)$$

where  $d\lambda$  is the wavelength interval scanned. For the example above,  $ds'_t = -2.05$  mm for  $d\lambda = 50$  nm. To keep the spectrum in focus on a fixed exit slit, it is necessary to simultaneously translate and rotate the grating. It is not difficult to show that a rotation about an appropriate axis displaced from the grating face gives the required motion. Details on location of this axis are given in the reference by Schroeder (1966).

It is evident from Eq. (15.1.8) that the Monk-Gillieson scanner is limited to relatively slow beams to keep the coma small, particularly if a large spectral range about the zero-coma wavelength is scanned. A scanning Czerny-Turner or Ebert-Fastie is clearly superior in this regard. One attractive feature of the Monk-Gillieson is its two reflections, hence the entrance and exit slits are on opposite ends of the instrument.

## 15.2. PIXEL MATCHING

Efficient use of any grating spectrometer requires matching the projected slit width to the pixel size. According to the Nyquist criterion the optimum match is two pixels per projected slit width. If the projected slit is undersampled with less than two pixels there is a loss in resolution, while if the slit width is oversampled the per pixel signal is less for a given exposure time and readout noise is more significant. We now determine the relation between spectral resolving power and pixel size for an optimum match.

The relevant relations for slit- and seeing-limited cases are Eqs. (13.4.12) and (12.2.1a), repeated here for convenience,

$$\mathcal{R}\phi = \frac{2d_1}{D} \frac{\sin \delta \cos \theta}{\cos \alpha}, \quad (\text{in general}) \quad (15.2.1)$$

$$= \frac{2d_1}{D} \tan \delta, \quad (\text{Littrow}) \quad (15.2.2)$$

$$w' = rw(f_2/f_1) = r\phi DF_2, \quad (15.2.3)$$

$$= 2\Delta \quad (\text{optimum match})$$

$$\phi F_2 = 2\Delta/D \quad (\text{optimum match}) \quad (15.2.4)$$

where  $F_2 = f_2/d_1$  and  $\Delta$  is the pixel width.

To illustrate the utility of these relations, we apply Eqs. (15.2.2) and (15.2.4) to an echelle spectrometer in Littrow mode on a 4-m telescope with  $\tan \delta = 2$ ,  $d_1 = 200$  mm, and  $\Delta = 20$   $\mu$ m. The results are  $\mathcal{R}\phi = 0.2 \cong 40,000$  arc-sec,  $\phi F_2 = 2$  arc-sec. Note that a change to an 8-m telescope, with unchanged spectrometer parameters, gives  $\mathcal{R}\phi = 0.1 \cong 20,000$  arc-sec,  $\phi F_2 = 1$  arc-sec. The need for larger gratings with larger telescopes to maintain resolving power is evident from a comparison of these numbers.

A study of these relations, along with the flux-resolution product  $\mathcal{F}\mathcal{R}$  in Eq. (12.2.13), also shows the importance of better seeing for stellar spectroscopy. The product  $\mathcal{F}\mathcal{R}$  is larger for smaller  $\phi'$  (better seeing), hence for a given slit width  $\phi$  the fraction of the light passed by the slit is larger. Alternatively, the slit width  $\phi$  can be reduced and larger resolving power achieved. For a smaller  $\phi$  note also that  $F_2$  is larger for the optimum match. This can be used to advantage in the design of a new spectrometer if better average seeing can be ensured.

As a final item we note that the product  $\phi D$  in Eqs. (15.2.1)–(15.2.4) is replaced by  $\lambda$  for the diffraction-limited case.

### 15.3. FAST SPECTROMETERS

In this section we consider various types of plane grating mountings with different collimator and camera configurations. Among the choices for a collimator are an off-axis paraboloid, on-axis paraboloid with fold mirror, and a well-corrected lens. The choices for a camera include a standard or folded Schmidt, a Schmidt-Cassegrain, or a well-corrected lens. Because the focal ratio of the camera is typically several times smaller than that of the collimator, we choose to call spectrometers of this type fast.

The discussion in this section is not directed toward the dispersing elements between the collimator and camera. Such an element could be a low-order

grating, grism, or echelle with prism or grating cross-disperser. The various options for a cross-dispersed echelle are discussed in Section 15.5.

We also note that a field lens near the telescope focal surface may be part of any of the collimator-camera options discussed here. A field lens reimages the telescope exit pupil onto the dispersing element and may be required if the spectrometer is intended for long-slit or multiple-object spectroscopy.

### 15.3.a. COLLIMATOR OPTIONS

The choice of collimator is influenced in part by the focal ratio of the beam from the telescope. For slow beams, say  $f/15$  at a Nasmyth focus, a mirror is often chosen as the collimator. Aberrations of such a mirror are generally negligible and the beam folding may help reduce the overall length of the spectrometer. For faster beams, say  $f/5 - f/7$  at a Cassegrain focus, and fiber-fed spectrometers, the trend is toward lens collimators. One exception to this is the spherical collimator for Hectochelle, a multiobject echelle spectrometer for the  $f/5$  Cassegrain focus of the converted Multiple Mirror Telescope. Details on lens collimators are found in the conference proceedings cited at the end of this chapter; we consider only mirror collimators in our discussion.

The choice of a reflecting collimator for a fast spectrometer is generally a folded on-axis paraboloid or an off-axis paraboloid. The former is shown schematically in Fig. 14.5, the latter in Fig. 15.5. Either type has zero spherical aberration, but both have coma and astigmatism at off-axis points on a long slit. The off-axis aberrations are of no consequence for a stellar source, but do set a limit when extended sources are observed. In this latter case it is important to know the size of these aberrations as a function of position on the slit.

Consider first an on-axis paraboloid without the fold mirror, as shown in Fig. 15.6. The chief ray at height  $y$  on the entrance slit comes from the center of the

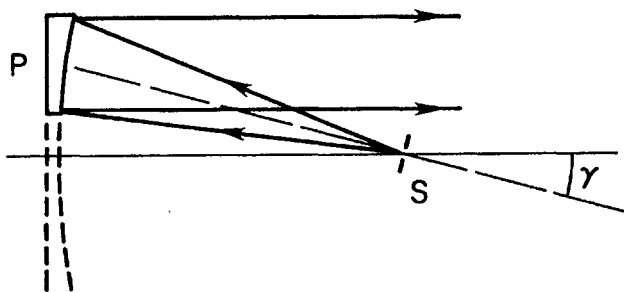


**Fig. 15.5.** Off-axis paraboloidal collimator P with angle  $\gamma$  between axes of telescope and mirror. S, entrance slit of spectrometer at telescope focus.

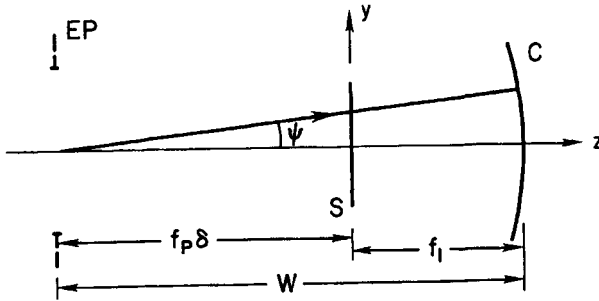


Fig. 15.6. Chief ray from center of telescope exit pupil at angle  $\psi$  with telescope axis. S, spectrometer entrance slit; C, on-axis collimator mirror.

telescope exit pupil at angle  $\psi$  with the  $z$  axis. The exit pupil is a distance  $f_p \delta$  from the slit, where  $f_p$  is the telescope primary focal length and  $\delta$  is given in Eq. (2.6.1). The pupil is distance  $W = -(f_p \delta + f_1)$  from the collimator, where  $W < 0$  by the sign convention and  $f_1$  is the collimator focal length. From Eq. (2.6.4) we get  $\psi = \theta(m/\delta)$ , where  $\theta$  is the angle on the sky.

Substituting these results in the coefficients in Table 5.6, with  $K = -1$  and  $n = 1$ , we find

$$B_1 = -\frac{\theta^2}{R} \frac{mD}{\delta d_1}, \quad B_2 = \frac{\theta}{R^2} \frac{D}{d_1}, \quad (15.3.1)$$

where  $R$  is the collimator radius of curvature, and  $d_1$  and  $D$  are the diameters of the collimator and telescope, respectively. In arriving at Eq. (15.3.1) we used the fact that  $f_p \delta / f_1$  is the ratio of the exit pupil diameter to the collimator diameter. As expected, given our discussion in Section 5.5, the coma coefficient does not depend on the pupil position.

The transverse aberrations are found by substituting Eqs. (15.3.1) into Eqs. (5.5.9), with  $s'$  replaced by the camera focal length  $f_2$ . The angular aberrations, projected on the sky, are found by dividing each transverse aberration by the system focal length  $f_s$ , where  $f_s = f(f_2/f_1) = F_2 D$ . With these substitutions we get

$$\text{AAS} = \frac{\theta^2}{2F} \frac{m}{\delta}, \quad \text{ATC} = \frac{3\theta}{16F^2}, \quad (15.3.2)$$

where  $F$  is the focal ratio of the collimator or telescope.

As an example, we take parameters for a Cassegrain telescope in Table 6.10 and evaluate Eqs. (15.3.2) at a field angle of 10 arc-min. The results are 0.28 and 1.13 arc-sec for the collimator astigmatism and coma, respectively. From these

results we see that coma sets the limit on allowable slit length; for typical seeing a slit 20 arc-min long gives negligible loss in spatial resolution along the slit.

Analysis including the telescope aberrations shows that the astigmatism of a Ritchey-Chretien is opposite that of the collimator, and the net astigmatism is smaller than that from Eq. (15.3.2) by nearly a factor of ten. With a classical Cassegrain, collimator and telescope aberrations cancel one another and spatial resolution along the slit is determined entirely by seeing.

An example of a collimator optically similar to that shown in Fig. 15.6 is the choice for the low resolution imaging spectrometer (LRIS) of the Keck telescope. In this case, however, only an off-axis portion of the full collimator shown in Fig. 15.6 is used. In effect, the LRIS collimator is an off-axis paraboloid that reimages an off-axis portion of the telescope focal surface and whose axis coincides with that of the telescope.

For the off-axis paraboloid shown in Fig. 15.5,  $\gamma$  is the angle between the axes of the telescope and paraboloid. The usual arrangement has the slit length perpendicular to the plane defined by the telescope and paraboloid axes. For this collimator we give results derived from ray traces. With  $\gamma = 10^\circ$  we find blur diameters of approximately 0.5 and 1.5 arc-sec at  $\theta = 1$  and 3 arc-min, respectively. For this example the total slit length is limited to about 4 arc-min.

Ray trace results for an off-axis paraboloid show that the blur diameter for different  $\gamma$  and  $\theta$  is approximately proportional to the product of the angles. An empirical relation for blur diameter is  $\text{blur (arc-sec)} = 0.05\gamma(\text{deg}) \cdot \theta(\text{arc-min})$ . This relation is an approximate one, and ray trace results are required for more exact measures of blur. The results given here also hold for a slit in the plane defined by the axes of the telescope and paraboloid.

In summary, for slit spectroscopy of extended objects, the on-axis paraboloid is the better choice for the collimator, if a slit more than a few arc-min in length or a fiber-sampled field more than a few arc-min on a side is required. This is achieved at the expense of an additional optical element, the folding flat. The echelle spectrograph on the 4-m Mayall telescope at Kitt Peak has an on-axis paraboloid collimator; the RC spectrograph on the same telescope has an off-axis paraboloid.

### 15.3.b. CAMERA OPTIONS

As pointed out numerous times, spectrometer cameras almost always are fast with monochromator focal ratios of two or even less. Capturing all of the dispersed light often requires a camera whose clear aperture/focal length ratio is one or less. The options for such fast systems include Schmidt and catadioptric cameras, as discussed in Chapters 7 and 8, and all-refractive lens systems. For spectrometers on telescopes in the 8-m class, the trend is toward lens systems. We

do not attempt to discuss the myriad lens systems that have been built, but suggest the reader consult the conference proceedings at the end of the chapter.

Design considerations for a Schmidt-type camera are covered in Chapter 7. As noted there, requirements on cameras for direct imaging are different in some respects from those for spectrometer cameras. For example, chromatic focal shifts in solid and semisolid cameras, intolerable in direct imaging, are accommodated in spectrometer cameras by tilting the detector to match the focal surface.

Spectrometers also require a wider camera in the direction of primary dispersion to accommodate beam expansion due to anamorphic magnification and to avoid vignetting of the dispersed beams. This is true for both gratings used in a single order and cross-dispersed echelles. Unlike the case of a direct camera, the pupil in a spectrometer is usually displaced from the corrector, and this means a somewhat larger corrector and camera mirror to cover the same field. A way to reduce the size of the camera optics in a cross-dispersed echelle is to reimagine the dispersed light from the echelle onto the cross-dispersing element. This so-called *white pupil* design is discussed in Section 15.5.

A final significant difference between the modes of operation is the location of the focal surface. It is usually internal in a large Schmidt telescope, but almost always external in a spectrometer camera. A schematic of a folded Schmidt camera is shown in Fig. 15.7, with the fold mirror roughly midway between the corrector and spherical mirror.

A study of the layout in Fig. 15.7 shows that careful placement of the fold mirror is required to ensure an efficient camera. It is essential that the detector not see collimated light, and this requires that the detector be in the shadow of the

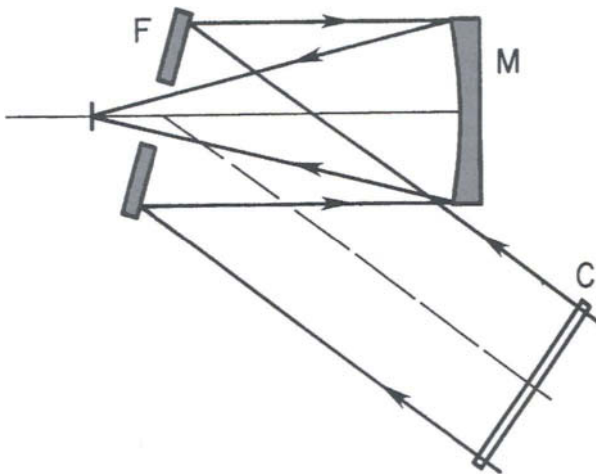


Fig. 15.7. Folded Schmidt camera. C, corrector plate; F, folding flat; M, spherical mirror.

fold mirror, as seen from the corrector. If the distance from the fold mirror vertex to detector is large, the size of the hole in the fold mirror must also be large to avoid vignetting the beam from the spherical mirror. But the hole in the fold mirror should be as small as possible to minimize vignetting of the beam from the corrector. The tradeoff between these competing requirements sets the design of a folded Schmidt.

For catadioptric systems of the type discussed in Chapter 8, the size of the central obscuration is often a serious problem. For these systems the advantage of an external focus must be weighed against the disadvantage of vignetting of the central obscuration.

Lens systems have the advantages of both an external focus and no central obscuration, and have become the choice for most large spectrometers. Although many of these systems have many separate lens elements to achieve the necessary image quality over a wide spectral range, high-efficiency antireflection coatings make them nearly as efficient as simpler reflecting cameras.

## 15.4. FIBER-FED SPECTROMETERS

Plane grating instruments have traditionally been used to observe stellar or near-stellar sources one at a time with the object centered on the entrance slit. For an observing program requiring spectra of many objects of comparable brightness in close proximity on the sky, the observing time can be reduced significantly by recording the spectra of many sources in the same exposure. As pointed out in Section 12.3, this is accomplished by using flexible glass fibers to transfer the light from separate sources in the telescope focal plane to the spectrometer slit. Each fiber is positioned at a source on one end and aligned along the slit at the other end. This technique of *multiobject spectroscopy* is applicable to objects within a cluster of stars or galaxies, as demonstrated by a number of observers.

As an illustration of the thinking that goes into designing a fiber-fed instrument, we take a telescope designed expressly for multiobject spectroscopy and show the parameters coming out of a design study.

### 15.4.a. A DESIGN EXERCISE

The telescope and configuration we choose for our design exercise is the 6.5-m converted MMT of the Smithsonian Astrophysical Observatory set up as an  $f/5$  Cassegrain. This focus has a  $1^\circ$  diameter field suitable for fiber-fed spectroscopy with one of the instruments, Hectospec, designed for moderate resolving power in the range 1000–5000. Some of its optical parameters, as given by Fabricant et al. (1994), are provided in Table 15.3.

Table 15.3

Optical Parameters of Hectospec<sup>a</sup>

300 fibers, 250 $\mu\text{m}$ core diameter, 0.5 mm spacing	
collimator diameter $d_1$	260 mm
camera focal length $f_2$	400 mm
camera-collimator angle	$35^\circ$
pixel size	13.5 $\mu\text{m}$
$f_2/f_1 = 1/3.25$	$rf_2/f_1 = 1/3.45$

<sup>a</sup> Hectospec is a moderate-resolution fiber-fed spectrometer on the modified 6.5-m MMT of the Smithsonian Astrophysical Observatory.

Of the several grating configurations of Hectospec, we choose the one with a 270 groove/mm grating and a blaze angle  $\delta = 5.3^\circ$ . To simplify our exercise we choose Eq. (15.2.2) rather than the more accurate Eq. (15.2.1); for this grating the error made by this simplification is only a few percent. Substituting  $d_1$  and  $\Delta$  from Table 15.3 into Eqs. (15.2.2) and (15.2.4) we get

$$\mathcal{R}\phi = 0.0074 = 1500 \text{ arc-sec}, \quad \phi F_2 = 0.86 \text{ arc-sec}. \quad (15.4.1)$$

With a telescope scale of approximately 160  $\mu\text{m}/\text{arc-sec}$ , each fiber subtends an angle of about 1.5 arc-sec on the sky. Putting this value into Eq. (15.4.1) gives  $\mathcal{R} \cong 1000$  and  $F_2 \cong 0.57$ . This value of  $F_2$  for an optimum pixel match is obviously not feasible; the choice made by the system designers is  $F_2 = 1.5$ . Hence each projected fiber end spans about 5.5 pixels.

This exercise indicates some of the tradeoffs made by the system designers for this instrument. The fiber size chosen is a tradeoff between ease of positioning and maximum light from a distant galaxy, better with a large fiber, and resolving power, larger with a small fiber. There is also the obvious tradeoff between pixel matching and camera focal ratio, a choice faced by nearly all designers of spectrometers for large telescopes.

## 15.5. ECHELLE SPECTROMETERS

For high-resolution astronomical spectroscopy,  $R \approx 4\text{E}4$  or larger, an echelle is the choice over a grating used in low order. The principal reasons for this are larger luminosity, discussed in Section 13.3, and the 2D format of the spectrum, which permits broad spectral coverage on efficient detectors. Because the echelle has a large groove spacing it is used at high-order numbers, as the example to

follow illustrates. Thus it is necessary to provide cross-dispersion to separate the orders, or use a filter to isolate a single order.

In this section we discuss the form of the 2D format with different cross-dispersers and possible locations of a cross-disperser within an echelle spectrometer. We give a design exercise to illustrate the choice of parameters appropriate for an echelle instrument on a 4-m telescope. Finally, we point out some of the different collimator and camera possibilities selected for echelle spectrometers on large telescopes.

### 15.5.a. SPECTRUM FORMATS

If wavelengths in different orders are to be recorded without confusion, a cross-disperser must be put in series with the echelle. A cross-disperser is simply another element, usually a prism or another grating, whose dispersion is at right angles to that of the echelle and whose function is to separate the orders. The angular dispersion of the order separator is usually many times smaller, and the combination of elements gives a 2D spectrum format. The format outline is set by the relative dispersions of the two elements; in this section we discuss the factors that determine a spectrum format.

We consider first the factors that determine the length of the spectrum in a given echelle order. With a camera of focal length  $f_2$ , the spectrum in the focal plane has length  $f_2 \Delta\beta$ , where  $\Delta\beta$  is the angular length of one free spectral range  $\Delta\lambda$ . Combining Eqs. (13.2.2a) and (13.2.6) we get

$$\Delta\beta = \frac{d\beta}{d\lambda} \Delta\lambda = \frac{\lambda_b}{\sigma \cos \beta_b}, \quad (15.5.1)$$

where  $\lambda_b$  is the blaze wavelength in the  $m$ th order and  $\beta_b$  is its angle of diffraction. This relation is not exact but for  $m > 10$  is a good approximation to the exact angular width. The free spectral range within this  $\Delta\beta$  is

$$\Delta\lambda = \frac{\lambda_b}{m} = \frac{\lambda_b^2}{2\sigma \sin \delta \cos \theta}. \quad (15.5.2)$$

As noted in Section 13.3,  $\Delta\lambda$  is the spectral range between the approximate half-intensity points of the blaze function; it is also the separation between blaze wavelengths in adjacent orders. For the echelle example to follow,  $\Delta\beta = 4.33^\circ$  and  $\Delta\lambda = 11.1 \text{ nm}$  with  $\theta = 5^\circ$  in order  $m = 45$ .

From Eqs. (15.5.1) and (15.5.2) it is evident that  $\sigma$  is the controlling parameter for a given blaze angle and wavelength. Recall also that the parameters that set the resolving power are the blaze angle and diameters of the collimator and telescope. Because the camera design depends on both beam diameter and focal

Table 15.4

Equations for Echelle at Blaze Peak

$m\lambda_b = \sigma(\sin \beta_b + \sin \alpha) = 2\sigma \sin \delta \cos \theta$	
$\beta_b = \delta - \theta, \quad \alpha = \delta + \theta$	
$A = \frac{2 \sin \delta \cos \theta}{\lambda_b \cos \beta_b}$	$\Delta\lambda = \frac{\lambda_b^2}{2\sigma \sin \delta \cos \theta}$
$\mathcal{R} = \frac{2d_1 \sin \delta \cos \theta}{\phi D \cos \alpha}$	$\Delta\beta = A\Delta\lambda = \frac{\lambda_b}{\sigma \cos \beta_b}$

length, it is clear that the order length  $f_2 \Delta\beta$  also depends on parameters other than the groove spacing.

For convenient reference, we give the important relations for an echelle at the blaze peak in Table 15.4, including those for order length and free spectral range. Note that angular dispersion and resolving power, as given in general in Table 13.1, are not constant over a single order. Their values at the blaze peak in Table 15.4 are essentially an average over each order.

Assuming a cross-disperser with angular dispersion  $A_c$ , the separation  $\Delta y$  between adjacent orders is given by  $\Delta y = f_2 A_c \Delta\lambda$ . If  $A$  and  $A_c$  are assumed constant over a free spectral range, that echelle order is tilted by an angle  $\psi$  with respect to the direction of echelle dispersion, where  $\tan \psi = A_c/A$ . This tilt of orders is shown schematically in Fig. 15.8.

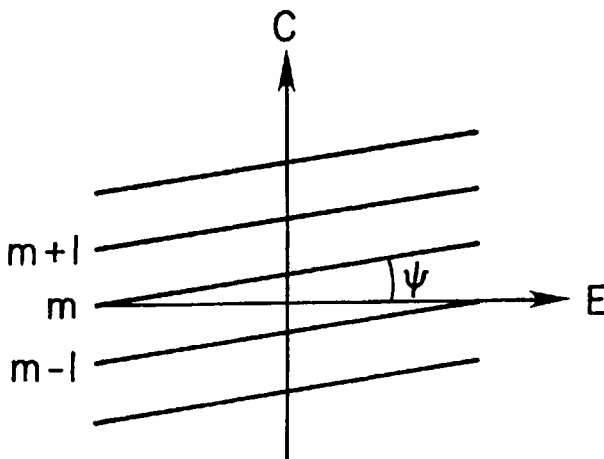


Fig. 15.8. Tilt of echelle orders relative to directions of echelle dispersion (E) and cross dispersion (C).

We consider first a grating cross-disperser with  $A_c = m_c/\sigma_c \cos \beta_c$  from Eq. (13.3.2a). Although  $A_c$  is essentially constant over a typical echelle order,  $A$  for the echelle increases as  $\beta$  increases, hence it is not constant along an order. Typically  $\tan \psi$  changes by a few percent from one end to the other and the order is slightly curved. At the blaze peak of the echelle the tilt of the echelle orders with a cross-dispersing grating is given by

$$\tan \psi = \frac{m_c}{\sigma_c \cos \beta_c} \frac{\lambda_b \cos \beta_b}{2 \sin \delta \cos \theta} = \text{constant} \cdot \lambda_b. \quad (15.5.3)$$

Given the angular dispersion  $A_c$  of the grating, we can write the order separation  $\Delta y$  in terms of the blaze wavelength. The result is

$$\Delta y (\text{grating}) = f_2 \frac{m_c}{\sigma_c \cos \beta_c} \frac{\lambda_b^2}{2 \sigma \sin \delta \cos \theta} = C \lambda_b^2, \quad (15.5.4)$$

where  $C$  is constant for a given echelle-grating combination.

For a prism cross-disperser,  $A_c$  is approximately proportional to  $\lambda^{-3}$ , as shown in Section 3.2. The combination of changing dispersions for both the prism and echelle along a given order results in more significant curvature for each order. In the case of a prism cross-disperser the tilt of an order and the separation between orders, both at the blaze peak, are given by

$$\tan \psi \approx \text{constant} \cdot \lambda_b^{-2}, \quad (15.5.5)$$

$$\Delta y (\text{prism}) \approx C \lambda_b^{-1}. \quad (15.5.6)$$

Comparing Eqs. (15.5.4) and (15.5.6) we see that gratings give larger order separation at longer wavelengths, while the reverse is true for prisms. When detector area is limited, a prism cross-disperser makes better use of the available area because  $y$  changes less rapidly with wavelength.

To illustrate the formats given by different cross-dispersers, we take a 31.6 groove/mm echelle with  $\tan \delta = 2$  and  $\theta = 5^\circ$ . For a grating cross-disperser, we assume one with 158 grooves/mm used in first order; for a prism cross-disperser we assume two  $45^\circ$  UBK7 prisms in series. The formats, to the same scale, are shown in Figs. 15.9 and 15.10 for the grating and prism, respectively. Each pattern has 66 orders over a wavelength range from 400 to 750 nm, with  $m = 141$  and 76 at these wavelengths, respectively.

The linear size of the formats shown in Figs. 15.9 and 15.10 is proportional to the camera focal length, as is the linear separation between orders. The angular separation between orders, projected on the sky, is proportional to the beam diameter and is independent of the camera focal length. We give numerical values for these formats in our discussion of a particular echelle spectrometer design to follow.

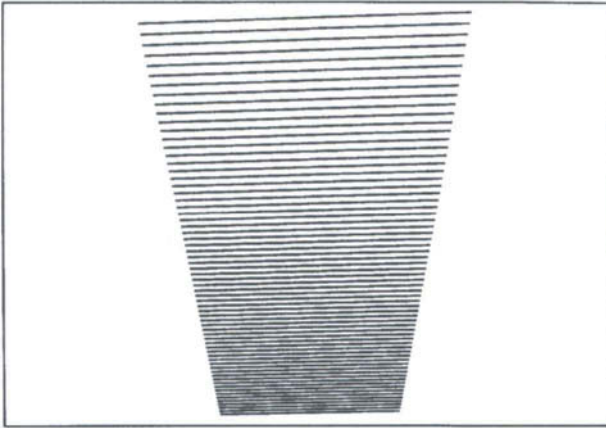


**Fig. 15.9.** Echelle format with grating cross-disperser. See text, Section 15.5.a, for parameter values of echelle and grating.

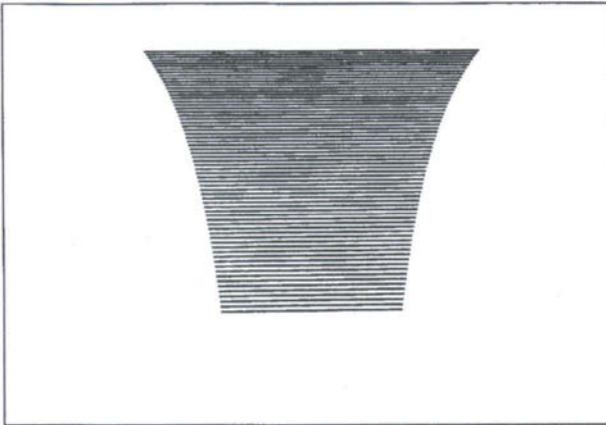


**Fig. 15.10.** Echelle format with prism cross-disperser. See text, Section 15.5.a, for parameter values of echelle and prism train.

### 15.5.b. CROSS-DISPERSION MODES

Several different methods of order separation are possible. The simplest way to suppress unwanted orders is with a narrowband filter between the telescope and spectrometer. Cross-dispersion can also be done with a separate prism or grating spectrometer following an echelle instrument, but such a system is less efficient

and more prone to misalignment than an echelle spectrometer with internal cross-dispersion. We choose to limit our discussion to internal cross-dispersion.

For internal cross-dispersion modes, the three principal options are a prism (or prism train) or plane grating located:

- (1) between the echelle and camera optics and used single-pass;
- (2) between the collimator and echelle and used single-pass; or
- (3) close to the echelle and used double-pass.

It is possible to devise an echelle instrument with either a concave grating used as both camera and cross-disperser or a concave grating predisperser also doubling as the collimator. Configurations with concave gratings, however, are not practical in the fast systems required for large telescopes.

In addition to the possible locations of the cross-disperser noted in the preceding text, the choice of angles of the chief ray to and from the echelle is an important part in the design of an echelle spectrometer. Although we make reference to angles in this section, we defer the main discussion of this topic to the following section.

We first consider mode (1), in which the disperser follows the echelle, oriented with  $\alpha > \beta$ , as shown schematically in Fig. 15.11. The direction of the echelle dispersion is in the plane of Fig. 15.11, and the prism or grating must be clear of the collimator beam and large enough to accept the dispersed light in each echelle order. In the direction perpendicular to the echelle dispersion, the width of the cross-disperser is the diameter of the collimator beam.

It is evident from Fig. 15.11 that the cross-disperser can be placed closer to the echelle if the angle  $\theta$  is larger, hence the height of the cross-disperser is less. Larger  $\theta$ , however, also means a larger dispersed beam height because of anamorphic magnification. The latter effect largely cancels the reduction in size obtained by putting the cross-disperser closer to the echelle; the net effect

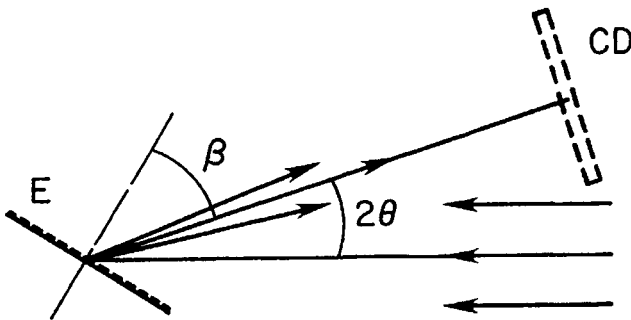


Fig. 15.11. Echelle (E) with postdisperser (CD), denoted as mode (1) in text, in off-plane configuration.

is that the size of the cross-disperser depends only weakly on the choice of  $\theta$ , except for  $\theta$  near zero.

We pointed out in Section 13.4 that the efficiency at the blaze peak and the average efficiency over each order decreases as  $\theta$  increases. In order to keep the efficiency as high as possible,  $\theta$  is chosen as small as possible, within the constraint of having the dispersed beam clear the collimator beam. Given these competing effects, it turns out that  $\theta$  in the range  $4\text{--}6^\circ$  is a good compromise between beam clearance and efficiency for this arrangement.

A variant of mode (1) is one in which  $\alpha = \beta$ , hence  $\theta = 0$ , but  $\gamma \neq 0$ , as shown in Fig. 15.12. We discuss the important features of this choice of angles in a following section.

The option listed here as mode (2) has the cross-disperser located in the collimator beam and used single-pass, as shown schematically in Fig. 15.13. In this mode the required size of the disperser is simply that of the collimator beam and the discussion for mode (1) relative to anamorphic magnification applies to the size of the camera optics. An example of an echelle spectrometer with this mode of cross-dispersion is the University College London Echelle Spectrograph

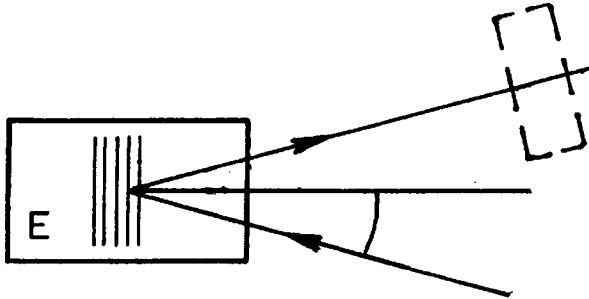


Fig. 15.12. Echelle (E) with postdisperser (CD) in quasi-Littrow or in-plane configuration.

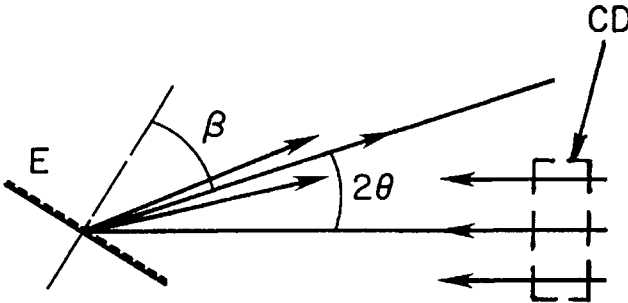


Fig. 15.13. Echelle (E) with predisperser (CD) in collimator beam.

(UCLES) for the Anglo-Australian Telescope (AAT). The disperser in this instrument is a train of three fused silica prisms.

The final cross-disperser option is mode (3), a prism(s) or transmission grating close to the echelle and used double-pass. Of the two choices of disperser for this mode, the prism is the only viable choice because of its constant efficiency. The efficiency curve for a transmission grating is sharply peaked if double-passed and this option cannot compete with a prism. An obvious advantage of a double-pass prism(s) is larger-order separation compared with a single-pass prism as used in mode (1). An example of an echelle spectrometer with this type of cross-disperser is an instrument for the 2.7-m telescope at the McDonald Observatory, Texas.

A double-pass prism arrangement is an attractive option for quasi-Littrow configurations in which  $\alpha = \beta = \delta$ . As pointed out in the discussion of Table 13.4 in Section 13.4, echelles approaching R-4 are almost forced into the quasi-Littrow mode because of problems with echelle size and anamorphic magnification.

Of the three modes discussed in this section the one most often chosen is mode (1). This mode has the advantage of allowing either gratings or prisms to be used and is not subject to tilt of the projected slit on the detector. We discuss this latter effect in Section 15.5.d.

### 15.5.c. GRATINGS VERSUS PRISMS AS CROSS-DISPERSERS

The choice of a grating versus a prism depends on many factors including required order separation, spectral range coverage, transmission efficiency, efficient use of detector area, and cost. Gratings usually have higher dispersion and, if a camera with a short focal length is used, may be the only practical option. One disadvantage of a grating is its changing efficiency over a wide spectral range, as shown in Fig. 13.10, and thus several may be needed. Another disadvantage of a grating is the less than optimum use of detector area, as shown by Eq. (15.5.4). The main advantage of gratings is a wide selection of available groove spacings to give a range of cross-dispersions.

A prism has high and constant efficiency over its range of transmittance, but lower dispersion than a grating, hence more than one prism may be required to get the necessary order separation in a spectrometer with a fast camera. Large prisms are generally more expensive than gratings of comparable size, and the choice of transparent glasses for near ultraviolet wavelengths, especially to the atmospheric cutoff, is limited. A significant advantage of a prism over a grating is that it gives a format that makes better use of detector area.

It is interesting to note the history of the choice of cross-disperser. Gratings were the choice for the first echelle spectrometers built in the 1960s and 1970s. These instruments typically had beam diameters of 100 mm or less, and used image tubes or photographic plates. Almost without exception, echelle instru-

ments designed and built in the 1980s used prism cross-dispersion. These systems typically had beam diameters of approximately 200 mm and use CCD detectors. For the largest echelle spectrometer in operation at the time of this writing, HIRES at the Keck 10-m telescope, the beam diameter is 300 mm and a grating cross-disperser is used. For this instrument both the grating and echelle are mosaics, as the size of single prisms required for this beam size precluded their use. Walker et al. (1994) have suggested prism mosaic configurations as cross-dispersers for beams of this size.

#### 15.5.d. ECHELLE SPECTROMETER CONFIGURATIONS

Echelle spectrometers have been built in many different configurations, but each is a variant of one of two choices of angles of the chief ray relative to the echelle. One choice is the so-called *in-plane* design in which  $\gamma = 0$ . In this design the collimator and camera beams are separated by choosing  $\alpha > \beta$ . The other choice is the *off-plane* design with  $\gamma \neq 0$ . Choosing  $\alpha = \beta$  gives a quasi-Littrow design, hence no anamorphic magnification in the direction of echelle dispersion. Figures 15.11 and 15.12 show off-plane and in-plane schematic layouts, respectively. A summary of the characteristics and modes for selected echelle spectrometers is given in Table 15.5.

**Table 15.5**  
Characteristics and Modes of Selected Echelle Spectrometers

	R-value	$W$ (mm)	Mode	Cross-Disperser
<b>In-Plane Designs</b>				
HIRES <sup>a</sup>	2.8	1260	1	Gratings
Hectochelle <sup>b</sup>	2.1	840	filter	—
HROS <sup>c</sup>	2.0	410	2	Prisms
immersed echelle				
CARCES <sup>d</sup>	2.0	410	1	Prisms
<b>Off-Plane Designs</b>				
HDS <sup>e</sup>	2.8	840	1	Gratings
HRS <sup>f</sup>	3.8	840	1	Gratings
white-pupil				

<sup>a</sup> High Resolution Echelle Spectrograph—Keck 10-m Telescope.

<sup>b</sup> Echelle Spectrograph—Modified 6.5-m Multiple Mirror Telescope.

<sup>c</sup> High-Resolution Optical Spectrograph—Gemini 8-m Telescope.

<sup>d</sup> Chicago ARC Echelle Spectrograph—Apache Point 3.5-m Telescope.

<sup>e</sup> High Dispersion Spectrograph—Subaru 8.2-m Telescope.

<sup>f</sup> High Resolution Spectrograph—Hobby-Eberly 9-m Telescope.

A consequence of nonzero  $\gamma$  in the off-plane design is that the entrance slit is reimaged by the spectrometer optics with a tilt, as discussed in Section 14.1, with the tilt proportional to  $\gamma$  and the slope given by Eq. (14.1.9). Substituting  $A$  from Table 15.4 into Eq. (14.1.9), the slope or tilt of the reimaged slit is, to a good approximation,  $d\beta/d\gamma = 2 \tan \gamma \tan \delta$ . This tilt is of little consequence for a single point source at the entrance slit, but must be taken into account in data reduction for a long slit.

The choices for collimator and camera optics are about as varied as the number of operating echelle spectrometers; examples of some of these choices are listed in Table 15.6. Details on the designs of these spectrometers, and versions based on a modified Czerny-Turner arrangement, are found in the references at the end of the chapter.

One optical layout of echelle spectrometers not yet discussed is the so-called *white-pupil* design. In this design additional optics between the echelle and the cross-disperser in mode (1) reimagine the echelle onto the cross-disperser with unit magnification. Thus the beam size at the prism or grating is the same as that of a monochromatic beam emerging from the echelle and the extra cross-disperser size needed to capture the dispersed light in each echelle order in an in-plane design is not required. Examples of designs that incorporate the white-pupil concept are the UV-Visual Echelle Spectrograph (UVES) for the ESO Very Large Telescope (VLT) and the fiber-fed High Resolution Spectrograph (HRS) for the Hobby-Eberly Telescope designed by Tull (1994). Both of these instruments use an R-4 echelle to get the largest possible  $\mathcal{R}\phi$  product from existing echelles. A schematic layout of a white-pupil design is shown in Fig. 15.14.

A final approach to increasing the  $\mathcal{R}\phi$  product is to use an immersed echelle, as discussed in Section 13.3. This is the choice for the high-resolution optical spectrograph (HROS) for a Gemini 8-m Telescope.

Table 15.6

Optics of Selected Echelle Spectrometers<sup>a</sup>

	Focus	Collimator	Camera
HIRES	Nasmyth	$f/14$ Tilted Sphere	Catadioptric
Hectoehelle	Bench <sup>b</sup>	Off-axis Paraboloid	Catadioptric
HROS	Cassegrain	$f/16$ Paraboloid	Catadioptric
CARCES	Nasmyth	$f/10$ Paraboloid	Schmidt
HDS	Nasmyth	$f/13$ Paraboloid	Catadioptric
HRS	Bench <sup>b</sup>	Off-axis Paraboloid	All-Reflective

<sup>a</sup> See Table 15.5 for definitions of acronyms.<sup>b</sup> Bench spectrometers are fiber-fed.

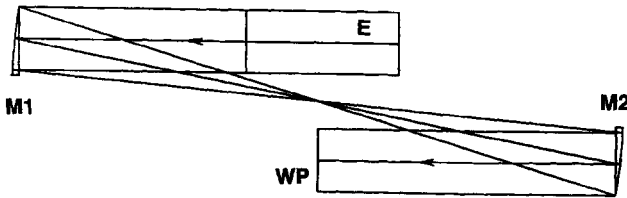


Fig. 15.14. Schematic layout of intermediate optics for white-pupil spectrometer design. Dispersed light from the echelle (E) is recollimated by the M1, M2 mirror pair and the pupil at the echelle is reimaged at the white pupil (WP).

### 15.5.e. ECHELLE DESIGN EXERCISE

To illustrate some of the considerations that go into the design of an echelle spectrometer, we take some specific parameters and determine the characteristics of the instrument and spectrum format. The assumed parameters include a telescope diameter  $D = 4$  m and an R-2 ( $\delta = 63.5^\circ$ ) echelle with 31.6 grooves/mm used at  $\theta = 5^\circ$ . We aim for a system capable of spectral resolving power  $\mathcal{R} = 5E4$  when the slit width  $\phi = 1$  arc-sec and the projected slit width  $w' = 30 \mu\text{m}$ .

Defining  $\Gamma = 2 \sin \delta \cos \theta / \cos \alpha$ , we can rewrite  $\mathcal{R}$  from Table 15.3 and Eq. (15.2.3) in suitable units as

$$\mathcal{R}\phi \text{ (arc-sec)} = 200\Gamma \frac{d_1 \text{ (mm)}}{D \text{ (m)}}, \quad (15.5.7)$$

$$w' (\mu\text{m}) = 5r\phi \text{ (arc-sec)}D \text{ (m)}F_2, \quad (15.5.8)$$

where  $\Gamma = 4.87$  and  $r = 0.70$  for the echelle angles chosen. Solving for  $d_1$  and  $F_2$  gives  $d_1 = 205$  mm and  $F_2 = 2.14$ , hence the camera focal length  $f_2 = 440$  mm. From these results we see that the only possible instrument configuration is one with a fast camera, such as a folded Schmidt. The projected slit width is covered by two pixels if the pixel size  $\Delta = 15 \mu\text{m}$ .

Note that the results derived so far are independent of the echelle groove spacing; this parameter is used to find the length  $f_2 \Delta\beta$  of each echelle order. With our chosen echelle, the order lengths are 10.7 and 19.8 mm, respectively, at 400 and 750 nm, with corresponding plate factors of 2.67 and 5.0  $\text{\AA}/\text{mm}$ .

The order separation and format width is determined by the cross-disperser, so far unspecified. If a first-order grating with 158 grooves/mm is used, the orders at 400 and 750 nm are separated by 23.3 mm; if two  $45^\circ$  UBK7 prisms are used, the orders at these wavelengths are separated by 15.7 mm. The echelle and cross-

disperser parameters used in this example are the same as those used for the formats shown in Figs. 15.9 and 15.10.

The spacings of the orders within the formats depend on the wavelength according to Eqs. (15.5.4) and (15.5.6). For the grating the angular separations between adjacent orders, projected on the sky, are 4.7 and 16.1 arc-sec at 400 and 750 nm, respectively. The corresponding separations for the prism cross-disperser are 7.6 and 4.5 arc-sec, with smaller separation at the long wavelength end of the format.

Our calculated parameters for this example assumed a 4-m telescope,  $\mathcal{R} = 50,000$  and  $\phi = 1$  arc-sec. Suppose we want a spectrometer with the same  $\mathcal{R}$  and  $\phi$  on an 8-m telescope. For the same  $\Gamma$  we find  $d_1 = 410$  mm from Eq. (15.5.7). Given the largest echelle width of 305 mm now available, the only viable way to reach the desired resolving power is an echelle with a larger  $\tan \delta$ . If, for example, we choose a quasi-Littrow configuration with an R-4 echelle, then we find  $\Gamma = 2$   $\tan \delta = 8$  and  $d_1 = 250$  mm.

In addition to the beam and echelle size problem, there is also a camera problem. From Eq. (15.5.8) we find  $\phi F_2 = 0.75$  arc-sec when  $w' = 30 \mu\text{m}$  for our assumed quasi-Littrow echelle on an 8-m telescope. This projected slit width was chosen to satisfy the Nyquist sampling criterion with  $15 \mu\text{m}$  pixels, but that is no longer possible for an 8-m telescope unless the slit width is reduced. If we choose  $w' = 60 \mu\text{m}$ , then  $F_2 = 1.5$  is a reasonable choice for the camera if the requirement  $\phi = 1$  arc-sec is kept.

Although these examples for a 4- and 8-m telescope illustrate the approach in the design of particular echelle instruments, the same procedures apply to the design of any echelle or grating spectrometer. Once the basic outline of a design is found, the choice of an optical system that fits this outline can be made.

Calculated values of  $\mathcal{R}\phi$  for selected echelle spectrometer and telescope combinations are found in Table 15.7.

Table 15.7

Resolution-Slit Width Products of Selected Echelle Spectrometers<sup>a</sup>

	$d_1$ (mm)	$f_2$ (mm)	$\delta$ (°)	$\zeta$ (°)	$\mathcal{R}\phi$ (arc-sec)
HIRES	300	760	70.5	5	45,000
Hectochelle	210	620	64.5	7.5	46,000
HROS <sup>b</sup>	160		63.5		29,000
CARCES	200	540	63.5	6	60,000
HDS	270	770	70.5	6	38,000
HRS	210	500	75	1	35,000

<sup>a</sup>  $\zeta = \theta$  for in-plane designs;  $\zeta = \gamma$  and  $\theta = 0$  for off-plane designs.

<sup>b</sup>  $\mathcal{R}\phi$  product includes gain factor of 1.46 from immersed echelle.

## 15.5.f. CONCLUDING REMARKS

Although our discussion of echelle formats and spectrometer configurations is given in terms of echelles with  $\tan \delta = 2$  or larger, the relations used apply to any blaze angle. An echellette grating can also be used with a cross disperser to separate orders. Consider, for example, a grating with 300 grooves/mm and  $\tan \delta = 0.75$ . From the grating equation in Table 15.4 we get  $m\lambda_0$  ( $\mu\text{m}$ ) =  $4 \cos \theta$ , hence most of the visible spectrum is covered in four orders,  $m = 6$  through  $m = 9$ . These orders are easily separated with a crossed prism in the configuration shown in Fig. 15.11. Because of the smaller  $\sin \delta$  compared to an echelle, such a system is appropriate for medium spectral resolution over a wide wavelength range in a 2D format.

The range of possibilities for echelle spectrometer designs is impressive, as shown by the data in Tables 15.5–15.7. Instruments such as these, either fiber-fed or with direct slit illumination, are transforming the field of high-resolution astronomical spectroscopy. Our discussion is only an introduction to a large subject area, and the interested reader should study the many papers describing these instruments in detail.

## 15.6. NONOBJECTIVE SLITLESS SPECTROMETERS

An important technique for low-dispersion spectroscopy with large telescopes is the nonobjective mode. This mode is one in which a dispersing element, prism, blazed transmission grating, or a combination of the two, is placed in the converging beam near the telescope focal surface, as shown in Fig. 12.3. We discuss the characteristics of each of these in the nonobjective mode. The plate factor  $P$  and spectral purity  $\delta\lambda$  for this mode are given by Eqs. (12.1.3b) and (12.4.1), respectively, and are repeated here for convenient reference.

$$P = (sA)^{-1}, \quad (15.6.1)$$

$$\delta\lambda = \frac{\phi'f}{As}, \quad \delta\lambda_c = \text{TTC} \cdot P \quad (15.6.2)$$

where  $s$  is the distance from the element to the focus,  $f$  is the telescope focal length,  $A$  is the angular dispersion, and  $\delta\lambda_c$  is the spectral coma as defined in Eq. (15.1.11).

The term “nonobjective” is used to distinguish this type of slitless instrument from the classical objective mode in which a prism or grating covers the aperture of a telescope. The disperser in the objective mode is in collimated light and the spectral resolution is determined by the seeing or telescope aberrations. The discussion in Sections 12.4 and 13.1 is sufficient for the objective mode.

The advantages of the nonobjective mode include ease of mounting a disperser on any telescope with a minimum of effort and cost, as no auxiliary optics are needed. Hence slitless spectroscopy is not limited to telescopes of modest size. Another advantage is that within broad limits set by aberrations and disperser size any plate factor is possible. A disadvantage of this mode is that aberrations are present when the disperser is placed in a converging beam but, as we show, their effect can often be reduced to a negligible level compared to the seeing limit. It is also important to note that this mode is not an alternative to the objective mode, but is complementary. The objective mode is typically used to give  $P$  in the range of 10–30 nm/mm, while the nonobjective mode is suitable for larger plate factors.

We now consider in turn the aberrations of the prism, grating, grism, and prism-grating in a converging beam. In each case we apply the paraxial approximation to all angles, an assumption that is justified for all practical configurations. Any significant deviations from results so derived are noted.

#### 15.6.a. NONOBJECTIVE PRISM

Although a prism or wedge is rarely used in this mode, its characteristics are important when combined with a grating. Thus we determine prism aberrations in anticipation of the discussion of a grism.

Consider a thin prism of index  $N$  with apex angle  $\gamma$ , as shown in Fig. 15.15, and angles of incidence  $\theta_1$  and  $\theta_2$  at the first and second surfaces, respectively. It is convenient to express these angles in terms of the apex angle. If  $\theta_1 = \varepsilon\gamma$  then, from Snell's law, we find  $\theta_2 = -\gamma(1 - \varepsilon/N)$ . The parameter  $\varepsilon$  determines the prism orientation with respect to the chief ray; when  $\varepsilon = 0$  the incident chief ray is perpendicular to the first surface, and when  $\varepsilon = N/2$  the prism is set for minimum deviation.

The pertinent aberration coefficients for each surface are those of astigmatism and coma, and from Table 5.1 we get

$$A_{11} = -\frac{\theta_1^2(N^2 - 1)}{2N^2s_1}, \quad A_{12} = \frac{\theta_2^2N(N^2 - 1)}{2s_2}, \quad (15.6.3)$$

$$A_{21} = -\frac{\theta_1(N^2 - 1)}{2N^2s_1^2}, \quad A_{22} = \frac{\theta_2N(N^2 - 1)}{2s_2^2}, \quad (15.6.4)$$

where  $s_1$  and  $s_2$  are the object distances at the first and second surfaces, respectively. The astigmatism coefficients are reversed in sign from those in Table 5.1 to reflect the change from sagittal to tangential image, as discussed in Section 15.1.a.

Assuming the prism thickness is small compared to the distance to the focal surface we have  $s_2 = Ns_1$ . This assumption, in turn, implies that the beam size is

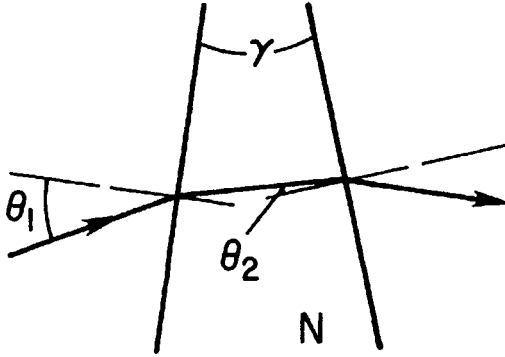


Fig. 15.15. Cross section of prism of index  $N$  with apex angle  $\gamma$ .  $\theta_1$  and  $\theta_2$  are angles of incidence at the first and second faces, respectively.

the same at the two surfaces, hence each prism aberration coefficient is simply the sum of surface coefficients. Substituting for  $\theta_1$  and  $\theta_2$ , with  $s_1 = s$ , we find

$$A_{1w} = \frac{\gamma^2(N^2 - 1)}{2s} \left( 1 - \frac{2\epsilon}{N} \right), \tag{15.6.5}$$

$$A_{2w} = -\frac{\gamma(N^2 - 1)}{2Ns^2}, \tag{15.6.6}$$

where the subscript  $w$  denotes a wedge or a prism. Note that the coma coefficient is independent of  $\epsilon$ , hence coma does not depend on the prism orientation. For the astigmatism coefficient we see that it is zero when  $\epsilon = N/2$ , the prism orientation at minimum deviation.

An analysis including the wedge thickness shows that, to a good approximation, the wedge coma coefficient is the sum of Eqs. (15.6.6) and (7.2.11), where the latter is the coefficient for a plate of thickness  $t$ . The contribution of the thickness term is smaller than that of Eq. (15.6.6) by a factor of  $\epsilon t/N^2s$ , and can be ignored.

The transverse and spectral coma are given by

$$\text{TTC} = 3A_{2w}x^2s = \frac{3\gamma(N^2 - 1)}{8NF^2}s, \tag{15.6.7}$$

$$\delta\lambda_c = \frac{3(N^2 - 1)}{8NF^2} \frac{d\lambda}{dN}, \tag{15.6.8}$$

where  $F$  is the focal ratio of the converging beam, and the angular dispersion  $A$  of a thin prism is  $\gamma dN/d\lambda$ . Note that the spectral coma is independent of the prism angle and distance from the focal surface.

As an example, consider a thin UBK7 prism in an  $f/8$  beam. At a wavelength of 400 nm,  $N = 1.53$  and, with  $dN/d\lambda$  from Fig. 13.1, we get  $\delta\lambda_c = 40$  nm. Thus a prism in the nonobjective mode is useful only for very low resolution, of order 10 in this example.

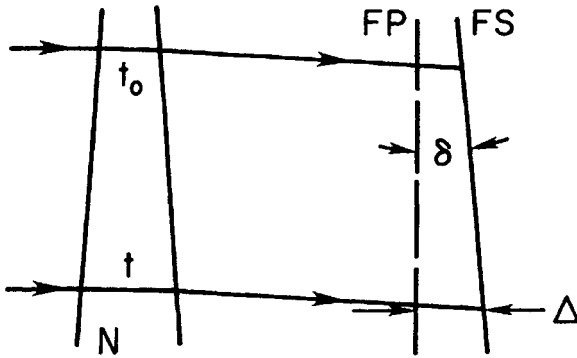


Fig. 15.16. Tilt of focal surface FS, shift from nominal telescope focal plane FP, due to prism in converging beam.

A final feature to note for a prism is the tilt of the focal surface. Figure 15.16 shows chief rays from sources in different parts of the field passing through different prism thicknesses. Neglecting the prism angle, we use Eq. (2.4.5) to find the shift in focus from the nominal telescope focal surface. Because the shift in focus is proportional to  $t$ , the average local prism thickness, the surface on which the spectrum is imaged is tilted with respect to the telescope focal surface. Using Eq. (2.4.5) we find that the angle  $\delta$  between these two surfaces, in terms of the prism angle, is given by  $\delta = \gamma(N - 1)/N$ . This relation is relevant to our discussions of the grism and prism-grating.

### 15.6.b. NONOBJECTIVE TRANSMISSION GRATING

We now consider a transmission grating in a converging beam at distance  $s$  from the telescope focal surface. The thickness of the grating blank contributes to the aberrations only if the grating face is not normal to the incident chief ray. Compared to the grating aberrations, the contribution of the blank thickness is roughly  $t/3s$  smaller for practical tilt angles and is ignored.

The relations for this mode are those for the Monk-Gillieson mounting in Tables 14.1–14.4, with the appropriate sign for a transmission grating. In the paraxial approximation these are

$$A_{1g} = (\beta^2 - \alpha^2)/2s, \quad (15.6.9)$$

$$A_{2g} = (\beta - \alpha)/2s^2 = (1/2s^2)m\lambda/\sigma, \quad (15.6.10)$$

$$\kappa_t = -3/s, \quad (15.6.11)$$

where the grating equation is used to rewrite the coma coefficient in Eq. (15.6.10). Considering first the coma, we find

$$\text{TTC} = 3A_{2g}x^2s = \frac{3s}{8F^2} \frac{m\lambda}{\sigma} = \frac{3\lambda}{8F^2P}, \quad (15.6.12)$$

$$\delta\lambda_c = 3\lambda/8F^2, \quad \mathcal{R} = 8F^2/3, \quad (15.6.13)$$

where  $F$  is the focal ratio of the converging beam, and  $\mathcal{R}$  is the spectral resolving power. Note that the spectral coma and resolving power are independent of the grating parameters and distance to the focal surface.

As an example, a grating in an  $f/8$  beam has  $\delta\lambda_c = 2.3$  nm at a wavelength of 400 nm, with  $\mathcal{R} = 170$ . Compared to the preceding prism example, the improvement in spectral resolution is indeed substantial. Given the size of the spectral coma, a grating in this mode can be used at significantly higher dispersion or lower plate factor than a nonobjective prism.

The spectral resolution achievable with a nonobjective grating is set by spectral coma if the dispersion is large and by seeing if the dispersion is small. The boundary between these is found by setting  $\delta\lambda_c = \delta\lambda$ , where the latter is given in Eq. (15.6.2).

Solving this relation for  $P$  gives, in the units specified,

$$P(\text{nm/mm}) = 75\lambda(\text{nm})/F^3D(\text{m})\phi'(\text{arc-sec}), \quad (15.6.14)$$

where  $D$  is the telescope diameter. The seeing blur is larger than the coma blur for any  $P$  larger than that given by Eq. (15.6.14). Results from this relation are plotted in Fig. 15.17 for a selected set of focal ratios.

The constraint put on the plate factor by this relation is a conservative one because the entire width of the comatic image is used in the spectral coma. Because about 80% of the light in a comatic image is within a width  $\text{TTC}/2$ , a plate factor limit that is one-half that given in Eq. (15.6.14) and Fig. 15.17 is somewhat more realistic.

We now determine the characteristics of the astigmatic image. It is evident from Eq. (15.6.9) that the astigmatism can be made zero at a wavelength  $\lambda_0$  by setting  $\beta = -\alpha$ , hence  $2\alpha = -m\lambda/\sigma$ . If the grating is tilted by angle  $\alpha$ , however, the detector is also at angle  $\alpha$  with respect to the grating surface. As a result of this tilt the plate factor now varies across the detector, and the fractional change in  $P$  across a detector of width  $W$  is  $|\alpha|W/s$ .

The transverse astigmatism is

$$\text{TAS} = 2A_{1g}ys = \frac{(\beta^2 - \alpha^2)}{2F}s = \frac{\lambda(\lambda - \lambda_0)}{2FP^2s}, \quad (15.6.15)$$

where the image length is  $2 \cdot \text{TAS}$ . For a given  $P$  and  $F$  we see that TAS varies inversely as  $s$ . To keep  $P$  constant for a larger  $s$  means choosing a grating with

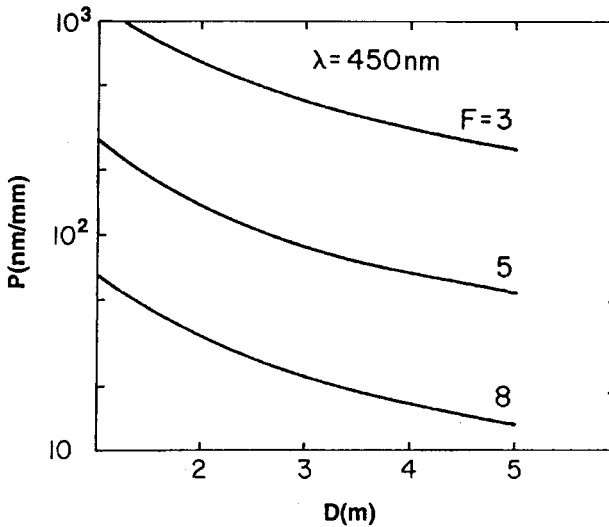


Fig. 15.17. Plate factor  $P$  at which spectral coma equals seeing blur of 1 arc-sec for nonobjective transmission grating. See Eq. (15.6.14).

fewer grooves per millimeter. Alternatively, for a given grating at different distances from the focal surface, the size of TAS is directly proportional to  $s$ .

As an example, take a first-order grating with 150 grooves/mm in an  $f/8$  beam. This grating has a plate factor of 100 nm/mm when  $s$  is 67 mm. At wavelengths of 400 and 600 nm, respectively, the astigmatic image lengths are 30 and 68  $\mu\text{m}$  when  $\alpha = 0$ . If  $\lambda_0$  is 500 nm, hence  $\alpha = -2.15^\circ$ , the image lengths are 7 and 11  $\mu\text{m}$  at 400 and 600 nm, respectively. Choosing a grating with 75 grooves/mm and letting  $s = 133$  mm reduces the image lengths by a factor of two. Although astigmatism does not affect spectral resolution, it is evident that it is desirable to keep the image lengths short to maintain spectrographic speed.

From Eq. (15.6.11) we see that the spectrum of each source has its own curved surface with radius  $s/3$ , with the surface concave as seen from the grating. Because all of the spectra are recorded on a flat detector, this curvature results in a defocus blur and can degrade the spectral resolution.

The image surfaces for the examples with  $\alpha = 0$  and  $\alpha = -2.15^\circ$  are shown in Fig. 15.18, with a line for each representing the optimum location of a detector for the 400–600 nm range. It is evident from Fig. 15.18 that the detector “fits” the image surface somewhat better for the tilted grating, with the zero-order image also in better focus. Simple geometry can be used in each case to determine the defocus blur at the ends of the spectral range.

A final important feature of the nonobjective grating mode is the presence of a zero-order reference for each spectrum, a reference not present for a prism in any

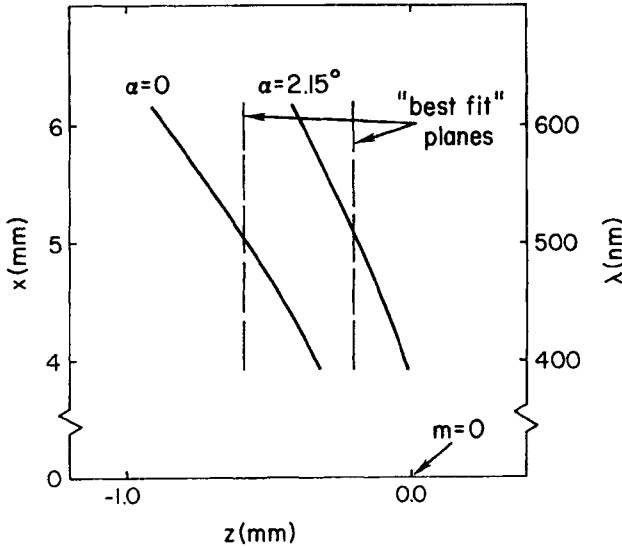


**Fig. 15.18.** Tilted image surfaces for nonobjective transmission mode with  $P = 100 \text{ nm/mm}$ . Horizontal scale is stretched by 2.5 times relative to vertical scale. Zero order and spectrum are in focus on surface with radius of curvature 22 mm.

slitless mode. This is a significant advantage in that quantitative measures of line positions are now possible. This is important, for example, for approximate measures of redshifts in emission-line objects. For a typical blazed grating with  $P \approx 100 \text{ nm/mm}$ , it turns out that the brightness in the zero order is comparable to that in the dispersed spectrum. Examples of such spectra are shown in the reference by Hoag and Schroeder (1970).

15.6.c. NONOBJECTIVE GRISM

The principal defects in spectra taken with a nonobjective grating are coma across the spectral range and defocus at the ends of the range. These defects are significantly reduced with a grism, a prism with a grating replicated on one of its faces. The characteristics of a grism in convergent light were first described by Bowen and Vaughan (1973); in our discussion we reproduce the main results from their treatment.

A cross-section of a grism is shown in Fig. 15.19, with the same notation for the angles as in Fig. 15.15. We again assume the paraxial approximation and neglect the prism thickness. In this approximation, the aberration coefficients of

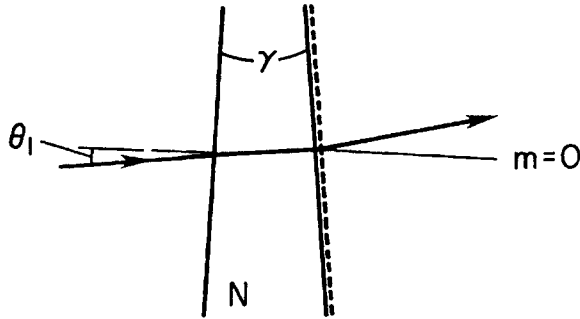


**Fig. 15.19.** Cross section of grism with apex angle  $\gamma$ .  $\theta_1$  is the angle of incidence at the first face; the grating is on the second face.

the grism are the sum of the corresponding coefficients of the prism and grating. Taking results from the previous sections, we get

$$A_{1s} = \frac{\gamma^2(N^2 - 1)}{2s} \left(1 - \frac{2\varepsilon}{N}\right) + \frac{\beta^2 - \alpha^2}{2s}, \quad (15.6.16)$$

$$A_{2s} = \frac{1}{2s^2} \left[ \frac{m\lambda}{\sigma} - \frac{\gamma(N^2 - 1)}{N} \right]. \quad (15.6.17)$$

The coma coefficient is zero for  $\lambda = \lambda_0$  when the prism angle  $\gamma$  is given by

$$\gamma = \frac{m\lambda_0}{\sigma} \frac{N}{N^2 - 1}, \quad (15.6.18)$$

and therefore

$$\text{TTC} = \frac{3s}{8F^2} \frac{m}{\sigma} |\Delta\lambda| = \frac{3|\Delta\lambda|}{8F^2P}, \quad (15.6.19)$$

where  $\Delta\lambda = \lambda - \lambda_0$ . Comparing the spectral coma for a grism from Eq. (15.6.19) with that for a grating given in Eq. (15.6.13) we see that the coma for the grism is several times smaller. This implies, in turn, that a grism can be used at a plate factor that is smaller by the same amount, or at a faster focal ratio, before the coma and seeing blurs are equal.

The direction of the diffracted chief ray at the zero-coma wavelength is shown in Fig. 15.19. In this direction the dispersions of the prism and grating add; the grism dispersion is typically a few percent larger than that of the grating alone.

The astigmatism coefficient, unlike the coma, depends on  $\varepsilon$  and the grism orientation. With the grating equation,  $m\lambda = \sigma(\beta - \alpha)$ , and  $\alpha = \gamma(\varepsilon - N)$ , we can rewrite Eq. (15.6.16) as

$$A_{1s} = -\frac{\gamma^2(N^2 - 1)}{2N^2s} [\zeta^2 + 2N\varepsilon(1 - \zeta) - N^2(1 - \zeta)^2], \quad (15.6.20)$$

where  $\zeta = \lambda/\lambda_0$ . Note that  $A_{1s}$  is independent of  $\varepsilon$  when  $\zeta = 1$ . Setting  $dA_{1s}/d\zeta = 0$  and evaluating at  $\zeta = 1$  gives  $\varepsilon = 1/N$ . With this choice of  $\varepsilon$  we have astigmatism constant near  $\lambda_0$  and, to a good approximation, constant over a significant range centered on  $\lambda_0$ . Note that  $\beta = 0$  at the corrected wavelength for this grism orientation. We show shortly that this choice of  $\varepsilon$  also significantly reduces defocus due to image surface curvature.

With  $\varepsilon = 1/N$ , substitution of  $A_{1s}$  into Eq. (14.2.4) gives

$$\text{TAS} = \frac{d\gamma^2(N^2 - 1)}{2N^2} [1 - (N^2 - 1)(1 - \zeta)^2], \quad (15.6.21)$$

where  $d$  is the beam diameter at the grating surface. Note that TAS is largest at  $\lambda_0$  and decreases slowly as  $\lambda$  changes.

We now illustrate these results with an example using a grating with 75 grooves/mm and a fused silica prism with  $\gamma = 2.76^\circ$ , hence  $\lambda_0 = 500$  nm. Assume an  $f/8$  beam and  $s = 240$  mm, hence  $P \approx 55$  nm/mm. With these parameters we get  $\text{TTC} = 11$   $\mu\text{m}$  for  $\Delta\lambda \pm 100$  nm, and image length of 38  $\mu\text{m}$  at the corrected wavelength. Results from ray traces of a 10-mm-thick grism show that the zero-coma wavelength is 510 nm, with a plate factor of 53.5 nm/mm in this vicinity. Aberrations from ray traces are in excellent agreement with those given by the relations for TTC and TAS.

If this grism is placed in an  $f/4$  beam at  $s = 120$  mm, the plate factor  $P \approx 110$  nm/mm. With these changes the image length is unchanged and TTC is two times larger. Because the beam is faster, aberrations due to the thickness of the grism are larger and a ray-trace analysis is necessary to determine whether they are significant.

We noted in our discussion of the nonobjective prism that the nominal surface on which the spectra are in focus is tilted by an angle  $\delta = \gamma(N - 1)/N$  to the telescope focal plane. With  $\varepsilon = 1/N$ , the second surface of the grism is tilted by the same angle. Because the grating is on this surface, the perpendicular distance between the grating and detector is constant and the plate factor is the same over the field.

The fit between a tilted detector and the curved image surface of a single spectrum is shown in Fig. 15.20 for the grism example already given here, with tilt  $\delta = 0.87^\circ$ . Comparing this diagram with Fig. 15.18, it is evident that the fit is better for the grism mode. A better fit is obtained for the grism example if  $\theta_1$  is  $0.5^\circ$  smaller, but at the expense of variable  $P$  in the dispersion direction. Thus the grism corrects the two major defects of the nonobjective grating, but with the slight added complication of a tilted detector.

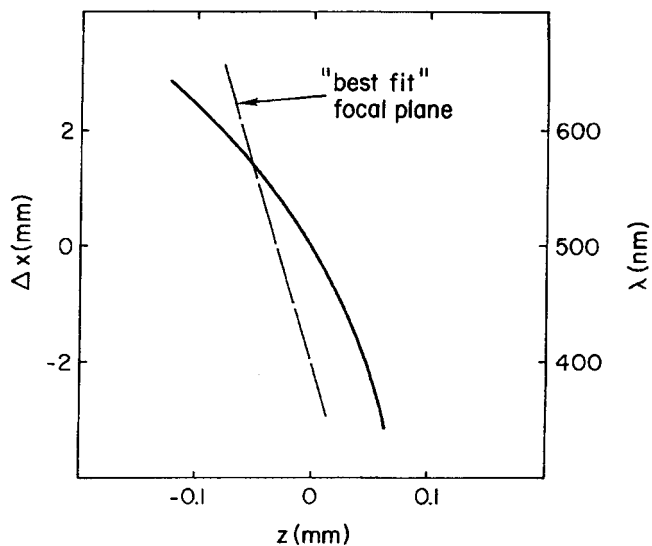


Fig. 15.20. Tilted, curved image surface for grism mode with  $P = 55$  nm/mm. Grism parameters are  $\alpha = 1.89^\circ$ ,  $\gamma = 2.76^\circ$ ,  $\delta = 0.87^\circ$ . Horizontal scale is stretched by 20 times relative to vertical scale.

In our discussion we have ignored the grism thickness and variation of grism index with wavelength. Their effects change some of the preceding results, though not significantly, and were included by Bowen and Vaughan in their analysis.

#### 15.6.d. NONOBJECTIVE PRISM-GRATING

The final nonobjective device considered consists of a separate prism and grating, as shown in Fig. 15.21. In this system there are two additional degrees of freedom: the separation between the elements and their relative orientations. With

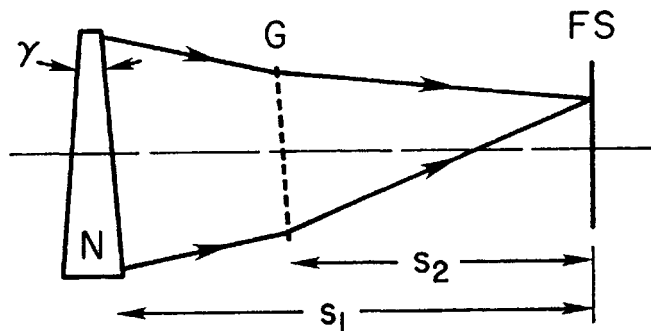


Fig. 15.21. Nonobjective prism-grating. FS, focal surface.

this system it is possible to eliminate both coma and astigmatism at one wavelength in the desired spectral range. This type of device is then suitable for fast beams and has been used, for example, at the  $f/2.7$  prime foci of the 4-m telescopes at the Kitt Peak (Tucson, Arizona) and Cerro Tololo Observatories (Chile).

Because of the several degrees of freedom for a prism-grating, we make no attempt at a thorough analysis but only give selected results without derivation. The aberration coefficients for the prism-grating are easily found by substituting the prism and grating coefficients into Eq. (5.6.7), with the results

$$A_{1s} = \frac{1}{2s_2} \left[ \gamma^2(N^2 - 1) \left( 1 - \frac{2\varepsilon}{N} \right) \left( \frac{s_1}{s_2} \right) + \beta^2 - \alpha^2 \right], \quad (15.6.22)$$

$$A_{1s} = \frac{1}{2s_2^2} \left[ \frac{m\lambda}{\sigma} - \frac{\gamma(N^2 - 1)}{N} \left( \frac{s_1}{s_2} \right) \right], \quad (15.6.23)$$

where  $s_1$  and  $s_2$  are the distances from the prism and grating, respectively, to the focal surface. Note that these relations reduce to those for the grism when  $s_1 = s_2$ . Setting  $A_{2s}$  to zero gives

$$\gamma = \frac{s_2}{s_1} \frac{m\lambda_0}{\sigma} \frac{N}{N^2 - 1}. \quad (15.6.24)$$

Because the prism is farther from the focus than the grating in the arrangement in Fig. 15.21, coma correction is achieved with a smaller apex angle compared with the grism.

The way in which astigmatism varies is most easily seen by taking the prism and grating tilt angles of the grism, hence  $\varepsilon = 1/N$  and  $\delta = \gamma(N - 1)/N$ , respectively. With these values as starting points, and assuming  $s_2$  and  $\lambda_0$  are fixed, Eq. (15.6.22) can be evaluated at  $\lambda_0$  for different  $s_1$ . Assigning the grism parameters to the grating and prism, astigmatism is zero when  $s_1 = 1.88s_2$ . If  $\varepsilon$  is made smaller, then astigmatism is zero at a smaller value of  $s_1$ . Ray traces show good agreement with the calculated values for an  $f/8$  beam. In faster beams, say,  $f/3$ , the relations above are a good first approximation, but ray traces are necessary to optimize the system and find the best grating orientation to fit the curved image surface to the tilted detector.

The slitless modes already discussed here assume a dispersing element in the converging beam ahead of the telescope focal surface. It is also possible to place a disperser in the diverging beam behind the focal surface and use a separate camera to focus the spectra. Because of the added optical elements this arrangement is less efficient than those previously discussed here, but has the advantage that the focal ratio of the final beam can be chosen as different from that of the telescope. A system of this type with a transmission grating and Schmidt camera has been built at the Royal Greenwich Observatory in Great Britain.

## 15.7. CONCLUDING REMARKS

With the exception of the nonobjective mountings, the discussion in this chapter has made little mention of the appropriate telescope focus for each instrument type. Instruments of smaller size are usually used at the Cassegrain focus, while large-beam spectrometers are usually placed at a Nasmyth focus on a platform that rotates with the telescope. Fiber-fed spectrometers are generally placed on a fixed platform near the telescope.

Older telescope facilities often included a Coudé room below the telescope, with a three-mirror system redirecting the light from a Cassegrain telescope along the polar axis. Large low-order diffraction gratings were the principal dispersing elements, with Coudé beam diameters as large as 300 mm. The dispersed light most often was sent to one of several Schmidt cameras. Examples of telescopes with such facilities include the Hale 5-m and Shane 3-m (see Bowen (1960)).

Spectrometer designs have become increasingly sophisticated in order to take advantage of the gains possible in observing efficiency with large telescopes at sites with superb seeing. This is especially true at the camera end with large, fast refractive and catadioptric cameras, such as those designed by Harland Epps for the Keck and other large telescopes. The changes at the input ends of spectrometers have been almost as dramatic, especially in instruments with hundreds of fibers feeding a single entrance slit. These spectrometers will certainly revolutionize the gathering of spectral information from celestial sources.

## REFERENCES

- Bowen, I. (1960). *Stars and Stellar Systems I, Telescopes*, Chap. 4, Chicago: University of Chicago Press.
- Hoag, A. and Schroeder, D. (1970). *Publ. Astron. Soc. Pac.*, **82**: 1141.
- Willstrop, R. (1965). *Mon. Not. R. Astr. Soc.*, **130**: 16.

## BIBLIOGRAPHY

### *All types of spectrometers*

James, J. and Sternberg, R. (1969). *The Design of Optical Spectrometers*, London: Chapman & Hall.

### *Czerny-Turner mounting*

Namioka, T. and Seya, M. (1967). *Sci. Light*, **16**: 169.

Reader, J. (1969). *J. Opt. Soc. Am.*, **59**: 1189.

Rosendahl, G. (1962). *J. Opt. Soc. Am.*, **52**: 408, 412.

*Ebert-Fastie mounting*

Fastie, W. (1952). *J. Opt. Soc. Am.*, **42**: 641, 647.

Welford, W. (1965). *Progress in Optics*, vol. 4, Chap. 6, Amsterdam: North-Holland.

*Monk-Gillieson mounting*

Kaneko, T., Namioka, T. and Seya, M. (1971). *Appl. Opt.*, **10**: 367.

Schroeder, D. (1966). *Appl. Opt.*, **5**: 545.

*Fiber-Fed spectrometers*

Fabricant, D., Hertz, E., and Szentgyorgyi, A. (1994). *Proc. SPIE Int. Soc. Opt. Eng.*, **2198**: 251.

*Echelle spectrometers*

Chaffee, F. and Schroeder, D. (1976). *Annual Review of Astronomy and Astrophysics*, **14**: 23, Palo Alto, CA: Annual Reviews.

Pilachowski, C., Dekker, H., Hinkle, K., Tull, R., Vogt, S., Walker, D., Diego, F., and Angel, R. (1995). *Publ. Astron. Soc. Pac.*, **107**: 983.

Schroeder, D. (1970). *Publ. Astron. Soc. Pac.*, **82**: 1253.

Schroeder, D. and Anderson, C. (1971). *Publ. Astron. Soc. Pac.*, **83**: 438.

Tull, R. (1994). *Proc. SPIE Int. Soc. Opt. Eng.*, **2198**: 674.

Tull, R. (1995). *Publ. Astron. Soc. Pac.*, **107**: 251.

Vogt, S., Allen, S., Bigelow, B., Bresee, L., Brown, B., Cantrall, T., Conrad, A., Couture, M., Delancy, C., Epps, H., Hilyard, D., Hilyard, D., Horn, E., Jern, N., Kanto, D., Keane, M., Kibrick, R., Lewis, J., Osborne, C., Osborne, J., Pardeilhan, G., Pfister, T., Ricketts, T., Robinson, L., Stover, R., Tucker, D., Ward, J., and Wei, M. (1994). *Proc. SPIE Int. Soc. Opt. Eng.*, **2198**: 362.

Walker, D., Radley, A., Diego, F., Charalambous, A., Dryburgh, M., Bigelow, B. (1994). *Proc. SPIE Int. Soc. Opt. Eng.*, **2198**: 1083.

*Dispersers in convergent light*

Bowen, I. and Vaughan, A. (1973). *Publ. Astron. Soc. Pac.*, **85**: 174.

Buchroeder, R. (1974). Unpublished study for Kitt Peak National Observatory.

Hoag, A. and Schroeder, D. (1970). *Publ. Astron. Soc. Pac.*, **82**: 1141.

*Conference Proceedings*

Crawford, D. (ed.) (1990). *Proc. SPIE Int. Soc. Opt. Eng.*, **1235**.

Crawford, D. and Craine, E. (eds.) (1994). *Proc. SPIE Int. Soc. Opt. Eng.*, **2198**.

D'Odorico, S. (ed.) (1998). *Proc. SPIE Int. Soc. Opt. Eng.*, **3355**.

The magnitude limits that can be reached by a ground-based telescope depend on many factors, of which the image size of a stellar source due to atmospheric effects is an important one. A powerful tool for reducing or eliminating seeing effects, and thereby reducing the image size, is *adaptive optics*. The techniques of adaptive optics are those by which telescope optics are adjusted on a rapid time scale to compensate for distortions in the wavefront entering a telescope. These adjustments are generally applied to a relatively small optical element in an optical train following the Cassegrain or Nasmyth focus and continuously readjusted on a time scale measured in milliseconds. For a good overview of the principles of adaptive optics, see the paper by Beckers and Goad (1987) and a review article by Beckers (1993).

Techniques of adaptive optics are to be distinguished from those of *active optics* for which adjustments are relatively much slower, often on a time scale of hours. Adjustments of this latter type are usually made to the primary mirror by actuators that adjust the shape of the mirror. The goal of active optics corrections is usually to reduce the aberrations of a telescope.

In this chapter we discuss the basic principles of adaptive optics and consider techniques by which a distorted wavefront is corrected before detection. It is also possible to apply postdetection corrections to images and achieve high angular resolution on bright sources with ground-based telescopes. For information on such techniques, and the fields of speckle imaging and speckle interferometry, the reader should consult the reference by McAlister (1985).

We describe some of the effects of the atmosphere on images, including selected relations based on the theory of atmospheric turbulence. The relations given by this theory are not derived; for thorough discussions of the theory of turbulence applied to optical astronomy the reader should consult the references by Roddier (1981) and Coulman (1985). We consider the effects of turbulence from the point of view of the time-averaged modulation transfer function (MTF) of the atmosphere.

### 16.1. EFFECTS OF ATMOSPHERIC TURBULENCE

The most notable effect of a turbulent atmosphere is a blurred image in the focal plane of a telescope. For a large telescope the image size, often called the seeing disk, is usually larger than the diffraction disk. The angular radius of the Airy disk and the limit of resolution  $\alpha_1$ , from Eq. (10.2.9), can be written as

$$\alpha_1(\text{arc-sec}) = 0.25 \lambda(\mu\text{m})/D(\text{m}). \quad (16.1.1)$$

If the radius  $\alpha$  of the seeing disk is 0.5 arcsec and  $\lambda = 0.5 \mu\text{m}$ , we get  $\alpha = \alpha_1$  for a 25-cm telescope. Thus for visible wavelengths and 1-m or larger telescopes, the image size is determined by atmospheric effects. Because  $\alpha_1 \propto \lambda/D$  the seeing disk may be comparable to the diffraction disk at infrared wavelengths for large telescopes, especially at the longest wavelengths that reach the ground.

#### 16.1.a. SEEING AND SCINTILLATION

The effect of atmospheric turbulence on stellar images is usually separated into two distinct phenomena. *Seeing* is the term used to describe random changes in the direction of light entering a telescope, while *scintillation* refers to random fluctuations in the intensity. Both of these effects arise from variations in the index of refraction and give rise to a distorted wavefront. A cross section of such a wavefront reaching the ground at a given instant of time is shown schematically in Fig. 16.1.

We first describe the effects of seeing and scintillation on a stellar image as observed with the eye. Scintillation is most evident to the unaided eye as the phenomenon called “twinkling.” In a telescope the twinkling is usually not seen, and a photometer is needed to record the fluctuations in intensity. In general, the larger the aperture the smaller are the fractional changes in the intensity.

The effect of seeing is a function of the telescope aperture. In good seeing, with a 10-cm aperture or less, the Airy disk of a star moves randomly about its mean position in the focal plane with excursions of 1 or 2 arc-seconds. In a large telescope, 1 m or larger, a blurred image is seen with little or no motion of the

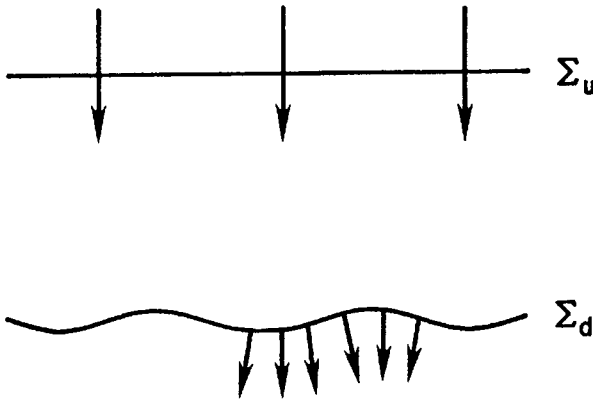


**Fig. 16.1.** Cross sections of undistorted wavefront  $\Sigma_u$  at top of atmosphere and distorted wavefront  $\Sigma_d$  at ground, after passage through turbulent atmosphere.

image as a whole. If the eye could follow the rapid changes within the image, it would see a changing pattern of speckles, each speckle having a size comparable to an Airy disk. A given speckle pattern is stationary over times on the order of 10–50 msec, with two patterns similar only for point sources within about 10 arc-sec of one another.

From these observations we deduce that the curvature of the wavefront is negligible over distances of the order of 10 cm, with instantaneous slopes of 1 or 2 arc-sec from an undistorted wavefront. The image seen in a large telescope is thus the average over many sections of the wavefront, each with a different instantaneous slope.

### 16.1.b. MODULATION TRANSFER FUNCTIONS

The demonstration that wavefront distortions arise from variations in index of refraction was discussed in Chapter 3 from the point of view of Fermat's Principle. This approach was adequate for showing the origin of seeing, but a more fruitful approach is one based on a theory of atmospheric turbulence. We now present selected results derived from a statistical approach, with results taken from Roddier (1981).

We first consider the image of a point source that has been broadened by seeing to a width large compared to the diffraction width. An approximate form for the distribution of energy within such an image is a Gaussian, with the normalized intensity given by

$$i(\alpha) = \exp(-\alpha^2/2\sigma^2), \quad (16.1.2)$$

where  $\alpha$  is the angular distance from the image peak and  $\sigma'$  is the rms deviation in a given direction from the peak. To find the MTF we substitute Eq. (16.1.2) into Eq. (11.1.8), adjust the normalization factor to give  $T(0) = 1$ , and get

$$T_a(v) = \exp(-2\pi^2\sigma'^2v^2). \quad (16.1.3)$$

If the unit of  $\sigma'$  is arc-seconds, the unit of  $v$  is cycles per arc-sec. Note the correspondence between these relations for  $i(\alpha)$  and  $T(v)$  with Eqs. (11.1.17) and (11.1.18). Equation (11.1.18) gives the pointing degradation function, and its product with the telescope MTF is the system MTF in the presence of pointing error. Equation (16.1.3) can be taken as the system MTF provided the telescope MTF is essentially unity over the range where  $T(v)$  is effectively nonzero.

As an illustration, we choose  $\sigma'$  to give an image whose FWHM is 0.5 arc-sec. Setting  $i(\alpha) = 0.5$  with  $\alpha = 0.25$  arc-sec in Eq. (16.1.2) gives  $\sigma' = 0.212$  arc-sec. Substituting this value of  $\sigma'$  in Eq. (16.1.3), we find  $T = 0.029$  for  $v = 2$  cycle/arc-sec. This is the effective cutoff frequency and is small compared to the diffraction cutoff frequency  $D/\lambda$  for a large telescope. For an 8-m telescope at  $\lambda = 500$  nm we get  $v_c = D/\lambda = 77.6$  cycles/arc-sec, and in this case we are justified in taking Eq. (16.1.3) as the system MTF.

Following the procedure in Section 11.1 we rewrite Eq. (16.1.3) in terms of the normalized spatial frequency. The resulting *atmospheric degradation function* is

$$T_a(v_n) = \exp(-2\pi^2\sigma^2v_n^2), \quad (16.1.4)$$

where  $\sigma = \sigma'(D/\lambda)$ ,  $v_n = v(\lambda/D)$ , and the subscript  $a$  denotes the atmosphere. Figure 16.2 shows  $T_a$  from Eq. (16.1.4) for  $D = 8$  m and  $\sigma' = 0.212$  arc-sec, at  $\lambda = 0.5$  and  $2 \mu\text{m}$ , superposed on the MTF for a perfect telescope with no central obscuration.

Although Eq. (16.1.3) is a reasonable approximation to the MTF of a large ground-based telescope, it is an ad hoc relation based solely on a statistical approach. This relation does not, for example, indicate how the rms seeing value might depend on wavelength or zenith angle.

An approach based on the physics of the so-called Kolmogorov turbulence gives an MTF that leads to a better description of the observed image profile. A detailed discussion of this approach and the resulting MTF and degradation function, both as given by Roddier (1981), are

$$T_K(v) = \exp\left[-3.44\left(\frac{\lambda v}{r_0}\right)^{5/3}\right]. \quad (16.1.5)$$

$$T_K(v_n) = \exp\left[-3.44\left(\frac{D}{r_0}v_n\right)^{5/3}\right], \quad (16.1.6)$$

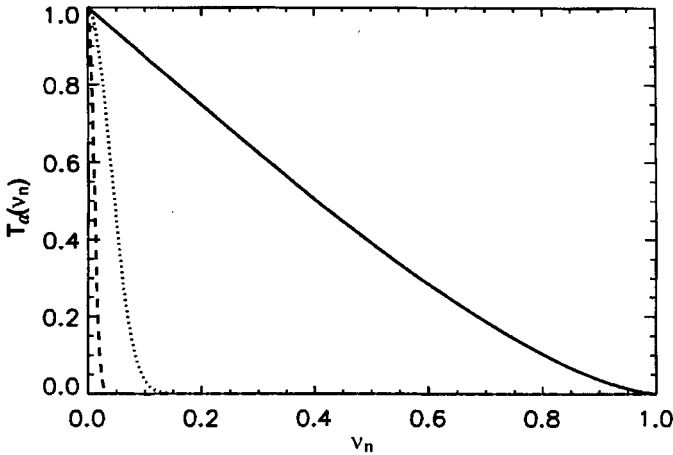


Fig. 16.2. Degradation function  $T_a(v_n)$  for atmospheric turbulence according to Eq. (16.1.4) superposed on MTF for perfect telescope. Perfect MTF (solid line);  $\lambda = 0.5 \mu\text{m}$  (dashed line);  $\lambda = 2 \mu\text{m}$  (dotted line). See text following Eq. (16.1.4) for values of the other parameters.

where  $v$  is the angular frequency and  $r_0$  is a wavelength-dependent length that is a measure of the seeing quality. As noted by Roddier, these  $T(v)$  are appropriate for a long-exposure image.

The parameter  $r_0$  is defined such that the angular resolution of a telescope is set by the atmosphere when  $D > r_0$ , and set by the telescope when  $D < r_0$ . For a large telescope limited by seeing, the limiting angular resolution for an unobstructed circular aperture is approximately

$$\alpha_0 \cong 1.22(\lambda/r_0). \quad (16.1.7)$$

The specific form of  $r_0$  is given by

$$r_0 = 0.185\lambda^{6/5}(\cos \gamma)^{3/5}\Sigma^{-3/5}, \quad (16.1.8)$$

where  $\gamma$  is the zenith angle and  $\Sigma$  is a function integrated through the atmosphere that is a measure of the turbulence. The reader should consult the reference by Roddier cited here for details on the function  $\Sigma$ .

It is evident from Eq. (16.1.8) that  $r_0$  increases with increasing wavelength and decreases with increasing zenith angle. At  $\gamma = 45^\circ$ ,  $r_0$  is approximately 20% smaller than at the zenith. In the examples to follow, we assume  $\gamma$  is zero.

Figure 16.3 shows  $T_K(v)$  from Eq. (16.1.5) for  $\lambda = 0.5 \mu\text{m}$  and  $r_0 = 26 \text{ cm}$ , with the latter value chosen to give  $\alpha_0 = 0.5 \text{ arc-sec}$ . Also shown in Fig. 16.3 for comparison is  $T_a(v)$  from Eq. (16.1.3) with the FWHM = 0.5 arc-sec.

The profile of a point spread function (PSF) is the Fourier transform of the corresponding  $T(v)$ , as discussed in Section 11.1. For the long-exposure MTF in

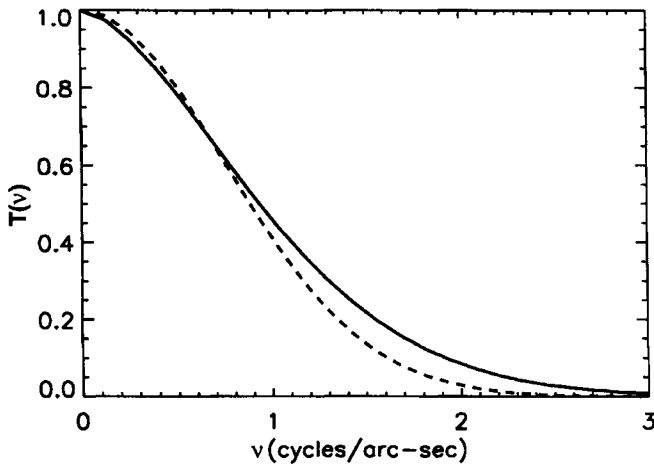


**Fig. 16.3.** Modulation transfer functions  $T_K(v)$  (solid line) at  $\lambda = 0.5 \mu\text{m}$  and  $r_0 = 26 \text{ cm}$  and  $T_a(v)$  (dashed line) with FWHM = 0.5 arc-sec. The curves are computed for an 8-m telescope with Eqs. (16.1.5) and (16.1.3), respectively.

Eqs. (16.1.5) or (16.1.6) we use Eq. (11.1.9) or (11.1.12), respectively, to find the PSF profile. Substituting Eq. (16.1.6) into Eq. (11.1.12) we get the PSFs at  $\lambda = 0.5$  and  $1 \mu\text{m}$  shown in Fig. 16.4. The parameters used are the same as those in Fig. 16.3. Because  $T_K(v)$  is approximately a Gaussian function, so also is its PSF. A comparison of the profiles in Fig. 16.4 with those found using the Gaussian MTF in Eq. (16.1.4) shows similar image cores, but a more rapid decrease in the wings of the Gaussian PSF.

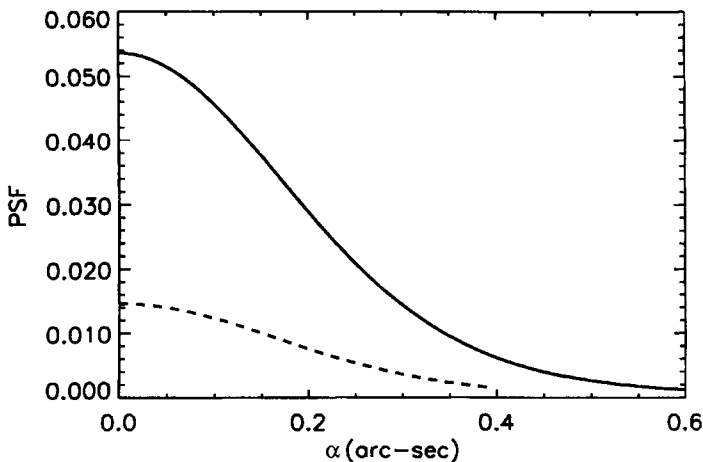


**Fig. 16.4.** Point spread functions for 2-m telescope at  $\lambda = 0.5 \mu\text{m}$  (dashed line) and  $1 \mu\text{m}$  (solid line) for  $T_K(v)$  from Fig. 16.3.

Table 16.1

Angular Resolution for Constant Turbulence<sup>a</sup>

$\lambda(\mu\text{m})$	$r_0(\text{cm})$	$\alpha_0(\text{arc-sec})$	$\alpha_1(\text{arc-sec})$
0.5	26	0.50	0.016
2.2	150	0.37	0.07
10.0	940	0.28	0.31

<sup>a</sup> $\Sigma$  in Eq. (16.1.8) is held constant.

An important feature of note in Fig. 16.4 is the Strehl ratio  $S$ , the normalized intensity at the peak of each PSF. A diffraction-limited PSF has  $S \geq 0.80$ , hence the effect of the turbulence used to find the PSFs in Fig. 16.4 is to dramatically decrease the Strehl ratio. This decrease, in turn, affects the limiting magnitude and provides an incentive to correct for wavefront distortion.

Table 16.1 gives values of  $r_0$ ,  $\alpha_0$ , and  $\alpha_1$  for several wavelengths, assuming the same constant  $\Sigma$  in Eq. (16.1.8), hence same turbulence, for each. The values of  $\alpha_1$  are calculated from Eq. (16.1.1) assuming an 8-m telescope. The improvement in resolution with increasing wavelength is evident from these results. Note also that diffraction, negligible in the visible compared to seeing, grows in significance in the infrared and is larger than the turbulence effect at  $\lambda = 10 \mu\text{m}$ .

All of the preceding results are based on the long-exposure MTF given in Eq. (16.1.5). Roddier (1981) also gives an expression for a short-exposure MTF, and the reader should consult this reference for details.

## 16.2. CORRECTION OF WAVEFRONT DISTORTION

From our results in the previous section, especially Fig. 16.4, it is clear that atmospheric turbulence has a drastic negative effect on angular resolution and limiting magnitude of ground-based telescopes. Given that the seeing parameter  $r_0 \propto \lambda^{6/5}$ , these negative effects are larger for shorter wavelengths and it not surprising that the techniques of adaptive optics were first applied at infrared wavelengths. The ease of correction depends strongly on the size of  $r_0$ , hence on the wavelength, as examples in this section demonstrate.

### 16.2.a. SOME BASIC RELATIONS

In order to illustrate the requirements for adaptive optics systems, we first present some of the necessary relations needed in our discussion. In this section, we draw on an excellent review by Beckers (1993).

Detection and compensation of the phase variations on the wavefront are usually done by measuring the wavefront of a reference object near the target object. This method succeeds if the angular separation between these two objects is less than the *isoplanatic angle*  $\theta_0$ . A good approximation to this angle is

$$\theta_0 \cong 0.3(r_0/H), \quad (16.2.1)$$

where  $H$  is the average distance of the turbulent layer. This angle corresponds to a lateral shift of  $0.3r_0$  between wavefronts from sources separated by  $\theta_0$ , hence the overlap in common area between the wavefronts is approximately 60%.

At separations of  $\theta_0$  the rms difference between the reference and target wavefronts is  $\cong \lambda/6$ . For  $r_0 = 26$  cm, from the first line in Table 16.1, and  $H = 5$  km, we find  $\theta_0 = 3.4$  arc-sec. In the visual range only a small fraction of the desired targets have suitable reference objects within the isoplanatic angle. This has led to development of laser guide stars, a topic we comment on briefly in the following section. The situation for natural reference objects in the infrared is decidedly more favorable.

Another angle related to  $\theta_0$  is the *isoplanatic angle for image motion*  $\theta_m$ . This is the angular distance over which image motions are very similar. An approximate relation for this angle is  $\theta_m \cong 0.3(D/H) \cong \theta_0(D/r_0)$ .

Another factor of crucial importance in applying the techniques of adaptive optics to correct for the phase variations is the rate at which the wavefront changes. This rate depends on wind velocities at different heights in the atmosphere. An approximate time scale for significant change is

$$\tau_0 \approx 0.3(r_0/V_{\text{wind}}). \quad (16.2.2)$$

For  $r_0 = 26$  cm and  $V_{\text{wind}} = 10$  m/sec, we find  $\tau_0 \cong 0.008$  sec. It is again evident that the situation for detection and compensation of phase variations is more favorable in the infrared than in the visual range.

### 16.2.b. PARTIAL WAVEFRONT CORRECTION

The parameter  $r_0$ , formally called the Fried parameter, can be thought of as the maximum diameter of a telescope whose performance is not seriously limited by atmospheric turbulence. Thus  $r_0$  is effectively the diameter of an undistorted seeing cell with the number of cells over a telescope aperture  $\sim (D/r_0)^2$ . Correction of a wavefront requires sensors to detect the deviations of an actual wavefront from an ideal plane wavefront and act on a deformable mirror to correct in real time. For a telescope of diameter  $D$ , the number of sensors required to approach correction giving diffraction-limited performance equals the number of seeing cells over the aperture. With  $r_0 \sim 10$ – $20$  cm for visible wavelengths, it

is evident that reaching near complete correction with a large telescope is very difficult, at best, in the visual range and challenging in the infrared.

The phase or path differences of a wavefront entering a telescope relative to a plane wavefront can be characterized in terms of any set of orthogonal functions, although Zernike polynomials are those most often used. Beckers states that the uncorrected rms phase variation across a circular aperture for variations caused by Kolmogorov turbulence is

$$\omega_0 \text{ (waves)} = 0.162(D/r_0)^{5/6}. \quad (16.2.3)$$

Note that setting  $r_0 = D$  gives  $\omega \cong \lambda/6$ . This is not diffraction-limited performance as defined in Chapter 10, but the Airy peak is still prominent.

If the lowest Zernike modes, those of *tip-tilt* ( $x$ - and  $y$ -tilt in Table 10.5), are compensated, then the residual mean square wavefront error is 13% of that for the uncompensated wavefront. If the next three Zernike modes are removed, focus and astigmatism in Table 10.5, the residual mean square error is 6%. The corresponding rms wavefront errors remaining for these two cases are

$$\omega_2 \text{ (waves)} = 0.058(D/r_0)^{5/6}, \quad (16.2.4)$$

$$\omega_5 \text{ (waves)} = 0.040(D/r_0)^{5/6}, \quad (16.2.5)$$

where the subscript on  $\omega$  denotes the total number of compensated modes. For a large number of compensated modes, the rms wavefront error remaining is

$$\omega_j \text{ (waves)} = 0.086j^{-5/12}(D/r_0)^{5/6}. \quad (16.2.6)$$

A comparison of Eqs. (16.2.3) and (16.2.4) shows that the dominant effect of turbulence on the wavefront entering a telescope is tilt of the entire wavefront.

It is instructive to take Eqs. (16.2.3)–(16.2.5) and find  $D/r_0$  that corresponds to the diffraction limit of  $\sim \lambda/14$  or 0.071 waves. Applying this to Eq. (16.2.4), for example, gives  $D/r_0 = 1.28$ . Thus a relatively simple tip-tilt device sufficient to achieve diffraction-limited performance in the far infrared would not be able to do the same in the visual range. From Eq. (16.2.6) we find that the number of compensated modes needed to reach the diffraction limit is  $\sim (D/r_0)^2$ .

It is also important to note that partial compensation of atmospheric turbulence leads to a larger Strehl ratio  $S$  and fainter limiting magnitude. For the two cases corresponding to Eqs. (16.2.4) and (16.2.5), Roddier states that the maximum improvement factors for  $S$  are 5 and 10, respectively.

The impact of atmospheric turbulence on the Strehl ratio is evident from the PSFs in Fig. 16.4. Following the procedure in Section 16.1 for computing PSFs using Eqs. (16.1.6) and (11.1.12), we find values of  $S$  for a range of  $D/r_0$ . The results are shown in Fig. 16.5 as a function of wavefront error given by Eq. (16.2.3). Also shown in Fig. 16.5 is a line for the ratio  $(r_0/D)^2$  plotted versus  $\omega_0$ .

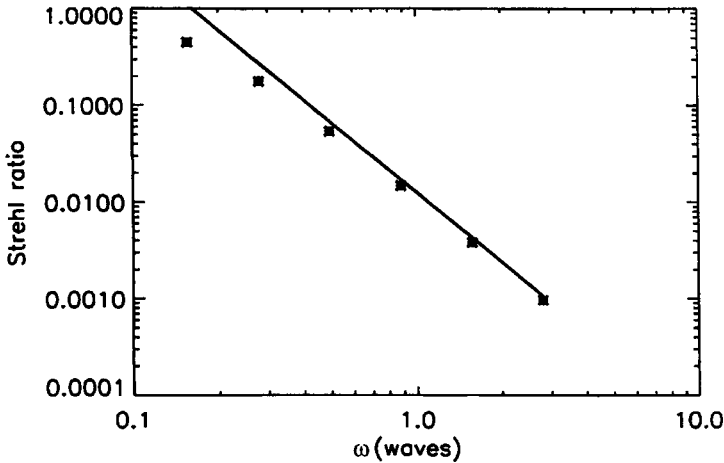


Fig. 16.5. Strehl ratios for PSFs blurred by atmospheric turbulence as a function of the uncorrected rms wavefront error. The solid line is  $(r_0/D)^2$ . See text for discussion.

For large wavefront errors the average intensity over a blurred image and the normalized peak intensity are proportional to this ratio, the area of the Airy disk divided by the area of the blurred image.

Partial correction of the wavefront gives an increased  $S$  and the emergence of a peak whose FWHM is  $\sim \lambda/D$ . These changes in the PSF are easily illustrated by taking the MTF degradation factor for midfrequency statistical error given in Eq. (11.1.15). The correlation length  $l$  in  $c(v_n)$  is a measure of the structure on a wavefront and, for atmospheric turbulence, we take  $l = (r_0/D)$ . With this change in Eq. (11.1.15), we get MTF degradation factor for partial correction

$$T_{pc} = \exp \{-k^2 \omega^2 [1 - c(v_n)]\}, \tag{16.2.7}$$

where  $k = 2\pi/\lambda$ ,  $\omega$  is the remaining rms wavefront error, and  $c(v_n)$  is modeled as a Gaussian in the form

$$c(v_n) = \exp (-4v_n^2(D/r_0)^2). \tag{16.2.8}$$

As an example, we take the PSF for  $\lambda = 1 \mu\text{m}$  in Fig. 16.4, with  $D = 2 \text{ m}$  and  $\alpha_0 = 0.5 \text{ arc-sec}$  as the remaining parameters. From Eqs. (16.1.7) and (16.2.3) we get  $r_0 = 0.524 \text{ m}$  and  $\omega_0 = 0.50 \text{ waves}$ . Choosing  $\omega = 0.2 \text{ waves}$ , we find  $T_{pc}$  from Eqs. (16.2.7) and (16.2.8), multiply by  $T_d$  for a perfect system, and use the resulting  $T$  in Eq. (11.1.12) to find the PSF.

The MTFs for this example are shown in Fig. 16.6, including the uncorrected MTF degradation factor from Eq. (16.1.6). Note that the MTF for the partially corrected system has an extended tail not present in the MTF for the uncorrected

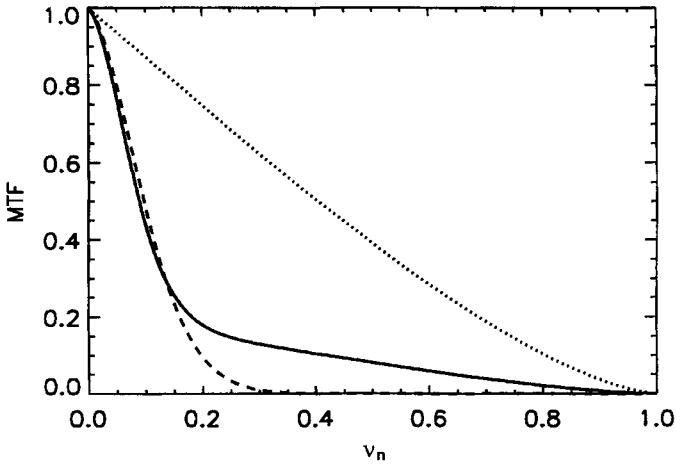


**Fig. 16.6.** The MTF for a partially corrected wavefront (solid line) with  $\omega = 0.2$  waves according to Eq. (16.2.7). Perfect MTF (dotted line); uncorrected MTF (dashed line). See text following Eq. (16.2.8) for values of the other parameters.

system. The PSFs for these MTFs are shown in Fig. 16.7. Note the presence of a diffraction-limited core whose FWHM  $\cong 0.12$  arc-sec and an increase in  $S$  of a factor of 4.4. In effect, the partial correction has moved some of the energy from the inner part of the blurred image into a sharp core and left the outer parts essentially unchanged.

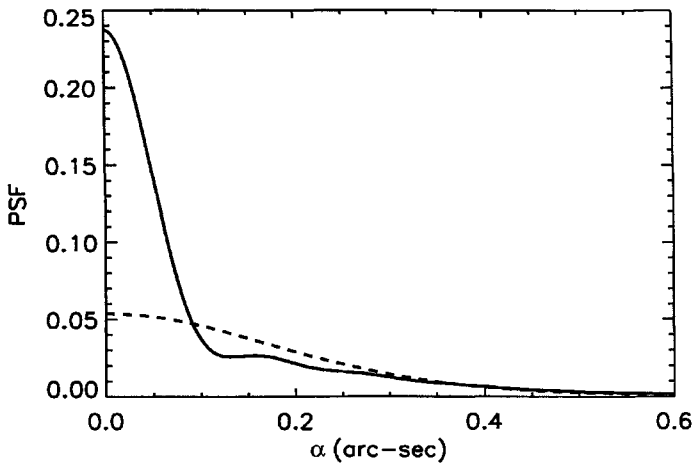


**Fig. 16.7.** The PSFs at  $\lambda = 1 \mu\text{m}$  for partially corrected MTF (solid line) and uncorrected MTF (dashed line). The MTFs are shown in Fig. 16.6.

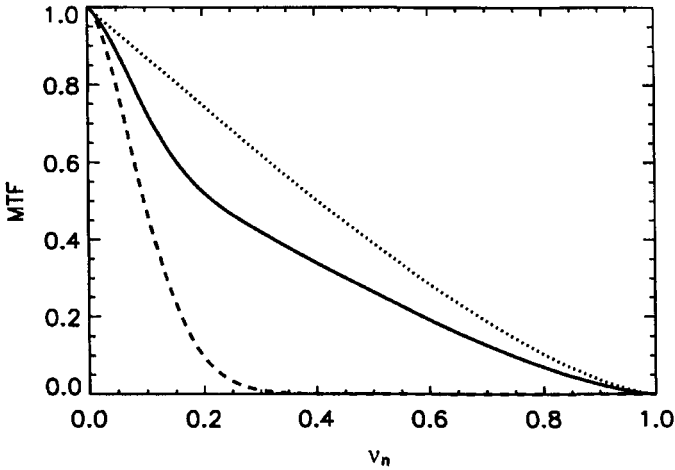


**Fig. 16.8.** The MTF for a partially corrected wavefront (solid line) with  $\omega = 0.1$  waves according to Eq. (16.2.7). Perfect MTF (dotted line); uncorrected MTF (dashed line). Other parameters are the same as those for Fig. 16.6.

Following the same procedure, but choosing  $\omega = 0.1$  waves, we get the results shown in Fig. 16.8 for the MTF and Fig. 16.9 for the PSF. With this choice of  $\omega$  the system is approaching the diffraction limit at which  $S = 0.80$ . A semilog plot of the PSF with  $\omega = 0.1$  waves shows the presence of several bright Airy rings around the main Airy peak.

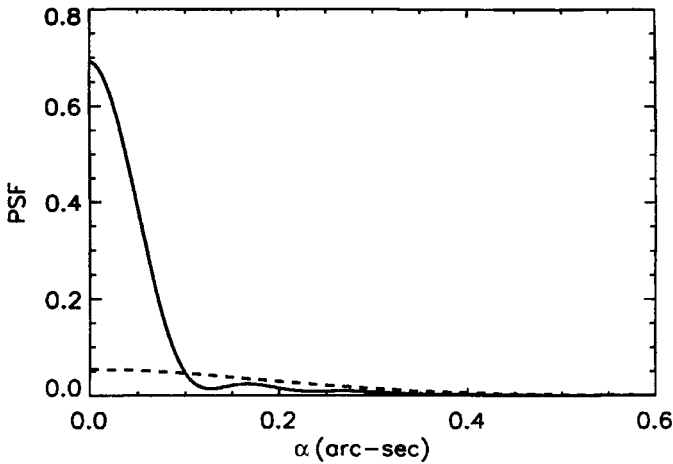


**Fig. 16.9.** The PSFs at  $\lambda = 1 \mu\text{m}$  for partially corrected MTF (solid line) and uncorrected MTF (dashed line). The MTFs are shown in Fig. 16.8.

This discussion of the effects of atmospheric turbulence on image characteristics and their partial correction is only an overview of a large subject area, but should suffice to give the reader an idea of the basic concepts. For a thorough discussion of the many facets of adaptive optics, consult the text by Tyson (1991).

### 16.3. ADAPTIVE OPTICS: SYSTEMS AND COMPONENTS

From our preceding discussion we see that the requirement for an adaptive optics system is a means of measuring the phase variations over an incoming wavefront and using that information to effectively flatten the wavefront in real time. In this section we consider some of the basics of the optical elements used in adaptive optics systems.

#### 16.3.a. AN OVERVIEW

A schematic diagram illustrating the essential components of an adaptive optics system is shown in Fig. 16.10. Light from the images of a target object and a reference source at an angular separation less than the isoplanatic angle  $\theta_0$  is collimated by a mirror or lens. The collimator forms an image of the entrance pupil on a deformable mirror DM and a second optical system following a tip-tilt mirror TTM reimages the target and reference objects. For a system making tip-tilt corrections only, the deformable mirror is not a part of the optical train.

Light from the target is sent to a reimaging camera or to a spectrometer, while the light from the reference is sent to a wavefront sensor. All of the optics in the reference beam is configured to reimage the pupil on the wavefront sensor. The

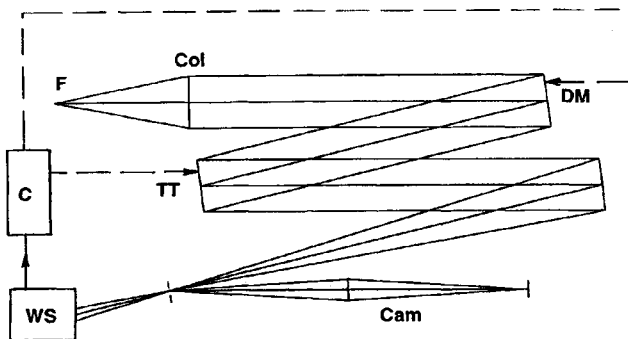


**Fig. 16.10.** Schematic of an adaptive optics system. F, telescope focus; Col, collimator; DM, deformable mirror; TT, Tip-tilt mirror; Cam, camera; WS, wavefront sensor; C, computer.

computer-processed signal from the wavefront sensor is then fed back to DM and TTM to compensate for the detected phase errors in the beam at the sensor. Thus the target beam is reflected from two mirrors that have been adjusted to correct for the detected atmospheric turbulence.

The number of sensor elements needed to correctly sample the distortions of the incoming beam and achieve near diffraction-limited performance is  $\sim(D/r_0)^2$  and the rate at which the sampling is done is governed by  $\tau_0$  in Eq. (16.2.2). Sampling at time intervals longer than  $\tau_0$  results in degraded correction. Other important considerations include the number of detected photons within one sampling time and the SNR for this sample.

### 16.3.b. ADAPTIVE MIRRORS

A deformable mirror is generally one of two types, a segmented mirror or a mirror with a continuous faceplate. Each mirror in a segmented mirror is adjusted separately in tip-tilt and piston (in an axial direction). Tip-tilt adjustments are controlled by the wavefront sensor, but axial adjustments must be controlled separately to ensure approximate continuity of the overall surface. The desired number of separate mirrors is  $\sim(D/r_0)^2$ , each with its own set of actuators.

Continuous faceplate mirrors are usually driven by bidirectional actuators using piezoelectric materials, with fewer actuators required because continuity is automatically ensured. This type of mirror also avoids the problems of light loss and diffraction caused by the gaps between the elements of a segmented mirror. Continuous mirrors are the usual choice for adaptive optics systems intended for faint sources.

### 16.3.c. WAVEFRONT SENSORS

A commonly used wavefront sensor is the Hartmann-Shack sensor shown schematically in cross-section in Fig. 16.11. An image of the telescope pupil is located on an array of lenslets, each of which reimages a portion of the incident wavefront on a detector array. For a fully adaptive system the size of each lenslet is approximately  $r_0$ . The image from each lenslet is shifted if the part of the wavefront being reimaged is tilted, with the magnitude of the shift at the detector proportional to the tilt angle and the direction of the shift giving the azimuth of this angle.

The composite of these numbers gives the information needed to find the overall tilt of the entire wavefront in azimuth and angle, while the separate shifts give similar information on each portion of the wavefront. The former is fed to the tip-tilt mirror and, for a fully adaptive system, the latter to the deformable mirror.

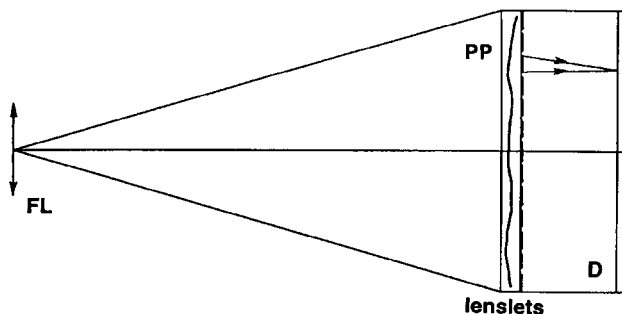


**Fig. 16.11.** Schematic cross section of a Hartmann-Shack wavefront sensor. The FL, field lens; PP, pupil plane; D, detector. Edge-rays are shown for one lenslet.

Advantages of a sensor of this type include simplicity, compactness, and sensitivity over a broad wavelength range with nearly all of the light from the reference object sent to the detector. The CCD arrays with low read-out noise and high quantum efficiency are the detector of choice for visible and near infrared wavelengths. Beckers gives a table of limiting magnitudes per lenslet for different spectral bands and a set of assumptions about seeing conditions and the detector. For the R-band this limit is about  $V = 10$ . The reader should consult the review by Beckers (1993) for details.

## 16.4. CONCLUDING REMARKS

In this chapter we have provided some of the basics needed to understand the importance of the field of adaptive optics. We have not discussed the variety of wavefront sensors used in these systems or the details of adaptive mirrors. Nor have we discussed in detail the important area of laser guide stars. Here we give a brief look at the impetus behind the work in this latter area, but leave the specifics to specialists in the field.

The principal limitation in applying adaptive optics is the lack of natural reference stars of sufficient brightness near any given target object. The small size of the isoplanatic angle in the visible range, typically 1 or 2 arc-sec, translates into the likelihood of finding a suitable reference star of roughly 1 in 10,000 at an average galactic latitude. For infrared wavelengths this limit is less severe, with a likelihood of about 1% at  $2.2 \mu\text{m}$  and near unity at a wavelength of  $10 \mu\text{m}$ . This limitation can be largely removed by using an artificial guide star provided by the reemission of light from sodium atoms in a layer in the upper atmosphere illuminated by a sodium laser beam. A good introduction to this rapidly developing field is given by Beckers (1993).

Our final comments are directed toward the applications of adaptive optics, especially in an era of 8- to 10-m telescopes. The advantages for imaging are obvious when the difference between diffraction-limited and seeing-limited resolution is large. The diffraction limit from Eq. (16.1.1) is approximately 0.01 arc-sec for an 8-m telescope, or about 1 parsec at the distance of the Virgo cluster. Better resolution is also accompanied by a fainter limiting magnitude for point sources, a topic we discuss further in the Chapter 17.

The advantages of adaptive optics for spectrometry are equally impressive. Our discussion in Chapter 15, especially that based on Eq. (15.2.1), shows the need for larger spectrometers if the resolving power-slit width product is to be maintained with larger telescopes. In the diffraction limit we substitute  $\lambda$  for  $\phi D$  to get the limiting spectral resolving power, as pointed out in Section 12.5. To ensure that most of the light in a diffraction-limited image passes through the aperture of a spectrometer, a more practical substitution is  $2\lambda$  for  $\phi D$ . By replacing  $\phi D$  with  $2\lambda$  in Eqs. (15.2.1) and (15.2.3), we find that the dependence on the telescope diameter vanishes. As pointed out in an example in Section 12.5, this also means that the need for fast cameras also vanishes.

We leave it to the reader to further explore the advantages of adaptive optics.

## REFERENCES

- Beckers, J. (1993). *Annual Review of Astronomy and Astrophysics*, **31**: 13, Palo Alto, CA: Annual Reviews.
- Beckers, J. and Goad, L. (1987). in *Instrumentation for Ground-Based Astronomy*, Robinson, L. (ed). p. 315, New York: Springer-Verlag.
- Coulman, C. (1985). *Annual Review of Astronomy and Astrophysics*, **23**: 19, Palo Alto, CA: Annual Reviews.
- Roddier, F. (1981). *Progress in Optics*, **19**, Chap. 5, Amsterdam: North-Holland.
- Tyson, R. (1991). *Principles of Adaptive Optics*, New York: Academic Press.

## BIBLIOGRAPHY

### *Speckle interferometry*

- McAlister, H. (1985). *Annual Review of Astronomy and Astrophysics*, **23**, 59. Palo Alto, CA: Annual Reviews.

### *Reviews and Conference Proceedings*

- Ealey, M. and Merkle, F. (eds.). (1994). *Proc. SPIE Int. Soc. Opt. Eng.* **2201**.
- Fugate, R. (ed.). (1992). *Laser Guide Star Adaptive Optics Workshop*, Albuquerque, New Mexico.
- Roddier, F. (ed.). (1989). *Proc. SPIE Int. Soc. Opt. Eng.* **1114**.
- Woolf, N. (1982). *Annual Review of Astronomy and Astrophysics*, **20**, 367, Palo Alto, CA: Annual Reviews.

Given a particular telescope and instrument combination, it is essential to know its capabilities for making a specific type of observation. To determine these capabilities requires not only a knowledge of the telescope and instrument characteristics, but also those of other parts of the overall system. The system as used here includes the detector and, in the case of ground-based telescopes, the atmosphere. The ability of a given system to measure a given signal is then determined by including all of these factors in a system analysis.

In this chapter we discuss those characteristics of detectors that are important for the detection and resolution of point sources. We consider a detector in terms of its modulation transfer function (MTF) and the effect this has on resolution of images. We discuss the characteristics of some types of solid-state detectors and use these results in examples of limiting magnitude calculations. We do not discuss the physics of detectors.

In most cases the output of a detector includes both the desired signal from the source being observed and “noise” from unwanted sources. This noise can arise from many different sources, such as light from the sky background in the vicinity of the object under study, and noise intrinsic to the detector in the form of dark current for a photomultiplier or dark counts for a photon-counting detector. For solid-state detectors there is also read noise introduced during the process of reading out the accumulated information stored on the array of pixels.

In the absence of sky background and detector noise, the recorded signal shows fluctuations due to “photon noise.” The source of this noise arises from statistical fluctuations in the number of recorded photons about some average value, where the average number of detected photons is found from a large number of identical exposures. Analysis of the effect of any noise contributor is done in terms of SNR, the topic of one of the sections in this chapter.

The final section of this chapter is a discussion of the detection limits in the presence of noise for different types of observations. Included are relations appropriate to direct imaging, and spectrometric observations for both slit-limited and slitless modes. Examples of selected modes are given for both ground-based telescopes and HST.

## 17.1. DETECTOR CHARACTERISTICS

With few exceptions, the detectors used for imaging and spectroscopy in the visible and infrared are solid-state devices, such as the charge-coupled device (CCD), based on the properties of semiconductors. The details of the physics of these devices can be found in monographs on detectors; characteristics of typical large solid-state detectors of interest in this chapter are given in Table 17.1.

For our purposes the important detector parameters are pixel size, quantum efficiency, intrinsic noise, MTF, and Nyquist sampling. We discuss each of these in turn in this section.

### 17.1.a. PIXELS, QUANTUM EFFICIENCY, AND INTRINSIC NOISE

A *pixel* or picture element is a single detector element in an array of elements, for example, as a single diode on a detector such as those in Table 17.1. Pixel

**Table 17.1**  
Nominal Characteristics of Large Solid-State Arrays

	CCD	HgCdTe	InSb
Format	2048 × 4096	1024 × 1024	1024 × 1024
Pixel ( $\mu\text{m}$ )	15 × 15	20 × 20	27 × 27
Size (mm)	30 × 60	20 × 20	30 × 30
Dark/Pixel	1 $e^-$ /hour	0.1 $e^-$ /sec	0.1 $e^-$ /sec
Quantum Efficiency	400–700 nm > 70%	1–2 $\mu\text{m}$ ~ 70%	1–5 $\mu\text{m}$ ~ 80%
Longwave Limit	~ 1 $\mu\text{m}$	~ 2.5 $\mu\text{m}$	~ 5.5 $\mu\text{m}$
Read Noise ( $e^-$ rms)	4	20	25
Full Well	200,000	100,000	300,000

sizes are typically in the range 10–30  $\mu\text{m}$ . Matching pixel size to image or spectral resolution is an important consideration in the design of most systems, as has been noted on numerous occasions in earlier chapters.

If  $n_i$  is the number of photons per sec incident on a detector and  $n_0$  is the number of detected photons, the *quantum efficiency*  $Q$  is defined as  $Q = n_0/n_i$ . For a sensitive photographic plate  $Q$  is a few percent at best, while for a CCD detector the quantum efficiency approaches unity for red wavelengths. Given the rapid development of CCD technology, especially in area and number of pixels, this detector is now the choice for nearly all spectrometric and direct imaging systems in the visible and near infrared.

The principal noise contribution in the output of most electronic detectors is the *dark current* or, equivalently, the *dark count*, or number of electrons per sec per pixel generated in the absence of an input light signal. The size of the dark count is reduced by cooling the detector and can often be reduced to a negligible level. For detectors such as those in Table 17.1 an additional noise contributor is the *read noise*, usually given as some number of equivalent electrons rms. These noise factors are included in the discussion of SNR and relations for detection limits in later sections.

For more details on particular detectors the reader should consult data sheets prepared by manufacturers and references devoted to discussions of detectors.

### 17.1.b. MODULATION TRANSFER FUNCTION OF IDEAL PIXEL

The detection characteristics of a pixel array are determined in large part by the pixel size, which, in turn, can be described in terms of a detector MTF. An ideal detector is one for which the counts from a given pixel are completely independent of those from neighboring pixels, hence an ideal pixel can be represented as a rectangular well.

Consider such a pixel of dimensions  $a$  and  $b$  in the  $x$ - and  $y$ -directions, respectively. We derive an MTF by defining this rectangular aperture as a PSF according to

$$\begin{aligned} i(x, y) &= 1, & |x| < a/2 & \text{ and } |y| < b/2, \\ &= 0, & |x| > a/2 & \text{ or } |y| > b/2, \end{aligned} \quad (17.1.1)$$

where the pixel center is at  $x = y = 0$ . Substituting Eq. (17.1.1) into Eq. (11.1.6) gives the normalized MTF as

$$T_{\Delta}(v_x, v_y) = \text{sinc}(\pi v_x a) \text{sinc}(\pi v_y b), \quad (17.1.2)$$

where  $\text{sinc}(z) = (\sin z)/z$ . The spatial frequencies in Eq. (17.1.2) are defined following Eq. (11.1.6), where  $\gamma$  is the orientation of the input sine target, discussed in Section 11.1, relative to the  $x, y$  coordinate system. If the lines of

the sine target are parallel to  $x$  or  $y$ , one sinc function in Eq. (17.1.2) becomes one.

Assuming square pixels of side  $\Delta$  and  $v_x = v$ , Eq. (17.1.2) becomes

$$\begin{aligned} T_{\Delta}(v) &= \text{sinc}(\pi v \Delta), \\ T_{\Delta}(v'_n) &= \text{sinc}(\pi v'_n), \end{aligned} \quad (17.1.3)$$

where we define a detector normalized frequency  $v'_n = v\Delta$ . Note that the MTF and normalized detector frequency are independent of wavelength. In the discussion to follow we take Eq. (17.1.3) as the representation of an ideal pixel array.

The system MTF, including detector, is the product  $T(v)T_{\Delta}(v)$ , where  $T(v)$  includes the factors in Eq. (11.1.14) for a system with aberrations. Following the procedure in Chapter 11, we rewrite this product in terms of the normalized spatial frequency of the system. Denoting the overall system MTF by  $T_s$  we get

$$T_s(v_n) = T(v_n) \text{sinc} \left[ \pi \left( \frac{\Delta}{\lambda F} \right) v_n \right] = T(v_n) \text{sinc} \left( \frac{\pi v_n}{N} \right), \quad (17.1.4)$$

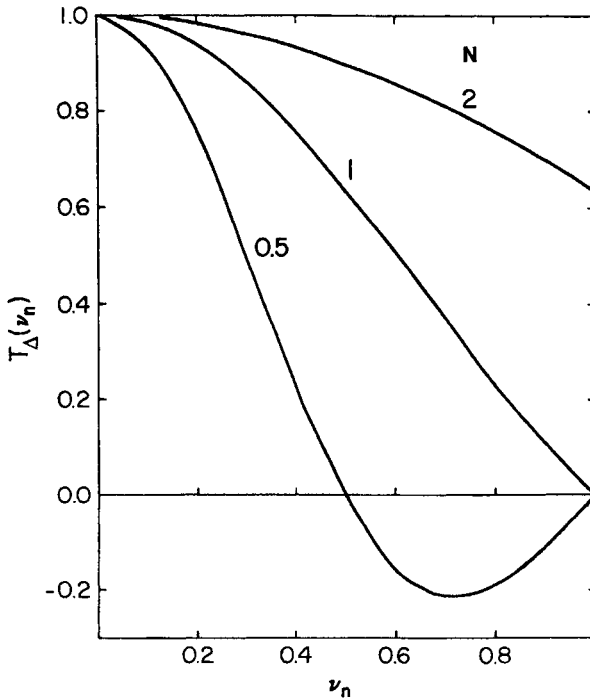


**Fig. 17.1.** Pixel MTF for different values of  $N$  based on Eq. (17.1.4). Here  $N = \lambda F/\Delta$ , where  $\Delta$  is the pixel size.

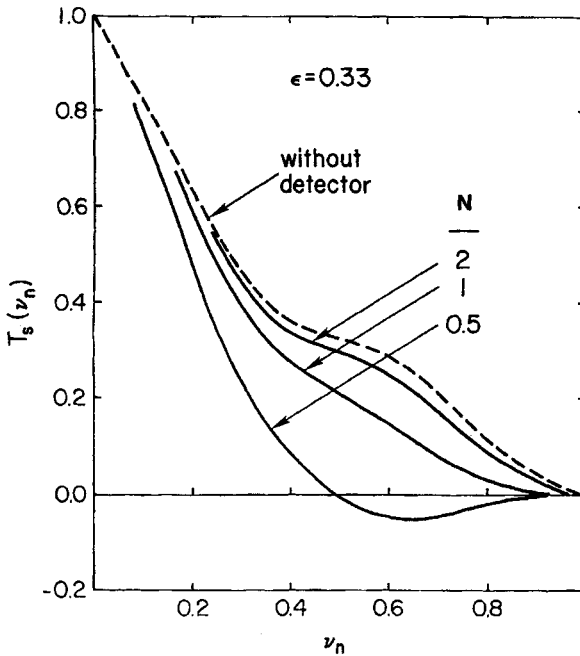


**Fig. 17.2.** System MTF including detector for circular aperture with central obscuration. Detector MTF is shown in Fig. 17.1.

where  $N = \lambda F / \Delta =$  number of pixels per length  $\lambda F$ . From Eq. (10.2.9) we see that  $\lambda F$  is the approximate radius of the Airy disk.

Figure 17.1 shows pixel MTFs for three different values of  $N$ . Note that the MTF is negative for some  $v_n < 1$  when  $N < 1$ . System MTFs for a perfect system with a circular aperture and  $\epsilon = 0.33$  are shown in Fig. 17.2 for each detector MTF in Fig. 17.1. The effect of the detector MTF is evident by inspection of the curves in Fig. 17.2. For  $N = 2$  there is little change of the MTF due to the optics only, with progressively greater change as  $N$  decreases. Note that high-frequency information is lost or masked for  $N = 0.5$ . This is not surprising, given that a single pixel spans an Airy disk diameter in this case.

### 17.1.c. MODULATION TRANSFER FUNCTION AND NYQUIST SAMPLING

According to the Nyquist criterion for discrete sampling, two samples per resolution element are required for unambiguous resolution of images that are

just resolved according to the Rayleigh criterion. With a linear separation at the Rayleigh limit given by  $\lambda F$ , the Nyquist criterion is satisfied with a pixel size  $\Delta = \lambda F/2$ , hence  $N = 2$ . Strictly speaking, this criterion applies to a sampling in one direction, but it is also appropriate for panoramic sampling.

Given  $N = \lambda F/\Delta$ , the curves in Fig. 17.1 change in proportion to wavelength with  $F/\Delta$  held constant. If, for example, the curve for  $N = 2$  is appropriate for wavelength  $\lambda$ , then the  $N = 1$  curve is appropriate for  $\lambda/2$  with the same pixel size and focal ratio. In this case, therefore, an image that is correctly sampled at longer wavelengths is not adequately sampled at shorter wavelengths.

We now apply these results to selected HST cameras assuming: (1) a perfect telescope; and (2) a pixel MTF of the form given in Eq. (17.1.4). The first assumption is not far from correct for visible and longer wavelengths but is a poor assumption in the far ultraviolet. The second assumption presumes an ideal pixel and may not be strictly valid for a real detector. Nevertheless, we proceed with these assumptions to illustrate the general characteristics of HST cameras in selected modes.

Listed in Table 17.2 are the focal ratios of the direct imaging modes of the advanced camera for surveys (ACS) in the visible and near infrared and the near-infrared camera and multiobject spectrometer (NICMOS). Also given in Table 17.2 is the width of a pixel projected on the sky for each mode. Note that the pixel size of the  $f/17.2$  wide-field mode of NICMOS is larger than the FWHM, given in Fig. 11.15, for all wavelengths to which it is sensitive. For the wide-field mode of ACS we see that the Nyquist criterion is nearly satisfied at a wavelength of  $1 \mu\text{m}$ , the longwave limit of the CCD. The Nyquist criterion is satisfied for the  $f/80$  camera of NICMOS at  $1 \mu\text{m}$ , but in this case the range of sensitivity extends to about  $2.5 \mu\text{m}$ .

Taking the entries for  $F/\Delta$  in Table 17.2, we get the lines representing  $N$  for each of the camera modes shown in Fig. 17.3. For each mode the range of

**Table 17.2**

Selected Characteristics of HST Cameras<sup>a</sup>

ACS			NICMOS		
$F$	$\Delta(\text{arc-sec})$	$F/\Delta^b$	$F$	$\Delta(\text{arc-sec})$	$F/\Delta$
26	0.050	1.73	17.2	0.20	0.43
72	0.025	3.43	45	0.076	1.13
			80	0.043	2.00

<sup>a</sup> ACS:  $\Delta = 15 \mu\text{m}$  for  $f/26$  mode (Wide Field Camera);  $\Delta = 21 \mu\text{m}$  for  $f/72$  mode (High-resolution Camera); and NICMOS:  $\Delta = 40 \mu\text{m}$ .

<sup>b</sup> The unit of  $F/\Delta$  is  $\mu\text{m}^{-1}$ .

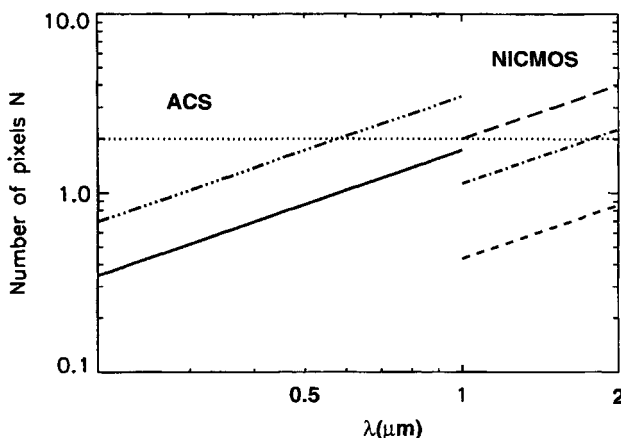


**Fig. 17.3.** Number of pixels spanning length  $\lambda F$  for selected camera modes of the Hubble Space Telescope. See Table 17.2 for values of  $F/\Delta$ . ACS:  $f/72$  (dash-dot-dot-dot),  $f/26$  (solid); NICMOS:  $f/80$  (long dash),  $f/45$  (dash-dot),  $f/17.2$  (short dash).

wavelengths for which  $N > 2$  is the range in which the image of a point source is oversampled. When  $N = 2$  there are approximately twelve pixels covering the Airy disk.

It is important to note that detection of a single point source does not require a large number of pixels covering the Airy disk. For the  $f/26$  mode of the WFC of ACS, for example, most of the energy of a single star image in the blue and near ultraviolet is recorded on four pixels, sufficient for many types of observations.

#### 17.1.d. APPROXIMATE PIXEL MODULATION TRANSFER FUNCTION

An approximate relation often used to represent the MTF of a square pixel is a Gaussian profile of the form

$$T_{\Delta}(v) = \exp[-0.282(\pi v \Delta)^2], \quad (17.1.5)$$

where the constant 0.282 is chosen to make  $T_{\Delta} = 0.5$  at  $v = 1/2\Delta$ . Figure 17.4 shows  $T_{\Delta}$  for a sinc function and Gaussian, the former according to Eq. (17.1.3) and the latter from Eq. (17.1.5). If curves like those in Fig. 17.2 are generated using Eq. (17.1.5) rather than Eq. (17.1.3), the resulting system MTFs are little different except that the curve for  $N = 0.5$  does not go negative. The general comments made about Fig. 17.2 are also true for the modified MTFs. Because the MTF and PSF are a Fourier transform pair, the PSF for Eq. (17.1.5) is also a Gaussian.

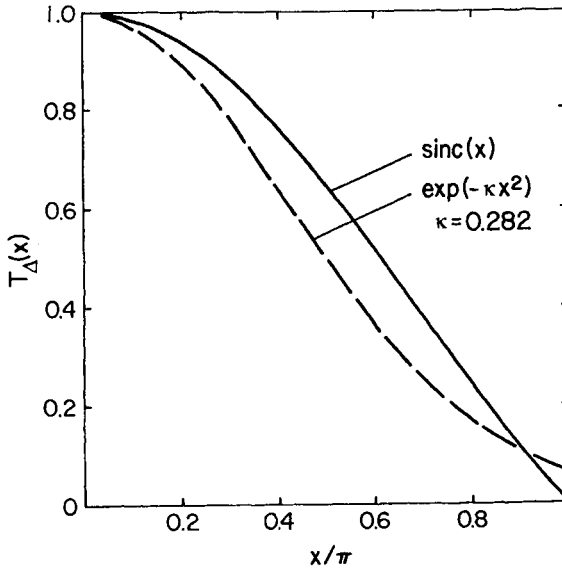


Fig. 17.4. Plot of sinc and Gaussian representations of pixel MTF. See Eq. (17.1.5) and the following discussion.

#### 17.1.e. IMAGE SHARPNESS AND SAMPLING

The importance of Nyquist sampling is shown by an application involving finding the best focus of a camera or telescope. If an image is diffraction-limited or nearly so, then the following *sharpness algorithm* provides a means of finding the optimum focus. This algorithm has the form

$$\Sigma = \sum_{i,k} I_{ik}^2 \div \left( \sum_{i,k} I_{ik} \right)^2, \quad (17.1.6)$$

where  $I_{ik}$  is the intensity of the image for pixel  $(i, k)$  of an  $(M \times M)$  array centered on the image. The value of  $M$  selected is not critical but it should be large enough to span one or two bright rings around the Airy disk. For a properly sampled image with  $N = 2$  pixels per length  $\lambda F$ , a good choice is  $M = 7$ .

The intensity is measured for an image at each of several focus positions. In a Cassegrain telescope, such as HST, this is simply done by moving the secondary mirror. The value of  $\Sigma$  is then computed for each image according to Eq. (17.1.6). These results, when plotted on a graph, show a maximum for  $\Sigma$  at best focus.

We now outline an exercise applying this algorithm to diffraction-limited images of different wavelengths imaged with a given detector. If we choose

$\lambda = 1 \mu\text{m}$ ,  $F = 30$ , and pixel size  $\Delta = 15 \mu\text{m}$ , then there are two pixels spanning length  $\lambda F$ . For this correctly sampled wavelength, the value of  $\Sigma$  does not depend on the precise position of the peak of the PSF on the pixel array. Whether this peak is centered on one pixel or is at a corner of a pixel is of no consequence. If, however, a PSF of a shorter wavelength is used, then the PSF is undersampled ( $\lambda F < 2\Delta$ ) and the position of the PSF on the array does affect the value of  $\Sigma$ . Not surprisingly,  $\Sigma$  is largest for an undersampled wavelength when the peak of the PSF is centered on one pixel.

## 17.2. SIGNAL-TO-NOISE RATIO

The performance of a system is most often given in terms of a quantity called the *signal-to-noise ratio* (SNR). The signal is the total number of detected photons on a given pixel, denoted here by  $n_s$ . If the signal is recorded a large number of times under identical conditions, the mean signal is  $\langle n_s \rangle$  with a statistical fluctuation in the number of detected photons about the mean. This fluctuation is a consequence of the random arrival rate of the photons at the detector and the random selection of those that are detected.

The variance or mean square noise in the signal is  $\langle n_s \rangle$ , and the standard deviation or noise is  $\sqrt{\langle n_s \rangle}$ . For an ideal detector, one giving only counts from the incident light, the SNR in the presence of photon noise is

$$\text{SNR} = \langle n_s \rangle / \sqrt{\langle n_s \rangle} = \sqrt{\langle n_s \rangle}. \quad (17.2.1)$$

For a real detector measuring a signal in the presence of a background source, the mean square noise from uncorrelated sources is the sum of the variances of the separate sources, and the SNR is

$$\text{SNR} = \langle n_s \rangle / \sqrt{\langle n_s \rangle + \langle n_b \rangle + \langle n_d \rangle}, \quad (17.2.2)$$

where  $\langle n_b \rangle$  is the noise from the background, and  $\langle n_d \rangle$  is the number of extraneous counts from the detector. The extra detector counts are due to dark counts and, in the case of solid-state detectors, read noise. The *fractional accuracy* for a given SNR is defined as  $1/\text{SNR}$ , thus an observation with 1% accuracy requires a SNR of 100. It is evident from Eq. (17.2.2) that better accuracy is achieved with smaller  $\langle n_d \rangle$ .

We now consider two limiting cases of SNR for an ideal detector, one with zero background, the other with background large compared to the signal. Let  $S$  and  $B$  denote the incident signal and background flux, respectively, in photons per

second on an ideal detector. If the exposure time is  $t$  and the quantum efficiency is  $Q$ , then the SNRs are

$$\text{SNR} = \sqrt{SQt}, \quad B \ll S, \quad (17.2.3a)$$

$$\text{SNR} = \sqrt{SQt} \cdot \sqrt{S/B}, \quad B \gg S. \quad (17.2.3b)$$

It is instructive to examine these relations for SNR from two different perspectives. Consider first the situation where  $S$  and  $B$  are constant, and observations are made of the same source with different detectors and/or exposure times. In both cases we see that the  $\text{SNR} \propto \sqrt{Qt}$ , hence a larger  $Q$  with a given exposure time or a longer exposure with the same  $Q$  gives a larger SNR. It is also evident that increasing the SNR by a factor of  $k$  requires a  $Qt$  product that is  $k^2$  times larger.

Alternatively, consider two sources with signal flux  $S_1$  and  $S_2$ , respectively, observed against the same background  $B$  to the same SNR level. From Eq. (17.2.3a,b) we get

$$\frac{S_1}{S_2} = \frac{Q_2 t_2}{Q_1 t_1}, \quad \text{signal-limited}, \quad (17.2.4a)$$

$$\frac{S_1}{S_2} = \left( \frac{Q_2 t_2}{Q_1 t_1} \right)^{1/2}, \quad \text{background-limited}. \quad (17.2.4b)$$

As a numerical example, let  $t_1 = t_2$  and  $Q_2/Q_1 = 6.3$ . In the signal-limited case  $S_2 = S_1/6.3$ ; in the background-limited case we have  $S_2 = S_1/2.5$ . Thus the more sensitive detector can observe a source that is two stellar magnitudes fainter in the signal-limited case, but only one magnitude fainter in the other case, for the same exposure time and SNR.

From Eqs. (17.2.3) it is evident that the SNR achieved with a given detector is larger with a longer exposure time. Consider a single exposure of length  $t$  compared to  $k$  separate exposures, each of length  $t/k$ . For each short exposure, the SNR is  $\sqrt{k}$  smaller than for the single long exposure for either case in Eqs. (17.2.3). By replacing  $t$  by  $k \cdot t/k$  in Eq. (17.2.3) we see that

$$\text{SNR}_1 = \sqrt{k \cdot \text{SNR}_k}, \quad (17.2.5)$$

where the subscripts 1 and  $k$  refer to the long and short exposures, respectively. It follows, therefore, that the SNR of  $k$  added exposures is the same as that of a single long exposure, where the total exposure time is the same for both.

As a final limiting case, consider the situation where the detector noise is large compared to either the background or signal. Assuming the detector noise is due

to both dark counts and read noise, the SNR for the detector-limited case can be written as

$$\text{SNR} = SQ_t / \sqrt{Ct + R^2}, \quad (17.2.6)$$

where  $C$  is the dark count per second and  $R$  is the rms read noise. If read noise is negligible compared to dark count, the addition of  $k$  separate short exposures leads to the result given in Eq. (17.2.5). If  $R$  is dominant, however, then the SNR for  $k$  added exposures is smaller than that of a single long exposure by a factor of  $\sqrt{k}$ .

This treatment is sufficient to illustrate how system performance is specified in terms of SNR. We now use this parameter to give a more detailed analysis for both photometry and spectroscopy.

### 17.3. DETECTION LIMITS AND SIGNAL-TO-NOISE RATIO

Most telescope/instrument systems are used for observations that are at or near the limits of the system. These limits are due to source faintness, sky background, limited observing time, detector noise, or any combination of these. It is therefore important to determine how each of these affects the magnitude limit that can be reached at a given SNR. Treatments like the one that follows have been given by several authors, including Baum (1962), Code (1973), and Bowen (1964). References are listed at the end of the chapter.

In this section we consider three types of observations and the relation between source brightness, exposure time, and SNR in the presence of various factors that degrade the SNR. Types of observations discussed include stellar photometry, slit-limited spectroscopy at various resolutions, and slitless spectroscopy. For each observation mode we illustrate the general results with graphs for the HST and large ground-based telescopes of various diameters, using detector characteristics suitable for each. We assume in all cases that the light is collected by a single telescope; situations in which an array of telescopes sends light to one or more instruments are discussed by Cede (1973).

We begin with the expression for the photon flux collected by a telescope of diameter  $D$  and transmitted to the detector. For a star of apparent magnitude  $m$ , the signal flux is

$$\begin{aligned} S &= N_0 \tau \frac{\pi}{4} (1 - \varepsilon^2) D^2 \Delta\lambda \cdot 10^{-0.4m}, \\ &= 0.7 N_0 \tau D^2 \Delta\lambda \cdot 10^{-0.4m}, \end{aligned} \quad (17.3.1)$$

where we set  $\pi(1 - \varepsilon^2)/4 = 0.7$ , assuming a typical  $\varepsilon$  for a Cassegrain telescope. This factor is included in all the relations that follow. The remaining factors in Eq.

(17.3.1) are defined as follows:  $N_0 = 10^4$  photons/(sec cm<sup>2</sup> nm) for a zero-magnitude A0 star at a wavelength of 550 nm,  $\tau$  is the system transmittance from the top of the atmosphere to the detector (not including slit losses), and  $\Delta\lambda$  is the bandpass of the instrument used. For photometry the bandpass is defined by a filter; for spectroscopy the bandpass is set by the spectrometer.

The photon flux from the sky background is given by

$$B = 0.7N_0\tau D^2\Delta\lambda' \cdot 10^{-0.4m'}\phi\phi', \quad (17.3.2)$$

where  $\Delta\lambda'$  is the bandpass of sky on the detector,  $m'$  is sky brightness in magnitudes per arc-second squared, and  $\phi\phi'$  is the detector area in arc-seconds squared projected on the sky. For stellar photometry and slit spectroscopy  $\Delta\lambda' = \Delta\lambda$ ; for slitless spectroscopy the two bandpasses are different.

In terms of photon flux, quantum efficiency  $Q$ , and exposure time  $t$ , we write Eq. (17.2.2) as

$$\text{SNR} = \frac{\kappa SQt}{\sqrt{(\kappa S + B)Qt + Ct + R^2}} = \frac{\kappa SQt}{\sqrt{\kappa SQt + \langle n_u \rangle}}, \quad (17.3.3)$$

where  $C$  and  $R$  are the dark counts per sec and rms read noise, respectively, as used in Eq. (17.2.6), and  $\langle n_u \rangle$  is the sum of all contributors to the noise.

The factor  $\kappa$  in Eq. (17.3.3) is included to account for factors not included in the transmittance of the system. In some photometric modes, for example, some fraction of the flux in a stellar image may not fall on a given pixel or group of pixels. For the HST, for example, the fraction of the energy on a set of pixels centered on the image depends on the camera mode. The same is true for a ground-based telescope measuring an image with a Gaussian profile. For slit spectroscopy part of the image at the entrance slit may be intercepted by the slit jaws and not reach the detector, or the signal of interest may be the core of an absorption line. The factor  $\kappa$  can account for these factors.

Other useful forms of Eq. (17.3.3) are obtained by solving this relation for either  $m$  or  $t$ . We choose to solve Eq. (17.3.3) for  $m$ , with Eq. (17.3.1) substituted for  $S$ . The result is

$$m = -2.5 \log \left[ \frac{(\text{SNR})^2}{1.4N_0\kappa\tau\Delta\lambda D^2Qt} \left( 1 + \left( 1 + \frac{4\langle n_u \rangle}{(\text{SNR})^2} \right)^{1/2} \right) \right]. \quad (17.3.4)$$

Representative results obtained from Eq. (17.3.4) for various combinations of parameters in different observation modes are given in the sections that follow.

Before considering specific telescope and detector combinations, it is instructive to look at two limiting cases for a noise-free detector, signal-limited and background-limited. In the former case we assume  $\langle n_u \rangle$  is negligible; in the latter case  $\langle n_u \rangle = BQt$  and is large compared to the signal.

In the signal-limited case Eq. (17.3.4) becomes

$$m = -2.5 \log \left[ \frac{(\text{SNR})^2}{0.7 N_0 \kappa \tau \Delta \lambda D^2 Q t} \right], \quad (17.3.5)$$

while in the background-limited case

$$m = 0.5 m' - 1.25 \log \left[ \frac{(\text{SNR})^2 \phi \phi'}{0.7 N_0 \kappa \tau \Delta \lambda D^2 Q t} \right]. \quad (17.3.6)$$

We first consider the situation where observations for a fixed bandpass are made with different telescopes and/or detectors to the same SNR level. We also assume  $\phi = \phi'$  and constant sky brightness. Starting with Eq. (17.3.5) or Eq. (17.3.6), we find the difference of the magnitudes reached as a function of the remaining variables, for the same SNR. For the signal-limited case we get

$$m_2 - m_1 = 2.5 \log \left[ \left( \frac{D_2}{D_1} \right)^2 \frac{\tau_2 Q_2 t_2}{\tau_1 Q_1 t_1} \right], \quad (17.3.7)$$

and for the background-limited case

$$m_2 - m_1 = 1.25 \log \left[ \left( \frac{D_2 \phi_1}{D_1 \phi_2} \right)^2 \frac{\tau_2 Q_2 t_2}{\tau_1 Q_1 t_1} \right]. \quad (17.3.8)$$

From Eq. (17.3.7) we see that doubling the telescope diameter with all other parameters held constant gives  $\Delta m = 1.5$ ; for Eq. (17.3.8) the same conditions give  $\Delta m = 0.75$ . Thus the faintness of a star observed to the same SNR is proportional to the telescope area in the signal-limited case, but only proportional to the telescope diameter in the background-limited case.

We see from Eq. (17.3.8) that the faintness of a star observed to the same SNR is inversely proportional to the image area with all other parameters constant. For ground-based telescopes the importance of good seeing in reaching faint magnitudes is therefore evident. In the event that the image diameter is determined by diffraction rather than seeing, Eq. (17.3.8) is modified by replacing  $\phi_1/\phi_2$  by  $D_2/D_1$ , and the faintness of a star observed to the same SNR is again proportional to the telescope area.

We now consider the situation where the same telescope and detector are used for observations made to different SNR levels. In this case the result for signal-limited observations is

$$m_2 - m_1 = -5 \log (\text{SNR}_2/\text{SNR}_1), \quad (17.3.9)$$

and for background-limited observations

$$m_2 - m_1 = -2.5 \log (\text{SNR}_2/\text{SNR}_1). \quad (17.3.10)$$

Therefore the slope in a log (SNR) versus magnitude plot is different by a factor of two in the two regions.

#### 17.4. DETECTION LIMITS: STELLAR PHOTOMETRY

We now take Eq. (17.3.4) and give results for HST and ground-based telescopes of different aperture, each with the same detector and filter characteristics. The parameters used for the calculations are given in Table 17.3, with characteristics for the CCD taken from Table 17.1.

We choose  $\kappa = 0.8$  for all telescopes and assume this fraction of the transmitted light contributes to the detected signal. For the wide-field mode of ACS, the fraction  $\kappa$  of a stellar image falls on a few pixels. For a large ground-based telescope, the fraction  $\kappa$  of an image with a Gaussian profile typically covers many pixels. The number of pixels  $j$  spanning the image is given, in appropriate units, as

$$j = \frac{\text{width}}{\text{pixel size}} = \frac{5FD(m)\phi(\text{arc-sec})}{\Delta(\mu\text{m})}. \quad (17.4.1)$$

We assume the total read noise is proportional to  $j^2$ , hence there is no on-chip summing before readout. The dark count is also, of course, proportional to  $j^2$ .

Results obtained from Eq. (17.3.4) with the parameters in Table 17.3 are shown in Fig. 17.5 for an exposure time of 2400 sec, the approximate time available in the dark part of one HST orbit. From the results in Fig. 17.5 it is evident that the ground-based observations are primarily in the background-

Table 17.3

Detector and Telescope Parameters

Other	$m'$ [mag/(arc-sec) <sup>2</sup> ]	$\phi$ (arc-sec)	$F$
Detector	$\Delta = 15 \mu\text{m}$ , $R = 5e^-$ rms/pixel, $C = 0.003e^-$ /(pixel sec), $\kappa = 0.8$ , $Q = 0.8$ ,		
Telescope	$\tau = (0.9)^2 = 0.81$		
Filter	$\tau = 0.8$ , $\Delta\lambda = 100 \text{ nm}$ (V-band)		
Relay Optics	$\tau = 0.5$		
WFC of ACS	23	0.1	26
Ground	22	1.0	2.5

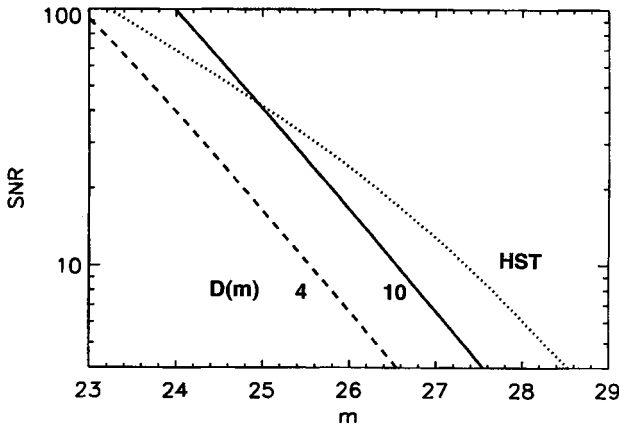


Fig. 17.5. Representative SNR-apparent magnitude diagram for photometry. Values of the parameters are given in Table 17.3.  $D = 4$  m (dashed line);  $D = 10$  m (solid line); HST (dotted line).

limited region, while those with the WFC of ACS are in the transition between the signal-limited and background-limited regimes.

It is also of interest to note that the noise contribution of the detector is negligible, compared to the sky background, for each of the ground-based telescopes at the chosen focal ratio. For each of these telescopes the sky contribution is approximately 1000 times larger than the detector noise. For the HST, on the other hand, both the sky and detector noise are smaller, especially the former. The net result for this camera mode of the HST is detector noise comparable to the sky noise. At small SNR the effect of the detector noise is to reduce the limiting magnitude by about 0.4 magnitudes.

The results for the ground-based telescopes in Fig. 17.5 are based on a sky brightness of 22 mag/square arc-sec. If the sky is fainter by 0.5 magnitudes, the curves for these telescopes are shifted to the right by 0.25 magnitudes, as shown by Eq. (17.3.6). This change is not as pronounced as that obtained with better seeing; for an image diameter smaller by a factor of two the curves are shifted to the right by 0.75 magnitudes.

The effect of better seeing is especially significant if adaptive optics are used to sharpen the image and increase the Strehl ratio. If, for example, the effective image size is reduced to 0.2 arc-sec, then the curves for the ground-based telescopes in Fig. 17.5 are shifted to the right by 1.75 magnitudes.

The results in Fig. 17.5 are intended only as an illustration of the relation between SNR and limiting magnitude for one given set of parameters. Because of the many variables that influence this relation, each particular telescope-filter combination requires its own set of calculations.

### 17.5. DETECTION LIMITS: SPECTROSCOPY

Calculation of detection limits for spectroscopy requires a careful analysis of the type of spectrometer and the mode in which it is used. In this section we consider slit and slitless modes, and stellar and extended sources. Selected examples of representative telescope/spectrometer combinations are given.

#### 17.5.a. SLIT SPECTROSCOPY-STELLAR SOURCES

The calculation of SNR for slit spectrometers proceeds by using Eqs. (17.3.3) and (17.3.4) modified for different source or observing conditions. For a stellar source there are two cases—the star image fits entirely within the slit, or part of the image falls on the slit jaws. If the star image is entirely within the slit we set  $\kappa = \kappa_0$ ; if part of the image is intercepted by the slit we set  $\kappa = \kappa_0(\phi/\phi')$ , where  $\phi'$  is the diameter of the image and  $\phi$  is the slit width projected on the sky. The slit-limited case is the usual one with large telescopes, especially at high resolution. The factor  $\kappa_0$  is the level of the signal relative to the continuum. For an emission line  $\kappa_0 > 1$ ; in the core of an absorption line  $\kappa_0 < 1$ .

Incorporating this factor into Eq. (17.3.4) gives

$$m = -2.5 \log \left[ \frac{(\text{SNR})^2(\phi'/\phi)}{1.4N_0\kappa_0\tau\Delta\lambda D^2 Q t} \left( 1 + \left( 1 + \frac{4(n_u)}{(\text{SNR})^2} \right)^{1/2} \right) \right]. \quad (17.5.1)$$

In the case where  $\phi = \phi'$ , Eq. (17.5.1) is the same as Eq. (17.3.4) at the continuum level and the limiting cases for a noise-free detector are given by Eqs. (17.3.5) and (17.3.6). The only difference for a spectrometer is  $\Delta\lambda = Pw'$ , where  $P$  is the plate factor and  $w'$  is the projected slit width in the spectrometer focal plane.

In the slit-limited case we use Eq. (12.2.1) to express  $\phi$  in terms of the projected slit width, hence  $\phi = w'/rDF_2$ . This is required because  $\phi$  and  $\Delta\lambda$  are not independent of one another. With this substitution into Eq. (17.5.1) we see that one factor of  $D$  is canceled. The limiting cases for a noise-free detector are

$$m = -2.5 \log \left[ \frac{(\text{SNR})^2 r F_2 \phi'}{0.7N_0\kappa_0\tau P w'^2 D Q t} \right] \quad (17.5.2)$$

in the signal-limited case, and

$$m = 0.5m' - 1.25 \log \left[ \frac{(\text{SNR})^2 r F_2 \phi'^3}{0.7N_0\kappa_0^2\tau P w'^2 D Q t} \right] \quad (17.5.3)$$

in the background-limited case.

**Table 17.4**  
Spectrometer Parameters

	Grating 600 grooves/mm, $m = 1$	Echelle $\tan \delta = 2.0$
$F_2$	1.5	2.0
$r$	0.9	0.7
$P$ (nm/mm)	5.56	0.368
$\mathcal{R}$ (at 500 nm)	3000	45,000
$\tau$ (system)	0.15	0.10
Other: $\phi' = 1$ arc-sec, $\kappa_0 = 1$ , $d_1 = 200$ mm. Projected slit $w'$ spans two pixels (30 $\mu$ m). Sky background = 22 mag/(arc-sec) <sup>2</sup> .		

From these relations we see that the faintness of a star observed to the same SNR is proportional to  $D$  in the signal-limited case, and proportional to  $\sqrt{D}$  in the background-limited case. Note that for a diffraction-limited telescope we have  $\phi' \propto 1/D$ , and the faintness reached at a given SNR is proportional to  $D^2$ .

If a given system is used to make observations to different SNR levels, the relations obtained from Eqs. (17.5.2) and (17.5.3) are the same as those given in Eqs. (17.3.9) and (17.3.10), respectively. Hence the slope in a log (SNR) versus magnitude plot is again different by a factor of two in the two regions.

We now give results derived using Eq. (17.5.1) for ground-based telescopes with representative spectrometers. The parameters of each spectrometer are given in Table 17.4; the detector used is a CCD with parameters given in Table 17.3. Results obtained from Eq. (17.5.1) with the given parameters are shown in Fig. 17.6 for an exposure time of 2400 sec. The choice of  $\kappa_0 = 1$  indicates observations at the continuum level of the stellar spectra. The detector noise is larger than the sky noise in the echelle mode by a factor of about 40; the detector and sky noise are comparable for the grating mode. Entrance slit widths are approximately 1.1 and 0.45 arc-sec for the 4- and 10-m telescopes, respectively.

In both modes the magnitude reached at SNR = 100 is close to that found from Eq. (17.5.2) for the signal-limited case. The curvature evident in Fig. 17.6 as SNR decreases indicates a transition to the detector-limited regime.

### 17.5.b. SLIT SPECTROSCOPY-EXTENDED SOURCES

The photon flux of an extended source collected by a telescope of diameter  $D$  and transmitted to the detector is given by

$$S = 0.7N_0\tau D^2\Delta\lambda \cdot 10^{-0.4m}\phi\phi', \quad (17.5.4)$$

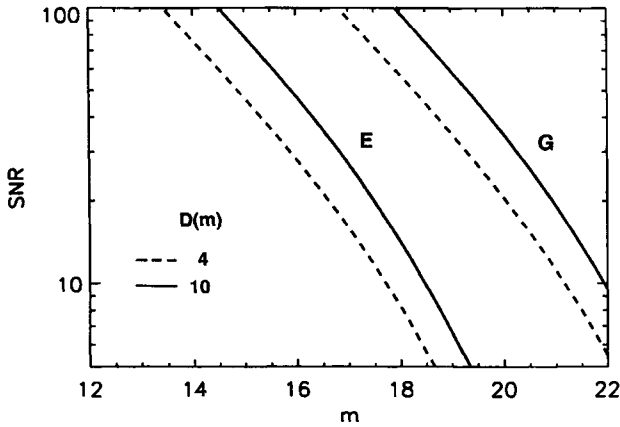


Fig. 17.6. Representative SNR-apparent magnitude diagram for spectrometry. Parameters for the detector are in Table 17.3, for the spectrometers in Table 17.4.  $D = 4$  m (dashed line);  $D = 10$  m (solid line). Curves on the left are for an echelle, those on the right for a first-order grating.

where  $m$  is the source brightness in magnitudes per square arc-sec and  $\phi\phi'$  is again the detector area in square arc-sec projected on the sky. For a source whose spectrum is a composite of stellar spectra, the parameter  $N_0$  has the nominal value given following Eq. (17.3.1); for an emission line source the product  $N_0\Delta\lambda$  is adjusted to the proper flux value. The flux from the sky background is given by Eq. (17.3.2).

For both source and sky the flux is proportional to  $D^2\phi\phi'$ , and using Eq. (12.2.1) we get  $D^2\phi\phi' = w'h'/rF_2^2$ . Hence the SNR depends on the camera focal ratio but is independent of the telescope diameter. Substituting this result in Eq. (17.3.3), we find that

$$\text{SNR} \propto (rF_2^2)^{-1/2}. \quad (17.5.5)$$

It is evident from Eq. (17.5.5) that SNR is larger for smaller  $F_2$ . This result is in accord with that given in Eq. (12.2.17) for the irradiance of an image. Thus observations of an extended source to a given SNR level, either through a spectrometer or filter, is done in a shorter time with a faster camera.

### 17.5.c. SLITLESS SPECTROSCOPY

For observations of stellar sources in the slitless mode, the source and background signals are given by Eqs. (17.3.1) and (17.3.2), respectively. In this mode  $\Delta\lambda = Pw'$  for the star signal, while  $\Delta\lambda'$  is the bandpass for all wavelengths

transmitted to the detector. For the background-limited case, assuming a noise-free detector, the only one considered here, we find

$$m = 0.5m' - 1.25 \log \left[ \frac{(\text{SNR})^2 \phi' \phi}{0.7N_0 \tau \Delta \lambda D^2 Q t} \left( \frac{\Delta \lambda'}{\Delta \lambda} \right) \right], \quad (17.5.6)$$

where  $\kappa$  is set equal to one. Note that Eq. (17.5.6) is simply Eq. (17.3.6) modified for the case of different spectral and sky bandpasses. The effect of the bandpass ratio is to give a brighter magnitude reached for a given SNR, assuming all other parameters are the same.

To illustrate the effect we assume a nonobjective transmission grating mode with a spectral resolving power  $\mathcal{R} = 100$ . If  $\Delta \lambda'$  is taken as  $\lambda/2$ , where  $\lambda$  is the wavelength at the blaze peak, then the bandpass ratio  $\Delta \lambda'/\Delta \lambda$  is approximately 50. The difference in magnitude with and without this factor is  $\Delta m = -1.25 \log(50)$ , or about 2.1 magnitudes. Although the limiting magnitude is brighter for this slitless mode, the gain is 50 spectral elements per source compared to one obtained with a narrow filter in a photometry mode.

## REFERENCES

- Baum, W. (1962). *Stars and Stellar Systems II, Astrophysical Techniques*, Chap. 1, Chicago: Univ. of Chicago Press.
- Bowen, I. (1964). *Astron. J.*, **69**, 816.
- Code, A. (1973). *Annual Review of Astronomy and Astrophysics*, **11**: 239, Palo Alto, CA: Annual Reviews.

## BIBLIOGRAPHY

*Instrument Handbooks*. Published periodically by the Space Telescope Science Institute, Baltimore, MD.

The most challenging aspect in constructing a telescope with large light gathering power and a capability of achieving high angular resolution is the primary mirror. In this chapter we discuss various aspects of building and testing mirrors, especially large concave mirrors, and the effects of residual errors on image quality, including errors that arise in the support of such mirrors. We also consider telescopes used in concert to achieve angular resolution beyond that possible with a single telescope.

### **18.1. LARGE MIRRORS**

The history of large mirrors is closely linked to the technologies of casting glass and polishing the surface to the desired shape. As these technologies developed it became possible to make both larger and faster monolithic mirrors. During the 1970s and 1980s it also became clear that the mass per unit collecting area had to be reduced. It also became evident during this time that mirrors in the 8-m class were approaching the size limit for single glass slabs and that segmented mirrors would be required for larger primaries. The outcome of these developments is a wide variety of mirror types, as shown in Table 18.1, with the order of the mirror examples given decreasing in mass per unit collecting area from top to bottom.

**Table 18.1**  
Types and Examples of Large Primary Mirrors

Type	Example
Monolithic (rigid)	
Solid (thick)	Hooker 2.5-m
Cast with cores	Hale 5-m
Spin-cast honeycomb	MMT conversion 6.5-m
Slumped honeycomb	HST 2.4-m
Monolithic (flexible)	
Solid (thin)	Gemini, VLT 8-m
Segmented	
Sphere (91 segments)	Hobby-Eberly 9-m
Paraboloid (36 segments)	Keck 10-m

### 18.1.a. MIRROR SHAPING

The figure is the basic prescription for the shape of a mirror, as given by Eq. (5.1.1). Most telescope primaries, either monolithic or segmented, have an aspheric figure, paraboloidal or hyperboloidal, although spherical mirrors are the likely choice for mirrors of the future, say 15 m or larger. Techniques for shaping large mirrors have evolved in response to the demands for faster mirrors.

For an aspheric mirror of conic constant  $K$  the local curvature on the surface is a function of the radial distance  $r$  from its center, as shown by Eq. (3.5.6) and restated here. The local radius of curvature is

$$R_{lc} = R[1 - K(\varepsilon^2/16F^2)]^{3/2}, \quad (18.1.1)$$

where  $F = |f|/D$ ,  $R$  is the vertex radius of curvature, and  $r = \varepsilon D/2$ , with  $0 < \varepsilon < 1$ . The change in curvature is more significant for smaller focal ratios and faster mirrors. As an example, for a paraboloid with  $K = -1$  and  $F = 1.25$ , the radius of curvature at the edge is about 6% larger than at the center.

These significant differences in curvature across a mirror have resulted in new techniques for polishing mirrors to the required precision. One such technique is *computer-controlled polishing* with small tools, such as used on the  $f/2.3$  primary of HST with a lap approximately 5 cm in diameter. Another technique is *stressed-lap polishing* in which the surface of a rotating lap is continuously adjusted to conform in radius to that part of the mirror below it, as used for the 6.5-m,  $f/1.25$  primary mirror of the MMT conversion (see Martin et al. (1998)).

The segmented approach has been adopted for primaries of diameter larger than about 8 m. The 9-m primary of the Hobby-Eberly Telescope (HET) and the primaries of the Keck 10-m telescopes (TMT) are examples of segmented

mirrors. The figure of each hexagonal section of HET is spherical and making high quality segments is relatively easy. For the TMTs, on the other hand, the overall figure is paraboloidal and the figure of a hexagonal section depends on the location of that section in the primary.

The technique used to polish the sections of the TMTs is called *stressed-mirror polishing*. A hexagonal mirror is bent to a prescribed shape and a spherical shape is polished onto the surface of the stressed glass. When the stresses are removed and the glass returns to its unstressed state, the surface has the desired shape of a section of an off-axis paraboloid (see Mast and Nelson (1990)).

An advantage of the segmented approach is that primaries of very large size are possible. An obvious disadvantage of this approach is the complexity of the structure required to hold the individual modules in their proper positions. For details on the modular approach to primary mirrors, the interested reader should consult the literature on the TMT project.

#### 18.1.b. TESTING

Aberration characteristics of telescopes discussed in previous chapters are derived assuming the mirrors are essentially perfect. A mirror produced in the optical shop is not perfect, however, but if the actual figure agrees with the prescription to within a specified tolerance the telescope performance is not noticeably degraded. In this section we discuss briefly the principal method used to ensure that a mirror figure is within a given tolerance. This discussion is only a quick look at a large subject and the interested reader should consult the literature for details. A good overview of a large number of testing methods is given in the book edited by Malacara (1978) cited at the end of the chapter.

For our discussion we assume that a mirror is perfect if it is diffraction-limited, that is, the rms deviation of the reflected wavefront compared to the ideal wavefront is  $< \lambda/14$ , where  $\lambda$  is the test wavelength. The definition of rms wavefront error and details on the origin of the stated condition are given in Section 10.3. The sensitivity of the test method discussed here is considerably better than the diffraction-limited criterion; wavefront errors of  $\sim \lambda/100$  can be measured.

The method most widely used for testing large concave mirrors is *Twyman-Green interferometry*, and the test device is a modified Michelson interferometer, as shown in Fig. 18.1. For testing a concave mirror, a Michelson interferometer, shown schematically in Fig. 13.16, is converted into a Twyman-Green by replacing the moveable mirror B in Fig. 13.16 with a positive lens, usually called a null lens, and the test mirror. The lens and mirror are placed so their optical axes coincide, with the focal point of the lens coincident with the center of curvature of the mirror. The other change is to use a laser plus beam expander as

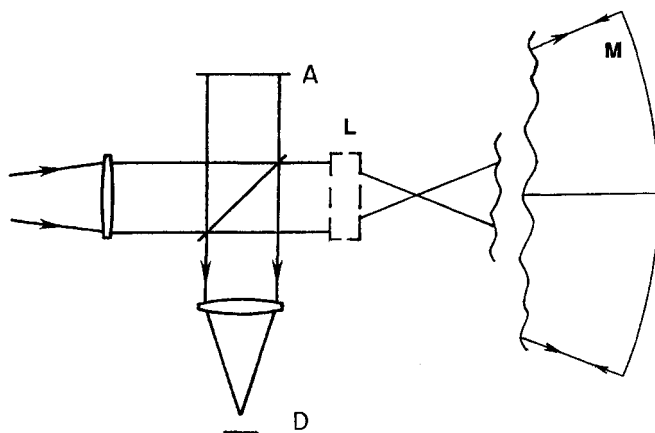


Fig. 18.1. Twyman-Green interferometer. A, fixed mirror; L, null lens; M, test mirror; D, detector.

the light source, with the pinhole in the beam expander placed at the focal point of the input collimator lens.

The beamsplitter divides the amplitude of the incident plane wavefront, which, after reflection in the two arms of the interferometer, returns to the beamsplitter. A portion of the two reflected beams is recombined at the beamsplitter and the superposition of the beams is directed toward the output lens and an array detector, the latter designated *D* in Fig. 18.1. The detector *D* must be placed in a plane conjugate to the pupil of the instrument and the interferogram at the pupil must represent the wavefront distortions introduced by the mirror under test.

If the null lens-mirror combination is perfect, and the reflected beam in each arm retraces exactly the path of the light from the beamsplitter, then the illumination at *D* is uniform. If, instead, the plane mirror designated *A* in Fig. 18.1 is tilted, a set of straight fringes with equal spacing is recorded by the detector. The spacing of the fringes is inversely proportional to the tilt angle. Each fringe traces a zone of equal optical path difference between the two interferometer arms; the recorded fringes are of the equal thickness type.

If the lens-mirror combination is not perfect and mirror *A* is tilted, then a set of distorted or curved fringes is seen. From measurements of the positions of the fringes at many points on the interferogram it is possible to find the shape of the distorted wavefront, including tilt. If this tilted wavefront is then represented in terms of a linear combination of Zernike polynomials, it is a simple matter to remove the tilt and recover the actual wavefront. Examples of fringe patterns seen with various types of aberrations in the test element and various tilts of mirror *A* are displayed in the book edited by Malacara (1978).

It should be evident from this discussion that the test using the Twyman-Green interferometer is one of the null lens and mirror combination, not of the mirror by itself. It is necessary, therefore, to test the lens independently and verify that it has the required characteristics. If, for example, the test mirror is a sphere, then the null lens by itself must be perfect. If, on the other hand, the test mirror is a conic other than a sphere, then the null lens must introduce an amount of spherical aberration that exactly compensates the spherical aberration of the mirror in the test setup. Such a null lens was required, for example, in the testing of the 2.4-m hyperboloidal primary of the Hubble Space Telescope with a Twyman-Green interferometer. Unfortunately, this lens was not independently checked following reassembly of its elements and the result was an HST primary built to a different conic constant than called for by the design.

As noted at the start of this section, this is only an introduction to one method of optical testing. We have not considered other methods used in the past with large mirrors, such as the Foucault or knife-edge test and Hartmann screen test. The latter method was used to test the 4-m mirrors made at the Kitt Peak National Observatory during the early 1970s. We have also omitted any discussion of test methods for convex conic mirrors, such as Hindle type tests. For details on these and other test methods, and further references to the literature, the reader should consult the Malacara reference.

### 18.1.c. RESIDUAL ERRORS AND SCATTERED LIGHT

Analysis of interferograms obtained during the testing of a mirror leads to a detailed contour map of the hills and valleys of the mirror surface relative to the prescribed surface. Terms in the Zernike expansion representing the errors of low spatial frequency on the wavefront, such as spherical aberration, coma, and astigmatism, provide an approximate measure of the mirror quality. Polishing and testing continue until these aberrations are brought to a specified level expressed in waves rms.

If these low frequency errors are removed from the interferogram, the residuals are attributed to randomly generated mid- and high-frequency spatial errors. From our discussion in Section 11.1 we find the representation of these errors in terms of degradation functions in Eqs. (11.1.15) and (11.1.16). These equations, repeated here, are

$$T_m = \exp \{-k^2 \omega_m^2 [1 - c(v_n)]\}, \quad (18.1.2)$$

$$T_h = \exp (-k^2 \omega_h^2), \quad (18.1.3)$$

where  $m$  and  $h$  denote mid- and high-frequency, respectively,  $k = 2\pi/\lambda$ ,  $\omega$  is the rms random wavefront error,  $v_n$  is the normalized spatial frequency, and  $c(v_n)$  is

the normalized autocorrelation function. See Section 11.1 for a discussion of these degradation factors.

As the errors represented by these factors are independent of one another and of the figure error, they can be combined in quadrature. Hence

$$\omega^2 = \omega_f^2 + \omega_m^2 + \omega_h^2, \quad (18.1.4)$$

where  $\omega^2$  is the mean square error (mse) on the wavefront for errors at all spatial frequencies. The overall quality of the mirror is thus given in terms of the separate errors and the combined error.

We discussed some of the effects of the mid- and high-frequency errors on the point spread function (PSF) in Section 11.1, and extend that discussion here. As noted in Section 11.1.d, the effect of  $T_h$  on the PSF computed with Eq. (11.1.12) is to decrease the PSF by this factor at all points on an image. The same reduction also occurs in the encircled energy (EE), as seen by inspection of Eq. (11.1.13).

Thus the fractional changes in the PSF and EE are given by

$$\frac{\Delta\text{PSF}}{\text{PSF}} = \frac{\Delta\text{EE}}{\text{EE}} = 1 - \exp(-k^2\omega^2) \cong k^2\omega^2. \quad (18.1.5)$$

The approximation in Eq. (18.1.5) is good for  $\omega \approx \lambda/20$  or smaller.

The effect of the high frequency error on the mirror is to scatter a fraction of the light at large angles from the PSF, hence the light is effectively lost. A similar displacement of light from the core of the PSF also occurs when mid-frequency errors are present on a mirror. For these errors the scattered light from the inner part of the PSF appears in the outer rings of the Airy pattern, as shown in Figs. 11.7 and 11.8. The fractional changes in the Strehl ratio and EE within a few Airy rings for mid-frequency errors are also given by Eq. (18.1.5).

#### 18.1.d. MIRROR SUPPORT AND PRINT-THROUGH

Another factor affecting image quality is *print-through*, undulations on a mirror surface introduced either during the polishing process or by the support structure. For rigid honeycomb mirrors the thickness of the mirror across its face varies in a regular pattern. If the thinner sections of the mirror face are depressed slightly during the polishing, the result is a regular pattern of bumps when the polishing tool is removed. A similar pattern can be polished into a thin flexible mirror supported at a finite number of points during the polishing process. Even with a perfect thin mirror, print-through can be introduced if the support structure in the telescope does not have sufficient support points.

In this section we consider briefly the print-through for a square array and outline the approach to analyzing its effect. As a starting point we assume a surface deformation  $\delta\zeta$  of the form

$$\delta\zeta = A \cos\left(\frac{2\pi\xi}{l}\right) \cos\left(\frac{2\pi\eta}{l}\right), \quad (18.1.6)$$

where  $\delta\zeta$  is the difference from the prescribed figure,  $2A$  is the peak-to-valley amplitude,  $(\xi, \eta)$  is the coordinate frame on the mirror, and  $l$  is the center-to-center spacing between undulations. A contour map for this  $\delta\zeta$  is shown in Fig. 18.2.

The effect of this surface error on the PSF is found by noting that the wavefront error  $\Phi = 2\delta\zeta$ , substituting  $\Phi$  into the aperture function in Eq. (10.5.1), and integrating Eq. (10.5.1) to find the amplitude  $U(x, y)$  in the image plane. For our purposes we consider only the effect on the peak intensity  $i(0)$ . Following the procedure in Section 10.3 for a square aperture of side  $l$  we find

$$\langle \Phi^n \rangle = \frac{1}{l^2} \iint_{-l/2}^{l/2} \Phi^n d\xi d\eta. \quad (18.1.7)$$

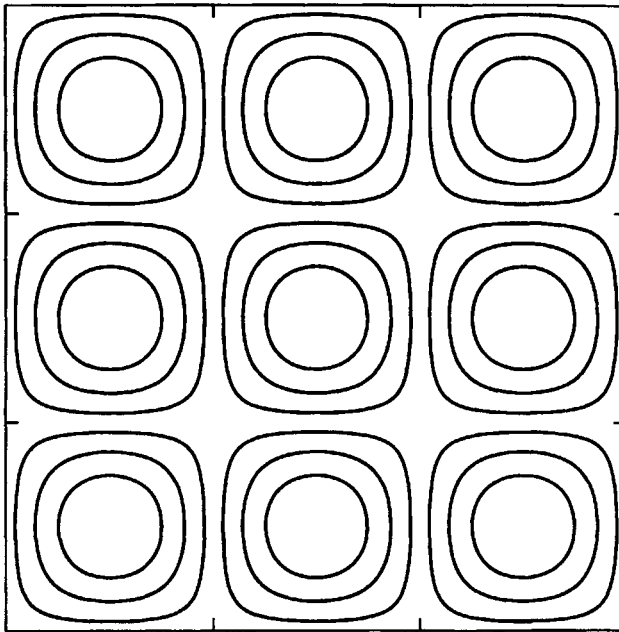


Fig. 18.2. Print-through pattern according to Eq. (18.1.6).

Computing the rms wavefront error according to Eq. (10.3.8) gives  $\omega = A$ . For an otherwise perfect mirror, the Strehl ratio  $S = 1 - k^2\omega^2$ . As an example, if  $S = 0.9$  at  $\lambda = 500$  nm, then  $A = 25$  nm,  $\omega = 0.05$  waves, and the peak-to-valley amplitude is 50 nm.

Thus the effect of the print-through pattern is to remove light from the core of the PSF and transfer it outward in the PSF. Unlike the radial scattering from random errors, the regular pattern of the undulations causes the light to appear in subsidiary peaks around the otherwise radially symmetric PSF. These side peaks are located at the secondary maxima derived from Eq. (10.1.6), with the main subsidiary peaks located at angles of approximately  $\lambda/l$  from the PSF peak. Calculations for this example show that the maximum intensity of a subsidiary peak is  $\sim 1\%$  of that of the main PSF.

Similar calculations for other patterns, such as hexagonal undulations, give comparable results. The principal difference is the location of the subsidiary peaks around the PSF.

#### 18.1.e. CONCLUDING REMARKS

The art and science of putting the proper figure on a large concave mirror must deal with many factors, as the discussion in this section has indicated. From lack of smoothness at a microscopic level to a large scale print-through pattern, errors over a large range of spatial frequencies contribute to image degradation.

Given the typical requirement that a telescope system from end-to-end, not including the atmosphere, be approximately diffraction-limited, it is not surprising that the requirement for its large primary mirror must be set at  $\lambda/20$  or smaller. For a space telescope the specification for the primary mirror is typically  $\lambda/40$  or smaller. Except for the built-in spherical aberration of the HST primary, this specification was met.

## 18.2. TELESCOPE ARRAYS; INTERFEROMETERS

The usual configuration of an optical telescope is one with a single circular aperture and an angular resolution in the diffraction limit of order  $\lambda/D$ . This dependence on wavelength and diameter applies to any telescope, thus the largest single aperture radio telescope has an angular resolution several orders of magnitude poorer than that of any optical telescope of modest size. To overcome this limitation, radio telescope configurations with multiple apertures have long been used to achieve high angular resolution. Given the resolution limit of  $\lambda/D$ , this means a large effective  $D$ , hence a long baseline across an array of phased telescopes or interferometers.

In contrast to the case for radio telescopes, angular resolution of ground-based optical telescopes is almost always limited by the atmosphere; in addition, stringent requirements for optical interferometers worked against their development. With the drive for higher angular resolution, however, increased attention has been given to the possibility of phased arrays, especially at infrared wavelengths.

Optical path differences between the elements of an interferometer are measured in fractions of a wavelength and the technical problems of maintaining differences to this accuracy are formidable. Our approach is to assume that the technical problems are solved and that the elements of an array are properly phased.

### 18.2.a. DIFFRACTION IMAGES

In this section we describe the diffraction image given by selected phased array configurations, each of which has some number  $N$  of identical telescopes with circular apertures. Arrangements discussed include linear arrays with an even number of equally spaced telescopes, and a square array with  $N = 4$ . For a discussion of these and other types of arrays, including an atlas of diffraction images, the reader should consult the excellent article by Meinel et al. (1983) listed in the references.

The calculation of the diffraction image of an array of telescopes is done by using the array theorem given in Section 10.5.c. Consider a set of identical telescopes or, equivalently, exit pupils distributed as shown in Fig. 18.3. For perfect telescopes the wavefront at each exit pupil is part of a spherical surface whose center is at  $O$  in Fig. 18.3. The amplitude  $U$  at a point  $P$  in the image is found by evaluating Eq. (10.5.5), where each term in the sum locates the center of one of the  $N$  telescopes. When this is done for  $N$  circular apertures, each of diameter  $D$  and focal length  $f$ , the result is

$$U(x, y) = C \frac{2J_1(v)}{v} \sum_{j=1}^N \exp[-ik(p\xi_j + q\eta_j)], \quad (18.2.1)$$

where  $C$  is a normalization constant,  $v = \pi D\alpha/\lambda$  [see Eq. (10.2.10)],  $p = x/f$ ,  $q = y/f$ , and  $(\xi_j, \eta_j)$  are the coordinates at the center of the  $j$ th telescope.

Note that the factor in front of the sum in Eq. (18.2.1) is the amplitude for a single circular clear aperture, as given in Eq. (10.2.7). The sum in Eq. (18.2.1) represents the superposition of the amplitudes from the  $N$  apertures treated as coherent sources, where  $k(p\xi_j + q\eta_j)$  is the phase difference between a wave from the center of the  $j$ th telescope and one from the origin of the  $(\xi, \eta)$  coordinate system.

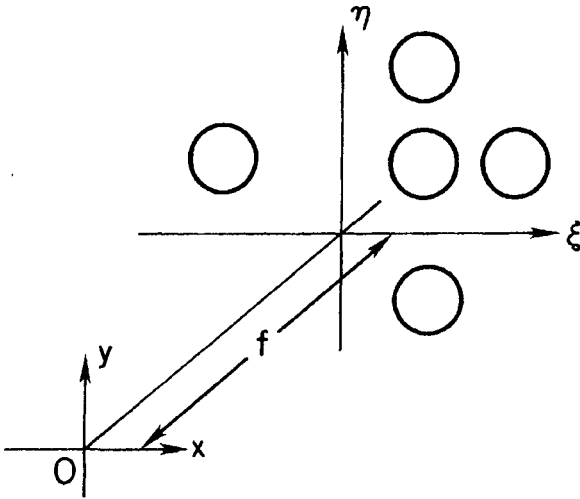


**Fig. 18.3.** Schematic layout of telescopes, each of focal length  $f$ , with pupils in the  $\xi\eta$ -plane and combined image in the  $xy$  plane.

The intensity at point  $P$  of the diffraction pattern is given by  $I(P) = |U(P)|^2$ , with the normalized intensity  $i(P) = I(P)/I(O)$ . In effect, the intensity of the diffraction pattern is that of a single telescope modulated by an interference pattern produced by the separate telescopes. This is similar to the result given in Eq. (13.4.1) for a diffraction grating, with the intensity the product of a blaze function and an interference factor. We now evaluate Eq. (18.2.1) for selected arrays of telescopes.

### 18.2.b. LINEAR ARRAYS

A linear array of  $N$  equally spaced telescopes, where  $N$  is even, is shown in Fig. 18.4. We put the origin of the  $(\xi, \eta)$  coordinate system in the center of the

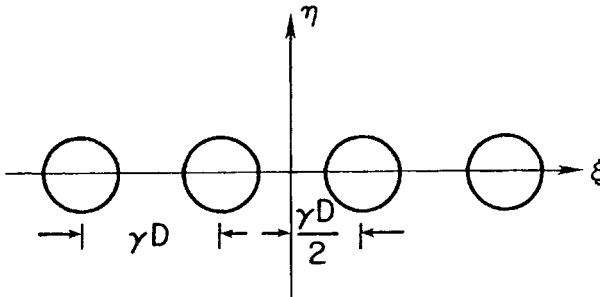


**Fig. 18.4.** Linear array of telescopes, each of diameter  $D$ , with spacing  $\gamma D$  between centers.

array for convenience in evaluating the sum in Eq. (18.2.1). The center-to-center spacing of adjacent telescopes is  $\gamma D$ , with  $\gamma > 1$  to ensure no overlap. The  $\xi$ -coordinates at the centers of the telescopes are  $\pm\gamma D/2, \pm 3\gamma D/2, \dots, \pm(2N - 1)\gamma D/2$ . Substituting into Eq. (18.2.1) we find

$$\Sigma = 2 \sum_{j=1}^{N/2} \cos [(2j - 1)\gamma v_x] = \frac{\sin (N\gamma v_x)}{\sin (\gamma v_x)}, \tag{18.2.2}$$

where  $v_x = \pi D x / \lambda f$ . Therefore the normalized intensity is

$$i(P) = \frac{1}{N^2} \left( \frac{2J_1(v)}{v} \right)^2 \left( \frac{\sin(N\gamma v_x)}{\sin(\gamma v_x)} \right)^2. \tag{18.2.3}$$

The smallest value of  $v_x$  for which  $i(P) = 0$  is given by  $N\gamma v_x = \pi$ , hence  $\alpha_x = \lambda / DN\gamma$ , where  $\alpha_x$  is the angular resolution in the  $x$  direction.

Note that the distance spanned by the telescopes of the array is  $\gamma(N - 1)D + D$ , hence the angular resolution in this direction is essentially that of a single telescope of this diameter. The resolution in the  $y$  direction is the same as that of a single telescope of diameter  $D$ , as is evident by setting  $v_x = 0$  in Eq. (18.2.3).

Results obtained from Eq. (18.2.3) are shown in Fig. 18.5 for  $N = 2$  and two values of  $\gamma$ , in a slice across the image in the  $x$  direction. Note the narrowing of

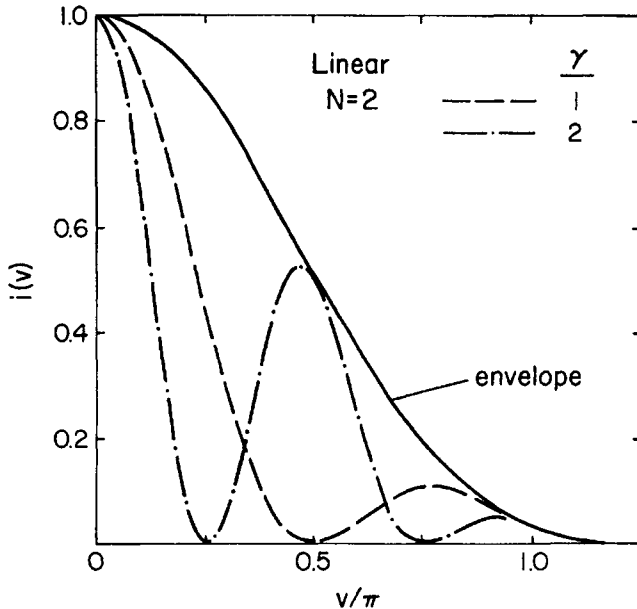
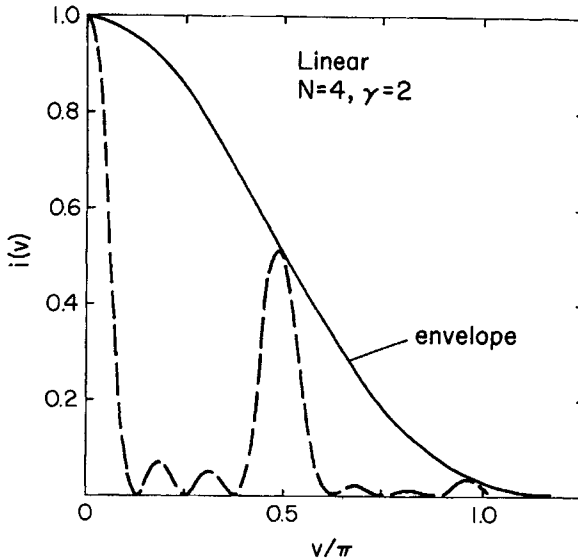


Fig. 18.5. Normalized PSFs for pairs of two telescopes. Angular distance from peak to first minimum is  $\lambda/2\gamma D$ .



**Fig. 18.6.** Normalized PSF for linear array of four telescopes. Angular distance from peak to first minimum is  $\lambda/N\gamma D$ .

the central peak in Fig. 18.5 as  $\gamma$  increases. We also see that there are more subsidiary peaks under the diffraction envelope when  $\gamma$  is larger, with a larger fraction of the total energy in these peaks. These additional peaks make it more difficult to achieve the resolution given by the central peak.

In Fig. 18.6 we show a slice across the image in the  $x$  direction for  $N = 4$  and  $\gamma = 2$ . Note that the principal peaks under the diffraction envelope are sharper, a consequence of the larger  $N\gamma$  product, with weak subsidiary bands between the principal peaks. In general, there are  $N - 2$  weak bands between adjacent strong bands. Contour maps of the images with  $N = 2$ ,  $\gamma = 2$ , and  $N = 4$ ,  $\gamma = 2$  are shown in Fig. 18.7.

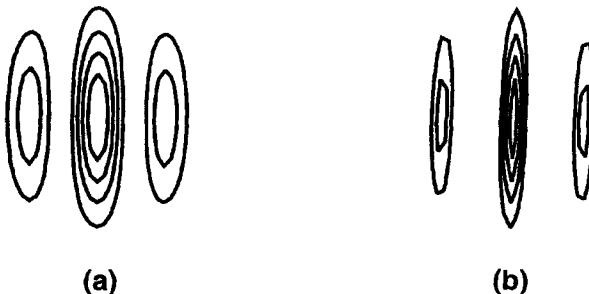


**Fig. 18.7.** Contour maps of PSFs from linear arrays with  $\gamma = 2$ : (a)  $N = 2$ , (b)  $N = 4$ .

## 18.2.c. SQUARE ARRAY

As a final example we consider the square array shown in Fig. 18.8. Applying Eq. (18.2.1) to a square array we find that the normalized intensity is

$$i(P) = \frac{1}{16} \left( \frac{2J_1(v)}{v} \right)^2 \left( \frac{\sin(2\gamma v_x)}{\sin(\gamma v_x)} \frac{\sin(2\gamma v_y)}{\sin(\gamma v_y)} \right)^2. \quad (18.2.4)$$

Results from Eq. (18.2.4) are shown in Fig. 18.9 for  $\gamma = 2$ . Note that the profile along the  $x$  and  $y$  directions is the same as that given in Fig. 18.5 for  $\gamma = 2$ . This is expected because the array spans the same distance,  $2D$  between centers, in both cases. In general, the FWHM of the central peak is inversely proportional to the spacing factor  $\gamma$ . The contour map for the square array with  $\gamma = 2$  shows a set of nine peaks in a  $3 \times 3$  array.

## 18.2.d. CONCLUDING REMARKS

These examples are sufficient to illustrate the general features of diffraction images of telescope arrays, with Eq. (18.2.1) as the basis for treating other configurations. We assumed the same  $D$  for telescopes in each of our examples, but this is not a requirement when using Eq. (18.2.1).

For a discussion of arrays of small telescopes utilized as stellar interferometers, the reader should consult the reviews by Labeyrie (1978) and by Shao and Colavita (1978). Examples of large telescopes projects planning for an interfero-

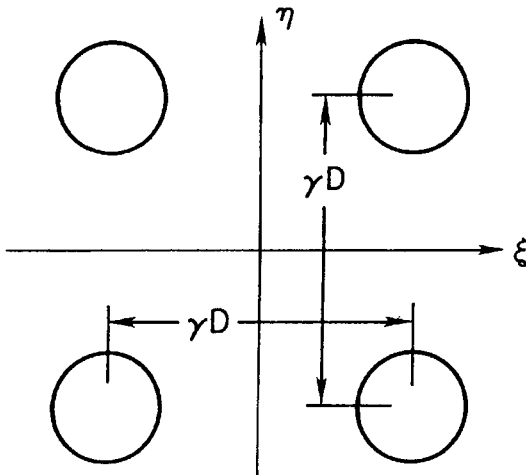


Fig. 18.8. Square array of telescopes of diameter  $D$ , spacing  $\gamma D$ .

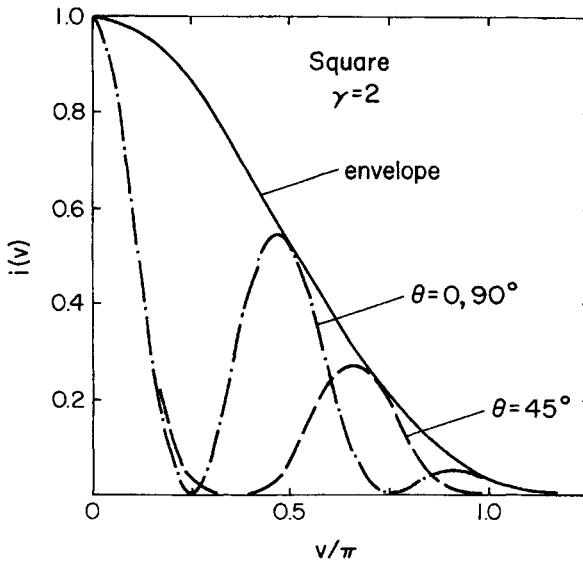


Fig. 18.9. Profiles of normalized PSFs for square array with  $\gamma = 2$ .

metric mode are the twin Keck 10-m telescopes, the Very Large Telescope array, and the Large Binocular Telescope. Although most observing will continue to be done with individual telescopes, it is evident that interferometers will make possible observations of unprecedented angular resolution.

## REFERENCES

- Malacara, D. (ed). (1978). *Optical Shop Testing*, New York: John Wiley.
- Martin, H. Allen, R., Angel, R., Burge, J., Davison, W., DeRigne, S., Dettmann, L., Ketelsen, D., Kittrell, W., Miller, S., Strittmatter, P., and West, S. (1998). *Proc. SPIE Int. Soc. Opt. Eng.*, **3352**: 194.
- Mast, T. and Nelson, J. (1990). *Proc. SPIE Int. Soc. Opt. Eng.* **1236**: 670.
- Meinel, A., Meinel, M. and Woolf, N. (1983). *Applied Optics and Optical Engineering*, vol. 9, Chap. 5. New York: Academic Press.

## BIBLIOGRAPHY

- Code, A. (1973). *Annual Review of Astronomy and Astrophysics*, **11**: 239. Palo Alto, CA: Annual Reviews.

- Hewitt, A. (ed). (1980) *Optical and Infrared Telescopes for the 1990s*, vols. 1 and 2. Tucson, AZ: Kitt Peak National Observatory.
- Hill, J. and Salinari, P. (1998). *Proc. SPIE Int. Soc. Opt. Eng.* **3352**, 23.
- Labeyrie, A. (1978). *Annual Review of Astronomy and Astrophysics*, **16**: 77. Palo Alto, CA: Annual Reviews.
- Optical Telescopes of the Future. (1977). *Proceedings of ESO Conference*. Geneva: European Southern Observatory.
- Shao, M. and Colavita, M. (1978). *Annual Review of Astronomy and Astrophysics*, **30**: 457, Palo Alto, CA: Annual Reviews.

*Conference Proceedings*

- Ardeberg, A. (ed.). (1997). *Proc. SPIE Int. Soc. Opt. Eng.*, **2871**.
- Barr, L. (ed.). (1986). *Proc. SPIE Int. Soc. Opt. Eng.*, **628**.
- Barr, L. (ed.). (1990). *Proc. SPIE Int. Soc. Opt. Eng.*, **1236**.
- Breckinridge, J. (ed.). (1994). *Proc. SPIE Int. Soc. Opt. Eng.*, **2200**.
- Stepp, L. (ed.). (1994). *Proc. SPIE Int. Soc. Opt. Eng.*, **2199**.
- Stepp, L. (ed.). (1998). *Proc. SPIE Int. Soc. Opt. Eng.*, **3352**.

## Table of Symbols

### Chapter 2

Symbol	Meaning
$d$	distance between surfaces
$D$	diameter of lens or mirror
$f, f'$	focal length; object (image) distance for image (object) at infinity
$f$	focal ratio
$h, h'$	object (image) height
$H$	Lagrange invariant
$i, i'$	angle of incidence (refraction)
$m$	transverse magnification
$M$	angular magnification
$n, n'$	index of refraction in space with incident (refracted) ray
$P$	power of surface or optical system
$R$	radius of curvature at vertex of surface
$s, s'$	object (image) distance
$S$	telescope scale
$u, u'$	slope angle of ray before (after) refraction
$W$	distance from stop to surface
$z$	coordinate direction along axis of optical system
$\delta$	normalized distance from exit pupil to telescope focus
$\Delta$	displacement of object point by plane-parallel plate

$\phi$	slope angle of normal to surface
$\theta$	angle between chief ray projected on sky and telescope axis
$\psi$	angle between chief ray from exit pupil and telescope axis

Normalized parameters for two-mirror telescopes—see Table 2.1.

### Chapter 3

Symbol	Meaning
$a$	projected width of prism face
$e$	eccentricity of conic section
$F$	shorthand representation of optical path length
$K$	conic constant
$l, l'$	length of oblique ray before (after) refraction
$L$	optical length
OPD	optical path difference
OPL	optical path length
$R_{lc}$	local radius of curvature on optical surface
$t$	prism base length
$z$	coordinate on optical surface
$\alpha$	slope angle of ray
$\alpha_0$	zenith angle of ray
$\Delta$	sag of mirror surface
$\gamma$	prism angle
$\lambda$	wavelength
$\kappa$	curvature of path of light ray in space

### Chapter 4

Symbol	Meaning
AA	angular aberration
ASA	angular spherical aberration
LSA	longitudinal spherical aberration
$r$	transverse distance from axis of optical system
TSA	transverse spherical aberration
$\alpha, \beta, \phi$	angles of rays
$\delta$	angular deviation of ray by Schmidt corrector plate
$\gamma$	wedge angle of corrector plate
$\eta$	normalized distance from axis of Schmidt camera
$\tau$	thickness of Schmidt corrector plate

**Chapter 5**

<b>Symbol</b>	<b>Meaning</b>
$A_i$	aberration coefficient
AAS	angular astigmatism
ADI	angular distortion
ASC	angular sagittal coma
ATC	angular tangential coma
$b$	aspheric coefficient
$B_i$	aberration coefficient
$L$	transverse offset of chief ray intersection at surface
$L'$	transverse offset of pupil or stop
$s'_p$	location of Petzval surface
$s'_s$	location of sagittal astigmatic image
$s'_t$	location of tangential astigmatic image
TA	transverse aberration
TAS	transverse astigmatism
TSC	transverse sagittal coma
TTC	transverse tangential coma
TDI	transverse distortion
$u_a$	sag of object or image surface
$\kappa_a$	curvature of object or image surface
$\Phi$	optical path difference (OPD)
$\Omega$	astigmatism factor

**Chapter 6**

<b>Symbol</b>	<b>Meaning</b>
LCA	longitudinal chromatic aberration
$\Omega$	wavefront error

**Chapter 7**

<b>Symbol</b>	<b>Meaning</b>
$c$	vertex curvature of optical surface
CSA	chromatic spherical aberration
$E$	fourth-order coefficient for aspheric surface
$F$	sixth-order coefficient for aspheric surface
$g$	distance from stop to corrector plate
$V$	Abbé number for glass
$\Gamma$	expansion factor for Schmidt plate with displaced stop

**Chapter 8****Symbol    Meaning**

$\sigma$             normalized distance of corrector plate in Schmidt-Cassegrain

**Chapter 10****Symbol    Meaning**

$a_{mn}$           aberration coefficients in fractions of waves  
 $a, b$           sides of rectangle  
 $A$             area  
 $A(\xi, \eta)$       aperture function  
 $dS$           area element at pupil  
 $EE$           enclosed energy fraction  
 $FWHM$         full-width at half-maximum of peak intensity  
 $\mathcal{F}$           energy or light flux  
 $i$             normalized intensity  
 $I$             intensity or irradiance  
 $k$              $2\pi/\lambda$   
 $OE$           1-EE  
 $p, q$         direction cosines  
 $PSF$         point spread function  
 $R$           radius of spherical wavefront  
 $S$           Strehl ratio  
 $u$           dimensionless diffraction variable in axial direction  
 $U$           wave amplitude  
 $v$           dimensionless diffraction variable in radial direction  
 $w$            $v/\pi$   
 $\alpha$         field angle projected on the sky  
 $\varepsilon$         linear obscuration ratio  
 $\xi, \eta, \zeta$       coordinates for wavefront at pupil  
 $\rho$         fractional radius of point within a circular aperture  
 $\omega$         root-mean-square (rms) wavefront error

**Chapter 11****Symbol    Meaning**

$c(v_n)$         normalized autocorrelation function  
 $C_a$           contrast  
 $l$             normalized autocorrelation length

$p_a$	spatial period
$T$	modulation transfer function (MTF)
$T_j$	MTF degradation factor
$v, v_n$	spatial frequency, normalized spatial frequency
$v_c$	cutoff spatial frequency
$\sigma', \sigma$	standard deviation, normalized standard deviation
$\Upsilon$	optical transfer function (OTF)

## Chapter 12

Symbol	Meaning
$A$	angular dispersion
$B$	photometric brightness
$d$	spectrometer beam width
$E$	irradiance
FRD	focal ratio degradation
$h, h'$	slit height, actual and projected
$\mathcal{L}$	luminosity
$P$	plate factor
$r$	anamorphic magnification
$\mathcal{R}$	spectral resolving power
$S$	area
$U$	etendue
$w, w'$	slit width, actual and projected
$\alpha, \beta$	angles before (after) dispersing element
$\Delta$	pixel size
$\delta\lambda$	limit of resolution
$\phi, \phi'$	subtended angles on the sky
$\tau$	transmittance
$\Omega$	solid angle

## Chapter 13

Symbol	Meaning
$b, b'$	actual (effective) groove width
BF	blaze function
$m$	diffraction grating order number
$N$	total number of grooves on grating
$N_R$	reflective finesse
$R$	reflectance

$T$	transmittance
$W$	grating width
$\alpha, \beta$	grating angle of incidence (diffraction)
$\delta$	grating blaze angle
$\Delta\lambda$	free spectral range
$\lambda_b$	blaze wavelength
$\theta$	in-plane grating angle
$\sigma$	diffraction grating groove spacing

### Chapter 14

#### Symbol    Meaning

$\gamma$	off-plane grating angle
$\rho$	radius of curvature of spectral line image

### Chapter 15

#### Symbol    Meaning

$N$	prism index of refraction
$\delta\lambda_c$	spectral coma
$\varepsilon$	prism orientation parameter
$\gamma$	prism angle

### Chapter 16

#### Symbol    Meaning

$c(v_n)$	normalized autocorrelation function
$H$	height of turbulent layer in atmosphere
$r_0$	seeing parameter, Fried parameter
$T$	modulation transfer function (MTF)
$T_j$	MTF degradation factor
$\alpha_0$	angular limit of resolution
$\gamma$	zenith angle
$v, v_n$	spatial frequency, normalized spatial frequency
$v_c$	cutoff spatial frequency
$\theta_0$	isoplanatic angle
$\theta_m$	isoplanatic angle for image motion
$\sigma', \sigma$	rms deviation from image peak, normalized deviation

## Chapter 17

Symbol	Meaning
$B$	incident background flux
$C$	dark count rate
$m$	apparent stellar magnitude
$m'$	sky brightness in magnitudes per arc-second squared
$\langle n \rangle$	mean signal
$N$	number of pixels per length $\lambda F$
$Q$	quantum efficiency
$R$	rms read noise
$S$	incident signal flux
SNR	signal-to-noise ratio
$t$	exposure time
$\kappa$	transmittance modifier
$\phi, \phi'$	subtended angles on the sky
$\tau$	transmittance

This Page Intentionally Left Blank

# Index

## A

Abbe number, 177

### Aberration

- astigmatism, 74–77, 86, 87, 92
- character of, 86
- chromatic, 65–68, 151, 167–170
- classical, 261–263
- coma, 82, 83, 86
- distortion, 78, 86
- field curvature, 97–103
- introduction to, 50–61
- multi-surface systems, 93–95
- orthogonal, 264–266
- ray and wavefront, 78–84
- spherical
  - fifth-order, 59, 174
  - third-order, 51–57, 86

Aberration, angular, *see* Angular aberration

### Aberration coefficients

- decentered pupil, 105
- displaced stop or pupil, 91
- grating, 358–360
- plane-parallel plate, 172
- prism, 398
- stop at surface
  - general surface, 84
  - mirror, 85

Aberration coefficients, element

- aspheric Schmidt plate, 166, 172, 173
- concentric meniscus lens, 199
- diffraction grating, 360, 399
- grism, 403
- prism, 398
- Schmidt-Cassegrain
  - primary, 187
  - secondary, 188

Aberration coefficients, grating mounting

- Czerny-Turner
  - monochromator, 370
  - spectrograph, 372
- nonobjective
  - grating, 399
  - grism, 403
  - prism-grating, 406

Aberration coefficients, system

- atmospheric dispersion corrector, 233
- Bouwers camera, 199
- Cassegrain focus corrector, 216
- grism, 403
- prime focus corrector, 211, 214
- prism-grating, 406
- Schmidt
  - focal reducer, 223
  - general, 165
- Schmidt-Cassegrain
  - all-spherical, 194

- Aberration coefficients, system (*cont.*)
  - flat field anastigmat, 190
  - general, 189
  - three-mirror telescope, 145
    - Paul-Baker, 147
  - two-mirror telescope
    - afocal, 132
    - corrected Ritchey-Chretien, 216
    - general, 117
    - hybrid, 130
    - with misaligned secondary, 134
- Aberration, longitudinal, *see* Longitudinal aberration
- Aberration, transverse, *see* Transverse aberration
- Achromatic corrector
  - Maksutov, 202
  - Schmidt, 177–181
- Active optics, 258
- Adaptive optics, 258, 409–424
  - deformable mirrors, 422
  - tip-tilt correction, 417
  - wavefront sensor, 422
- Afocal telescope, *see* Telescope type
- Airy disk, 248, 250, 256
- Airy pattern
  - asymptotic form, 251
  - encircled energy, 252–255
  - general, 248
  - peak intensity, 252, 256
  - point spread function, 246–250
  - radii of dark rings, 250
  - Strehl ratio, 260
- Alignment errors
  - aberration coefficients, 134, 138
  - decenter, 104, 133
  - despace, 143
  - image shift, 134
  - Schmidt camera, 105–107
  - tilt, 104, 133
  - two-mirror telescope, 132–144
- Anamorphic magnification
  - definition, 308
  - diffraction grating, 325
  - prism, 321
- Anastigmatic telescope
  - Schmidt-Cassegrain, 190–193
  - two-mirror, 124–126, 131
- Angular aberration
  - corrected Ritchey-Chretien, 212
  - definition, 52, 60
  - fifth-order spherical
    - aspheric plate, 174
    - conic mirror, 59
    - spherical mirror, 174
  - paraboloid, 113
  - prime focus plus aspheric plate, 217
  - relation to transverse, 80
  - Schmidt with misaligned plate, 105–107
  - Schmidt-Cassegrain aplanat, 194
  - two-mirror telescope
    - aplanatic, 122
    - classical, 119
    - despaced secondary, 143, 144
    - general, 118
    - hybrid, 131
    - misaligned secondary, 135, 139
- Angular dispersion, *see* Dispersion
- Angular magnification, *see* Magnification
- Angular resolution, 46, 257
  - limit due to atmosphere, 411–415
  - limit due to diffraction, 257, 410
- Aperture function
  - definition, 272
  - example, spider, 272
- Aperture stop, 22
  - see also* Stop; Pupil
- Aplanatic condition, 87
- Aplanatic telescope, 121–123, 126–129
- Array, 451–457
  - general, 452
  - linear, 453
  - square, 456
  - theorem, 274, 452
- Aspheric corrector
  - aberration coefficients, 106, 171
  - achromatic, 177–180
  - aspheric coefficient, 166, 173
  - chromatic aberration, 65–68, 167–170
  - fifth-order spherical, 174
  - prime focus, 211–214
  - radius of curvature, 67, 169
  - Ritchey-Chretien focus, 216–219
  - size, 170
  - surface figure, 67, 167
  - surface parameters, 167
  - zonal deviations, 168
- Astigmatism, *see also* Aberration; Aberration coefficients
  - angular, 60, 86

- misalignment, 138–142
    - sagittal, 74, 86, 92
    - tangential, 74, 86, 92
    - transverse, 77, 86
  - Atmosphere
    - dispersion corrector, 225–237
    - degradation function, 412
    - differential refraction, 43, 226
    - Fried parameter, 413, 416
    - isoplanatic angle, 416
    - long-exposure modulation transfer function (MTF), 412
    - refraction, 43
    - turbulence, 44
      - Kolmogorov, 412–415
      - scintillation, 410
      - seeing, 44, 410
      - speckle, 411
  - Atmospheric dispersion corrector, 225–237
    - chromatic focal error, 229, 231
    - in collimated light, 227
    - in convergent light, 228
    - in Ritchey-Chretien telescope, 235
  - Autocorrelation, 281, 283, 286
- B**
- Back focal distance, 18, 115
  - Baker-Schmidt telescope
    - aberration coefficients, 190
    - chromatic aberration, 192
    - conic constants, 191
  - Blaze, grating
    - angle, 328, 334
    - function, 332–338
    - wavelength, 334
  - Bouwers camera, 198–202
    - aberration coefficient, 199
    - chromatic aberration, 201
    - concentric meniscus corrector, 198
    - parameters, 201
  - Brightness, *see also* Intensity; Irradiance, 312
    - extended source, 314
    - stellar source, 314
- C**
- Camera
    - Bouwers, 198–202
    - Maksutov, 202
    - Schmidt, 64–68, 164–184
    - Schmidt-Cassegrain, 185–197
  - Cassegrain telescope, *see also* Telescope type
    - aberration coefficients, 117
    - angular aberrations, 118, 119, 122
    - diameter of secondary, 21
    - exit pupil, 23, 24
    - power, 19
    - type
      - classical, 61–64, 119–121
      - Couder, 125
      - Dall-Kirkham, 63, 123
      - hybrid, 129–131
      - Ritchey-Chretien, 121–123
      - Schwarzschild, 125
  - Catadioptric telescope, *see also* Schmidt-Cassegrain camera
    - Bouwers, 198–202
    - Maksutov, 202
    - Schmidt
      - solid, semi-solid, 181–184
    - Schmidt-Cassegrain, 185–187
  - Chief ray, 24, 72
  - Chromatic aberration
    - meniscus corrector, 201
    - Schmidt camera, 66–68, 167–170
    - Schmidt-Cassegrain, 192
    - solid Schmidt, 182
  - Classical Cassegrain, *see* Cassegrain telescope
  - Collimator
    - paraboloid
      - off-axis, 379
      - on-axis, 380
    - spherical mirror, 379
  - Coma, *see also* Aberration; Aberration coefficients
    - angular, 60, 86
    - misalignment, 106, 135–138
    - sagittal, 82, 87, 92
    - spectral, 376, 400
    - tangential, 82, 87, 92
    - transverse, 82, 86
  - Conic constant
    - definition, 41
    - relation to eccentricity, 41
  - Conic section, 41
  - Conjugate points, 10
  - Contrast, 278
  - Coude focus, *see* Focus
  - Couder telescope, *see* Cassegrain telescope
  - Cross dispersion, 385–392

- Cross dispersion (*cont.*)  
 grating, 387  
 modes, 388–391  
 prism, 387
- Curvature  
 in inhomogeneous medium, 30  
 of field, *see* Field curvature  
 local, on surface, 42, 445  
 spectrum line, 356
- Cutoff frequency, 278, 280  
*see also* Modulation transfer function
- Czerny-Turner mounting, 369–374  
 monochromator, 371  
 spectrograph, 373
- D**
- Dall-Kirkham telescope, *see* Cassegrain telescope
- Decenter, *see* Alignment errors
- Defocus, 261, 263, 266
- Degradation function, *see also* Modulation transfer function, 285–288  
 atmosphere, 412  
 correlation length, 286  
 microripple, 286  
 mid-frequency ripple, 286  
 root-mean-square pointing error, 288
- Despace, *see* Alignment errors
- Detection limits, 435–443  
 stellar photometry, 438  
 stellar spectroscopy, 440–443  
 slit-limited, 440  
 slitless, 442
- Detector  
 charge coupled device (CCD), 426  
 dark count, 427  
 read noise, 427  
 infrared, 426  
 modulation transfer function, 427–431  
 quantum efficiency, 427  
 signal-to-noise ratio, 433–435
- Differential refraction, *see* Atmosphere
- Diffraction  
 focus, 262, 268  
 shift from paraxial focus, 263  
 Fraunhofer, *see* Fraunhofer diffraction image  
 annular aperture, 248–257  
 array, 452–457  
 circular aperture, 248–257  
 rectangular aperture, 243–246  
 slit, 246  
 integral  
 array, 452  
 in presence of aberrations, 259, 272  
 perfect, 243, 248  
 limit, 46, 250, 257, 270  
 variables, 243, 247, 250
- Diffraction grating  
 anamorphic magnification, 325  
 angles, 323  
 angular dispersion, 324  
 blaze  
 angle, 328, 334  
 function, 332–338  
 wavelength, 334  
 constant, 323  
 efficiency, 331–339  
 equation, 323, 355  
 free spectral range, 327  
 grism, 356, 402–405  
 holographic  
 surface, 341  
 volume-phase, 342  
 interference function, 333  
 Littrow mode, 328  
 luminosity-resolution product, 339  
 polarization, 339  
 reflection, 323, 355  
 resolving power, 326  
 resolving power-slit width product, 339  
 sign convention, 323, 324, 355  
 transmission, 324, 355
- Diffraction grating mounting, *see also* Aberration coefficients, element; Aberration coefficients, grating mounting; Spectrometer type  
 concave  
 inverse Wadsworth, 365  
 Rowland, 361–363  
 Wadsworth, 361, 364  
 plane  
 Czerny-Turner, 369–374  
 Ebert-Fastie, 374  
 Monk-Gillieson, 375–377  
 transmission  
 nonobjective, 399, 405
- Dispersion  
 angular, 35, 305

- prism, 321
    - grating, 324
  - curves, glass, 322
  - linear, 306
  - Distortion, *see* Aberration; Aberration coefficients
- E**
- Ebert-Fastie
    - grating mounting, 374
    - as 1 : 1 reimager, 107–109
  - Eccentricity, 41
  - Echelle, 325, 327–331, 384–396
    - blaze
      - angle, 334, 337
      - function, 337
      - wavelength, 334
    - blaze peak
      - efficiency, 337–339
      - equations, 386
    - cross-dispersion modes, 388–391
    - design example, 394
    - effective groove width, 337
    - free spectral range, 385
    - immersed, 330, 395
    - Littrow mode, 328
    - order
      - length, 385
      - separation, 387
      - tilt, 386
    - overfilling, 341
    - polarization, 339
    - R-value, 328
    - spectrometer configuration
      - in-plane, 392
      - off-plane, 392
      - white pupil, 393
    - spectrum format, 385–388
  - Echelle, *see also* Diffraction grating, 325
    - crossed, 396
  - Ellipsoid, 39, 41
  - Encircled energy (EE), 252–255
    - annular aperture, 253
    - asymptotic approximation, 255
    - circular aperture, 253
    - definition, 252
    - in presence of
      - figure error, 269
      - random wavefront error, 289
      - rms pointing error, 291
      - small errors, 449
    - relation to modulation transfer function (MTF), 282
  - Enclosed energy, *see also* Encircled energy, 245
  - Entrance pupil, 22
  - Etendue
    - definition, 312, 313
    - diffraction limit, 319
    - Fabry-Perot, 345
    - Fourier transform spectrometer, 349
    - spectrometer, 313
  - Exit pupil
    - definition, 23
    - two-mirror telescope, 23, 24
- F**
- Fabry lens, 210
  - Fabry-Perot interferometer, 342–347
    - Airy function, 343
    - comparison with echelle, 346
    - etendue, 345
    - free spectral range, 344
    - luminosity-resolution product, 345
    - reflective finesse, 344
    - spectral purity, 344
    - spectral resolution, 344
    - type
      - imaging, 345
      - scanning, 344
  - Fermat's Principle
    - aberration compensation example
      - Cassegrain telescope, 61–64
      - Schmidt camera, 64–68
    - application to,
      - atmosphere, 42–45
      - conic mirrors, 37–41
      - diffraction grating, 353–356
      - general surface, 70–74
      - prism, 34
      - spherical surface, 32
      - thin lens, 33
    - general statement, 28
    - laws of refraction & reflection, 31, 32
    - physical interpretation, 36
  - Fiber optics, 237–239
    - focal ratio degradation (FRD), 238, 317
    - as input
      - integral field spectrometer (IFS), 305

- Fiber optics (*cont.*)
    - multiple object spectrometer (MOS), 305, 383
  - Field curvature, 97–103
    - introduction to, 60
    - median, 101
    - Petzval, 98
    - sagittal, 100
    - tangential, 100
  - Field curvature, system
    - grating, mountings
      - Czerny-Turner, 374
      - Monk-Gillieson, 362
      - nonobjective, 399
      - Rowland, 362
      - Wadsworth, 362
    - prime focus with corrector, 212
    - Schmidt-Cassegrain aplanat, 194
    - spherical mirror, 101
    - two-mirror telescope
      - aplanatic, 122
      - classical, 119
      - general, 118
  - Field flattener lens
    - aberrations, 207
    - Ritchey-Chretien telescope, 207
    - Schmidt camera, 102, 208–210
  - Field lens, 207, 210
  - Field stop, 22
  - Flux, 256, 312, 313, 315, 435, 436
  - Flux-resolution product, *see also* Luminosity-resolution product
    - diffraction limit, 319
    - general, 314
  - Focal length
    - mirror, 13, 38
    - thick lens, 15
    - thin lens, 15, 33
    - two-mirror telescope, 19
  - Focal ratio, 18
  - Focal reducer
    - general configuration, 220–222
    - Schmidt camera example, 222–225
    - types, 222
  - Focus
    - Cassegrain, 18, 207
    - coude, 131, 407
    - diffraction, 262
    - Gregorian, 18
    - Nasmyth, 131, 393, 407
    - prime, 210
  - Folded Schmidt camera, 382
  - Fourier transform, *see* Fraunhofer diffraction
  - Fourier transform spectrometer, 347–350
  - Four-mirror telescope, 154–161
    - examples, 155–158
    - pupil alignment, 159–161
  - Fraunhofer diffraction
    - annular aperture, 246–252
    - aperture function, 272
    - circular aperture, 246–252
    - definition, 242
    - Fourier transform, 272
    - rectangular aperture, 242–246
    - slit, 246
  - Free spectral range
    - diffraction grating, 326
    - Fabry-Perot, 344
  - Frequency, *see* Spatial frequency
  - Full Width Half Maximum, *see* Point spread function
- G**
- Gaussian equation, *see* Paraxial equation
  - Gaussian profile
    - image motion, 288
    - intensity, 411
    - modulation transfer function, 412
  - Glass
    - Abbe number, 177
    - dispersion, 322
    - index of refraction, 28, 35
  - Grating, *see* Diffraction grating
  - Gregorian telescope, *see also* Telescope type
    - aberration coefficients, 117
    - angular aberrations, 118, 119, 122
    - aplanatic, 121–123
    - classical, 119–121
    - exit pupil, 23, 24
    - power, 19
  - Grism, 356, 402–405
- H**
- Holographic grating, *see* Diffraction grating
  - Hubble Space Telescope
    - astigmatism, 270
    - COSTAR, 301
    - image characteristics
      - as-built, 298–302

predicted, 291–297  
 intensity, 256, 257  
 optical fix, 159, 160, 301  
 original instrument complement, 292  
 parameters, 292  
 replacement instruments  
   advanced camera system (ACS), 430,  
   431, 438  
   near infrared camera and multiple object  
   spectrometer (NICMOS), 430, 431  
 Huygens-Fresnel principle, 241  
   diffraction integral, 242, 259, 272  
 Hybrid telescope, 129–131  
 Hyperboloid, 40, 41

## I

Image  
   brightness, *see* Intensity; Irradiance  
   diffraction, *see* Diffraction image  
   sharpness, 432  
   slicer, 316  
 Index of refraction, 8, 28, 35  
 Intensity, *see also* Irradiance, 255–257  
   asymptotic average, 245, 252  
   average over Airy disk, 256  
   definition, 243  
   multiple aperture telescope  
     linear array, 454  
     square array, 456  
   normalized, 244, 248  
   peak, 252, 256  
   radial dependence, 252  
   Strehl, 260  
 Interferometer  
   Fabry-Perot, 342–347  
   Michelson, 347  
   telescope array, 451–457  
   Twyman-Green, 446, 447  
 Inverse Wadsworth, *see* Diffraction grating  
   mounting  
 Irradiance, *see also* Intensity, 255–257, 315  
   definition, 256, 315  
   pixel, 315  
   spectral, 315

## L

Lagrange invariant, 12, 313  
 Lateral magnification, *see* Magnification  
 Limit of resolution, *see* Resolution

Limiting magnitude  
   general form, 436, 440  
   stellar photometry  
     background-limited, 437  
     signal-limited, 437  
   slit-limited spectroscopy  
     extended source, 441  
     stellar source, 440  
   slitless spectroscopy, 442  
 Longitudinal aberration  
   chromatic, 151, 201, 229  
   spherical, 51  
 Luminosity, *see also* Etendue, 312, 313  
 Luminosity-resolution product, *see also* Flux-  
   resolution product  
   diffraction limit, 319  
   Fabry-Perot, 345  
   Fourier transform spectrometer, 349  
   general, 314  
   grating, 339

## M

Magnification  
   anamorphic, *see* Anamorphic magnification  
   angular, 11  
   lateral or transverse  
     mirror, 13  
     refracting surface, 11  
     sign, 11, 19  
     thin lens, 15  
   pupil, 160  
 Maksutov camera, 202–204  
 Meniscus corrector  
   achromatic, 202  
   concentric, 198–202  
 Michelson interferometer, 347  
 Mirror  
   print-through, 449  
   residual error, 448  
   shaping, 445  
   testing, 446  
 Modulation transfer function (MTF), 277–291,  
   411–415, 427–431  
   annular aperture, 282–284  
   atmosphere, 411–415  
   cutoff frequency, 280  
   definition, 278  
   and degradation functions, 285–290  
   in presence of aberrations, 283–285

- Modulation transfer function (MTF) (*cont.*)
  - pixel, 427–431
  - relation to
    - encircled energy, 282
    - point spread function, 282
- Monk-Gillieson mounting, 375–377
- Monochromator, *see also* Spectrometer type
  - Czerny-Turner, 369–371
  - Ebert-Fastie, 374
  - Monk-Gillieson, 375–377
- Multiple aperture telescope, *see* Array

### N

- Nasmyth focus, *see* Focus
- Neutral point, 136
- Noise, *see also* Signal-to-noise ratio
  - dark count, 427, 435
  - photon, 433
  - read, 427, 435
- Nonobjective
  - grating, 399–402
  - grism, 402–405
  - prism, 397–399
  - prism-grating, 405, 406
- Normalized intensity, *see* Strehl ratio
- Normalized parameters, two-mirror telescopes
  - definitions, 18, 115
  - table, 18, 115
- Nyquist criterion
  - image sharpness, 432
  - pixel matching, 377
  - sampling, 310, 429–431

### O

- Objective prism, 322
- Objective mode, 318, 322
- Obscuration, 21, 128
- Off-axis paraboloid, *see* Paraboloid
- Optical path difference (OPD)
  - diffraction grating, 358
  - displaced stop, 89
  - multi-surface system, 93
  - relation to transverse aberration, 79, 94
  - single surface, 73, 79
- Optical path length (OPL)
  - general, 28
  - grating, 353–355
  - refracting surface, 31, 32, 71–73

- Optical transfer function (OTF), *see* Transfer function

### P

- Paraboloid, 38, 113–115
  - angular aberrations, 113, 114
  - image surface curvature, 113
  - off-axis, 379
  - reimager at 1:1, 107–109
- Paraxial approximation, 9
- Paraxial equation
  - mirror, 12
  - refracting surface, 10, 33
  - thin lens, 15
- Paul-Baker telescope, 145–152
- Petzval
  - curvature, 98, 99
  - spherical mirror, 101
  - plus thin lens, 102
  - surface, 98
  - two-mirror telescope, 103
- Phase transfer function, *see* Transfer function
- Photometry, 438, 439
- Pixel, 315, 317, 426
  - irradiance, 315
  - matching, 317
- Pixel modulation transfer function
  - approximation, 431
  - ideal square well, 427–431
- Plane-parallel plate
  - aberration coefficients, 172
  - image displacement, 16
- Plate factor, 307
- Point spread function (PSF), 243–252, 282–290
  - annular aperture, 246
  - array, 454, 456
  - asymptotic approximation, 245, 252
  - encircled energy, *see* Encircled energy
  - enclosed energy, 245
  - full width half maximum (FWHM), 244, 251
  - Gaussian profile, 411
  - in presence of aberrations, 266–269
  - relation to modulation transfer function, 282
  - with random
    - rms pointing error, 290
    - wavefront error, 288
  - rectangular aperture, 243–246
- Power
  - mirror, 13

- refracting surface, 10
  - separated thin lens doublet, 15
  - thick lens, 15
  - thin lens, 15
  - two-mirror telescope, 19
  - Prime focus telescope, 113–115
  - Prime focus corrector, 210–216
    - aspheric plate, 211–213
    - multiple aspheric plates, 214
    - Wynne triplet, 215
  - Print-through, 449–451
  - Prism
    - aberration coefficients, 397
    - angular dispersion, 35, 321
    - deviation, 66
    - transverse aberrations, 233, 234
    - zero-deviation, 225, 234
  - Pupil
    - alignment, 159–161
    - entrance, 22
    - exit, 23
    - decentered, 103–105
    - displaced, 88–90
    - magnification, 160
    - shear, 160
    - two-mirror telescope, 23, 24
- Q**
- Quantum efficiency, 427
- R**
- Radius of curvature
    - sign convention, 8
    - image surfaces, 97–103
    - spectral image, 357
  - Ray coordinate system, 8, 70–72, 353–355
  - Rayleigh criterion, 257, 271, 280, 318
  - Reflection, law of, 12, 31
  - Refraction
    - atmospheric, 43
    - constant of, 43
    - differential atmospheric, 43, 225, 226
    - law of, 9, 31, 73
  - Resolution, *see also* Spectral resolving power
    - angular, 46, 257, 280, 455
    - atmospheric limit, typical, 114, 410–415
    - diffraction limit, 257, 280, 318–320
    - limit of
      - slit spectroscopy, 318
      - slitless spectroscopy, 318
  - Resolving power, *see* Spectral resolving power
  - Ritchey-Chretien telescope
    - angular aberrations, 122
    - conic constants, 121
    - corrected at Cassegrain focus, 216–219
    - field curvature, 122
    - field-flattened, 207
    - misaligned, 135–142
    - modified flat-field, 219
  - Root-mean-square wavefront error, *see* Wavefront
  - Rowland mounting, 360–363
- S**
- Sagittal
    - astigmatic image location, 74, 92
    - astigmatism, 75, 77
    - coma, 82, 87, 92
    - image surface curvature, 100, 102
  - Scale, telescope, 20
  - Schmidt camera, 64–68, 102, 164–184
    - aberration coefficients, 165
      - with misaligned corrector, 102
    - achromatic, 177–181
    - all-reflecting, 204
    - aspheric coefficient, 67, 166, 173
    - chromatic aberration, 66–68, 167–170
    - field-flattened, 102, 208–210
    - fifth-order spherical aberration, 174
    - focal reducer, 222–225
    - folded, 382
    - solid, semi-solid, 181–184
  - Schmidt telescope, *see* Schmidt camera
  - Schmidt-Cassegrain camera, 185–197
    - aberration coefficients
      - flat-field, 190
      - general, 189
    - all-spherical mirrors, 193–195
    - anastigmatic flat-field, 190–193
    - aplanat, 195
    - chromatic aberration, 192
    - compact, 195–197
  - Schwarzschild telescope, *see* Telescope type
  - Secondary mirror
    - alignment errors and aberrations, 132–144
    - diameter
      - Schmidt-Cassegrain, 190
      - two-mirror, 21

- Secondary mirror (*cont.*)  
 distance from focus, 21  
 neutral point, 136
- Seeing, atmospheric, *see* Atmosphere
- Segmented mirror telescope, 162, 445
- Seidel coefficients, 111
- Semi-solid Schmidt camera, *see* Schmidt camera
- Shift, focal surface, 20, 21
- Sign convention, 9, 355  
 angles, 9  
 distances, 8  
 indices of refraction, 13  
 surface radii, 8, 97
- Signal-to-noise ratio (SNR), 433–438  
 background-limited case, 434, 437  
 definition, 433  
 detector-limited case, 435  
 fractional accuracy, 433  
 ideal case, 433  
 signal-limited case, 434, 437
- Slit spectroscopy, limiting magnitude  
 extended source, 441  
 stellar source, 440
- Slitless spectroscopy  
 limiting magnitude, 443  
 spectral purity, 318
- Snell's law  
 reflection, 12, 31  
 refraction, 9, 31, 73
- Solid Schmidt camera, *see* Schmidt camera
- Space Telescope, *see* Hubble Space Telescope
- Spatial frequency, 278–280  
 cutoff, 278, 280  
 normalized, 280
- Speckle, 411
- Spectral purity  
 definition, 310  
 diffraction limit, 319  
 slitless mode, 318
- Spectral resolving power  
 definition, 311  
 diffraction limit, 319  
 Fabry-Perot, 344  
 grating, 326  
 prism, 322
- Spectrograph, *see* Spectrometer parameters;  
 Spectrometer type
- Spectrometer parameters  
 anamorphic magnification, 308, 321, 325  
 dispersion  
 angular, 305, 321, 323  
 linear, 306  
 etendue, 312  
 flux, 312  
 flux-resolution product, 314  
 free spectral range, 327, 344  
 irradiance, 315  
 limit of resolution, 310, 318  
 luminosity, 312  
 luminosity-resolution product, 314, 319  
 plate factor, 307  
 projected slit, 308, 318  
 resolving power-slit width product, 339  
 spectral purity, 310, 319  
 spectral resolving power, 311, 317, 319, 322,  
 326, 344  
 spectrum line  
 curvature, 356  
 tilt, 356  
 speed, 315
- Spectrometer type  
 Czerny-Turner, 369–374  
 Ebert-Fastie, 374  
 echelle, *see* Echelle  
 Fabry-Perot, 342–347  
 fiber-fed, 317  
 design example, 383  
 Fourier transform, 347–350  
 inverse Wadsworth, 365  
 Monk-Gillieson, 375–377  
 Rowland, 360–364  
 slitless, nonobjective  
 grating, 399  
 grism, 402  
 prism, 397  
 prism-grating, 405  
 Wadsworth, 360–362, 364
- Spectrum line  
 curvature, 356  
 tilt, 356
- Speed, *see* Spectrometer parameters
- Spherical aberration, *see also* Aberration;  
 Aberration coefficients  
 angular, 52  
 circle of least confusion, 56  
 definition, 50  
 fifth-order conic, 59  
 fifth-order, in collimated light  
 aspheric plate, 174

- spherical mirror, 174
    - longitudinal, 51
    - third-order, 51, 59
    - transverse, 50, 86
  - Stop, *see also* Pupil aperture
    - definition, 22
    - displaced from surface, 88–90
    - field, 22
  - Stop-shift statements, 89, 90
  - Strehl ratio, 260, 262, 263, 293, 296, 418
  - Super-Schmidt camera, *see* Telescope type
  - Surface curvature, image, 97–103
    - median, 101
    - Petzval, 98
    - sagittal, 100
    - tangential, 100
  - Surface equation
    - aspheric, 167
    - conic mirror, 41, 42
    - general, 50, 71
- T**
- Tangential
    - astigmatic image location
      - general, 74, 92
      - grating, 359
    - astigmatism, 75, 77, 360
    - coma, 82, 87, 92
    - image surface curvature,
      - general, 100, 102
      - grating, 362
  - Telescope type
    - afocal, 131
    - all-reflecting, 204
    - aplanatic
      - flat-field, 126
      - two-mirror, 121–123, 125
    - anastigmatic
      - Couder, 125
      - Schwarzschild, 125
    - array, *see* Array
    - Baker-Schmidt, *see* Schmidt-Cassegrain camera
    - Bouwers meniscus, 198–202
    - Cassegrain, 17, 61–64, 119–121, 126–129
    - classical, 61–64, 119–121
    - Couder, 125
    - Dall-Kirkham, 63, 123
    - four-mirror, 154–161
    - Gregorian, 17, 126–129
    - hybrid, 129–131
    - inverse Cassegrain, 126
    - Maksutov, 202
    - paraboloid, 113–115
    - Paul-Baker, 145–152
    - prime focus corrected, 210–216
    - Ritchey-Chretien, 121–123
      - corrected, 216–219
      - field-flattened, 207
    - Schmidt, *see* Schmidt camera
    - Schmidt-Cassegrain, *see* Schmidt-Cassegrain camera
    - Schwarzschild, 125
    - three-mirror, 144–153
  - Thick lens, 14
  - Thick plate, 16
    - aberration coefficients, 172
    - image displacement, 16
  - Thin lens
    - focal length, 15, 33, 34
    - paraxial equation, 15
    - power, 15
  - Three-mirror telescope, 144–153
  - Korsch
    - flat-field, 152
    - two-axis, 153
  - Paul-Baker, 145–152
  - Robb, 153
  - Transfer function, *see also* Modulation transfer function
    - definition
      - modulation, 278
      - optical, 280
      - phase, 280
    - relation to
      - encircled energy, 282
      - point spread function, 282
  - Transverse aberration
    - chromatic
      - Schmidt camera, 66–68, 167–170
      - Schmidt-Cassegrain camera, 192
    - definitions, 50, 77, 79, 86
    - diffraction grating, 359–361
    - grating mounting
      - Czerny-Turner monochromator, 371
      - spectrograph, 373
      - inverse Wadsworth, 366

- Transverse aberration (*cont.*)
    - Monk-Gillieson, 360, 376
    - Rowland, 360
    - Wadsworth, 360
  - in limit of small object distance, 207
  - multi-surface system, 93–95
  - nonobjective mode
    - grating, 400
    - grism, 403
    - prism, 233, 398
  - plane-parallel plate, 232
  - prism, doublet, 234
  - relation to angular, 80
  - single surface, stop at surface, 85
  - Transverse magnification, *see* Magnification
  - Turbulence, *see* Atmosphere
  - Two-mirror telescope, *see also* Telescope type
    - aberration coefficients, 117
    - alignment errors, 132–144
    - angular aberrations, 118, 119, 122
    - comparison between types, 126–129
    - conic constants, 119, 121
    - image surface curvatures, 118
    - neutral point, 136
    - normalized parameters, 18, 115
    - parameter combinations, 116
    - Petzval curvature, 103, 118
    - power, 19
    - Twyman-Green interferometer, 446, 447
- V**
- Vignetting, 128, 149, 340, 383
- W**
- Wadsworth mounting, 360–362, 364
  - Wavefront
    - aberration, 78–84, 258
    - definition, 45
    - distortion
      - Fried parameter, 413, 416
      - isoplanatic angle, 416
      - partial correction, 416–421
      - root-mean-square error, 260–269
  - Wynne triplet, 215, 216
- Z**
- ZEMAX, 6
  - Zernike polynomials, 264–269